DISSERTATION | DOCTORAL THESIS

Titel | Title

Studies of Macroautophagy in *Arabidopsis thaliana*

verfasst von | submitted by

Jierui Zhao

angestrebter akademischer Grad | in partial fulfilment of the requirements for the degree of

Doctor of Philosophy (PhD)

Wien | Vienna, 2025

Studienkennzahl lt. Studienblatt | Degree programme code as it appears on the student record sheet:	UA 794 685 490
Dissertationsgebiet lt. Studienblatt | Field of study as it appears on the student record sheet:	Molekulare Biologie
Betreut von | Supervisor:	Yasin Dagdas PhD

Acknowledgments

The past six years as a PhD candidate in Yasin's lab have been transformative, shaping not only my scientific journey but also my personal growth. Through this experience, I have emerged more confident, enthusiastic, and sincere in both my professional and personal pursuits. None of this would have been possible without the unwavering support of my supervisor, colleagues, collaborators, and everyone who contributed to my PhD journey.

First and foremost, I am deeply grateful to Yasin for granting me the extraordinary opportunity to pursue my PhD in his lab. After completing my Master degree, I faced significant challenges in securing a PhD position in Europe. Yasin not only welcomed me into his team but also entrusted me with exciting projects in plant molecular and cell biology. His comprehensive guidance, both in research and career development, has been instrumental in shaping my path as a scientist.

I extend my sincere appreciation to my Thesis Advisory Committee members, Gang Dong and Shotaro Otsuka, for their invaluable feedback on my research and their mentorship in navigating my future career.

My heartfelt thanks go to my colleagues and collaborators for their indispensable contributions to my project. I am especially indebted to Mai Thu Bai for her exceptional dedication to the CFS1 project. I am also profoundly grateful to Byung-Ho Kang and Juncai Ma from the Chinese University of Hong Kong for their generous collaboration and expertise. Additionally, I would like to acknowledge the interns I supervised, Yixuan Chen and Kai Ching Yeung, for their hard work and commitment.

To all current and former members of the Yasin Dagdas lab—thank you for fostering an environment that is not only scientifically rigorous but also supportive, united, and inspiring. The camaraderie and teamwork I experienced here are unparalleled. Each of you has taught me something invaluable, whether in science, technology, or interpersonal dynamics. Though I cannot name everyone individually, I will carry the lessons and spirit of this lab with me throughout my career.

Finally, I wish to express my gratitude to the VBC PhD program for providing me with the opportunity to work in such an exceptional research environment. My sincere thanks also go to the VBC and GMI staff for their indispensable support in my daily work and life. A special acknowledgment goes to the Biooptics facility for their efficient and professional assistance with my microscopy experiments.

This journey has been unforgettable, and I will forever cherish the knowledge, friendships, and experiences gained along the way.

Table of Contents

1. Abstracts

1.1. English abstract

Autophagy is an evolutionarily conserved degradation pathway essential for cellular homeostasis, stress adaptation, and development in eukaryotes. While the core autophagy machinery is well-characterized, key aspects of plant autophagy–particularly autophagosome maturation and cell-type-specific regulation—remain poorly understood. This thesis addresses these gaps through two interconnected projects investigating selective autophagy in Arabidopsis thaliana.

The first project identifies CELL DEATH RELATED ENDOSOMAL FYVE/SYLF PROTEIN 1 (CFS1) as a novel plant-specific autophagy adaptor. Using affinity purification-mass spectrometry (AP-MS), we discovered that CFS1 interacts with ATG8 via an ATG8-interacting motif (AIM) and localizes to autophagosome membranes. Functional studies revealed that CFS1 does not participate in autophagosome biogenesis but instead mediates autophagosome-vacuole delivery by bridging autophagosomes with the ESCRT-I component VPS23A. Disrupting the CFS1-VPS23A interaction impaired autophagic flux, leading to defective cargo degradation and stress sensitivity. Ultrastructural and biochemical analyses demonstrated that CFS1 promotes the formation of amphisomes–hybrid organelles resulting from autophagosome-multivesicular body (MVB) fusion–revealing a previously unknown maturation step in plant autophagy.

The second project explores cell-type-specific autophagy in the root epidermis, where trichoblasts (root hair-forming cells) exhibit higher autophagic flux than adjacent atrichoblasts (non-hair cells). Genetic dissection showed this disparity arises from developmental programming rather than morphological differences, as mutants disrupting trichoblast-atrichoblast identity abolished the autophagy asymmetry. Tissue-specific CRISPR knockout and complementation experiments demonstrated that trichoblast autophagy is essential for salt stress tolerance, enabling preferential vacuolar sodium sequestration. Disrupting autophagy solely in trichoblasts impaired ion compartmentalization and increased salt sensitivity, while restoring it rescued these defects. These findings establish how developmental pathways spatially regulate autophagy to optimize stress resilience.

Collectively, this thesis advances our understanding of plant autophagy by (1) elucidating CFS1's role in amphisome formation and (2) revealing how cell-type-specific autophagy contributes to salt stress adaptation. These findings not only deepen fundamental knowledge of autophagy regulation but also offer potential strategies for improving crop stress tolerance through targeted autophagy modulation.

1.2. Zusammenfassung

Die Autophagie ist ein evolutionär konservierter Abbauweg, der für die zelluläre Homöostase, die Anpassung an Stress und die Entwicklung von Eukaryonten wesentlich ist. Während der Kern der Autophagie-Maschinerie gut charakterisiert ist, sind Schlüsselaspekte der pflanzlichen Autophagie - insbesondere die Reifung von Autophagosomen und die zelltypspezifische Regulierung - nach wie vor schlecht verstanden. In dieser Arbeit werden diese Lücken durch zwei miteinander verbundene Projekte zur Untersuchung der selektiven Autophagie in Arabidopsis thaliana geschlossen.

Das erste Projekt identifiziert CELL DEATH RELATED ENDOSOMAL FYVE/SYLF PROTEIN 1 (CFS1) als einen neuartigen pflanzenspezifischen Autophagie-Adaptor. Mithilfe von Affinitätsreinigungs-Massenspektrometrie (AP-MS) entdeckten wir, dass CFS1 über ein ATG8-interagierendes Motiv (AIM) mit ATG8 interagiert und an Autophagosomenmembranen lokalisiert ist. Funktionelle Studien zeigten, dass CFS1 nicht an der Autophagosomen-Biogenese beteiligt ist, sondern stattdessen den Transport von Autophagosomen zu Vakuolen vermittelt, indem es eine Brücke zwischen Autophagosomen und der ESCRT-I-Komponente VPS23A schlägt. Die Unterbrechung der Interaktion zwischen CFS1 und VPS23A führte zu einer Beeinträchtigung des autophagischen Flusses und damit zu einem gestörten Abbau der Ladung und einer erhöhten Stressempfindlichkeit. Ultrastrukturelle und biochemische Analysen zeigten, dass CFS1 die Bildung von Amphisomen fördert - hybride Organellen, die aus der Fusion von Autophagosom und multivesikulärem Körper (MVB) entstehen - und damit einen bisher unbekannten Reifungsschritt in der pflanzlichen Autophagie aufzeigt.

Das zweite Projekt untersucht die zelltypspezifische Autophagie in der Wurzelepidermis, wo Trichoblasten (Wurzelhaar bildende Zellen) einen höheren Autophagiefluss aufweisen als benachbarte Atrichoblasten (Nicht-Haar-Zellen). Genetische Untersuchungen zeigten, dass diese Ungleichheit eher auf eine Entwicklungsprogrammierung als auf morphologische Unterschiede zurückzuführen ist, da Mutanten, die die Identität von Trichoblasten und Atrichoblasten stören, die Autophagie-Asymmetrie aufheben. Gewebespezifische CRISPR-Knockout- und Komplementationsexperimente zeigten, dass die Trichoblasten-Autophagie für die Salzstresstoleranz wesentlich ist und eine bevorzugte vakuoläre Natriumbindung ermöglicht. Die Unterbrechung der Autophagie ausschließlich in Trichoblasten beeinträchtigte die Ionenkompartimentierung und erhöhte die Salzempfindlichkeit, während die Wiederherstellung der Autophagie diese Defekte wieder beheben konnte. Diese Ergebnisse zeigen, wie Entwicklungswege die Autophagie räumlich regulieren, um die Stressresilienz zu optimieren.

Insgesamt trägt diese Arbeit zu unserem Verständnis der pflanzlichen Autophagie bei, indem sie (1) die Rolle von CFS1 bei der Bildung von Amphisomen aufklärt und (2) zeigt, wie zelltypspezifische Autophagie zur Anpassung an Salzstress beiträgt. Diese Erkenntnisse vertiefen nicht nur das grundlegende Wissen über die Regulierung der Autophagie, sondern bieten auch potenzielle Strategien zur Verbesserung der Stresstoleranz von Pflanzen durch gezielte Modulation der Autophagie.

2. Introduction

2.1. Autophagy: a conserved cellular degradation pathway

Macroautophagy (hereafter referred to as autophagy) is an evolutionarily conserved catabolic process in eukaryotes that facilitates the degradation of superfluous or damaged cellular components and eliminates pathogenic invaders (Marshall et al., 2018; Gross et al., 2025). The study of autophagy has a rich historical foundation, with the term first emerging in the 1860s to describe a self-sustaining nutrient recycling system essential for survival under starvation conditions (Mizushima et al., 2018). The modern conceptualization of autophagy, however, was established following Christian de Duve's discovery of lysosomes in 1955 and his subsequent redefinition of autophagy in 1963 as a process in which intracellular materials are delivered to lysosomes for degradation (Mizushima et al., 2018). A pivotal advancement in the field occurred in the 1990s with Yoshinori Ohsumi's identification of autophagy-related genes (ATGs) in yeast, a breakthrough that earned him the 2016 Nobel Prize in Physiology or Medicine (Kirkin et al., 2020).

Initially characterized as a non-selective "bulk" degradation mechanism, autophagy was understood to indiscriminately degrade large portions of the cytoplasm, including proteins and organelles, in response to cellular stress such as nutrient deprivation (Gross et al., 2025). This process serves as a critical survival strategy by recycling macromolecules to sustain energy and nutrient homeostasis (Gross et al., 2025). Over recent decades, research has revealed the existence of selective autophagy, a specialized branch of the pathway that targets specific substrates for degradation via autophagy receptors such as p62/SQSTM1, NBR1, and OPTN (Stephani et al., 2020; Mizushima et al., 2023). These receptors recognize cargo and tether it to the autophagic machinery through interactions with ATG8 family proteins (e.g., LC3, GABARAP) via ATG8-interacting motifs (AIMs) [Vargas et al., 2023]. So far, extensive studies have elucidated core ATG proteins and their roles in autophagosome formation, membrane elongation, and substrate degradation, highlighting the complexity of selective autophagy and its critical functions in cellular quality control, immunity, and disease pathogenesis (Cadena-Ramos et al., 2024).

2.2. Autophagy in plants: roles in development and stress adaptation

In plant cells, autophagy operates as a conserved quality control mechanism, mediating the targeted degradation of damaged organelles, misfolded proteins, and invasive pathogens (Wang et al., 2021). This process is indispensable for plant development, stress resilience, and immune defense (Wang et al., 2018).

During plant development, autophagy plays a regulatory role across multiple stages, from seed formation to senescence (Yoshimoto et al., 2024). In seed development, autophagy facilitates nutrient remobilization from senescing tissues to the developing embryo, ensuring proper storage protein processing and maturation (Guiboileau et al., 2012; Lornac et al., 2020). During germination, autophagy mobilizes stored reserves to support seedling establishment (Erlichman et al., 2023). Throughout vegetative growth, autophagy maintains cellular homeostasis by degrading damaged organelles and proteins, thereby sustaining tissue and organ function (Yoshimoto et al., 2024). In reproductive development, autophagy influences flowering time and pollen

development, with defects leading to male sterility due to impaired nutrient supply and dysregulated programmed cell death (PCD) in tapetal cells (Kurusu et al.,2014; Kurusu et al., 2017). Additionally, autophagy contributes to somatic cell reprogramming, facilitating dedifferentiation and callus formation, processes essential for tissue regeneration and stress responses (Rodriguez et al., 2020).

Under stress conditions, autophagy is crucial for plant survival, mitigating damage caused by nutrient deprivation, oxidative stress, drought, salinity, and pathogen invasion (Han et al., 2011). During nutrient limitation, autophagy-related genes such as *AtATG4a*, *AtATG8a-AtATG8i*, and *AtATG7* are upregulated in Arabidopsis, promoting nutrient recycling and survival (Rose et al., 2006; Han et al., 2011; Chen et al., 2021). Under oxidative stress, autophagy degrades oxidized proteins, as evidenced by the hypersensitivity of *atg2* and *atg5* mutants to oxidative damage (Minibayeva et al., 2012). Similarly, autophagy is activated in response to high salinity and drought, with *AtATG18a* induction being critical for stress tolerance (Liu et al., 2009).

Autophagy also exhibits a dual role in plant-pathogen interactions. In incompatible interactions, autophagy restricts hypersensitive response (HR) cell death, as demonstrated in tobacco infected with tobacco mosaic virus, where ATG6/Beclin1 silencing leads to uncontrolled cell death (Hofius et al., 2017; Sertsuvalkul et al., 2022). Conversely, in compatible interactions, autophagy can either enhance or suppress resistance depending on the pathogen type. For instance, Arabidopsis *atg* mutants display increased susceptibility to necrotrophic pathogens but enhanced resistance to biotrophic pathogens such as *Pseudomonas syringae pv. tomato* (Lenz et al., 2011). These findings underscore the multifaceted role of selective autophagy in maintaining cellular homeostasis and enhancing plant resilience across developmental and environmental contexts.

Given its pivotal functions, plant autophagy holds significant potential for improving agricultural productivity and stress resilience (Li et al., 2023). Emerging strategies, such as nanoparticle-based autophagy modulation and synthetic biology approaches to engineer cargo-specific receptors, offer non-transgenic avenues to enhance autophagy efficiency (Thanthrige et al., 2021). Integrating these advances with precision breeding and agroecological practices could mitigate yield losses, reduce fertilizer dependency, and improve climate adaptation (Thanthrige et al., 2021; Li et al., 2023). However, a comprehensive understanding of the selective autophagy machinery in plants is a prerequisite for such applications.

2.3. The autophagy machinery in plant cells

In plant cells, autophagy is initiated by developmental or stress signals, including nutrient starvation, salinity, drought, or pathogen attack, etc (Zhuang et al., 2024). Upon induction, a cup-shaped isolation membrane forms, marking the onset of autophagosome biogenesis (Figure 1). This process is orchestrated by the ATG1 kinase complex, which is regulated by the AMP-activated protein kinase (AMPK) and target of rapamycin (TOR) kinase pathways (Marshall et al., 2018; Gross et al., 2025). The ATG1 complex, comprising ATG1, ATG13, ATG11, and ATG101, initiates phagophore assembly site (PAS) formation, where autophagic machinery components converge (Suttangkakul et al., 2013; Gross et al., 2025). Following initiation, the phosphatidylinositol-3 kinase complex, consisting of ATG6/VPS30/Beclin1, VPS15,

and VPS34, is recruited to the PAS to facilitate membrane expansion (Liu et al., 2020; Gross et al., 2025). The endoplasmic reticulum (ER) serves as a primary lipid source, with proteins such as SH3P2 and ORP2A mediating ER-autophagosome membrane contact sites (EACS) to support autophagosome formation (Zhuant et al., 2013; Ye et al., 2022; Gross et al., 2025). ATG9, the sole integral membrane protein in the autophagy apparatus, delivers lipids and regulatory molecules to the PAS via cytosolic vesicles (Zhuang et al., 2017). ATG9 also acts as a scramblase, ensuring phospholipid symmetry (Zhuang et al., 2017; Gross et al., 2025). The lipid-binding protein ATG18 recruits ATG2 to the expanding phagophore, where ATG2 functions as a lipid transporter, shuttling phospholipids from the ER to the autophagosome membrane (Xiong et al., 2005; Luo et al., 2023).

As the autophagosome matures, the ubiquitin-like conjugation systems ATG8 and ATG12-ATG5-ATG16 mediate ATG8 lipidation with phosphatidylethanolamine (PE), facilitating membrane closure (Phillips et al., 2008; Gross et al., 2025). The endosomal sorting complex required for transport (ESCRT) machinery, including FREE1 and AMSH3, plays a critical role in autophagosome maturation and sealing (Nagel et al., 2017; Gao et al., 2015; Gao et al., 2017; Zeng et al., 2023). Finally, mature autophagosomes are transported to and fused with the vacuole, releasing their inner vesicles (autophagic bodies) for degradation by vacuolar hydrolases, thereby recycling cellular components (Figure 1). This tightly regulated hierarchical assembly ensures a tightly regulated process that is essential for plant development and stress resilience.

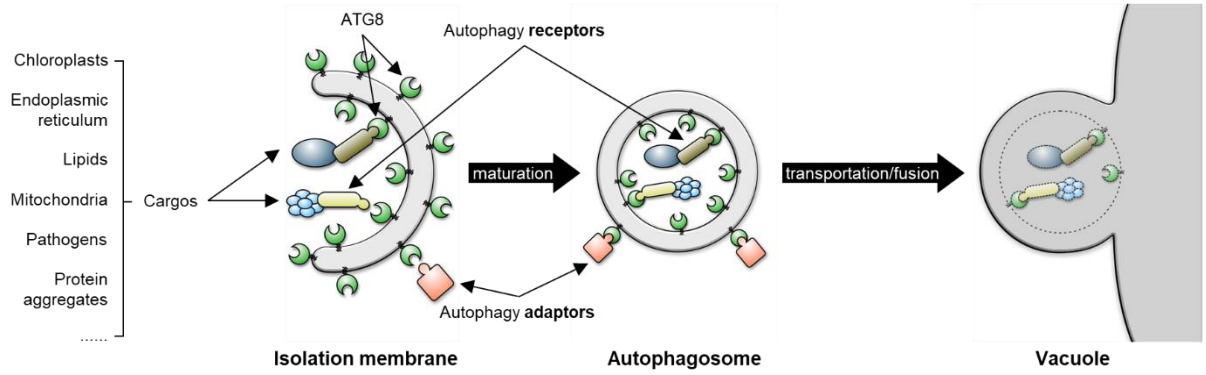

Figure 1. Schematic graph of the plant autophagy pathway. Autophagy receptors and adaptors bind ATG8 proteins on autophagosome membranes. In contrast to autophagy receptors, autophagy adaptors bind ATG8 at the outer membrane of the autophagosome and do not undergo autophagic degradation.

2.4. The cytoplasm-to-vacuole journey of the autophagosomes remains unrevealed as autophagy adaptors are missing in plant cells

A key mediator of autophagic cargo selection is ATG8, a ubiquitin-like protein conjugated to PE on both sides of the isolation membrane (Bu et al., 2020). During membrane expansion, ATG8-PE interacts with autophagy receptors on the inner membrane to recruit specific cargo (Kim et al., 2012). While numerous plant autophagy receptors (e.g., NBR1, ATI1, ATI2) have been identified (Youshimoto et al., 2018), autophagy adaptors, which bind ATG8-PE on the outer autophagosome membrane without undergoing autophagic degradation, remain elusive in plants (Stolz et al., 2014). Both autophagy receptors and adaptors bind to ATG8 via AIMs, which are denoted as [W/F/Y]XX[L/I/V] (X represents any amino acid) [Liu et al., 2021]. However,

unlike receptors, adaptors do not participate in cargo recognition but instead regulate autophagosome biogenesis and transport (Galluzzi et al., 2017). For instance, in human cells, sorting nexin 18 (SNX18) facilitates autophagosome formation while no homolog of SNX18 is found in plants (Knævelsrud et al., 2013; Stolz et al., 2014). In addition, FYCO1 (FYVE and coiled-coil domain-containing protein 1) mediates autophagosome-lysosome transport via interactions with ATG8 and PI3P in mammalian (Pankiv et al., 2010; Olsvik et al., 2015). However, although Arabidopsis possesses a FYCO1 homolog, it appears nonfunctional in autophagosome transport (Youshimoto et al., 2018). Consequently, fundamental questions remain unresolved: How autophagosomes are transported to and fused with the vacuole in plant cells? And how these events are coordinated with other vacuolar trafficking pathways? Do autophagosomes in plant cells also fuse with multivesicular bodies (MVBs) to form amphisomes prior to vacuolar delivery? Addressing these gaps is critical for understanding plant autophagy regulation.

2.5. CFS1: A candidate autophagy adaptor in plants

My first PhD project aims to figure out whether there are plant-specific autophagy adaptors functioning during the transportation of autophagosomes to the vacuole. As described in detail in **Chapter 4.1** (Zhao et al., 2022), I and my colleagues performed an affinity purification-mass spectrometry (AP-MS) assay of mCherry-fused ATG8E in Arabidopsis and identified a novel Arabidopsis FYVE domain-containing protein called CELL DEATH RELATED ENDOSOMAL FYVE/SYLF PROTEIN 1 (CFS1). CFS1 harbors a putative AIM for ATG8 interaction, a FYVE (Fab1, YOTB, Vac1, and EEA1) domain for PI3P binding, and a SYLF domain (SH3YL1 Ysc84/Lsb4p Lsb3p plant FYVE) that interacts with PI3P and actin (Figure 2, Sutipatanasomboon et al., 2017). Additionally, CFS1 contains a PSAPP motif mediating VPS23 interaction (Figure 2, Bilodeau et al., 2003).

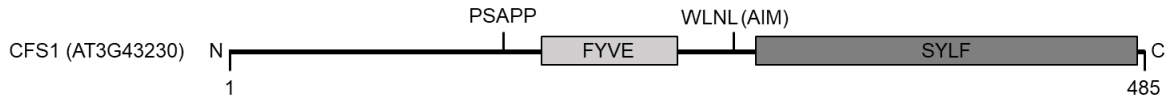

Figure 2. Schematic graph showing the structure of Arabidopsis CFS1.

Previous studies have implicated CFS1 in autophagy-related processes in Arabidopsis thaliana. Disruption of CFS1 results in premature senescence, a phenotype reminiscent of known autophagy-deficient mutants (Sutipatanasomboon et al., 2017), suggesting a potential role in autophagic regulation. Furthermore, transcriptomic analyses revealed a strong correlation between CFS1 expression levels and ATG11 (Li et al., 2014), a key mediator of selective autophagy, further supporting its involvement in this pathway. However, the precise mechanistic role of CFS1 in selective autophagy remains unclear. Given that plant FYVE-domain proteins are known to integrate phosphoinositide signaling with membrane trafficking processes, we hypothesize that CFS1 functions as a novel autophagy adaptor, modulating autophagic flux through interactions with the ESCRT machinery. How we decipher the roles of CFS1 in Arabidopsis selective autophagy pathway is comprehensively described in **Chapter 3.1**, **4.1** and **5.1** (Zhao et al.,2022).

2.6. Cell-type-specific autophagy in plants

Plant autophagy serves as a vital adaptive mechanism, promoting survival under environmental stressors by reallocating cellular resources to maintain essential metabolic processes and delay senescence (Bassham et al., 2012; Avin-Wittenberg, 2019). The functional significance of autophagy is evident in autophagy-deficient mutants, which display developmental abnormalities, premature aging, heightened sensitivity to biotic/abiotic stresses, and disrupted metabolic homeostasis (Yoshimoto et al., 2004; Minina et al., 2018; Yagyu & Yoshimoto, 2024).

Beyond these organism-wide effects, recent studies highlight autophagy's cell-type-specific roles, enabling localized regulation of physiological and developmental processes. For instance, in Arabidopsis root cap, autophagy mediates the programmed death and removal of border cells, a mechanism essential for coordinated cell separation and root growth (Feng et al., 2022; Goh et al., 2022). Targeted knockout of ATG5 in this tissue via CRISPR mutagenesis inhibits vacuolization and clearance of dying cells, underscoring autophagy's developmental precision in spatially restricted contexts (Feng et al., 2022). Similar tissue-specific autophagy mechanisms govern petal abscission, further illustrating its nuanced regulatory roles (Htwe et al., 2011; Furuta et al., 2024). Despite these insights, the extent to which cell-type-specific autophagy pathways contributes to stress tolerance remains poorly characterized, presenting a critical gap in understanding its adaptive versatility.

2.7. Trichoblasts and atrichoblasts: a model for cell-type-specific autophagy

In Arabidopsis thaliana, the developmental specification of root epidermal cells into trichoblasts (root hair-forming cells, T cells) and atrichoblasts (non-hair cells, A cells) is governed by a position-dependent signaling cascade that integrates intrinsic transcriptional regulation and extrinsic environmental cues (Datta et al., 2011). Epidermal cell fate determination follows a type III patterning system, where trichoblasts and atrichoblasts are organized into distinct, alternating longitudinal files (Salazar-Henaoet al., 2016). This spatial arrangement is dictated by the positional relationship between epidermal cells and the underlying cortical tissue: trichoblasts arise from epidermal cells overlying the junction between two cortical cells (T position), while atrichoblasts develop from cells contacting a single cortical cell (A position) [Balcerowicz et al., 2015; Salazar-Henaoet al., 2016]. The molecular basis of this patterning involves a competitive regulatory network centered on R2R3 MYB transcription factors (Figure 3). In A-positioned cells, the WEREWOLF (WER) MYB protein forms a complex with bHLH partners GL3/EGL3 (GLABRA3 /ENHANCER OF GLABRA3) and the WD40 protein TRANSPARENT TESTA GLABRA1 (TTG1), which activates GLABRA2 (GL2) expression to suppress root hair fate and promote atrichoblast differentiation (Balcerowicz et al., 2015; Salazar-Henaoet al., 2016). Conversely, T-positioned cells exhibit reduced WER activity due to positional signaling mediated by SCRAMBLED (SCM), a leucine-rich repeat receptor-like kinase. This allows dominance of R3 MYB inhibitors like CAPRICE (CPC), which translocate from T-positioned cellss to A-positioned cells, sequestering the bHLH-TTG1 complex and derepressing root hair initiation (Balcerowicz et al., 2015; Salazar-Henaoet al., 2016). Notably, this developmental program exhibits phenotypic plasticity, as a series of Arabidopsis mutants of which the root-hair development related genes were mutagenized showed distinct T/A cell patterning.

Despite their proximity, T and A cells exhibit distinct morphological and physiological traits. Trichoblasts are shorter, wider, and divide more frequently in the meristematic zone compared to atrichoblasts (Löfke et al., 2013). In addition, trichoblasts display delayed vacuolization and retain a denser cytoplasm, while atrichoblasts undergo earlier vacuole expansion (Löfke et al., 2013). During elongation, both cell types polarize and elongate significantly, but trichoblasts initiate elongation later and achieve shorter final lengths than atrichoblasts (Löfke et al., 2013).

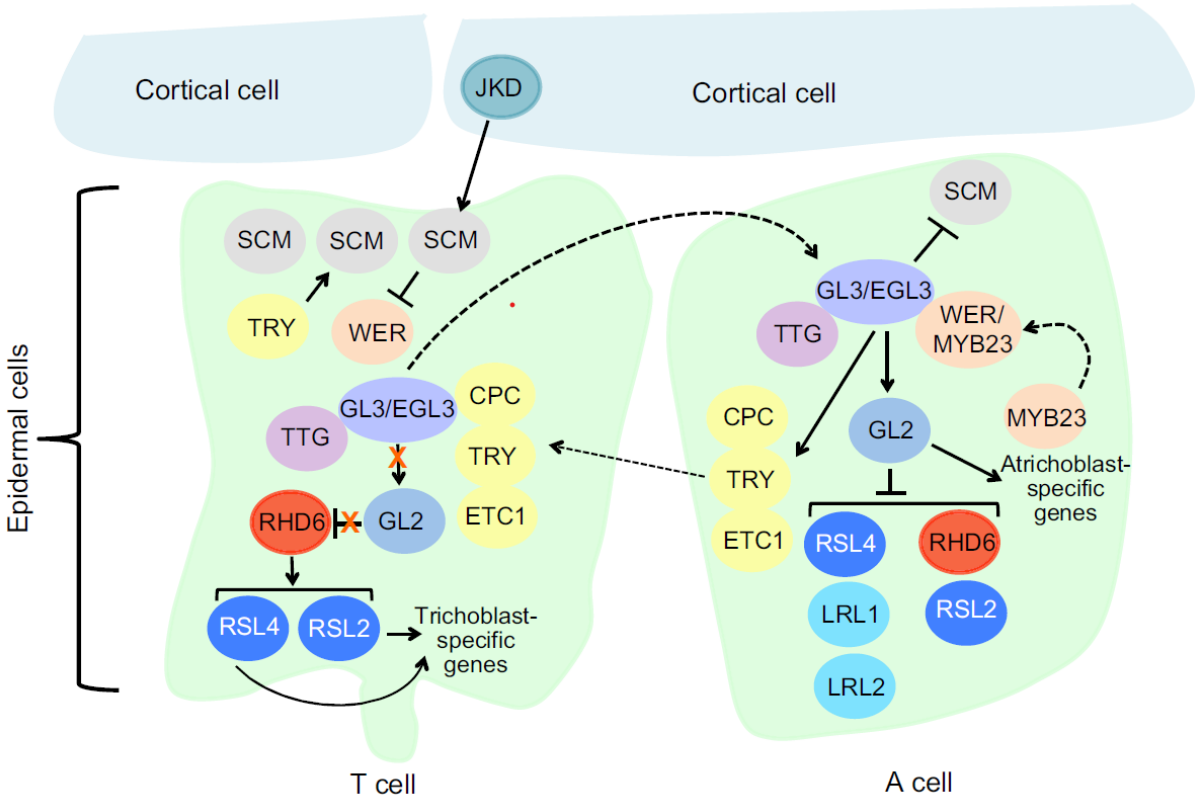

Figure 3. Spatially regulated cell fate determination in the Arabidopsis root epidermis (adapted from Salazar-Henaoet al., 2016).

Given the striking morphological and physiological distinctions between trichoblasts and atrichoblasts, we sought to investigate whether autophagic activity also differs between these two cell types. Intriguingly, our preliminary experiments revealed a significantly higher autophagic flux in trichoblasts compared to atrichoblasts (Figure 4). This finding aligns with prior observations (Guichard et al., 2024), reinforcing the notion that the trichoblast-atrichoblast system in Arabidopsis serves as an excellent model for studying cell-type-specific selective autophagy in plants. In my second PhD project, using the trichoblast-atrichoblast system as research model, I demonstrate that Arabidopsis trichoblasts exhibit cell-type specific autophagy essential for salt stress tolerance. The details of this project are comprehensively described in **Chapter 3.2**, **4.2** and **5.2** (Zhao et al., 2025).

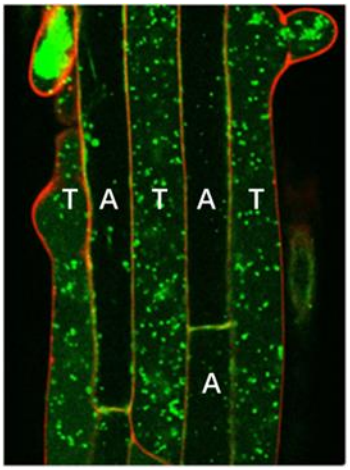

Figure 4. Preliminary results showed trichoblasts possess significantly higher autophagic flux than atrichoblasts. Five-day-old Arabidopsis seedlings were treated with liquid 1/2 MS media containing 2 μM concanamycin A for 3 h before confocal imaging. Green fluorescent puncta indicated GFP-ATG8A-labeled autophagosomes. Red fluorescence indicated cell wall. T, trichoblasts. A, atrichoblasts.

3. Aims of the thesis

This thesis comprises two independent yet interrelated projects, both focusing on autophagy in *Arabidopsis thaliana*. The first project elucidates the role of CFS1 in the Arabidopsis autophagy pathway, while the second investigates cell-type-specific autophagy using the trichoblast-atrichoblast system of the Arabidopsis root epidermis as a model.

3.1. Characterization of CFS1 as a novel autophagy adaptor in Arabidopsis

As described in **Chapter 2.5**, we identified CFS1 as a potential autophagy adaptor via affinity purification-mass spectrometry (AP-MS). To validate its role, we employed live-cell confocal microscopy, electron microscopy, and biochemical assays to assess three key aspects:

(1) Autophagosome recruitment – whether CFS1 localizes to autophagosomes.
(2) ATG8 interaction – whether CFS1 binds ATG8 via an AIM (ATG8-interacting motif).
(3) Subcellular localization and stability – whether CFS1 could reside on the outer autophagosome membrane and evades autophagic degradation.

To further dissect CFS1's functional role, we conducted autophagic flux assays and phenotypic analyses to determine its regulatory impact on autophagy. Additionally, phylogenetic and functional comparisons between CFS1 and its homolog CFS2 confirmed that only CFS1 functions as an autophagy adaptor. To explore evolutionary conservation, we extended our study to *Marchantia polymorpha*, assessing whether CFS1's autophagy-related function is conserved across plant species.

Through yeast two-hybrid screening, we identified VPS23A, an ESCRT-I component involved in endocytic trafficking, as a novel CFS1 interactor. Subsequent protein-protein interaction assays, confocal microscopy, and phenotypic analyses were performed to elucidate how CFS1 mediates crosstalk between autophagy and the ESCRT machinery.

3.2. Dissecting autophagic flux differences between trichoblasts and atrichoblasts in Arabidopsis root maturation zone

As outlined in **Chapter 2.7**, prior study and our preliminary data indicate that trichoblasts exhibit higher autophagic flux than atrichoblasts at root maturation zone. In this project, we systematically employed all ATG8 isoforms as autophagic flux markers under various conditions, using confocal microscopy to robustly confirm this phenomenon in the root maturation zone. Furthermore, we utilized root-hair development mutants to determine whether the observed flux difference stems from cell-type identity or morphological variation.

To explore the physiological significance of this disparity, we developed two kinds of tool plant lines:

(1) CRISPR-TSKO (tissue-specific knockout) lines, where autophagy is selectively disrupted in trichoblasts of Arabidopsis wild-type Col-0.

(2) ATG5-complementation lines, where autophagy is specifically restored in trichoblasts of *atg5* mutants.

Through confocal imaging and phenotypic characterization of these genetic tools, we aim to uncover the cell-type-specific role of selective autophagy in trichoblasts and its contribution to Arabidopsis adaptation.

4. Synopsis of the manuscripts

4.1. Manuscript 1: “Plant autophagosomes mature into amphisomes prior to their delivery to the central vacuole”

Authors: **Jierui Zhao**, Mai Thu Bui, Juncai Ma, Fabian Künzl, Lorenzo Picchianti, Juan Carlos De La Concepcion, Yixuan Chen, Sofia Petsangouraki, Azadeh Mohseni, Marta García-Leon, Marta Salas Gomez, Caterina Giannini, Dubois Gwennogan, Roksolana Kobylinska, Marion Clavel, Swen Schellmann, Yvon Jaillais, Jiri Friml, Byung-Ho Kang, Yasin Dagdas

Contribution: All the confocal microscopy experiments except PIN2 endocytosis and time-lapse videos were designed and done by me. I also generated plasmids and transgenic Arabidopsis lines for required experiments, performed co-IP experiments, autophagic flux assays and the phenotypic assays. For the manuscript writing, I analyzed data, prepared figures, wrote and revised the manuscript.

Status: This manuscript is published in Journal of Cell Biology (volume 221, issue 12) on October 19, 2022.

DOI: https://doi.org/10.1083/jcb.202203139

JCB Journal of Cell Biology

ARTICLE

Plant autophagosomes mature into amphisomes prior to their delivery to the central vacuole

Jierui Zhao[1,2*], Mai Thu Bui[1*], Juncai Ma[3*], Fabian Künzl[1], Lorenzo Picchianti[1,2], Juan Carlos De La Concepcion[1], Yixuan Chen[1], Sofia Petsangouraki[1], Azadeh Mohseni[1], Marta García-Leon[1], Marta Salas Gomez[1], Caterina Giannini[4], Dubois Gwennogan[5], Roksolana Kobylinska[1], Marion Clavel[1], Swen Schellmann[6], Yvon Jaillais[5], Jiri Friml[4], Byung-Ho Kang[3], and Yasin Dagdas[1]

Autophagosomes are double-membraned vesicles that traffic harmful or unwanted cellular macromolecules to the vacuole for recycling. Although autophagosome biogenesis has been extensively studied, autophagosome maturation, i.e., delivery and fusion with the vacuole, remains largely unknown in plants. Here, we have identified an autophagy adaptor, CFS1, that directly interacts with the autophagosome marker ATG8 and localizes on both membranes of the autophagosome. Autophagosomes form normally in *Arabidopsis thaliana cfs1* mutants, but their delivery to the vacuole is disrupted. CFS1's function is evolutionarily conserved in plants, as it also localizes to the autophagosomes and plays a role in autophagic flux in the liverwort *Marchantia polymorpha*. CFS1 regulates autophagic flux by bridging autophagosomes with the multivesicular body-localized ESCRT-I component VPS23A, leading to the formation of amphisomes. Similar to CFS1-ATG8 interaction, disrupting the CFS1-VPS23A interaction blocks autophagic flux and renders plants sensitive to nitrogen starvation. Altogether, our results reveal a conserved vacuolar sorting hub that regulates autophagic flux in plants.

Introduction

Macroautophagy (hereafter autophagy) is a conserved vacuolar trafficking pathway that mediates three Rs in eukaryotic cells, including plants: (i) It *remodels* the cellular environment for developmental and temporary reprogramming events that underlie cellular differentiation and adaptation. In plants, for example, autophagy is essential for callus regeneration in *Arabidopsis thaliana*, wound-induced de-differentiation in *Physcomitrium patens*, sperm maturation in *Marchantia polymorpha*, and pollen formation in rice (Rodriguez et al., 2020; Norizuki et al., 2021 *Preprint*; Kurusu et al., 2014). Autophagy-mediated cellular adaptation is also crucial for stress tolerance including drought, infection, and high temperature stress. Studies involving *Arabidopsis*, maize, and rice have shown that autophagy mutants such as *atg2*, *atg5*, and *atg7* are highly susceptible to biotic and abiotic stress factors and undergo early senescence (Signorelli et al., 2019; McLoughlin et al., 2018; Wada et al., 2015). (ii) At the cellular level, autophagy *renovates* the cell by removing the organelles, protein complexes, and other dysfunctional macromolecules that would otherwise reduce cellular fitness (Dikic, 2017; Marshall and Vierstra, 2018). Finally, (iii) during nutrient limitation, autophagy *replenishes* cellular energy pools and prolongs survival by recycling surplus cellular material (McLoughlin et al., 2020; Rabinowitz and White, 2010). Thus, autophagy is a major degradation and recycling pathway that keeps the cell in tune with the ever-changing environment and maintains cellular homeostasis.

The main vehicle of autophagy is a de novo formed, double-membrane vesicle termed the autophagosome. Autophagosomes capture their cargo and deliver them to the vacuole (or lysosomes in metazoans) for recycling. Autophagosome biogenesis involves the concerted action of highly conserved autophagy-related gene (ATG) proteins that coordinate the nucleation and growth of a cup-shaped phagophore around the autophagic cargo (Nakatogawa, 2020; Chang et al., 2021; Weidberg et al., 2011). The two opposing membranes are then sealed with endosomal sorting complex required for transport (ESCRT) proteins to form the autophagosome (Chang et al., 2021). Both autophagosome membranes are labeled with lipidated ATG8 family proteins that interact with (i) other ATG proteins to coordinate autophagosome formation, (ii) cargo receptors that selectively recruit cargo macromolecules and underlie selective autophagy, and (iii) adaptor proteins that mediate the

[1]Gregor Mendel Institute, Austrian Academy of Sciences, Vienna BioCenter, Vienna, Austria; [2]Vienna BioCenter PhD Program, Doctoral School of the University at Vienna and Medical University of Vienna, Vienna, Austria; [3]School of Life Sciences, Centre for Cell & Developmental Biology and State Key Laboratory of Agrobiotechnology, The Chinese University of Hong Kong, Shatin, New Territories, Hong Kong, China; [4]Institute of Science and Technology Austria, Klosterneuburg, Austria; [5]Laboratoire Reproduction et Développement des Plantes, Université de Lyon, École normale supérieure de Lyon, Centre national de la recherche scientifique (CNRS), Institut National de la Recherche Agronomique (INRAE), Lyon, France; [6]Botanik III, Biocenter, University of Cologne, Cologne, Germany.

*J. Zhao, M.T. Bui, and J. Ma contributed equally to this paper. Correspondence to Byung-Ho Kang: bkang@cuhk.edu.hk; Yasin Dagdas: yasin.dagdas@gmi.oeaw.ac.at.

trafficking and vacuolar fusion of autophagosomes (Stolz et al., 2014). Most of these ATG8-interacting proteins contain highly conserved short linear motifs termed as the ATG8-interacting motif (AIM). The core AIM is denoted as [W/F/Y]xx[L/I/V], where x represents any amino acid. The AIM peptide is bound by the highly conserved W and L loops, collectively known as the AIM-docking site (ADS), on ATG8 (Birgisdottir et al., 2013). Despite recent advances in cargo receptor identification and characterization, no autophagy adaptors have been characterized in plants. As a result, we have only a limited understanding of how autophagosomes are delivered to the vacuole in plants.

Autophagosome maturation is logistically different in yeast, metazoans, and plants. In yeast, autophagosome biogenesis and maturation happen in the vicinity of the vacuole; the coordination of these processes is aided by spatial proximity (Zhao and Zhang, 2019). In metazoans, autophagosomes are formed at various sites around the cell and subsequently fuse with endosomes or lysosomes (Zhao et al., 2021). Autophagosome-endosome fusions create amphisomes, which mature into autolysosomes by acquiring lytic enzymes (Sanchez-Wandelmer and Reggiori, 2013). Despite these logistical differences, in both yeast and metazoans, the concerted action of dedicated soluble *N*-ethylmaleimide-sensitive factor attachment protein receptor (SNARE) proteins, tethering factors, and adaptors mediate the fusion of autophagosomes with the lytic compartments (Zhao et al., 2021). In plants, autophagosomes are formed at sites around the cell and are then delivered to the central vacuole, which can occupy as much as 80% of the cell volume (Marshall and Vierstra, 2018). The molecular details of autophagosome trafficking, fusion with the vacuole, and how these events are coordinated with other vacuolar trafficking pathways are currently unknown in plants. Whether or not plant autophagosomes converge into amphisomes before arriving to the central vacuole also remains unknown.

To address these questions, we focused on the identification of autophagy adaptors. We developed a differential centrifugation protocol to enrich for intact autophagosomes prior to affinity purification-mass spectrometry (AP-MS) with ATG8 as bait. This approach identified CFS1 (cell death related endosomal FYVE/SYLF protein 1), a highly conserved FYVE (Fab-1, YGL023, Vps27, and EEA1) and SYLF (SH3YL1, Ysc84p/Lsb4p, Lsb3p, and plant FYVE) domain-containing protein that was previously linked to autophagy (Sutipatanasomboon et al., 2017; Kim et al., 2022). Characterization of CFS1 revealed that it interacts with ATG8 in an AIM-dependent manner and specifically regulates autophagic flux in both *A. thaliana* and *M. polymorpha*. Genome-wide yeast two hybrid screening showed that CFS1 also interacts with the multivesicular body-localized ESCRT-I complex protein VPS23A. Live cell imaging and electron microscopy analyses demonstrate that CFS1 colocalizes with VPS23A at amphisomes. Further flux assays and phenotypic studies showed that the CFS1-VPS23A interaction is crucial for autophagic flux. Altogether, our data suggest that plants employ a prevacuolar sorting hub to coordinate vacuolar trafficking pathways in plants.

Results

Differential centrifugation coupled to affinity purification-mass spectrometry (AP-MS) revealed autophagosome-associated proteins in *A. thaliana*

Since autophagy adaptors play crucial roles in autophagic flux but are unknown in plants, we first set out to identify autophagy adaptors. We induced autophagy in GFP-ATG8A expressing *A. thaliana* seedlings with Torin1 treatment and performed differential centrifugation experiments to enrich for small membranous compartments, including intact autophagosomes, while removing larger, bulkier compartments such as organelles (Liu and Bassham, 2010; LaMontagne et al., 2016; Fig. 1 A). To test whether the membrane-associated fractions (P4) contain intact autophagosomes, we performed protease protection assays. Both NBR1, a well-characterized autophagy receptor that is localized within the autophagosomes, and ATG8, which localizes on both sides of the autophagosome, were protected in these assays (Svenning et al., 2011; Stolz et al., 2014; Fig. S1, A and B). After addition of Triton X-100, a detergent that destabilizes membranes, both proteins became sensitive to protease treatment (Fig. S1 B). These experiments suggested that we could enrich for intact autophagosomes (Borner et al., 2005). We then combined this approach with AP-MS of mCherry-ATG8E expressing lines and screened for protease-sensitive proteins (i.e., those localized on the outer autophagosome membrane) in the membrane-enriched fractions (Fig. 1 A). Mass spectrometry analysis revealed 48 proteins that are ATG8E-associated, P4-enriched, and proteinase K-sensitive, including SH3P2, FRA3, NUP93A, and NUP98A (Fig. 1, B and C; and Tables S1 and S2). One of these 48 proteins was the FYVE and SYLF domain-containing protein CFS1 (At3g43230; Fig. 1, B and C). Since CFS1 has previously been linked to autophagy and FYVE and SYLF domain-containing proteins are well-known players in vesicle trafficking (Sutipatanasomboon et al., 2017; Kim et al., 2022; Melia et al., 2020), we decided to characterize CFS1 in depth.

CFS1 localizes to the autophagosomes

To map the cellular distribution of CFS1, we generated transgenic *Arabidopsis* lines that stably co-express mCherry-CFS1 with endomembrane compartment markers, including NAG1-EGFP (Golgi bodies), VHAa1-GFP (trans-Golgi network), GFP-ARA7 (late endosomes), and GFP-ATG8A (autophagosomes; Geldner et al., 2009; Bassham, 2015). Live-cell confocal imaging and quantification under control and two different autophagy inducing conditions (nitrogen starvation and salt stress) showed that mCherry-CFS1 puncta specifically colocalize with the autophagosomes (Thompson et al., 2005; Liu et al., 2009; Fig. S1, C and E; and Fig. 1 D). Mander's colocalization coefficients showed that both the M1 and M2 between mCherry-CFS1 and GFP-ATG8A are higher than 0.4, while the M1 and M2 between mCherry-CFS1 and other GFP markers are <0.2 (Fig. S1, D, F, and E). We also performed microscopy experiments with the amphiphilic styryl dye FM4-64, a stain that is widely used for tracing endocytic vesicles (Rigal et al., 2015). CFS1 did not colocalize with FM4-64 even under autophagy-inducing conditions (Fig. S1, G and H).

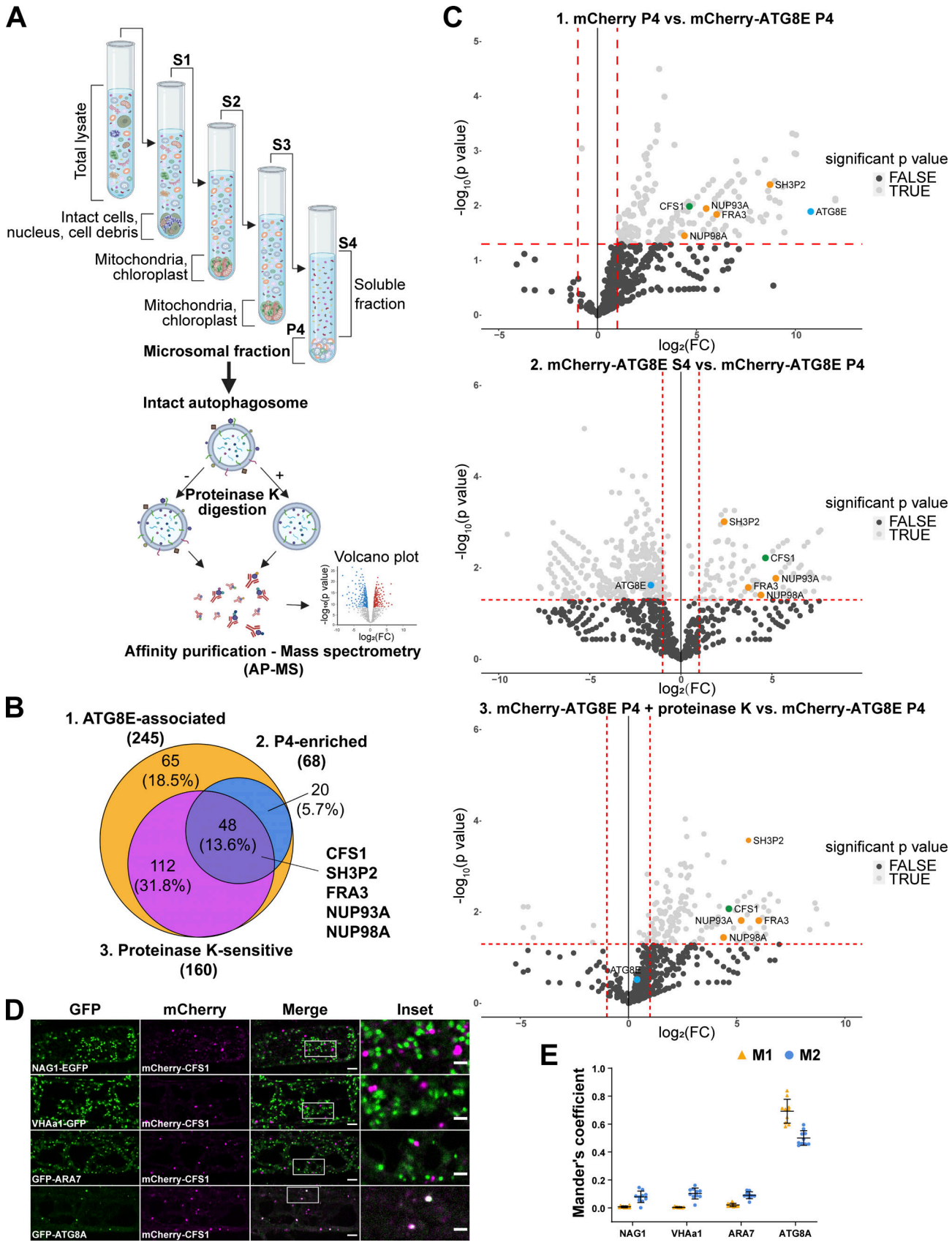

Figure 1. **Differential centrifugation coupled to affinity purification-mass spectrometry (AP-MS) revealed autophagosome-associated proteins in *A. thaliana*. (A)** Schematic diagram showing the differential centrifugation coupled to affinity purification-mass spectrometry (AP-MS) workflow. Total lysate of *Arabidopsis* seedlings underwent several differential centrifugation steps, where each time the supernatant (S) was transferred, and the pellet (P) was left

untouched. Samples were spun for 10 min at 1,000 *g* (S1), to remove intact cells, nuclei, and cell debris; 10 min at 10,000 *g*, to remove bigger organelles like mitochondria and chloroplasts (S2); 10 min at 15,000 *g*, to further remove organelles (S3) and finally 60 min at 100,000 *g* (S4 and P4; LaMontagne et al., 2016). The P4 fraction, containing small vesicles and microsomes (microsomal fraction), i.e., autophagosomes, was further subjected to 30 ng/µl proteinase K treatment (P4 + proteinase K). All S4, P4, and P4 + proteinase K samples were processed for AP-MS. **(B)** Venn diagram showing the overlap between ATG8E-associated, P4-enriched, and protease K-sensitive proteins that were identified by the AP-MS workflow described in A. 7-d-old *Arabidopsis* seedlings expressing pUBQ::mCherry or pUBQ::mCherry-ATG8E were treated with 3 µM Torin 1 for 90 min for autophagy induction before lysing. Diagram was generated using Venny 2.1.0 (Oliveros, 2016). **(C)** Volcano plots of mCherry-ATG8E AP-MS datasets identified CFS1 in all three pairwise comparisons. Upper panel, volcano plot of the pairwise comparison of "mCherry P4" and "mCherry-ATG8E P4" shows proteins enriched by the bait mCherry-ATG8E. X- and Y-axis displays $\log_2$ fold-change ($\log_2$[FC]) and $-\log_{10}$(P value), respectively. Dashed lines represent threshold for $\log_2$(FC) > 1 and P value <0.05. Only proteins passing both P value <0.05 and $\log_2$(FC) < 0 filter were considered in the first set "ATG8E-associated" in B. Middle panel, volcano plot of the pairwise comparison of "mCherry-ATG8E S4" and "mCherry-ATG8E P4," shows proteins enriched by mCherry-ATG8E in the pellet (P4) relative to the supernatant (S4). X-axis and Y-axis display $\log_2$(FC) and $-\log_{10}$(P value), respectively. Dashed lines represent threshold for $\log_2$(FC) > 1 and P value <0.05. Only proteins passing both P value <0.05 and $\log_2$(FC) < 0 filter were considered in the second set "P4-enriched" in B. Lower panel, volcano plot of the pairwise comparison of "mCherry-ATG8E P4 + proteinase K" and "mCherry-ATG8E P4", shows proteins enriched by mCherry-ATG8E in the pellet (P4) before proteinase K treatment. X-axis and Y-axis display $\log_2$(FC) and $-\log_{10}$(P value), respectively. Dashed lines represent threshold for $\log_2$(FC) > 1 and P value <0.05. Only proteins passing both P value <0.05 and $\log_2$(FC) < 0 filter were considered in the third set "Proteinase K-sensitive" in B. For all volcano plots, CFS1, interested proteins, and ATG8E are labeled by green, orange, or light blue dots, respectively. **(D)** Confocal microscopy images of *Arabidopsis* root epidermal cells co-expressing pUBQ::mCherry-CFS1 with either Golgi body marker p35S::NAG1-EGFP, trans-Golgi network marker pa1::VHAa1-GFP, MVB marker pRPS5a::GFP-ARA7 or autophagosome marker pUBQ::GFP-ATG8A under nitrogen starvation. 5-d-old *Arabidopsis* seedlings were incubated in nitrogen-deficient 1/2 MS media for 4 h for autophagy induction before imaging. Representative images of 10 replicates are shown. Area highlighted in the white-boxed region in the merge panel was further enlarged and presented in the inset panel. Scale bars, 5 µm. Inset scale bars, 2 µm. **(E)** Quantification of confocal experiments in D showing the Mander's colocalization coefficients between mCherry-CFS1 and the GFP-fused marker proteins NAG1, VHAa1, ARA7, or ATG8A. M1, fraction of GFP-fused marker signal that overlaps with mCherry-CFS1 signal. M2, fraction of mCherry-CFS1 signal that overlaps with GFP-fused marker signal. Bars indicate the mean ± SD of 10 replicates.

To further corroborate the autophagosome localization of CFS1, we visualized it with two other autophagosome-localized proteins: ATG11, a core autophagy protein that is crucial for recruitment of selective autophagy receptors and cargoes to the autophagosome, and NBR1 (Zientara-Rytter and Subramani, 2020; Svenning et al., 2011). mCherry-CFS1 colocalized with both GFP-ATG11 and NBR1-GFP upon induction of autophagy with salt stress (Fig. S1, I and J). Finally, we performed spinning disc time-lapse imaging of *Arabidopsis* lines that stably co-express mCherry-CFS1 with GFP-ATG8A or NBR1-GFP. Consistent with our confocal microscopy data, these time course experiments showed that CFS1 moves together with ATG8 and NBR1 puncta (Videos 1 and 2). Altogether, these results demonstrate that CFS1 specifically labels autophagic compartments.

A previous study analyzing FYVE domain-containing proteins in *Arabidopsis* identified another protein (CFS2, At1g29800) that also has FYVE and SYLF domains and shares 57.3% identity with CFS1 (Wywial and Singh, 2010; Fig. S2 A). Our phylogenetic analysis of CFS1 proteins across the plant kingdom detected no homology between CFS1 and CFS2 (Fig. S2 B). CFS1 and CFS2 formed separate, well-supported clades with different evolutionary histories. Nevertheless, we tested whether CFS2 plays a role in autophagy. We first carried out microscopy experiments similar to those described above. Although CFS2 was stably expressed, it did not form any puncta and had a diffuse localization pattern, even under autophagy inducing conditions (Fig. S2, C and D). Nitrogen starvation plate assays, which are typically used to evaluate autophagy defects in *Arabidopsis*, showed no difference between *cfs2* mutants and wild-type Col-0 plants (Phillips et al., 2008; Fig. S2 E). In contrast, *cfs1* mutants showed early senescence after 10 d of nitrogen starvation, similar to the autophagy-deficient *atg5* mutant (Thompson et al., 2005; Fig. S2 E). We then compared autophagic flux in *cfs1* and *cfs2* mutants. NBR1 is degraded upon induction of autophagy, and this is used as a proxy for autophagic flux measurements (Bassham, 2015). Under both nitrogen starvation and salt-stress conditions, *cfs1* mutants had higher NBR1 levels compared to wild-type plants (Fig. S2, F–I). However, *cfs2* mutants showed no significant difference, and *cfs1cfs2* double mutants were comparable to *cfs1* (Fig. S2, F–I). Altogether, these results suggest that CFS2 is not involved in autophagy and prompted us to focus on CFS1 for further characterization.

CFS1 interacts with ATG8 in an AIM-dependent manner

Autophagy adaptors interact with ATG8 directly through an AIM (Birgisdottir et al., 2013; Stolz et al., 2014; Zaffagnini and Martens, 2016). To investigate whether CFS1 interacts with ATG8, we first performed GST pull-down assays with *Arabidopsis* lysates expressing mCherry-CFS1 and *Escherichia coli* crude extracts expressing all nine GST-tagged *Arabidopsis* ATG8 isoforms or GST alone. mCherry-CFS1 interacted with GST-ATG8A to GST-ATG8F with similar affinities, but did not interact with GST-ATG8G, GST-ATG8H, and GST-ATG8I (Fig. S3 A). To further study whether CFS1 interacts with ATG8 in an AIM-dependent manner, we mixed crude extracts from *E. coli* expressing WT GST-ATG8A, an ADS mutant of ATG8 (GST-ATG8A^{ADS}), or GST alone with *Arabidopsis* lysates expressing mCherry-CFS1 and performed GST pull-down assays. mCherry-CFS1 interacted with GST-ATG8A, but not with GST-ATG8A^{ADS} or GST alone (Fig. 2 A). Consistently, the interaction between CFS1 and ATG8 could be outcompeted with a high-affinity AIM peptide, but not with an AIM mutant peptide (Stephani et al., 2020; Fig. 2 A). We then set out to identify the AIM in CFS1. Amino acid sequence alignments revealed a highly conserved candidate AIM between the FYVE and SYLF domains of CFS1 (Fig. S4). To test whether this motif is important for ATG8 interaction, we mutated the core AIM residues into alanine (WLNL-267-ALNA) and expressed the resulting mCherry-CFS1^{AIM} in the *cfs1* mutant. This mutation did not affect CFS1

stability as both proteins accumulate to similar levels (Fig. 2 B). Pull-down experiments showed that, in contrast to mCherry-CFS1, mCherry-CFS1^{AIM} interacted significantly less with GST-ATG8A (Fig. 2 B). We then performed in vivo co-immunoprecipitation (co-IP) experiments using plants stably co-expressing mCherry-CFS1 with GFP-ATG8A. We observed a strong association between CFS1 and ATG8A (Fig. 2 C). This association was further strengthened during nitrogen starvation, suggesting recruitment of CFS1 to the autophagosomes upon autophagy induction (Fig. 2 C). In contrast, mCherry-CFS1^{AIM}-GFP-ATG8A association was substantially weaker under both control and nitrogen-starved conditions (Fig. 2 C).

We then performed nitrogen starvation plate assays to test the physiological relevance of the CFS1 AIM. Expression of wild-type mCherry-CFS1 rescued the nitrogen-sensitivity phenotype of *cfs1* mutants. mCherry-CFS1^{AIM} expressing plants remained sensitive to nitrogen starvation, similar to the *cfs1* and *atg5* mutants (Fig. 2 D). Finally, we compared the localization patterns of mCherry-CFS1 and mCherry-CFS1^{AIM} relative to GFP-ATG8A. mCherry-CFS1 formed a significantly higher number of colocalizing puncta compared to mCherry-CFS1^{AIM} under both control and autophagy-inducing conditions (Fig. 2, E and F). Collectively, these results suggest that CFS1 interacts with ATG8 in an AIM-dependent manner and that the CFS1–ATG8 interaction is essential for CFS1 function and autophagosome localization.

To further study the residual puncta formed by mCherry-CFS1^{AIM}, we crossed mCherry-ATG8E with the *atg5* mutant, which does not form autophagosomes (Thompson et al., 2005). mCherry-CFS1 was still able to form a limited number of puncta in both basal and autophagy-inducing conditions, indicating that CFS1 forms puncta independently of autophagosomes (Fig. 2, G and H). To understand how CFS1 could still form puncta in the absence of autophagy, we looked at the other functional domains on CFS1. CFS1 has well-defined FYVE and SYLF domains that bind phosphatidylinositol-3-phosphate (Pi3P) and actin, respectively (Sutipatanasomboon et al., 2017; Fig. S2, A and B). We point-mutated the FYVE domain (RHHCR-195-AHACA) or the SYLF domain (K282A, R288A, K320A) of CFS1 to generatemCherry-CFS1^{FYVE} and mCherry-CFS1^{SYLF}. We also combined the mutations from mCherry-CFS1^{AIM}, mCherry-CFS1^{FYVE}, and mCherry-CFS1^{SYLF} to generate a triple CFS1 mutant, mCherry-CFS1^{tri}. Confocal microscopy results showed that mutating these domains, either individually or in combination, did not alter protein stability but did lead to diffuse localization patterns and disrupted ATG8A co-localization (Fig. S3, C and D), suggesting that CFS1 bridges Pi3P-rich endomembrane compartments with autophagosomes. In addition, in vivo co-IP experiments showed that compared to the wild-type mCherry-CFS1, mCherry-CFS1^{FYVE}, mCherry-CFS1^{SYLF}, and mCherry-CFS1^{tri} associated less with GFP-ATG8A (Fig. S3 D). Altogether, these results suggest that in addition to the AIM, FYVE and SYLF domains are also important for CFS1–ATG8 interaction.

CFS1 functions as an autophagy adaptor

We next explored the molecular function of CFS1 in autophagy. Three types of autophagy-related proteins contain AIMs: (i) core autophagy proteins involved in autophagosome biogenesis, (ii) autophagy receptors that mediate selective cargo recruitment and undergo autophagic degradation together with their respective cargoes, and (iii) autophagy adaptors, which interact with ATG8 on the outer autophagosome membrane and mediate autophagosome trafficking and maturation (Stolz et al., 2014). To determine whether CFS1 is involved in autophagosome biogenesis, we performed transmission electron microscopy (TEM) experiments in *Arabidopsis* root cells. Ultrastructural analysis of autophagosomes in *cfs1* mutants showed fully formed autophagosomes, indistinguishable from those in wild-type cells, ruling out a role for CFS1 in autophagosome biogenesis (Fig. 3 A). To test whether CFS1 functions as an autophagy receptor or adaptor, we performed comparative vacuolar flux analysis, using NBR1 as a representative autophagy receptor. We stained the vacuolar lumen with BCECF-AM and blocked vacuolar degradation with the vATPase inhibitor concanamycin A (conA; Krebs et al., 2010; Bassham, 2015), which enabled us to quantify puncta within the vacuolar lumen. Upon induction of autophagy with salt stress, we found significantly less CFS1 puncta compared to ATG8 or NBR1 puncta (Fig. 3, B and C). Consistently, although both CFS1 and NBR1 colocalize with ATG8E at cytosolic autophagosomes, upon conA treatment there were fewer co-localizing CFS1-ATG8E puncta inside the vacuole compared to NBR1-ATG8E puncta (Fig. 3, D and E). These results suggest that CFS1 functions as an autophagy adaptor. Since autophagy adaptors should localize on the outer autophagosome membrane, we performed immunogold-labeling TEM experiments on *Arabidopsis* seedlings expressing mCherry-CFS1. We could readily detect gold particles on the outer autophagosome membranes (Fig. 3, F and G), consistent with CFS1 having an adaptor function. Of note, we also detected gold particles at the inner autophagosome membrane (Fig. 3 F), suggesting CFS1 is recruited to the autophagosomes during phagophore growth. In sum, the comparative vacuolar flux analysis and the ultrastructural localization experiments support the role of CFS1 as an autophagy adaptor.

CFS1 is crucial for autophagic flux

Autophagy adaptors regulate the delivery or fusion of autophagosomes to the vacuole, known as autophagic flux (Stolz et al., 2014). We next examined the role of CFS1 in this process. First, we expressed mCherry-ATG8E in wild-type Col-0, *cfs1*, or *atg5*, and quantified the number of mCherry-ATG8E-labeled autophagosomes in root epidermal cells of these lines. Upon autophagy induction with salt stress, significantly more autophagosomes accumulated in the cytosol of *cfs1* cells compared to Col-0 (Fig. 4, A and B). However, after treatment with conA, which stabilizes autophagic bodies in the vacuole, *cfs1* mutants had significantly less mCherry-ATG8E puncta (Fig. 4, A and B). *atg5* mutants had no autophagosomes in either condition (Fig. 4, A and B). These results suggest that *cfs1* mutants have defects in the delivery of autophagosomes to the vacuole, which leads to the accumulation of autophagosomes in the cytosol. To support these data, we performed GFP-release assays under the same conditions. When GFP-ATG8 is delivered to the vacuole, a stable GFP fragment is released due to vacuolar protease activity.

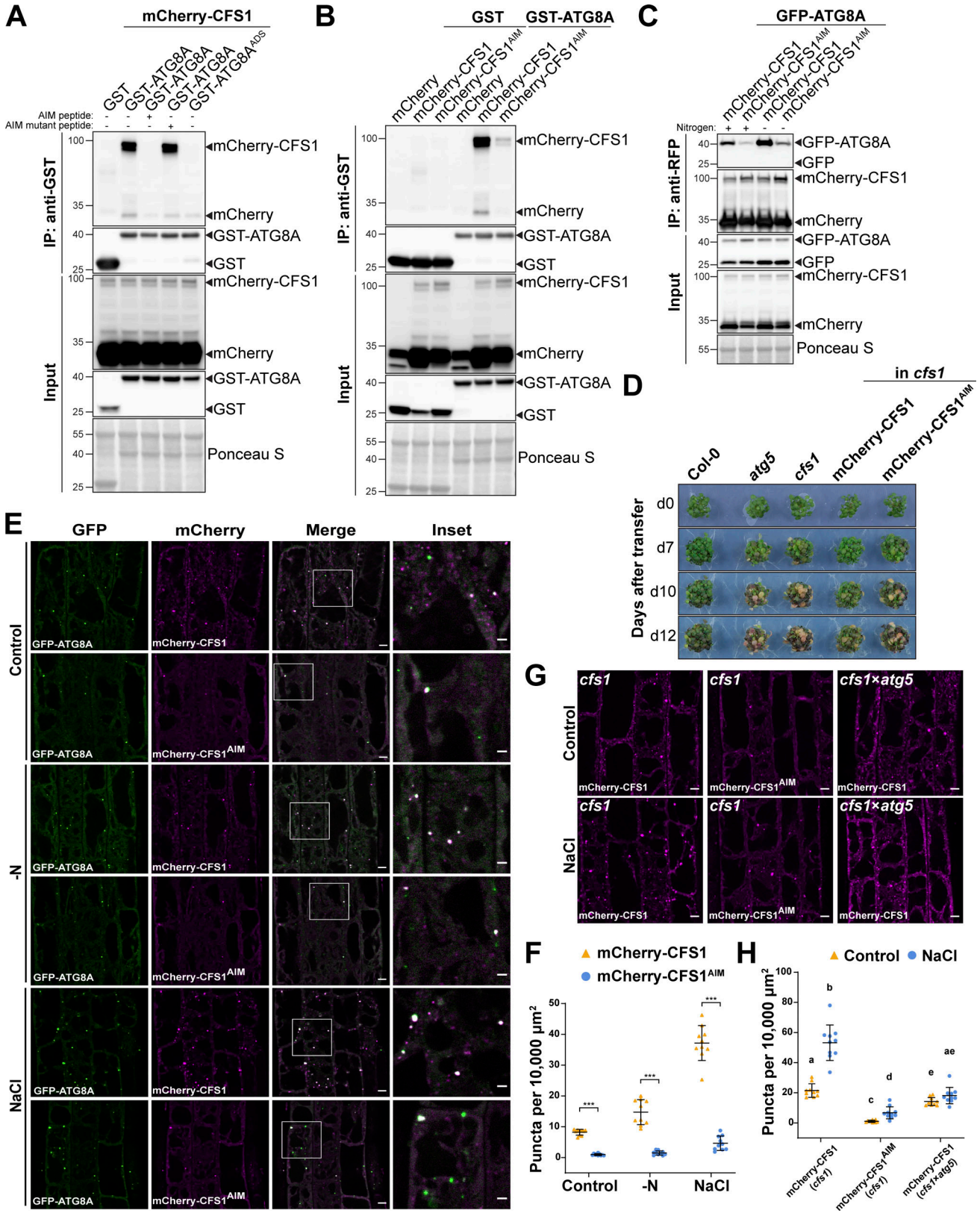

Figure 2. **CFS1 interacts with ATG8A in an AIM (ATG8 Interacting Motif)-dependent manner. (A)** GST pull-down coupled with peptide competition with *E. coli* lysates expressing either GST, GST-ATG8A, or GST-ATG8A^{ADS} and *A. thaliana* whole-seedling lysates expressing mCherry-CFS1. The peptides were added to a final concentration of 200 μM. Proteins were visualized by immunoblotting with anti-GST and anti-RFP antibodies. Representative images of three replicates are shown. Reference protein sizes are labeled as numbers at the left side of the blots (unit: kD). ADS, AIM docking site. **(B)** GST pull-down with *E. coli* lysates expressing either GST or GST-ATG8A and *A. thaliana* whole-seedling lysates expressing either mCherry, mCherry-CFS1, or mCherry-CFS1^{AIM}. Proteins

were visualized by immunoblotting with anti-GST and anti-RFP antibodies. Representative images of three replicates are shown. Reference protein sizes are labeled as numbers at the left side of the blots (unit: kD). **(C)** RFP-Trap pull-down of *Arabidopsis* seedlings co-expressing pUBQ::GFP-ATG8A with either pUBQ::mCherry-CFS1 or pUBQ::mCherry-CFS1^{AIM}. 7-d-old seedlings were incubated in either control (+) or nitrogen-deficient (–) 1/2 MS media for 12 h. Protein extracts were immunoblotted with anti-GFP and anti-RFP antibodies. Representative images of four replicates are shown. Reference protein sizes are labeled as numbers at the left side of the blots (unit: kD). **(D)** Phenotypic characterization of Col-0, *atg5*, *cfs1*, *cfs1* complemented with pUBQ::mCherry-CFS1 or *cfs1* complemented with pUBQ::mCherry-CFS1^{AIM} upon nitrogen starvation. 25 seeds per genotype were grown on 1/2 MS media plates (+1% plant agar) for 1-wk and 7-d-old seedlings were subsequently transferred to nitrogen-deficient 1/2 MS media plates (+0.8% plant agar) and grown for 2 wk. Plants were grown at 21°C under LEDs with 85 μM/m^2/s and a 14 h light/10 h dark photoperiod. d0 depicts the day of transfer. Brightness of pictures was enhanced ≤19% with Adobe Photoshop (2020). Representative images of four replicates are shown. **(E)** Confocal microscopy images of *Arabidopsis* root epidermal cells co-expressing pUBQ::GFP-ATG8A with either pUBQ::mCherry-CFS1 or pUBQ::mCherry-CFS1^{AIM}. 5-d-old *Arabidopsis* seedlings were incubated in either control, nitrogen-deficient (–N) or 150 mM NaCl-containing 1/2 MS media before imaging. Representative images of 10 replicates are shown. Area highlighted in the white-boxed region in the merge panel was further enlarged and presented in the inset panel. Scale bars, 5 μm. Inset scale bars, 2 μm. **(F)** Quantification of confocal experiments in E showing the number of mCherry-CFS1 puncta per normalized area (10,000 μm^2). Bars indicate the mean ± SD of 10 replicates. Two-tailed and paired Student *t* tests were performed to analyze the significance differences of the mCherry-CFS1 puncta number. ***, P value <0.001. **(G)** Confocal microscopy images of root epidermal cells of *cfs1* expressing pUBQ::mCherry-CFS1 or pUBQ::mCherry-CFS1^{AIM}, or *cfs1* × *atg5* expressing pUBQ::mCherry-CFS1. 5-d-old *Arabidopsis* seedlings were incubated in either control or 150 mM NaCl-containing 1/2 MS media for 2 h before imaging. Representative images of 10 replicates are shown. Scale bars, 5 μm. **(H)** Quantification of confocal experiments in G showing the number of mCherry-CFS1 puncta per normalized area (10,000 μm^2). Bars indicate the mean ± SD of 10 replicates. Brown–Forsythe and Welch one-way ANOVA test were performed to analyze the differences of the mCherry-CFS1 puncta number between each group. Unpaired *t* tests with Welch's correction were used for multiple comparisons. Family-wise significance and confidence level, 0.05 (95% confidence interval), were used for analysis. Source data are available for this figure: SourceData F2.

The ratio of free GFP to GFP-ATG8 can thus be used to quantify autophagic flux (Bassham, 2015; Yoshii and Mizushima, 2017). Quantification of five independent experiments showed that *cfs1* had higher levels of full-length GFP-ATG8A and lower levels of free GFP under nitrogen starvation or salt-stress conditions compared to wild type (Fig. 4, C and D). As mentioned above, the rate of NBR1 degradation can be also used to measure autophagic flux (Bassham, 2015; Yoshii and Mizushima, 2017). Following autophagy induction with salt stress, NBR1 levels remained high in *cfs1* compared to wild type (Fig. S2, F–I; and Fig. 4, C and E). Collectively, these results show that CFS1 is crucial for autophagic flux in *A. thaliana*.

We then tested whether CFS1 is involved in autophagic flux during selective autophagy. Using our recently established uncoupler-induced mitophagy assays, we compared mitophagic flux in wild type and *cfs1* cells (Ma et al., 2021). Ultrastructural analysis of uncoupler-treated *cfs1* cells showed fully formed mitophagosomes, further confirming that CFS1 does not play a role in autophagosome biogenesis (Fig. 4 F). We then measured mitophagic flux using western blots. Uncoupler treatment led to a decrease in levels of the mitochondrial matrix protein isocitrate dehydrogenase (IDH). This decrease was restored upon conA treatment, confirming the induction of mitophagy. *cfs1* mutants had higher IDH levels upon uncoupler treatment, suggesting a defect in mitophagic flux (Fig. 4, G and H). When we examined mitochondrial ultrastructure in *cfs1* by electron microscopy, we saw accumulation of damaged mitochondria with distinctive electron dense precipitates, which were rare in wild type, but common in *atg5* mutant (Fig. 4 I). Altogether, these results suggest CFS1 is also crucial for selective autophagy flux in *A. thaliana*.

We next asked whether the function of CFS1 is conserved across plants by studying the *M. polymorpha* (Mp) CFS1 homolog. Stable *M. polymorpha* plants co-expressing mScarlet-MpCFS1 with GFP-MpATG8A or GFP-MpATG8B showed that MpCFS1 colocalizes with both MpATG8 isoforms (Fig. 5, A and B). Heterologous expression of MpCFS1 in *A. thaliana* also showed colocalization of MpCFS1 with GFP-ATG8A (Fig. 5, C and D). Finally, GFP-release assays in *Marchantia* showed that *Mpcfs1* mutants have a defect in GFP-ATG8 degradation (Fig. 5, E and F). Together, these results suggest that CFS1 function is conserved across plants.

Since autophagic flux measurements assess vacuolar delivery, we decided to test if other vacuolar trafficking pathways are also affected in *cfs1* mutants. First, we measured the endocytic delivery of FM4-64 in Col-0, *cfs1*, *cfs2*, *cfs1cfs2*, and *cfs1* complementation lines. We quantified FM4-64 positive puncta upon conA treatment, which stabilizes endocytic vesicles. There was no difference between Col-0 and the mutant lines (Fig. 6, A and B). We then measured the uptake of a proteinaceous endocytic cargo, the auxin efflux carrier protein PIN2, in Col-0 and *cfs1* (Kleine-Vehn et al., 2008). Similar to FM4-64, upon induction of PIN2 endocytosis with dark treatment, we did not observe any difference between Col-0 and *cfs1* (Fig. 6, C and D). In addition, we compared the vacuolar morphology in Col-0, *cfs1*, *cfs2*, *cfs1cfs2*, and *cfs1* complementation lines, using BCECF-AM staining. We observed multiple small vacuoles in the epidermal cells of the root meristematic zone (Fig. 6 E) and intact central vacuoles at the transition zone in all lines (Fig. 6 F). Altogether, these results indicate that CFS1 specifically regulates autophagic flux without affecting other vacuolar pathways or vacuolar morphology.

CFS1 interacts with VPS23A and mediates the formation of amphisomes

How then does CFS1 regulate autophagic flux? We hypothesized that it may interact with tethering factors, such as the CORVET or the HOPS complex, and thereby bridge the autophagosomes with the tonoplast (Takemoto et al., 2018). To test this hypothesis, we generated *Arabidopsis* lines that co-expressed mCherry-CFS1 with the CORVET complex component VPS3, the HOPS complex component VPS39, and the tonoplast localized SNARE protein VAMP711 (Takemoto et al., 2018; Geldner et al., 2009). Under both control and autophagy-inducing conditions, CFS1 did not colocalize with any of those proteins, negating out our hypothesis (Fig. S5, A–F).

This prompted us to step back and investigate the CFS1 interactome. We performed a genome-wide yeast two hybrid

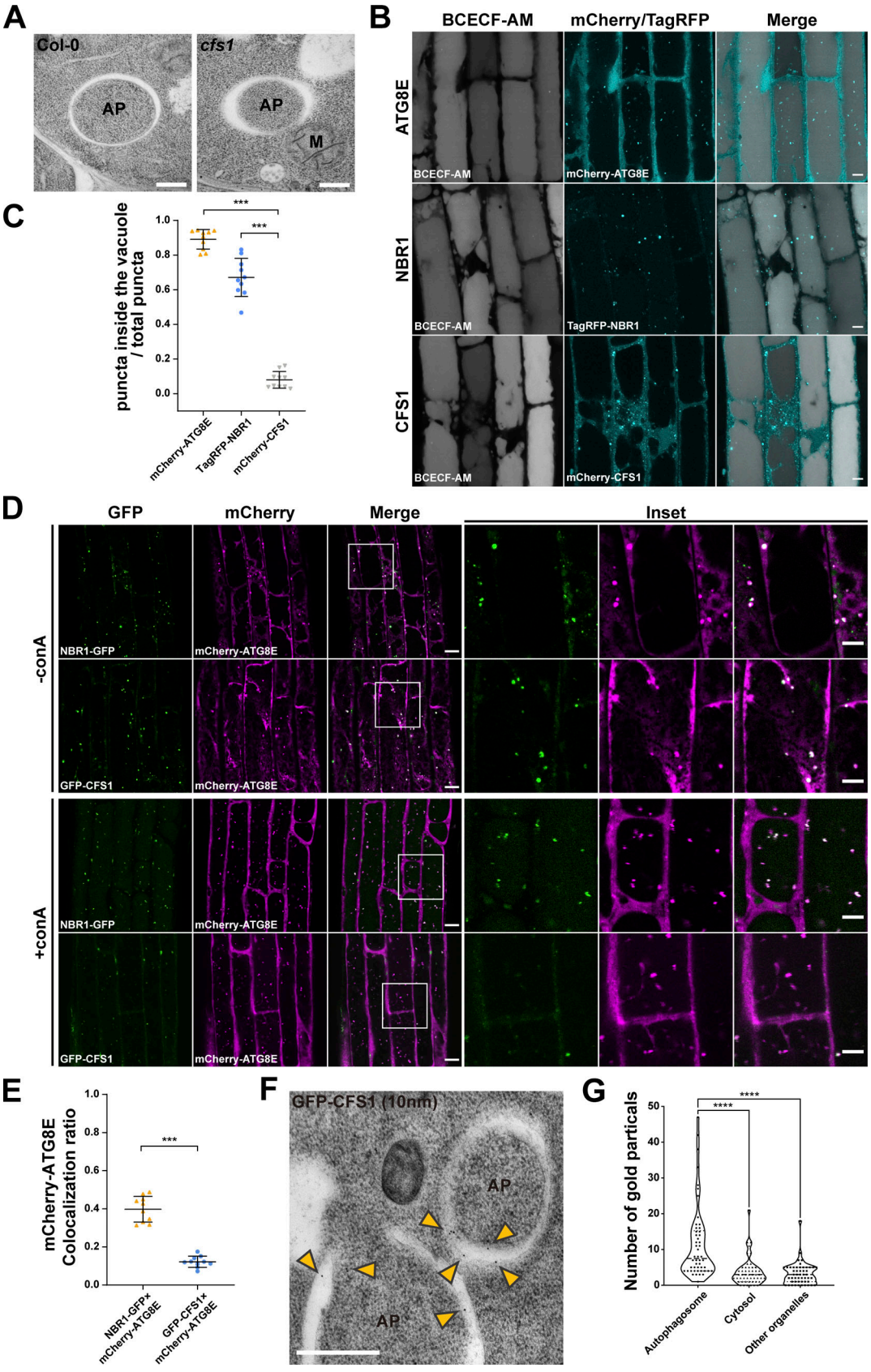

Figure 3. **CFS1 functions as an autophagy adaptor. (A)** Transmission electron microscopy (TEM) micrographs showing fully formed autophagosomes in the root cells of Col-0 and *cfs1*. 7-d-old *Arabidopsis* seedlings were incubated in 150 mM NaCl-containing 1/2 MS media for 1 h for autophagy induction before cryofixation. Scale bars, 500 nm. AP, autophagosome. M, mitochondrion. **(B)** Confocal microscopy images of *Arabidopsis* root epidermal cells expressing either

pUBQ::mCherry-ATG8E, pNBR1::TagRFP-NBR1 or pUBQ::mCherry-CFS1. 5-d-old seedlings were first incubated in 5 µM BCECF-AM-containing 1/2 MS media for 30 min for vacuole staining and were subsequently transferred to 1/2 MS media containing 90 mM NaCl and 1 µM concanamycin A (conA) for 2 h before imaging. Representative images of 10 replicates are shown. Scale bars, 5 µm. **(C)** Quantification of confocal experiments in B showing the ratio between the number of mCherry-ATG8E, TagRFP-NBR1, or mCherry-CFS1 puncta inside the vacuole, compared to the total number of mCherry-ATG8E, TagRFP-NBR1, or mCherry-CFS1 puncta. Bars indicate the mean ± SD of 10 replicates. Two-tailed and unpaired *t* tests with Welch's corrections were performed to analyze the differences of puncta numbers between mCherry-ATG8E and mCherry-CFS1 or between TagRFP-NBR1 and mCherry-CFS1. ***, P value <0.001. **(D)** Confocal microscopy images of *Arabidopsis* root epidermal cells co-expressing pUBQ::mCherry-ATG8E with either pUBQ::GFP-CFS1 or pNBR1::NBR1-GFP. 5-d-old *Arabidopsis* seedlings were incubated in 1/2 MS media containing either 150 mM NaCl (without conA; -conA), or 90 mM NaCl and 1 µM conA (+conA) for 2 h before imaging. Representative images of 10 replicates are shown. Area highlighted in the boxed region in the merge panel was further enlarged and presented in the inset panel. Scale bars, 10 µm. Inset scale bars, 5 µm. **(E)** Quantification of confocal experiments in D showing the mCherry-ATG8E colocalization ratio of NBR1-GFP and GFP-CFS1 to mCherry-ATG8E under +conA treatment conditions. The mCherry-ATG8E colocalization ratio is calculated as the ratio between the number of mCherry-ATG8E puncta that colocalize with NBR1-GFP or GFP-CFS1 puncta compared with the number of total mCherry-ATG8E puncta. Bars indicate the mean ± SD of 10 replicates. Two-tailed and unpaired *t* tests with Welch's corrections were performed to analyze the differences of mCherry-ATG8E colocalization ratio between GFP-CFS1 and NBR1-GFP. ***, P value <0.001. **(F)** TEM images showing immuno-gold labeled GFP-CFS1 at the autophagosomes in *Arabidopsis* root cells. 7-d-old seedlings were incubated in 150 mM NaCl-containing 1/2 MS media for 2 h for autophagy induction before cryofixation. Sections from pUBQ::GFP-CFS1 expressing samples were labeled with an anti-GFP primary antibody and a secondary antibody conjugated to 10 nm gold particles. Yellow arrowheads mark the gold particles associated with autophagosomes. Scale bars, 500 nm. AP, autophagosome. **(G)** Quantification of the localization of the GFP-specific gold particles imaged in the experiment shown in F. Approximately 900 gold particles in 50 TEM images captured from five independent samples were grouped into autophagosomes, cytosol or other organelles according to their locations. One-way ANOVA was performed to analyze the significant difference between different gold particle locations. ****, P value <0.0001.

screens, which revealed 51 confident interactors (Table S4). Notably, one of these interactors was VPS23A, an ESCRT-I complex component that is known to regulate endomembrane trafficking (Nagel et al., 2017; Shen et al., 2018; Gao et al., 2015). Confocal microscopy analyses showed that CFS1 colocalize with VPS23A under both control and salt-stressed conditions (Fig. 7, A and B). To further test the association between CFS1 and the ESCRT-I complex, we colocalized CFS1 with two other ESCRT-localized adaptor proteins, FREE1 and ALIX (Gao et al., 2015; Kalinowska et al., 2015). Similar to VPS23A, both proteins partially colocalized with CFS1 (Fig. S5, G and H). Interestingly, our airyscan and spinning disc microscopy analysis showed that two GFP-CFS1 puncta localized on distinct regions of VPS23A-TagRFP puncta (Fig. 7 C) and CFS1 move together with VPS23A (Video 3). These results suggest that CFS1 could bridge autophagosomes with VPS23A-labeled multivesicular bodies.

We then performed immunogold labeling TEM experiments to visualize the compartments where CFS1 and VPS23A colocalize. We used two differently sized gold particles conjugated to anti-GFP or anti-RFP antibodies, recognizing GFP-CFS1 and VPS23A-TagRFP, respectively. Electron micrographs obtained from cryo-fixed *Arabidopsis* root cells revealed that CFS1 and VPS23A colocalized at amphisomes, hybrid structures where autophagosomes fuse with intraluminal vesicle containing multivesicular bodies (Sanchez-Wandelmer and Reggiori, 2013; Fig. 7 D) This demonstrates that, similar to metazoans, plants have amphisomes where CFS1 colocalizes with VPS23A.

This prompted us to test the significance of amphisomes in autophagic flux. We first measured autophagic flux in *vps23* mutants. *Arabidopsis* has two VPS23 isoforms, VPS23A/VPS23.1 and VPS23B/VPS23.2 (Nagel et al., 2017). Since *Arabidopsis vps23avps23b* double mutants are lethal, we measured autophagic flux on single *vps23a* or *vps23b* mutants (Nagel et al., 2017). We expressed GFP-ATG8A in Col-0, *cfs1*, *vps23a*, and *vps23b* and quantified the GFP-ATG8A-marked autophagic bodies with and without salt stress and conA treatment. Neither *vps23a* nor *vps23b* mutants showed a significant difference compared to Col-0 (Fig. 7, E and F). Consistently, neither *vps23a* nor *vps23b* mutants showed autophagic flux defects in NBR1 degradation assays (Fig. 7, G and H). Finally, *vps23a* and *vps23b* were indistinguishable from wild type in nitrogen starvation plate assays (Fig. 7 I). Altogether, these data indicate that VPS23A and VPS23B may act redundantly or do not play a role in autophagy.

To circumvent the potential redundancy between VPS23A and VPS23B, we mutated CFS1 residues likely to mediate the CFS1–VPS23A interaction. Previous studies have shown that VPS23 interacting proteins contain a "PSAPP" motif, which docks into the ubiquitin E2 variant domain on VPS23 (Pornillos et al., 2003; Sutipatanasomboon et al., 2017). Consistently, Alphafold prediction suggested CFS1 and VPS23A interacted in a PSAPP-dependent manner (Jumper and Hassabis, 2022; Fig. 8 A). We thus generated the mCherry-CFS1^{PSAPP} mutant, where the PSAPP motif is mutated to alanines (PSAPP-145-AAAAA) and expressed it in the *cfs1* background. We also generated the mCherry-CFS1$^{AIM+PSAPP}$ double mutant, where both the AIM and the PSAPP motifs were mutated. The PSAPP mutation did not affect the stability of mCherry-CFS1 and its interaction with GFP-ATG8A (Fig. 8 B). We then tested whether the PSAPP motif is important for CFS1–VPS23A interaction. We stably co-expressed VPS23A-mTurquoise2 and GFP-ATG8A with mCherry-CFS1 or mCherry-CFS1^{PSAPP}. RFP pull-down experiments showed that mCherry-CFS1, mCherry-CFS1^{PSAPP} had similar association levels with GFP-ATG8A. However, the PSAPP mutant associated significantly less with VPS23A (Fig. 8 C). Furthermore, confocal microscopy experiments on *Arabidopsis* lines co-expressing GFP-VPS23A with either mCherry-CFS1 or mCherry-CFS1^{PSAPP} showed that mCherry-CFS1^{PSAPP} did not colocalize with GFP-VPS23A anymore (Fig. 8, D and E). Of note, in several cases, mCherry-CFS1^{PSAPP} puncta were in close proximity of the VPS23 puncta, but were unable to fully colocalize, consistent with the loss of association that we observed in the co-IP experiments (Fig. 8, C and D). Altogether, these findings suggest that CFS1 interacts with VPS23A in a PSAPP-dependent manner.

We next wanted to understand the physiological importance of the CFS1–VPS23A interaction in *Arabidopsis*. We measured

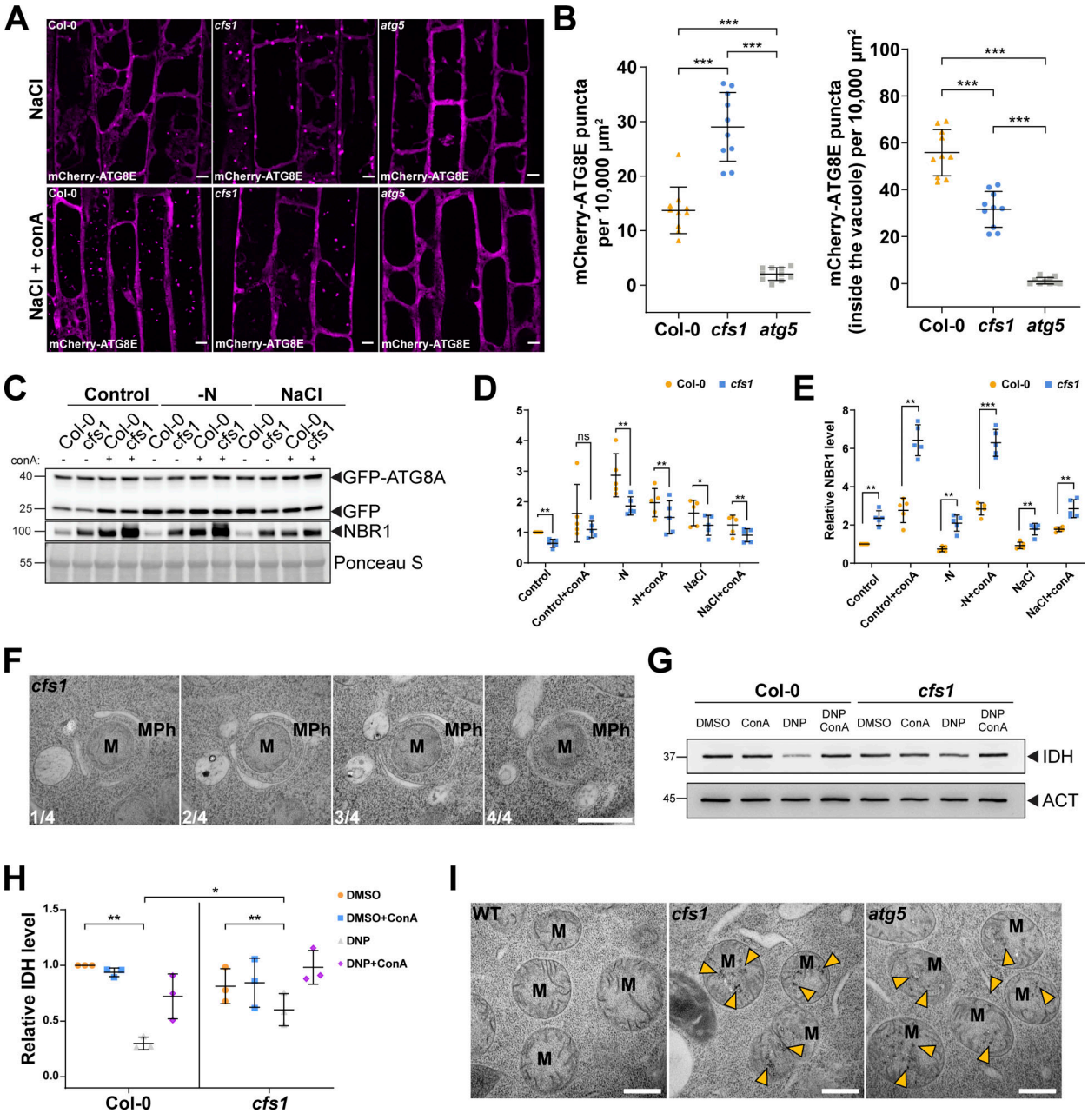

Figure 4. **CFS1 is crucial for autophagic flux in *A. thaliana*. (A)** Confocal microscopy images of root epidermal cells of Col-0, *cfs1*, or *atg5* expressing pUBQ::mCherry-ATG8E under NaCl or NaCl + conA treatment. 5-d-old *Arabidopsis* seedlings were incubated in 1/2 MS media containing either 150 mM NaCl (NaCl) or 90 mM NaCl and 1 µM conA (NaCl + conA) for 2 h before imaging. Representative images of 10 replicates are shown. Scale bars, 5 µm. **(B)** Left panel, quantification of the mCherry-ATG8E puncta per normalized area (10,000 µm^2) of the NaCl-treated cells imaged in A. Right panel, quantification of the mCherry-ATG8E puncta inside the vacuole per normalized area (10,000 µm^2) of the NaCl + conA-treated cells imaged in A. Bars indicate the mean ± SD of 10 replicates. Two-tailed and unpaired Student *t* tests with Welch's correction were performed to analyze the significance of mCherry-ATG8E puncta density differences between Col-0 and *cfs1*, Col-0 and *atg5*, or *cfs1* and *atg5*. ***, P value <0.001. **(C)** Western blots showing GFP-ATG8A cleavage level and endogenous NBR1 level in Col-0 or *cfs1* mutants under control, nitrogen-deficient (–N) or salt-stressed (NaCl) conditions. *Arabidopsis* seedlings were grown under continuous light in 1/2 MS media for 1-wk and 7-d-old seedlings were subsequently transferred to 1/2 MS media ±1 µM conA, nitrogen-deficient (–N) 1/2 MS media ±1 µM conA, or 1/2 MS media containing 150 mM NaCl ±1 µM conA for 12 h. 15 µg of total protein extract was loaded and immunoblotted with anti-GFP and anti-NBR1 antibodies. Representative images of five replicates are shown. Reference protein sizes are labeled as numbers at the left side of the blots (unit: kD). **(D)** Quantification of the relative autophagic flux in C. Values were calculated through protein band intensities of GFP divided by GFP-ATG8A and normalized to untreated (Control) Col-0. Results are shown as the mean ± SD of five replicates. One-tailed and paired Student *t* tests were performed to analyze the significance of the relative autophagic flux differences. ns, not significant. *, P < 0.05. **, P < 0.01. **(E)** Quantification of the relative NBR1 level in C compared to untreated (control) Col-0. Values were calculated through normalization of protein bands to Ponceau S and shown as the mean ± SD of five replicates. One-tailed and paired Student *t* tests were performed to analyze the significance of the relative NBR1 level differences. **, P < 0.01. ***, P < 0.001. **(F)** Serial sections of transmission electron microscopy micrographs showing a mitophagosome engulfing a mitochondrion. 7-d-old *Arabidopsis cfs1* seedlings were incubated in 1/2 MS media containing 50 µM DNP for 1 h before cryofixation. Scale bar, 500 nm. MPh, mitophagosome. M, mitochondrion. **(G)** Immunoblot

assay of uncoupler-induced mitochondrial protein degradation in *Arabidopsis* Col-0 and *cfs1* seedlings. 7-d-old seedlings were incubated in 1/2 MS media containing 50 µM DNP ±1 µM conA for 4 h before protein extraction. A mitochondrial matrix protein, isocitrate dehydrogenase (IDH), was immunoblotted by anti-IDH antibodies. Actin (ACT) was immunoblotted by anti-ACT antibodies and was used as a loading control. Representative images of three replicates are shown. Reference protein sizes are labeled as numbers at the left side of the blots (unit: kD). **(H)** Quantification of relative IDH intensities in G compared to untreated (control) Col-0. Values were calculated via normalization of protein bands to ACT and shown as the mean ± SD of three replicates. One-tailed and paired Student's *t* tests were performed to analyze the significance of the relative IDH level differences. ns, not significant. *, $P < 0.05$. **, $P < 0.01$. **(I)** TEM micrographs of mitochondria in *Arabidopsis* Col-0, *cfs1* and *atg5* root cells. 7-d-old seedlings were incubated in 150 mM NaCl-containing 1/2 MS media for 2 h for autophagy induction before cryofixation. Yellow arrowheads mark the distinctive electron dense precipitates of compromised mitochondria that appear after NaCl treatment. Scale bars, 500 nm. M, mitochondria. Source data are available for this figure: SourceData F4.

autophagic flux in mCherry-CFS1 and mCherry-CFS1^{PSAPP} expressing *A. thaliana* lines, using three different assays. First, we quantified vacuolar GFP-ATG8A puncta under autophagy inducing salt stress conditions. mCherry-CFS1^{PSAPP} lines had significantly fewer autophagic bodies in the vacuole (Fig. 8, G and H). Consistently, GFP-release assays showed that mCherry-CFS1^{PSAPP} lines phenocopied the mCherry-CFS1^{AIM} lines, with an autophagic flux defect under nitrogen starvation conditions (Fig. 8, I and J). NBR1 flux measurements also indicated a defect in autophagic flux (Fig. 8, I and K). Ultimately, to test the physiological importance of the CFS1–VPS23A interaction, we performed nitrogen starvation plate assays. Similar to the expression of mCherry-CFS1^{AIM}, the expression of mCherry-CFS1^{PSAPP} failed to rescue the nitrogen starvation-sensitivity phenotype of *cfs1* (Fig. 8 L). Altogether, these findings demonstrate that the CFS1–VPS23A interaction is critical for autophagic flux.

Discussion

Autophagosome maturation involves the trafficking and fusion of double-membraned autophagosomes with lytic compartments. Studies in yeast and metazoans have shown that this maturation step has several similarities with endocytic vesicle fusion and trafficking. Tethering complexes, RAB GTPases, SNARE proteins, and adaptors facilitate the trafficking and fusion of autophagosomes with the endolysosomal compartments (Zhao and Zhang, 2019; Zhao et al., 2021). While well studied in yeast and metazoans, a systematic analysis of autophagosome maturation is still missing in plants. In addition, plant genomes lack homologs of key maturation proteins, such as the autophagic SNARE, Syntaxin 17, suggesting plants have evolved different components for autophagosome maturation. Here, we show that CFS1 is an autophagy adaptor that bridges autophagosomes with multivesicular bodies and mediates the formation of amphisomes. We propose that CFS1 functions as a licensing factor that tethers autophagosomes to multivesicular bodies through the ESCRT-I complex. This is reminiscent of COPII tethering factor p115 that targets a subpopulation of COPII vesicles to cis-Golgi (Allan et al., 2000).

Previous studies in *Arabidopsis* showed that ESCRT-III subunits VPS2.1 and CHMP1A and B are involved in autophagy and regulate carbon starvation-induced bulk and selective autophagic degradation (Spitzer et al., 2015; Katsiarimpa et al., 2013). Similarly, in mammalians, ESCRT-III complex have been shown to mediate the closure of autophagosomes (Takahashi et al., 2018; Takahashi et al., 2019). Our findings now further extend ESCRT-autophagy crosstalk and show that ESCRT-I subunits are also involved in autophagic degradation.

Our findings are consistent with a role of CFS1 in autophagosome maturation as opposed to autophagosome biogenesis, which was suggested recently (Kim et al., 2022): (i) our differential centrifugation-based autophagosome enrichment procedure selects for proteins that associate with closed, mature autophagosomes. AP-MS did not identify biogenesis components but did identify trafficking-related proteins such as Myosin 14 (Fig. 1 B and Table S3); (ii) we observe fully formed autophagosomes in micrographs obtained from *cfs1* mutants indistinguishable from and in similar numbers to wild type (Fig. 3 A and Fig. 4 F); and (iii) we observe a clear colocalization with the ESCRT-I protein VPS23A in both confocal and electron micrographs (Fig. 7). Although we see significant defects in bulk and selective autophagic flux in *cfs1*, CFS1^{AIM}, and CFS1^{PSAPP} mutants, autophagic flux is not fully blocked in any of them. These findings suggest two, not mutually exclusive, explanations: (i) There could be other autophagy adaptors that mediate the maturation of a sub-population of autophagosomes. Consistently, in metazoans, there are several autophagy adaptors that are either involved in SNARE recruitment, Rab GTPase activation or autophagosome trafficking (Zhao et al., 2021). Performing autophagosome enrichment experiments in a GFP-ATG8A/*cfs1* line or using reporter lines of GFP-ATG8G, H or I that do not interact with CFS1 could reveal these adaptors. (ii) Some autophagosomes may be trafficked directly to the vacuole without an intermediary amphisome step. A systematic characterization of the autophagosome fusion machinery would shed light on both of these possibilities.

There are multiple trafficking routes to the vacuole: endocytic trafficking, post-Golgi trafficking, ER to vacuole transport, and autophagy (Aniento et al., 2022). Although we are starting to understand how these routes operate individually, how distinct vacuolar trafficking pathways are coordinated in response to changes in metabolic demands and external stimuli remains elusive. Here, based on our findings, we propose that vacuolar trafficking is organized as a "hub and spoke" type distribution system, where amphisomes serve as sorting hubs for multivesicular bodies and autophagosomes (Fig. 9). The "hub and spoke" model was developed by Delta Airlines in the 1950s and has since been successfully employed by various types of supply chain logistics and aviation industry. The model implies that, rather than transportation taking place from A to B as in the point-to-point system, all materials transit through centralized hubs. It thereby reduces logistical costs as fewer routes are necessary. It also permits economies of scale, since complicated

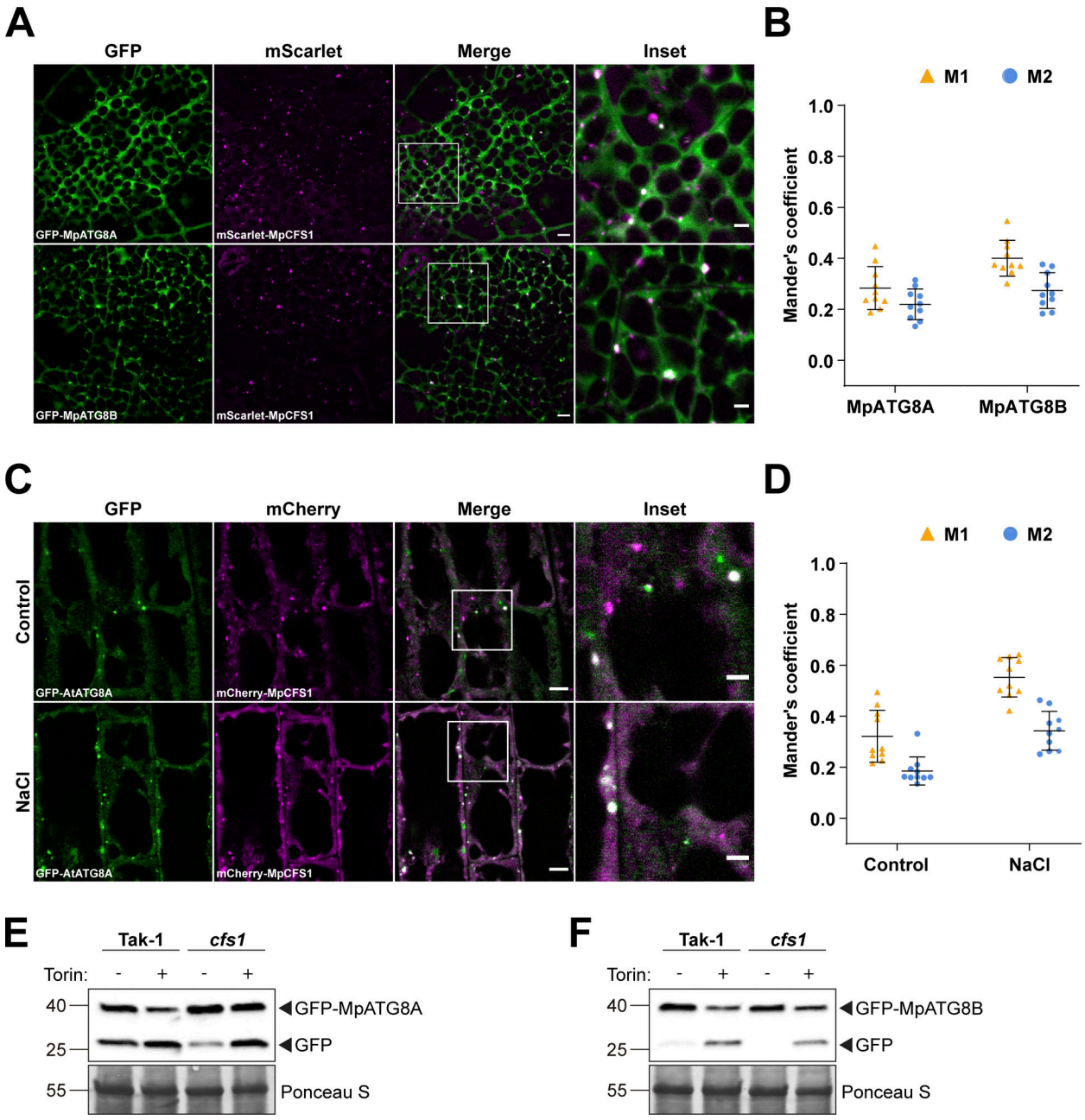

Figure 5. **CFS1 function is conserved in *M. polymorpha*. (A)** Confocal microscopy images of *M. polymorpha* thallus cells co-expressing pEF1::mScarlet-MpCFS1 with either pEF1::GFP-MpATG8A or pEF1::GFP-MpATG8B. 2-d-old thalli were incubated in 1/2 Gamborg B5 media before imaging. Representative images of 10 replicates are shown. Area highlighted in the white-boxed region in the merge panel was further enlarged and presented in the inset panel. Scale bars, 5 µm. Inset scale bars, 2 µm. **(B)** Quantification of confocal experiments in A showing the Mander's colocalization coefficients between mScarlet-MpCFS1 and GFP-fused MpATG8A or MpATG8B. M1, fraction of the GFP-fused MpATG8A or MpATG8B signals that overlaps with mScarlet-MpCFS1 signal. M2, fraction of mScarlet-MpCFS1 signal that overlaps with GFP-fused MpATG8A or MpATG8B signals. Bars indicate the mean ± SD of 10 replicates. **(C)** Confocal microscopy images of *Arabidopsis* root epidermal cells co-expressing pUBQ::mCherry-MpCFS1 and pUBQ::GFP-AtATG8A. 5-d-old seedlings were incubated in either control or 150 mM NaCl-containing 1/2 MS media for 1 h before imaging. Representative images of 10 replicates are shown. Scale bars, 5 µm. Inset scale bars, 2 µm. **(D)** Quantification of confocal experiments in (C) showing the Mander's colocalization coefficients between mCherry-MpCFS1 and GFP-AtATG8A under control or salt-stressed (NaCl) conditions. M1, fraction of the GFP-AtATG8A signal that overlaps with the mCherry-MpCFS1 signal. M2, fraction of the mCherry-MpCFS1 signal that overlaps with the GFP-AtATG8A signal. Bars indicate the mean ± SD of 10 replicates. **(E)** GFP cleavage assay of pEF1::GFP-MpATG8A in *M. polymorpha* wild type (Tak-1) or *cfs1* mutants. 10-d-old propagules were treated with 12 µM Torin for 5 h before protein extraction. 15 µg of total protein extract was loaded and immunoblotted with anti-GFP antibodies. Representative images of two replicates are shown. Reference protein sizes are labeled as numbers at the left side of the blots (unit: kD). **(F)** GFP cleavage assay of pEF1::GFP-MpATG8B in *M. polymorpha* wild type (Tak-1) or *cfs1* mutants. 10-d-old propagules were treated with 12 µM Torin for 5 h before protein extraction. 15 µg of total protein extract was loaded and was immunoblotted with anti-GFP antibodies. Representative images of two replicates are shown. Reference protein sizes are labeled as numbers at the left side of the blots (unit: kD). Source data are available for this figure: SourceData F5.

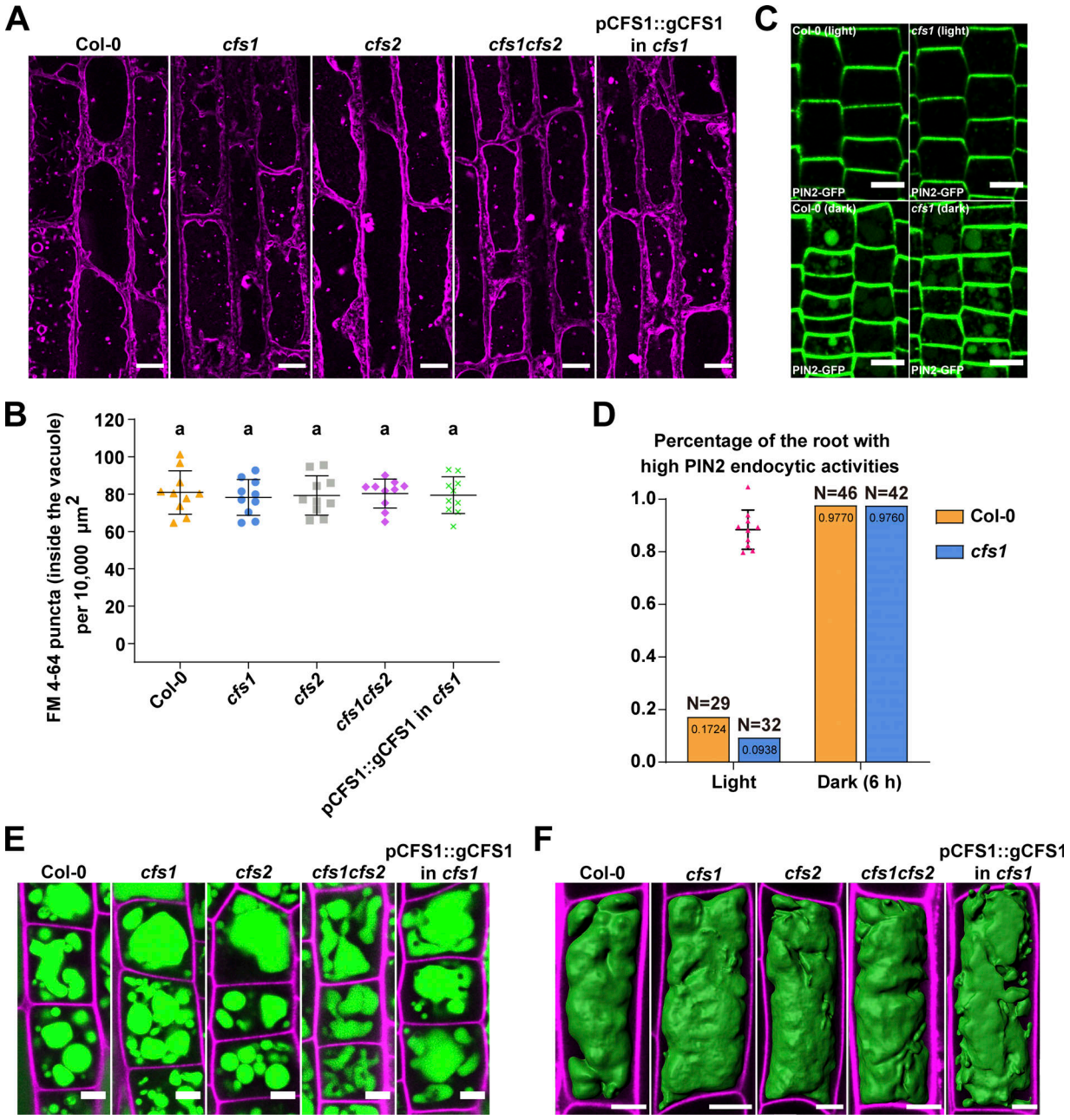

Figure 6. **Endocytic trafficking or vacuolar morphology is not affected in *cfs1* mutants. (A)** Confocal microscopy images of *Arabidopsis* root epidermal cells of Col-0, *cfs1*, *cfs2*, *cfs1cfs2*, and *cfs1* complemented with pCFS1::gCFS1(pCFS1::gCFS1 in *cfs1*). 5-d-old *Arabidopsis* seedlings were first incubated in 4 μM FM 4-64-containing 1/2 MS media for 30 min and then transferred to 1 μM concanamycin A-containing 1/2 MS media for 2 h before imaging. Representative images of 10 replicates are shown. Scale bars, 10 μm. **(B)** Quantification of the FM 4-64 stained puncta inside the vacuole per normalized area (10,000 μm^2) of the cells imaged in A. Bars indicate the mean ± SD of 10 replicates. One-way ANOVA tests were performed to analyze the differences of the number of FM 4-64 stained puncta between each group. Tukey's multiple comparison tests were used for multiple comparisons. Family-wise significance and confidence level, 0.05 (95% confidence interval). **(C)** Representative microscopy images showing PIN2 endocytosis in the epidermal cells in the root tip meristem region of Col-0 and *cfs1* under light or 6 h dark conditions. 5-d-old *Arabidopsis* seedlings expressing pPIN2::PIN2-GFP were grown on 1/2 MS media plates (+1% plant agar) under light or 6 h dark conditions before imaging. Scale bars, 10 μm. **(D)** Quantification of PIN2 endocytic activities in Col-0 and *cfs1* shown in C. The *Arabidopsis* seedlings with at least five root epidermal cells that contained visible PIN2-GFP in the vacuole were considered as high PIN2 endocytic activities. The percentage of Col-0 and *cfs1* with high PIN2 endocytic activities under light or 6-h dark conditions are shown in the graph. Numbers inside the bars represent the exact value (4 decimals) of each bar. N represents the total number of the Col-0 or *cfs1* seedlings used for imaging and quantification in three independent experiments. **(E)** Confocal microscopy images showing the BCECF-AM-stained root epidermal cells in the meristem region of Col-0, *cfs1*, *cfs2*, *cfs1cfs2*, or pCFS1::gCFS1 in *cfs1*. 5-d-old *Arabidopsis* seedlings were incubated in 1/2 MS media containing 5 μM BCECF-AM for 30 min before imaging. Samples were mounted on slides with 0.002 mg/ml propidium iodide. Representative images of three replicates are shown. Green signals indicate the BCECF-AM-stained vacuole. Magenta signals indicate the propidium iodide-stained cell wall. Scale bars, 5 μm. **(F)** Three-dimensional images showing the vacuolar structure of the BCECF-AM-stained root epidermal cells in the transition region of Col-0, *cfs1*, *cfs2*, *cfs1cfs2*, or pCFS1::gCFS1 in *cfs1*. 5-d-old *Arabidopsis* seedlings were incubated in 1/2 MS media containing 5 μM BCECF-AM for 30 min before imaging. Samples were mounted on slides with 0.002 mg/ml propidium iodide. Representative images of three replicates are shown. Green signals indicate the BCECF-AM-stained vacuole. Magenta signals indicate the propidium iodide-stained cell wall. Scale bars, 10 μm.

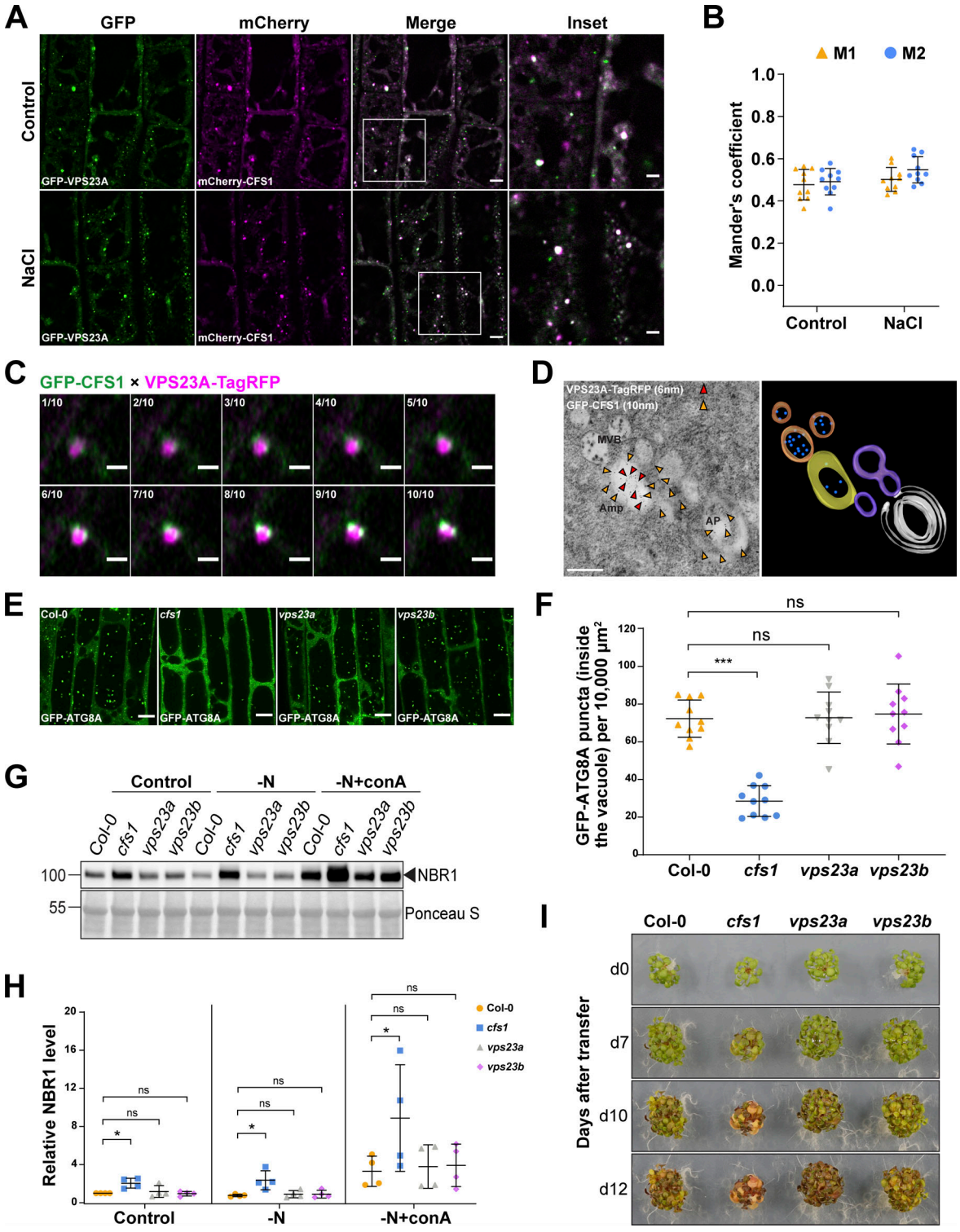

Figure 7. **Functional analysis of CFS1-VPS23 interaction revealed the amphisome in *A. thaliana*. (A)** Confocal microscopy images of *Arabidopsis* root epidermal cells co-expressing pUBQ::mCherry-CFS1 with pUBQ::GFP-VPS23A. 5-d-old *Arabidopsis* seedlings were incubated in either control or 150 mM NaCl-containing 1/2 MS media for 1 h before imaging. Representative images of 10 replicates are shown. Area highlighted in the white-boxed region in the merge panel was further enlarged and presented in the inset panel. Scale bars, 5 μm. Inset scale bars, 2 μm. **(B)** Quantification of confocal experiments in A showing the Mander's colocalization coefficients between mCherry-CFS1 and GFP-VPS23A. M1, fraction of GFP-VPS23A signal that overlaps with mCherry-CFS1 signal. M2, fraction of mCherry-CFS1 signal that overlaps with GFP-VPS23A signal. Bars indicate the mean ± SD of 10 replicates. **(C)** Airyscan time-lapse microscopy images of *Arabidopsis* root epidermal cells showing the partial colocalization between GFP-CFS1 and VPS23A-TagRFP. 5-d-old *Arabidopsis* seedlings co-expressing pVPS23A::VPS23A-TagRFP and pUBQ::GFP-CFS1 were incubated in 150 mM NaCl-containing 1/2 MS media for 1 h for autophagy induction before imaging. 10 continuous layers from one Z-stack image are shown separately in order. Interval of the Z-stack image, 0.15 μm. Scale bars, 1 μm. **(D)** Left panel, transmission electron microscopy micrographs showing the colocalization of VPS23A-TagRFP and GFP-CFS1 in *Arabidopsis* root cells co-expressing

pVPS23A::VPS23A-TagRFP and pUBQ::GFP-CFS1. 5-d-old seedlings were incubated in 150 mM NaCl-containing 1/2 MS media for 2 h for autophagy induction before cryofixation. Sections were labeled with rabbit anti-RFP and chicken anti-GFP primary antibodies and secondary antibodies conjugated to 6- or 10-nm gold particles. Yellow and red arrowheads mark the representative RFP and GFP-specific gold particles, respectively. MVB, multivesicular bodies; Amp, amphisome; AP, autophagosome. Scale bars, 400 nm. Right panel, the three-dimensional model of the amphisome and its associated compartments shown in the left panel. The model was generated from serial sections flanking the section shown in the left panel. Autophagosome (white), autophagosome-associated vesicles (purple), amphisome (yellow), multivesicular bodies (orange), and internal vesicles (blue) were rendered into 3D surfaces. **(E)** Confocal microscopy images of root epidermal cells of Col-0, *cfs1*, *vps23a*, or *vps23b* seedlings expressing pUBQ::GFP-ATG8A under NaCl + concanamycin A (conA) treatment. 5-d-old *Arabidopsis* seedlings were incubated in 1/2 MS media containing 90 mM NaCl and 1 µM conA for 2 h before imaging. Representative images of 10 replicates are shown. Scale bars, 10 µm. **(F)** Quantification of the number of GFP-ATG8A puncta inside the vacuole per normalized area (10,000 µm^2) of the cells imaged in E. Bars indicate the mean ± SD of 10 replicates. Two-tailed and unpaired Student *t* tests were performed to analyze the significance of GFP-ATG8A puncta density differences between Col-0 and *cfs1*, Col-0 and *vps23a*, or Col-0 and *vps23b*. ns, not significant. ***, P value <0.001. **(G)** Western blot showing the endogenous NBR1 level in Col-0, *cfs1*, *vps23a,* or *vps23b* under control or nitrogen-deficient ± conA conditions. *Arabidopsis* seeds were first grown in 1/2 MS media under continuous light for 1-wk and 7-d-old seedlings were subsequently transferred to 1/2 MS media (Control), nitrogen-deficient 1/2 MS media (–N) or nitrogen-deficient 1/2 MS media containing 1 µM conA (–N + conA) for 12 h. 10 µg of total protein extract was loaded and immunoblotted with anti-NBR1 antibodies. Representative images of four replicates are shown. Reference protein sizes are labeled as numbers at the left side of the blots (unit: kD). **(H)** Quantification of the relative NBR1 level in G compared to untreated (control) Col-0. Values were normalized to untreated (Control) Col-0 and calculated through normalization of protein bands to Ponceau S and shown as the mean ± SD of four replicates. One-tailed and paired Student *t* tests were performed to analyze the significance of the relative NBR1 level difference. ns, not significant. *, P < 0.05. **(I)** Phenotypic characterization of *Arabidopsis cfs1*, *vps23a*, and *vps23b* mutants during nitrogen starvation. 25 seeds per genotype were grown on 1/2 MS media plates (+1% plant agar) for 1-wk and 7-d-old seedlings were subsequently transferred to nitrogen-deficient 1/2 MS media plates (+0.8% plant agar) and grown for 2 wk. Plants were grown at 21°C under LEDs with 85 µM/m^2/s and a 14 h light/10 h dark photoperiod. d0 depicts the day of transfer. Brightness of pictures was enhanced ≤30% with Adobe Photoshop (2020). Representative images of four replicates are shown. Source data are available for this figure: SourceData F7.

operations can be performed in the hubs rather than separately organized in each node (Oti, 2013). Organizing vacuolar trafficking through hubs (i) could allow the cell to intricately balance the anabolic and catabolic needs and seamlessly integrate various intrinsic and extrinsic signals, (ii) could facilitate the crosstalk between post-Golgi trafficking, endocytosis, and autophagy, and (iii) could provide a route for loading and secretion of extracellular vesicles.

One well-known drawback of "hub and spoke" distribution models is that the hub represents a single point of failure. Any congestion in the hub can severely impact the whole system. Therefore, building a robust hub is critical for a successful supply chain (Oti, 2013). This could be informative for translational approaches that aim to increase plant stress tolerance by engineering plant endomembrane trafficking.

Speculation

One of our time-lapse videos analyzing CFS1-NBR1 co-trafficking showed an intriguing pattern: A CFS1-NBR1 positive punctum squeezed through a membrane, which looks like movement from one cell to another, and separated from each other after moving to the adjacent cell (Video 4). We would like to share it with the community and discuss the implications of cell-to-cell movement of autophagosomes: (i) In *Arabidopsis* roots, central vacuoles mature and acidify by fusion of small vacuoles in a developmentally regulated manner (Cui et al., 2019; Cui et al., 2020; Krüger and Schumacher, 2018). So, in meristematic cells, vacuoles may not be hydrolytically active. Autophagosomes in such cells may need to traffic to the neighboring cells to deliver autophagic cargo to an active lytic compartment. Intriguingly, we observed that mCherry-CFS1 highly accumulates in the quiescent center cells of *Arabidopsis*, where vacuoles have not matured yet (Fig. 10). (ii) Alternatively, they may be loaded with cargo that are involved in cell-to-cell communication. In both cases, the amphisomes formed through CFS1–VPS23A interaction may act as the "porter" role (Fig. 9). However, as the title of the section implies, these scenarios need to be supported or refuted by further studies.

Materials and methods

Plant material and cloning procedure

All *Arabidopsis thaliana* lines used in this study originate from the Columbia (Col-0) ecotype and are listed below (Table 1). The primers used for genotyping are listed in Table 3. Coding sequences from gene of interest were amplified from Col-0 cDNA with primers listed in Table 3. Plasmids were assembled through the GreenGate cloning method (Lampropoulos et al., 2013). In short, CFS1 (At3g43230) and CFS2 (At1g29800) were cloned into two parts to remove internal *Bsa*I sites (see Table 3 for primers). For introducing point mutations in mCherry-CFS1^{AIM} (WLNL-267-ALNA), mCherry-CFS1^{FYVE} (RHHCR-195-AHACA), and mCherry-CFS1^{PSAPP} (PSAPP-145-AAAAA), site-directed mutagenesis was applied using primers listed in Table 3. For mCherry-CFS1^{SYLF} (K282A, R288A, K320A), the SYLF domain was mutagenized by ordering a synthetic DNA sequence carrying point mutations (Table 3) and replaced by restriction enzyme digestion with *Nco*I (NEB) and *Xba*I (NEB). All constructs used in this study are listed in Table 2. Transgenic plant lines were generated through the Agrobacterium-mediated floral-dip method (Clough and Bent, 1998) and are listed in Table 1.

For *M. polymorpha*, all lines are derived from the Takaragaike-1 (Tak-1) ecotype. Plants were maintained and cultivated asexually on half-strength (1/2) Gamborg B5 media (Gamborg B5 medium basal salt mixture [Duchefa] supplemented with 0.5 g/l MES and 1% sucrose, pH 5.5) plates (+1% plant agar [Duchefa]) under continuous white light with a light intensity of 50 µM/m^2/s at 21°C. For cloning, MpATG8A (Mp1g21590) and MpATG8B (Mp5g05930) primers are listed in Table 3. For MpCFS1 (Mp3g11370), a synthetic DNA construct (Table 3) with GreenGate compatible *Bsa*I overhangs was ordered. Plasmids were assembled through the Gateway (Ishizaki et al., 2015) or

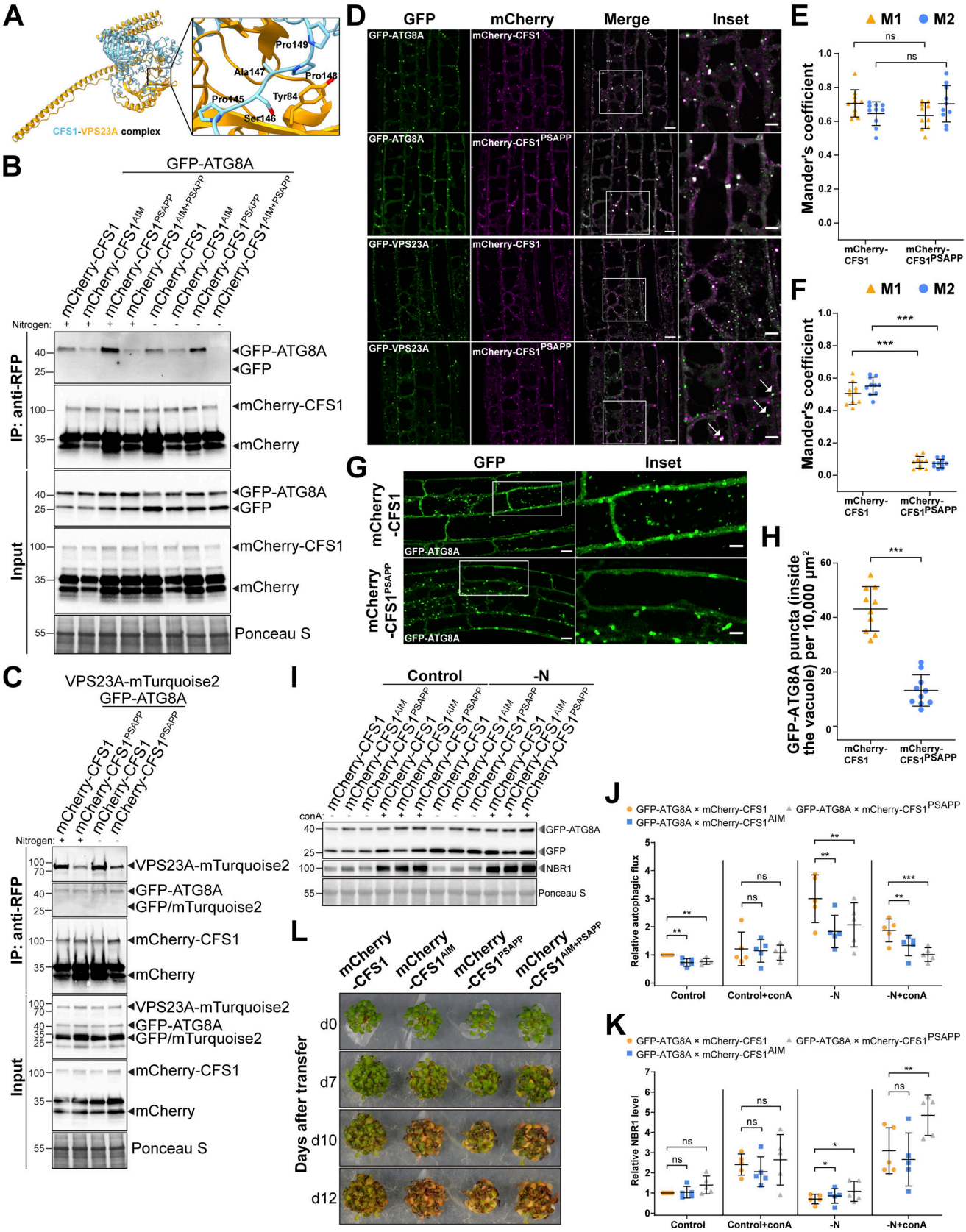

Figure 8. **PSAPP motif of CFS1 is crucial for CFS1-VPS23A interaction and autophagic flux. (A)** Homology modeling of CFS1/VPS23A complex. Prediction of CFS1-VPS23A heterocomplex formation generated by AlphaFold2 as implemented by ColabFold (Jumper et al., 2021; Mirdita et al., 2022). Structure of CFS1 and VPS23A is represented as ribbons and colored in light blue and orange, respectively. The predicted complex interaction interface involving AtCFS1 PSAPP motif is highlighted as a zoom in with the side chains of relevant residues represented as sticks. **(B)** RFP-Trap pull-down of *Arabidopsis* seedlings co-expressing

pUBQ::GFP-ATG8A with either pUBQ::mCherry-CFS1, pUBQ::mCherry-CFS1^{AIM}, pUBQ::mCherry-CFS^{PSAPP} or pUBQ::mCherry-CFS1$^{AIM+PSAPP}$. 7-d-old seedlings were incubated in either control (+) or nitrogen-deficient (−) 1/2 MS media for 12 h. Protein extracts were immunoblotted with anti-GFP and anti-RFP antibodies. Representative images of two replicates are shown. Reference protein sizes are labeled as numbers at the left side of the blots (unit: kD). **(C)** RFP-Trap pull-down of *Arabidopsis* seedlings co-expressing pUBQ::GFP-ATG8A and pUBQ::VPS23A-mTurquoise2 with either pUBQ::mCherry-CFS1 or pUBQ::mCherry-CFS1^{PSAPP}. 7-d-old seedlings were incubated in either control (+) or nitrogen-deficient (−) 1/2 MS media for 12 h. Protein extracts were immunoblotted with anti-GFP and anti-RFP antibodies. Representative images of two replicates are shown. Reference protein sizes are labeled as numbers at the left side of the blots (unit: kD). **(D)** Confocal microscopy images of *Arabidopsis* root epidermal cells co-expressing either pUBQ::GFP-ATG8A or pUBQ::GFP-VPS23A with either pUBQ::mCherry-CFS1 or pUBQ::mCherry-CFS1^{PSAPP} under salt stress. 5-d-old *Arabidopsis* seedlings were incubated in 150 mM NaCl-containing media for 1 h for autophagy induction before imaging. Representative images of 10 replicates are shown. Area highlighted in the white-boxed region in the merge panel was further enlarged and presented in the inset panel. Arrows point out the partial colocalization of GFP-VPS23A puncta and mCherry-CFS1^{PSAPP} puncta. Scale bars, 10 µm. Inset scale bars, 5 µm. **(E)** Quantification of confocal experiments in (D) showing the Mander's colocalization coefficients between GFP-ATG8A and either mCherry-CFS1 or mCherry-CFS1^{PSAPP}. M1, fraction of GFP-ATG8A signal that overlaps with mCherry-CFS1 or mCherry-CFS1^{PSAPP} signal. M2, fraction of mCherry-CFS1 or mCherry-CFS1^{PSAPP} signal that overlaps with GFP-ATG8A signal. Bars indicate the mean ± SD of 10 replicates. **(F)** Quantification of confocal experiments in D showing the Mander's colocalization coefficients between GFP-VPS23A and either mCherry-CFS1 or mCherry-CFS1^{PSAPP}. M1, fraction of GFP-VPS23A signal that overlaps with mCherry-CFS1 or mCherry-CFS1^{PSAPP} signal. M2, fraction of mCherry-CFS1 or mCherry-CFS1^{PSAPP} signal that overlaps with GFP-VPS23A signal. Bars indicate the mean ± SD of 10 replicates. **(G)** Confocal microscopy images of *Arabidopsis* root epidermal cells co-expressing pUBQ::GFP-ATG8A with either pUBQ::mCherry-CFS1 or pUBQ::mCherry-CFS1^{PSAPP} under NaCl + concanamycin A (conA) treatment. 5-d-old *Arabidopsis* seedlings were incubated in 1/2 MS media containing 90 mM NaCl and 1µM conA for 2 h before imaging. Scale bars, 10 µm. Inset scale bars, 5 µm. **(H)** Quantification of GFP-ATG8A puncta inside the vacuole per normalized area (10,000 µm^2) of the cells imaged in G. Bars indicate the mean ± SD of 10 replicates. Two-tailed and unpaired Student's *t* test were performed to analyze the significance of difference between mCherry-CFS1 and mCherry-CFS1^{PSAPP}. ***, P value <0.001. **(I)** Western blots showing the GFP-ATG8A cleavage level and the endogenous NBR1 level in *Arabidopsis cfs1* mutants co-expressing pUBQ::GFP-ATG8A with either pUBQ::mCherry-CFS1, pUBQ::mCherry-CFS1^{AIM}, or pUBQ::mCherry-CFS1^{PSAPP} under control ± conA or nitrogen-deficient (−N) ± conA conditions. *Arabidopsis* seeds were first grown in 1/2 MS media under continuous light for 1-wk and 7-d-old seedlings were subsequently transferred to 1/2 MS media ±1 µM conA or nitrogen-deficient 1/2 MS media ±1 µM conA for 12 h. 10 µg of total protein extract was loaded and immunoblotted with anti-GFP and anti-NBR1 antibodies. Representative images of five replicates are shown. Reference protein sizes are labeled as numbers at the left side of the blots (unit: kD). **(J)** Quantification of I showing the relative autophagic flux. Values were calculated as the protein band intensities of GFP divided by the protein band intensity of GFP-ATG8A and were normalized to untreated (Control) Col-0. Results are shown as the mean ± SD of five replicates. One-tailed and paired Student's *t* tests were performed to analyze the significance of the relative autophagic flux differences. ns, not significant. **, P < 0.01. ***, P < 0.001. **(K)** Quantification of I showing the relative NBR1 level in respect to untreated (Control) Col-0. Values were calculated through normalization of protein bands to Ponceau S and shown as the mean ± SD of five replicates. One-tailed and paired Student *t* tests were performed to analyze the significance of the relative NBR1 level difference. ns, not significant. *, P < 0.05. **, P < 0.01. **(L)** Phenotypic characterization of *Arabidopsis cfs1* mutants complemented with either pUBQ::mCherry-CFS1, pUBQ::mCherry-CFS1^{AIM}, pUBQ::mCherry-CFS1^{PSAPP}, or pUBQ::mCherry-CFS1$^{AIM+PSAPP}$ upon nitrogen starvation. 25 seeds per genotype were grown on 1/2 MS media plates (+1% plant agar) for 1-wk and 7-d-old seedlings were subsequently transferred to nitrogen-deficient 1/2 MS media plates (+0.8% plant agar) and grown for 2 wk. Plants were grown at 21°C under LEDs with 85 µM/m^2/s and a 14 h light/10 h dark photoperiod. d0 depicts the day of transfer. Brightness of pictures was enhanced ≤19% with Adobe Photoshop (2020). Representative images of four replicates are shown. Source data are available for this figure: SourceData F8.

GreenGate (Lampropoulos et al., 2013) system and introduced through *Agrobacterium tumefaciens* transformation (Kubota et al., 2013). *cfs1* knockout mutants were achieved through CRISPR/Cas9 gene editing through 2 gRNAs. gRNAs were inserted at the *Bsa*I (NEB) sites of the pMpGE_En03 entry vector and subsequently inserted into the pMpGE010 destination vector through LR clonase II reaction (Invitrogen; Sugano et al., 2018). Successful transformants were verified through sequencing of PCR products from amplified genomic DNA. Stable plant lines and constructs used are listed in Tables 4 and 2, respectively.

Plant phenotypic assays

Arabidopsis seedlings were grown as described in Jia et al. (2019). Briefly, 25 *Arabidopsis* seeds per bundle were vapor-phase sterilized (90% sodium hypochlorite 13 and 10% HCl 36%) and sown on plates which were layered with a thin nylon mesh on top of 1/2 MS media (Murashige and Skoog salt + Gamborg B5 vitamin mixture [Duchefa] supplemented with 0.5 g/liter MES and 1% sucrose, pH 5.7) plates (with 1% plant agar [Duchefa]) followed by 3 d of vernalization at 4°C in dark. Vernalized seeds were grown at 21°C under LEDs with 85 µM/m^2/s with a 14 h light/10 h dark photoperiod for 7 d. 7-d-old seedlings were subsequently transferred to 1/2 MS media (CaissonLabs) or nitrogen-deficient 1/2 MS media (Murashige and Skoog salt without nitrogen [CaissonLabs] + Gamborg B5 vitamin mixture [Duchefa] supplemented with 0.5 g/liter MES and 1% sucrose, pH 5.7) plates (+0.8% plant agar [Duchefa]) and grown for 2 wk.

Sample preparation before protein extraction

Unless stated otherwise, 20–40 *A. thaliana* seeds were grown in 1/2 MS media in 12-well plates under continuous light and constant shaking at 80 rpm for 7 d. 7-d-old seedlings were subjected to indicated treatments. For nitrogen starvation, 1/2 MS media was replaced with nitrogen-deficient 1/2 MS media. For salt stress, 150 mM NaCl was added to 1/2 MS media. For drug-treatments, all drugs used were dissolved in DMSO and added to the desired concentration (3 µM Torin1 (CAS 1222998-36-8; Santa Cruz); 1 µM concanamycin A (conA; CAS 80890-47-7; Santa Cruz); and 50 µM 2,4-dinitrophenol (DNP; CAS 51-28-5; Sigma-Aldrich). Equal amount of pure DMSO was added to control samples. Seedlings were harvested in microcentrifugation tubes with different-sized glass beads (2.85–3.45, 1.7–2.1, and 0.75–1.00 mm; Lactan GmbH) and flash-frozen in liquid nitrogen. Plants were ground with a mixer mill MM400 (3 × 30 s, 30 Hz; Retsch).

For protein extraction of *M. polymorpha*, the propagules were grown for 10 d in 1/2 Gamborg B5 media under continuous light

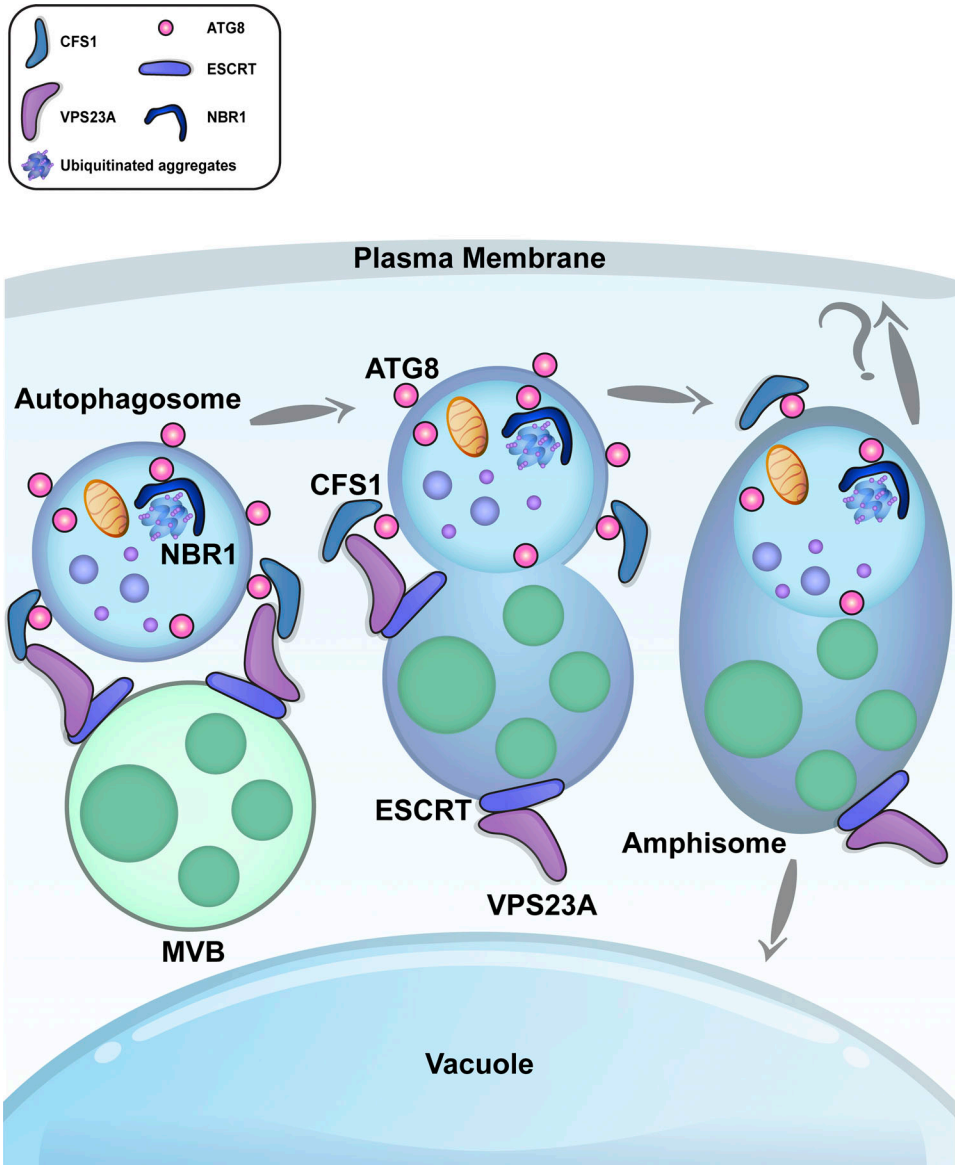

Figure 9. **Current working model: Vacuolar trafficking is organized as a "hub and spoke" type distribution system.** CFS1 interacts with both ATG8 and VPS23A and mediates the formation of amphisomes—hybrid prevacuolar compartments that are formed by the fusion of multivesicular bodies and autophagosomes.

with a light intensity of 50 μM/m^2/s at 21°C and subjected to indicated treatments. Samples were flash-frozen in liquid nitrogen and ground using a mortar and pestle.

Western blotting

Arabidopsis protein extraction was achieved by adding 250 μl of protein extraction buffer (100 mM Tris [pH 7.5], 200 mM NaCl, 1 mM EDTA, 2% 2-Mercaptoethanol, 0.2% Triton X-100 and 1 tablet/50 ml Complete, EDTA-free Protease Inhibitor Cocktail [Sigma-Aldrich], pH 7.8) to grinded samples. Samples were subsequently well mixed and centrifuged at 15,000 rpm at 4°C for 10 min. The whole supernatant was transferred to a new tube. After another round of centrifugation at 15,000 rpm at 4°C for 10 min, resulting supernatant was diluted with 2× Laemmli buffer (4% SDS, 20% glycerol, 10% 2-mercaptoethanol, 0.004% bromophenol blue and 0.125 M Tris HCl, pH 6.8) and boiled at 95°C for 10 min as the final protein extract sample.

For *M. polymorpha* protein extraction, grinded plant powder was weighed and added with 2× volume of buffer (10% glycerol, 25 mM Tris [pH 7.5], 150 mM NaCl, 1 mM EDTA, 2% PVPP, 1 mM DTT, 0.2% Nonidet P-40/Igepal and 1 tablet/50 ml cOmplete, EDTA-free Protease Inhibitor Cocktail [Sigma-Aldrich]) for lysing. Protein lysates were cleared through centrifuging samples at 12,000 rpm twice. Resulting supernatant was diluted in 4× Laemmli buffer and boiled at 70°C for 10 min as the final protein extract sample.

For *Arabidopsis*, protein concentration was measured using the Amido black method (Popov et al., 1975). 10 μl of protein sample was diluted in 190 μl water and added with 1 ml Amido black staining solution (90% methanol, 10% acetic acid, 0.005%

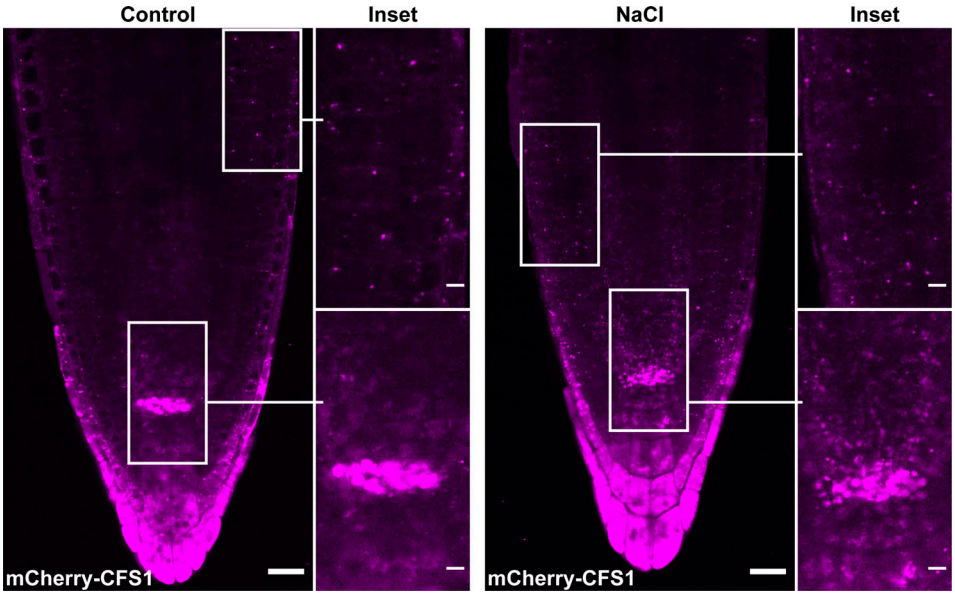

Figure 10. **CFS1 accumulates at the quiescent center cells of *A. thaliana*.** Confocal microscopy images showing that pUBQ::mCherry-CFS1 strongly accumulates at the quiescent center cells of *A. thaliana*. 5-d-old *Arabidopsis* seedlings were incubated in either control or 150 mM NaCl-containing 1/2 MS media for 1 h before imaging. Representative images of three replicates are shown. Area highlighted in the white-boxed region was further enlarged and presented in the inset panel. Scale bars, 20 µm. Inset scale bars, 5 µm.

[w/v] Amido black 10B [Sigma-Aldrich]). Samples were mixed thoroughly and centrifuged at 15,000 rpm for 10 min. After removal of supernatant, pellets were washed with 1-ml washing solution (90% ethanol and 10% acetic acid) and centrifuged at 15,000 rpm for 10 min. Resulting pellets were dissolved in 1 ml 0.2 N NaOH and the corresponding optical density (OD) at 630 nm was measured through a plate reader (Synergy HTX Multi-Mode Microplate Reader; BioTek). Protein concentration (C) was calculated through the formula C = (OD−b)/10a, where a and b were calibrated by the Bovine Serum Albumin (BSA) standard curve of the staining solution. For Marchantia, protein concentration was quantified using Bradford assay (Sigma-Aldrich). Chemiluminescence was acquired through iBright Imaging System (Invitrogen).

For Western blotting, indicated amount of protein was loaded on 4–20% Mini-PROTEAN TGX precast gel (Bio-Rad) and blotted on nitrocellulose using the semi-dry Trans-Blot Turbo Transfer System (Bio-Rad). Protein extract was immunoblotted with either rabbit anti-NBR1 (1:2,000, AS14 2805; Agrisera), rabbit anti-IDH (1:5,000, AS06 203A; Agrisera), rabbit anti-ACT (1:5,000; Agrisera, AS13 2,640), mouse anti-GFP (1:3,000, 11814460001; Roche), or mouse anti-RFP (1:3,000, AB_2631395; Chromotek) antibodies. Images were captured through Chem-iDoc Touch Imaging System (Bio-Rad) or iBright Imaging System (Invitrogen) by developing with SuperSignal West Pico PLUS Chemiluminescent Substrate (Thermo Fisher Scientific). Protein band intensities were quantified through Image Lab 6 (Bio-Rad) as previously described in Stephani et al. (2020).

Protease protection assay

Roughly 5–10 mg of *Arabidopsis* seeds were grown in 6-well plates under continuous light and continuous shaking for 7 d. 7-d-old *Arabidopsis* seedlings were subjected to Torin1 treatment (3 µM for 90 min) for autophagy induction and immediately grinded in GTEN-based buffer (GTEN [10% glycerol, 30 mM Tris [pH 7.5], 150 mM NaCl, 1 mM EDTA [pH 8], 0.4 M sorbitol, 5 mM MgCl2, 1 mM Dithiothreitol [DTT], 100× liquid protease inhibitor cocktail [Sigma-Aldrich], and 1% Polyvinylpolypyrrolidon [PVPP]) in a 3:1 v/w ratio. Afterwards lysates underwent several differential centrifugation steps where each time the supernatant was transferred. Samples were spun for (i) 10 min at 1,000 *g*, to remove cell debris and nuclei; (ii) 10 min at 10,000 *g*, to remove bigger organelles like mitochondria and chloroplasts; (iii) 10 min at 15,000 *g*, to further remove organelles (S3 fraction); and finally (iv) 60 min at 100,000 *g* (S4 and P4 fraction; LaMontagne et al., 2016). Protein concentration in S3 was normalized through Bradford (Sigma-Aldrich) to ensure that equal amount of protein was loaded before ultracentrifugation step. The P4 fraction was dissolved gently in GTEN-based buffer (without PVPP) and was further subjected to 30 ng/µl proteinase K (Sigma-Aldrich) and 1% Triton X-100 treatment for 30 min on ice. The reaction was stopped with 5 mM phenylmethylsulfonyl fluoride (PMSF). Proteins were then precipitated overnight with 0.1% sodium deoxycholate (NaDOC) and 11% trichloroacetic acid (TCA). Resulting pellets were washed twice with 100% acetone and dissolved in 2× Laemmli buffer. Proteins were quantified again through the Amido black method as described above and 5 µg were loaded on the gel.

In vitro pull-down assays

Recombinant proteins were expressed using Rosetta2(DE3) pLysS *E. coli* strain. Bacteria were grown to an OD_{600} of 0.6–0.7 followed by induction with 300 µM IPTG and overnight incubation at room temperature (RT). 50 ml of culture was pelleted

Table 1. ***A. thaliana*** **lines used in this study**

Name	Accession Number	Source or reference
Col-0		
cfs1-2	At3g43230	SALK_024058; Sutipatanasomboon et al. (2017) Sci. Rep.
cfs2-1	At1g29800	SALK_02775; this study
atg5-1	At5g17290	SAIL_129B07L; Thompson et al. (2005) Plant Physiol.
vps23.1-3	At3g12400	SAIL_1233E07_2-4; Nagel et al. (2017) PNAS.
vps23.2-1	At5g13860	SAIL_237G05_3-4; Nagel et al. (2017) PNAS.
cfs1-2 × *cfs2-1*	At3g43230 (CFS1); At1g29800 (CFS2)	This study
pUBQ::mCherry		Geldner et al. (2009) Plant J.
pUBQ::mCherry		This study
pUBQ::GFP-ATG8A	At4g21980	Munch et al. (2015) The Plant Cell.
pUBQ::GFP-ATG8A × *cfs1-2*	At4g21980 (ATG8A); At3g43230 (CFS1)	This study
pUBQ::mCherry-ATG8E	At2g45170	Hu et al. (2020) J. Integr. Plant Biol.
pUBQ::mCherry-ATG8E × *cfs1-2*	At2g45170 (ATG8E); At3g43230 (CFS1)	This study
pUBQ::mCherry-ATG8E × *atg5-1*	At2g45170 (ATG8E); At5g17290 (ATG5)	This study
pCFS1::gCFS1 in *cfs1-2*	At3g43230	Sutipatanasomboon et al. (2017) Sci Rep.
pUBQ::mCherry-CFS1 in *cfs1-2*	At3g43230	This study
pUBQ::mCherry-CFS1^{AIM} in *cfs1-2*	At3g43230	This study
pUBQ::GFP-CFS1 in *cfs1-2*	At3g43230	This study
pUBQ::mScarlett-CFS2 in pUBQ::GFP-CFS1 in *cfs1-2*	At1g29800 (CFS2); At3g43230 (CFS1)	This study
pUBQ::mCherry-CFS1^{FYVE} in pUBQ::GFP-ATG8A × *cfs1-2*	At3g43230 (CFS1); At4g21980 (ATG8A)	This study
pUBQ::mCherry-CFS1^{SYLF} in pUBQ::GFP-ATG8A × *cfs1-2*	At3g43230 (CFS1); At4g21980 (ATG8A)	This study
pUBQ::mCherry-CFS1^{tri} in pUBQ::GFP-ATG8A × *cfs1-2*	At3g43230 (CFS1); At4g21980 (ATG8A)	This study
pUBQ::mCherry-CFS1^{PSAPP} in *cfs1-2*	At3g43230	This study
pUBQ::mCherry-CFS1^{PSAPP} in pUBQ::GFP-ATG8A × *cfs1-2*	At3g43230 (CFS1); At4g21980 (ATG8A)	This study
pUBQ::mCherry-CFS1$^{AIM+PSAPP}$ in *cfs1-2*	At3g43230	This study
pUBQ::mCherry-CFS1$^{AIM+PSAPP}$ in pUBQ::GFP-ATG8A × *cfs1-2*	At3g43230 (CFS1); At4g21980 (ATG8A)	This study
pUBQ::GFP-VPS23A in pUBQ::mCherry-CFS1 in *cfs1-2*	At3g12400 (VPS23A); At3g43230 (CFS1)	This study
pUBQ::GFP-VPS23A in pUBQ::mCherry-CFS1^{PSAPP} in *cfs1-2*	At3g12400 (VPS23A); At3g43230 (CFS1)	This study
pUBQ::VPS23A-mTurquoise2 in pUBQ::GFP-ATG8A × pUBQ::mCherry-CFS1 in *cfs1-2*	At3g12400 (VPS23A); At4g21980 (ATG8A); At3g43230 (CFS1)	This study
pUBQ::VPS23A-mTurquoise2 in pUBQ::mCherry-CFS1^{PSAPP} in pUBQ::GFP-ATG8A × *cfs1-2*	At3g12400 (VPS23A); At4g21980 (ATG8A); At3g43230 (CFS1)	This study
pUBQ::mCherry-MpCFS1 in pUBQ::GFP-ATG8A × cfs1-2	Mp3g11370 (CFS1); At4g21980 (ATG8A); At3g43230 (CFS1)	This study
p35S::GFP-FREE1 in pUBQ::mCherry-CFS1 in *cfs1-2*	At1g20110 (FREE1); At3g43230 (CFS1)	This study
atg5-1 × pUBQ::mCherry-CFS1 in *cfs1-2*	At5g17290 (ATG5); At3g43230 (CFS1)	This study
pUBQ::GFP-ATG8A × pUBQ::mCherry-CFS1 in *cfs1-2*	At4g21980 (ATG8A); At3g43230 (CFS1)	This study
pUBQ::GFP-ATG8A × pUBQ::mCherry-CFS1^{AIM} in *cfs1-2*	At4g21980 (ATG8A); At3g43230 (CFS1)	This study
pUBQ::mCherry-ATG8E × pUBQ::GFP-CFS1 in *cfs1-2*	At2g45170 (ATG8E); At3g43230 (CFS1)	This study
pVPS3::mGFP-VPS3	At1g22860	Takemoto et al. (2018) PNAS.
pVPS3::mGFP-VPS3 × pUBQ::mCherry-CFS1 in *cfs1-2*	At1g22860 (VPS3); At3g43230 (CFS1)	This study
pVPS39::VPS39-mGFP	At4g36630	Takemoto et al. (2018) PNAS.
pVPS39::VPS39-mGFP × pUBQ::mCherry-CFS1 in *cfs1-2*	At4g36630 (VPS39); At3g43230 (CFS1)	This study
pUBQ::YFP-VAMP711	At4g32150	Geldner et al. (2009) Plant J.

Table 1. ***A. thaliana* lines used in this study (*Continued*)**

Name	Accession Number	Source or reference
pUBQ::YFP-VAMP711 × pUBQ::mCherry-CFS1 in *cfs1-2*	At4g32150 (VAMP711); At3g43230 (CFS1)	This study
p35S::NAG1-EGFP	At4g38240	Grebe et al. (2003) Curr Biol.
p35S::NAG1-EGFP × pUBQ::mCherry-CFS1 in *cfs1-2*	At4g38240(NAG1); At3g43230 (CFS1)	This study
pa1::VHA-a1-GFP	At2g28520	Dettmer et al. (2006) The Plant Cell.
pa1::VHA-a1-GFP × pUBQ::mCherry-CFS1 in *cfs1-2*	At2g28520 (VHA-a1); At3g43230 (CFS1)	This study
pRPS5a::GFP-ARA7	At4g19640	Richter et al. (2007) Nature.
pRPS5a::GFP-ARA7 × pUBQ::mCherry-CFS1 in *cfs1-2*	At4g19640 (ARA7); At3g43230 (CFS1)	This study
pPIN::PIN2-GFP	At5g57090	Xu and Scheres (2005) The Plant Cell.
pPIN2::PIN2-GFP × *cfs1-2*	At5g57090 (PIN2); At3g43230 (CFS1)	This study
pNBR1::TagRFP-NBR1	At4g24690	Provided by Alyona Minina
pNBR1::NBR1-GFP	At4g24690	Hafrén et al. (2017) PNAS.
pNBR1::NBR1-GFP × pUBQ::mCherry-CFS1 in *cfs1-2*	At4g24690 (NBR1); At3g43230 (CFS1)	This study
pUBQ::mCherry-ATG8E × pNBR1::NBR1-GFP	At2g45170 (ATG8E); At4g24691 (NBR1)	This study
pUBQ::GFP-ATG11	At4g30790	Li et al. (2014) The Plant Cell.
pUBQ::GFP-ATG11 × pUBQ::mCherry-CFS1 in *cfs1-2*	At4g30790 (ATG11); At3g43230 (CFS1)	This study
pALIX::GFP-3Gly-ALIX	At1g15130	Cardona-López et al. (2015) The Plant Cell.
pALIX::GFP-3Gly-ALIX × pUBQ::mCherry-CFS1 in *cfs1-2*	At1g15130 (ALIX); At3g43230 (CFS1)	This study
pVPS23A::VPS23A-TagRFP	At3g12400	Nagel et al. (2017) PNAS.
pVPS23A::VPS23A-TagRFP × pUBQ::GFP-CFS1 in *cfs1-2*	At3g12400 (VPS23A); At3g43230 (CFS1)	This study
pVPS23A::VPS23A-TagRFP × pUBQ::GFP-ATG8A	At3g12400 (VPS23A); At4g21980 (ATG8A)	This study
pUBQ::GFP-ATG8A × *vps23.1-3*	At4g21980 (ATG8A); At3g12400 (VPS23A)	This study
pUBQ::GFP-ATG8A × *vps23.2-1*	At4g21980 (ATG8A); At3g13860 (VPS23B)	This study

and resuspended in 5 ml of EDTA-free buffer (10% Glycerol, 25 mM Tris/HCl pH 7.5, 150 mM NaCl, 0.1 mM TCEP, 0.1% Nonidet P-40/Igepal, 10 µM $ZnCl_2$ and 1 tablet/50 ml cOmplete, EDTA-free Protease Inhibitor Cocktail [Sigma-Aldrich]) containing 10× FastBreak Cell Lysis reagent (Promega) and Benzonase. Cells were broken open through incubation on a spinning wheel at room temperature for 10–20 min. Lysates were clarified through centrifugation at 15,000 rpm at 4°C for 10 min. For proteins expressed in planta, 40 seeds per genotype were grown. Frozen plant tissue was homogenized as described above and 700 µl EDTA-free buffer containing 2% PVPP was added. Lysates were centrifuged twice at 15,000 rpm at 4°C for 10 min. 100 µl of *E. coli* lysate and 400 µl of plant lysate were mixed and incubated with 10 µl of equilibrated Glutathione High-Capacity Magnetic Agarose Beads (Sigma-Aldrich) for 1 h at 4°C on a spinning wheel. For peptide competition, peptides were added to a final concentration of 200 µM as described in Stephani et al. (2020). Beads were washed five times with EDTA-free buffer, without TCEP, eventually eluted in 50 µl 2× Laemmli buffer and boiled for 10 min at 95°C. Gels were loaded with 15 µl of sample per well. Anti-GST HRP conjugate (Sigma-Aldrich) was used in a 1:2,000 dilution.

In vivo co-immunoprecipitation

For co-immunoprecipitation, 40 seeds per genotype were grown in 1/2 MS media for 7 d. Proteins were extracted by adding 800 µl of EDTA-free buffer with 2% PVPP. Lysates were cleared by centrifugation at 15,000 rpm at 4°C for 10 min twice. 500 µl supernatant was incubated with 20 µl RFP-Trap Magnetic Agarose beads (Chromotek) for 1 h. Beads were washed three and five times with EDTA-free buffer, without TCEP, before and after incubation with lysate, respectively. Beads were eluted in 50 µl 2× Laemmli buffer, boiled for 10 min at 95°C and subjected to Western blot analysis with indicated antibodies.

Affinity purification-mass spectrometry (AP-MS)

For affinity purification, S4, P4, and P4 + proteinase K samples described in Fig. 1 A were prepared as same as the method described above for the protease protection sample preparation, except that 0.1% Nonidet P-40/Igepal was added and samples were incubated for 1 h with 40 µl RFP-Trap Magnetic Agarose beads (Chromotek) after proteinase K treatment. Mass spectrometry sample preparation and measurement were performed as previously described in Stephani and Picchianti et al., 2020 (Stephani et al., 2020).

Mass spectrometry data processing

The total number of MS/MS fragmentation spectra was used to quantify each protein (Table S1). The data matrix of spectral count values (Table S2) was submitted to a negative-binomial test using the R package IPinquiry4 (https://github.com/hzuber67/IPinquiry4) that calculates fold change and P values

Table 2. **List of plasmids used in this study**

Name	Accession number	Expression system	Backbone	Additional information	Source or reference
pUBQ::mCherry		*A. thaliana*	pGGZ003		This study
pUBQ::mCherry-CFS1	At3g43230	*A. thaliana*	pGGZ003		This study
pUBQ::GFP-CFS1	At3g43230	*A. thaliana*	pGGZ003		This study
pUBQ::mCherry-CFS1^{AIM}	At3g43230	*A. thaliana*	pGGZ003	WLNL267ALNA	This study
pUBQ::mCherry-CFS1^{FYVE}	At3g43230	*A. thaliana*	pGGZ003	RHHCR195AHACA	This study
pUBQ::mCherry-CFS1^{SYLF}	At3g43230	*A. thaliana*	pGGZ003	K282A, R288A, K320A	This study
pUBQ::mCherry-CFS1^{tri}	At3g43230	*A. thaliana*	pGGZ003	RHHCR195AHACA (FYVE); K282A, R288A, K320A (SYLF); WLNL267ALNA (AIM)	This study
pUBQ::mCherry-CFS1^{PSAPP}	At3g43230	*A. thaliana*	pGGZ003	PSAPP145AAAAA (PSAPP)	This study
pUBQ::mCherry-CFS1$^{AIM+PSAPP}$	At3g43230	*A. thaliana*	pGGZ003	PSAPP145AAAAA (PSAPP); WLNL267ALNA (AIM)	This study
pUBQ::mScarlett-CFS2	At1g29800	*A. thaliana*	pGGZ003		This study
pUBQ::mCherry-MpCFS1	Mp3g11370	*A. thaliana*	pGGZ003		This study
p35S::GFP-FREE1	At1g20110	*A. thaliana*	pMDC43		Provided by Pedro L. Rodriguez
pUBQ::GFP-VPS23A	At3g12400	*A. thaliana*	pGGZ003		
pUBQ::VPS23A-mTurquoise2	At3g12400	*A. thaliana*	pGGZ003		
GST		*E. coli*			Stephani et al. (2020)
GST-ATG8A	At4g21980	*E. coli*			Stephani et al. (2020)
GST-ATG8A^{ADS}	At4g21980	*E. coli*		YL50AA	Stephani et al. (2020)
GST-ATG8B	At4g04620	*E. coli*			Stephani et al. (2020)
GST-ATG8C	At1g62040	*E. coli*			Stephani et al. (2020)
GST-ATG8D	At2g05630	*E. coli*			Stephani et al. (2020)
GST-ATG8E	At2g45170	*E. coli*			Stephani et al. (2020)
GST-ATG8F	At4g21980	*E. coli*			Stephani et al. (2020)
GST-ATG8G	At3g60640	*E. coli*			Stephani et al. (2020)
GST-ATG8H	At3g06420	*E. coli*			Stephani et al. (2020)
GST-ATG8I	At3g15580	*E. coli*			Stephani et al. (2020)
pEF::GFP-ATG8A	Mp1g21590	*M. polymorpha*	pMpGWB303		
pEF::GFP-ATG8B	Mp5g05930	*M. polymorpha*	pMpGWB303		This study
pEF::mScarlet-CFS1	Mp3g11370	*M. polymorpha*	pGGSUN		This study
pMpGE010_CFS1g1g2	Mp3g11370	*M. polymorpha*	pMpGE010		This study

using the quasi-likelihood negative binomial generalized log-linear model implemented in the edgeR package. The pairwise comparisons were the following: (i) mCherry P4 vs. mCherry-ATG8E P4, (ii) mCherry-ATG8E S4 vs. mCherry-ATG8E P4, and (iii) mCherry-ATG8E P4 + protease K vs. mCherry-ATG8E P4. In each case, comparisons were obtained from two independent biological replicates. Only proteins with log(FC) > 0 and P value <0.05 were considered to build the Venn diagram in Fig. 1 B. Venn diagram was built using the Venny 2.1.0 online tool (https://bioinfogp.cnb.csic.es/tools/venny/index.html) and then redrawn manually. Analysis results are shown in Table S3. The mass spectrometry proteomics data have been deposited to the ProteomeXchange Consortium through the PRIDE (Perez-Riverol et al., 2019) partner repository.

Yeast two hybrid screening

The screening was performed by Hybrigenics against the *Arabidopsis* cDNA library. Results are shown in Table S4.

Preparation of *A. thaliana* samples for confocal microscopy

For all experiments except PIN2 endocytosis imaging, *Arabidopsis* seeds were vapor-phase sterilized by chlorine (generated by a 10:1 mixture of 13% sodium hypochlorite and 36% HCl) for 15 min and were subsequently stored at 4°C for 2 d for vernalization. Vernalized seeds were spread on 1/2 MS media plates

Table 3. **Primer and synthetic sequences used in this study for genotyping, cloning, and mutagenesis**

Name	Sequence	Additional information	Source or reference
LBb1.3 (SAIL)	5′-ATTTTGCCGATTTCGGAAC-3′	For genotyping	SIGnAL. 2017.
cfs1-2 (LP)	5′-GCTCGACTAAGAACAGCATGC-3′	For genotyping	SIGnAL. 2017.
cfs1-2 (RP)	5′-TACATGGGTTTGGATGAGCG-3′	For genotyping	This study
cfs2-1 (LP)	5′-TGGTGAGTTTTACGCTTACCG-3′	For genotyping	SIGnAL. 2017.
cfs2-1 (RP)	5′-TTGGTCCATCAAATAAGGCTG-3′	For genotyping	SIGnAL. 2017.
LB3 (SALK)	5′-AATTTCATAACCAATCTCGATACAC-3′	For genotyping	Nagel et al. (2017) PNAS.
vps23.1-3 (LP)	5′-AACTTTGGACTTTGGAACATGTCCACTCCTTACA-3′	For genotyping	Nagel et al. (2017) PNAS.
vps23.1-3 (RP)	5′-AGGAACCATCATCACACGCATAGCCACAG-3′	For genotyping	Nagel et al. (2017) PNAS.
vps23.2-1 (LP)	5′-TCGTCATCTGTCGTCGTCTTCAAG-3′	For genotyping	Nagel et al. (2017) PNAS.
vps23.2-1 (RP)	5′-GTATCACGAATGCAACCTAGCTGCAATGGAAG-3′	For genotyping	Nagel et al. (2017) PNAS.
CFS1_part1_fwd	5′-AACAGGTCTCAGGCTCTATGGCTACTCTCAACGGAAA-3′	For cloning CDS, part 1	This study
CFS1_part1_rev	3′-AACAGGTCTCACGAGATATTACCAGACCAGT-5′	For cloning CDS, part 1	This study
CFS1_part2_fwd	5′-AACAGGTCTCTCTCGTAGACCAGACGGGTCATGG-3′	For cloning CDS, part 2	This study
CFS1_part2_rev	3′-AACAGGTCTCACTGACGGGCGCAAACGAGCATA-5′	For cloning CDS, part 2	This study
CFS2_part1_fwd	5′-ACCCTCTGCCATCTCTTCATTTGGT-3′	For cloning CDS, part 1	This study
CFS2_part1_rev	3′-AACAGGTCTCAGGGTGGTGACCAGGAGCCATCATCT-5′	For cloning CDS, part 1	This study
CFS2_part2_fwd	5′-TCCTGGTCTCCACCCTCTGC-3′	For cloning CDS, part 2	This study
CFS2_part2_rev	3′-AACAGGTCTCACTGAGTCTTCAGACAATGGAGAAATTGCCGGTGACCGAACAGTTTCA-5′	For cloning CDS, part 2	This study
MpCFS1	5′-AACAGGTCTCAGGCTCTATGGAGGAGAATGAGTACAACGGACTCTGCCGGACAGATACCG TCGAAGAGGAGAAATATTCTGAGAAAAGTGGTCGATACAAGGGTGTCATTCGTGATGAGA AACCCACTTGTGCTGTCTGTATGGAAGTTCTAGGAACTCATGGTGGGCCTGCATCTCTCGCCT GCGGCCACAATGGATGTCTCGAGTGCTTACAACAGGTCCAGATGCACTCGAACATGCCTG TCTGTCCTCTTTGTCGTACACCCTTTGATGGAGATATCAATTTGGCCCCGAACTTAGACTTAC GGGCTGCACTCGAGTGTGCCGAACAAGCCGCCGCAGCTGCGCGAGCTGCCGAGGATCGGA GGATGGTTGCTGTGTACAATTCTAAGCAGATTGTGAAGCCGAGCAGAGATAAAACCACCA GGTCACACCAACAGCGATTCATCTATGATTTGCCCTATCCTGAGGAAACAGGACCTTGGATTC CGGTGTCAATTCCGCCCAAGGGCTCGAAGGACTTTGATGGGCCTGACATGGGCAGTATAT ATGGAGATGTTTTTCCGGAACCCTTGATGACAGTGGGTGTCCGACAAGGGGCTCCGGACA TCAACCTTTGGAATGTTTTGAGTGGATTTCTTGCAATCATATCGGGAAGGGGTGGTACACAAA GCCAGAATTTCCACTCACAGTCCGGTTATTCTGATAGTAGAACATCTACGTACTACCGAGAAA GTTCTGGTCATGGAAGATCTAACAGCAATTCATGGAGTGGGAATTTACACAGGCCAAGTG CACCTCCACTGCTCCTTGGCACTAATGATTCCGATGTCAGCCTCATACGAGCTATTCTCGAAG CAGAGCCCCCGGACTGGATGCCTGACAGTTCGGCCCTTTCCTGTATGCTCTGTGGCGCTG CCTTTAGGGCAATAACTTGTGGAAGACATCATTGTCGGTTCTGCGGGGGAATTTTTTGTAGGA GATGCTCTTCCGGGAGATGTCTTTTACCTGTGAAGTTCCGGGACAGGGACCCGAAAAGAG TTTGCGATACCTGCTGGGAGAGACTGGAACCTGTACAGAAGAATCTTGCCGACCGAGTTA GTAATGCAGCACAAATCGCTCTACATGATGTGACTGACTTCAGCTGTATGACAGCATGGATAA ACAGTCCACTTGGGCTTTCGATGGAGCAAGAAATTTTTAAGGCAACAAATGCCTTGCGTAGCT ATTTGGAGATTGGAGTACTCAAACCAGAAAGATCCATCCCCGACGCTGTTCTGAAAGGAG CCTGTGGCTTGGCAATCATCACAGTGTTCAAGGCCGGGTTTATGATGACCTACAAATTTGGTA CGGGATTGGTTGTTTCACGGAGGAGAGATGGGTCCTGGTCTGCACCATCAGCTATCGCAT CGTGTGGTCTGGGATGGGGAGCTCAGGCTGGTGGGGAGCTGACTGATTTCATCATAGTCC TAAGGACAGAAGAAGCTGTGAAGGCCTTTAGTGGGAGAGTACATTTGTCAGTTGGTGCCG GCCTAAGCGTCGCTGCCGGACCTGTTGGAAGAGCTGCGGAAGCAGATCTTAGAGCTGGTG ATGGGGGTACTGCAGCTTGTTACACTTACAGTCGAAGCAAAGGAGCGTTCGTCGGATGTT CAATCGAAGGCAATGTTGTGGCGACACGGTCCTCCGCCAACATGCGCTTTTATGGAGAAT CTGGTGTCACTGCAGTCGACATTCTTCTTGGAGACGTTCCAAGACCTCGGGCTGCAGCTC CGCTTTATAGTGCTTTGGATGAACTTTTTGTAAAGGTGGACACATCAGTGAGACCTGTT-3′	For cloning CDS	This study
MpATG8A_fwd	5′-AACAGGTCTCAGGCTCCATGGGAGAGAGCGAGTTTCAAT-3′	For cloning CDS	This study

Table 3. **Primer and synthetic sequences used in this study for genotyping, cloning, and mutagenesis (*Continued*)**

Name	Sequence	Additional information	Source or reference
MpATG8A_rev	3′-AACAGGTCTCACTGATCAGCCAACGAGGGCGAC-5′	For cloning CDS	This study
MpATG8B_fwd	5′-AACAGGTCTCAGGCTCCATGACGGGGAAGAGGAGTTC-3′	For cloning CDS	This study
MpATG8B_rev	3′-AACAGGTCTCACTGACTAAACCAGAGGAAGGCAATTG-5′	For cloning CDS	This study
gRNA_MpCFS1_1_fwd	5′-CTCGAAGTTCTAGGAACTCATGGT-3′	For CRISPR/Cas9	This study
gRNA_MpCFS1_1_rev	5′-AAACACCATGAGTTCCTAGAACTT-3′	For CRISPR/Cas9	This study
gRNA_MpCFS1_2_fwd	5′-CTCGACTTCAGCTGTATGACAGCA-3′	For CRISPR/Cas9	This study
gRNA_MpCFS1_2_rev	5′-AAACTGCTGTCATACAGCTGAAGT-3′	For CRISPR/Cas9	This study
CFS1_mutAIM_fwd	5′-TGGACTTGCTCAAGAGGAGCGTTGAATGCCCCTGTTGGTCTATCCAT-3′	For site-directed mutagenesis	PrimerX. 2017.
CFS1_mutAIM_rev	3′-ATGGATAGACCAACAGGGGCATTCAACGCTCCTCTTGAGCAAGTCCA-5′	For site-directed mutagenesis	PrimerX. 2017.
CFS1_mutFYVE_fwd	5′-GGTGCTCATGCTTGTGCTTTCTGCGGAGGGATATTTTGTAGA-3′	For site-directed mutagenesis	PrimerX. 2019.
CFS1_mutFYVE_rev	3′-GAAAGCACAAGCATGAGCACCACACGTAATTGCAGTAAAAGG-5′	For site-directed mutagenesis	PrimerX. 2019.
CFS1_mutSYLF	5′-AGTCTCCATGGAAGATGAGATATACGCAGCTGCTAATACGTTGGCAGGTTACTGCCAGGT AGCAAGACTAGACCCTGAGAAATCCATACCGCATGCTGTTCTTAGTCGAGCTAAAGGTTTGGC AATCATAACGGTTGCCGCTGCTGGGGCTTTACTGTCATACAAACTCGGGACTGGTCTGGTAAT ATCTCGTAGACCAGACGGGTCATGGTCTGCTCCATCTGCCATACTATCAGTAGGTCTTGGATG GGGTGCACAGATTGGAGGTGAGTTGATGGACTTCATAATAGTGCTTCATGATGTGAAAGC CGTGAAGACATTCTGCAGCAGAATGCACTTCTCTCTAGGCGCGGGATGCAGTGCAGCAGC AGGGCCTATCGGGAGAGTGTTGGAGGCTGACCTTCGAGCTGGTGACAAAGGCTCTGGTGT CTGCTATACTTACAGCCGCAGCAAAGGGGCATTTGTGGGAGTATCTCTAGAGAGACT-3′	For mutagenesis	This study
CFS1_mutPSAPP_fwd	5′-CATTCGTCTGTTTACATAGCGGCTGCTGCGGCTCTACTTGAACCTAGTG-3′	For site-directed mutagenesis	PrimerX. 2018.
CFS1_mutPSAPP_rev	3′-CACTAGGTTCAAGTAGAGCCGCAGCAGCCGCTATGTAAACAGACGAATG-5′	For site-directed mutagenesis	PrimerX. 2018.
VPS23A_fwd	5′-AACAGGTCTCAGGCTCTATGGTTCCCCCGCCGTCTAATCC-3′	For cloning CDS, part 1	This study
VPS23A-Bsa1_rev	3′-AACAGGTCTCAGAAACGAGGCCAGAAGGAGTGACAT-5′	For cloning CDS, part 1	This study
VPS23A-Bsa1_fwd	5′-AACAGGTCTCATTTCTCTTCCGTACCTTCAGAATTGG-3′	For cloning CDS, part 2	This study
VPS23A_rev	3′-AACAGGTCTCACTGATGAATGTAACCTACCTGCGATGGCTG-5′	For cloning CDS, part 2	This study

(+1% plant agar [Duchefa]) and grown at 21°C at 60% humidity under LEDs with 50 mM/m^{2}s a and a 16 h light/8 h dark photoperiod for 5 d. Plates were placed vertically to let the roots elongate along the media surface. 5-d-old seedlings were placed in 1/2 MS media and treated with salt or chemicals as indicated in each experiment before confocal imaging. For nitrogen starvation, 1/2 MS media was replaced by nitrogen-deficient 1/2 MS media. For PIN2 endocytosis imaging, *Arabidopsis* seeds were vapor-phase sterilized by chlorine (generated by a 25:1 mixture of 2.6% sodium hypochlorite and 36% HCl) for 3–4 h. The sterilized seeds were spread on 1/2 MS media plates (+1% plant agar [Duchefa]). The plated seeds were subsequently stored at 4°C for 2 d for vernalization. Vernalized seeds were then grown at 21°C at 60% humidity under LEDs with 50 mM/m^{2}s a and a 16 h light/8 h dark photoperiod for 5 d. Plates were placed vertically to let the roots elongate along the media surface. 5-d-old *Arabidopsis* seedlings were grown on 1/2 MS media plates under light or 6-h dark conditions before imaging.

For confocal microscopy, *Arabidopsis* seedlings were placed on a microscope slide with water or water with 0.002 mg/ml propidium iodide and covered with a coverslip. The epidermal cells of root meristem zone were used for CFS1 and FM 4-64 colocalization imaging, PIN2 endocytosis imaging, or vacuolar morphology imaging. The epidermal cells of root elongation zone were used for confocal imaging in Fig. 3 D and time-lapse imaging in Videos 1, 2, and 3. For all other experiments, the epidermal cells of root transition zone were used for image acquisition.

Preparation of *M. polymorpha* samples for confocal microscopy

The *M. polymorpha* asexual gemmae were incubated in 1/2 Gamborg B5 media for 2 d before imaging. 2-d-old *M. polymorpha* thalli were placed on a microscope slide with water and covered with a coverslip. The meristem region was used for image acquisition.

Confocal microscopy

All images except for Airyscan imaging, PIN2 endocytosis imaging and time-lapse imaging were acquired by an upright point laser scanning confocal microscope ZEISS LSM800 Axio Imager.Z2 (Carl Zeiss) equipped with high-sensitive GaAsP detectors (Gallium Arsenide), a LD C-Apochromat 40X objective lens (numerical aperture 1.1, water immersion), and ZEN software (blue edition, Carl Zeiss). For Fig. 10, a Plan-Apochromat 20X objective lens (numerical aperture 0.8, dry) is used instead of the 40X one. GFP and BCECF-AM fluorescence were excited at 488 nm and detected between 488 and 545 nm. TagRFP, mCherry, and mScarlet fluorescence were excited at 561 nm and detected between 570 and 617 nm. FM 4-64 fluorescence was excited at 561 nm and detected between 656 and 700 nm (Fig. S4 A) or 576 and 700 nm. For Z-stack imaging, interval between the layers was set as 1 µm. For each experiment, all replicate images were acquired using identical confocal microscopic parameters. Confocal images were processed with Fiji (version 1.52, Fiji) and Imaris (version 9.0.1, BITPLANE). For Airyscan imaging, Z-stack images were acquired by an inverted point laser scanning confocal microscope ZEISS LSM980 Axio Observer.Z1/7 (Carl Zeiss) equipped with a hexagonal GaAsP detector Airyscan II (Gallium Arsenide), a plan-Apochromat 63x objective lens (numerical aperture 1.40, oil immersion), and ZEN software (blue edition, Carl Zeiss) under room temperature. GFP fluorescence was excited at 488 nm and detected between 495 and 550 nm. TagRFP fluorescence was excited at 561 nm and detected between 573 and 627 nm. Interval between layers was set as 0.15 µm. Original images were deconvoluted by ZEN software using the default mode (blue edition, Carl Zeiss). Deconvoluted images were processed with Fiji (version 1.52, Fiji).

For PIN2 endocytosis imaging, images were acquired by an inverted Zeiss microscope AxioObserver Z1 (Carl Zeiss) equipped with a spinning disk module CSU-W1-T3 (Yokogawa), a Prime 95B camera (http://www.photometrics.com/), a Plan-Apochromat 63× objective lens (numerical aperture 1.4, oil immersion), and the Metamorph acquisition software (Molecular Devices). GFP was excited with a 488 nm laser (150 mW) and was detected by a 525/50 nm BrightLine single-band bandpass filter (Semrock). Confocal images were processed with Fiji (version 1.52, Fiji).

For time-lapse imaging, images were acquired by an Andor Dragonfly confocal platform (Andor) equipped with a spinning disc confocal microscope (Nikon Ti2E inverted microscope). A 40X objective lens (numerical aperture 1.15, water immersion) was installed for acquiring images. The pinhole disk pattern was set as 40 µm. Green fluorescence signals were excited by 488 nm laser and detected through an Andor Zyla sCMOS camera. Red fluorescence signals were excited by 561 nm laser and detected through an Andor iXon 888 EMCCD camera. The two cameras acquired the image at the same time. For time-lapse mode imaging, the total imaging time is 60 s, with an interval of 1 s. Confocal images were processed with Fiji (version 1.52, Fiji).

Table 4. ***M. polymorpha*** **lines used in this study**

Name	Accession Number	Source or reference
Tak-1		
pEF::GFP-ATG8A	Mp1g21590	This study
cfs1 in pEF::GFP-ATG8A	Mp3g11370 (CFS1); Mp1g21590 (ATG8A)	This study
pEF::mScarlet-CFS1 in pEF::GFP-ATG8A	Mp3g11370 (CFS1); Mp1g21590 (ATG8A)	This study
pEF::GFP-ATG8B	Mp5g05930	This study
cfs1 in pEF::GFP-ATG8B	Mp3g11370 (CFS1); Mp5g05930 (ATG8B)	This study
pEF::mScarlet-CFS1 in pEF::GFP-ATG8B	Mp3g11370 (CFS1); Mp5g05930 (ATG8B)	This study

Image processing and quantification

Mander's colocalization analyses were performed by Fiji (version 1.52, Fiji). Confocal images were background-subtracted with 25 pixels of rolling ball radius. Mander's coefficients M1 and M2 were calculated through JACoP plugin (Bolte and Cordelières, 2006). Thresholds in JACoP plugin settings were adjusted according to the puncta signals in original confocal images.

Puncta quantification was performed by Fiji (version 1.52, Fiji). Z-stack images (at least five layers) were background-subtracted with 25 pixels of rolling ball radius. Each Z-stack image was subsequently thresholded using the MaxEntropy method and was converted to an 8-bit grayscale image. Threshold values were adjusted according to the puncta signals in original confocal images. The number of puncta in thresholded images was counted by the Analyze Particles function in Fiji. For all puncta quantification, puncta with the size between 0.10 and –4.00 µm^2 were counted.

Imaris (version 9.0.1, BITPLANE) was used for 3D construction of the vacuole structure. Default settings were used for 3D construction while the surface signals were smoothed with a surface detail of 0.25 µm.

TEM

For TEM samples preparation, high-pressure freezing, freeze substitution, resin embedding, and ultramicrotomy were performed as described before (Ma et al., 2021; Kang, 2010; Wang et al., 2017). Briefly, 7-d-old *Arabidopsis* seedlings were incubated in 150 mM NaCl or 50 µM DNP for 1 h and were then rapidly frozen with an EM ICE high-pressure freezer (Leica Microsystems).

For Epon resin-embedded samples, the samples were freeze-substituted in 2% OsO_4 with acetone at –80°C for 24 h and were then slowly warmed up to room temperature over 48 h. Excess OsO_4 was removed by rinsing with acetone at room temperature. Root samples were separated from planchettes and embedded in Embed-812 resin (cat. no. 14120; Electron Microscopy Sciences), and the resin was polymerized at 65°C. Ultrathin (100 nm) sections from the samples were collected on copper slot grids coated with formvar.

For immuno-gold labeling samples, frozen specimens were freeze-substituted in anhydrous acetone containing 0.25% glutaraldehyde and 0.1% uranyl acetate at −80°C for 24 h and were slowly warmed up to −45°C. After rinsing with precooled acetone, the cells were embedded in Lowicryl HM20 resin at −45°C and the resin was polymerized by ultraviolet illumination. Ultrathin (100 nm) sections from the samples were collected on nickel slot grids coated with formvar. The sections were probed with rabbit anti-ATG8 (Agrisera), rabbit anti-RFP (Abcam), or chicken anti-GFP polyclonal primary antibodies (Abcam) and gold particles (6, 10 nm) conjugated secondary antibodies (Ted Pella). Sections were post-stained and examined with a Hitachi 7400 TEM (Hitachi-High Technologies) operated at 80 kV.

For the quantification of immuno-gold labeling samples, ∼900 gold particles in 50 TEM images from 8 TEM sections (5–10 micrographs per section) were grouped into autophagosomes, cytosol, or other organelles according to their locations. The sections were collected from five individual plastic-embedded *Arabidopsis* roots with three times of replicates for cryo-fixation and sample embedding.

Statistical analyses

All quantification analyses and statistical tests were performed with GraphPad Prism 8 software. F-test was used to check whether the variances were significantly different ($P < 0.05$). For comparing the significance of differences between two experimental groups, Student's *t* tests were performed as indicated in each experiment. The significance level of differences between two experimental groups was marked as *, $P < 0.05$; **, $P < 0.01$; ***, $P < 0.001$; ns, not significant. For comparing the significance of differences between multiple experimental groups, one-way ANOVA was performed as indicated in each experiment.

For PIN2 endocytosis qualitative quantification, the *Arabidopsis* seedling with at least five root epidermal cells that contain visible PIN2-GFP in the vacuole is considered as the one with high PIN2 endocytic activities.

Phylogenic tree analysis

Coding sequences of CFS1 and CFS2 homologs were obtained using the BLAST tool against representative species of different plant lineages in Phytozome (Goodstein et al., 2012). The tree was inferred from a 2283-nt-long alignment using the maximum likelihood method and Tamura-Nei model as implemented by MEGA X (Tamura and Nei, 1993; Kumar et al., 2018). 100 bootstrap method and a discrete Gamma distribution were used to model evolutionary rate differences among sites (5 categories [+G, parameter = 0.8072]; Felsenstein, 1985). Best-scoring ML tree (−98686.19) is shown with purple circles indicating bootstrap values above 80 on their respective clades. The tree is represented using Interactive Tree Of Life (iTOL) v4 (Letunic and Bork, 2019).

Homology modeling

Cartoon representations of AtCFS1 structure and prediction of AtCFS1-VPS23A heterocomplex formation were generated by homology modeling using AlphaFold2 (Jumper et al., 2021) as implemented by ColabFold (Mirdita et al., 2022).

Online supplemental material

Fig. S1 shows differential centrifugation coupled to AP-MS revealed CFS1 as an autophagosome-associated protein in *A. thaliana*. Fig. S2 shows that CFS2 does not play a role in autophagic flux. Fig. S3 shows functional characterization of CFS1-ATG8 interaction. Fig. S4 shows AIM between the FYVE and SYLF domains of CFS1 is conserved in plants. Fig. S5 shows CFS1 does not colocalize with VPS3, VPS39, or VAMP711, but partially colocalizes with FREE1 and ALIX. Source Data files include the uncropped blots used in the corresponding figures. Table S1 shows MS dataset that is used for analysis in Fig. 1. Table S2 shows spectral count of the mass spec data used in Fig. 1. Table S3 shows the final list of proteins identified in analysis described in Fig. 1. Table S4 shows yeast two hybrid dataset. Video 1 shows ATG8-CFS1 co-movement. Video 2 shows NBR1-CFS1 co-movement. Video 3 shows CFS1-VPS23 co-movement. Video 4 shows autophagosome movement from one cell to another.

Data availability

All the raw images, blots, and replicates associated with figures are uploaded to the Zenodo server and can be accessed under the DOI: doi.org/10.5281/zenodo.7139130 and doi.org/10.5281/zenodo.7139412. Proteomics data are available via ProteomeXchange with identifier PXD031787.

Acknowledgments

We thank Suayip Üstün, Karin Schumacher, Erika Isono, Gerd Juergens, Takashi Ueda, Daniel Hofius, and Liwen Jiang for sharing published materials.

We acknowledge funding from Austrian Academy of Sciences, Austrian Science Fund (FWF, P 32355, P 34944), Austrian Science Fund (FWF-SFB F79), Vienna Science and Technology Fund (WWTF, LS17-047) to Y. Dagdas; Austrian Academy of Sciences DOC Fellowship to J. Zhao, Marie Curie VIP2 Fellowship to J.C. De La Concepcion and M. Clavel; Hong Kong Research Grant Council (GRF14121019, 14113921, AoE/M-05/12, C4002-17G) to B.-H. Kang. We thank Vienna Biocenter Core Facilities (VBCF) Protein Chemistry, Biooptics, Plant Sciences, Molecular Biology, and Protein Technologies. We thank J. Matthew Watson and members of the Dagdas lab for the critical reading and editing of the manuscript.

The authors declare no competing financial interests.

Author contributions: J. Zhao performed microscopy experiments, flux measurements, phenotypic plate assays, and in vivo pull-down assays, prepared figures, and wrote the draft. M.T. Bui generated *Arabidopsis* lines, performed flux measurements, protease protection assays, phenotypic plate assays, and AP-MS experiments, and wrote the draft. J. Ma performed electron microscopy experiments and mitophagy flux assays, prepared figures, and wrote the draft. F. Künzl generated *Arabidopsis* lines. L. Picchianti performed in vitro pull-down assays and drew the model. J.C. De La Concepcion performed

phylogenetic analysis and Alphafold models, and wrote the draft. Y. Chen contributed to protease protection assays. S. Petsangouraki contributed to phenotypic characterization experiments. A. Mohseni, M. García-Leon, and M.S. Gomez performed the Marchantia-related experiments. C. Giannini performed the time-lapse imaging experiments. D. Gwennogan performed the PIN2 endocytosis experiments. R. Kobylinska performed the AP-MS experiments. M. Clavel performed the IP-MS experiments, analyzed data, prepared figures, and wrote the draft. S. Schellmann generated transgenic *Arabidopsis* lines. Y. Jaillais and J. Friml supervised students and contributed to the draft. B.-H. Kang supervised students and wrote the draft. Y. Dagdas supervised students and postdocs and wrote the draft.

Submitted: 31 March 2022
Revised: 12 August 2022
Accepted: 14 September 2022

References

Allan, B.B., B.D. Moyer, and W.E. Balch. 2000. Rab1 recruitment of p115 into a cis-SNARE complex: Programming budding COPII vesicles for fusion. *Science*. 289:444–448. https://doi.org/10.1126/science.289.5478.444

Aniento, F., V. Sánchez de Medina Hernández, Y. Dagdas, M. Rojas-Pierce, and E. Russinova. 2022. Molecular mechanisms of endomembrane trafficking in plants. *The Plant Cell*. 34:146–173. https://doi.org/10.1093/plcell/koab235

Bassham, D.C. 2015. Methods for analysis of autophagy in plants. *Methods*. 75:181–188. https://doi.org/10.1016/j.ymeth.2014.09.003

Birgisdottir, Å.B., T. Lamark, and T. Johansen. 2013. The LIR motif: Crucial for selective autophagy. *J. Cell Sci.* 126:3237–3247. https://doi.org/10.1242/jcs.126128

Bolte, S., and F. P. Cordelières. 2006. A guided tour into subcellular colocalization analysis in light microscopy. *Journal of Microscopy*. 224:213–232.

Borner, G.H.H., D.J. Sherrier, T. Weimar, L.V. Michaelson, N.D. Hawkins, A. Macaskill, J.A. Napier, M.H. Beale, K.S. Lilley, and P. Dupree. 2005. Analysis of detergent-resistant membranes in *Arabidopsis*. Evidence for plasma membrane lipid rafts. *Plant Physiol.* 137:104–116. https://doi.org/10.1104/pp.104.053041

Cardona-López, X., L. Cuyas, E. Marín, C. Rajulu, M. L. Irigoyen, E. Gil, M. I. Puga, R. Bligny, L. Nussaume, N. Geldner, et al. 2015. ESCRT-III-Associated Protein ALIX Mediates High-Affinity Phosphate Transporter Trafficking to Maintain Phosphate Homeostasis in Arabidopsis. *The Plant Cell*. 27:2560–2581.

Chang, C., L.E. Jensen, and J.H. Hurley. 2021. Autophagosome biogenesis comes out of the black box. *Nat. Cell Biol.* 23:450–456. https://doi.org/10.1038/s41556-021-00669-y

Clough, S.J., and A.F. Bent. 1998. Floral dip: A simplified method for Agrobacterium-mediated transformation of Arabidopsis thaliana. *Plant J.* 16:735–743. https://doi.org/10.1046/j.1365-313x.1998.00343.x

Cui, Y., W. Cao, Y. He, Q. Zhao, M. Wakazaki, X. Zhuang, J. Gao, Y. Zeng, C. Gao, Y. Ding, et al. 2019. A whole-cell electron tomography model of vacuole biogenesis in *Arabidopsis* root cells. *Nat. Plants*. 5:95–105. https://doi.org/10.1038/s41477-018-0328-1

Cui, Y., Q. Zhao, S. Hu, and L. Jiang. 2020. Vacuole biogenesis in plants: How many vacuoles, how many models? *Trends Plant Sci.* 25:538–548. https://doi.org/10.1016/j.tplants.2020.01.008

Dettmer, J., A. Hong-Hermesdorf, Y. D. Stierhof, and K. Schumacher. 2006. Vacuolar H^+-ATPase Activity Is Required for Endocytic and Secretory Trafficking in *Arabidopsis*. *The Plant Cell*. 18:715–730.

Dikic, I. 2017. Proteasomal and autophagic degradation systems. *Annu. Rev. Biochem.* 86:193–224. https://doi.org/10.1146/annurev-biochem-061516-044908

Felsenstein, J. 1985. Confidence limits on phylogenies: AN approach using the bootstrap. *Evol. Int. J. Org. Evol.* 39:783–791. https://doi.org/10.1111/j.1558-5646.1985.tb00420.x

Gao, C., X. Zhuang, Y. Cui, X. Fu, Y. He, Q. Zhao, Y. Zeng, J. Shen, M. Luo, and L. Jiang. 2015. Dual roles of an *Arabidopsis* ESCRT component FREE1 in regulating vacuolar protein transport and autophagic degradation. *Proc. Natl. Acad. Sci. USA*. 112:1886–1891. https://doi.org/10.1073/pnas.1421271112

Geldner, N., V. Dénervaud-Tendon, D.L. Hyman, U. Mayer, Y.-D. Stierhof, and J. Chory. 2009. Rapid, combinatorial analysis of membrane compartments in intact plants with a multicolor marker set. *Plant J.* 59:169–178. https://doi.org/10.1111/j.1365-313x.2009.03851.x

Goodstein, D.M., S. Shu, R. Howson, R. Neupane, R.D. Hayes, J. Fazo, T. Mitros, W. Dirks, U. Hellsten, N. Putnam, and D.S. Rokhsar. 2012. Phytozome: A comparative platform for green plant genomics. *Nucleic Acids Res.* 40:D1178–D1186. https://doi.org/10.1093/nar/gkr944

Grebe, M., J. Xu, W. Möbius, T. Ueda, A. Nakano, H. J. Geuze, M. B. Rook, and B. Scheres. 2003. *Arabidopsis* Sterol Endocytosis Involves Actin-Mediated Trafficking via ARA6-Positive Early Endosomes. *Curr Biol.* 13:1378–1387.

Hafrén, A., J. L. Macia, A. J. Love, J. J. Milner, M. Drucker, and D. Hofius. 2017. Selective autophagy limits cauliflower mosaic virus infection by NBR1-mediated targeting of viral capsid protein and particles. *Proc. Natl. Acad. Sci. USA*. 114:E2026–E2035.

Hu, S., H. Ye, Y. Cui, and L. Jiang. 2020. AtSec62 is critical for plant development and is involved in ER-phagy in *Arabidopsis thaliana*. *J. Integr. Plant Biol.* 62:181–200.

Ishizaki, K., R. Nishihama, M. Ueda, K. Inoue, S. Ishida, Y. Nishimura, T. Shikanai, and T. Kohchi. 2015. Development of gateway binary vector series with four different selection markers for the liverwort *Marchantia polymorpha*. *PLoS One*. 10:e0138876. https://doi.org/10.1371/journal.pone.0138876

Jia, M., X. Liu, H. Xue, Y. Wu, L. Shi, R. Wang, Y. Chen, N. Xu, J. Zhao, J. Shao, et al. 2019. Noncanonical ATG8-ABS3 interaction controls senescence in plants. *Nat. Plants*. 5:212–224. https://doi.org/10.1038/s41477-018-0348-x

Jumper, J., and D. Hassabis. 2022. Protein structure predictions to atomic accuracy with AlphaFold. *Nat. Methods*. 19:11–12. https://doi.org/10.1038/s41592-021-01362-6

Jumper, J., R. Evans, A. Pritzel, T. Green, M. Figurnov, O. Ronneberger, K. Tunyasuvunakool, R. Bates, A. Žídek, A. Potapenko, et al. 2021. Highly accurate protein structure prediction with AlphaFold. *Nature*. 596:583–589.

Kalinowska, K., M.-K. Nagel, K. Goodman, L. Cuyas, F. Anzenberger, A. Alkofer, J. Paz-Ares, P. Braun, V. Rubio, M.S. Otegui, and E. Isono. 2015. Arabidopsis ALIX is required for the endosomal localization of the deubiquitinating enzyme AMSH3. *Proc. Natl. Acad. Sci. USA*. 112:E5543–E5551. https://doi.org/10.1073/pnas.1510516112

Kang, B.-H. 2010. Electron microscopy and high-pressure freezing of *Arabidopsis*. *Methods Cell Biol.* 96:259–283. https://doi.org/10.1016/S0091-679X(10)96012-3

Katsiarimpa, A., K. Kalinowska, F. Anzenberger, C. Weis, M. Ostertag, C. Tsutsumi, C. Schwechheimer, F. Brunner, R. Hückelhoven, and E. Isono. 2013. The deubiquitinating enzyme AMSH1 and the ESCRT-III subunit VPS2.1 are required for autophagic degradation in *Arabidopsis*. *The Plant Cell*. 25:2236–2252. https://doi.org/10.1105/tpc.113.113399

Kim, J.H., H.N. Lee, X. Huang, H. Jung, M.S. Otegui, F. Li, and T. Chung. 2022. FYVE2, a phosphatidylinositol 3-phosphate effector, interacts with the COPII machinery to control autophagosome formation in *Arabidopsis*. *The Plant Cell*. 34:351–373. https://doi.org/10.1093/plcell/koab263

Kleine-Vehn, J., J. Leitner, M. Zwiewka, M. Sauer, L. Abas, C. Luschnig, and J. Friml. 2008. Differential degradation of PIN2 auxin efflux carrier by retromer-dependent vacuolar targeting. *Proc. Natl. Acad. Sci. USA*. 105:17812–17817. https://doi.org/10.1073/pnas.0808073105

Krebs, M., D. Beyhl, E. Görlich, K.A.S. Al-Rasheid, I. Marten, Y.-D. Stierhof, R. Hedrich, and K. Schumacher. 2010. Arabidopsis V-ATPase activity at the tonoplast is required for efficient nutrient storage but not for sodium accumulation. *Proc. Natl. Acad. Sci. USA*. 107:3251–3256. https://doi.org/10.1073/pnas.0913035107

Krüger, F., and K. Schumacher. 2018. Pumping up the volume- vacuole biogenesis in *Arabidopsis* thaliana. *Semin. Cell Dev. Biol.* 80:106–112. https://doi.org/10.1016/j.semcdb.2017.07.008

Kubota, A., K. Ishizaki, M. Hosaka, and T. Kohchi. 2013. Efficient Agrobacterium-mediated transformation of the liverwort *Marchantia polymorpha* using regenerating thalli. *Biosci. Biotechnol. Biochem.* 77:167–172. https://doi.org/10.1271/bbb.120700

Kumar, S., G. Stecher, M. Li, C. Knyaz, and K. Tamura. 2018. MEGA X: Molecular evolutionary genetics analysis across computing platforms. *Mol. Biol. Evol.* 35:1547–1549. https://doi.org/10.1093/molbev/msy096

Kurusu, T., T. Koyano, S. Hanamata, T. Kubo, Y. Noguchi, C. Yagi, N. Nagata, T. Yamamoto, T. Ohnishi, Y. Okazaki, et al. 2014. OsATG7 is required for autophagy-dependent lipid metabolism in rice

postmeiotic anther development. *Autophagy*. 10:878–888. https://doi.org/10.4161/auto.28279
LaMontagne, E.D., C.A. Collins, S.C. Peck, and A. Heese. 2016. Isolation of microsomal membrane proteins from *Arabidopsis thaliana*. *Curr. Protoc. Plant Biol.* 1:217–234. https://doi.org/10.1002/cppb.20020
Lampropoulos, A., Z. Sutikovic, C. Wenzl, I. Maegele, J.U. Lohmann, and J. Forner. 2013. GreenGate---a novel, versatile, and efficient cloning system for plant transgenesis. *PLoS One*. 8:e83043. https://doi.org/10.1371/journal.pone.0083043
Letunic, I., and P. Bork. 2019. Interactive tree of Life (iTOL) v4: Recent updates and new developments. *Nucleic Acids Res.* 47:W256–W259. https://doi.org/10.1093/nar/gkz239
Li, F., T. Chung, and R. D. Vierstra. 2014. AUTOPHAGY-RELATED11 Plays a Critical Role in General Autophagy- and Senescence-Induced Mitophagy in *Arabidopsis*. *The Plant Cell*. 26:788–807.
Liu, Y., and D.C. Bassham. 2010. TOR is a negative regulator of autophagy in *Arabidopsis thaliana*. *PLoS One*. 5:e11883. https://doi.org/10.1371/journal.pone.0011883
Liu, Y., Y. Xiong, and D.C. Bassham. 2009. Autophagy is required for tolerance of drought and salt stress in plants. *Autophagy*. 5:954–963. https://doi.org/10.4161/auto.5.7.9290
Ma, J., Z. Liang, J. Zhao, P. Wang, W. Ma, K.K. Mai, J.A. Fernandez Andrade, Y. Zeng, N. Grujic, L. Jiang, et al. 2021. Friendly mediates membrane depolarization-induced mitophagy in *Arabidopsis*. *Curr. Biol.* 31:1931–1944.e4. https://doi.org/10.1016/j.cub.2021.02.034
Marshall, R.S., and R.D. Vierstra. 2018. Autophagy: The master of bulk and selective recycling. *Annu. Rev. Plant Biol.* 69:173–208. https://doi.org/10.1146/annurev-arplant-042817-040606
McLoughlin, F., R.C. Augustine, R.S. Marshall, F. Li, L.D. Kirkpatrick, M.S. Otegui, and R.D. Vierstra. 2018. Maize multi-omics reveal roles for autophagic recycling in proteome remodelling and lipid turnover. *Nat. Plants*. 4:1056–1070. https://doi.org/10.1038/s41477-018-0299-2
McLoughlin, F., R.S. Marshall, X. Ding, E.C. Chatt, L.D. Kirkpatrick, R.C. Augustine, F. Li, M.S. Otegui, and R.D. Vierstra. 2020. Autophagy plays prominent roles in amino acid, nucleotide, and carbohydrate metabolism during fixed-carbon starvation in maize. *The Plant Cell*. 32:2699–2724. https://doi.org/10.1105/tpc.20.00226
Melia, T.J., A.H. Lystad, and A. Simonsen. 2020. Autophagosome biogenesis: From membrane growth to closure. *J. Cell Biol.* 219:e202002085. https://doi.org/10.1083/jcb.202002085
Mirdita, M., K. Schütze, Y. Moriwaki, L. Heo, S. Ovchinnikov, and M. Steinegger. 2022. ColabFold: making protein folding accessible to all. *Nature Methods*. 19:679–682.
Munch, D., O. K. Teh, F. G. Malinovsky, Q. Liu, R. R. Vetukuri, F. El Kasmi, P. Broderson, I. Hara-Nishimura, J. L. Dangl, M. Peterson, et al. 2015. Retromer Contributes to Immunity-Associated Cell Death in Arabidopsis. *The Plant Cell*. 27:463–479.
Nagel, M.-K., K. Kalinowska, K. Vogel, G.D. Reynolds, Z. Wu, F. Anzenberger, M. Ichikawa, C. Tsutsumi, M.H. Sato, B. Kuster, et al. 2017. Arabidopsis SH3P2 is an ubiquitin-binding protein that functions together with ESCRT-I and the deubiquitylating enzyme AMSH3. *Proc. Natl. Acad. Sci. USA*. 114:E7197–E7204. https://doi.org/10.1073/pnas.1710866114
Nakatogawa, H. 2020. Mechanisms governing autophagosome biogenesis. *Nat. Rev. Mol. Cell Biol.* 21:439–458. https://doi.org/10.1038/s41580-020-0241-0
Norizuki, T., N. Minamino, H. Tsukaya, and T. Ueda. 2021. Bryophyte spermiogenesis occurs through multimode autophagic and nonautophagic degradation. *bioRxiv*. (Preprint posted August 17, 2021). https://doi.org/10.1101/2021.08.17.456730
Oti, O.O. 2013. Hub and spoke network design for the inbound supply chain. Massachusetts Institute of Technology, Sloan School of Management; and, (S.M.)–Massachusetts Institute of Technology, Engineering Systems Division; in conjunction with the Leaders for Global Operations Program at MIT, Cambridge, MA. 74 pp..
Perez-Riverol, Y., A. Csordas, J. Bai, M. Bernal-Llinares, S. Hewapathirana, D.J. Kundu, A. Inuganti, J. Griss, G. Mayer, M. Eisenacher, et al. 2019. The PRIDE database and related tools and resources in 2019: Improving support for quantification data. *Nucleic Acids Res.* 47:D442–D450. https://doi.org/10.1093/nar/gky1106
Phillips, A.R., A. Suttangkakul, and R.D. Vierstra. 2008. The ATG12-conjugating enzyme ATG10 Is essential for autophagic vesicle formation in *Arabidopsis thaliana*. *Genetics*. 178:1339–1353. https://doi.org/10.1534/genetics.107.086199
Popov, N., M. Schmitt, S. Schulzeck, and H. Matthies. 1975. Reliable micromethod for determination of the protein content in tissue homogenates. *Acta biol. Med. Ger.* 34:1441–1446
Pornillos, O., D.S. Higginson, K.M. Stray, R.D. Fisher, J.E. Garrus, M. Payne, G.-P. He, H.E. Wang, S.G. Morham, and W.I. Sundquist. 2003. HIV Gag mimics the Tsg101-recruiting activity of the human Hrs protein. *J. Cell Biol.* 162:425–434. https://doi.org/10.1083/jcb.200302138
Rabinowitz, J.D., and E. White. 2010. Autophagy and metabolism. *Science*. 330:1344–1348. https://doi.org/10.1126/science.1193497
Richter, S., N. Geldner, J. Schrader, H. Wolters, Y. D. Stierhof, G. Rios, C. Koncz, D. G. Robinson, and G. Jürgens. 2007. Functional diversification of closely related ARF-GEFs in protein secretion and recycling. *Nature*. 448:488–492.
Rigal, A., S.M. Doyle, and S. Robert. 2015. Live cell imaging of FM4-64, a tool for tracing the endocytic pathways in *Arabidopsis* root cells. *Methods Mol. Biol.* 1242:93–103. https://doi.org/10.1007/978-1-4939-1902-4_9
Rodriguez, E., J. Chevalier, J. Olsen, J. Ansbøl, V. Kapousidou, Z. Zuo, S. Svenning, C. Loefke, S. Koemeda, P.S. Drozdowskyj, et al. 2020. Autophagy mediates temporary reprogramming and dedifferentiation in plant somatic cells. *EMBO J.* 39:e103315. https://doi.org/10.15252/embj.2019103315
Sanchez-Wandelmer, J., and F. Reggiori. 2013. Amphisomes: Out of the autophagosome shadow? *EMBO J.* 32:3116–3118. https://doi.org/10.1038/emboj.2013.246
Shen, J., Q. Zhao, X. Wang, C. Gao, Y. Zhu, Y. Zeng, and L. Jiang. 2018. A plant Bro1 domain protein BRAF regulates multivesicular body biogenesis and membrane protein homeostasis. *Nat. Commun.* 9:3784. https://doi.org/10.1038/s41467-018-05913-y
Signorelli, S., Ł.P. Tarkowski, W. Van den Ende, and D.C. Bassham. 2019. Linking autophagy to abiotic and biotic stress responses. *Trends Plant Sci.* 24:413–430. https://doi.org/10.1016/j.tplants.2019.02.001
Spitzer, C., F. Li, R. Buono, H. Roschzttardtz, T. Chung, M. Zhang, K.W. Osteryoung, R.D. Vierstra, and M.S. Otegui. 2015. The endosomal protein CHARGED MULTIVESICULAR BODY PROTEIN1 regulates the autophagic turnover of plastids in *Arabidopsis*. *The Plant Cell*. 27:391–402. https://doi.org/10.1105/tpc.114.135939
Stephani, M., L. Picchianti, A. Gajic, R. Beveridge, E. Skarwan, V. Sanchez de Medina Hernandez, A. Mohseni, M. Clavel, Y. Zeng, C. Naumann, et al. 2020. A cross-kingdom conserved ER-phagy receptor maintains endoplasmic reticulum homeostasis during stress. *Elife*. 9:e58396. https://doi.org/10.7554/eLife.58396
Stolz, A., A. Ernst, and I. Dikic. 2014. Cargo recognition and trafficking in selective autophagy. *Nat. Cell Biol.* 16:495–501. https://doi.org/10.1038/ncb2979
Sugano, S.S., R. Nishihama, M. Shirakawa, J. Takagi, Y. Matsuda, S. Ishida, T. Shimada, I. Hara-Nishimura, K. Osakabe, and T. Kohchi. 2018. Efficient CRISPR/Cas9-based genome editing and its application to conditional genetic analysis in *Marchantia polymorpha*. *PLoS One*. 13:e0205117. https://doi.org/10.1371/journal.pone.0205117
Sutipatanasomboon, A., S. Herberth, E.G. Alwood, H. Häweker, B. Müller, M. Shahriari, A.Y. Zienert, B. Marin, S. Robatzek, G.J.K. Praefcke, et al. 2017. Disruption of the plant-specific CFS 1 gene impairs autophagosome turnover and triggers EDS1-dependent cell death. *Sci. Rep.* 7:1–14. https://doi.org/10.1038/s41598-017-08577-8
Svenning, S., T. Lamark, K. Krause, and T. Johansen. 2011. Plant NBR1 is a selective autophagy substrate and a functional hybrid of the mammalian autophagic adapters NBR1 and p62/SQSTM1. *Autophagy*. 7:993–1010. https://doi.org/10.4161/auto.7.9.16389
Takahashi, Y., H. He, Z. Tang, T. Hattori, Y. Liu, M.M. Young, J.M. Serfass, L. Chen, M. Gebru, C. Chen, et al. 2018. An autophagy assay reveals the ESCRT-III component CHMP2A as a regulator of phagophore closure. *Nat. Commun.* 9:2855. https://doi.org/10.1038/s41467-018-05254-w
Takahashi, Y., X. Liang, T. Hattori, Z. Tang, H. He, H. Chen, X. Liu, T. Abraham, Y. Imamura-Kawasawa, N.J. Buchkovich, et al. 2019. VPS37A directs ESCRT recruitment for phagophore closure. *J. Cell Biol.* 218:3336–3354. https://doi.org/10.1083/jcb.201902170
Takemoto, K., K. Ebine, J.C. Askani, F. Krüger, Z.A. Gonzalez, E. Ito, T. Goh, K. Schumacher, A. Nakano, and T. Ueda. 2018. Distinct sets of tethering complexes, SNARE complexes, and Rab GTPases mediate membrane fusion at the vacuole in *Arabidopsis*. *Proc. Natl. Acad. Sci. USA*. 115:E2457–E2466. https://doi.org/10.1073/pnas.1717839115
Tamura, K., and M. Nei. 1993. Estimation of the number of nucleotide substitutions in the control region of mitochondrial DNA in humans and chimpanzees. *Mol. Biol. Evol.* 10:512–526. https://doi.org/10.1093/oxfordjournals.molbev.a040023
Thompson, A.R., J.H. Doelling, A. Suttangkakul, and R.D. Vierstra. 2005. Autophagic nutrient recycling in *Arabidopsis* directed by the ATG8 and

ATG12 conjugation pathways. *Plant Physiol.* 138:2097–2110. https://doi.org/10.1104/pp.105.060673

Wada, S., Y. Hayashida, M. Izumi, T. Kurusu, S. Hanamata, K. Kanno, S. Kojima, T. Yamaya, K. Kuchitsu, A. Makino, and H. Ishida. 2015. Autophagy supports biomass production and nitrogen use efficiency at the vegetative stage in rice. *Plant Physiol.* 168:60–73. https://doi.org/10.1104/pp.15.00242

Wang, P., X. Chen, C. Goldbeck, E. Chung, and B.-H. Kang. 2017. A distinct class of vesicles derived from the trans-Golgi mediates secretion of xylogalacturonan in the root border cell. *Plant J.* 92:596–610. https://doi.org/10.1111/tpj.13704

Weidberg, H., E. Shvets, and Z. Elazar. 2011. Biogenesis and cargo selectivity of autophagosomes. *Annu. Rev. Biochem.* 80:125–156. https://doi.org/10.1146/annurev-biochem-052709-094552

Wywial, E., and S.M. Singh. 2010. Identification and structural characterization of FYVE domain-containing proteins of *Arabidopsis thaliana*. *BMC Plant Biol.* 10:157. https://doi.org/10.1186/1471-2229-10-157

Xu, J., and B. Scheres. 2005. Dissection of Arabidopsis ADP-RIBOSYLATION FACTOR 1 Function in Epidermal Cell Polarity. *The Plant Cell.* 17: 525–536.

Yoshii, S.R., and N. Mizushima. 2017. Monitoring and measuring autophagy. *Int. J. Mol. Sci.* 18:E1865. https://doi.org/10.3390/ijms18091865

Zaffagnini, G., and S. Martens. 2016. Mechanisms of selective autophagy. *J. Mol. Biol.* 428:1714–1724. https://doi.org/10.1016/j.jmb.2016.02.004

Zhao, Y.G., P. Codogno, and H. Zhang. 2021. Machinery, regulation and pathophysiological implications of autophagosome maturation. *Nat. Rev. Mol. Cell Biol.* 22:733–750. https://doi.org/10.1038/s41580-021-00392-4

Zhao, Y.G., and H. Zhang. 2019. Autophagosome maturation: An epic journey from the ER to lysosomes. *J. Cell Biol.* 218:757–770. https://doi.org/10.1083/jcb.201810099

Zientara-Rytter, K., and S. Subramani. 2020. Mechanistic insights into the role of Atg11 in selective autophagy. *J. Mol. Biol.* 432:104–122. https://doi.org/10.1016/j.jmb.2019.06.017

Supplemental material

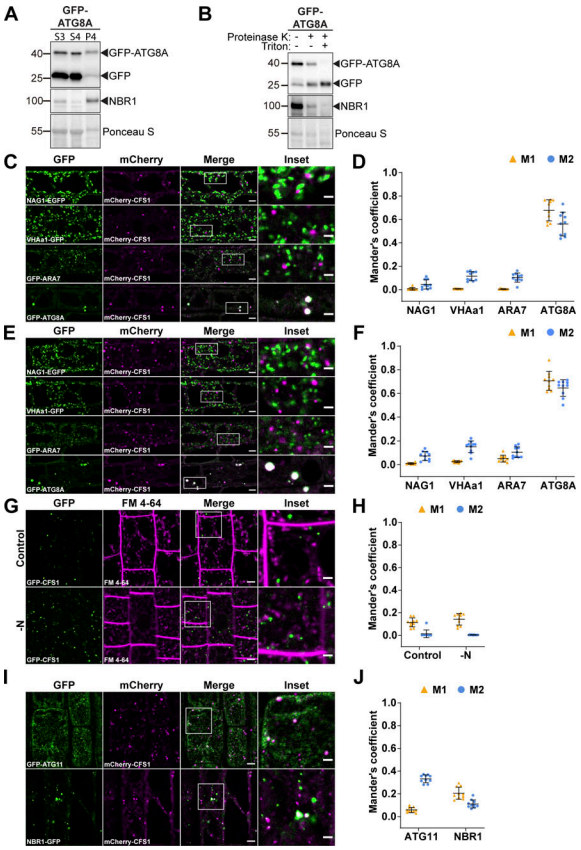

Figure S1. **Differential centrifugation coupled to affinity purification-mass spectrometry (AP-MS) revealed CFS1 as an autophagosome-associated protein in *A. thaliana*. (A and B)** Ultracentrifugation enriches for intact autophagosomes. **(A)** Western blot analysis of 7-d-old Col-0 seedlings expressing pUBQ::GFP-ATG8A. *Arabidopsis* seedlings were treated with 3 µM Torin 1 for 90 min prior to differential centrifugation described in Fig. 1 A. A total of 5 µg of protein was loaded in each lane. Protein extracts were immunoblotted with anti-GFP and anti-NBR1 antibodies. Representative images of four replicates are shown. Reference protein sizes are labeled as numbers at the left side of the blots (unit: kD). **(B)** Protease protection assay of enriched autophagosomes in A. Autophagosomes were treated with 30 ng/µl proteinase K in the absence or presence of 1% Triton X-100. A total of 5 µg of protein was loaded in each lane. Protein extracts were immunoblotted with anti-GFP and anti-NBR1 antibodies. Representative images of 4 replicates are shown. Reference protein sizes are labeled as numbers at the left side of the blots (unit: kD). **(C and D)** CFS1 localizes to the autophagosomes under control conditions. **(C)** Confocal microscopy images of *Arabidopsis* root epidermal cells co-expressing pUBQ::mCherry-CFS1 with either Golgi body marker p35S::NAG1-EGFP, trans-Golgi network marker pa1::VHAa1-GFP, late endosome marker pRPS5a::GFP-ARA7 or autophagosome marker pUBQ::GFP-ATG8A under control conditions. 5-d-old *Arabidopsis* seedlings were incubated in control 1/2 MS media before imaging. Representative images of 10 replicates are shown. Area highlighted in the white-boxed region in the merge panel was further enlarged and presented in the inset panel. Scale bars, 5 µm. Inset scale bars, 2 µm. **(D)** Quantification of confocal experiments in C showing the Mander's colocalization coefficients between mCherry-CFS1 and the GFP-fused marker NAG1, VHAa1, ARA7, or ATG8A. M1, fraction of GFP-fused marker signal that overlaps with mCherry-CFS1 signal. M2, fraction of mCherry-CFS1 signal that overlaps with GFP-fused marker signal. Bars indicate the mean ± SD of 10 replicates. **(E and F)** CFS1 localizes to the autophagosomes under salt stress. **(E)** Confocal microscopy images of *Arabidopsis* root epidermal cells co-expressing pUBQ::mCherry-CFS1 with either Golgi body marker p35S::NAG1-EGFP, trans-Golgi network marker pa1::VHAa1-GFP, MVB marker pRPS5a::GFP-ARA7 or autophagosome marker pUBQ::GFP-ATG8A under salt stress. 5-d-old *Arabidopsis* seedlings were incubated in 150 mM NaCl-containing 1/2 MS media for 1 h for autophagy induction before imaging. Representative images of 10 replicates are shown. Area highlighted in the white-boxed region in the merge panel was further enlarged and presented in the inset panel. Scale bars, 5 µm. Inset scale bars, 2 µm. **(F)** Quantification of confocal experiments in E showing the Mander's colocalization coefficients between mCherry-CFS1 and the GFP-fused marker NAG1, VHAa1, ARA7, or ATG8A. M1, fraction of GFP-fused marker signal that overlaps with mCherry-CFS1 signal. M2, fraction of mCherry-CFS1 signal that overlaps with GFP-fused marker signal. Bars indicate the mean ± SD of 10 replicates. **(G and H)** CFS1 does not colocalize with the endocytic marker dye FM 4-64. **(G)** Confocal microscopy images of *Arabidopsis* root epidermal cells expressing pUBQ::GFP-CFS1 and stained with FM 4-64. 5-d-old *Arabidopsis* seedlings were first incubated in either control or nitrogen-deficient (−N) 1/2 MS media for 4 h and were then incubated in either control or nitrogen-deficient 1/2 MS media containing 4 µM FM 4-64 for 30 min before imaging. Representative images of 10 replicates are shown. Area highlighted in the white-boxed region in the merge panel was further enlarged and presented in the inset panel. Scale bars, 5 µm. Inset scale bars, 2 µm. **(H)** Quantification of confocal experiments in G showing the Mander's colocalization coefficients between GFP-CFS1 and FM 4-64. M1, fraction of GFP-CFS1 signal that overlaps with FM 4-64 signal. M2, fraction of FM 4-64 signal that overlaps with GFP-CFS1 signal. Bars indicate the mean ± SD of 10 replicates. **(I and J)** CFS1 colocalizes with the autophagosome marker proteins ATG11 and NBR1 during salt stress. **(I)** Confocal microscopy images of *Arabidopsis* root epidermal cells co-expressing pUBQ::mCherry-CFS1 with either pUBQ::GFP-ATG11 or pNBR1::NBR1-GFP. 5-d-old *Arabidopsis* seedlings were incubated in 150 mM NaCl-containing 1/2 MS media for 1 h for autophagy induction before imaging. Representative images of 10 replicates are shown. Area highlighted in the white-boxed region in the merge panel was further enlarged and presented in the inset panel. Scale bars, 5 µm. Inset scale bars, 2 µm. **(J)** Quantification of confocal experiments in I showing the Mander's colocalization coefficients between mCherry-CFS1 and the GFP-fused marker ATG11 or NBR1. M1, fraction of GFP-fused marker signal that overlaps with mCherry-CFS1 signal. M2, fraction of mCherry-CFS1 signal that overlaps with GFP-fused marker signal. Bars indicate the mean ± SD of 10 biological replicates. Source data are available for this figure: SourceData FS1.

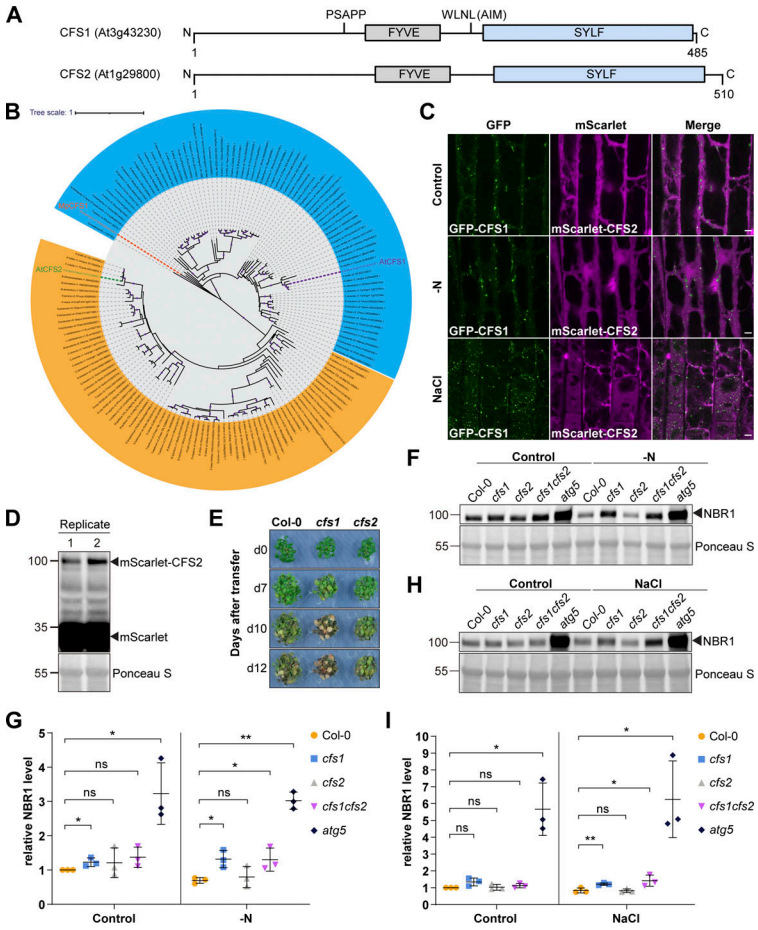

Figure S2. **CFS2 does not play a role in autophagic flux. (A)** Schematic diagrams showing the domain structures of *Arabidopsis* CFS1 and CFS2. **(B)** Maximum likelihood (ML) phylogenetic tree showing that across the plant kingdom, no homology could be detected between CFS1 homologs and CFS2 homologs. Coding sequences of CFS1 and CFS2 homologs were obtained using the BLAST tool against representative species of different plant lineages in Phytozome (Goodstein et al., 2012). The tree was inferred from a 2283-nt-long alignment using the ML method and Tamura-Nei model as implemented by MEGA X (Tamura and Nei, 1993; Kumar et al., 2018). 100 bootstrap method and a discrete Gamma distribution was used to model evolutionary rate differences among sites (5 categories [+G, parameter = 0.8072]) (Felsenstein, 1985). The tree is represented using Interactive Tree Of Life (iTOL) v4 (Letunic and Bork, 2019). Best-scoring ML tree (−98686.19) is shown with purple circles indicating bootstrap values above 80 on their respective clades. The scale bar indicates the evolutionary distance based on the nucleotide substitution rate. All CFS1 homologs are grouped in the blue region while all CFS2 homologs are grouped in the orange region. Genes that encode *A. thaliana* CFS1 (AtCFS1), *A. thaliana* CFS2 (AtCFS2), and *M. polymorpha* CFS1 (MpCFS1) are highlighted with purple, green, and orange colors, respectively. **(C)** Confocal microscopy images of *Arabidopsis* root epidermal cells co-expressing pUBQ::GFP-CFS1 and pUBQ::mScarlet-CFS2. 5-d-old *Arabidopsis* seedlings were incubated in either control, nitrogen-deficient (−N) or 150 mM NaCl-containing 1/2 MS media before imaging. Representative images of 10 replicates are shown. Note that no CFS2 puncta signals could be detected. Scale bars, 5 µm. **(D)** Western blot analysis of *Arabidopsis* seedlings expressing pUBQ::mScarlet-CFS2 used in C. Total lysates were immunoblotted with anti-RFP antibodies. Images of two replicates are shown. Reference protein sizes are labeled as numbers at the left side of the blots (unit: kD). **(E)** Phenotypic characterization of *Arabidopsis cfs1* and *cfs2* mutants upon nitrogen starvation. 25 *Arabidopsis* seeds per genotype were first grown on 1/2 MS media plates (+1% plant agar) for 1-wk and 7-d-old seedlings were subsequently transferred to nitrogen-deficient (−N) 1/2 MS media plates (+0.8% plant agar) and grown for 2 wk. Plants were grown at 21°C under LEDs with 85 µM/m^2/s and a 14 h light/10 h dark photoperiod. d0 depicts the day of transfer. Brightness of pictures was enhanced ≤19% with Adobe Photoshop (2020). Representative images of four replicates are shown. **(F)** Western blots showing the endogenous NBR1 level in Col-0, *cfs1*, *cfs2*, *cfs1cfs2*, or *atg5* under control or nitrogen-starved (−N) conditions. *Arabidopsis* seeds were first grown in 1/2 MS media under continuous light for 1 wk and 7-d-old seedlings were subsequently transferred to control or nitrogen-deficient 1/2 MS media for 12 h. 10 µl of total seedling extract was loaded and immunoblotted with anti-NBR1 antibodies. Representative images of three replicates are shown. Reference protein sizes are labeled as numbers at the left side of the blots (unit: kD). **(G)** Quantification of F showing the relative NBR1 level of Col-0, *cfs1*, *cfs2*, *cfs1cfs2*, or *atg5* under control or nitrogen-starved conditions. Values were calculated through normalization of protein bands to Ponceau S and to untreated (Control) Col-0 and shown as the mean ± SD of three replicates. One-tailed and paired Student's *t* tests were performed to analyze the significance of the relative NBR1 level differences between Col-0 and each mutant. ns, not significant. *, P value <0.05. **, P value <0.01. **(H)** Western blot showing the endogenous NBR1 level in Col-0, *cfs1*, *cfs2*, *cfs1cfs2*, or *atg5* under control or salt-stressed (NaCl) conditions. *Arabidopsis* seeds were first grown in 1/2 MS media under continuous light for 1-wk and 7-d-old seedlings were subsequently transferred to control or 150 mM NaCl-containing 1/2 MS media for 16 h. 10 µl of total seedling extract was loaded and immunoblotted with anti-NBR1 antibodies. Representative images of three replicates are shown. Reference protein sizes are labeled as numbers at the left side of the blots (unit: kD). **(I)** Quantification of H showing the relative NBR1 level of Col-0, *cfs1*, *cfs2*, *cfs1cfs2*, or *atg5* under control or salt stress (NaCl) conditions. Values were calculated through normalization of protein bands to Ponceau S and to untreated (Control) Col-0 and shown as the mean ± SD of three replicates. One-tailed and paired Student's *t* tests were performed to analyze the significance of the relative NBR1 level difference between Col-0 and each mutant. ns, not significant. *, P value <0.05. **, P value <0.01. Source data are available for this figure: SourceData FS2.

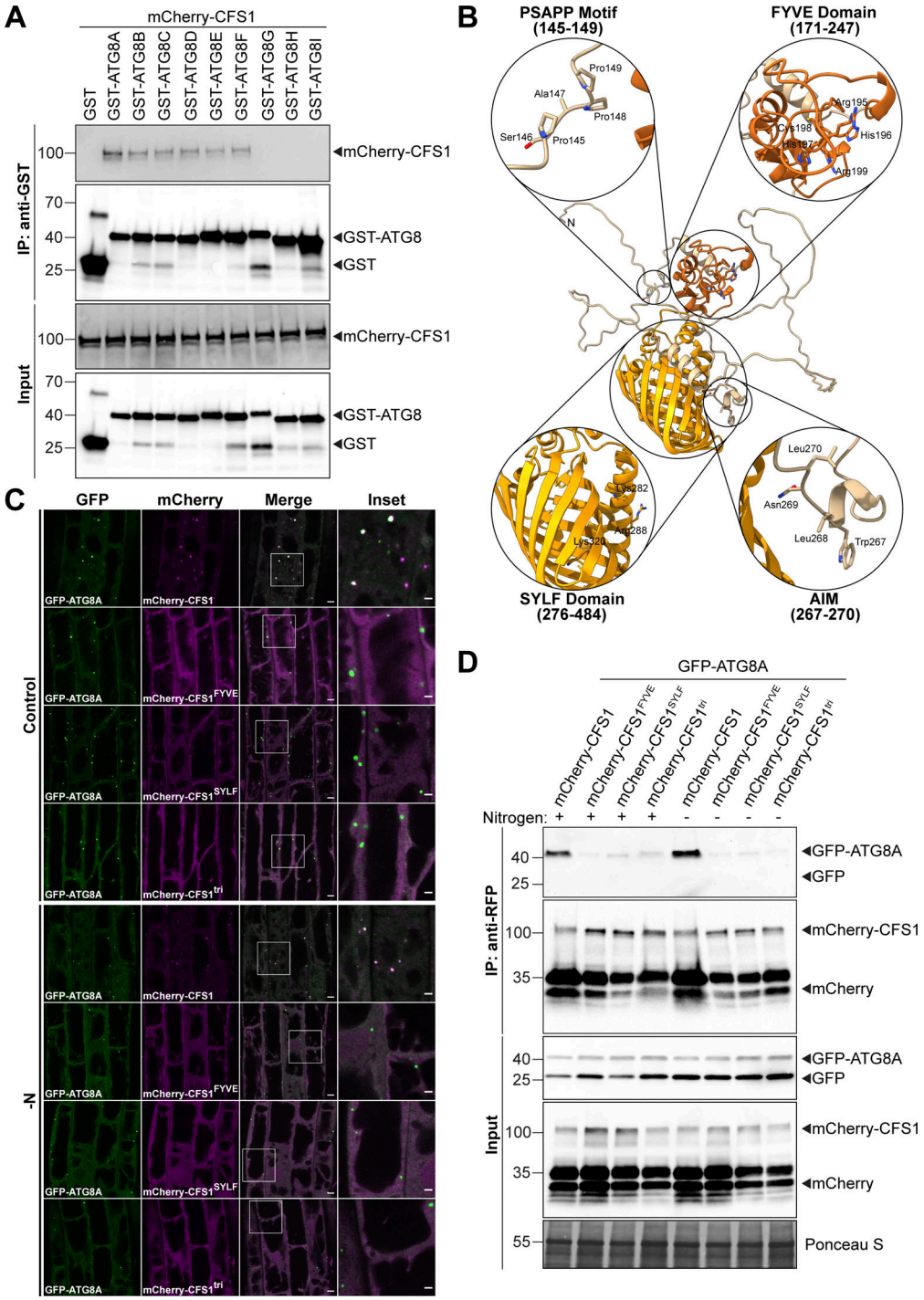

Figure S3. **Functional characterization of CFS1-ATG8 interaction. (A)** GST pull-downs of *E. coli* lysates expressing either GST, GST-ATG8A, GST-ATG8B, GST-ATG8C, GST-ATG8D, GST-ATG8E, GST-ATG8F, GST-ATG8G, GST-ATG8H or GST-ATG8I and *A. thaliana* whole-seedling lysates expressing mCherry-CFS1. Proteins were visualized by immunoblotting with anti-GST and anti-RFP antibodies. Representative images of two replicates are shown. Reference protein sizes are labeled as numbers at the left side of the blots (unit: kD). **(B)** Homology modeling and domain representation of CFS1. CFS1 structure is shown as ribbons, and relevant motifs and domains are highlighted as zoom-in, with the side chains of relevant residues represented as stick. For clarity, the FYVE and SYLF domains of CFS1 are colored in brick red and orange, respectively. **(C)** Confocal microscopy images of *cfs1* mutants co-expressing pUBQ::GFP-ATG8A with either pUBQ::mCherry-CFS1, pUBQ::mCherry-CFS1^{FYVE}, pUBQ::mCherry-CFS1^{SYLF} or pUBQ::mCherry-CFS1^{tri}. 5-d-old *Arabidopsis* seedlings were incubated in either control or nitrogen-deficient (–N) 1/2 MS media for 4 h before imaging. Representative images of 10 replicates are shown. Area highlighted in the white-boxed region in the merge panel was further enlarged and presented in the inset panel. Scale bars, 5 μm. Inset scale bars, 2 μm. **(D)** RFP-Trap pull-down of *Arabidopsis* seedlings co-expressing pUBQ::GFP-ATG8A with either pUBQ::mCherry-CFS1, pUBQ::mCherry-CFS1^{FYVE}, pUBQ::mCherry-CFS1^{SYLF} or pUBQ::mCherry-CFS1^{tri}. 7-d-old seedlings were incubated in either control (+) or nitrogen-deficient (–) 1/2 MS media for 12 h. Protein extracts were immunoblotted with anti-GFP and anti-RFP antibodies. Representative images of two replicates are shown. Reference protein sizes are labeled as numbers at the left side of the blots (unit: kD). Source data are available for this figure: SourceData FS3.

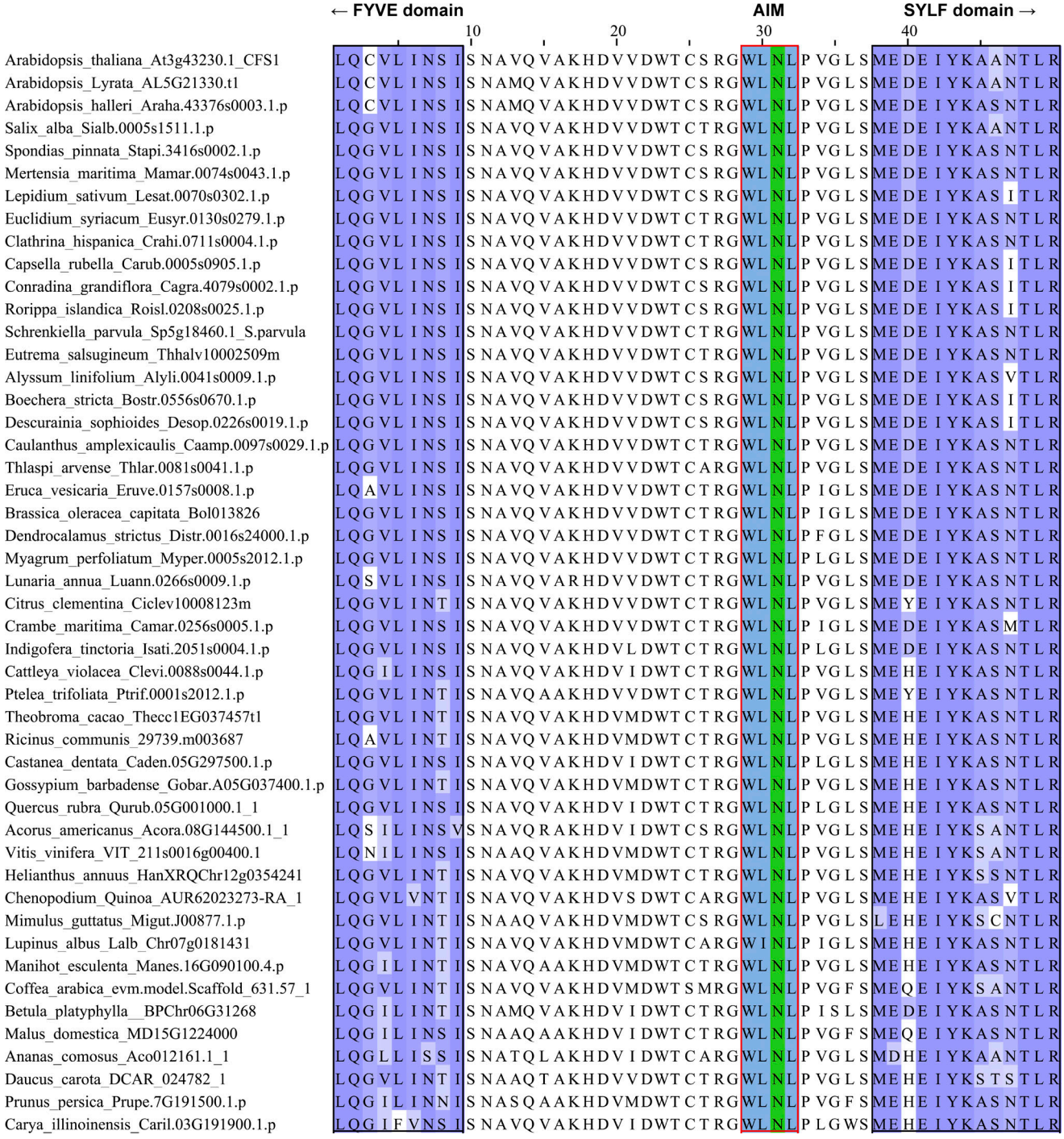

Figure S4. **The AIM between the FYVE and SYLF domains of CFS1 is conserved in plants.** Multiple sequencing alignments showing the conserved AIM (WLNL) between the FYVE and SYLF domains of CFS1. The regions that belong to FYVE or SYLF domains are labeled with black boxes.

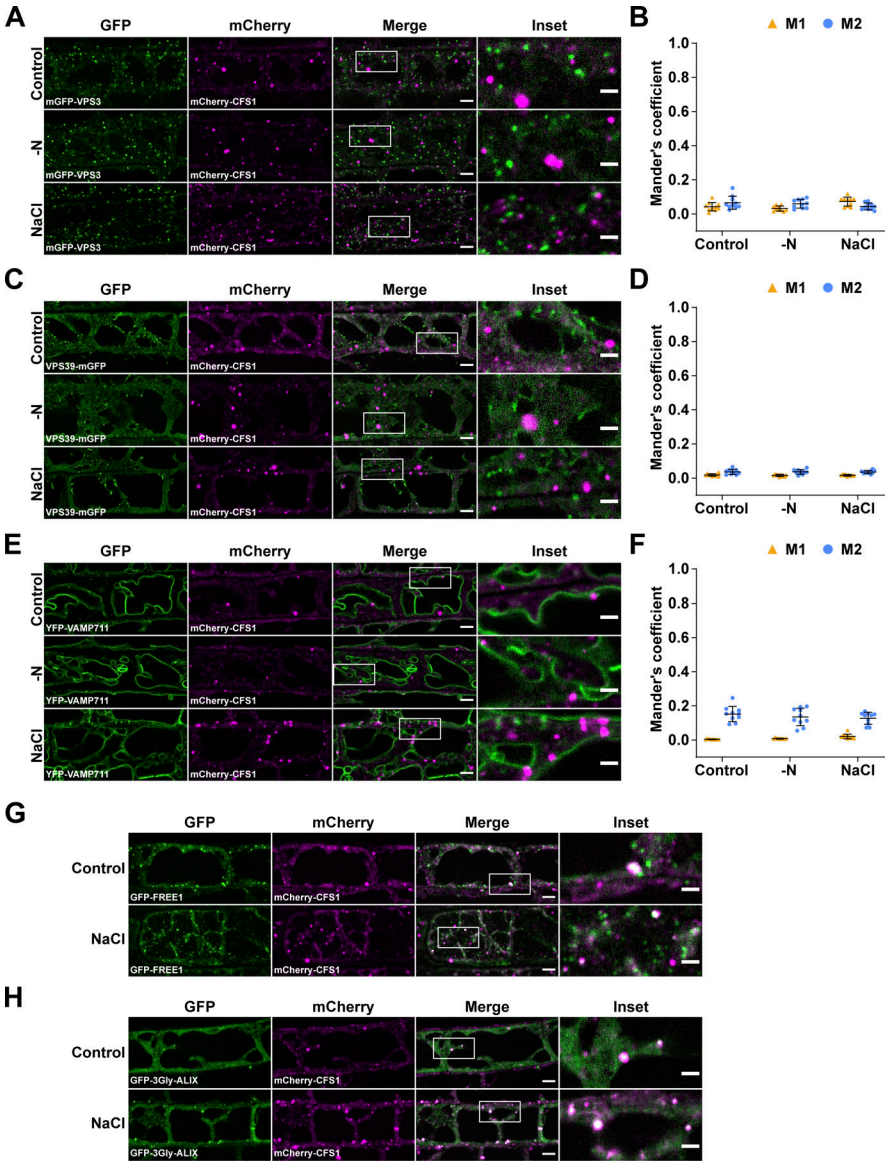

Figure S5. **CFS1 does not colocalize with VPS3, VPS39, or VAMP711, but partially colocalizes with FREE1 and ALIX. (A)** Confocal microscopy images of *Arabidopsis* root epidermal cells co-expressing pVPS3::mGFP-VPS3 with pUBQ::mCherry-CFS1. 5-d-old *Arabidopsis* seedlings were incubated in either control, nitrogen-deficient (–N) or 150 mM NaCl-containing 1/2 MS media before imaging. Representative images of 10 replicates are shown. Area highlighted in the white-boxed region in the merge panel was further enlarged and presented in the inset panel. Scale bars, 5 µm. Inset scale bars, 2 µm. **(B)** Quantification of confocal experiments in A showing the Mander's colocalization coefficients between mCherry-CFS1 and mGFP-VPS3. M1, fraction of mGFP-VPS3 signal that overlapped with the mCherry-CFS1 signal. M2, fraction of mCherry-CFS1 signal that overlapped with the mGFP-Vps3 signal. Bars indicate the mean ± SD of 10 replicates. **(C)** Confocal microscopy images of *Arabidopsis* root epidermal cells co-expressing pVPS39::VPS39-mGFP with pUBQ::mCherry-CFS1. 5-d-old *Arabidopsis* seedlings were incubated in either control, nitrogen-deficient (–N) or 150 mM NaCl-containing 1/2 MS media before imaging. Representative images of 10 replicates are shown. Area highlighted in the white-boxed region in the merge panel was further enlarged and presented in the inset panel. Scale bars, 5 µm. Inset scale bars, 2 µm. **(D)** Quantification of confocal experiments in C showing the Mander's colocalization coefficients between mCherry-CFS1 and VPS39-mGFP. M1, fraction of VPS39-mGFP signal that overlapped with the mCherry-CFS1 signal. M2, fraction of mCherry-CFS1 signal that overlapped with the VPS39-mGFP signal. Bars indicate the mean ± SD of 10 replicates. **(E)** Confocal microscopy images of *Arabidopsis* root epidermal cells co-expressing pUBQ::YFP-VAMP711 with pUBQ::mCherry-CFS1. 5-d-old *Arabidopsis* seedlings were incubated in either control, nitrogen-deficient (–N) or 150 mM NaCl-containing 1/2 MS media before imaging. Representative images of 10 replicates are shown. Area highlighted in the white-boxed region in the merge panel was further enlarged and presented in the inset panel. Scale bars, 5 µm. Inset scale bars, 2 µm. **(F)** Quantification of confocal experiments in E showing the Mander's colocalization coefficients between mCherry-CFS1 and YFP-VAMP711. M1, fraction of YFP-VAMP711 signal that overlapped with the mCherry-CFS1 signal. M2, fraction of mCherry-CFS1 signal that overlapped with the YFP-VAMP711 signal. Bars indicate the mean ± SD of 10 replicates. **(G)** Representative confocal microscopy images showing the colocalization of p35S::GFP-FREE1 and pUBQ::mCherry-CFS1 in *Arabidopsis* root epidermal cells. 5-d-old *Arabidopsis* seedlings were incubated in either control or 150 mM NaCl-containing 1/2 MS media for 1 h before imaging. Area highlighted in the white-boxed region in the merge panel was further enlarged and presented in the inset panel. Scale bars, 5 µm. Inset scale bars, 2 µm. **(H)** Representative confocal microscopy images showing the colocalization of pALIX::GFP-3Gly-ALIX and pUBQ::mCherry-CFS1 in *Arabidopsis* root epidermal cells. 5-d-old *Arabidopsis* seedlings were incubated in either control or 150 mM NaCl-containing 1/2 MS media for 1 h before imaging. Area highlighted in the white-boxed region in the merge panel was further enlarged and presented in the inset panel. Scale bars, 5 µm. Inset scale bars, 2 µm.

Video 1. **Time-lapse video showing that mCherry-CFS1 (magenta) moves together with GFP-ATG8A (green) in *Arabidopsis* root epidermal cells.** 5-d-old *Arabidopsis* seedlings co-expressing pUBQ::GFP-ATG8A and pUBQ::mCherry-CFS1 were incubated in 150 mM NaCl-containing 1/2 MS media for 1 h for autophagy induction before imaging. Total imaging time, 60 s. Interval, 1 s. Scale bar, 10 µm.

Video 2. **Time-lapse video showing that mCherry-CFS1 (magenta) moves together with NBR1-GFP (green) in *Arabidopsis* root epidermal cells.** 5-d-old *Arabidopsis* seedlings co-expressing pNBR1::NBR1-GFP and pUBQ::mCherry-CFS1 were incubated in 150 mM NaCl-containing 1/2 MS media for 1 h for autophagy induction before imaging. Total imaging time, 60 s. Interval, 1 s. Scale bar, 10 µm.

Video 3. **Time-lapse video showing the partial colocalization and the associated movement between GFP-CFS1 (green) and VPS23A-TagRFP (magenta) in *Arabidopsis* root epidermal cells.** 5-d-old *Arabidopsis* seedlings co-expressing pUBQ::GFP-CFS1 and pVPS23A::VPS23A-TagRFP were incubated in 150 mM NaCl-containing 1/2 MS media for 1 h for autophagy induction before imaging. Total imaging time, 60 s. Interval, 1 s. Scale bar, 10 µm.

Video 4. **Time-lapse video showing cell-to-cell movement of NBR1-GFP (green)/mCherry-CFS1 (magenta) punctum in *Arabidopsis* root cells.** 5-d-old *Arabidopsis* seedlings co-expressing pNBR1::NBR1-GFP and pUBQ::mCherry-CFS1 were incubated in 150 mM NaCl-containing 1/2 MS media for 1 h for autophagy induction before imaging. Total imaging time, 60 s. Interval, 1 s. Scale bar, 5 µm.

Provided online are Table S1, Table S2, Table S3, and Table S4. Table S1 shows original mass spectromertry dataset used for analysis. Table S2 shows spectral count of the mass spectromertry data. Table S3 shows final list of proteins identified in analysis. Table S4 shows yeast two hybrid dataset.

4.2. Manuscript 2: “Cell-type specific autophagy in root hair forming cells is essential for salt stress tolerance in *Arabidopsis thaliana*”

Authors: **Jierui Zhao**, Christian Löfke, Kai Ching Yeung, Yixuan Chen, Yasin Dagdas

Contribution: All the experiments showed in figures were desgined and done by me. I also generated plasmids and transgenic Arabidopsis lines for required experiments. For the manuscript writing, I analyzed data, prepared figures, wrote and revised the manuscript.

Status: This manuscript is currently a preprint on bioRxiv posted on March 18, 2025.

DOI: https://doi.org/10.1101/2025.03.18.643786

Cell-type specific autophagy in root hair forming cells is essential for salt stress tolerance in *Arabidopsis thaliana*

Jierui Zhao[1,2], Christian Löfke[1], Kai Ching Yeung[1], Yixuan Chen[1], Yasin Dagdas[1,3,*]

[1] Gregor Mendel Institute of Molecular Plant Biology, Austrian Academy of Sciences, Vienna BioCenter, Vienna, Austria

[2] Vienna BioCenter PhD Program, Doctoral School of the University at Vienna and Medical University of Vienna, Vienna, Austria

[3] Heidelberg University, Centre for Organismal Studies (COS), 69120 Heidelberg, Germany

* Correspondence: yasin.dagdas@cos.uni-heidelberg.de

Abstract

Autophagy is a vital cellular quality control pathway that enables plants to adapt to changing environments. By degrading damaged or unwanted components, autophagy maintains cellular homeostasis. While the organismal phenotypes of autophagy-deficient plants under stress are well-characterized, the contribution of cell-type-specific autophagy responses to whole-plant homeostasis remains poorly understood. Here, we show that root hair-forming cells (trichoblasts) of *Arabidopsis thaliana* exhibit higher autophagic flux than adjacent non-hair cells (atrichoblasts). This differential autophagy is genetically linked to cell fate determination during early development. Mutants disrupting trichoblast or atrichoblast identity lose the autophagy distinction between these cell types. Functional analyses reveal that elevated autophagy in trichoblasts is essential for sodium ion sequestration in vacuoles—a key mechanism for salt stress tolerance. Disrupting autophagy specifically in trichoblasts impairs sodium accumulation and reduces plant survival under salt stress. Conversely, cell-type-specific complementation restores both sodium sequestration and stress tolerance. Our findings uncover a cell-type-specific autophagy program in root hairs and demonstrate how developmental cues shape autophagy to enhance stress resilience. This work establishes a direct link between cell identity, autophagy, and environmental adaptation in plants.

Introduction

Autophagy, a conserved eukaryotic degradation pathway, plays a pivotal role in maintaining cellular homeostasis by recycling damaged organelles, protein aggregates, and microbes (Gross et al., 2025). It is orchestrated by a suite of autophagy-related (ATG) proteins that mediate the *de novo* formation of a double-membraned vesicle, termed the autophagosome, which captures and delivers the cargo to the vacuole for breakdown (Avin-Wittenberg et al., 2015; Marshall & Vierstra, 2018). Autophagosome biogenesis is initiated by the ATG1 kinase complex (comprising ATG1, ATG13, ATG11, and ATG101), which integrates stress signals from upstream regulators such as TOR and SnRK1 kinase complexes to initiate autophagosome biogenesis (Mizushima, 2018; Marshall & Vierstra, 2018). Phagophore expansion depends on the phosphatidylinositol 3-kinase (PI3K) complex (VPS34, ATG6, VPS15), and membrane transfer is facilitated by proteins like ATG9 and ATG2 (Huang & Bassham, 2015). Autophagosome maturation requires the ubiquitin-like conjugation systems (ATG3, ATG4, ATG7, ATG12-ATG5-ATG16) responsible for ATG8 lipidation—a hallmark of autophagosome formation (Chung et al., 2010). While ATG proteins orchestrate autophagosome biogenesis, cargo selection and recruitment are mediated by selective autophagy receptors (SARs), such as NBR1 and ATI1 (Stolz et al., 2014; Svenning et al., 2011; Honig et al., 2012; Michaeli et al., 2014). SARs on the one hand interact with ATG8 via conserved ATG-interacting motifs (AIMs) and on the other hand contain cargo recognition domains for selective cargo recruitment (Kirkin & Rogov, 2019; Luong et al., 2022; Gross et al., 2025).

Plant autophagy is a critical adaptive mechanism enabling survival during environmental stress (Bassham et al., 2012; Avin-Wittenberg, 2019). Under abiotic stress, such as nutrient deprivation, drought, and salinity, autophagy reallocates cellular resources to sustain metabolic functions and delay senescence (Guiboileau et al., 2012; Avin-Wittenberg, 2019). The functional importance of autophagy in plants is underscored by the phenotypic consequences observed in autophagy-deficient mutants (atg mutants), which exhibit abnormal organ development, premature senescence, hypersensitivity to biotic and abiotic stresses, and metabolic imbalances (Yoshimoto et al., 2004; Minina et al., 2018; Yagyu & Yoshimoto, 2024). While organismal outcomes of autophagy defects are well-established, emerging evidence emphasizes its cell type-specific functions, allowing tailored responses across plant

tissues (Feng et al., 2022). For example, in the Arabidopsis root cap, autophagy facilitates the programmed death and clearance of root cap border cells, a process critical for organized cell separation and root growth (Feng et al., 2022; Goh et al., 2022). Disruption of ATG5 in the root cap via tissue-specific CRISPR mutagenesis impairs vacuolarization and the removal of dying cells, demonstrating the developmental precision of autophagy in a spatially restricted context (Feng et al., 2022). Similarly, cell-type specific autophagy has been shown to play important roles in leaf abscission (Htwe et al., 2011; Furuta et al., 2024). However, the degree to which cell-type specific autophagy responses contribute to stress tolerance remains largely unknown.

Arabidopsis roots offer an ideal system to investigate cell type-specific autophagy as the patterning of cell types that have very different metabolic and homeostatic demands are well established. Particularly the trichoblasts and atrichoblasts, which are adjacent to each other and differentiate into root hair and non-root hair cells (Datta et al., 2011), provides an excellent system to study cell-type specific homeostatic responses. The differentiation of trichoblasts (root hair cells) and atrichoblasts (non-hair cells) in the Arabidopsis root epidermis is a complex process regulated by a combination of positional signaling, transcriptional networks, and hormonal cues (Balcerowicz et al., 2015; Salazar-Henaoet al., 2016). The fate of Arabidopsis root epidermal cells is determined by their position relative to the underlying cortical cells. Cells in contact with two cortical cells (T position) become trichoblasts, while those in contact with only one cortical cell (A position) become atrichoblasts (Balcerowicz et al., 2015; Salazar-Henaoet al., 2016). The differentiation of trichoblasts and atrichoblasts are regulated by a network of transcription factors. In A-positioned cells, the MYB transcription factor WEREWOLF (WER) forms a complex with the bHLH proteins GLABRA3 (GL3) or ENHANCER OF GLABRA3 (EGL3) and the WD40 protein TRANSPARENT TESTA GLABRA1 (TTG1) (Balcerowicz et al., 2015; Salazar-Henaoet al., 2016). This complex promotes the expression of the homeodomain protein GLABRA2 (GL2), which inhibits the expression of downstream genes related to root hair formation, leading to the atrichoblast fate (Balcerowicz et al., 2015; Salazar-Henaoet al., 2016). In T-positioned cells, the R3 MYB protein CAPRICE (CPC) (or its paralogs TRYPTYCHON [TRY] and ENHANCER OF TRY AND CPC1 [ETC1]) replaces WER in the complex, preventing GL2 expression and allowing the cells to adopt the trichoblast fate (Balcerowicz et al., 2015; Salazar-Henaoet al., 2016).

Previous studies reported autophagic flux differences between root hair cells and non-root hair cells (Guichard et al., 2024). However, the physiological and genetic basis underlying this difference remains unknown. Understanding how autophagy links with the cell type-specific transcriptional programs in Arabidopsis roots may reveal novel regulatory hubs that mediate stress adaptation and developmental plasticity.

Here, we dissected autophagic flux pattern in trichoblasts and atrichoblasts during salt stress. Using a large suite of reporters, we showed that trichoblast cells have higher autophagic flux compared the adjacent atrichoblast cells. This is encoded by the trichoblast developmental program as autophagic flux differences disappeared in genetic mutants that change cell fate. Cell-type specific CRISPR mutagenesis and complementation experiments revealed higher autophagic flux in trichoblasts is crucial for salt stress tolerance. Altogether, by mapping autophagy dynamics at cellular resolution, we uncovered a cell-type specific autophagy response that is crucial for stress resilience.

Results

Trichoblasts exhibit significantly higher autophagic flux compared to atrichoblasts in the root maturation zone of *Arabidopsis thaliana*

Trichoblasts and atrichoblasts are organized in a highly structured adjacent manner. To investigate whether these two cell types exhibit distinct autophagic activities, we first measured the autophagic flux in trichoblasts and atrichoblasts at the root maturation zone of Arabidopsis wildtype Col-0 expressing GFP-ATG8A, under control and two autophagy-inducing conditions (NaCl stress and nitrogen starvation), using confocal microscopy. To accurately identify trichoblasts and atrichoblasts in our live-cell imaging experiments, we adhered to the following criteria: an epidermal cell was classified as a trichoblast if it was adjacent to two cortical cells, whereas it was classified as an atrichoblast if it was adjacent to only one cortical cell (Figure S1). Under both control and autophagy-inducing conditions, confocal microscopy revealed that trichoblasts exhibit significantly higher autophagic flux compared to the adjacent atrichoblast cells (Figure 1 and S2). Similar to ATG8A, the other eight ATG8 isoforms (ATG8B to I) also exhibited higher autophagic flux in trichoblast cells compared to atrichoblasts at the root maturation zone under control, NaCl stress, and nitrogen-starvation conditions (Figure 1 and S2). Collectively, these results demonstrate that

trichoblasts in the root maturation zone exhibit significantly higher autophagic activity compared to the adjacent atrichoblast cells. This observation prompted us to further explore this cell type specific autophagic response in more detail.

Genetic basis of the higher autophagic flux in trichoblast cells

The development of trichoblasts and atrichoblasts is regulated by a well-characterized genetic program (Balcerowicz et al., 2015; Salazar-Henao et al., 2016). While the formation of root hairs from trichoblasts at the maturation zone results in obvious surface differences, the determination of cell type identity occurs at the meristematic zone (Löfke et al., 2013). Given that both root hair structure and cell type identity could contribute to the observed differences in autophagic activity, we investigated autophagic activity in a series of Arabidopsis root epidermal development mutants. We selected four representative mutants that were previously shown to affect cell fate and identity: *rhd6 rsl1*, *cpc try*, *gl2*, and *wer myb23* (Figure 2A). *rhd6 rsl1* exhibits ectopic non-hair cells at trichoblast positions, while *gl2* displays ectopic hair cells at atrichoblast positions. However, both *rhd6 rsl1* and *gl2* retain meristematic cell type determination, as evidenced by meristematic vacuolar biogenesis phenotype (Löfke et al., 2013). In contrast, *cpc try* and *wer myb23* lose cell type determination at the meristematic stage, despite *cpc try* having ectopic non-hair cells and *wer myb23* having ectopic hair cells (Figure 2A). To test the genetic basis of higher autophagic flux in trichoblast cells, we expressed GFP-ATG8A in these four mutants, as well as in *atg5* as an autophagy-defective control, and performed live-cell imaging experiments similar to those described in Figure 1. Analysis of autophagic flux in epidermal cells at trichoblast and atrichoblast positions revealed that *rhd6 rsl1* and *gl2* maintained the autophagic flux difference, whereas *cpc try* and *wer myb23* lost this difference. This suggests cell fate defined at the meristematic zone underlies the differential autophagic activity between trichoblasts and atrichoblasts (Figure 2B–2E and S3). However, the presence of root hair structures also appeared to slightly enhance autophagic flux, as evidenced by the slightly lower autophagic flux in trichoblast-positioned cells of *rhd6 rsl1* compared to Col-0 and *gl2*, and the slightly higher autophagic flux in atrichoblast-positioned cells of *gl2* compared to other lines (Figure 2B–2E and S3).

Notably, *wer myb23* exhibited an unexpected autophagic flux pattern, with all root epidermal cells displaying very low flux (Figure 2B–2E and S3). Strikingly, GFP-ATG8A signals in *wer myb23* were predominantly localized to the endoplasmic reticulum (ER) and ER bodies under both control and autophagy-inducing conditions (Figure S4A). Colocalization experiments in Col-0 and *wer myb23* that co-express GFP-ATG8A with the ER marker DDRGK1-mCherry (Gerakis et al., 2019) confirmed the entrapment of GFP-ATG8A signal at the ER (Figure S4B). These findings suggest the transcriptional network that underlies root epidermal cell development impinges on autophagosome biogenesis and cell-type identity dictates the higher autophagic flux in trichoblast cells.

Establishment of cell-type specific CRISPR mutagenesis and complementation lines to investigate the physiological relevance of higher autophagic flux in trichoblast cells

To further investigate the physiological significance of the differential autophagic activity between trichoblasts and atrichoblasts, we established two genetic approaches to modulate autophagic flux in trichoblasts. First, using trichoblast-specific promoters *ProEXP7* and *ProRHD6* (Figure S5) and tissue-specific CRISPR knockout (CRISPR-TSKO) technology, we aimed to disrupt autophagic flux specifically in trichoblasts. We expressed *ProEXP7*-driven and *ProRHD6*-driven Cas9 to knockout *ATG5* in Col-0 expressing ProUBQ10:mCherry-ATG8E (mCherry-ATG8E in Col-0), generating the lines TSKO-E (*ProEXP7*-driven) and TSKO-R (*ProRHD6*-driven) (Figure 3A). Interestingly, under both control and NaCl stress conditions, only TSKO-R exhibited a significant reduction in mCherry-ATG8E-marked autophagic flux in trichoblasts at the maturation zone, while TSKO-E maintained autophagic flux levels similar to Col-0 (Figure S6). Given that *ProEXP7* is expressed exclusively in trichoblasts at the maturation zone, whereas *ProRHD6* is also expressed in trichoblasts at the meristematic and elongation zones (Figure S5), we hypothesized that pre-existing ATG5 is stable enough to reach maturation zone cells. Additionally, we confirmed that TSKO-R did not exhibit reduced autophagic flux in cells that don't express *RHD6* , such as those in the stele and cotyledon epidermis (Figure S7), indicating that autophagy remained intact in non-*ProRHD6* expressing regions. Based on these results, we selected TSKO-R for further studies.

In parallel, we generated Arabidopsis lines in which autophagy was specifically rescued in trichoblasts. We expressed *ProEXP7*-driven and *ProRHD6*-driven *ATG5* in Arabidopsis *atg5* mutant expressing ProUBQ10:mCherry-ATG8E (mCherry-ATG8E in *atg5*), creating the complementation lines R-ATG5 (*ProRHD6*-driven) and E-ATG5 (*ProEXP7*-driven) (Figure 3B). Subsequently, we compared mCherry-ATG8E-marked autophagic flux in Col-0, TSKO-R, R-ATG5, E-ATG5, and *atg5* under control and NaCl stress conditions. TSKO-R lost the autophagic flux difference between trichoblasts and atrichoblasts, resembling *atg5* mutant. In contrast, both R-ATG5 and E-ATG5 restored the autophagic flux difference to levels comparable to mCherry-ATG8E in Col-0 (Figure 3C–3F). These results demonstrate that TSKO-R, R-ATG5, and E-ATG5 allow us to study the physiological relevance of higher autophagic flux in trichoblast cells.

Higher autophagic flux in trichoblasts is necessary and sufficient to compartmentalize sodium ions in trichoblast vacuoles, thereby contributing to salt stress tolerance.

Next, we set out to explore the physiological relevance of higher flux in trichoblast cells. Previous studies have shown that autophagy was required for sodium ion accumulation in the vacuole of root meristem cells (Luo et al., 2017). This finding inspired us to check if higher flux in trichoblast cells is correlated with the accumulation of sodium in trichoblast vacuoles. First, we measured sodium ion concentrations in the vacuoles of epidermal cells at the root maturation zone in Col-0 and three autophagy-deficient mutants (*atg5*, *atg8*, and *atg16*), using the CoroNa Green AM staining method (Park et al., 2009; Luo et al, 2017). Notably, only trichoblasts in Col-0 exhibited significantly higher sodium ion concentrations compared to atrichoblasts (CoroNa Green AM fluorescence ratios > 1.5), whereas all autophagy-defective mutants lost this difference (CoroNa Green AM fluorescence ratios around 1) (Figure 4A and 4B). This prompted us to hypothesize that sodium accumulation in trichoblast vacuoles could help plants tolerate NaCl stress. To test our hypothesis, we grew seeds of Col-0 and autophagy-deficient mutant lines on normal 1/2 MS media for 6 days, then transferred them to 1/2 MS media supplemented with 150 mM NaCl for 4 days. Col-0 seedlings displayed significantly higher survival rates (measured as the percentage of non-etiolated leaves) compared to the autophagy-deficient lines (Figure 4C and 4D), supporting our hypothesis.

Next, we tested if higher flux in trichoblast cells contribute to NaCl stress tolerance, using the tools we established. CoroNa Green AM staining results revealed that TSKO-R, which lacks autophagic flux differences between trichoblasts and atrichoblasts, also lost the sodium ion concentration difference (Figure 4E and 4F). Conversely, the complementation lines R-ATG5 and E-ATG5, which restored autophagic flux differences, also re-established the sodium ion concentration difference between trichoblasts and atrichoblasts (Figure 4E and 4F). Given that only a subset of cells in TSKO-R lost autophagy and only a subset in R-ATG5 and E-ATG5 regained autophagy, we predicted that these lines would exhibit intermediate survival rates between Col-0 and *atg5*. Indeed, phenotyping assays using the same approach as described above demonstrated significantly lower survival rate for TSKO-R line and significantly higher survival rates for R-ATG5 and E-ATG5 lines (Figure 4G and 4H).

Collectively, these results demonstrate that autophagy mediates sodium ion sequestration in trichoblast vacuoles, thereby contributing to NaCl stress tolerance in Arabidopsis seedlings. The precise mechanism underlying this process remains to be elucidated, but our findings highlight the importance of trichoblast-specific autophagy in salt stress responses.

Discussion

Our study uncovers a critical role for cell-type-specific autophagy in trichoblasts, linking higher autophagic flux to sodium ion sequestration and salt stress tolerance in *Arabidopsis thaliana*. Under both control and stress conditions, trichoblasts exhibit significantly higher autophagic activity than atrichoblasts and this difference is essential for vacuolar sodium accumulation and plant survival under salinity.

A recent study has demonstrated that under salt stress conditions, Arabidopsis transports sodium ions to the vacuole to prevent toxicity. This compartmentalization is mediated by SOS1-transporter that is localized at the tonoplast (Ramakrishna et al., 2025). Our findings suggest elevated autophagic flux in trichoblasts correlates with enhanced capacity to sequester sodium ions in vacuoles. We envision two scenarios that may explain autophagy-mediated sodium sequestration in the vacuole: (1) Autophagy could support sodium compartmentalization via modulating the turnover or activity of sodium transporters. Previous studies in mammalian cells have shown that ion channels could modulate autophagy by ion fluxes in and out of lysosomes and they

themselves could be modulated by autophagic recycling (Kondratskyi et al., 2018). It will be interesting to test if NHX family transporters, including SOS1 are regulated by autophagic turnover. (2) Alternatively, metalloproteins that can carry sodium ions in bulk could be delivered to the vacuole via autophagy. This is akin to ferritinophagy that is mediated by the NCOA4 selective autophagy receptor (Mancias et al., 2014). NCOA4 selectively binds ferritin and delivers ferritin molecules to the lysosomes to release iron (Wang et al., 2023). Similar to ferritinophagy, sodium binding metalloproteins could be targeted by autophagy to rapidly deliver sodium ions to the vacuole and prevent cytotoxicity. These two scenarios focus on degradative function of autophagy. Alternatively, higher autophagic flux could improve cellular homeostasis, enabling trichoblasts to maintain ion balance more effectively under stress. Future studies that investigate autophagic cargo under salt stress conditions could reveal which of these scenarios underlie elevated autophagic flux in trichoblasts.

The differential autophagic flux between trichoblasts and atrichoblasts originates during cell fate specification at the meristematic zone, as evidenced by epidermal mutants (Figure 2 and S3). Mutants disrupting early trichoblast/atrichoblast (T/A) identity (*cpc try*, *wer myb23*) abolished autophagic differences, while those retaining cell fate (*rhd6 rsl1*, *gl2*) preserved them. This suggests that developmental programs dictating T/A identity directly regulate autophagy. Transcription factors or signaling molecules common to both pathways may mediate this crosstalk. The striking mislocalization of ATG8A to the ER in *wer myb23* mutants further highlights this interplay, implying that cell fate regulators impinge on the autophagosome biogenesis machinery. This unexpected finding opens new avenues to explore how developmental signalling could spatially regulate autophagy.

Our findings underscore the importance of studying autophagy at cellular resolution. Whole-organism approaches may overlook critical tissue- or cell-type-specific dynamics, as demonstrated by the stark contrast between trichoblasts and atrichoblasts. Readily available high-resolution tools such as CRISPR-TSKO, single-cell omics, and live cell imaging allows us to move from whole organism to cell-type specific autophagy studies, and opens the door to address a fundamental yet unanswered question in cell biology: How autophagy responses in different cell types are coordinated to establish an organismal homeostatic response?

By manipulating autophagy specifically in trichoblasts using CRISPR-TSKO and ATG5 complementation lines, we demonstrated its necessity and sufficiency for sodium accumulation and salt tolerance. Disrupting autophagy in trichoblasts (TSKO-R) abolished sodium differences and reduced survival under salt stress, while restoring it (R-ATG5, E-ATG5) reinstated both. These results suggest that enhancing autophagy in stress-responsive cell types, such as trichoblasts, could improve crop resilience without compromising growth. For agriculture, this strategy could mitigate yield losses in saline soils, particularly in staple crops where root hair function is pivotal for nutrient uptake.

Materials and methods

Plant material and cloning procedure

All *Arabidopsis thaliana* lines used in this study are listed in Table 1. All the plasmids established in this study are listed in Table 2. The primers used for genotyping and cloning are listed in Table 3. Synthetic sequences for plasmid construction were also listed in Table 3.

All plasmids were assembled via the GreenGate cloning method (Lampropoulos et al., 2013). DNA sequences of *ProEXP7* and *ProRHD6* were cloned from Arbidopsis genome DNA using the primers listed in Table 3 and were subsequently ligated to pGGA000 to form the promoter entry modules pGG-A-ProEXP7-B and pGG-A-ProRHD6-B, respectively. These two modules and the promoter entry module pGG-A-ProUBQ10+Ω-B (Zhao et al., 2022) were further assembled with other GreenGate modules pGGB003 (Lampropoulos et al., 2013), pSW596-mTurquoise2 (Addgene plasmid # 115985; Schürholz et al., 2018), pGGD007 (Lampropoulos et al., 2013), pGGE009 (Lampropoulos et al., 2013), pGG-F-Alired-G (Zhao et al., 2022) and pGGZ003 (Lampropoulos et al., 2013) to form the plasmids ProUBQ10:mTurquoise2-NLS, ProRHD6:mTurquoise2-NLS and ProEXP7:mTurquoise2-NLS, respectively.

For constructing plasmids for CRISPR-TSKO, we used an adapted method from Decaestecker et al., 2019. The DNA fragments of two ProU6-26-driven guide RNAs for knocking out ATG5 (ProU6-26-gATG5-1_ProU6-26-gATG5-2; Table 3) were cloned and inserted into pGGF000 to form the entry module pGG-F-gATG5-G. This entry module, together with other GreenGate modules pGG-B-Linker-C, pGG-C-Cas9PTA*-

D, pGG-D-P2A-GFP-NLS-E, pGG-E-G7T-F, pFASTR-A-G, was assmebled with either pGG-A-ProEXP7-B or pGG-A-ProRHD6-B to form the recombinant plasmids ProEXP7:Cas9-GFP_gATG5 and ProRHD6:Cas9-GFP_gATG5, respectively.

The coding sequence of Arabidopsis *ATG5* (Table 3) were cloned into pTwist Amp High Copy to form the entry module pTwist-C-ATG5-D (Twist Bioscience). The GreenGate modules pGGB003 (Lampropoulos et al., 2013), pTwist-C-ATG5-D (Twist Bioscience), pGGD002 (Lampropoulos et al., 2013), pGGE009 (Lampropoulos et al., 2013), pGG-F-Alired-G (Zhao et al., 2022) and pGGZ003 (Lampropoulos et al., 2013) were assembled with either pGG-A-ProEXP7-B or pGG-A-ProRHD6-B to form the recombinant plasmids ProEXP7:ATG5 and ProRHD6:ATG5, respectively.

All transgenic Arabidopsis lines were generated through the Agrobacterium-mediated floral-dip method (Clough and Bent, 1998). ProEXP7:Cas9-GFP_gATG5 and ProRHD6:Cas9-GFP_gATG5 were transformed into Arabidopsis wildtype Col-0 plants and the positive transformants were labeled as the line TSKO-E and TSKO-R, respectively. ProEXP7:ATG5 and ProRHD6:ATG5 were transformed into Arabidopsis *atg5-1* mutant plants and the positive transformants were labeled as the line E-ATG5 and R-ATG5, respectively.

Plant phenotypic assays

Arabidopsis seeds were sterilized with 70% ethanol + 0.5‰ Tween 20 for 15 min and then with 100% ethanol for 15 min. Sterilized seeds were subsequently stored at 4˚C for 2 d for vernalization. Vernalized seeds were sown 1/2 MS media (Murashige and Skoog salt + Gamborg B5 vitamin mixture [Duchefa] supplemented with 0.5 g/liter MES and 1% sucrose, pH 5.7) plates (+ 1% plant agar [Duchefa]) and vertically grown at 21˚C at 60% humidity under LEDs with 70 mM/m^2s a and a 16 h light/8 h dark photoperiod for 6 d. 6-d-old seedlings were subsequently transferred to 1/2 MS media plates (+1% plant agar [Duchefa]) containing 150 mM NaCl and vertically grown for 4 d. The seedlings were imaged at the day of transfer (d0) and at the fourth day after transfer (d4). The percentage of non-etiolated leaves to total leaves (including the cotyledons) of Arabidopsis seedlings at d4 were calculated for statistical analysis.

Preparation of *Arabidopsis thaliana* samples for confocal microscopy

Arabidopsis seeds were were sterilized with 70% ethanol + 0.5‰ Tween 20 for 15 min and then with 100% ethanol for 15 min. Sterilized seeds were subsequently stored at 4˚C for 2 d for vernalization. Vernalized seeds were spread on 1/2 MS media plates (+ 1% plant agar [Duchefa]) and vertically grown at 21˚C at 60% humidity under LEDs with 50 mM/m^2s a and a 16 h light/8 h dark photoperiod for 5 d. 5-day-old seedlings were placed in 1/2 MS media and treated with salt or chemicals as indicated in each experiment before confocal imaging. For nitrogen starvation, 1/2 MS media was replaced by nitrogen-deficient 1/2 MS media (Murashige and Skoog salt without nitrogen [CaissonLabs] + Gamborg B5 vitamin mixture [Duchefa] supplemented with 0.5 g/liter MES and 1% sucrose, pH 5.7).

For confocal microscopy, 5-d-old Arabidopsis seedlings were placed on a microscope slide with either water or water with 0.002 mg/ml propidium iodide and covered with a coverslip.

Confocal microscopy

All images except the cotyledon epidermis imaging (Figure S7) were acquired by an upright point laser scanning confocal microscope ZEISS LSM800 Axio Imager.Z2 (Carl Zeiss) equipped with high-sensitive GaAsP detectors (Gallium Arsenide), a Plan-Apochromat 20X objective lens (numerical aperture 0.8, dry) and ZEN software (blue edition, Carl Zeiss). For cotyledon epidermis imaging (Figure S7), a LD C-Apochromat 40X objective lens (numerical aperture 1.1, water) was used instead of the 20X one. The GFP, mTurquoise2 and CoroNa Green AM fluorescence were excited at 488 nm and detected between 488 nm and 545 nm. The propidium iodide and mCherry fluorescence was excited at 561 nm and detected between 570 nm and 617 nm. For Z-stack imaging, interval between layers was set as 1 µm. Confocal images were processed with Fiji (version 1.54f, Fiji).

Statistical analyses

All quantification analyses and statistical tests were performed with GraphPad Prism 8 software (version 8.1.1). For comparing the significance of differences between two experimental groups, paired and two-tailed student’s t-tests were performed as indicated in each experiment. For comparing the significance of differences between

multiple experimental groups, Paired repeated measures one-way ANOVA and Fisher's LSD tests were performed as indicated in each experiment.

Acknowledgments

We thank George Haughn, Moritz Nowack, Ni Zhan and Qiangnan Feng for sharing experimental materials. We acknowledge funding from Austrian Academy of Sciences, Austrian Science Fund (FWF, P32355, P34944, I 6760, SFB F79, DOC 111), Vienna Science and Technology Fund (WWTF, LS17-047, LS21-009), European Research Council Grant (Project number: 101043370), and DFG-Heisenberg Professorship to Y.D. lab. We thank Vienna Biocenter Core Facilities (VBCF) Biooptics, Plant Sciences and Molecular Biology Service.

The authors declare no competing financial interests.

Author contributions

J. Zhao designed the experiments, constructed plasmids, generated Arabidopsis lines, performed microscopy experiments and phenotypic assays, prepared figures, and wrote the draft. C. Löfke constructed plasmids, generated Arabidopsis lines and performed preliminary microscopy experiments. K. C. Yueng constructed plasmids and generated Arabidopsis lines. Y. Chen performed microscopy experiments and generated Arabidopsis lines. Y. Dagdas designed the experiments, supervised students and wrote the draft.

Data availability

All the source data associated with the data presented in this manuscript is available at Zenodo. DOI: 10.5281/zenodo.15034967 and DOI: 10.5281/zenodo.15034948

Table 1. *Arabidopsis thaliana* lines used in this study.

Name	Background	Accession Number	Source or reference
Col-0	Col-0		
atg5-1	Col-0	AT5G17290 (*ATG5*)	SAIL_129B07L; Thompson et. al. (2005) Plant Physiol.
atg8 (*ATG8* nonuple mutant)	Col-0	AT4G21980 (*ATG8A*); AT4G04620 (*ATG8B*); AT1G62040 (*ATG8C*); AT2G05630 (*ATG8D*); AT2G45170 (*ATG8E*); AT4G16520 (*ATG8F*); AT3G60640 (*ATG8G*); AT3G06420 (*ATG8H*); AT3G15580 (*ATG8I*)	Del Chiaro et al. (2024) bioRxiv.
atg16	Col-0	AT5G50230 (*ATG16*)	Julian et al. (2025) Nat Plants.
rhd6-3 rsl1-1	Col-0	AT1G66470 (*RHD6*); AT2G26130 (*RSL1*)	Menand et al. (2007) Science.
cpc-1 try-82	Col-0	AT2G46410 (*CPC*); AT5G53200 (*TRY*)	Schellmann et al. (2002) EMBO J.
wer-1 myb23-1	Col-0	AT5G14750 (*WER*); AT5G40330 (*MYB23*)	Lee and Schiefelbein (1999) Cell; Lee and Schiefelbein (2001) Development.
gl2-8	Col-0	AT1G79840 (*GL2*)	SALK_130213
ProUBQ10:GFP-ATG8A	Col-0	AT4G21980 (*ATG8A*)	Munch et. al. (2015) The Plant Cell.
ProUBQ10:GFP-ATG8B	Col-0	AT4G04620 (*ATG8B*)	Stephani et al. (2020) eLife.
ProUBQ10:GFP-ATG8C	Col-0	AT1G62040 (*ATG8C*)	Stephani et al. (2020) eLife.
ProUBQ10:GFP-ATG8D	Col-0	AT2G05630 (*ATG8D*)	Stephani et al. (2020) eLife.
ProUBQ10:GFP-ATG8E	Col-0	AT2G45170 (*ATG8E*)	Stephani et al. (2020) eLife.
ProUBQ10:GFP-ATG8F	Col-0	AT4G16520 (*ATG8F*)	Stephani et al. (2020) eLife.
ProUBQ10:GFP-ATG8G	Col-0	AT3G60640 (*ATG8G*)	Stephani et al. (2020) eLife.
ProUBQ10:GFP-ATG8H	Col-0	AT3G06420 (*ATG8H*)	Stephani et al. (2020) eLife.
ProUBQ10:GFP-ATG8I	Col-0	AT3G15580 (*ATG8I*)	Stephani et al. (2020) eLife.
ProUBQ10:GFP-ATG8A x *atg5*	*atg5-1*	AT4G21980 (*ATG8A*); AT5G17290 (*ATG5*)	This study
ProUBQ10:GFP-ATG8A x *rhd6 rsl1*	*rhd6-3 rsl1-1*	AT4G21980 (*ATG8A*); AT1G66470 (*RHD6*); AT2G26130 (*RSL1*)	This study
ProUBQ10:GFP-ATG8A x *cpc try*	*cpc-1 try-82*	AT4G21980 (*ATG8A*); AT2G46410 (*CPC*); AT5G53200 (*TRY*)	This study
ProUBQ10:GFP-ATG8A x *wer myb23*	*wer-1 myb23-1*	AT4G21980 (*ATG8A*); AT5G14750 (*WER*); AT5G40330 (*MYB23*)	This study
ProUBQ10:GFP-ATG8A x *gl2-8*	*gl2-8*	AT4G21980 (*ATG8A*); AT1G79840 (*GL2*)	This study
ProUBQ10:mTurquoise2-NLS	Col-0	AT4G05320 (*UBQ10*)	This study
ProEXP7:mTurquoise2-NLS	Col-0	AT1G12560 (*EXP7*)	This study

Table 1. *Arabidopsis thaliana* lines used in this study. (*Continued*)

ProRHD6:mTurquoise2-NLS	Col-0	AT1G66470 (*RHD6*)	This study
ProUBQ10:mCherry-ATG8E (mCherry-ATG8E in Col-0)	Col-0	AT2G45170 (*ATG8E*)	Hu et. al. (2020) J Integr Plant Biol.
ProUBQ10:mCherry-ATG8E x *atg5* (mCherry-ATG8E in *atg5*)	*atg5-1*	AT2G45170 (*ATG8E*); AT5G17290 (*ATG5*)	Zhao et al. (2022) J Cell Biol.
ProEXP7:Cas9-GFP_gATG5 (TSKO-E)	Col-0	AT5G17290 (*ATG5*)	This study
ProRHD7:Cas9-GFP_gATG5 (TSKO-R)	Col-0	AT5G17290 (*ATG5*)	This study
ProEXP7:ATG5 in mCherry-ATG8E in *atg5* (E-ATG5)	*atg5-1*	AT5G17290 (*ATG5*)	This study
ProRHD6:ATG5 in mCherry-ATG8E in *atg5* (R-ATG5)	*atg5-1*	AT5G17290 (*ATG5*)	This study
ProUBQ10:GFP-ATG8A x ProUBQ10:DDRGK1-mCherry in Col-0	Col-0	AT4G21980 (*ATG8A*); AT4G27120 (*DDRGK1*)	This study
ProUBQ10:GFP-ATG8A x ProUBQ10:DDRGK1-mCherry in *wer myb23*	*wer-1* *myb23-1*	AT4G21980 (*ATG8A*); AT4G27120 (*DDRGK1*); AT5G14750 (*WER*); AT5G40330 (*MYB23*)	This study

Table 2. List of plasmids used in this study.

Name	Accession number	Expression System	Backbone	Source or reference
pGG-A-ProEXP7-B	AT1G12560 (*EXP7*)	*Escherichia coli*	pGGA000	This study
pGG-A-ProRHD6-B	AT1G66470 (*RHD6*)	*Escherichia coli*	pGGA000	This study
ProUBQ10:mTurquoise2-NLS	AT4G05320 (*UBQ10*)	*Arabidopsis thaliana*	pGGZ003	This study
ProEXP7:mTurquoise2-NLS	AT1G12560 (*EXP7*)	*Arabidopsis thaliana*	pGGZ003	This study
ProRHD6:mTurquoise2-NLS	AT1G66470 (*RHD6*)	*Arabidopsis thaliana*	pGGZ003	This study
pGG-F-gATG5-G	AT5G17290 (*ATG5*)	*Escherichia coli*	pGGF000	Adapted from Decaestecker et al. (2019) The Plant Cell.
ProEXP7:Cas9-GFP_gATG5	AT1G12560 (EXP7); AT5G17290 (*ATG5*)	*Arabidopsis thaliana*	pFASTR-AG	Adapted from Decaestecker et al. (2019) The Plant Cell.
ProRHD6:Cas9-GFP_gATG5	AT1G66470 (RHD6); AT5G17290 (*ATG5*)	*Arabidopsis thaliana*	pFASTR-AG	Adapted from Decaestecker et al. (2019) The Plant Cell.
pTwist-C-ATG5-D	AT5G17290 (*ATG5*)	*Escherichia coli*	pTwist Amp High Copy	Twist Bioscience
ProEXP7:ATG5	AT1G12560 (EXP7); AT5G17290 (*ATG5*)	*Arabidopsis thaliana*	pGGZ003	This study
ProRHD6:ATG5	AT1G66470 (RHD6); AT5G17290 (*ATG5*)	*Arabidopsis thaliana*	pGGZ003	This study

Table 3. Primers and synthetic sequences used in this study.

Name	Sequence	Note	Source or reference
LBb1.3 (SAIK)	ATTTTGCCGATTTCGGAAC	For genotyping	SIGnAL. 2017.
gl2-8 (LP)	ACCACCGATCAGATCAGACAC	For genotyping	SIGnAL. 2017.
gl2-8 (RP)	GGAGTTTTCGAGGTGGAGATC	For genotyping	SIGnAL. 2017.
wer-1-F	TCATTAGGCTCCACAAGTTG	For genotyping	Lee and Schiefelbein (1999) Cell.
wer-1-R	GATGCGTGTTCCAATAGTTC	For genotyping	Lee and Schiefelbein (1999) Cell.
myb23-1 (LP)	AAAAGCTACAAGCAAATATTCGG	For genotyping	SIGnAL. 2017.
myb23-1 (RP)	TGTTCGATCCTTAGTTCACGG	For genotyping	SIGnAL. 2017.
ProEXP7-F	AACAGGTCTCAACCTCTTTGCTTTCTCCGGTTCAATTG	For cloning ProEXP7	This study
ProEXP7-R	AACAGGTCTCATGTTTCTAGCCTCTTTTTCTTTATTCTTAG	For cloning ProEXP7	This study
ProRHD6-1F	AACAGGTCTCAACCTCTCAAAGAGGGACAAGACCAAAG	For cloning ProRHD6 part 1	This study
ProRHD6-1R	AACAGGTCTCATACCAAAACATGCTAAAACCTT	For cloning ProRHD6 part 1	This study
ProRHD6-2F	AACAGGTCTCAGGTATCTAAACCCAAAGAATGG	For cloning ProRHD6 part 2	This study
ProRHD6-2R	AACAGGTCTCATGTTTAGACACTAATAAGTTTGATAAG	For cloning ProRHD6 part 2	This study
ProU6-26-gATG5-1_ProU6-26-gATG5-2 (Sequence inserted to pGGF000 to form the recombinant plasmid pGG-F-gATG5-G)	CTCTTTTTTTCTTCTTCTTCGTTCATACAGTTTTTTTTGTTTATCAGCTTACATTTTCTTGAACCGTAGCTTTCGTTTTCTTCTTTTTAACTTTCCATTCGGAGTTTTTGTATCTTGTTTCATAGTTTGTCCCAGGATTAGAATGATTAGGCATCGAACCTTCAAGAATTTGATTGAATAAAACATCTTCATTCTTAAGATATGAAGATAATCTTCAAAAGGCCCCTGGGAATCTGAAAGAAGAGAAGCAGGCCCATTTATATGGGAAAGAACAATAGTATTTCTTATATAGGCCCATTTAAGTTGAAAACAATCTTCAAAAGTCCCACATCGCTTAGATAAGAAAACGAAGCTGAGTTTATATACAGCTAGAGTCGAAGTAGTGATTGACTCGTACCGTTCATGACAGGTTTTAGAGCTAGAAATAGCAAGTTAAAATAAGGCTAGTCCGTTATCAACTTGAAAAAGTGGCACCGAGTCGGTGCTTTTTTTAACAGTATTCAGTCGACTGGTACCAACAGGCTCTCTTTTTTTCTTCTTCTTCGTTCATACAGTTTTTTTTTGTTTATCAGCTTACATTTTCTTGAACCGTAGCTTTCGTTTTCTTCTTTTTAACTTTCCATTCGGAGTTTTTGTATCTTGTTTCATAGTTTGTCCCAGGATTAGAATGATTAGGCATCGAACCTTCAAGAATTTGATTGAATAAAACATCTTCATTCTTAAGATATGAAGATAATCTTCAAAAGGCCCCTGGGAATCTGAAAGAAGAGAAGCAGGCCCATTTATATGGGAAAGAACAATAGTATTTCTTATATAGGCCCATTTAAGTTGAAAACAATCTTCAAAAGTCCCACATCGCTTAGATAAGAAAACGAAGCTGAGTTTATATAC	Sequence for Greengate entry module cloning	Adapted from Decaestecker et al. (2019) The Plant Cell.

	AGCTAGAGTCGAAGTAGTGATTGAACATACTGAT ACCATGTGAGTTTTAGAGCTAGAAATAGCAAGTT AAAATAAGGCTAGTCCGTTATCAACTTGAAAAAG TGGCACCGAGTCGGTGCTTTTTTT		
AtATG5 CDS (Sequence inserted to pTwist Amp High Copy to form the recombinant plasmid pTwist-C-ATG5-D	ATGGCGAAGGAAGCGGTCAAGTATGTATGGGAA GGAGCAATTCCTCTGCAGATTCATCTCCACAAAT CCGACGTCGCTTCTCACCCTGCTCCTCCTCCTG CTCTTGTGTTAGCACCAAGAATAGGATATTTGCC TCTGTTGATTCCTCTTATAAAGCCTTATTTCAAGG ATTCACTTCCTCCTGGTGAAGATTCAATTTGGTT TGATTACAAAGGATTTCCTCTAAAATGGTATATA CCAACAGGTGTTCTTTTCGATCTCCTTTGTGCAG AACCCGAAAGACCATGGAATCTCACGATACACTT TAGAGGATATCCTTGCAACATACTGATACCATGT GAAGGAGAAGATTCTGTAAAATGGAACTTTGTTA ATTCTTTGAAAGAGGCACAATATATCATCAATGG AAATTGCAAGAATGTTATGAACATGTCTCAGAGT GATCAAGAGGATCTATGGACCTCTGTCATGAAC GGTGATCTTGATGCCTATACAAGATTATCACCCA AGCTTAAAATGGGAACAGTCGAAGATGAGTTTTC AAGGAAAACAAGTTTGTCATCTCCACAATCTCAA CAAGTTGTGCCTGAGACGGAGGTGGCTGGACAA GTTAAGACAGCAAGAATTCCTGTTCGGTTGTATG TTCGAAGTCTAAATAAAGATTTCGAGAATCTTGA AGATGTACCGGAGATCGATACCTGGGATGACAT CTCGTACCTTAATCGCCCTGTTGAGTTCCTCAAA GAAGAAGGGAAATGCTTTACGTTACGTGACGCC ATTAAAAGTCTCCTCCCTGAGTTTATGGGAGACA GAGCGCAAACGAGTGGTGAAGAAAGAAGCATAG ATGATACAGAAGAAGCAGATGGGTCGAGGGAGA TGGGTGAAATCAAATTGGTAAGGATACAAGGGA TAGAAATGAAGCTAGAGATACCGTTTTCGTGGGT GGTAAATAACTTGATGAACCCAGAATTCTATCTC CATATCTCTGTCCTTGTGAAAGCTCCTCAAAGGT GA	Arabidopsis ATG5 coding sequence for Greengate entry module cloning	Accession number AT5G17290

References

Avin-Wittenberg, T., Bajdzienko, K., Wittenberg, G., Alseekh, S., Tohge, T., Bock, R., Giavalisco, P., & Fernie, A. R. (2015). Global analysis of the role of autophagy in cellular metabolism and energy homeostasis in arabidopsis seedlings under carbon starvation. *Plant Cell*, *27*(2), 306–322. https://doi.org/10.1105/tpc.114.134205

Balcerowicz, D., Schoenaers, S., & Vissenberg, K. (2015). Cell fate determination and the switch from diffuse growth to planar polarity in arabidopsis root epidermal cells. *Frontiers in Plant Science*, *6*(DEC), 1–13. https://doi.org/10.3389/fpls.2015.01163

Chen, W., Hu, Z., Yu, M. T., Zhu, S., Xing, J., Song, L., Pu, W., & Yu, F. (2022). A molecular link between autophagy and circadian rhythm in plants. *Journal of Integrative Plant Biology*, *64*(5), 1044–1058. https://doi.org/10.1111/jipb.13250

Clough, S. J., & Bent, A. F. (1998). Floral dip: A simplified method for Agrobacterium-mediated transformation of Arabidopsis thaliana. *Plant Journal*, *16*(6), 735–743. https://doi.org/10.1046/j.1365-313X.1998.00343.x

Decaestecker, W., Buono, R. A., Pfeiffer, M. L., Vangheluwe, N., Jourquin, J., Karimi, M., van Isterdael, G., Beeckman, T., Nowack, M. K., & Jacobs, T. B. (2019). CRISPR-Tsko: A technique for efficient mutagenesis in specific cell types, tissues, or organs in Arabidopsis[open]. *Plant Cell*, *31*(12), 2868–2887. https://doi.org/10.1105/tpc.19.00454

Del Chiaro, A., Grujic, N., Zhao, J., Papareddy, R. K., Gao, P., Ma, J., Lofke, C., Bhattacharya, A., Gruetzner, R., & Bourguet, P. (2024). Nonuple atg8 mutant provides genetic evidence for functional specialization of ATG8 isoforms in Arabidopsis thaliana. *BioRxiv*, 2012–2024.

Feng, Q., De Rycke, R., Dagdas, Y., & Nowack, M. K. (2022). Erratum: Autophagy promotes programmed cell death and corpse clearance in specific cell types of the Arabidopsis root cap (Current biology : CB (2022) 32 9 (2110-2119.e3) PII: S0960-9822(22)01614-1). *Current Biology : CB*, *32*(20), 4548. https://doi.org/10.1016/j.cub.2022.10.006

Furuta, Y., Yamamoto, H., Hirakawa, T., Uemura, A., Pelayo, M. A., Iimura, H.,

Katagiri, N., Takeda-Kamiya, N., Kumaishi, K., Shirakawa, M., Ishiguro, S., Ichihashi, Y., Suzuki, T., Goh, T., Toyooka, K., Ito, T., & Yamaguchi, N. (2024). Petal abscission is promoted by jasmonic acid-induced autophagy at Arabidopsis petal bases. *Nature Communications*, *15*(1), 1098. https://doi.org/10.1038/s41467-024-45371-3

Gerakis, Y., Quintero, M., Li, H., & Hetz, C. (2019). The UFMylation System in Proteostasis and Beyond. *Trends in Cell Biology*, *29*(12), 974–986. https://doi.org/10.1016/j.tcb.2019.09.005

Goh, T., Sakamoto, K., Wang, P., Kozono, S., Ueno, K., Miyashima, S., Toyokura, K., Fukaki, H., Kang, B. H., & Nakajima, K. (2022). Autophagy promotes organelle clearance and organized cell separation of living root cap cells in Arabidopsis thaliana. *Development (Cambridge)*, *149*(11), dev200593. https://doi.org/10.1242/dev.200593

Guiboileau, A., Yoshimoto, K., Soulay, F., Bataillé, M. P., Avice, J. C., & Masclaux-Daubresse, C. (2012). Autophagy machinery controls nitrogen remobilization at the whole-plant level under both limiting and ample nitrate conditions in Arabidopsis. *New Phytologist*, *194*(3), 732–740. https://doi.org/10.1111/j.1469-8137.2012.04084.x

Guichard, M., Holla, S., Wernerová, D., Grossmann, G., & Minina, E. A. (2024). RoPod, a customizable toolkit for non-invasive root imaging, reveals cell type-specific dynamics of plant autophagy. *Scientific Reports*, *14*(1), 12664. https://doi.org/10.1038/s41598-024-63226-1

Honig, A., Avin-Wittenberg, T., Ufaz, S., & Galili, G. (2012). A new type of compartment, defined by plant-specific Atg8-interacting proteins, is induced upon exposure of Arabidopsis plants to carbon starvation. *Plant Cell*, *24*(1), 288–303. https://doi.org/10.1105/tpc.111.093112

Htwe, N. M. P. S., Yuasa, T., Ishibashi, Y., Tanigawa, H., Okuda, M., Zheng, S. H., & Iwaya-Inoue, M. (2011). Leaf Senescence of Soybean at Reproductive Stage is Associated with Induction of Autophagy-Related Genes, GmATG8c, GmATG8i and GmATG4. *Plant Production Science*, *14*(2), 141–147. https://doi.org/10.1626/pps.14.141

Hu, S., Ye, H., Cui, Y., & Jiang, L. (2020). AtSec62 is critical for plant development

464 and is involved in ER-phagy in Arabidopsis thaliana. *Journal of Integrative Plant*
465 *Biology*, *62*(2), 181–200. https://doi.org/10.1111/jipb.12872

466 Julian, J., Gao, P., del Chiaro, A., De la Concepcion, J. C., Armengot, L., Somssich,
467 M., Duverge, H., Clavel, M., Grujic, N., Kobylinska, R., Polivka, I., Besten, M.,
468 Dank, C., Korbei, B., Bachmair, A., Coll, N. S., Sprakel, J., & Dagdas, Y. F.
469 (2024). ATG8ylation of vacuolar membrane protects plants against cell wall
470 damage. *BioRxiv*, 590262. https://doi.org/10.1101/2024.04.21.590262

471 Kirkin, V., & Rogov, V. V. (2019). A Diversity of Selective Autophagy Receptors
472 Determines the Specificity of the Autophagy Pathway. *Molecular Cell*, *76*(2),
473 268–285. https://doi.org/10.1016/j.molcel.2019.09.005

474 Kondratskyi, A., Kondratska, K., Skryma, R., Klionsky, D. J., & Prevarskaya, N.
475 (2018). Ion channels in the regulation of autophagy. *Autophagy*, *14*(1), 3–21.
476 https://doi.org/10.1080/15548627.2017.1384887

477 Lampropoulos, A., Sutikovic, Z., Wenzl, C., Maegele, I., Lohmann, J. U., & Forner, J.
478 (2013). GreenGate - A novel, versatile, and efficient cloning system for plant
479 transgenesis. *PLoS ONE*, *8*(12), e83043.
480 https://doi.org/10.1371/journal.pone.0083043

481 Lee, M. M., & Schiefelbein, J. (1999). WEREWOLF, a MYB-related protein in
482 Arabidopsis, is a position-dependent regulator of epidermal cell patterning. *Cell*,
483 *99*(5), 473–483. https://doi.org/10.1016/S0092-8674(00)81536-6

484 Lee, M. M., & Schiefelbein, J. (2001). Developmentally distinct MYB genes encode
485 functionally equivalent proteins in Arabidopsis. *Development*, *128*(9), 1539–
486 1546. https://doi.org/10.1242/dev.128.9.1539

487 Liu, Y., & Bassham, D. C. (2012). Autophagy: Pathways for self-eating in plant cells.
488 *Annual Review of Plant Biology*, *63*(1), 215–237.
489 https://doi.org/10.1146/annurev-arplant-042811-105441

490 Löfke, C., Dünser, K., & Kleine-Vehn, J. (2013). Epidermal patterning genes impose
491 non-cell autonomous cell size determination and have additional roles in root
492 meristem size control. *Journal of Integrative Plant Biology*, *55*(9), 864–875.
493 https://doi.org/10.1111/jipb.12097

494 Luo, L., Zhang, P., Zhu, R., Fu, J., Su, J., Zheng, J., Wang, Z., Wang, D., & Gong, Q.

(2017). Autophagy is rapidly induced by salt stress and is required for salt tolerance in arabidopsis. *Frontiers in Plant Science*, *8*, 1459. https://doi.org/10.3389/fpls.2017.01459

Luong, A. M., Koestel, J., Bhati, K. K., & Batoko, H. (2022). Cargo receptors and adaptors for selective autophagy in plant cells. *FEBS Letters*, *596*(17), 2104–2132. https://doi.org/10.1002/1873-3468.14412

Mancias, J. D., Wang, X., Gygi, S. P., Harper, J. W., & Kimmelman, A. C. (2014). Quantitative proteomics identifies NCOA4 as the cargo receptor mediating ferritinophagy. *Nature*, *508*(7498), 105–109. https://doi.org/10.1038/nature13148

Marshall, R. S., & Vierstra, R. D. (2018). Autophagy: The Master of Bulk and Selective Recycling. *Annual Review of Plant Biology*, *69*, 173–208. https://doi.org/10.1146/annurev-arplant-042817-040606

Menand, B., Yi, K., Jouannic, S., Hoffmann, L., Ryan, E., Linstead, P., Schaefer, D. G., & Dolan, L. (2007). An ancient mechanism controls the development of cells with a rooting function in land plants. *Science*, *316*(5830), 1477–1480. https://doi.org/10.1126/science.1142618

Michaeli, S., Honig, A., Levanony, H., Peled-Zehavi, H., & Galili, G. (2014). Arabidopsis ATG8-INTERACTING PROTEIN1 is involved in autophagy-dependent vesicular trafficking of plastid proteins to the vacuole. *Plant Cell*, *26*(10), 4084–4101. https://doi.org/10.1105/tpc.114.129999

Minina, E. A., Moschou, P. N., Vetukuri, R. R., Sanchez-Vera, V., Cardoso, C., Liu, Q., Elander, P. H., Dalman, K., Beganovic, M., Lindberg Yilmaz, J., Marmon, S., Shabala, L., Suarez, M. F., Ljung, K., Novák, O., Shabala, S., Stymne, S., Hofius, D., & Bozhkov, P. V. (2018). Transcriptional stimulation of rate-limiting components of the autophagic pathway improves plant fitness. *Journal of Experimental Botany*, *69*(6), 1415–1432. https://doi.org/10.1093/jxb/ery010

Mizushima, N. (2018). A brief history of autophagy from cell biology to physiology and disease. *Nature Cell Biology*, *20*(5), 521–527. https://doi.org/10.1038/s41556-018-0092-5

Munch, D., Teh, O. K., Malinovsky, F. G., Liu, Q., Vetukuri, R. R., Kasmi, F. El, Brodersen, P., Hara-Nishimura, I., Dangl, J. L., Petersen, M., Mundy, J., &

526 Hofius, D. (2015). Retromer contributes to immunity-associated cell death in
527 arabidopsis. *Plant Cell*, *27*(2), 463–479. https://doi.org/10.1105/tpc.114.132043

528 Park, M., Lee, H., Lee, J. S., Byun, M. O., & Kim, B. G. (2009). In planta
529 measurements of Na+ using fluorescent dye CoroNa Green. *Journal of Plant*
530 *Biology*, *52*(4), 298–302. https://doi.org/10.1007/s12374-009-9036-8

531 Ramakrishna, P., Gámez-Arjona, F. M., Bellani, E., Martin-Olmos, C., Escrig, S., De
532 Bellis, D., De Luca, A., Pardo, J. M., Quintero, F. J., Genoud, C., Sánchez-
533 Rodriguez, C., Geldner, N., & Meibom, A. (2025). Elemental cryo-imaging
534 reveals SOS1-dependent vacuolar sodium accumulation. *Nature*, *637*(8048),
535 1228–1233. https://doi.org/10.1038/s41586-024-08403-y

536 Rothermel, B. A., & Diwan, A. (2021). Autophagy in Health and Disease. *Autophagy*
537 *in Health and Disease*, *76*, 1–433. https://doi.org/10.1016/B978-0-12-822003-
538 0.01001-9

539 Salazar-Henao, J. E., Vélez-Bermúdez, I. C., & Schmidt, W. (2016). The regulation
540 and plasticity of root hair patterning and morphogenesis. *Development*
541 *(Cambridge)*, *143*(11), 1848–1858. https://doi.org/10.1242/dev.132845

542 Schellmann, S., Schnittger, A., Kirik, V., Wada, T., Okada, K., Beerman, A.,
543 Thumfahrt, J., Jürgens, G., & Hülskamp, M. (2002). TRIPTYCHON and
544 CAPRICE mediate lateral inhibition during trichome and root hair patterning in
545 Arabidopsis. *EMBO Journal*, *21*(19), 5036–5046.
546 https://doi.org/10.1093/emboj/cdf524

547 Schürholz, A. K., López-Salmerón, V., Li, Z., Forner, J., Wenzl, C., Gaillochet, C.,
548 Augustin, S., Barro, A. V., Fuchs, M., Gebert, M., Lohmann, J. U., Greb, T., &
549 Wolf, S. (2018). A comprehensive toolkit for inducible, cell type-specific gene
550 expression in Arabidopsis. *Plant Physiology*, *178*(1), 40–53.
551 https://doi.org/10.1104/pp.18.00463

552 Stephani, M., Picchianti, L., Gajic, A., Beveridge, R., Skarwan, E., Hernandez, V. S.
553 de M., Mohseni, A., Clavel, M., Zeng, Y., Naumann, C., Matuszkiewicz, M.,
554 Turco, E., Loefke, C., Li, B., Durnberger, G., Schutzbier, M., Chen, H. T.,
555 Abdrakhmanov, A., Savova, A., … Dagdas, Y. (2020). A cross-kingdom
556 conserved er-phagy receptor maintains endoplasmic reticulum homeostasis
557 during stress. *ELife*, *9*, 1–105. https://doi.org/10.7554/ELIFE.58396

Stolz, A., Ernst, A., & Dikic, I. (2014). Cargo recognition and trafficking in selective autophagy. *Nature Cell Biology*, *16*(6), 495–501. https://doi.org/10.1038/ncb2979

Svenning, S., Lamark, T., Krause, K., & Johansen, T. (2011). Plant NBR1 is a selective autophagy substrate and a functional hybrid of the mammalian autophagic adapters NBR1 and p62/SQSTM1. *Autophagy*, *7*(9), 993–1010. https://doi.org/10.4161/auto.7.9.16389

Thompson, A. R., Doelling, J. H., Suttangkakul, A., & Vierstra, R. D. (2005). Autophagic nutrient recycling in Arabidopsis directed by the ATG8 and ATG12 conjugation pathways. *Plant Physiology*, *138*(4), 2097–2110. https://doi.org/10.1104/pp.105.060673

Wang, J., Wu, N., Peng, M., Oyang, L., Jiang, X., Peng, Q., Zhou, Y., He, Z., & Liao, Q. (2023). Ferritinophagy: research advance and clinical significance in cancers. *Cell Death Discovery*, *9*(1), 463. https://doi.org/10.1038/s41420-023-01753-y

Yagyu, M., & Yoshimoto, K. (2024). New insights into plant autophagy: molecular mechanisms and roles in development and stress responses. *Journal of Experimental Botany*, *75*(5), 1234–1251. https://doi.org/10.1093/jxb/erad459

Yoshimoto, K., Hanaoka, H., Sato, S., Kato, T., Tabata, S., Noda, T., & Ohsumi, Y. (2004). Processing of ATG8s, ubiquitin-like proteins, and their deconjugation by ATG4s are essential for plant autophagy. *Plant Cell*, *16*(11), 2967–2983. https://doi.org/10.1105/tpc.104.025395

Zhao, J., Bui, M. T., Ma, J., Künzl, F., Picchianti, L., de la Concepcion, J. C., Chen, Y., Petsangouraki, S., Mohseni, A., García-Leon, M., Gomez, M. S., Giannini, C., Gwennogan, D., Kobylinska, R., Clavel, M., Schellmann, S., Jaillais, Y., Friml, J., Kang, B. H., & Dagdas, Y. (2022). Plant autophagosomes mature into amphisomes prior to their delivery to the central vacuole. *Journal of Cell Biology*, *221*(12), e202203139. https://doi.org/10.1083/jcb.202203139

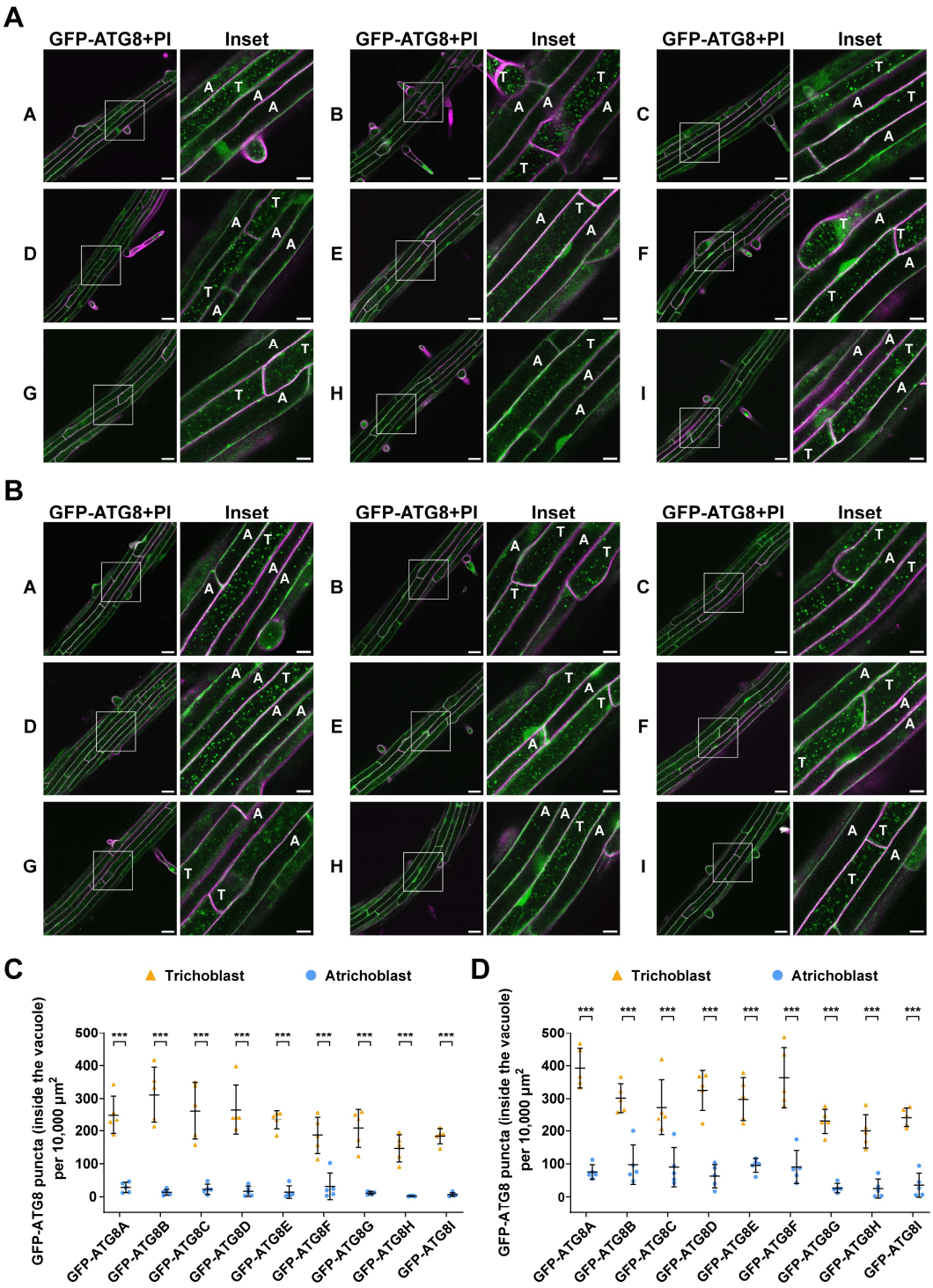

Figure 1. Trichoblasts exhibit significantly higher autophagic flux than neighboring atrichoblasts under both control and NaCl treatments in *Arabidopsis thaliana* root maturation zone.

(A) Confocal microscopy images of the trichoblasts and atrichoblasts at root maturation zone of Arabidopsis wildtype Col-0 expressing ProUBQ10:GFP-ATG8A–I isoforms under control treatment. 5-d-old Arabidopsis seedlings were incubated in control 1/2 MS media containing 2 µm concanamycin A for 2 h before imaging. Representative images of 5 replicates are shown. Area highlighted in the white-boxed region in the GFP-ATG8+PI panel was further enlarged and presented in the inset panel. Scale bars, 30 µm. Inset scale bars, 10 µm. Green color, GFP-ATG8A–I isoforms. Magenta color, propidium iodide dye. T, trichoblasts. A, atrichoblasts.

(B) Confocal microscopy images of the trichoblasts and atrichoblasts at root maturation zone of Arabidopsis wildtype Col-0 expressing ProUBQ10:GFP-ATG8A–I isoforms under NaCl treatment. 5-d-old Arabidopsis seedlings were incubated in 1/2 MS media containing 50 mM NaCl + 1 µm concanamycin A for 40-60 min before imaging. Representative images of 5 replicates are shown. Area highlighted in the white-boxed region in the GFP-ATG8+PI panel was further enlarged and presented in the inset panel. Scale bars, 30 µm. Inset scale bars, 10 µm. Green color, GFP-ATG8A–I isoforms. Magenta color, propidium iodide dye. T, trichoblasts. A, atrichoblasts.

(C) Quantification of the GFP-ATG8 puncta inside the vacuole per normalized area (10,000 μm^2) of the trichoblasts and atrichoblasts imaged in A. Bars indicate the mean ± SD of 5 replicates. Two-tailed and paired student t-tests were performed to analyze the significance of GFP-ATG8 puncta density differences between the trichoblasts and the atrichoblasts. ***, $P < 0.001$.

(D) Quantification of the GFP-ATG8 puncta inside the vacuole per normalized area (10,000 μm^2) of the trichoblasts and atrichoblasts imaged in B. Bars indicate the mean ± SD of 5 replicates. Two-tailed and paired student t-tests were performed to analyze the significance of GFP-ATG8 puncta density differences between the trichoblasts and the atrichoblasts. ***, $P < 0.001$.

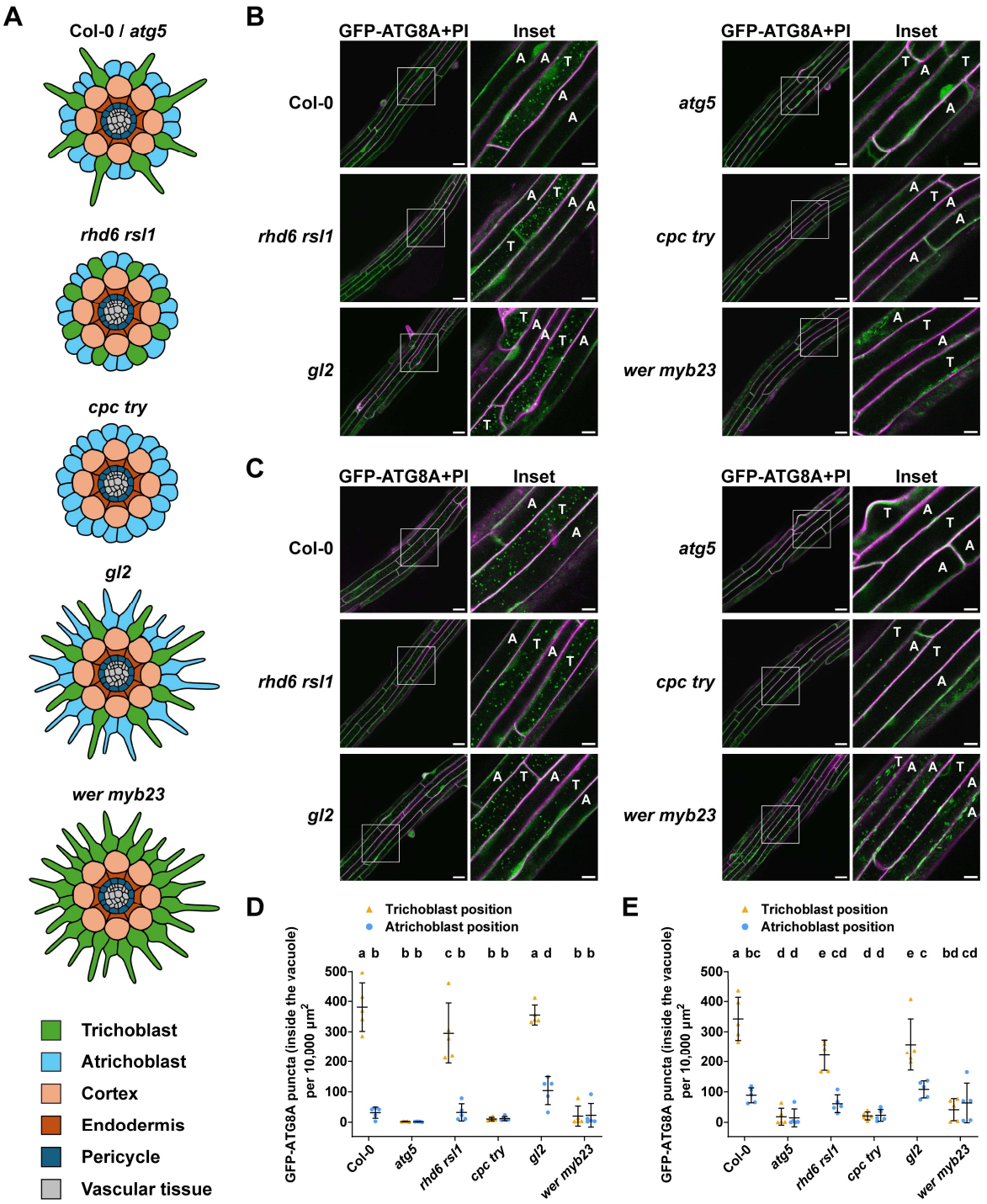

Figure 2. Genetic basis of the autophagic flux difference between trichoblasts and atrichoblasts.

(A) Schematic diagram showing the trichoblast-atrichoblast distribution pattern in Arabidopsis wildtype Col-0, the autophagy-defective mutant *atg5* and different root-hair development mutant lines *rhd6 rsl1*, *cpc try*, *gl2* and *wer myb23*.

(B) Confocal microscopy images of epidermal cells at the root maturation zone of Col-0, *atg5*, *rhd6 rsl1*, *cpc try*, *gl2* and *wer myb23* expressing ProUBQ10:GFP-ATG8A under control treatment. 5-d-old Arabidopsis seedlings were incubated in control 1/2 MS media containing 2 μm concanamycin A for 2 h before imaging. Representative images of 5 replicates are shown. Area highlighted in the white-boxed region in the GFP-ATG8A+PI panel was further enlarged and presented in the inset panel. Scale bars, 30 μm. Inset scale bars, 10 μm. Green color, GFP-ATG8A. Magenta color, propidium iodide dye. Note, T indicates the trichoblast positions (adjacent to two cortex cells) and A indicates the atrichoblast positions (adjacent to only one cortex cell), rather than the cell identities as mutants are affected in cell identity development.

(C) Confocal microscopy images of epidermal cells at the root maturation zone of Col-0, *atg5*, *rhd6 rsl1*, *cpc try*, *gl2* and *wer myb23* expressing ProUBQ10:GFP-ATG8A under NaCl treatment. 5-d-old Arabidopsis seedlings were incubated in 1/2 MS media containing 50 mM NaCl + 1 μm concanamycin A for 40-60 min before imaging. Representative images of 5 replicates are shown. Area highlighted in the white-boxed region in the GFP-ATG8A+PI panel was further enlarged and presented in the inset panel. Scale bars, 30 μm. Inset scale bars, 10 μm. Green color, GFP-ATG8A. Magenta color, propidium iodide dye. Note, T indicates the trichoblast positions (adjacent to two cortex cells) and A indicates the atrichoblast positions (adjacent to only one cortex cell), rather than the cell identities as mutants are affected in cell identity development.

(D) Quantification of the GFP-ATG8A puncta inside the vacuole per normalized area (10,000 μm^2) of the cells at the trichoblast positions and the atrichoblast positions imaged in B. Bars indicate the mean ± SD of 5 replicates. Paired repeated measures one-way ANOVA and Fisher's LSD tests were used to analyze the differences of the number of the GFP-ATG8A puncta between each group. Family-wise significance and confidence level, 0.05 (95% confidence interval).

(E) Quantification of the GFP-ATG8A puncta inside the vacuole per normalized area (10,000 μm^2) of the cells at the trichoblast positions and the atrichoblast positions imaged in C. Bars indicate the mean ± SD of 5 replicates. Paired repeated measures one-way ANOVA and Fisher's LSD tests were used to analyze the differences of the number of the GFP-ATG8A puncta between each group. Family-wise significance and confidence level, 0.05 (95% confidence interval).

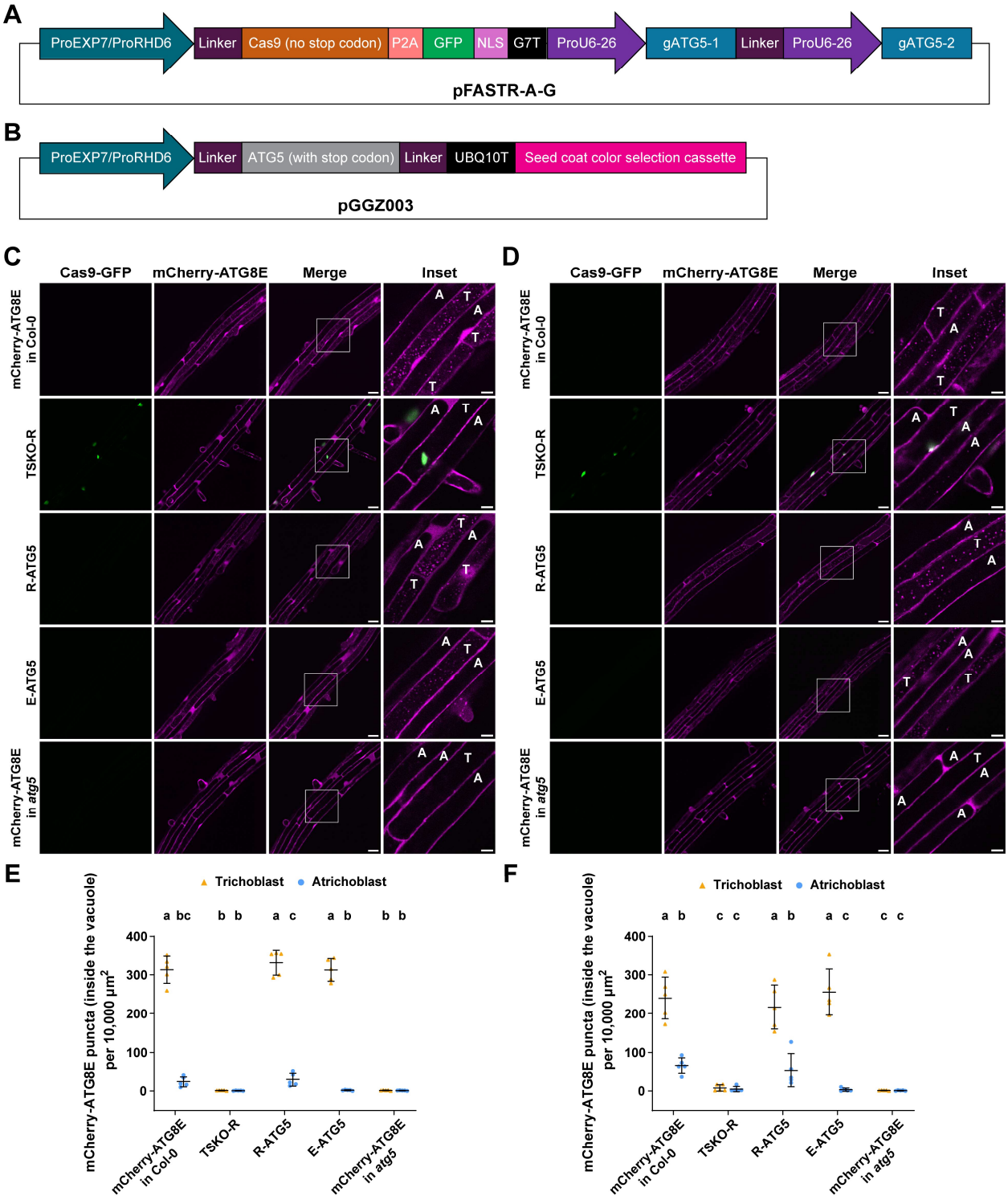

Figure 3. Tissue specific CRISPR mutagenesis and complementation of *ATG5* confirm higher autophagic flux in trichoblast cells.

(A) Schematic diagram showing the design of the trichoblast-specific *ATG5* CRISPR mutagenesis plasmid expressed in wild type Col-0 expressing ProUBQ10:mCherry-ATG8E(mCherry-ATG8E in Col-0).

(B) Schematic diagram showing the design of the trichoblast-specific *ATG5* complementation plasmid transformed to complement the autophagy-defective mutant *atg5* rexpressing ProUBQ10:mCherry-ATG8E (mCherry-ATG8E in *atg5*).

(C) Confocal microscopy images of trichoblasts and atrichoblasts of Arabidopsis lines mCherry-ATG8E in Col-0, TSKO-R (*ATG5* mutagenized using *ProRHD6*-driven Cas9), R-ATG5 (*atg5* mutant complemented with *ProRHD6*-driven *ATG5*), E-ATG5 (*atg5* mutant complemented with *ProEXP7*-driven *ATG5*) and mCherry-ATG8E in *atg5* under control treatment. 5-d-old Arabidopsis seedlings were incubated in control 1/2 MS media containing 2 µm concanamycin A for 2 h before imaging. Representative images of 5 replicates are shown. Area highlighted in the white-boxed region in the merge panel was further enlarged and presented in the inset panel. Scale bars, 30 µm. Inset scale bars, 10 µm. T, trichoblasts. A, atrichoblasts.

(D) Confocal microscopy images of trichoblasts and atrichoblasts of Arabidopsis lines mCherry-ATG8E in Col-0, TSKO-R (*ATG5* mutagenized using *ProRHD6*-driven Cas9), R-ATG5 (*atg5* mutant complemented with *ProRHD6*-driven *ATG5*), E-ATG5 (*atg5* mutant complemented with *ProEXP7*-driven *ATG5*) and mCherry-ATG8E in *atg5* under NaCl stress treatment. 5-d-old Arabidopsis seedlings were incubated in 1/2 MS media containing 50 mM NaCl + 1 µm concanamycin A for 1 h before imaging. Representative images of 5 replicates are shown. Area highlighted in the white-boxed region in the merge panel was further enlarged and presented in the inset panel. Scale bars, 30 µm. Inset scale bars, 10 µm. T, trichoblasts. A, atrichoblasts.

(E) Quantification of the mCherry-ATG8E puncta inside the vacuole per normalized area (10,000 μm^2) of the trichoblasts and atrichoblasts imaged in C. Bars indicate the mean ± SD of 5 replicates. Paired repeated measures one-way ANOVA and Fisher's LSD tests were used to analyze the differences of the number of the mCherry-ATG8E puncta between each group. Family-wise significance and confidence level, 0.05 (95% confidence interval).

(F) Quantification of the mCherry-ATG8E puncta inside the vacuole per normalized area (10,000 μm^2) of the trichoblasts and atrichoblasts imaged in D. Bars indicate the mean ± SD of 5 replicates. Paired repeated measures one-way ANOVA and Fisher's LSD tests were used to analyze the differences of the number of the mCherry-ATG8E puncta between each group. Family-wise significance and confidence level, 0.05 (95% confidence interval).

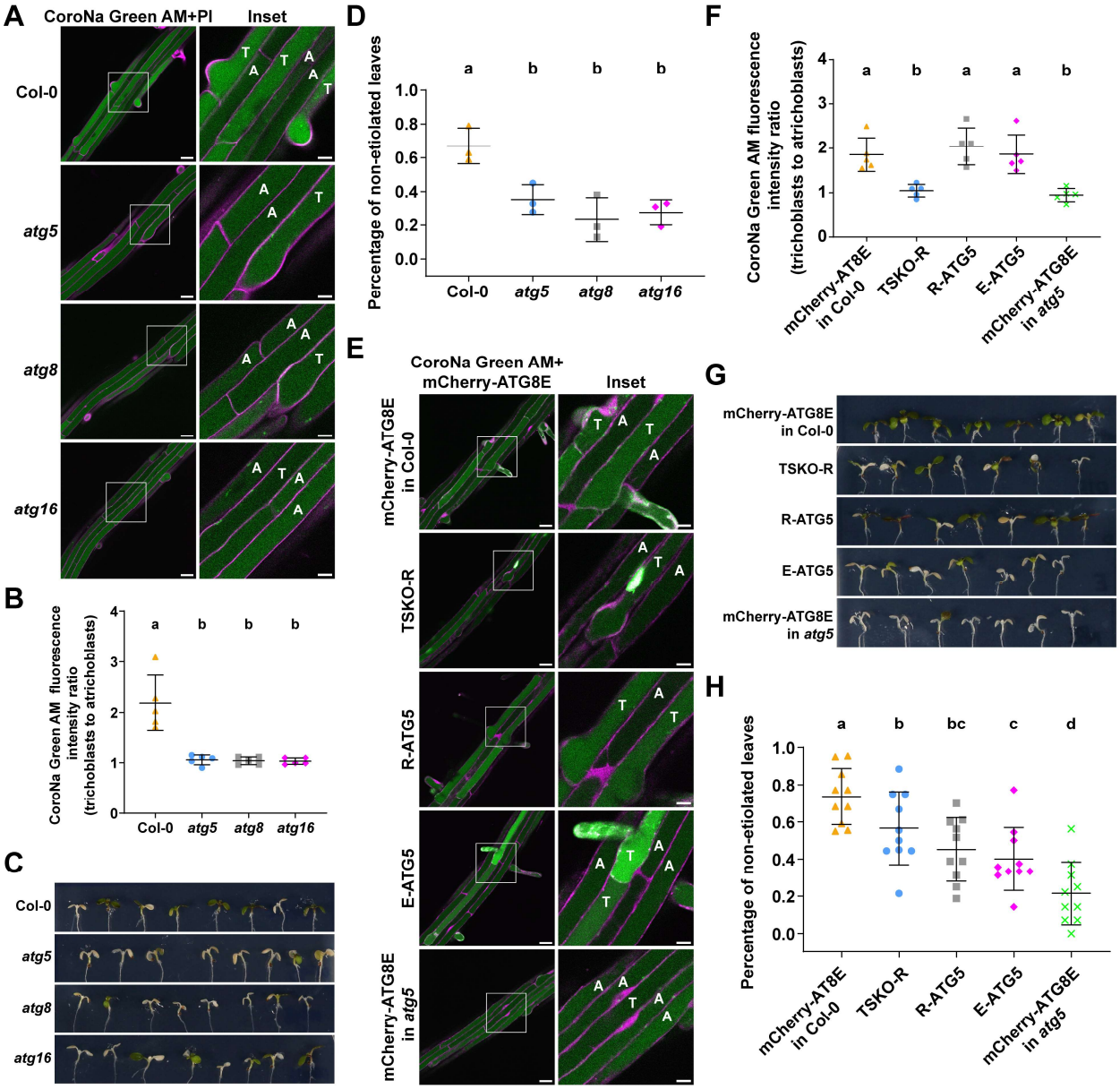

Figure 4. High autophagic flux in trichoblasts regulates sodium accumulation in the vacuole and is essential for coping with NaCl stress.

(A) Confocal microscopy images showing the sodium ion accumulation in the vacuoles of trichoblasts and atrichoblasts at the root maturation zone of Arabidopsis wildtype Col-0 and the autophagy-defective mutants *atg5*, *atg8* and *atg16* indicated by CoroNa Green AM staining. 5-d-old Arabidopsis seedlings were incubated in control 1/2 MS media for 30 min and were subsequently incubated in control 1/2 MS media containing 2 μm CoroNa Green AM for 30 min before imaging. Representative images of 5 replicates are shown. Area highlighted in the white-boxed region in the CoroNa Green+PI panel was further enlarged and presented in the inset panel. Scale bars, 30 μm. Inset scale bars, 10 μm. Green color, CoroNa Green AM sodium indicator. Magenta color, propidium iodide dye. T, trichoblasts. A, atrichoblasts.

(B) Quantitative analysis of the vacuolar CoroNa Green AM fluorescence intensity ratio between trichoblasts and atrichoblasts of the Arabidopsis seedlings imaged in A. Bars indicate the mean ± SD of 5 replicates. Paired repeated measures one-way ANOVA and Fisher's LSD tests were performed to analyze the significance of the CoroNa Green AM fluorescence intensity ratio differences between each group. Family-wise significance and confidence level, 0.05 (95% confidence interval).

(C) Phenotypic characterization of the seedlings of Arabidopsis wildtype Col-0 and the autophagy-defective mutants *atg5*, *atg8* and *atg16* under NaCl stress treatment. Arabidopsis seeds were vertically grown on 1/2 MS media plates (+1% plant agar) for 6 d and the 6-d-old seedlings were subsequently transferred to 1/2 MS media plates (+1% plant agar) containing 150 mM NaCl and vertically grown for 4 d. Plants were grown at 21°C under LEDs with 70 μM/m^2/s and a 14 h light/10 h dark photoperiod. Representative images of 3 replicates are shown.

(D) Quantitative analysis of the percentage of non-etiolated leaves of Arabidopsis seedlings imaged in C. Bars indicate the mean ± SD of 3 replicates. Paired repeated measures one-way ANOVA and Fisher's LSD tests were performed to analyze the significance of the percentage differences between each group. Family-wise significance and confidence level, 0.05 (95% confidence interval).

(E) Confocal microscopy images showing the sodium ion concentrations in the vacuoles of trichoblasts and atrichoblasts at the root maturation zone of Arabidopsis lines mCherry-ATG8E in Col-0, TSKO-R (*ATG5* mutagenized using *ProRHD6*-driven Cas9), R-ATG5 (*atg5* mutant complemented with *ProRHD6*-driven *ATG5*), E-ATG5 (*atg5* mutant complemented with *ProEXP7*-driven *ATG5*) and mCherry-ATG8E in *atg5* indicated by CoroNa Green AM staining. 5-d-old Arabidopsis seedlings were incubated in control 1/2 MS media for 30 min and were subsequently incubated in control 1/2 MS media containing 2 μm CoroNa Green AM for 30 min before imaging. Representative images of 5 replicates are shown. Area highlighted in the white-boxed region in the CoroNa Green AM+mCherry-ATG8E panel was further enlarged and presented in the inset panel. Scale bars, 30 μm. Inset scale bars, 10 μm. Green color, CoroNa Green AM sodium indicator (and the nuclear signals of Cas9-GFP in TSKO-R). Magenta color, mCherry-ATG8E. T, trichoblasts. A, atrichoblasts.

(F) Quantitative analysis of the vacuolar CoroNa Green AM fluorescence intensity ratio between trichoblasts and atrichoblasts of the Arabidopsis seedlings imaged in E. Bars

indicate the mean ± SD of 5 replicates. Paired repeated measures one-way ANOVA and Fisher's LSD tests were performed to analyze the significance of the CoroNa Green AM fluorescence intensity ratio differences between each group. Family-wise significance and confidence level, 0.05 (95% confidence interval).

(G) Phenotypic characterization of the seedlings of Arabidopsis lines mCherry-ATG8E in Col-0, TSKO-R (*ATG5* mutagenized using *ProRHD6*-driven Cas9), R-ATG5 (*atg5* mutant complemented with *ProRHD6*-driven *ATG5*), E-ATG5 (*atg5* mutant complemented with *ProEXP7*-driven *ATG5*) and mCherry-ATG8E in *atg5* under NaCl stress treatment. Arabidopsis seeds were vertically grown on 1/2 MS media plates (+1% plant agar) for 6 d and the 6-d-old seedlings were subsequently transferred to 1/2 MS media plates (+1% plant agar) containing 150 mM NaCl and vertically grown for 4 d. Plants were grown at 21°C under LEDs with 70 μM/m^2/s and a 14 h light/10 h dark photoperiod. Representative images of 10 replicates are shown.

(H) Quantitative analysis of the percentage of non-etiolated leaves of Arabidopsis seedlings imaged in G. Bars indicate the mean ± SD of 10 replicates. Paired repeated measures one-way ANOVA and Fisher's LSD tests were performed to analyze the significance of the percentage differences between each group. Family-wise significance and confidence level, 0.05 (95% confidence interval).

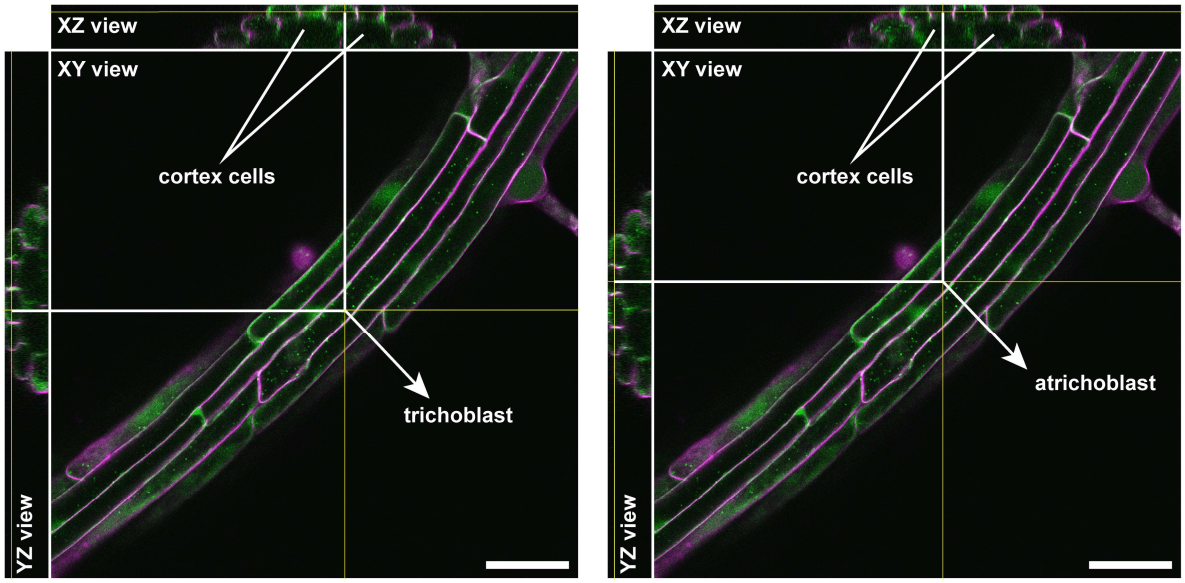

Figure S1. Schematic confocal images illustrating the approach used to distinguish trichoblasts from atrichoblasts through confocal microscopy. To identify trichoblast and atrichoblast cells, we analyzed XZ and YZ views of Z-stack images. Trichoblast (root hair forming) cells are identified as cells that are adjacent to two cortex cells and atrichoblast (non-root hair forming) cells as cells that are adjacent to one cortex cell. Green color, GFP-ATG8A. Magenta color, propidium iodide dye (for cell wall staining). Scale bars, 50 μm. Yellow lines show the alignment of XY, XZ and YZ views of the target cell.

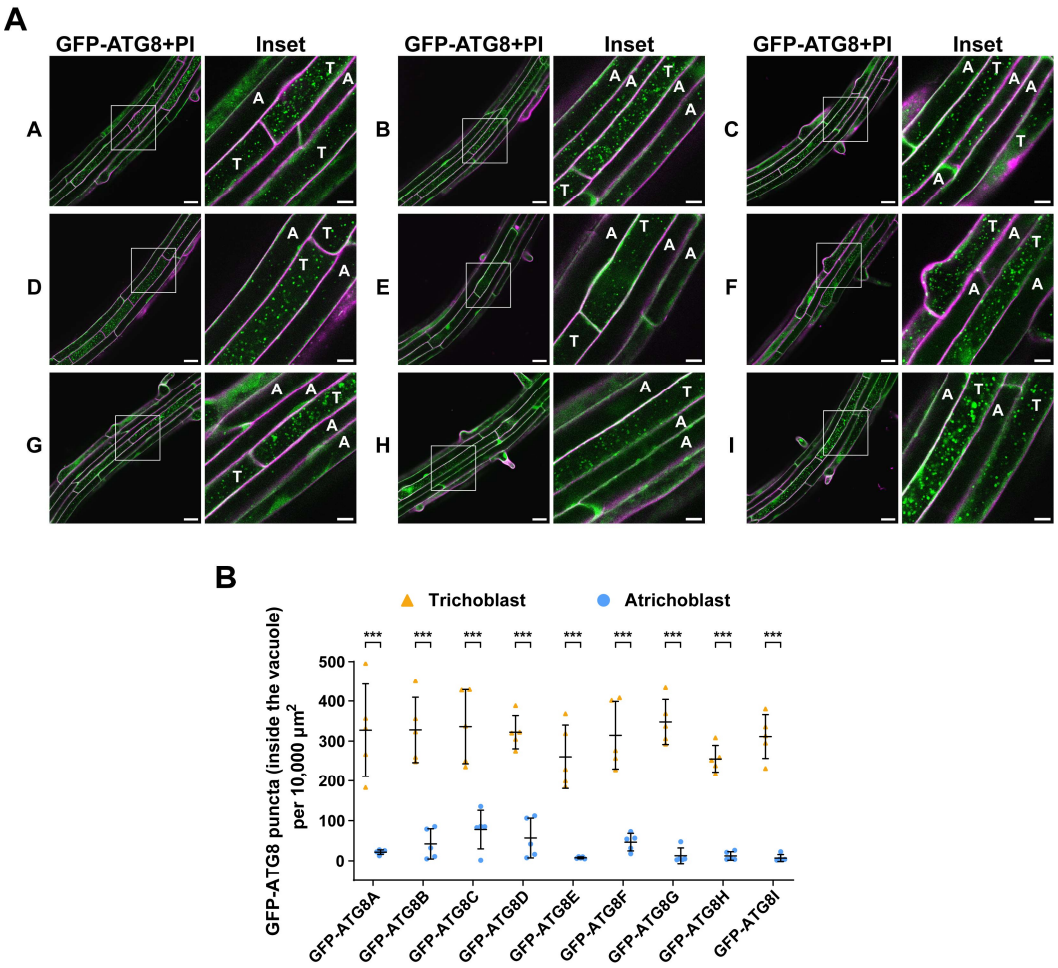

Figure S2. Trichoblasts exhibit higher autophagic flux than atrichoblasts under nitrogen-starvation conditions.

(A) Confocal microscopy images of the trichoblasts and atrichoblasts at the root maturation zone of Arabidopsis wildtype Col-0 expressing ProUBQ10:GFP-ATG8A–I isoforms under nitrogen-starvation conditions. 5-d-old Arabidopsis seedlings were incubated in nitrogen-deficient 1/2 MS media containing 2 µm concanamycin A for 2 h before imaging. Representative images of 5 replicates are shown. Area highlighted in the white-boxed region in the GFP-ATG8+PI panel was further enlarged and presented in the inset panel. Scale bars, 30 µm. Inset scale bars, 10 µm. Green color, GFP-ATG8A–I isoforms. Magenta color, propidium iodide dye. T, trichoblasts. A, atrichoblasts.

(B) Quantification of the GFP-ATG8 puncta inside the vacuole per normalized area (10,000 μm^2) of the trichoblasts and atrichoblasts imaged in A. Bars indicate the mean ± SD of 5 replicates. Two-tailed and paired student t tests were performed to analyze the significance of GFP-ATG8 puncta density differences between the trichoblasts and the atrichoblasts. ***, $P < 0.001$

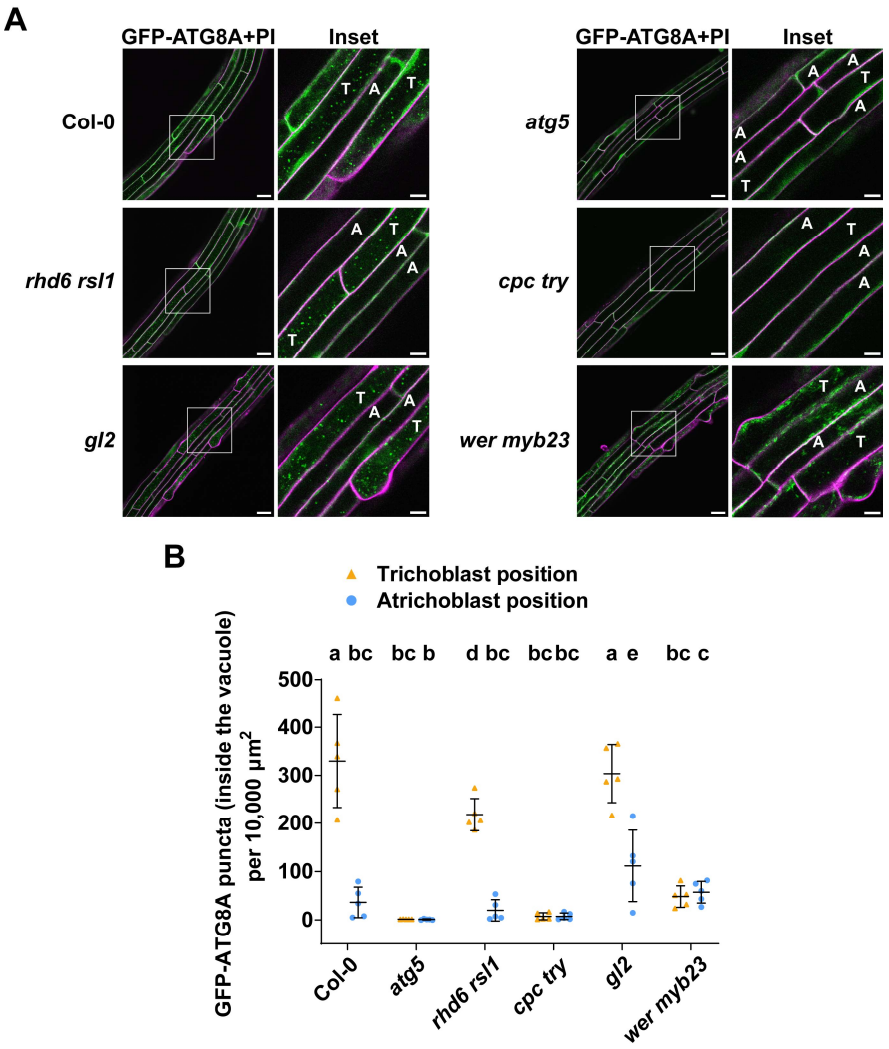

Figure S3. Genetic basis of the autophagic flux difference between trichoblasts and atrichoblasts.

(A) Confocal microscopy images of epidermal cells at the root maturation zone of Col-0, *atg5*, *rhd6 rsl1*, *cpc try*, *gl2* and *wer myb23* expressing ProUBQ10:GFP-ATG8A under nitrogen-starvation conditions. 5-d-old Arabidopsis seedlings were incubated in nitrogen-deficient 1/2 MS media containing 2 µm concanamycin A for 2 h before imaging. Representative images of 5 replicates are shown. Area highlighted in the white-boxed region in the GFP-ATG8A+PI panel was further enlarged and presented in the inset panel. Scale bars, 30 µm. Inset scale bars, 10 µm. Green color, GFP-ATG8A. Magenta color, propidium iodide dye. Note, T indicates the trichoblast positions (adjacent to two cortex cells) and the A indicates the atrichoblast positions (adjacent to only one cortex cell), rather than the cell identities as mutants are affected in cell identity development.

(B) Quantification of the GFP-ATG8A puncta inside the vacuole per normalized area (10,000 µm^2) of the cells at the trichoblast positions and the atrichoblast positions imaged in A. Bars indicate the mean ± SD of 5 replicates. Paired repeated measures one-way ANOVA and Fisher's LSD tests were used to analyze the differences of the number of the GFP-ATG8A puncta between each group. Family-wise significance and confidence level, 0.05 (95% confidence interval).

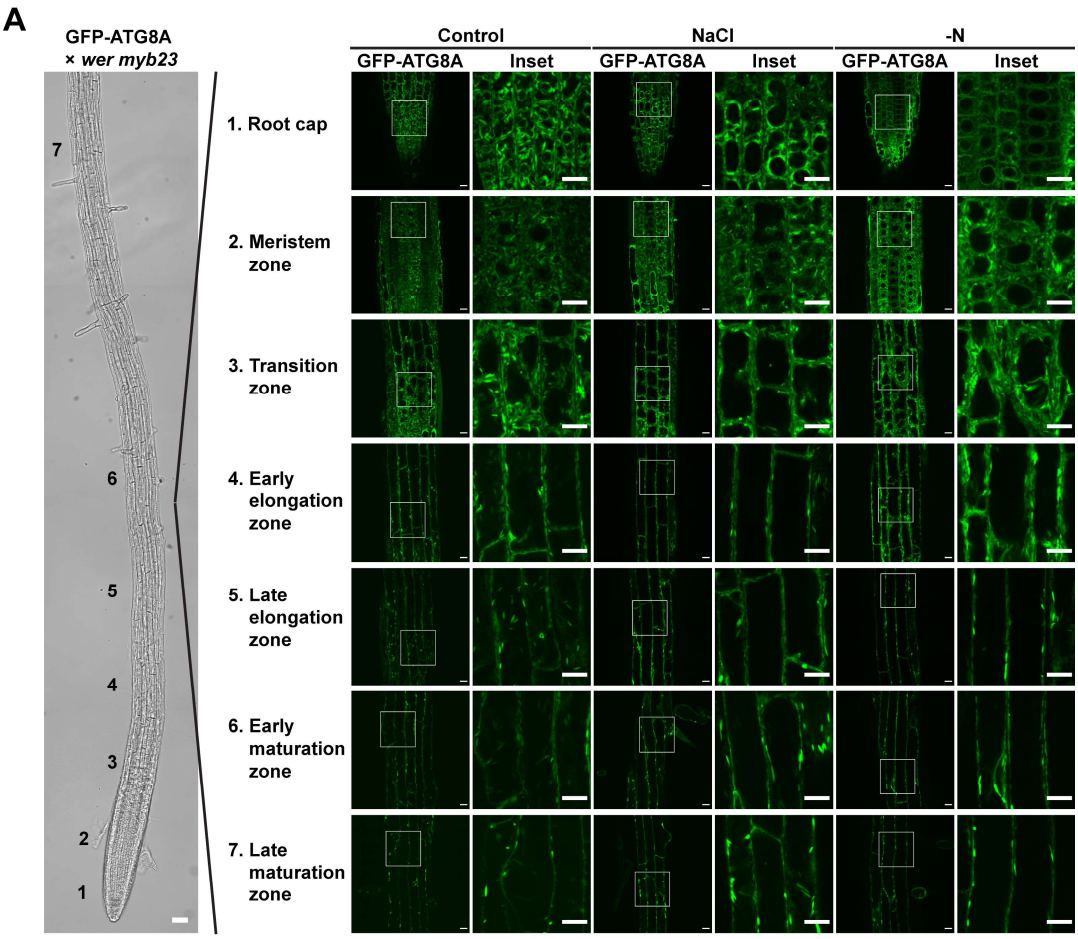

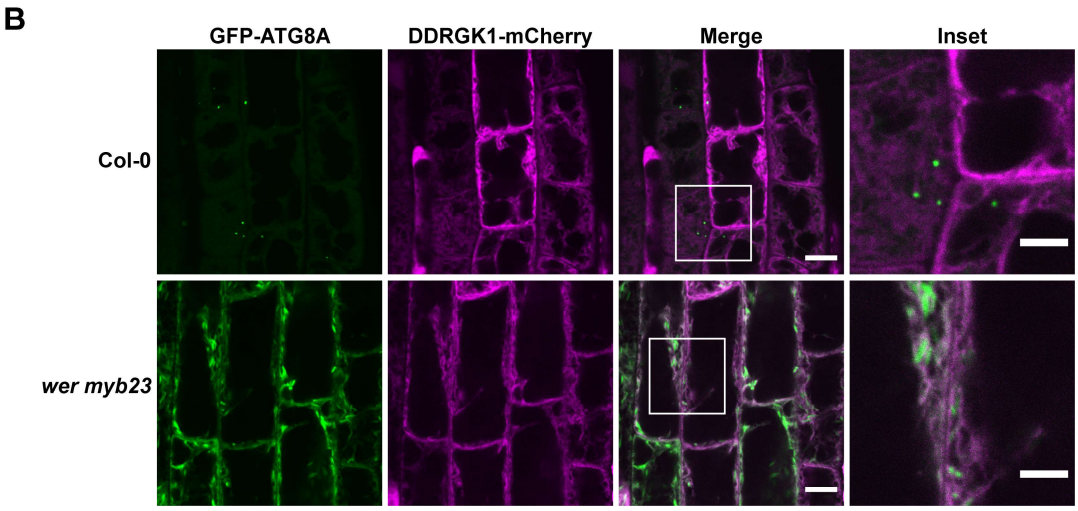

Figure S4. GFP-ATG8A is trapped at the endoplasmic reticulum in *wer myb23* mutant.

(A) Confocal microscopy images of cells from different root regions of *wer myb23* expressing ProUBQ10:GFP-ATG8A. 5-d-old Arabidopsis seedlings were incubated in either control 1/2 MS media (Control) for 3 h, 100 mM NaCl-containing 1/2 MS media (NaCl) for 45 min, or nitrogen-deficient 1/2 MS media (−N) for 3 h before imaging. Representative images of 3 replicates are shown. Area highlighted in the white-boxed region in the GFP-ATG8A panel was further enlarged and presented in the inset panel. Bright field scale bars, 50 μm. GFP-ATG8A panel scale bars, 10 μm. Inset scale bars, 10 μm.

(B) Confocal microscopy images of epidermal cells of the root transition zone of Arabidopsis wildtype Col-0 and *wer myb23* mutant lines co-expressing ProUBQ10:GFP-ATG8A and the endoplasmic reticulum marker ProUBQ10:DDRGK1-mCherry. 5-d-old Arabidopsis seedlings were incubated in 1/2 MS media for 3 h before imaging. Representative images of 2 replicates are shown. Area highlighted in the white-boxed region in the merge panel was further enlarged and presented in the inset panel. Scale bars, 10 μm. Inset scale bars, 5 μm.

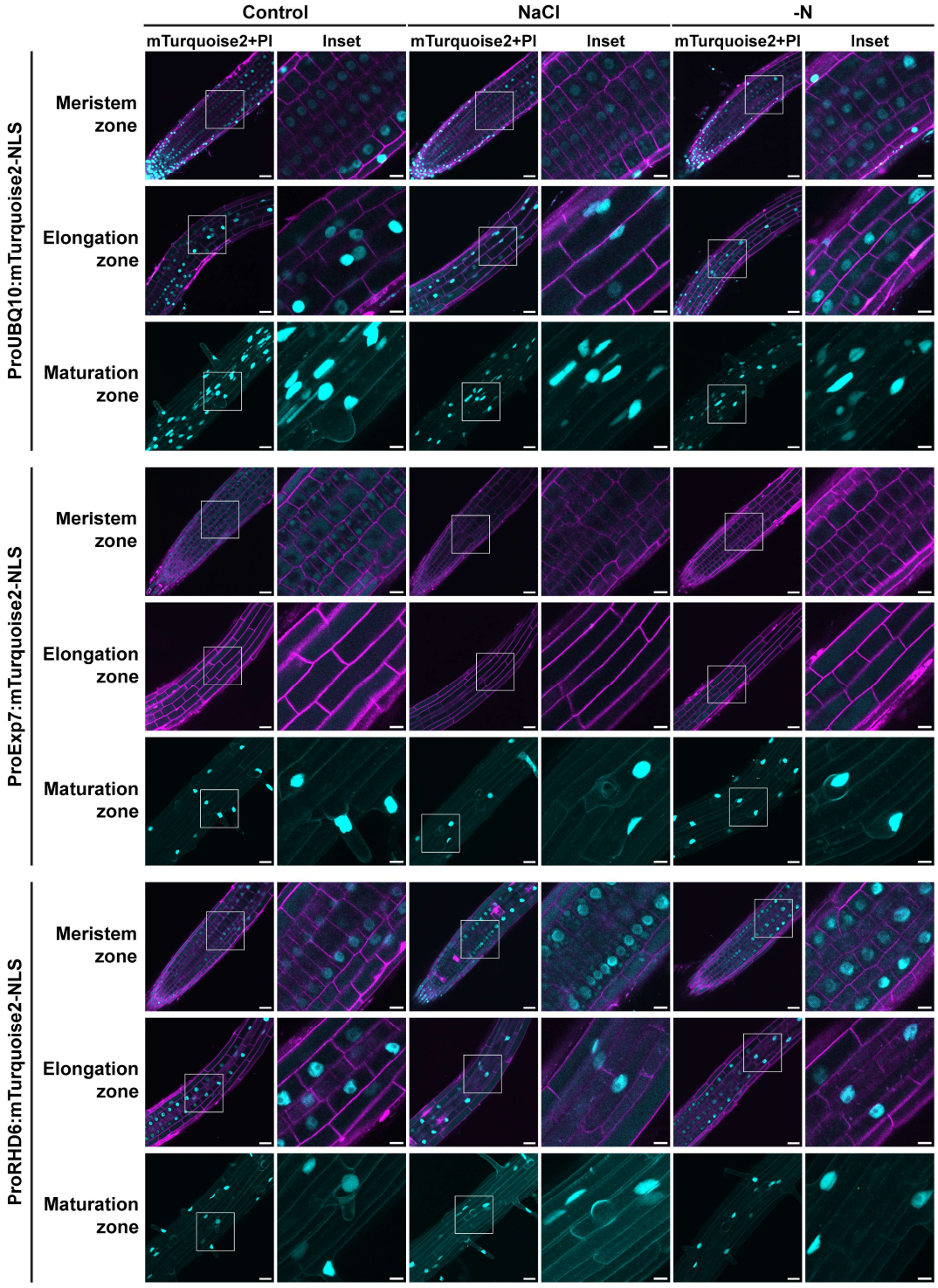

Figure S5. Expression patterns of *UBQ10*, *EXP7* and *RHD6* promoters in *Arabidopsis thaliana* roots.

Confocal microscopy images of root epidermal cells of different root regions of Arabidopsis wildtype Col-0 expressing either ProUBQ10:mTurquoise2-NLS, ProEXP7:mTurquoise2-NLS or ProRHD6:mTurquoise2-NLS. 5-d-old Arabidopsis seedlings were incubated in either control 1/2 MS media (Control) for 3 h, 100 mM NaCl-containing 1/2 MS media (NaCl) for 45 min, or nitrogen-deficient 1/2 MS media (−N) for 3 h before imaging. For images showing the maturation zone, an mTurquoise2-single channel Z-stack image was shown. Representative images of 3 replicates are shown. Area highlighted in the white-boxed region in the mTurquoise2+PI panel was further enlarged and presented in the inset panel. Scale bars, 30 μm. Inset scale bars, 10 μm. Cyan color, mTurquoise2-NLS. Magenta color, propidium iodide dye. NLS, nuclear location signal peptide.

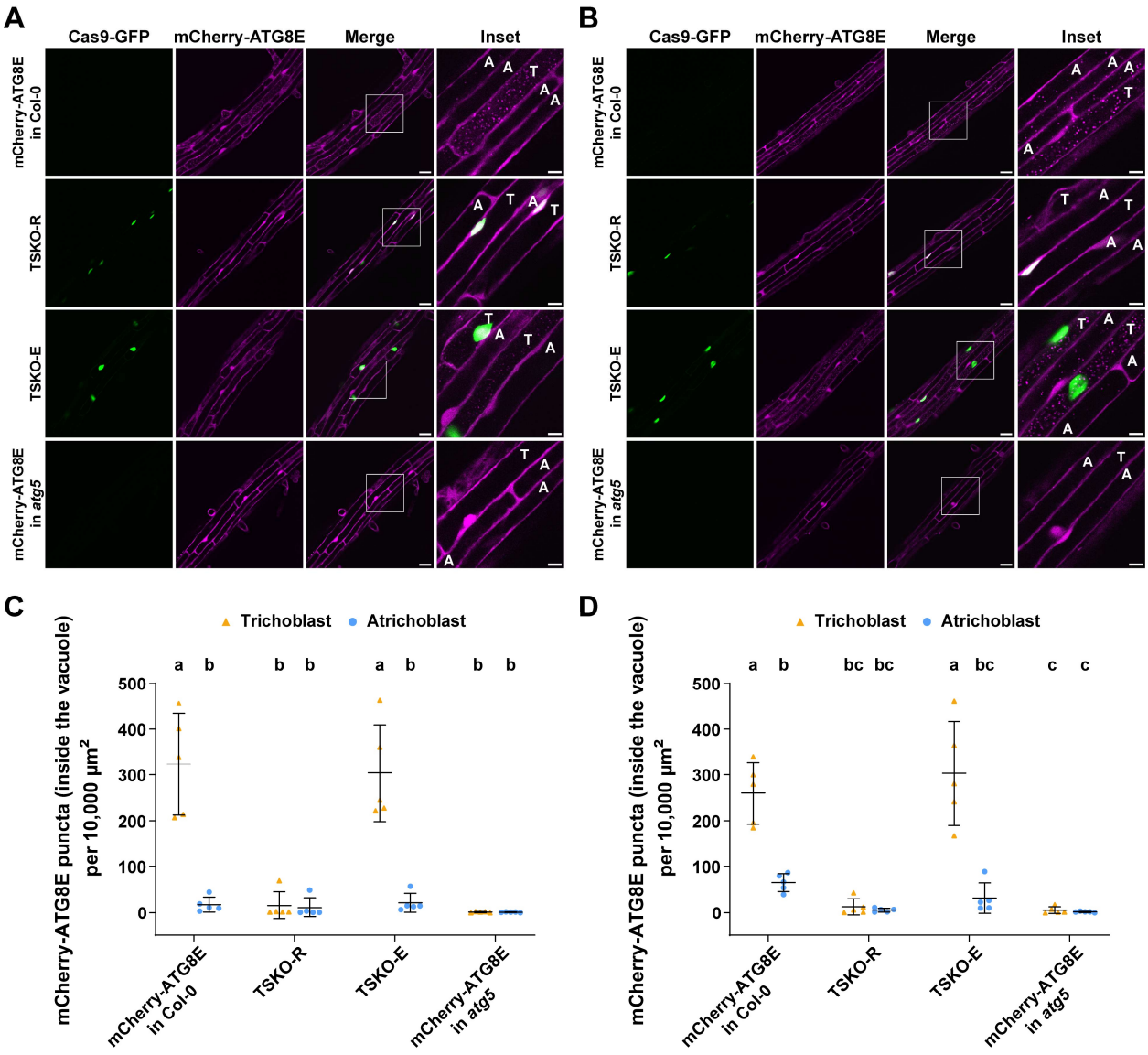

Figure S6. *RHD6* promoter was more efficient in disrupting autophagic flux in trichoblast cells compared to *EXP7* promoter in tissue specific CRISPR mutagenesis experiments.

(A) Confocal microscopy images of trichoblasts and atrichoblasts at the root maturation zone of Arabidopsis lines mCherry-ATG8E in Col-0, TSKO-R (*ATG5* mutagenized using *ProRHD6*-driven Cas9), TSKO-E (*ATG5* mutagenized using *ProEXP7*-driven Cas9) and mCherry-ATG8E in atg5 under control treatment. 5-d-old Arabidopsis seedlings were incubated in 1/2 MS media containing 2 μm concanamycin A for 2 h before imaging. Representative images of 5 replicates are shown. Area highlighted in the white-boxed region in the merge panel was further enlarged and presented in the inset panel. Scale bars, 30 μm. Inset scale bars, 10 μm. T, trichoblasts. A, atrichoblasts.

(B) Confocal microscopy images of trichoblasts and atrichoblasts at the root maturation zone of Arabidopsis lines mCherry-ATG8E in Col-0, TSKO-R (*ATG5* mutagenized using *ProRHD6*-driven Cas9), TSKO-E (*ATG5* mutagenized using *ProEXP7*-driven Cas9) and mCherry-ATG8E in atg5 under NaCl stress treatment. 5-d-old Arabidopsis seedlings were incubated in 1/2 MS media containing 50 mM NaCl + 1 μm concanamycin A for 1 h before imaging. Representative images of 5 replicates are shown. Area highlighted in the white-boxed region in the merge panel was further enlarged and presented in the inset panel. Scale bars, 30 μm. Inset scale bars, 10 μm. T, trichoblasts. A, atrichoblasts.

(C) Quantification of the mCherry-ATG8E puncta inside the vacuole per normalized area (10,000 μm^2) of the cells of the trichoblasts and atrichoblasts imaged in A. Bars indicate the mean ± SD of 5 replicates. Paired repeated measures one-way ANOVA and Fisher's LSD tests were used to analyze the differences of the number of the mCherry-ATG8E puncta between each group. Family-wise significance and confidence level, 0.05 (95% confidence interval).

(D) Quantification of the mCherry-ATG8E puncta inside the vacuole per normalized area (10,000 μm^2) of the cells of the trichoblasts and atrichoblasts imaged in B. Bars indicate the mean ± SD of 5 replicates. Paired repeated measures one-way ANOVA and Fisher's LSD tests were used to analyze the differences of the number of the mCherry-ATG8E puncta between each group. Family-wise significance and confidence level, 0.05 (95% confidence interval).

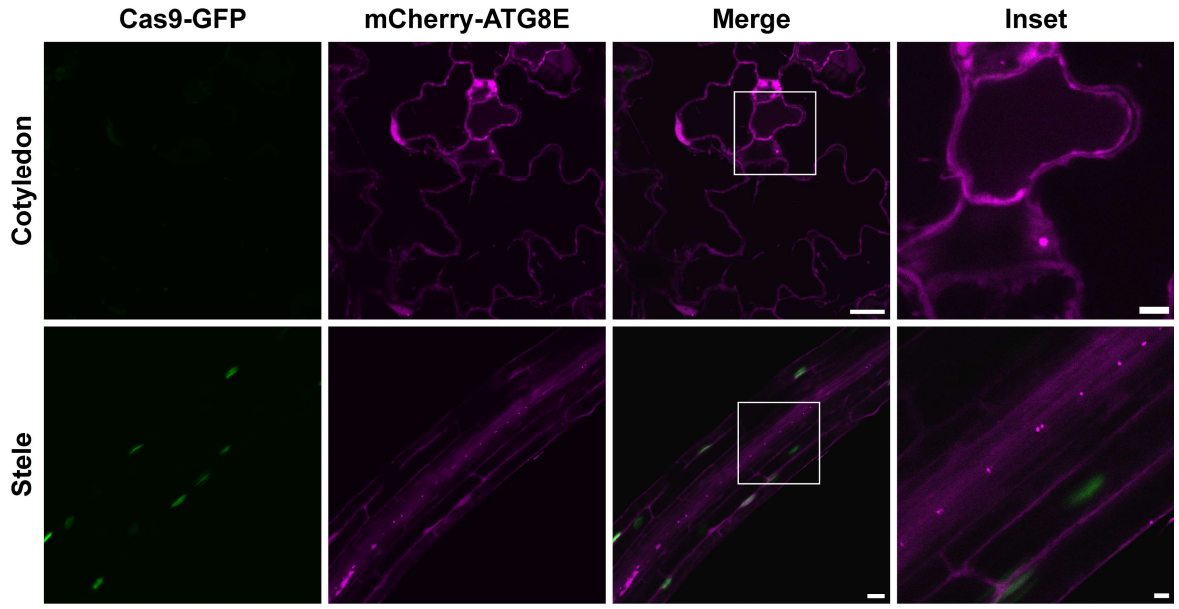

Figure S7. Normal autophagosome structures can be observed in cells that donot express Cas9 in TSKO-R lines.

Confocal microscopy images of cells of cotyledon epidermis and stele regions of TSKO-R (*ATG5* mutagenized using *ProRHD6*-driven Cas9). 5-d-old Arabidopsis seedlings were incubated in control 1/2 MS media for 30 min before imaging. Representative images of 3 replicates are shown. Area highlighted in the white-boxed region in the merge panel was further enlarged and presented in the inset panel. Scale bars, 20 μm. Inset scale bars, 5 μm.

5. Discussion

In the manuscript presented in **Chapter 4.1**, through differential centrifugation coupled with AP-MS and functional studies, CFS1 is screened out and characterized as a novel autophagy adaptor, which bridges autophagosomes with the ESCRT-1 component VPS23A to regulate autophagic flux and mediate the formation of amphisomes fused by autophagosomes and multivesicular bodies. This project showed first evidence that plants use amphisomes as intermediates during the transportation of autophagosome from cytoplasm to vacuole, differing from yeast and mammals but achieving similar cargo degradation. The details of this project will be comprehensively discussed in **Chapter 5.1**.

In the manuscript presented in **Chapter 4.2**, it is demonstrated that autophagy is specifically elevated in root hair-forming cells (trichoblasts) of Arabidopsis compared to neighboring non-hair cells (atrichoblasts). This difference is crucial for salt stress tolerance, as trichoblasts use autophagy to sequester sodium ions into vacuoles, preventing toxicity. The details of this project will be comprehensively discussed in **Chapter 5.2**.

5.1. CFS1 is a novel plant-specific autophagy adaptor that mediates the fusion of autophagosomes and multivesicular bodies to amphisomes via CFS1-VPS23A interaction

5.1.1. Identification of CFS1 as a candidate autophagy adaptor

In this study, we utilized an innovative AP-MS approach to systematically identify candidate autophagy adaptors. Autophagy adaptors are distinguished from other proteins by three defining characteristics: (i) the ability to interact with ATG8 family proteins, (ii) recruitment to autophagosome membranes upon autophagy induction, and (iii) localization to the outer membrane of autophagosomes. Accordingly, potential autophagy adaptors were selected based on their association with ATG8E, enrichment in the microsomal fraction, and sensitivity to proteinase K digestion (Sweeney and Walker, 1993). Through this stringent screening process, 48 candidate proteins, including CFS1, were identified.

CFS1 belongs to the plant FYVE domain-containing protein family, members of which are frequently implicated in vesicle trafficking processes. Given prior evidence that CFS1 is related to autophagy, we selected it as a prime candidate for further functional characterization as a putative autophagy adaptor.

5.1.2. CFS1 specifically localizes to autophagosomes

Under control conditions and two autophagy-inducing treatments (nitrogen deficiency and salt stress), mCherry-tagged CFS1 exhibited punctate structures that colocalized strongly with autophagosome markers (ATG8A, NBR1, and ATG11; Gross et al., 2025) but not with other vesicular or membrane markers, confirming its specific localization to autophagosomes. In contrast, CFS2, the Arabidopsis homolog of CFS1, displayed diffuse cytoplasmic fluorescence in confocal imaging, suggesting no functional role in autophagosome maturation or trafficking. Furthermore, phenotypic analysis revealed no discernible differences between the *cfs2* mutant and wild-type Col-0, reinforcing

that CFS2 is not involved in autophagy. Thus, we focused exclusively on CFS1 for subsequent investigations.

Notably, CFS1-marked puncta showed complete colocalization with ATG8A, indicating that CFS1, like ATG8, is uniformly distributed across the autophagosome membrane. This observation proved critical in interpreting later experiments, where partial colocalization of CFS1 with VPS23A reflects the connection of two distinct vesicle populations.

5.1.3. CFS1 binds ATG8A–F via an AIM-dependent mechanism

GST pull-down assays demonstrate that CFS1 specifically interacts with ATG8A–F but not ATG8G–I, validating the use of ATG8A and ATG8E in confocal microscopy studies. Further evidence from AIM peptide competition assays, GST pull-downs, and in vivo co-immunoprecipitation (co-IP) confirm that CFS1-ATG8 binding requires AIM, as mutation of this motif ($CFS1^{AIM}$) abolished the interaction. Microscopic analyses corroborate these findings, as $CFS1^{AIM}$ failed to localize to autophagosomes. Moreover, $CFS1^{AIM}$ could not rescue the nitrogen deficiency-induced etiolation phenotype of *cfs1* (which phenocopies *atg5*), underscoring the functional necessity of the CFS1-ATG8 interaction in autophagy.

5.1.4. CFS1 functions as an autophagy adaptor

To elucidate whether CFS1 acts as an autophagy adaptor involved in autophagosome trafficking and maturation rather than biogenesis, we performed comprehensive ultrastructural analysis using transmission electron microscopy (TEM). Our observations demonstrated that *cfs1* mutants exhibited normal autophagosome formation, indicating that CFS1 is dispensable for autophagosome biogenesis.

Comparative analysis of vacuolar flux revealed several key findings: (1) CFS1 puncta were significantly less abundant within vacuoles compared to ATG8 or the canonical autophagy receptor NBR1; (2) Concanamycin A treatment resulted in reduced colocalization of CFS1-ATG8E in vacuoles. These results collectively support the classification of CFS1 as an autophagy adaptor. Furthermore, immunogold-labeling TEM provided definitive evidence that CFS1 could steadily exist at the outer autophagosome membrane, consistent with its proposed adaptor function.

Taken together with the findings presented in **Chapter 5.1.2, 5.1.3**, and **5.1.4**, our data demonstrate that CFS1 serves as a bona fide autophagy adaptor which functions after the autophagosome biogenesis.

5.1.5. CFS1 regulates autophagic flux but not endocytic pathway functionality

To investigate whether CFS1 mediates autophagosome delivery to the vacuole, we initially compared autophagosome accumulation in the *cfs1* mutant with the wild-type Col-0 and the autophagy-deficient *atg5* mutant. Confocal microscopy quantification of mCherry-ATG8E-labeled autophagosomes under salt stress revealed significantly higher cytosolic autophagosome accumulation in *cfs1* mutants compared to wild-type. Notably, when treated with concanamycin A under salt stress conditions, *cfs1* mutants exhibited markedly reduced autophagic flux relative to Col-0 plants. These findings

demonstrate that CFS1 deficiency primarily impairs autophagosome clearance rather than formation.

To validate defective vacuolar delivery, we employed GFP-cleavage assays where vacuolar proteases process GFP-ATG8A to generate free GFP, serving as an autophagic flux indicator. *cfs1* mutants displayed substantially diminished free GFP levels during nitrogen starvation or salt stress, confirming impaired autophagosome degradation. Furthermore, we observed pronounced accumulation of the selective autophagy receptor NBR1 in *cfs1* mutants, consistent with compromised autophagic flux.

To assess CFS1's involvement in selective autophagy, we examined mitophagy using the uncoupler DNP (Ma et al., 2021). While *cfs1* mutants exhibited normal mitophagosome formation (verified by TEM), mitochondrial protein (IDH) degradation was defective, resembling the *atg5* phenotype. Electron microscopy further revealed accumulated damaged mitochondria in *cfs1*, underscoring that CFS1 is essential for efficient autophagic flux but dispensable for autophagosome biogenesis.

5.1.6. Evolutionary conservation of CFS1 function in *Marchantia polymorpha*

To evaluate the evolutionary conservation of CFS1 function, we investigated its ortholog in the basal land plant *Marchantia polymorpha*. Transgenic lines co-expressing mScarlet-MpCFS1 with Marchantia ATG8 isoforms (GFP-MpATG8A/B) demonstrated strong colocalization between MpCFS1 and MpATG8 puncta, recapitulating the Arabidopsis interaction pattern.

Functional complementation assays revealed that MpCFS1 expressed in Arabidopsis *cfs1* mutants maintained colocalization with GFP-ATG8A, indicating cross-species functional preservation. Crucially, GFP-ATG8 cleavage assays in *Mpcfs1* knockout mutants showed significantly reduced free GFP levels, mirroring the Arabidopsis *cfs1* phenotype. These results establish that CFS1's role in regulating autophagic flux is evolutionarily conserved in early-diverging plants.

5.1.7. CFS1 does not participate in endocytosis or vacuole morphogenesis

To exclude potential pleiotropic effects on membrane trafficking, we systematically evaluated endocytic function in *cfs1* mutants. FM4-64 uptake assays (Jelínková et al., 2019), which track endocytic vesicle trafficking to the vacuole, showed comparable internalization and vacuolar delivery patterns among *cfs1*, *cfs2*, *cfs1 cfs2* double mutants, and wild-type Col-0.

Using the well-characterized PIN2 endocytosis pathway for auxin transporter degradation, we observed normal PIN2 internalization in *cfs1* mutants following dark-induced endocytosis. Additionally, BCECF-AM staining (Ozkan et al., 2002) revealed no vacuolar morphology defects in *cfs1* or related mutants. Collectively, these data demonstrate that CFS1 specifically modulates autophagy without affecting endomembrane trafficking or vacuolar integrity.

5.1.8. CFS1 colocalizes with VPS23A at amphisomes

To elucidate the molecular mechanism by which CFS1 regulates autophagy, we sought to identify its interaction partners beyond ATG8. A genome-wide yeast two-hybrid screen identified VPS23A, a core component of the ESCRT-I complex, as a high-confidence interactor. Given that ESCRT-I regulates MVB formation, this interaction suggested a potential functional link between autophagosomes and endosomal trafficking.

To validate this interaction, we performed colocalization assays in Arabidopsis root cells co-expressing mCherry-CFS1 and GFP-VPS23A. Under both control and salt-stress conditions, CFS1 puncta exhibited strong colocalization with VPS23A, indicating a physical association. Airyscan super-resolution microscopy and spinning-disk time-lapse imaging further revealed dynamic interactions, with CFS1 and VPS23A puncta moving in tandem before merging, suggesting functional cooperation.

To determine whether these colocalized puncta represent fusion events, we performed immunogold TEM with dual labeling. Electron micrographs confirmed that gold particles for both proteins co-occupied vesicular structures displaying features of autophagosomes (double membranes) and MVBs (intraluminal vesicles). These findings provide ultrastructural evidence that CFS1 and VPS23A coexist at amphisomes, marking the first identification of amphisomes in plant cells.

5.1.9. The CFS1–VPS23A interaction is essential for autophagic flux

To assess the functional significance of the CFS1–VPS23A interaction, we sought to disrupt this interaction and examine its impact on autophagy. However, since *vps23a vps23b* double mutants are lethal, and single *vps23* mutants showed no significant autophagy defects (likely due to functional redundancy between the two VPS23 isoforms), we circumvented this limitation by generating a CFS1 variant with a mutated VPS23A-binding motif ($CFS1^{PSAPP}$).

Pull-down assays and *in vivo* co-IP experiments confirmed that while $CFS1^{PSAPP}$ retained binding to ATG8, its interaction with VPS23A was severely impaired. Confocal microscopy further demonstrated that $CFS1^{PSAPP}$ puncta no longer colocalized with VPS23A, despite maintaining association with autophagosomes (marked by GFP-ATG8A). These results suggest that the CFS1-VPS23A interaction is crucial for amphisome formation.

Although we could not definitively conclude whether amphisome formation was abolished in *cfs1* mutants or in *cfs1* mutants expressing $CFS1^{PSAPP}$, we were able to evaluate the functional consequences of disrupting the CFS1-VPS23A interaction. Using GFP-cleavage assays, NBR1 turnover assays, and phenotypic assays (as described in **Chapter 5.1.3**), we found that impairing the CFS1-VPS23A interaction led to a significant reduction in autophagic flux and conferred nitrogen starvation sensitivity comparable to *cfs1* mutants. In summary, these results demonstrate that the CFS1-VPS23A interaction is critical for efficient autophagic flux.

5.1.10. Concluding remarks

This study provides compelling evidence that plant autophagosomes mature into amphisomes before their delivery to the central vacuole, a process mediated by the autophagy adaptor CFS1. By bridging autophagosomes with the ESCRT-I component VPS23A, CFS1 facilitates the formation of amphisomes, ensuring efficient autophagic flux. Our findings reveal that CFS1 interacts with ATG8 via an AIM-dependent mechanism and with VPS23A through a PSAPP motif, both of which are essential for autophagosome-vacuole trafficking. Disruption of either interaction leads to defective autophagy, as demonstrated by the accumulation of autophagosomes in *cfs1* mutants and impaired degradation of cargoes like the autophagy receptor NBR1 and mitochondrial proteins. Importantly, CFS1's function is evolutionarily conserved, as its homolog in *Marchantia polymorpha* similarly regulates autophagic flux, underscoring its fundamental role in plant autophagy.

The discovery of amphisomes in plants fills a critical gap in our understanding of autophagosome maturation, which was previously well-characterized in yeast and metazoans but remained elusive in plants. Our work suggests that plants employ a prevacuolar sorting hub, i.e. the amphisome, to coordinate autophagic and endosomal trafficking. This finding aligns with the unique architecture of plant cells, where the large central vacuole necessitates specialized mechanisms for organelle turnover. Furthermore, our "hub and spoke" model proposes that amphisomes act as central hubs integrating multiple vacuolar trafficking pathways, optimizing cellular resource allocation during stress responses.

The implications of this work extend beyond fundamental cell biology. Given that autophagy is crucial for stress adaptation, nutrient recycling, and developmental transitions, understanding how CFS1 regulates autophagic flux opens new avenues for improving crop resilience. For instance, manipulating CFS1 or its interactors could enhance nitrogen remobilization under starvation or mitigate oxidative damage during abiotic stress. However, key questions remain, such as whether additional adaptors compensate for CFS1 loss and how autophagosome-ESCRT crosstalk is spatiotemporally regulated. Future studies should also explore the intriguing possibility of cell-to-cell autophagosome movement, hinted at in our live-imaging data, which could redefine our understanding of intercellular communication in plants.

In summary, this study establishes CFS1 as a central regulator of plant autophagy and provides the first mechanistic framework for amphisome-mediated autophagosome maturation in plants. By linking autophagosomes to the ESCRT machinery, our work not only advances the plant autophagy field but also sets the stage for translational research aimed at harnessing autophagy for agricultural improvement. Future investigations into the molecular players governing amphisome formation and their physiological roles will further illuminate the adaptability and complexity of plant autophagy.

5.2. Cell-type specific autophagy sequesters sodium ions in the vacuoles of root hair forming cells for salt stress resilience in *Arabidopsis thaliana*

5.2.1. Trichoblasts exhibit elevated autophagic flux compared to atrichoblasts in the root maturation zone

To validate our preliminary observation of differential autophagic activity between root hair-forming cells (trichoblasts) and non-hair cells (atrichoblasts) in the root maturation zone, we conducted a systematic analysis of autophagic flux in Arabidopsis thaliana Col-0 plants expressing GFP-tagged versions of all ATG8 isoforms (ATG8A-I). Under both basal conditions and autophagy-inducing treatments (salt stress and nitrogen starvation), trichoblasts consistently exhibited a greater abundance of vacuolar GFP-ATG8 puncta compared to adjacent atrichoblasts. These results demonstrate that trichoblasts maintain intrinsically higher autophagic activity independent of external stimuli.

5.2.2. Genetic determinants of autophagy differences between trichoblasts and atrichoblasts

To investigate whether this differential autophagy is developmentally programmed, we analyzed autophagy patterns in a panel of Arabidopsis mutants with disrupted root epidermal cell fate specification. These mutants allowed us to dissect whether the observed autophagic differences depend on cell identity established early in development or later root hair formation.

We employed four key mutant lines (Löfke et al., 2013):

(1) ***rhd6 rsl1*** - forms ectopic non-hair cells in trichoblast positions while maintaining proper meristematic identity;
(2) ***cpc try*** - lacks trichoblast identity due to disruption of the CAPRICE/TRYPTYCHON pathway;
(3) ***gl2*** - produces ectopic root hairs in atrichoblast positions while retaining normal early cell fate determination;
(4) ***wer myb23*** - lacks atrichoblast identity due to loss of WEREWOLF/MYB23 function.

Our analysis revealed distinct patterns:

In *rhd6 rsl1* and *gl2* mutants, which preserve correct meristematic identity, the autophagic disparity between trichoblast-positioned and atrichoblast-positioned cells persisted, albeit slightly attenuated. This suggests that while root hair structures may modestly augment autophagy, the primary regulation stems from developmental programming. Conversely, *cpc try* and *wer myb23* mutants, which are defective in early cell fate specification, completely abolished the autophagy distinction. This establishes that trichoblast/atrichoblast identity, rather than root hair presence per se, governs autophagic flux.

Notably, *wer myb23* mutants displayed globally impaired autophagy, with GFP-ATG8A mislocalized to the endoplasmic reticulum instead of forming autophagosomes. This unexpected finding reveals that the WER/MYB23 transcriptional network not only

controls cell fate but also modulates autophagosome biogenesis, uncovering a novel connection between developmental pathways and autophagy machinery.

5.2.3. Establishing the functional role of trichoblast-specific autophagy in salt stress tolerance

To definitively establish whether the observed differences in autophagic flux between trichoblasts and atrichoblasts had functional consequences for plant stress adaptation, we employed a combination of tissue-specific genetic manipulations and physiological assays.

We developed two strategies to selectively manipulate autophagy in trichoblasts while maintaining normal autophagy in other cell types. First, we created tissue-specific CRISPR knockout lines (CRISPR-TSKO) where ATG5, an essential autophagy gene, was disrupted specifically in trichoblasts using either the RHD6 or EXP7 promoters. The ProRHD6-driven knockout (TSKO-R) successfully reduced autophagic flux in trichoblasts while leaving other cells unaffected, whereas the ProEXP7-driven knockout had minimal effect, likely due to stable pre-existing ATG5 protein in mature trichoblasts. Second, we generated complementation lines where ATG5 expression was restored specifically in trichoblasts of *atg5* mutants, using the same promoters. These experiments demonstrated that the differential autophagy between cell types could be genetically controlled and that trichoblast identity was the primary determinant of elevated autophagic flux.

Building on these genetic tools, we reveal the critical physiological role of trichoblast-specific autophagy in salt stress adaptation. Using CoroNa Green AM staining (Luo et al., 2017), we showed that wild-type plants preferentially accumulate higher sodium ion levels in trichoblast vacuoles than in atrichoblasts, while autophagy-deficient mutants (*atg5*, *atg8* and *atg16*) lose this compartmentalization difference. Importantly, our tissue-specific manipulations confirmed this mechanism: TSKO-R plants (with trichoblast-specific ATG5 knockout) failed to sequester more sodium in trichoblasts, while the complementation lines (R-ATG5 and E-ATG5) restored the sodium accumulation. Phenotypic assays under salt stress conditions provided the ultimate functional validation, demonstrating that plants with disrupted trichoblast autophagy showed significantly reduced survival, whereas those with restored trichoblast autophagy maintained wild-type levels of tolerance.

5.2.4. Concluding remarks

This study establishes a crucial link between developmental programming, cell-type-specific autophagy, and environmental adaptation in Arabidopsis thaliana. By demonstrating that trichoblasts (root hair-forming cells) exhibit higher autophagic flux than adjacent atrichoblasts—a difference genetically encoded during early cell fate determination—we reveal how developmental cues fine-tune cellular homeostasis to optimize stress resilience. Our findings show that elevated autophagy in trichoblasts is not merely correlative but functionally essential, enabling vacuolar sodium sequestration and thereby conferring salt stress tolerance.

The use of tissue-specific genetic tools (CRISPR-TSKO and complementation) was pivotal in dissecting this mechanism, proving that autophagy localized to trichoblasts alone is both necessary and sufficient for salt adaptation. Strikingly, disrupting

autophagy specifically in trichoblasts abolished sodium compartmentalization and reduced survival, while restoring it rescued these phenotypes. This underscores the importance of studying autophagy at cellular resolution, as organism-wide approaches may mask critical tissue-specific adaptations.

Beyond salt tolerance, our work opens new questions: How do developmental transcription factors (e.g., WEREWOLF) mechanistically regulate autophagy? Could similar cell-type-specific autophagy programs operate in other stress responses or developmental contexts? From an applied perspective, these insights suggest strategies to engineer stress-resistant crops by modulating autophagy in specific cell types, such as root hairs, without compromising overall growth.

Ultimately, this study bridges developmental biology, cell biology, and environmental adaptation, illustrating how spatially restricted autophagy pathways contribute to organismal fitness. By decoding how developmental identity shapes cellular stress responses, we advance our understanding of plant resilience and provide a framework for exploring autophagy’s role in other multicellular systems.

6. Appendix

In this chapter, a list of manuscripts of which I am the co-author are presented. These manuscripts are not closely related to my main projects. However, these manuscripts also contribute to the plant autophagy field in general and represent an essential part of my achievements during PhD studies.

6.1. Functional specialization of ATG8 isoforms in Arabidopsis

Autophagy is a conserved cellular recycling process mediated by ATG proteins, with ATG8 playing a central role in autophagosome formation and cargo recruitment. While most ATG proteins are conserved as single isoforms, Arabidopsis encodes nine ATG8 isoforms, suggesting potential functional specialization. As detailed in **Chapter 6.2** (Del Chiaro et al., 2024), we generate a nonuple *atg8* mutant (Δ*atg8*) lacking all ATG8 isoforms to investigate their functional divergence. Transcriptional and translational reporters reveal tissue-specific expression patterns and distinct autophagosome subpopulations marked by different ATG8 isoforms. The Δ*atg8* mutant exhibits severe autophagy defects, including hypersensitivity to carbon (C) and nitrogen (N) starvation, impaired bulk autophagy, and defective selective autophagy (mitophagy and pexophagy). Functional complementation reveals that ATG8A restored plant viability under both C and N starvation, while ATG8H complements only C deprivation. Proximity-dependent proteomic profiling uncovers distinct protein interaction networks for each isoform during N starvation, which further supported their functional differentiation. Our findings provide genetic evidence for ATG8 isoform specialization in plants, revealing distinct roles in stress adaptation and selective autophagy.

6.2. Appendix Manuscript 1: “Nonuple atg8 mutant provides genetic evidence for functional specialization of ATG8 isoforms in *Arabidopsis thaliana*”

Authors: Alessia Del Chiaro, Nenad Grujic, **Jierui Zhao**, Ranjith Kumar Papareddy, Peng Gao, Juncai Ma, Christian Löfke, Anuradha Bhattacharya, Ramona Gruetzner, Pierre Bourguet, Frédéric Berger, Byung-Ho Kang, Sylvestre Marillonnet, Yasin Dagdas

Contribution: For this manuscript, I performed confocal experiments, analyzed data, and made the figures of Figure 1 and S2. I also wrote and revised the methods part related to confocal microscopy and statistics.

Status: This manuscript is currently a preprint on bioRxiv posted on December 10, 2024.

DOI: https://doi.org/10.1101/2024.12.10.627464

Nonuple atg8 mutant provides genetic evidence for functional specialization of ATG8 isoforms in *Arabidopsis thaliana*

Alessia Del Chiaro[1,2,*], Nenad Grujic[1,*], Jierui Zhao[1,2], Ranjith Kumar Papareddy[1], Peng Gao[1], Juncai Ma[3], Christian Lofke[1], Anuradha Bhattacharya[1], Ramona Gruetzner[4], Pierre Bourguet[1], Frédéric Berger[1], Byung-Ho Kang[3], Sylvestre Marillonnet[4], Yasin Dagdas[1]

Affiliations

[1]Gregor Mendel Institute, Austrian Academy of Sciences, Vienna BioCenter, Vienna, Austria.
[2]Vienna BioCenter PhD Program, Doctoral School of the University at Vienna and Medical University of Vienna, Vienna, Austria
[3]School of Life Sciences, Centre for Cell & Developmental Biology and State Key Laboratory of Agrobiotechnology, The Chinese University of Hong Kong, Shatin, New Territories, Hong Kong, China
[4]Leibniz-Institut für Pflanzenbiochemie, Department of Cell and Metabolic Biology, Halle, Germany.
* These authors contributed equally

Correspondence: Yasin Dagdas (yasin.dagdas@gmi.oeaw.ac.at)

Abstract

Autophagy sustains cellular health by recycling damaged or excess components through autophagosomes. It is mediated by conserved ATG proteins, which coordinate autophagosome biogenesis and selective cargo degradation. Among these, the ubiquitin-like ATG8 protein plays a central role by linking cargo to the growing autophagosomes through interacting with selective autophagy receptors. Unlike most ATG proteins, the ATG8 gene family is significantly expanded in vascular plants, but its functional specialization remains poorly understood. Using transcriptional and translational reporters in *Arabidopsis thaliana*, we revealed that ATG8 isoforms are differentially expressed across tissues and form distinct autophagosomes within the same cell. To explore ATG8 specialization, we generated the nonuple *Δatg8* mutant lacking all nine ATG8 isoforms. The mutant displayed hypersensitivity to carbon and nitrogen starvation, coupled with defects in bulk and selective autophagy as shown by biochemical and ultrastructural analyses. Complementation experiments demonstrated that ATG8A could rescue both carbon and nitrogen starvation phenotypes, whereas ATG8H could only complement carbon starvation. Proximity labeling proteomics further identified isoform-specific interactors under nitrogen starvation, underscoring their functional divergence. These findings provide genetic evidence for functional specialization of ATG8 isoforms in plants and lay the foundation for investigating their roles in diverse cell types and stress conditions.

Introduction

Autophagy is an evolutionarily conserved cellular quality control mechanism essential for maintaining homeostasis and adapting to environmental stresses (*1-3*). It functions by selectively degrading and recycling damaged, redundant, or harmful cellular components, ensuring cellular integrity and energy balance (*4-6*). Although autophagy occurs constitutively, it is highly inducible under stress conditions such as nutrient deprivation, hypoxia, or infection (*7-10*). During these challenges, autophagy sustains survival by facilitating the degradation of intracellular material, which is sequestered into specialized double-membrane compartments called autophagosomes (*11, 12*). These structures subsequently fuse with lytic organelles—the vacuole in plants and yeast or the lysosome in animals—where their contents are broken down and recycled (*3*).

Contrary to initial views of autophagy as a non-selective bulk degradation process, it is now recognized as a highly selective pathway (*13-16*). This selectivity is mediated by specific interactions between cargo receptors, known as selective autophagy receptors (SARs), and autophagy-related proteins such as ATG8 (*17, 18*). These interactions enable the precise targeting of a wide range of substrates, from protein aggregates to damaged organelles, thus tailoring autophagic responses to specific cellular needs (*19*).

Autophagosome biogenesis progresses through three tightly regulated stages: initiation, expansion, and maturation. This process is orchestrated by the autophagy-related (ATG) protein family, comprising approximately 40 conserved members (*20, 21*). Central to autophagy is ATG8, a ubiquitin-like protein crucial for autophagosome formation, cargo recruitment, and membrane trafficking (*22, 23*). Once processed and lipidated, ATG8 associates with the autophagosome membrane, acting as a scaffold for the assembly of other core autophagy machinery and cargo receptors (*24, 25*).

Interestingly, unlike most ATG proteins, which exist as single or a few isoforms, the ATG8 gene family has undergone significant expansion in vascular plants (*26, 27*). While yeast and eukaryotes from early branching groups encode a single ATG8, vascular plants possess multiple isoforms, with *Arabidopsis thaliana* containing nine distinct ATG8 genes (AtATG8a-i) forming two major clades. Clade I contains ATG8A-G, whereas Clade II contains ATG8H and ATG8I (*28*). Despite moderate sequence divergence and differential expression patterns (*29, 30*)the biological significance of ATG8 isoform expansion and its implications for selective autophagy remain poorly understood.

Here, we present genetic evidence for the functional specialization of ATG8 isoforms in *A. thaliana* by generating a nonuple ATG8 mutant lacking all nine ATG8 genes. Our study reveals that

ATG8 isoforms not only exhibit distinct tissue-specific expression and subcellular localization but also differ in their ability to mediate autophagic responses under specific stress conditions. These findings highlight the complex regulatory landscape of autophagy in plants and provide a foundation for unraveling the mechanisms underlying ATG8 specialization.

Results and Discussion

Arabidopsis thaliana ATG8 isoforms exhibit tissue-specific expression patterns and form distinct autophagosomes within root cells

To explore ATG8 specialization, we first checked the expression patterns of all the nine Arabidopsis ATG8 isoforms. We generated ATG8 promoter-GFP-GUS (pATG8X::GFP-GUS) expressing lines and performed β-glucuronidase (GUS) staining (Fig. 1A). Interestingly, AtATG8s exhibit distinct expression patterns and we only observed a partial overlap between different isoforms, indicating a certain degree of tissue specificity. ATG8E, ATG8F and ATG8G, show a more widespread expression pattern over different tissues and organs, whereas other isoforms, including ATG8A, ATG8B and ATG8I, appear to be restricted to the root (Fig. 1A). Furthermore, some isoforms exhibit peculiar tissue- or cell-type specificities, such as ATG8D being strongly induced in the apex of the cotyledon or ATG8C appearing specifically expressed in guard cells (Fig. 1A). These observations hint at a potential tissue- or cell-type-specific function of the different ATG8 isoforms.

Then, we decided to test the subcellular compartmentalization of ATG8 isoforms. We co-expressed mCherry-ATG8E translational fusion constructs with GFP-tagged versions of ATG8A, ATG8D and ATG8I and assessed their co-localization upon bulk autophagy inducing chemical Torin1 (*31*) and ER-stress inducer Tunicamycin (*32*) treatments (Fig. 1B and C). Irrespective of the treatment, ATG8E colocalized almost entirely with ATG8A. Conversely, ATG8D and ATG8I exhibit a lower degree of colocalization with ATG8E during Torin 1 treatment and even more pronouncedly upon Tunicamycin treatment. ATG8I, representative of the clade II of ATG8 isoforms, has the weakest level of colocalization with ATG8E. These data indicate there are distinct pools of autophagosomes that are labelled with different ATG8 isoforms. In sum, the expression site polymorphism as well as varying levels of colocalization upon different treatments, support the hypothesis that ATG8 isoforms might fulfill different functions or respond to different stimuli.

atg8 nonuple mutant (*Δatg8*) is deficient in autophagy

The partial overlap in expression and colocalization patterns of ATG8 isoforms prompted us to generate an ATG8-free *Arabidopsis thaliana* line that we could use as a tool to investigate ATG8 specialization. Using multiplex CRISPR mutagenesis, we combined 9 guide RNAs (one for each ATG8 isoform) in a construct containing an intronized Cas9 (*33*) and transformed it to generate a nonuple knock-out of *atg8*. We first confirmed the mutations using whole genome sequencing (Fig. 2A). To functionally verify *Δatg8* as an autophagy deficient mutant, we performed the typical nutrient starvation assays (*34*). We transferred 9-days old Arabidopsis seedlings to carbon or nitrogen deprived ½ MS liquid medium for 4 or 6 days, respectively. Similar to the autophagy-deficient mutants *atg2* and *atg5* (*35, 36*), *Δatg8* exhibits reduced growth and discoloration of the cotyledons (Fig. 2B and C). To biochemically validate *Δatg8* mutant, we performed autophagic flux assays under carbon and nitrogen starvation conditions, by measuring the endogenous levels of the stereotypical autophagy substrate NBR1 (Fig. 2D and E) (*37*). NBR1 accumulated at a comparable level in both *Δatg8* and *atg5* under all conditions and was insensitive to concanamycin A treatment that blocks vacuolar degradation (*38*), denoting that both mutants are defective in autophagic degradation (Fig. 2D and E). Collectively, these results suggest that atg8 nonuple mutant is deficient in autophagy.

Δatg8 mutant is defective in selective autophagy

Nitrogen and carbon starvation are considered to trigger bulk autophagy (*39, 40*). To test if *Δatg8* is also defective in selective autophagy, we tested its ability to perform mitophagy and pexophagy. For mitophagy, we measured the levels of the outer mitochondrial membrane voltage dependent anion channel I (VDAC) and the matrix protein isocitrate dehydrogenase (IDH) upon 2,4-dinitrophenol (DNP) treatment. DNP is an uncoupler that leads to mitochondrial depolarization and triggers mitophagy (*41, 42*) (Fig. 3A). Although both VDAC and IDH levels were decreased in the DNP treated wild type Col-0 plants, *Δatg8* behaved similar to *atg5* and showed no change in VDAC or IDH levels (*41*). Likewise, when we assessed peroxisome degradation using the catalase antibody, *Δatg8* mutant behaved similar to *atg5* mutant and was unable to perform pexophagy (*43*) (Fig. 3B). Altogether, these results suggest *Δatg8* mutant is defective in mitophagy and pexophagy.

Next, we performed transmission electron microscopy (TEM) analysis of mitophagy in Arabidopsis root cells. Although we could detect mitophagosomes in wild type Col-0 plants, we did not observe any mitophagosomes in *Δatg8* mutant (Fig. 3C). However, we could still detect double-membraned structures that resemble autophagosomes in the *Δatg8* mutant. These

vesicles appear to non-specifically engulf various types of cellular components. Although further studies are necessary to understand the nature of these compartments, a plausible source could be provacuoles, compartments that appear during vacuole biogenesis (*44*). Indeed, provacuole formation has been reported to be independent of autophagy as autophagy-deficient mutants can still form provacuoles (*44*). In summary, our data suggest *Δatg8* mutant is unable to carry out autophagic recycling.

Complementation of *Δatg8* with ATG8A or ATG8H reveals functional specialization

After confirming the autophagy-deficient phenotype of the *Δatg8* mutant, to assess the functional specialization of ATG8 isoforms, we complemented it with GFP tagged ATG8A and ATG8H, representing both clades. First, we analyzed the complemented lines with confocal microscopy. Both GFP-ATG8A and GFP-ATG8H formed cytoplasmic bright puncta, which further accumulated in the vacuole upon Concanamycin A treatment and underwent autophagic flux (Fig. S2A-B).

To assess to what extent they were able to recover the autophagic function and evaluate potential isoform-specific responses to different stressors, we subjected the two complementation lines to starvation assays. Upon carbon starvation, both complementation mutants exhibit a similar phenotype to Col-0 (Fig. 4A). This suggests that both ATG8A and ATG8H could mediate the autophagic recycling of cellular material that ensure survival during carbon deprivation. In contrast, during nitrogen starvation only GFP-ATG8A expression recovered the sensitivity to nitrogen starvation. GFP-ATG8H expressing lines were similar to the *Δatg8* mutant (Fig. 4B). These results provide functional genetic evidence for ATG8H specialization in *Arabidopsis thaliana*.

To support these findings, we performed autophagic flux assays under carbon and nitrogen starvation. Under carbon starvation conditions, both *Δatg8/+GFP-ATG8A* and *Δatg8/+GFP-ATG8H* had similar NBR1 flux, in contrast to the *Δatg8* mutant (Fig. 4C). This is consistent with the phenotyping results and indicates that both ATG8A and ATG8H are able to trigger bulk autophagy in response to carbon deprivation. However, during nitrogen starvation NBR1 flux in *Δatg8/+GFP-ATG8H* was similar to the *Δatg8* mutant (Fig. 4D), further corroborating the hypothesis that ATG8H, unlike ATG8A, is not able to fully operate autophagy in response to nitrogen deprivation.

ATG8A and ATG8H have distinct proxitomes during nitrogen starvation

Following the observation that ATG8A and ATG8H do not respond equally to N starvation stress, we reasoned that the two isoforms may be interacting with different proteins that are involved in autophagy signaling or cargo recognition. Indeed, our results could be explained by the inability of ATG8H to engage with the nitrogen starvation response signaling, or its failure to associate with

the selective autophagy receptors recognizing the cargoes that need to be degraded to cope with nitrogen deprivation. To test these hypotheses, we complemented the *Δatg8* mutant with the biotinylating enzyme TurboID fused ATG8A and ATG8H and determined the ATG8 proxitomes during nitrogen starvation (Fig. 4E). We used TurboID alone as negative control. 47 proteins exhibited specific association with both or only one of the two ATG8 isoforms (Supplementary Table 3). Among these, numerous well-known interactors were found, including several ATG proteins. Interestingly, whereas some ATG proteins showed similar levels of association with ATG8A and ATG8H, such as ATG3, ATG7, ATG14B and ATG18F, other ATG proteins appear to interact prevalently or exclusively with just one isoform (Supplementary Table 3). In the case of ATG1, ATG1A seems to interact with ATG8A uniquely, while ATG1B can associate with both isoforms but still exhibits a stronger association with ATG8A in the conditions tested. ATG1 kinase initiates autophagosome biogenesis and constitutes one of the major targets for autophagy regulation (*45, 46*). In light of this, our results may indicate that during N starvation ATG1A and ATG1B recruit ATG8A preferentially to promote nutrient replenishment. It is also interesting to observe that less than one third of the total ATG8 interactors are shared between ATG8A and ATG8H (Fig. 4F), whilst 22 proteins specifically interact with ATG8A, and 8 proteins interact with only ATG8H. As a proof on concept, our proximity labeling analysis suggested that the adaptor protein CFS1 specifically interacts with ATG8A but not with ATG8H, consistent with our previous results (*47*). While other interactors need to be further validated, these results suggest single-isoform TurboID lines provide an effective tool to study ATG8 specialization in a wide range of stress conditions.

Since the core autophagy machinery is shared across various selective autophagy pathways, the question of how cells achieve subcellular compartmentalization of these concurrent mechanisms remains unresolved. A plausible explanation is ATG8 isoform specialization, whereby distinct ATG8 variants interact with specific adaptors, receptors, or ATG proteins to direct and compartmentalize autophagic processes. Previous biochemical and proteomic analyses in potato supported this hypothesis, revealing isoform-specific interactomes (*48*). However, the co-occurrence of multiple ATG8 isoforms within individual autophagosomes (Fig. 1) suggests that some unique interactors might have been overlooked.

In this study, we provide genetic evidence for ATG8 specialization in plants using an Arabidopsis *Δatg8* nonuple mutant complemented with individual ATG8 isoforms. Unlike mitophagy observed in HeLa cells lacking multiple ATG8 genes, the Arabidopsis *Δatg8* mutant failed to perform mitophagy and pexophagy, as evidenced by the absence of mitophagosomes and the accumulation of autophagy substrates (Fig. 3). While double-membraned vesicles were

observed in *Δatg8* cells, these are likely provacuolar compartments, which are independent of autophagy.

Interestingly, complementation experiments revealed functional divergence among ATG8 isoforms. While both ATG8A and ATG8H restored carbon starvation sensitivity, only ATG8A was able to complement nitrogen starvation sensitivity (Fig. 4). Consistent with their specialization, proximity labeling proteomics demonstrated distinct interactomes for ATG8A and ATG8H. Further studies are necessary to link the nitrogen sensitivity phenotype to the differentially interacting proteins. Nevertheless, our findings establish the functional specialization of ATG8 isoforms in plants, providing a framework for understanding how cells fine-tune autophagic processes in response to diverse and overlapping signals.

Material and Methods

Plant material and cloning

All Arabidopsis thaliana lines used originate from the Columbia (Col-0) ecotype. The *Δatg8* mutant was generated with two rounds of CRISPR editing. First, the CRISPR/Cas9 construct including gRNAs for all nine AtATG8 genes and an intronized Cas9 was assembled according to a protocol previously described (*33*). The construct was assembled in binary vector pAGM62636 (*33*) that contains a p15 origin of replication for low copy number replication in *E. coli* and an *Agrobacterium rhizogenes* A4 ori for single copy replication in Agrobacterium, resulting in plasmid pAGM70811. This vector backbone was chosen to minimize the risk or recombination between the 9 guides RNA cassettes present on the same plasmid. The gRNAs sequences are the following:

```
ATG8A (AT4G21980): AGCTTACGGGAATTCTGTCA
ATG8B (AT4G04620): GAACTCAATACAGGTGATTG
ATG8C (AT1G62040): CAGTTAGATCAGCTGGAACA
ATG8D (AT2G05630): AAGAGGATGTTCATGCTTG
ATG8E (AT2G45170): CTGTTAGGTCTGATGGCACA
ATG8F (AT4G16520): TTCAGAGAAGAGAAGGGCAG
ATG8G (AT3G60640): GAGGAGACAGTACCGGTGGG
ATG8H (AT3G06420): AAACGCAGATCTGCCAGACA
ATG8I (AT3G15580): GATGAAAGGCTCGCGGAGTCG
```

Primary transformants were genotyped by amplicon sequencing. The data was analysed using a custom-built pipeline to retrieve indel frequencies in the ATG8 genes, using bwa and samtools *mpileup* (*49, 50*). Code and documentation are available at https://github.com/pierre-

bourguet/CRISPR_genotyping. Following sequencing, we could only confirm the successful mutation of eight of the nine isoforms. Therefore, a second CRISPR/Cas9 was employed to target the last gene (ATG8D – AT2G05630). The construct was assembled according to the protocol previously described (*51*), on pHEE401E plasmid, with the following gRNAs sequences: GAACAACAGAGACTCGACCA, GTGATGTCCCGGATATTGAT. The nuple mutant *Δatg8* contains both T-DNA CRISPR/Cas9 cassettes and is resistant to BASTA and Hygromycin. The mutations of nine ATG8 isoforms were confirmed via single cell sequencing.

All the plasmids, except pAGM7081, were assembled through the GreenGate cloning procedure (*52*) and were constructed as follows: pGGZ003_ATG8X::GFP-GUS (X represents the 9 ATG8 isoforms, from A to I), pGGSUN_RPS5::mCherry-TurboID; pGGSUN_RPS5::mCherry-TurboID-ATG8A; pGGSUN_RPS5::mCherry-TurboID-ATG8H; pGGSUN_HTR5::GFP-ATG8A; pGGSUN_HTR5::GFP-ATG8H. Apart from pATG8X::GFP-GUS expressing plants, which are hygromycin resistant, transformants were selected via seed coat fluorescence. The coding sequences of ATG8A and ATG8H carry silent mutations to avoid CRISPR/Cas9 targeting. The point mutations from the start codon are the following: ATG8A, 81bp T > A, 84bp C > T, 87bp A > G, 93bp C > G; for ATG8H, 123bp C > T, 126bp A > C, 129bp T > C, 135bp A > G, 138bp C > T.

DNA sequencing and analysis

High-quality DNA was extracted using the cetyltrimethylammonium bromide (CTAB) method and used to construct Illumina-compatible libraries with the Nextera XT DNA Library Preparation Kit, following the manufacturer's instructions. Sequencing was performed on an Illumina NextSeq instrument in paired-end 150 bp mode.

Raw FASTQ files obtained from sequencing were quality-checked and adapter-trimmed using TrimGalore (https://github.com/FelixKrueger/TrimGalore) with default settings. The trimmed FASTQ files were aligned to the TAIR10 genome using Bowtie2 (*51*) with the parameters `-D 15 -R 2 -N 0 -L 22 -i S,1,1.15`. The resulting aligned BAM files were sorted and indexed using SAMtools (*52*) and manually inspected for insertions or deletions using the Integrative Genomics Viewer (IGV). Deletions and insertions were manually inspected, and the corresponding changes in cDNA and protein sequences were catalogued (Supplementary Table 1).

Plant growth and treatments

For standard plant growth, Arabidopsis seeds were gas sterilized with sodium hypochlorite + HCl (10:1 v/v), sown on water-saturated soil and grown in 16h light/8h dark photoperiod with 165 µmol m^-2 s^-1 light intensity. For *in vitro* growth, Arabidopsis seeds were surface sterilized in 70%

ethanol for 10 minutes twice, then rinsed in absolute ethanol and dried on sterile paper. Seeds were sown in ½ MS liquid medium (Murashige and Skoog salt + Gamborg B5 vitamin mixture [Duchefa] supplemented with 0.5 g/liter MES and 1% sucrose, pH 5.7), vernalized at 4 °C in the dark for 2 days, and then grown under LEDs with 85µM/m^2/s with a 14 h light/10 h dark photoperiod.

For drug treatments, all drugs were dissolved in DMSO and added to the desired concentration: 3 µM Torin 1 (Santa Cruz Biotechnology – CAS 1222998-36-8), 10 µg/mL Tunicamycin (Santa Cruz Biotechnology – CAS 11089-65-9), 1-2 µM Concanamycin A (Santa Cruz Biotechnology – CAS 80890-47-7), 50 µM DNP (Sigma-Aldrich, D198501-1KG). An equal amount of pure DMSO was added to control samples.

For confocal microscopy, Arabidopsis seeds were sterilized by 70% ethanol + 0.05% Tween 20 (Sigma-Aldrich) for 5 min and were subsequently sterilized by 100% ethanol for 10 min. Sterilized seeds were stored in sterile water at 4°C for 1 d for vernalization. Vernalized seeds were spread on 1/2 MS media plates (+1% plant agar [Duchefa]) and vertically grown at 21°C at 60% humidity under LEDs with 50 mM/m^2s a and a 16 h light/8 h dark photoperiod for 5 days. 5-days old seedlings were incubated in ½ MS media containing either DMSO for 2 h, 3 µM Torin 1 for 2 h, 10 µg/mL Tunicamycin for 4 h or 2 µM Concanamycin for 2.5 h before imaging.

Carbon and Nitrogen starvation assays

A. thaliana seeds (~30 per sample, 3 replicates per condition) were sterilized with ethanol, sown in ½ MS liquid medium, vernalized at 4 °C in the dark for 2 days and grown at 21 °C under LEDs with 85µM/m2/s and a 14 h light/10 h dark photoperiod. The starvation treatments were performed on 9-days old seedlings, by replacing ½ MS liquid medium with the same medium (as control), ½ MS liquid medium without sucrose for C starvation or ½ MS liquid medium without nitrogen (Murashige & Skoog without Nitrogen, Caisson Laboratories – MSP21) for N starvation. Prior to medium replacement, the seedlings were washed twice with 1 mL of the new medium to ensure proper removal of the previous medium. For C starvation, the seedlings were kept in the dark. Pictures of the samples were taken after 4 days of C starvation and 6 days of N starvation.

Confocal microscopy

For confocal microscopy, Arabidopsis seedlings were placed on a microscope slide with water and covered with a coverslip. The epidermal cells of root transition and elongation zone were used for image acquisition.

Confocal images were acquired via an upright point laser scanning confocal microscope ZEISS LSM800 Axio Imager.Z2 (Carl Zeiss) equipped with high-sensitive GaAsP detectors (Gallium Arsenide), a LD C-Apochromat 40X objective lens (numerical aperture 1.1, water immersion), and ZEN software (blue edition 3.8, Carl Zeiss). GFP signals were excited at 488 nm and detected between 488 and 545 nm. mCherry signals were excited at 561 nm and detected between 570 and 617 nm.

Image processing and statistics

Confocal images were processed and quantified by Fiji (version 1.52, Fiji). The mCherry-ATG8E colocalization ratio was calculated as the ratio of the number of mCherry-ATG8E puncta that colocalized with GFP-ATG8 isoforms to the total number of mCherry-ATG8E puncta. Statistics tests were performed via GraphPad Prism 8.1.1.

Protein extraction and western blotting

20-40 *A. thaliana* seeds per sample were surface sterilized with ethanol, sown in ½ MS liquid medium, vernalized at 4 °C in the dark for 2 days and grown for 7 days at 21 °C under LEDs with 85µM/m2/s with a 14 h light/10 h dark photoperiod. For starvation treatments, performed overnight, the ½ MS liquid medium was replaced with the same medium (as control), ½ MS liquid medium without sucrose for C starvation or ½ MS liquid medium without nitrogen (Murashige & Skoog without Nitrogen, Caisson Laboratories – MSP21) for N starvation. For C starvation, the samples were kept in the dark. When required, 1 µM Concanamycin A (Santa Cruz Biotechnology – CAS 80890-47-7) was added to the new medium. The seedlings were harvested in safe lock Eppendorf tubes containing 2 mm Ø glass bead, flash frozen in liquid nitrogen and pulverized using a Silamat S7 (Ivoclar vivident). Total proteins were extracted in 2X Laemmli buffer by agitating the samples in the Silamat S7 for 20 s. The samples were boiled at 70 °C and 1000 rpm shaking for 10 min, then centrifuged at max speed with a benchtop centrifuge. Total proteins were quantified with the amido black method. 10 µl of supernatant was added to 190 µl of deionized water, vortexed and then mixed with 1 ml of Amido Black Buffer (10% acetic acid, 90% methanol, 0.05% [w/v] Amido Black (Napthol Blue Black, Sigma N3393)) by inverting the tubes. After 10 min centrifugation at max speed, pellets were washed with 1 ml of Wash Buffer (10% acetic acid, 90% ethanol), mixed by inversion, and centrifuged for another 10 minutes at max speed. Pellets were resuspended in 0.2N NaOH and $OD_{630\,nm}$ was measured, with NaOH solution as blank, to quantify protein concentration with the OD = a[C] + b determined curve. 15 µg of total protein extracts were separated on SDS-PAGE gels and blotted onto PVDF Immobilon-P membrane (Millipore). NBR1 was detected using the anti-NBR1 antibody (Rabbit polyclonal; Agrisera – AS14 2805)

diluted 1:10000. Catalase proteins were detected with Anti-Cat antibody (Rabbit polyclonal; Agrisera – AS09 501), diluted 1:1000. GFP was detected with the anti-GFP antibody (Mouse monoclonal; Roche – 11814460001), diluted 1:5000. Rabbit polyclonal antibody was detected with a goat anti-rabbit IgG HRP-linked antibody (Invitrogen, 65-6120) diluted 1:5000. Hybridized membranes were reacted with SuperSignal™ West Pico PLUS Chemiluminescent Substrate (Thermo Fisher Scientific) and imaged using an iBright CL1500 Imaging System (Invitrogen).

Protein bands were quantified with ImageJ according to the protocol previously described (*53*) and normalized on the loading control. The values reported on the figures correspond to mean values for 3 biological replicates.

For mitophagy assays, 5-days old Arabidopsis seedlings were treated with 50 µM DNP (Sigma-Aldrich, D198501-1KG), or an equal amount of DMSO, for 2-3 hours in the dark, then moved to liquid ½ MS medium for 1h recovery under light. Protein extraction and immunoblot analysis was performed as previously reported (*41*).

GUS staining

10-days old Arabidopsis seedlings expressing pATG8X::GFP-GUS (X represents the 9 ATG8 isoforms, from A to I) were first immersed in acetone for 20 minutes and then washed with the GUS buffer (50 mM $NaPO_4$, 2 mM K-ferrocyanide, 2mM K-ferricyanide, 0.2% Triton X-100). The washed samples were subsequently incubated in GUS staining buffer [GUS buffer + 2 mM X-Gluc (Thermo Scientific)] under 37°C until a blue coloration was visible. The stained samples were then washed and discolored with 100% ethanol and were ready for photographing.

Affinity purification of biotinylated proteins and nanoLC-MS/MS Analysis

A. thaliana seeds were surface sterilized with ethanol, stratified for 2 days at 4 °C in the dark and then grown in ½ MS (Duchefa)/0.5% MES/1% sucrose under LEDs with 85 µM/m2/s and a 14 h light/10 h dark photoperiod. 7-days old seedlings were washed and treated with N deficient ½ MS medium (or control ½ MS medium) overnight and the following morning 50 µM biotin was added to the medium. After 1 hour of biotin incubation, the seedlings were quickly rinsed in ice cold water, dried and frozen in liquid nitrogen. Around 1 gram of plant tissue was used for each sample and the affinity purification of biotinylated proteins was performed as previously described (*54*).

For MS Analysis, the nano HPLC system (UltiMate 3000 RSLC nano system) was coupled to an Orbitrap Exploris 480 mass spectrometer, equipped with a Nanospray Flex ion source (all parts Thermo Fisher Scientific). Peptides were loaded onto a trap column (PepMap Acclaim C18, 5 mm × 300 µm ID, 5 µm particles, 100 Å pore size, Thermo Fisher Scientific) at a flow rate of 25 µl/min

using 0.1% TFA as mobile phase. After loading, the trap column was switched in line with the analytical column (PepMap Acclaim C18, 500 mm × 75 µm ID, 2 µm, 100 Å,Thermo Fisher Scientific). Peptides were eluted using a flow rate of 230 nl/min, starting with the mobile phases 98% A (0.1% formic acid in water) and 2% B (80% acetonitrile, 0.1% formic acid) and linearly increasing to 35% B over the next 120min. This was followed by a steep gradient to 95% B in 1 min, stayed there for 6 min and ramped down in 2 min to the starting conditions of 98% A and 2% B for equilibration at 30°C. The Orbitrap Exploris 480 mass spectrometer was operated in data-dependent mode, performing a full scan (m/z range 350-1200, resolution 60,000, normalized AGC target 300%) at 3 different compensation voltages (CV -45V, -60V and -75V), followed by MS/MS scans of the most abundant ions for a cycle time of 0.9 seconds for each. MS/MS spectra were acquired using an isolation width of 1.2 m/z, normalized AGC target 200%, HCD collision energy of 30 %, maximum injection time mode set to custom and resolution of 30,000. Precursor ions selected for fragmentation (include charge state 2-6) were excluded for 45 s. The monoisotopic precursor selection (MIPS) mode was set to peptide and the exclude isotopes feature was enabled.

MS Data processing

For peptide identification, the RAW-files were loaded into Proteome Discoverer (version 2.5.0.400, Thermo Scientific). All MS/MS spectra were searched using MSAmanda v2.0.0.19924 (Dorfer V. et al., J. Proteome Res. 2014 Aug 1;13(8):3679- 84). The peptide mass tolerance was set to ±10 ppm and fragment mass tolerance to±10 ppm, the maximum number of missed cleavages was set to 2, using tryptic enzymatic specificity without proline restriction. The RAW-files were searched against the Arabidopsis database (32,785 sequences; 14,482,855 residues), supplemented with common contaminants and sequences of tagged proteins of interest. The following search parameters were used: Oxidation on methionine, phosphorylation on serine, threonine, and tyrosine, deamidation on asparagine and glutamine, iodoacetamide derivative on cysteine, beta-methylthiolation on cysteine, biotinylation on lysine, ubiquitinylation residue on lysine, ubiquitination on lysine, pyro-glu from q on peptide N-terminal glutamine, acetylation on protein N-Terminus were set as variable modifications. The result was filtered to 1 % FDR on protein level using the Percolator algorithm (Käll L. et al., Nat. Methods. 2007 Nov; 4(11):923-5) integrated in Proteome Discoverer. The localization of the post-translational modification sites within the peptides was performed with the tool ptmRS, based on the tool phosphoRS (Taus T. et al., J. Proteome Res. 2011, 10, 5354-62). Additionally, an Amanda score cut-off of at least 150 was applied. Protein areas have been computed in IMP-apQuant (Doblmann J. et. al, J Proteome Res 2019, 18(1):535-41) by summing up unique and razor peptides. Resulting protein areas were

normalized using iBAQ (Schwanhäusser B. et al., Nature 2011, 473(7347):337–42) and sum normalization was applied for normalization between samples. Match-between-runs (MBR) was applied for peptides with high confident peak area that were identified by MS/MS spectra in at least one run. Proteins were filtered to be identified by a minimum of 2 PSMs in at least 1 sample and quantified proteins were filtered to contain at least 3 quantified peptide groups. Statistical significance of differentially expressed proteins was determined using limma (Smyth, G. K. - Linear models and empirical Bayes methods for assessing differential expression in microarray experiments. Statistical Applications in Genetics and Molecular Biology, 2004, Volume 3, Article 3.) (Supplementary Table 2).

To identify potential interactors, log2FC was calculated comparing average PSMs in TID-ATG8A samples (n = 3) or TID-ATG8H samples (n = 3) against the TID control (n = 3). Proteins with average PSMs > 3, log2FC > 1 and p-value > 0,05 were selected as potential interactors. The list of potential interactors is provided in Supplementary Table 3.

TEM

The TEM assay was performed following the previously established method (*41, 55*). Briefly, 5-days old *Arabidopsis* seedlings were germinated on ½ MS plates and dissected under microscopy before freezing. For high-pressure freezing, the root tips were collected and immediately frozen with a high-pressure freezer (EM ICE, Leica). For freeze substitution, the root tips were substituted with 2% osmium tetroxide in anhydrous acetone and maintained at −80 °C for 24 hours using an AFS2 temperature-controlling system (Leica). Subsequently, the samples were subjected to three washes with precooled acetone and slowly warmed up to room temperature over a 60-h period before being embedded in EPON resin. After resin polymerization, samples were mounted and trimmed. For the ultrastructure studies, 100 nm thin sections were prepared using an ultramicrotome (EM UC7, Lecia) and examined with a Hitachi H-7650 TEM (Hitachi-High Technologies) operated at 80 kV.

Data availability

All the source data used to generate the main and supplementary figures are deposited to Zenodo (10.5281/zenodo.14277422). Genomic sequencing data generated in this study are deposited at the National Center for Biotechnology Information Gene Expression Omnibus (NCBI GEO, https://www.ncbi.nlm.nih.gov/geo/) under accession number GSE283481. The mass

spectrometry proteomics data have been deposited to the ProteomeXchange Consortium via the PRIDE partner repository.

Acknowledgements

We thank Vienna Biocenter Core Facilities (VBCF), particularly Proteomics, BioOptics and Plant Sciences. We thank the CLIP cluster (https://clip.science) for access for image analysis. We acknowledge funding from Austrian Academy of Sciences, Austrian Science Fund (FWF, P32355, P34944, SFB F79, DOC 111), Vienna Science and Technology Fund (WWTF, LS17-047, LS21-009), and European Research Council Grant (Project number: 101043370). Peng Gao is supported by the Vienna International Postdoctoral Program (VIP2) and Marie Curie Fellowship (Project number: 847548).

The authors declare no competing financial interest.

References

1. D. C. Bassham *et al.*, Autophagy in development and stress responses of plants. *Autophagy* **2**, 2-11 (2006).
2. T. Su *et al.*, Autophagy: An Intracellular Degradation Pathway Regulating Plant Survival and Stress Response. *Front Plant Sci* **11**, 164 (2020).
3. Y. Liu, D. C. Bassham, Autophagy: pathways for self-eating in plant cells. *Annu Rev Plant Biol* **63**, 215-237 (2012).
4. J. Zhou *et al.*, NBR1-mediated selective autophagy targets insoluble ubiquitinated protein aggregates in plant stress responses. *PLoS Genet* **9**, e1003196 (2013).
5. M. Izumi, K. Yoshimoto, H. Batoko, Editorial: Organelle Autophagy in Plant Development. *Front Plant Sci* **11**, 502 (2020).
6. R. S. Marshall, R. D. Vierstra, Autophagy: The Master of Bulk and Selective Recycling. *Annu Rev Plant Biol* **69**, 173-208 (2018).
7. E. A. Merkulova, A. Guiboileau, L. Naya, C. Masclaux-Daubresse, K. Yoshimoto, Assessment and optimization of autophagy monitoring methods in Arabidopsis roots indicate direct fusion of autophagosomes with vacuoles. *Plant Cell Physiol* **55**, 715-726 (2014).
8. L. Chen *et al.*, Autophagy contributes to regulation of the hypoxia response during submergence in Arabidopsis thaliana. *Autophagy* **11**, 2233-2246 (2015).
9. A. Ismayil, M. Yang, Y. Liu, Role of autophagy during plant-virus interactions. *Semin Cell Dev Biol* **101**, 36-40 (2020).
10. P. Wang, Y. Mugume, D. C. Bassham, New advances in autophagy in plants: Regulation, selectivity and function. *Semin Cell Dev Biol* **80**, 113-122 (2018).
11. R. Le Bars, J. Marion, R. Le Borgne, B. Satiat-Jeunemaitre, M. W. Bianchi, ATG5 defines a phagophore domain connected to the endoplasmic reticulum during autophagosome formation in plants. *Nat Commun* **5**, 4121 (2014).
12. W. G. van Doorn, A. Papini, Ultrastructure of autophagy in plant cells: a review. *Autophagy* **9**, 1922-1936 (2013).
13. M. Jin, X. Liu, D. J. Klionsky, SnapShot: Selective autophagy. *Cell* **152**, 368-368.e362 (2013).
14. A. Stolz, A. Ernst, I. Dikic, Cargo recognition and trafficking in selective autophagy. *Nat Cell Biol* **16**, 495-501 (2014).
15. J. C. Farré, S. Subramani, Mechanistic insights into selective autophagy pathways: lessons from yeast. *Nat Rev Mol Cell Biol* **17**, 537-552 (2016).
16. T. Lamark, T. Johansen, Mechanisms of Selective Autophagy. *Annu Rev Cell Dev Biol* **37**, 143-169 (2021).
17. T. Johansen, T. Lamark, Selective autophagy mediated by autophagic adapter proteins. *Autophagy* **7**, 279-296 (2011).
18. V. Rogov, V. Dötsch, T. Johansen, V. Kirkin, Interactions between autophagy receptors and ubiquitin-like proteins form the molecular basis for selective autophagy. *Mol Cell* **53**, 167-178 (2014).
19. S. Luo *et al.*, Cargo Recognition and Function of Selective Autophagy Receptors in Plants. *Int J Mol Sci* **22**, (2021).
20. X. Wen, D. J. Klionsky, An overview of macroautophagy in yeast. *J Mol Biol* **428**, 1681-1699 (2016).
21. H. Yamamoto, S. Zhang, N. Mizushima, Autophagy genes in biology and disease. *Nat Rev Genet* **24**, 382-400 (2023).
22. A. Kaufmann, V. Beier, H. G. Franquelim, T. Wollert, Molecular mechanism of autophagic membrane-scaffold assembly and disassembly. *Cell* **156**, 469-481 (2014).

23. A. Kaufmann, T. Wollert, Scaffolding the expansion of autophagosomes. *Autophagy* **10**, 1343-1345 (2014).
24. T. Johansen, T. Lamark, Selective Autophagy: ATG8 Family Proteins, LIR Motifs and Cargo Receptors. *J Mol Biol* **432**, 80-103 (2020).
25. W. Liu *et al.*, ATG8-Interacting Motif: Evolution and Function in Selective Autophagy of Targeting Biological Processes. *Front Plant Sci* **12**, 783881 (2021).
26. H. Popelka, D. J. Klionsky, Post-translationally-modified structures in the autophagy machinery: an integrative perspective. *Febs j* **282**, 3474-3488 (2015).
27. E. Seo *et al.*, Comparative analyses of ubiquitin-like ATG8 and cysteine protease ATG4 autophagy genes in the plant lineage and cross-kingdom processing of ATG8 by ATG4. *Autophagy* **12**, 2054-2068 (2016).
28. R. Kellner, J. C. De la Concepcion, A. Maqbool, S. Kamoun, Y. F. Dagdas, ATG8 Expansion: A Driver of Selective Autophagy Diversification? *Trends Plant Sci* **22**, 204-214 (2017).
29. D. Winter *et al.*, An "Electronic Fluorescent Pictograph" browser for exploring and analyzing large-scale biological data sets. *PLoS One* **2**, e718 (2007).
30. S. Sláviková *et al.*, The autophagy-associated Atg8 gene family operates both under favourable growth conditions and under starvation stresses in Arabidopsis plants. *J Exp Bot* **56**, 2839-2849 (2005).
31. C. C. Thoreen *et al.*, Correction: An ATP-competitive mammalian target of rapamycin inhibitor reveals rapamycin-resistant functions of mTORC1. *J Biol Chem* **295**, 2886 (2020).
32. M. Stephani *et al.*, A cross-kingdom conserved ER-phagy receptor maintains endoplasmic reticulum homeostasis during stress. *Elife* **9**, (2020).
33. R. Grützner *et al.*, High-efficiency genome editing in plants mediated by a Cas9 gene containing multiple introns. *Plant Commun* **2**, 100135 (2021).
34. T. Chung, A. R. Phillips, R. D. Vierstra, ATG8 lipidation and ATG8-mediated autophagy in Arabidopsis require ATG12 expressed from the differentially controlled ATG12A AND ATG12B loci. *Plant J* **62**, 483-493 (2010).
35. Y. Wang, M. T. Nishimura, T. Zhao, D. Tang, ATG2, an autophagy-related protein, negatively affects powdery mildew resistance and mildew-induced cell death in Arabidopsis. *Plant J* **68**, 74-87 (2011).
36. A. R. Thompson, J. H. Doelling, A. Suttangkakul, R. D. Vierstra, Autophagic nutrient recycling in Arabidopsis directed by the ATG8 and ATG12 conjugation pathways. *Plant Physiol* **138**, 2097-2110 (2005).
37. S. Svenning, T. Lamark, K. Krause, T. Johansen, Plant NBR1 is a selective autophagy substrate and a functional hybrid of the mammalian autophagic adapters NBR1 and p62/SQSTM1. *Autophagy* **7**, 993-1010 (2011).
38. M. Krebs *et al.*, Arabidopsis V-ATPase activity at the tonoplast is required for efficient nutrient storage but not for sodium accumulation. *Proc Natl Acad Sci U S A* **107**, 3251-3256 (2010).
39. J. H. Doelling, J. M. Walker, E. M. Friedman, A. R. Thompson, R. D. Vierstra, The APG8/12-activating enzyme APG7 is required for proper nutrient recycling and senescence in Arabidopsis thaliana. *J Biol Chem* **277**, 33105-33114 (2002).
40. Y. Xiong, A. L. Contento, D. C. Bassham, AtATG18a is required for the formation of autophagosomes during nutrient stress and senescence in Arabidopsis thaliana. *Plant J* **42**, 535-546 (2005).
41. J. Ma *et al.*, Friendly mediates membrane depolarization-induced mitophagy in Arabidopsis. *Curr Biol* **31**, 1931-1944.e1934 (2021).
42. N. D. Georgakopoulos, G. Wells, M. Campanella, The pharmacological regulation of cellular mitophagy. *Nat Chem Biol* **13**, 136-146 (2017).

43. K. Yoshimoto *et al.*, Organ-specific quality control of plant peroxisomes is mediated by autophagy. *J Cell Sci* **127**, 1161-1168 (2014).
44. C. Viotti *et al.*, The endoplasmic reticulum is the main membrane source for biogenesis of the lytic vacuole in Arabidopsis. *Plant Cell* **25**, 3434-3449 (2013).
45. Y. Kamada *et al.*, Tor directly controls the Atg1 kinase complex to regulate autophagy. *Mol Cell Biol* **30**, 1049-1058 (2010).
46. N. Mizushima, The role of the Atg1/ULK1 complex in autophagy regulation. *Curr Opin Cell Biol* **22**, 132-139 (2010).
47. J. Zhao *et al.*, Plant autophagosomes mature into amphisomes prior to their delivery to the central vacuole. *J Cell Biol* **221**, (2022).
48. E. K. Zess *et al.*, N-terminal β-strand underpins biochemical specialization of an ATG8 isoform. *PLoS Biol* **17**, e3000373 (2019).
49. H. L. Xing *et al.*, A CRISPR/Cas9 toolkit for multiplex genome editing in plants. *BMC Plant Biol* **14**, 327 (2014).
50. A. Lampropoulos *et al.*, GreenGate---a novel, versatile, and efficient cloning system for plant transgenesis. *PLoS One* **8**, e83043 (2013).
51. B. Langmead, S. L. Salzberg, Fast gapped-read alignment with Bowtie 2. *Nat Methods* **9**, 357-359 (2012).
52. P. Danecek *et al.*, Twelve years of SAMtools and BCFtools. *Gigascience* **10**, (2021).
53. S. Stael, L. P. Miller, D. Fernández-Fernández Á, F. Van Breusegem, Detection of Damage-Activated Metacaspase Activity by Western Blot in Plants. *Methods Mol Biol* **2447**, 127-137 (2022).
54. A. Mair, S. L. Xu, T. C. Branon, A. Y. Ting, D. C. Bergmann, Proximity labeling of protein complexes and cell-type-specific organellar proteomes in Arabidopsis enabled by TurboID. *Elife* **8**, (2019).
55. B. H. Kang, Electron microscopy and high-pressure freezing of Arabidopsis. *Methods Cell Biol* **96**, 259-283 (2010).

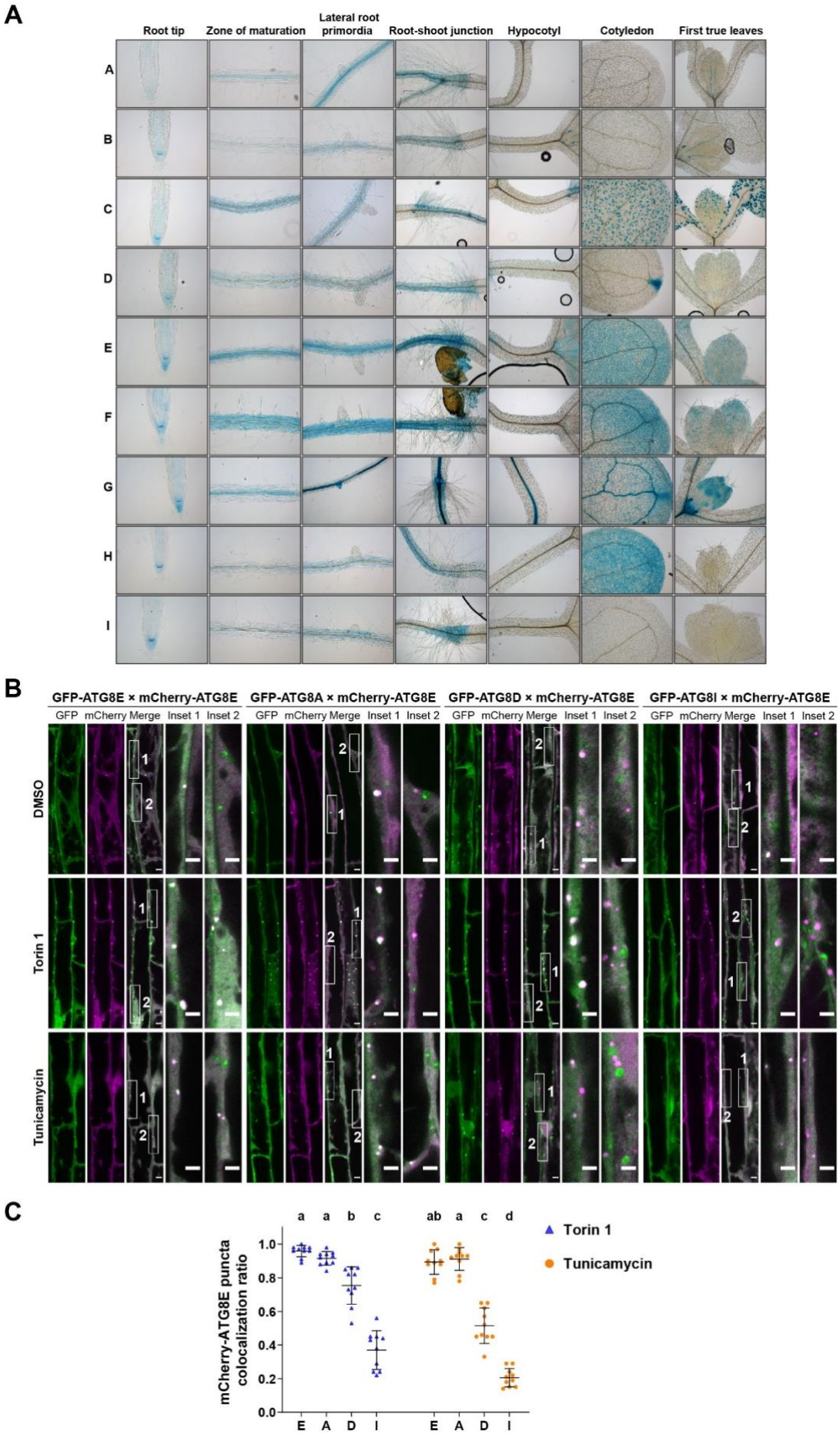

Figure 1. ***Arabidopsis thaliana*** **ATG8 isoforms exhibit tissue-specific expression patterns and form distinct autophagosomes within root cells**

(A) Representative GUS staining images showing the spatial-temporal expression patterns of 9 Arabidopsis ATG8 isoforms.10-days old Arabidopsis seedlings expressing pATG8X::GFP-GUS (X represents the 9 ATG8 isoforms, from A to I) were stained with GUS staining buffer. (B) Representative confocal microscopic images showing the colocalization of mCherry-ATG8E with different GFP-ATG8 isoforms in Arabidopsis root epidermal cells. 5-days old Arabidopsis seedlings co-expressing mCherry-ATG8E with GFP-ATG8E, GFP-ATG8A, GFP-ATG8D, or GFP-ATG8I were incubated in ½ MS liquid media containing either DMSO (as mock condition) for 2 h, 5 μM Torin1 for 2 h, or 10 μg/mL Tunicamycin for 4 h. Representative images of 10 replicates were shown here. Scale bars, 5μm. Inset scale bars, 3 μm. (C) Quantification of mCherry-ATG8E colocalization ratio of the Arabidopsis root epidermal cells imaged in (B). The mCherry-ATG8E colocalization ratio was calculated as the ratio of the number of mCherry-ATG8E puncta that colocalized with GFP-ATG8 isoforms to the total number of mCherry-ATG8E puncta. Bars indicate the mean ± SD of 10 replicates. Brown-Forsy and Welch ANOVA tests with Dunnett's T3 multiple comparisons tests were used for statistically comparing the colocalization difference between each treatment group.

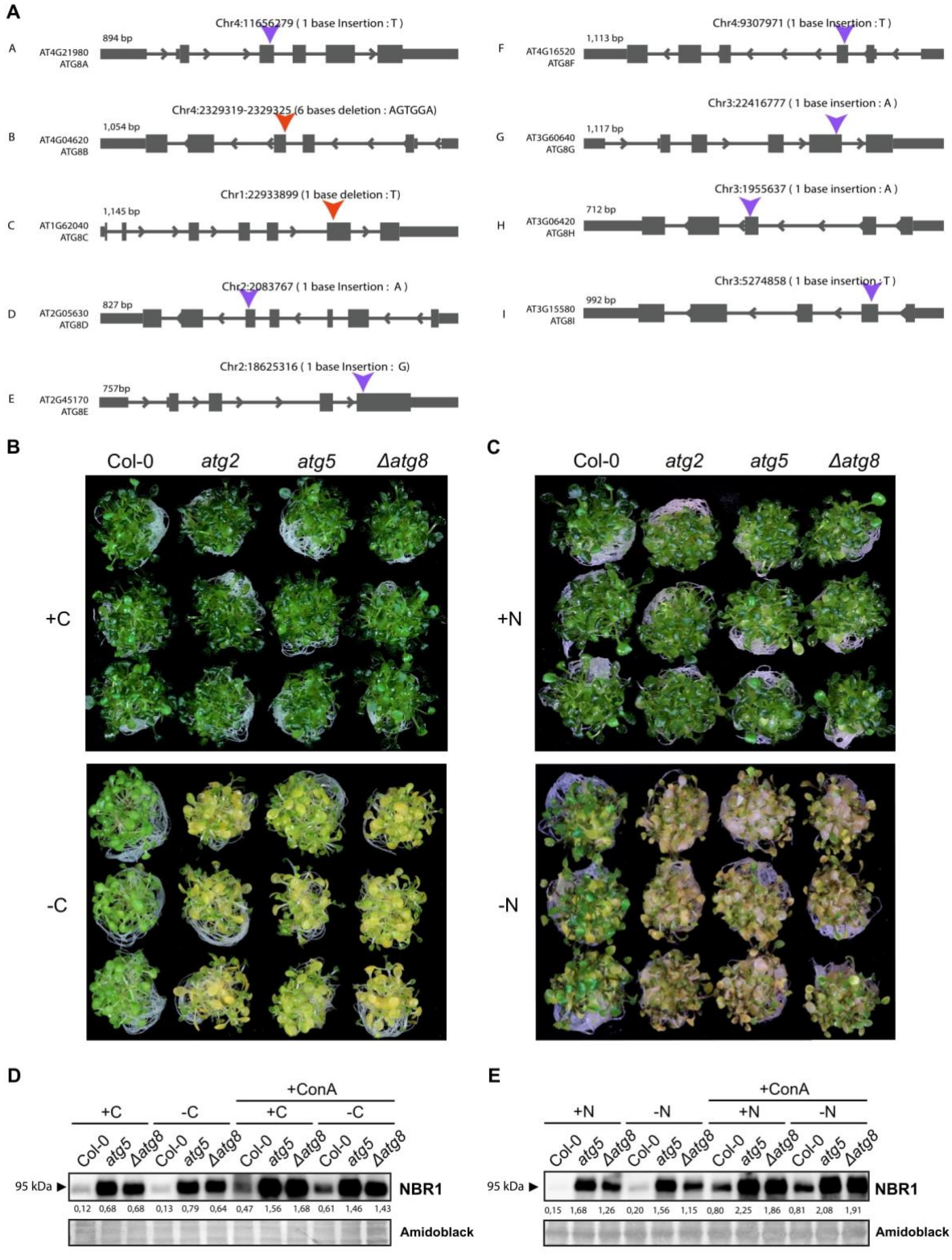

Figure 2. *atg8* nonuple mutant (*Δatg8*) is deficient in autophagy

(A) Schematic representation of gene models illustrating CRISPR-induced mutations in the ATG8 gene. Blue arrows denote insertion sites, while red arrows indicate deletion sites. The forward and reverse arrows within the gene model indicate the directionality of gene transcription, reflecting the strandedness of the gene. (B, C) Carbon (B) and nitrogen (C) starvation phenotypic
600 assays comparing Col-0, *atg5* and *Δatg8* (n = 3) in carbon-rich (+C) or carbon-deficient (-C) ½ MS liquid medium and nitrogen-rich (+N) or nitrogen-deficient (-N) ½ MS liquid medium. (D, E) Western blots comparing endogenous NBR1 levels in Col-0, *atg5* and *Δatg8* upon carbon (D) and nitrogen (E) starvation, in combination with Concanamycin A (1µM). Relative quantification of protein bands is reported below the blots.

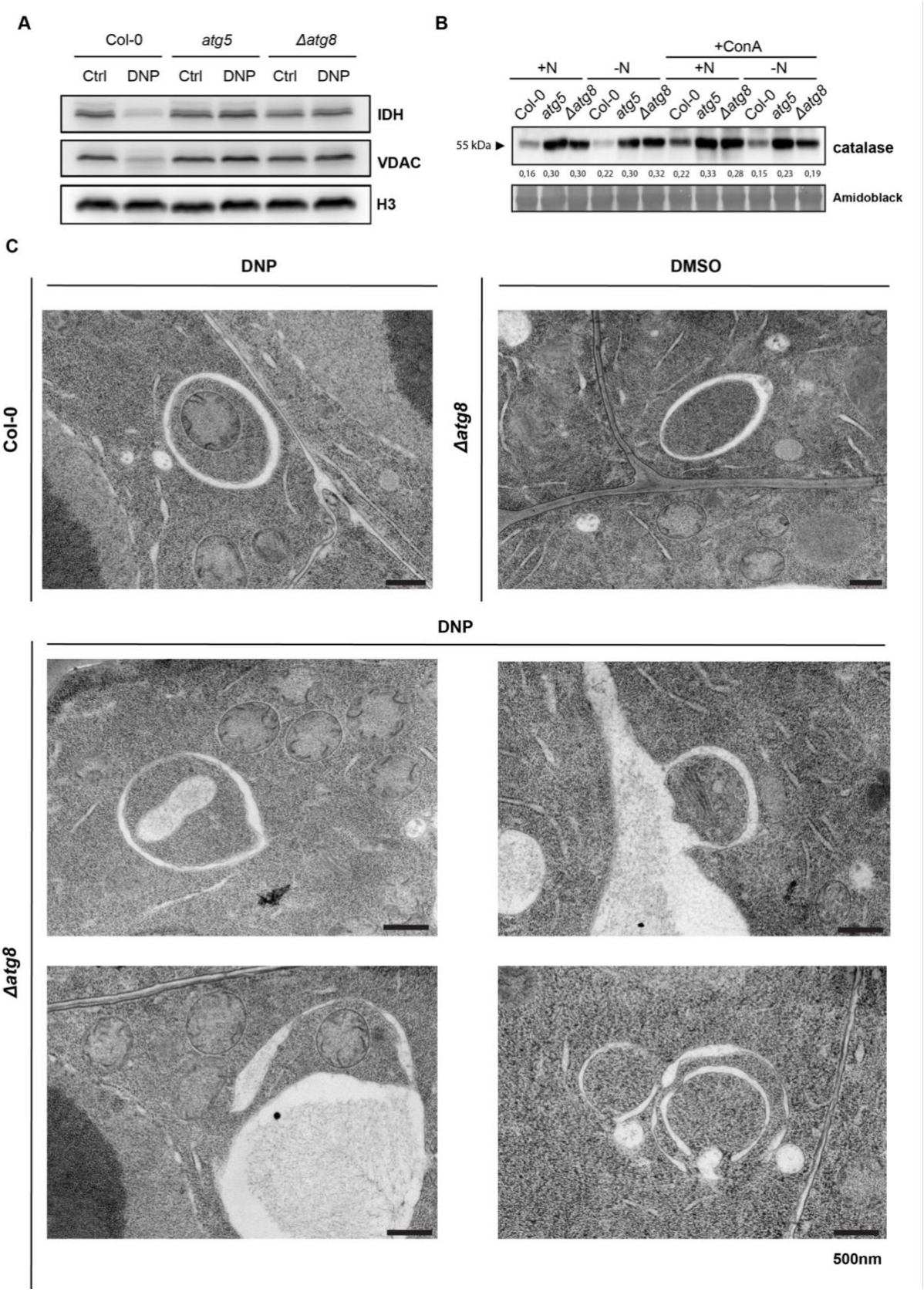

Figure 3. The *Δatg8* mutant is not able to perform mitophagy and pexophagy.

(A) Western blots comparing endogenous IDH and VDAC levels in Col-0, *atg5* and *Δatg8* upon DNP treatment. (B) Western blots comparing endogenous catalase levels in Col-0, *atg5* and *Δatg8* upon N starvation treatment. Relative quantification of protein bands is reported below the blot. (C) Electron micrographs of Col-0 and *Δatg8* root cells treated with DNP or DMSO. Scale bars, 500 nm.

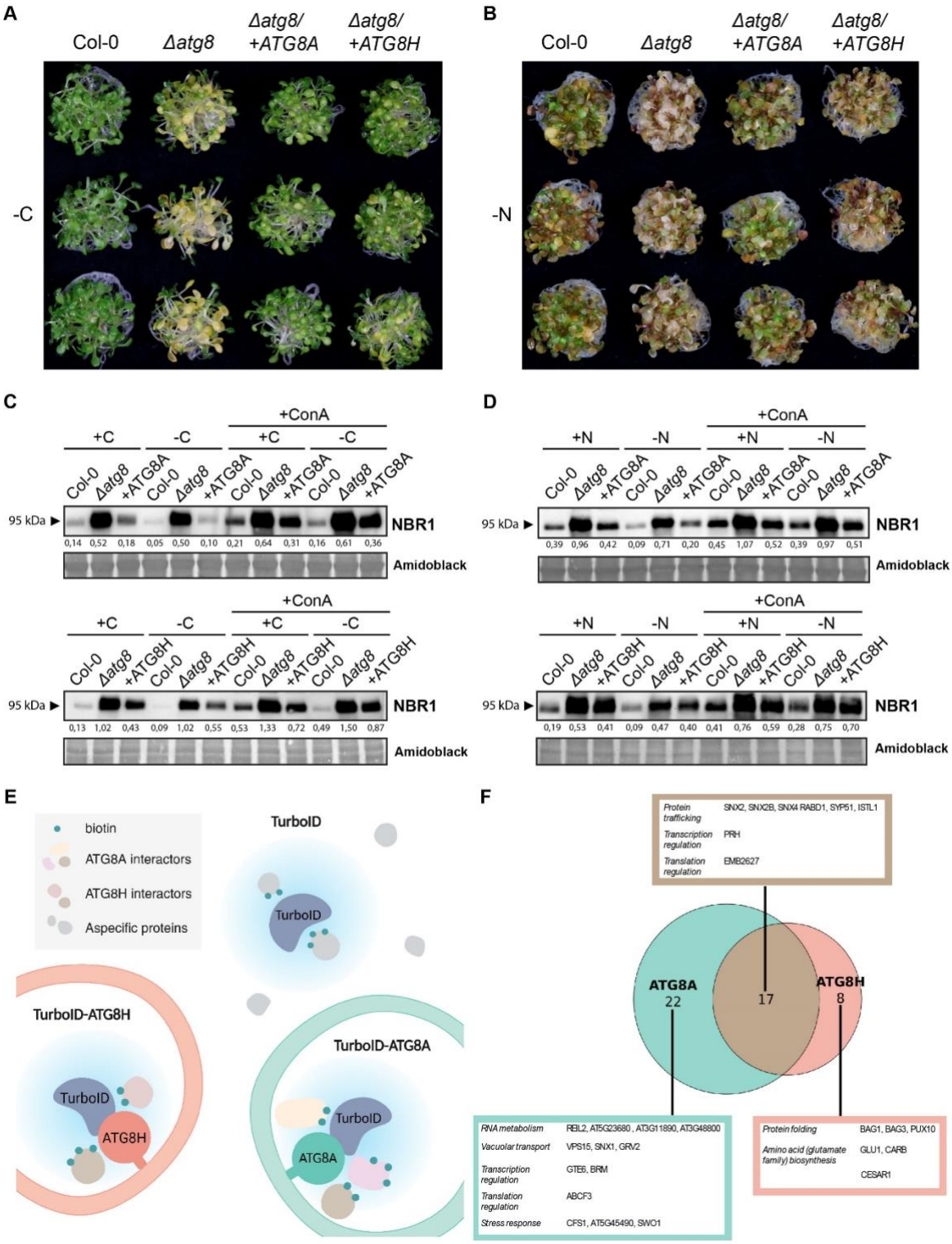

620 **Figure 4. Complementation of *Δatg8* with ATG8A or ATG8H reveals functional specialization of ATG8 isoforms**

(A, B) Carbon (A) and nitrogen (B) starvation phenotypic assays comparing Col-0, *Δatg8* and complementation lines *Δatg8* /+ATG8A, *Δatg8*/+ATG8H (n = 3) in carbon-deficient (-C) ½ MS liquid medium and nitrogen-deficient (-N) ½ MS liquid medium. (C, D) Western blots comparing endogenous NBR1 levels in Col-0, *Δatg8, Δatg8* /+ATG8A and *Δatg8* /+ATG8H upon carbon (C) and nitrogen (D) starvation, in combination with Concanamycin A (1 µM). Relative quantification of protein bands is reported below the blots. (E) Schematic representation of TurboID proximity labeling analysis. (F) Venn diagram reporting common and unique interactors of ATG8A and ATG8H under nitrogen starvation.

630

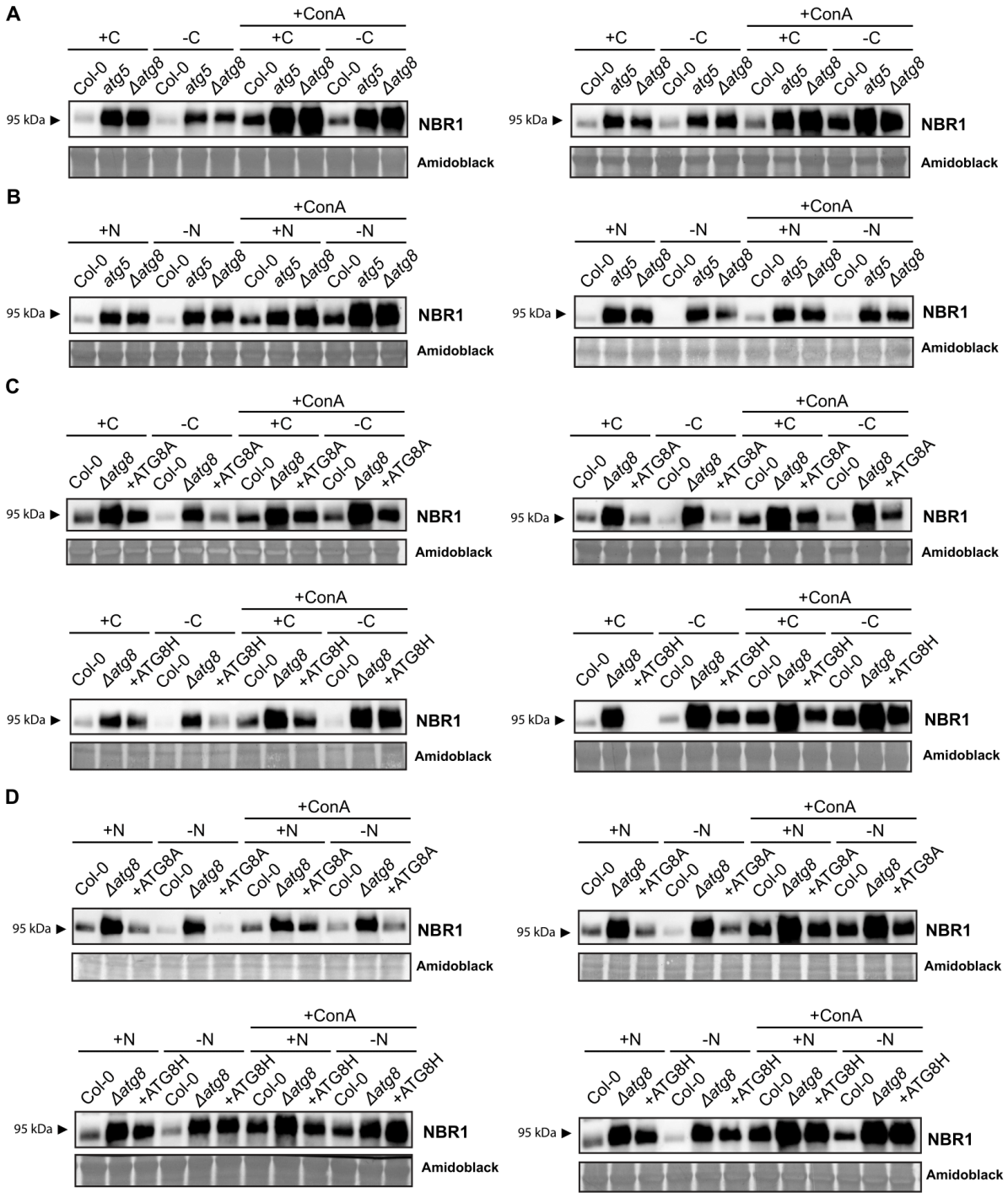

Supplementary Figure 1. Replicates of western blots in Figure 2 (A, B) and Figure 4 (C, D).

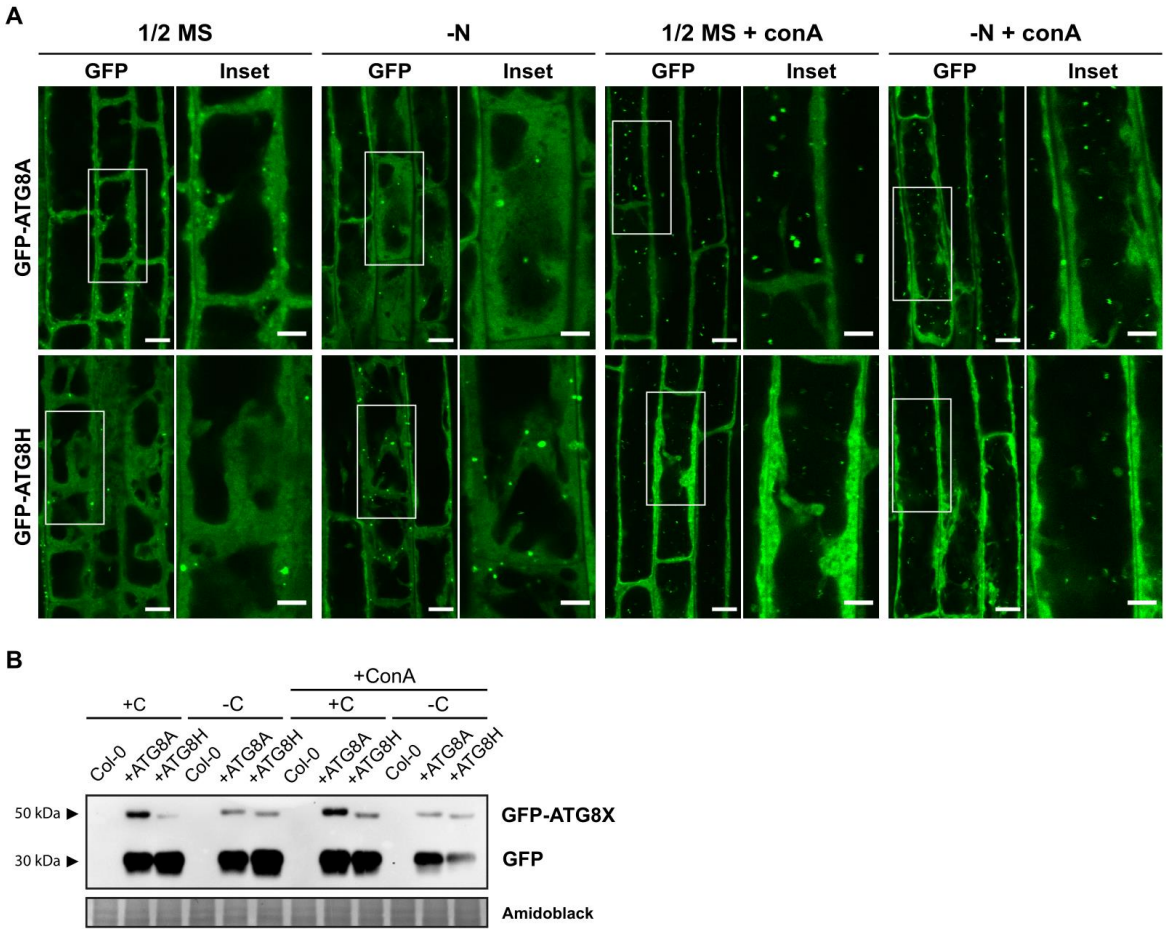

Supplementary Figure 2. Arabidopsis ATG8 complementation lines have normal autophagosome structure and autophagic flux under control and nutrient-deficient conditions. (A) Representative confocal microscopic images showing the autophagosomes and the autophagic bodies inside the vacuole in root epidermal cells of the complementation lines Δatg8 /+GFP-ATG8A and Δatg8 /+GFP-ATG8A. 5-days old Arabidopsis seedlings were incubated in ½ MS liquid media or nitrogen-deficient (-N) liquid media for 3 h, or ½ MS liquid media or nitrogen-deficient (-N) liquid media containing 2 μM concanamycin A for 2.5 h before imaging. Representative images of 3 replicates were shown here. Scale bars, 10 μm. Inset scale bars, 5 μm. (B) Western blot comparing autophagic flux of complementation lines Δatg8 /+GFP-ATG8A and Δatg8 /+GFP-ATG8A upon C starvation treatment, in combination with concanamycin A (1μM).

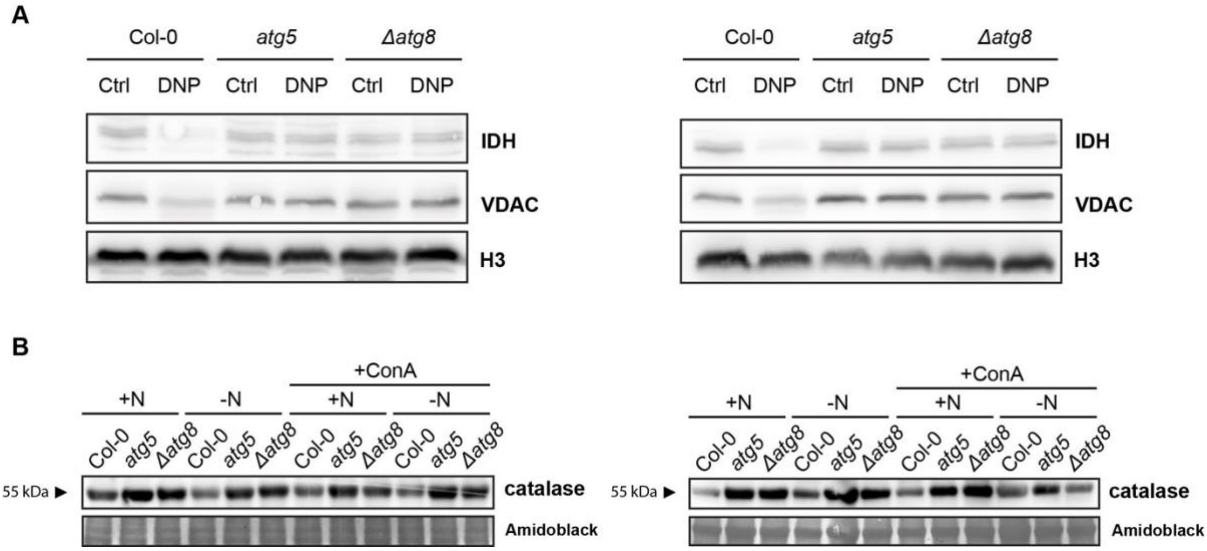

Supplementary Figure 3. Replicates of western blots in Figure 3.

6.3. Mitophagy in Arabidopsis is mediated by Friendly

Mitophagy, the selective degradation of damaged mitochondria via autophagy, is well-characterized in metazoans and yeast but remains poorly understood in plants. While mitochondrial quality control is critical for cellular homeostasis, the molecular mechanisms underlying plant mitophagy, particularly under stress or developmental transitions, are largely unexplored.

As shown in **Chapter 6.4** (Ma et al., 2021), we investigated depolarization-induced mitophagy in Arabidopsis thaliana using live-cell imaging, electron tomography, and biochemical assays, revealing that uncoupler (DNP and FCCP) treatments trigger mitochondrial membrane depolarization and ATG5-dependent recruitment of ATG8-labeled autophagosomes to degrade compromised mitochondria. We identify the CLU family protein FRIENDLY (FMT) as essential for mitophagy, as it translocates to depolarized mitochondria and mediates autophagosome formation, with *fmt* mutants exhibiting defective mitochondrial clearance. Furthermore, mitophagy is activated during de-etiolation, linking mitochondrial turnover to chloroplast biogenesis and metabolic reprogramming. Our findings establish FMT as a key regulator of plant mitophagy and provide insights into organelle quality control during stress and development.

6.4. Appendix Manuscript 2: “Friendly mediates membrane depolarization-induced mitophagy in *Arabidopsis*”

Authors: Juncai Ma, Zizhen Liang, **Jierui Zhao**, Pengfei Wang, Wenlong Ma, Keith K. Mai, Juan A. Fernandez Andrade, Yonglun Zeng, Nenad Grujic, Liwen Jiang, Yasin Dagdas, Byung-Ho Kang

Contribution: For this manuscript, I analyzed the data of confocal experiments and western blots and revised the manuscript.

Status: This manuscript was published in Current Biology (volume 31, issue 9) on May 10, 2021.

DOI: https://doi.org/10.1016/j.cub.2021.02.034

Article

Current Biology

Friendly mediates membrane depolarization-induced mitophagy in *Arabidopsis*

Graphical Abstract

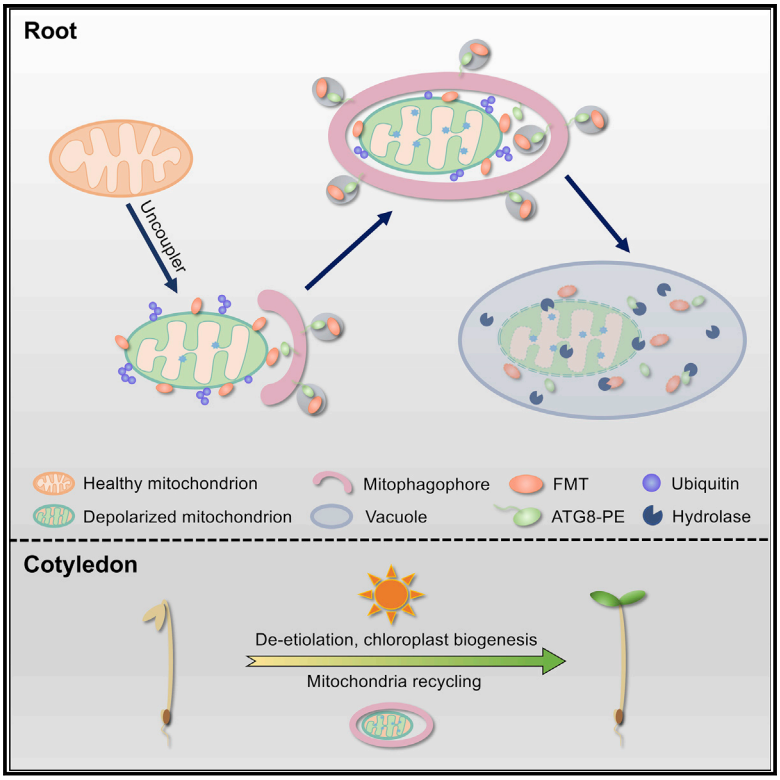

Authors

Juncai Ma, Zizhen Liang, Jierui Zhao, ..., Liwen Jiang, Yasin Dagdas, Byung-Ho Kang

Correspondence

bkang@cuhk.edu.hk (B.-H.K.), yasin.dagdas@gmi.oeaw.ac.at (Y.D.)

In brief

Mitophagy in plant cells is poorly understood in comparison with animal or fungal cells. Ma et al. show that depolarization stresses induce mitophagy in *Arabidopsis*, and Friendly is required for the removal of depolarized mitochondria. The Friendly-mediated mitophagy occurs during de-etiolation, suggesting its role in metabolic switching.

Highlights

- Uncouplers induce mitochondria depolarization and mitophagy in *Arabidopsis*
- ATG5 is required for ATG8 recruitment and mitochondrial protein degradation
- Friendly, a clustered mitochondria family protein, mediates the plant mitophagy
- Mitophagy is activated in *Arabidopsis* cotyledon cells during de-etiolation

Ma et al., 2021, Current Biology *31*, 1931–1944
May 10, 2021
https://doi.org/10.1016/j.cub.2021.02.034

CellPress

Current Biology

CellPress

Article

Friendly mediates membrane depolarization-induced mitophagy in *Arabidopsis*

Juncai Ma,[1] Zizhen Liang,[1] Jierui Zhao,[2] Pengfei Wang,[1] Wenlong Ma,[1] Keith K. Mai,[1] Juan A. Fernandez Andrade,[3] Yonglun Zeng,[1] Nenad Grujic,[2] Liwen Jiang,[1] Yasin Dagdas,[2,*] and Byung-Ho Kang[1,4,*]

[1]School of Life Sciences, Centre for Cell & Developmental Biology and State Key Laboratory of Agrobiotechnology, The Chinese University of Hong Kong, Shatin, New Territories, Hong Kong, China

[2]Gregor Mendel Institute (GMI), Austrian Academy of Sciences, Vienna BioCenter (VBC), Vienna, Austria

[3]Department of Physiology and Pharmacology, Western University, London, ON, Canada

[4]Lead contact

*Correspondence: yasin.dagdas@gmi.oeaw.ac.at (Y.D.), bkang@cuhk.edu.hk (B.-H.K.)

https://doi.org/10.1016/j.cub.2021.02.034

SUMMARY

The oxidative environment within the mitochondria makes them particularly vulnerable to proteotoxic stress. To maintain a healthy mitochondrial network, eukaryotes have evolved multi-tiered quality control pathways. If the stress cannot be alleviated, defective mitochondria are selectively removed by autophagy via a process termed mitophagy. Despite significant advances in metazoans and yeast, in plants, the molecular underpinnings of mitophagy are largely unknown. Here, using time-lapse imaging, electron tomography, and biochemical assays, we show that uncoupler treatments cause loss of mitochondrial membrane potential and induce autophagy in *Arabidopsis*. The damaged mitochondria are selectively engulfed by autophagosomes that are labeled by ATG8 proteins in an ATG5-dependent manner. Friendly, a member of the clustered mitochondria protein family, is recruited to the damaged mitochondria to mediate mitophagy. In addition to the stress, mitophagy is also induced during de-etiolation, a major cellular transformation during photomorphogenesis that involves chloroplast biogenesis. De-etiolation-triggered mitophagy is involved in cotyledon greening, pointing toward an inter-organellar crosstalk mechanism. Altogether, our results demonstrate how plants employ mitophagy to recycle damaged mitochondria during stress and development.

INTRODUCTION

Mitochondria are highly dynamic double-membraned organelles that function as cellular powerhouses. They generate energy via oxidative phosphorylation and mediate the synthesis of essential macromolecules, such as iron-sulfur clusters.[1,2] One of the by-products of the oxidative environment in mitochondria is the generation of toxic reactive oxygen species that damage mitochondrial DNA, lipids, and proteins. In addition, although most of the mitochondrial proteins are encoded by nuclear genes, 13 subunits of the oxidative phosphorylation complexes are still encoded by the mitochondrial genome. As the inter-genome coordination could be disrupted, and one cell could have thousands of times more copies of the mitochondrial genome than the nuclear genome, imbalances in stoichiometries of these multi-subunit oxidative phosphorylation (OXPHOS) complexes trigger proteotoxic stress.[3,4] To overcome these challenges and maintain a healthy mitochondrial network, eukaryotes have evolved multi-tiered and interconnected mitochondrial quality control pathways.[3]

One of the major mitochondrial quality control pathways is mitophagy, the selective removal of damaged or superfluous mitochondria via autophagy. As many players involved in mitophagy have been associated with diseases, and mitophagy allows us to visualize selective engulfment of an organelle into an autophagosome, mitophagy is one of the best-studied signaling mechanisms in metazoans.[5–8] One of the hallmarks of damaged mitochondria is the loss of membrane potential.[3] Various chemical protonophores, such as carbonyl cyanide p-trifluoro-methoxyphenylhydrazone (FCCP) or 2,4-dinitrophenol (DNP), have been used to induce mitochondrial membrane depolarization and mitophagy.[9] The loss of mitochondrial membrane potential leads to the stabilization of PINK1 on the mitochondrial outer membrane. PINK1 phosphorylates ubiquitin and activates Parkin on the mitochondrial membrane for polyubiquitination of various outer-membrane proteins. These eat-me signals create a positive feedback loop that results in the recruitment of selective autophagy receptors, such as p62, optineurin, or NDP52, to recruit the damaged mitochondria into autophagosomes for their subsequent degradation.[7,10,11] Although much has been learned about mitophagy in metazoans, molecular players that mediate mitophagy in plants are yet to be uncovered.[2,12]

Mounting evidence suggests plant mitochondria are also recycled by selective autophagy.[2,13] However, likely influenced by harboring another endosymbiotic organelle, plants lack homologs of known mitophagy receptors and regulators.[12] So far, most studies have used genetic and biochemical assays to analyze mitochondrial turnover in plants. Cell biological tools that would allow us to visualize different stages of mitophagy have not been established.

Similar to metazoans, ATG8 proteins are widely used to monitor and quantify autophagy in plants.[14] ATG8 is a ubiquitin-like protein inserted into the growing phagophore by phosphatidyl ethanolamine modification. ATG8 also directly interacts with selective autophagy receptors and adaptors and therefore plays key roles in selective autophagy processes.[15] During the course of evolution, ATG8 gene family has expanded from one isoform in unicellular algae to nine isoforms in the model plant *Arabidopsis thaliana*. Accumulating evidence suggests that ATG8 isoforms are functionally specialized, reminiscent of the specific functions of LC3 and GABARAP family proteins in metazoans.[16,17] In *Arabidopsis*, ATG8a and ATG8e are the most commonly used isoforms, as they are expressed in various tissues and induced by various starvation and stress conditions.[18,19] As lipidated ATG8 migrates faster in SDS-PAGE gel, the ratio of lipidated to unlipidated ATG8 serves as a readout for autophagic activity. When delivered to the vacuole, the ATG8 segment of GFP-ATG8 decays faster, leading to accumulation of free GFP. Therefore, the ratio of GFP-ATG8 to free GFP is an indicator of autophagic activity.[14] Although ATG8-based autophagic flux assays have been successfully employed to characterize starvation-induced autophagy mechanisms, so far, they have not been adopted for studying mitophagy in plants.

Here, we studied uncoupler-induced mitophagy in the model plant *Arabidopsis thaliana*. We used live-cell imaging and electron tomography to visualize the engulfment of the damaged mitochondria by mitophagosomes. We supported our cell biological findings with autophagic flux assays to show autophagy regulates the recycling of damaged mitochondria. We also showed that Friendly (FMT) protein linked to the regulation of mitochondria dynamics is recruited to mitochondria upon damage. Consistently, *fmt* mutants have defects in the formation of mitophagosomes and mitochondrial turnover. Finally, we demonstrate that de-etiolation also leads to the accumulation of compromised mitochondria and their recycling via mitophagy. Altogether, our findings establish a cell biological and biochemical platform to further dissect mitophagy and reveal a molecular player that is essential for mitophagy in plants.

RESULTS

Uncoupler treatments induce accumulation of depolarized mitochondria in *Arabidopsis* root cells

Uncouplers, such as DNP and FCCP, perturb the electrochemical potential of the inner mitochondrial membrane, triggering mitochondrial recycling in mammalian cells.[20] To test whether these compounds also affect mitochondria in plant root tip cells, we incubated *Arabidopsis* seedlings expressing mitochondrion-targeted GFP (mito-GFP) in liquid MS medium containing DNP or FCCP (Figure 1). Our live-cell imaging and electron microscopy/tomography of mitochondria were limited to cortex cells in the root elongation zone for consistency. However, loss of membrane potential and mitochondrial recycling were observed in all cell types. To differentiate depolarized mitochondria, we pre-stained root cells with tetramethylrhodamine ethyl ester (TMRE), a fluorescent dye sensitive to membrane potential.[21] Normal mitochondria are seen as yellow puncta from dual fluorescence emitted from GFP and TMRE, although depolarized mitochondria will be green as TMRE will not fluoresce upon membrane depolarization.

Under normal conditions, depolarized mitochondria were rare in mito-GFP roots (Figure 1A). When mito-GFP roots were incubated with DNP, the numbers of depolarized mitochondria increased significantly (Figures 1A and 1C). Inactivation of an essential macroautophagy gene, *ATG5*, in the mito-GFP line (*atg5-1::*mito-GFP) led to the accumulation of depolarized mitochondria in DNP-treated as well as untreated roots, indicating that removal of depolarized mitochondria requires *ATG5* (Figures 1B and 1D). The addition of concanamycin A (ConA), an inhibitor of vacuolar H^+-ATPase that disrupts protein transport to the vacuole, led to further buildup of mitochondria lacking membrane potential in mito-GFP roots, indicating vacuole is the final destination for these depolarized mitochondria. Interestingly, ConA did not lead to a similar buildup of depolarized mitochondria in *atg5-1*::mito-GFP roots (no significant difference [n.s.] in Figure 1D). These observations agree with the inhibition of autophagic degradation by ConA[15,22] and suggest that depolarized mitochondria are recycled via the macroautophagy machinery in *Arabidopsis* root cells.

FCCP was a more potent uncoupler than DNP, depolarizing almost all mitochondria at a lower concentration after 1 h (Figure 1). In the following analyses, however, we employed DNP to trigger mitophagy because its slower action facilitated the monitoring of the mitophagy dynamics via cell biological and biochemical assays.

Uncoupler treatments induce autophagy

To examine whether autophagosome formation is induced following the uncoupler stress, we visualized a member of the *Arabidopsis* ATG8 family, ATG8e, fused with a YFP (YFP-ATG8e). Under normal conditions, we rarely observed puncta; most of the ATG8 signal was diffuse. However, the number of YFP-ATG8e foci significantly increased in root cells upon DNP treatment in a time-dependent manner (Figures 2A and 2B). Immunoblot analyses of wild-type (WT) root cells with ATG8 antibody revealed a faint lower band, which became more abundant in root samples incubated with DNP (Figure 2C). The lower band was absent in *atg5-1* mutant root samples, irrespective of DNP exposure (Figure 2C). If protein extracts from DNP-treated WT root samples were incubated with phospholipase D (PLD), the lower band disappeared, confirming it represents the lipidated form of ATG8 (Figures 2D and 2E). Altogether, these results suggest that ATG8 lipidation, thereby autophagy, is induced upon DNP treatment in an *ATG5*-dependent manner.

We then performed fluorescent protein cleavage assay to measure autophagic flux in DNP-treated cells. A free YFP polypeptide was detected in YFP-ATG8e samples, and its amount increased over time with a concomitant drop in YFP-ATG8e (Figures 2F and 2G). No free mCherry was discerned in the immunoblot of mCherry-ATG8e::*atg5-1* by an anti-mCherry antibody (Figure 2C). DNP treatment did not affect the autophagic flux of Neighbor of BRCA1 (NBR1), a commonly used autophagy substrate (Figure 2F).[23] These data suggest that uncoupler treatment activates a selective autophagy pathway to recycle depolarized mitochondria.

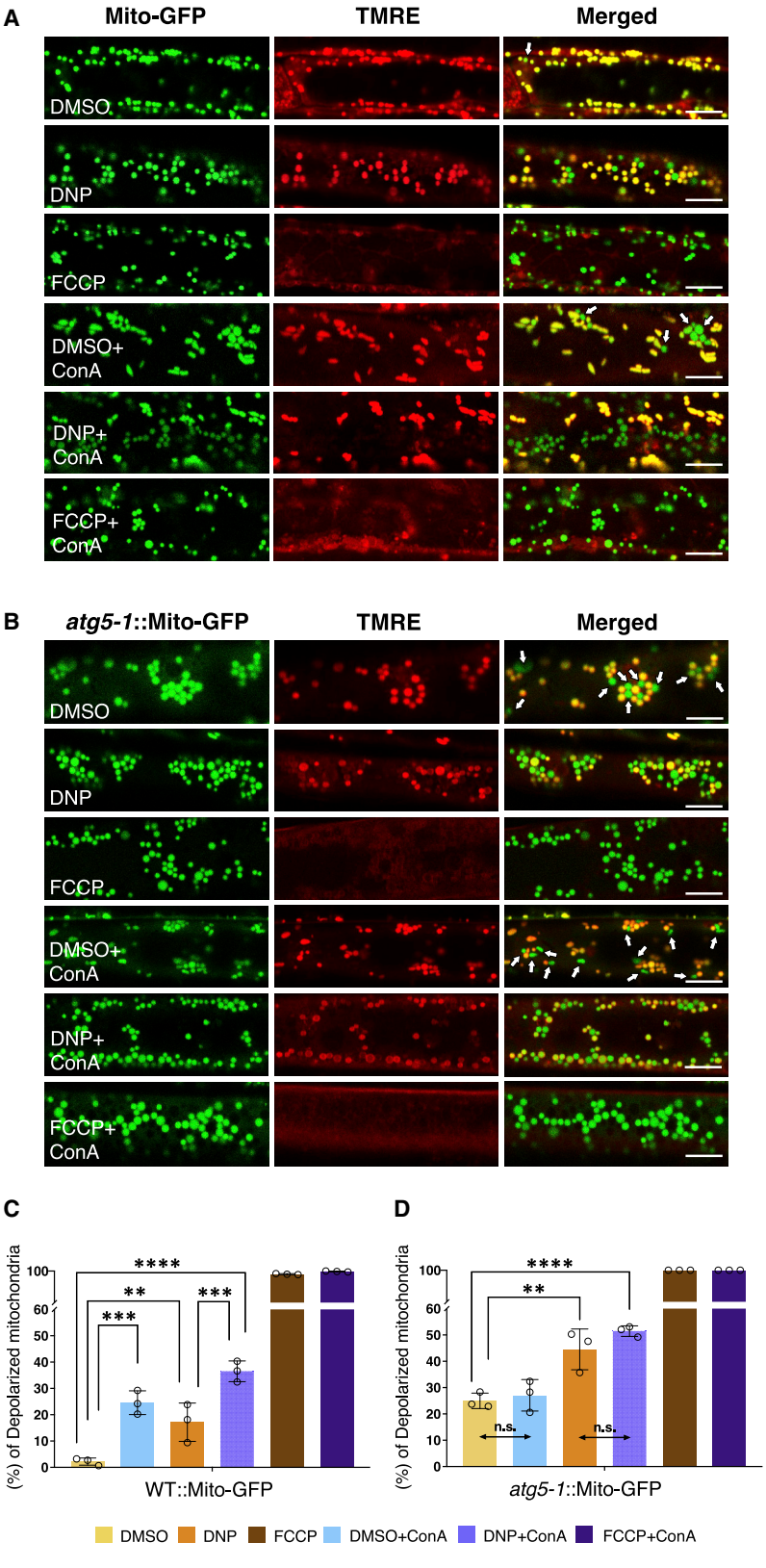

Figure 1. Accumulation of depolarized mitochondria in *Arabidopsis* after uncoupler treatments

(A and B) Uncoupler-treatment-induced mitochondria depolarization. Confocal micrographs of wild-type (A) and *atg5-1* (B) root cells expressing a mitochondrion-targeted GFP (mito-GFP) after incubation with DMSO (control), DNP (50 μM), FCCP (10 μM), ConA (0.5 μM), DNP + ConA, or FCCP + ConA for 1 h. Mitochondria were pre-stained with TMRE. Normal mitochondria exhibit yellow fluorescence, although depolarized mitochondria exhibit green fluorescence (arrows) in DMSO or DMSO + ConA panels in the merged image columns. Note that most mitochondria are round. Scale bars, 8 μm.

(C and D) Bar charts illustrating percentages of depolarized mitochondria in wild-type (WT) and *atg5-1* root cells expressing mito-GFP at each treatment condition. Bars represent the mean (±SD) of three biological replicates, each generated from three technical replicates. About 500 mitochondria from 10 cells (five root samples) were counted per condition. Asterisks (*) denote significant differences from the DMSO control (one-way ANOVA; **$p < 0.01$; ***$p < 0.001$; ****$p < 0.0001$; n.s., no significant difference).

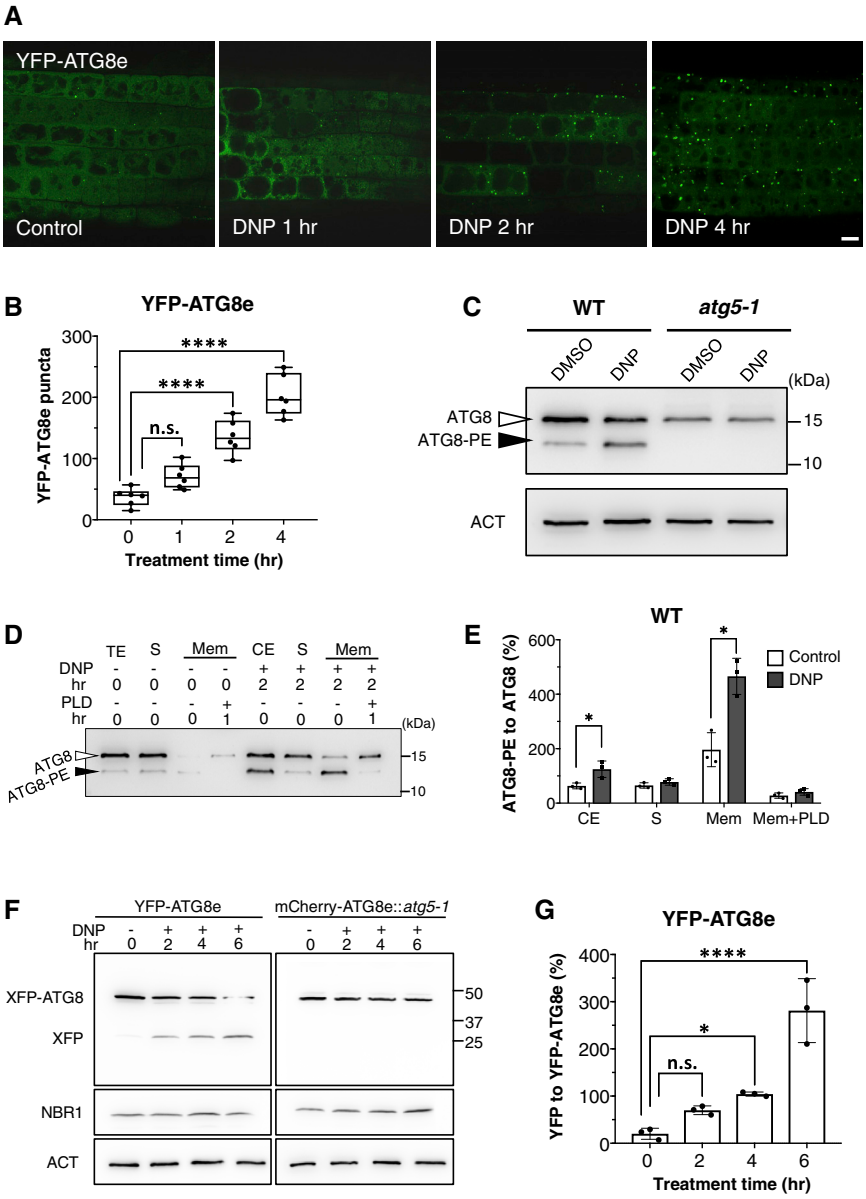

Figure 2. Uncoupler-induced autophagy in *Arabidopsis*

(A) Autophagosome formation is induced upon DNP treatment. *Arabidopsis* YFP-ATG8e seedlings were incubated in DNP solution (0–4 h) before imaging. Scale bars, 8 μm.

(B) Numbers of YFP-ATG8e puncta after incubating with DNP (50 μM). Confocal micrographs of 50 root cortex cells from five roots were examined for counting puncta at each time point (one-way ANOVA; ****$p < 0.0001$).

(C and D) DNP-induced ATG8 lipidation. Total protein extracts were prepared from *Arabidopsis* root cells following incubation in DNP for 2 h and examined by immunoblot analysis with an anti-ATG8 antibody. White arrowheads mark ATG8. An additional polypeptide became enriched in the membrane fraction when WT cells were incubated with DNP (black arrowhead), but not in *atg5-1* cells. For phospholipase D (PLD) digestion (D), total protein extract (TE), soluble (S), and membrane (mem) fractions were separated. The additional polypeptide (black arrowhead) became enriched in the membrane fraction from DNP-incubated samples, which was reduced after PLD treatment.

(E) Bar chart showing polypeptide intensity ratios of lipidated ATG8 to free ATG8 in (D). Bars represent the mean (±SD) of three biological replicates (unpaired t test; *$p < 0.05$).

(F) ATG8 cleavage assays of DNP-treated WT and *atg5-1* seedlings expressing YFP-ATG8e or mCherry-ATG8e, respectively. Protein extracts were prepared from *Arabidopsis* seedlings exposed to DNP (50 μM) and subjected to immunoblot analysis with anti-GFP or anti-mCherry antibody. Note that NBR1 amounts did not change. Actin (ACT) was used as loading control.

(G) Bar chart illustrating polypeptide intensity ratios of free YFP to YFP-ATG8e in (F). Bars represent the mean (±SD) of three biological replicates (one-way ANOVA; *$p < 0.05$; ****$p < 0.0001$).

Damaged mitochondria are selectively engulfed by autophagosomes in uncoupler-treated root cells

We then examined whether DNP-induced autophagosomes were indeed engulfing mitochondria by staining YFP-ATG8e root cells with MitoTracker Red (MTR). Unlike TMRE, which is quickly washed off from mitochondria upon depolarization, MTR is retained after depolarization, making it a better stain for monitoring mitophagy in live cells.[24] YFP-positive puncta were seen in the vicinity of mitochondria (Figure 3A). In higher magnification micrographs, we were able to identify ATG8e-specific fluorescent structures resembling open pouches that contain mitochondria (arrowheads, Figure 3B). We were also able to observe mitochondria that were entirely surrounded by YFP-ATG8e rings (white arrow, Figure 3B). In time-lapse, live-cell imaging analysis, YFP-ATG8e pockets partially enclosing a mitochondrion were seen to grow, eventually encapsulating the mitochondrion in a 300-s time frame (Figure 3C). These autophagic compartments (i.e., mitophagosomes) were approximately 1 to 2 μm in diameter, and each carried a single mitochondrion.

A time-lapse movie revealed that small YFP-ATG8e puncta arises near MTR-stained mitochondria and elongates to a semicircle, capturing a mitochondrion. This process took about 10 min (Video S1). Another video documented an incomplete mitophagosome that expanded to fully engulf a mitochondrion (Video S2). Elongating tips of phagophores stayed in contact with the mitochondrial surface throughout their growth (Figure S1). Based on these time-lapse, live-cell microscopy analyses, we estimate that it takes about 15 min for mature mitophagosomes to develop from an initial YFP-ATG8 puncta on a mitochondrion.

We then cryofixed root samples and performed transmission electron microscopy (TEM) analysis. Mitochondria in control

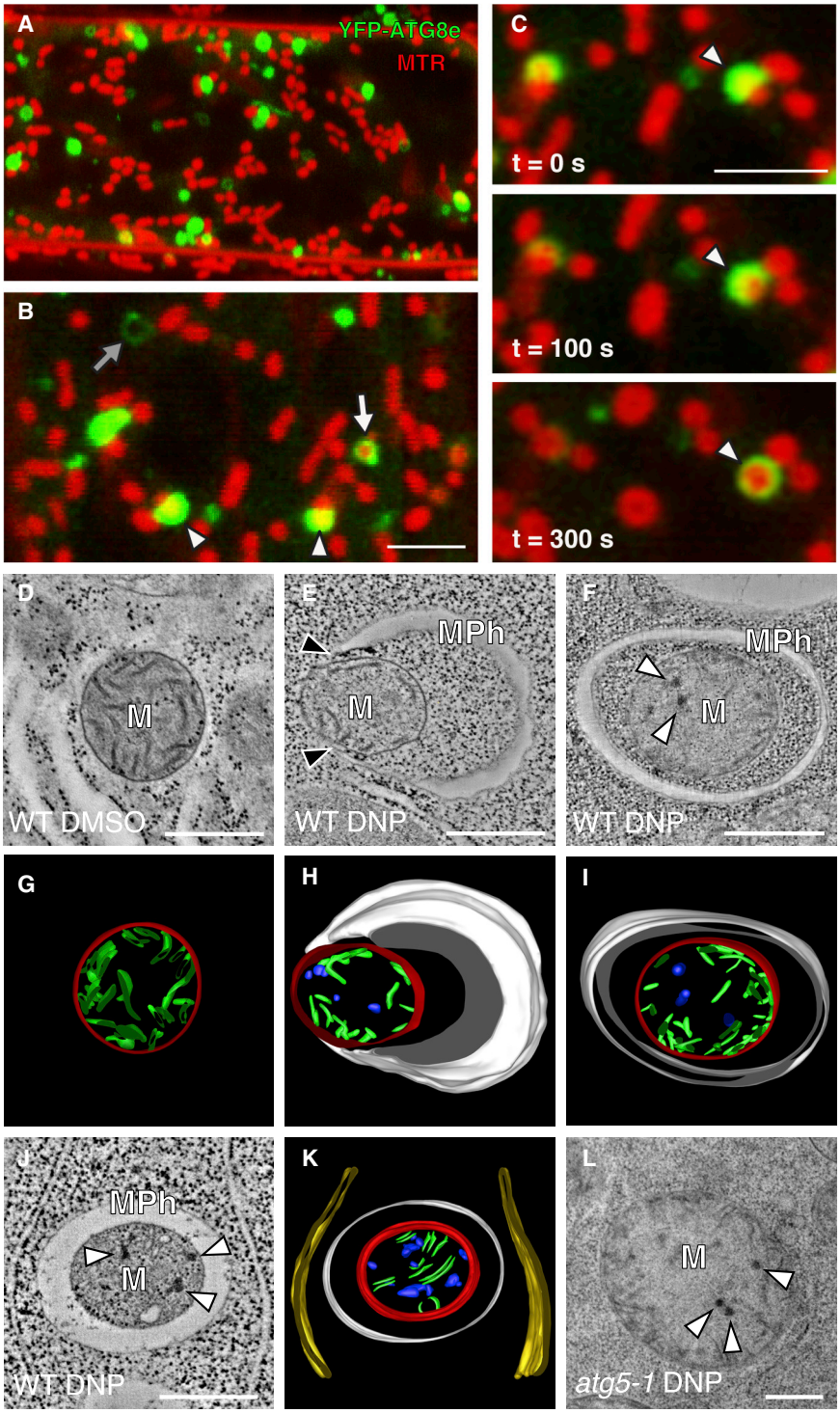

Figure 3. Selective engulfment of depolarized mitochondria by autophagosomes in *Arabidopsis* after uncoupler treatment

(A and B) Confocal micrographs of *Arabidopsis* root cells expressing YFP-ATG8e stained with MitoTracker Red (MTR) and incubated with DNP for 1 h. The mitochondria associated with YFP-ATG8e are indicated with arrowheads in (B). A mitochondrion completely enclosed in circular ATG8e fluorescence is marked with a white arrow. Empty YFP fluorescence circles were also observed (gray arrow in B). Scale bars, 5 μm.

(C) Time-lapse imaging of a mitophagy event in an *Arabidopsis* root cell. YFP-ATG8e encircled a mitochondrion (arrowhead) over 5 min. Scale bar, 5 μm.

(D–F and J) Electron tomograms of mitochondria (M) in *Arabidopsis* WT root cells incubated with DMSO or DNP. Mitophagosomes (MPh) are assembled in the vicinity of the mitochondria. Note that the phagophore tips (black arrowheads) are in contact with the mitochondrial surface in (E).

(G–I and K). Three-dimensional models of the mitophagosome (MPh) and its cargo (M) based on tomograms in (D)–(F) and (J). Mitophagosome (white), mitochondria outer membrane (red), cristae (green), aggregates in the matrix (blue), and ER (yellow) were rendered into 3D surfaces.

(L) TEM micrograph of abnormal mitochondria in an *atg5-1* mutant root cell. Mitophagosomes were not found in the mutant cells. Scale bars, 500 nm. See also Figure S1 and Videos S1 and S2.

samples had smooth cristae that are evenly dispersed in the matrix (Figures 3D and 3G). By contrast, mitochondria in DNP-treated cells had electron-dense precipitates in their matrix, some of which were engulfed by double-membraned mitophagosomes (Figures 3E–3K). Serial section TEM of mitophagosomes showed that one mitochondrion was contained per autophagosome, and no other organelles were identified in autophagosomes (Figures S1B and S1C), in agreement with our live-cell imaging results (Figures 3B and 3C). Electron tomography analysis revealed that, in contrast to free mitochondria, mitochondria sequestered in mitophagosomes have dark precipitates in the matrix and fewer cristae (Figures 3G–3K). *Arabidopsis atg5-1* root cells had many mitochondria exhibiting the signs of internal degradation (i.e., dark aggregates and collapsed cristae), but they were not associated with mitophagosomes (Figure 3L). Altogether, these results show that plant cells selectively recycle damaged mitochondria via autophagy that involves ATG5.

To further investigate mitochondria elimination during uncoupler-induced mitophagy, we carried out immunoblot assays to assess the levels of mitochondrial proteins in *Arabidopsis* WT and *atg5-1* mutant lines. Levels of outer mitochondrial membrane (OMM) proteins, peripheral-type benzodiazepine receptor (PBR), and voltage-dependent anion channel 1 (VDAC1); inner mitochondria membrane (IMM) proteins, cytochrome oxidase subunit II (COXII), and L-galactono-1,4-lactone dehydrogenase (GLDH); and mitochondria

matrix (MM) protein isocitrate dehydrogenase (IDH) were all reduced upon uncoupler treatment, and the extent of reduction increased in later time points (Figure 4A; 1–4 h). The protein decay was dependent on vacuolar transport, as the addition of ConA prevented the degradation (Figure 4C). Furthermore, mitochondrial protein levels did not change significantly in DNP-treated *atg5-1* mutant samples, indicating that ATG5 is required for protein degradation (Figures 4C–4E).

Interestingly, OMM proteins exhibited faster decay rates in comparison with IMM and matrix proteins. Because OMMs could also be recycled by the proteasome,[25] we assayed OMM protein amounts after inhibiting proteasome activity with MG132. Supplementing the inhibitor indeed stabilized OMM proteins, but not IMM or matrix proteins (Figures 4D and 4E). Consistently, when we isolated mitochondria-enriched fractions from DNP-treated *Arabidopsis* root samples by sucrose gradients, the amount of ubiquitinated proteins was further increased by MG132 treatment (Figure S2A). These experiments suggest that proteasome and autophagy cooperate to degrade OMM proteins, as was observed by Tanaka et al.,[26] whereas IMM and matrix proteins are primarily degraded by autophagy upon the loss of membrane potential. We also observed a reduction in mitochondrial protein amounts after inducing bulk autophagy by growing *Arabidopsis* seedlings in nitrogen starvation media. However, nitrogen-starvation-induced mitochondrial protein recycling was milder, indicating starvation induces basal mitophagy (Figure S2B). Altogether, these experiments suggest uncoupler treatments induce a rapid mitophagy process that is dependent on ATG5. Uncoupler treatments also induce ubiquitination of the outer mitochondrial membrane, where both autophagy and proteasome work together to recycle ubiquitinated proteins (Figure 4E).

Friendly is essential for uncoupler-induced mitophagy

Studies in metazoan cells have indicated that the mitochondrial network is fragmented prior to mitophagy.[27,28] In *Arabidopsis*, FMT, a clustered mitochondria (CLU) family protein, was shown to play essential roles in mitochondrial dynamics.[29] We tested whether FMT is implicated in mitophagy using our uncoupler-treatment-induced mitophagy setup. Root cells expressing FMT-YFP exhibited diffuse cytosolic fluorescence. Upon DNP treatment, FMT-YFP formed puncta that colocalized with mitochondria (Figure 5A). Strikingly, when we localized FMT-YFP and ATG8 with immunofluorescence microscopy, colocalization of FMT with ATG8 significantly increased upon DNP treatment, in contrast to control treatments (Figure 5B). Pull-down experiments further showed that uncoupler treatment led to a specific association of FMT-YFP with ATG8, suggesting that FMT-YFP is recruited to mitophagosomes (Figure 5C). In WT root cells expressing mCherry-ATG8e and mitochondria-targeted GFP, ATG8e-labeled vesicles engulfed mitochondria upon uncoupler treatment (Figure 5D, upper row). In *fmt* mutant, ATG8 puncta assembled on the mitochondrial surface. However, these puncta failed to engulf the mitochondria, forming incomplete mitophagosomes (Figure 5D, lower row). TEM imaging of the *fmt* mutant provided further evidence for stunted mitophagosomes with disconnected edges (Figure 5D, arrowheads). Quantification of mitophagosomes in WT and *fmt* mutant cells showed that, in contrast to the WT cells, *fmt* mutants had less mitophagosomes, most of which failed to develop into mature mitophagosomes (Figure 5E). Altogether, these experiments show that FMT is essential for depolarization-induced mitophagosome formation in *Arabidopsis* root cells.

We then set out to investigate mitophagy defects in *fmt* mutants using TMRE staining and immunoblot-based autophagic flux assays. Clusters of mitochondria is a distinctive feature of *fmt* root cells (Figure 6A). Depolarized mitochondria were more abundant in *fmt* than WT cells (Figures 6A–6C). Swollen mitochondria displaying indications of mitochondrial damage, such as dark aggregates and loss of cristae, were readily discerned in TEM micrographs of the mutant cells (Figures S3A and S3B). Such abnormal mitochondria were also enriched in *atg5-1* mutant cells (Figure 1). Immunoblot analyses using mitochondrial compartment-specific antibodies indicated that mitochondrial protein degradation was delayed in *fmt* mutant (Figures 6D and S3C). Even after 6 h of DNP stress, *fmt* mutants displayed a significant defect in mitochondrial protein elimination (Figure 6E), showing that FMT is required for mitophagy-mediated protein recycling in *Arabidopsis*.

Cotyledon greening during de-etiolation is affected in *atg5-1* mutant seedlings

The etioplast is a type of plastid that develops in seedlings germinated under darkness. Upon light exposure, seedlings undergo de-etiolation, which involves transformation of etioplasts into chloroplasts.[30] Because mitochondrial and chloroplast functions are interlinked,[31] we hypothesized that the mitochondrial population might be adjusted during de-etiolation. First, we monitored the greening of cotyledons when dark-grown seedlings were illuminated with light. Chlorophyll contents increased gradually over a 12-h period, with a significant rise 6 h after illumination (Figures 7A and 7B). When we measured amounts of mitochondrial proteins in cotyledon samples, levels of the proteins dropped in the 6- to 8-h period after illumination, but they recovered in the later time point (Figures 7C and S4B). The swing in the mitochondrial protein concentrations suggests a period of accelerated mitochondria recycling at around 8 h. To verify this observation and see whether de-etiolation-induced mitochondria recycling is linked to mitochondrial membrane depolarization, we examined cotyledon cells with TMRE staining. We observed a significant increase in the number of depolarized mitochondria at 6–8 h after light illumination (Figures 7D and S4A). In agreement with our western blot and TMRE staining assays, we frequently observed mitophagosomes in transmission electron micrographs of cotyledon cells that were fixed 6–8 h after illumination (Figures 7E, 7F, S4B, and S4C).

In *atg5-1* or *fmt* mutant seedlings, cotyledon greening was significantly delayed (Figures 7A and 7B). Furthermore, western blot-based flux assays with compartment-specific antibodies revealed lack of mitochondrial protein level fluctuations in both *atg5-1* and *fmt* mutant cells (Figure 7C). Finally, TEM micrographs obtained from cotyledons of 6–8 h illuminated *atg5-1* and *fmt* mutant cells showed accumulation of compromised mitochondria (indicated with arrows pointing to dark aggregates), without any discernable mitophagosome formation (Figures 7E, 7F, S4C, and S4D). In sum, these results indicate de-etiolation leads to loss of mitochondrial membrane potential and triggers ATG5- and FMT-dependent mitophagy in *Arabidopsis*.

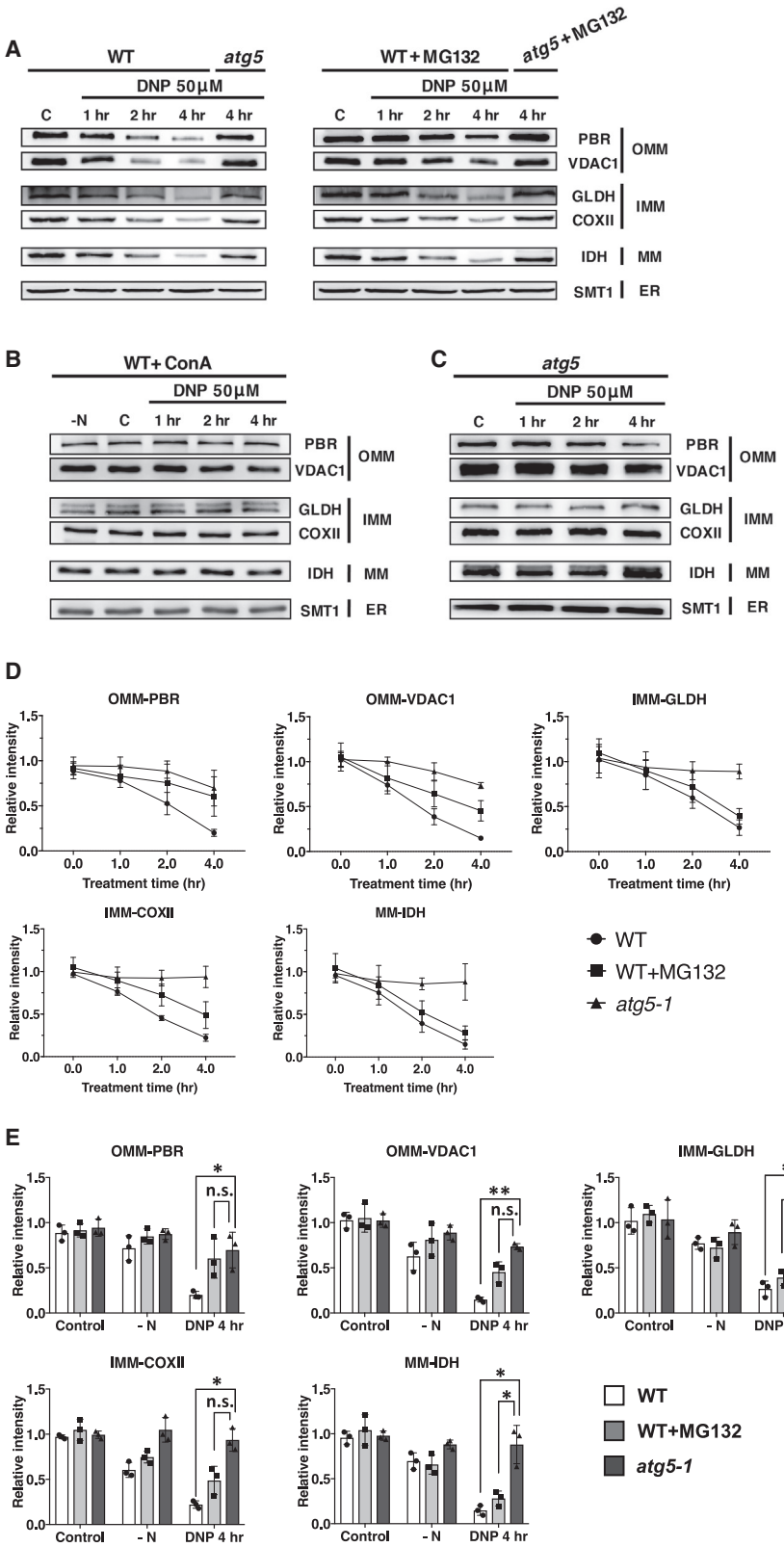

Figure 4. ATG5-dependent degradation of mitochondrial proteins in uncoupler-treated *Arabidopsis* root cells

(A–C) Immunoblot analyses of uncoupler-induced mitochondrial protein degradation in *Arabidopsis* WT and *atg5-1* seedlings. WT and *atg5-1* mutant *Arabidopsis* roots were incubated in DNP solution for 1–4 h or nitrogen starvation (−N) solutions for 1 day before analysis. For outer mitochondrial membrane (OMM) proteins, PBR and VDAC1; for inner mitochondrial membrane (IMM), COXII and GLDH; and mitochondrial matrix IDH were examined. Concanamycin A (ConA) was added to the treatment in (B). Proteasome inhibitor MG132 was added in (A). An ER membrane protein, SMT1, was used as a loading control.

(D) Line charts illustrating degradation rates of OMM, IMM, and MM protein in WT treated with DNP (WT), *atg5-1* treated with DNP (*atg5-1*), and WT treated with DNP and MG132 (WT + MG132).

(E) Bar charts showing amounts of mitochondria membrane proteins after the three treatments, namely, DMSO 4 h (control), DNP 4 h, and nitrogen starvation (−N). Protein extracts from WT, WT + MG132, and *atg5-1* were examined. The polypeptide intensity values were normalized to that of an endoplasmic reticulum (ER) protein, SMT1. Bars represent the mean (±SD), and asterisks (*) indicate significant decreases from that of the control (DMSO 4 h, C; two-way ANOVA; *$p < 0.05$; **$p < 0.01$).

See also Figure S2.

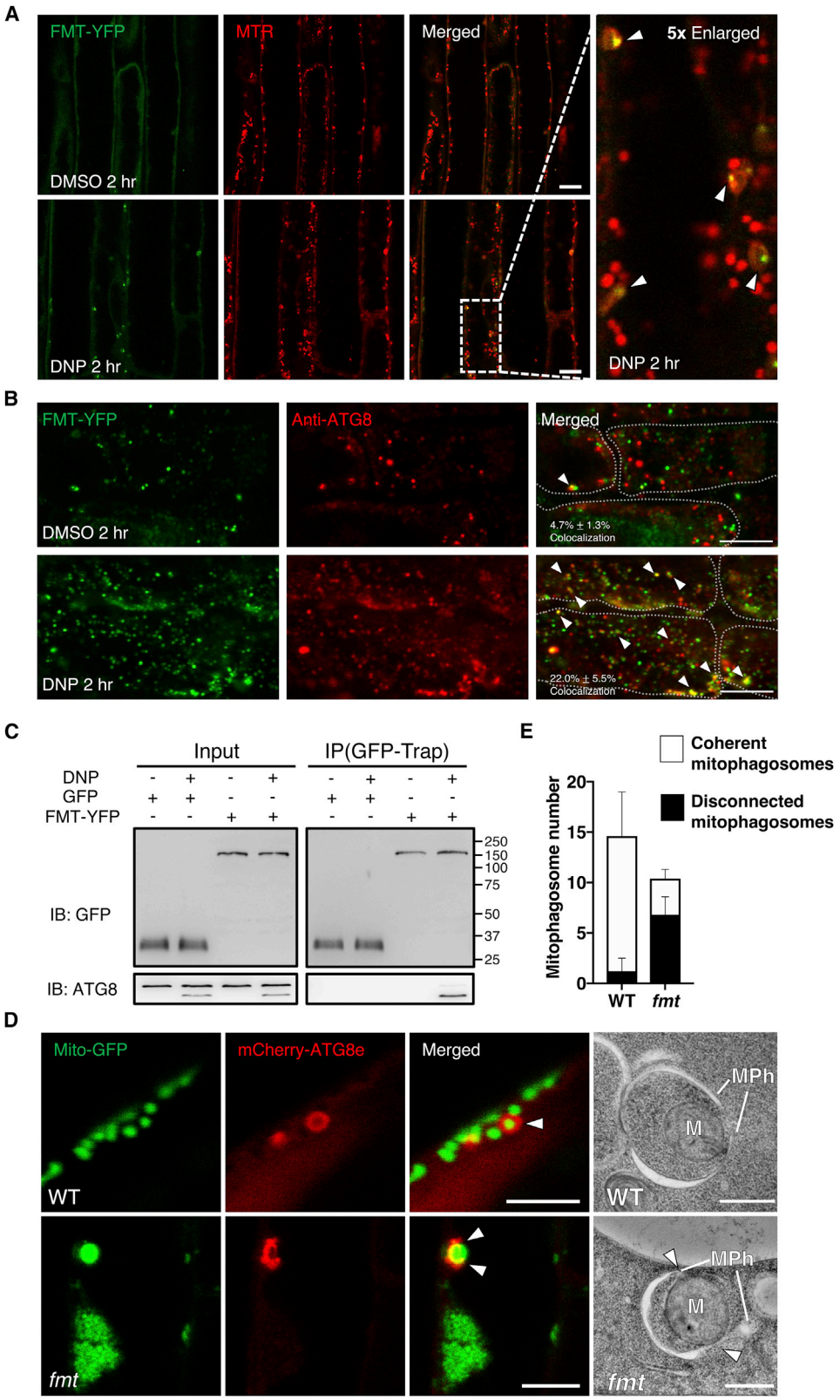

Figure 5. Association of Friendly with damaged mitochondria and ATG8 upon uncoupler treatment

(A) DNP treatment led to the recruitment of Friendly (FMT) to mitochondria. Confocal micrographs of *Arabidopsis* root cells expressing a YFP-tagged FMT (FMT-YFP) pre-stained with MTR are shown. FMT-YFP seedlings were incubated with DMSO or DNP for 2 h before imaging. Scale bars, 8 μm.

(legend continued on next page)

DISCUSSION

Research in the last decade has transformed autophagy from a bulk degradation system to a highly selective cellular quality control pathway that rapidly removes toxic or superfluous macromolecules.[32,33] Especially organelles that get damaged due to metabolic and physiological stress conditions are mainly recycled via distinct selective autophagy pathways.[6] Consistently, in all the eukaryotes tested so far, autophagy is essential for adapting to environmental changes.[12,34] Despite the significant advances made in the metazoan selective autophagy field, how plants recycle their organelles is still mostly unknown. Although the core autophagy machinery that mediates the autophagosome formation is highly conserved in plants, selective autophagy receptors and adaptors responsible for recognizing and recruiting damaged organelles to the autophagosomes are not well conserved.[12] For example, up to eight different receptor proteins and dozens of accessory proteins have been shown to mediate various mitophagy pathways in mammalian cells.[3] Homologs of most of those proteins are absent in plant genomes, implying plant mitophagy have followed a different evolutionary path, likely due to the presence of another endosymbiont in the cell.

Here, we have established a detailed toolbox to study mitophagy in plants. We have shown that protonophore uncouplers specifically induce mitophagy, similar to metazoans. Our findings also revealed high levels of mitophagy during de-etiolation, a fundamental developmental step that allows plants to harness daylight following germination. Our studies also revealed a molecular player, the FMT protein, that is essential for mitophagy.

Recycling of compromised mitochondria in plant cells

We were able to discern signs of damages in mitochondria after incubation with uncouplers (Figure 3). They had dark aggregates and shriveled cristae in the matrix, and these mitochondria were selectively captured by mitophagosomes. Impaired mitochondria were rare in DMSO control samples but frequently observed in TEM images of *atg5-1* and *fmt* mutants (Figures 7 and S3). These results indicated that the aberrant mitochondria correspond to depolarized mitochondria. Sperm mitochondria in cryofixed *C. elegans* oocytes also exhibited similar ultrastructural features, and they lose membrane potential upon fertilization.[21,35] However, we did not observe large ruptures in mitochondrial membranes reported in TEM analysis of mammalian mitophagy, where cells were preserved by chemical fixation.[36]

An intriguing feature that we noticed in our TEM analysis is that tips of the elongating phagophores were in contact with the mitochondrial surface (Figure 3E, arrowheads). This observation is consistent with the YFP-ATG8e fluorescence that expanded tightly over mitochondria in the time-lapse recordings (Figure 3C; Video S2). The affinity between the autophagosome membrane and mitochondria explains why mitophagosomes usually have one damaged mitochondrion, ensuring selective recycling. It also suggests highly specific protein interaction networks that involve mitophagosomes and mitochondrial surface proteins drive mitophagy.

In mammalian cells in which mitochondria undergo cycles of fusion and fission, it takes longer than 12 h of incubation with uncoupler compounds for inducing mitophagy. Mitochondria in *Arabidopsis* root cells are mostly round, indicating that mitochondria fission dominates over fusion,[37] and the differential mitochondrial organization could explain the rapid onset of mitophagy in our plant root cell system. The mitochondrial dynamics in mammalian cells collaborates for maintaining a healthy mitochondrial pool; fusion can rescue damaged mitochondria via diluting their injuries although fission singles out aberrant mitochondria for mitophagy.[38] Fission also keeps the mitophagy activity from spreading to uninjured regions of the mitochondria network.[39] By contrast, individual mitochondria in the root cell have to deal with the depolarization stress by themselves. Some plant cells, including seed cells after germination or shoot apical meristem cells, have elongated mitochondria constituting a network.[40,41] These cells are better for testing whether mitochondria fragment in response to uncoupler stresses and studying the roles of mitochondrial fission in plant mitophagy.

FMT is essential for mitophagy in plants

FMT is required for normal mitochondria distribution in the plant cell, possibly regulating the interaction between individual mitochondria before fusion.[29] We have shown that DNP-induced mitochondria recycling is affected in fmt mutant cells, and FMT associates with ATG8 after mitochondrial damage (Figure 5). These results suggest that FMT contributes to autophagosome assembly during mitophagy. Because FMT is a protein shuttling between the cytosol and mitochondria, it is tempting to speculate that FMT may engage in an autophagy receptor/adaptor complex through which the core autophagy machinery is recruited to mitochondria. Both *fmt* and *atg5-1* mutants exhibited increased depolarized mitochondria and inhibition of mitochondrial protein degradation after DNP treatment (Figures 1 and 6). However, inactivation of *ATG5* had stronger impacts on the elimination of damaged mitochondria than *FMT* mutation and

(B) FMT-YFP puncta colocalize with autophagosome marker ATG8 after DNP treatment. FMT-YFP seedlings were incubated with DMSO or DNP for 2 h and processed for immunofluorescence microscopy localization with an anti-GFP and an anti-ATG8 antibody. The percentages of FMT-YFP puncta overlapping with ATG8 puncta are indicated in the merged panels. Overlapping puncta were counted from five root samples. Cells were outlined with white dashed lines. Scale bars, 5 μm.

(C) FMT associates with ATG8 upon DNP treatment. *Arabidopsis* root cells expressing FMT-YFP were incubated with DMSO or DNP for 2 h, subjected to immunoprecipitation using GFP-trap, and analyzed with immunoblotting (IB).

(D) Confocal micrographs of *Arabidopsis* WT and *fmt* root cells expressing a mito-GFP and mCherry-targeted ATG8e (mCherry-ATG8e). WT or *fmt* plants seedlings were incubated with DNP for 1 h before imaging. Scale bars, 8 μm. TEM photos show mitochondrial phagophores (MPh) around mitochondria (M) under the condition in (A). Arrowheads point to defective phagophores in the *fmt* mutant cell in both confocal and TEM micrographs. An aggregate in the matrix is marked with an arrow. Scale bars, 500 nm.

(E) Ratio of coherent and disconnected mitophagosomes observed in confocal micrographs of WT and *fmt* root cells. Bars represent the mean (±SD) of three biological replicates from more than ten individual WT or *fmt* root samples after 1 h DNP treatment.

See also Figure S3.

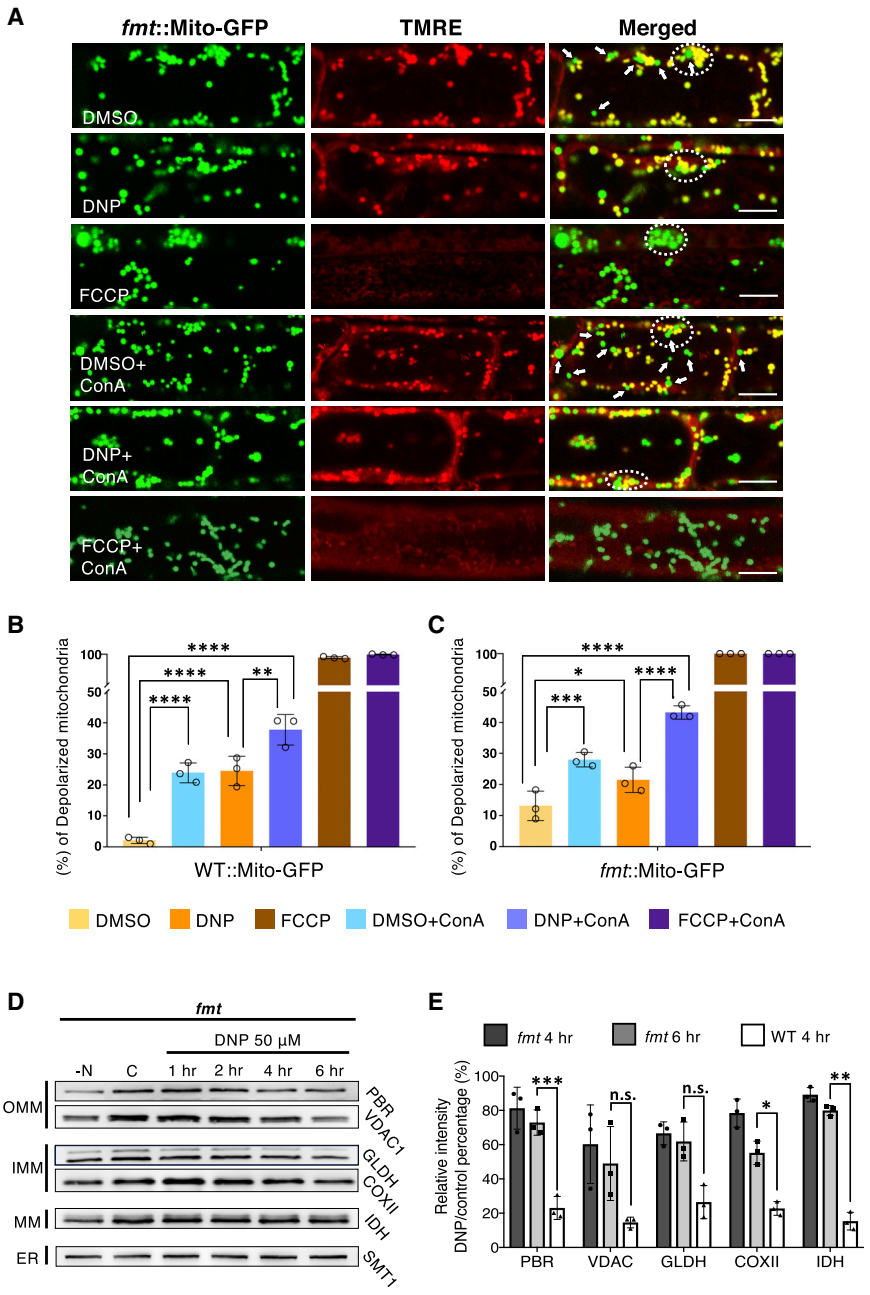

Figure 6. Defective elimination of depolarized mitochondria in the *Arabidopsis friendly* mutant

(A) Confocal micrographs of *fmt* root cells expressing a mito-GFP. *fmt* mutant roots were pre-stained with TMRE and incubated under conditions specified in each row for 1 h before imaging. Several normal mitochondria emitting yellow fluorescence and depolarized mitochondria emitting green fluorescence are denoted with arrows in the merged image column. Mitochondria clusters distinctive of *fmt* mutant cells are enclosed in dashed ovals. Scale bars, 8 μm.

(B and C) Bar charts illustrating percentages of depolarized mitochondria in WT and *fmt* (A) root cells expressing mito-GFP for each treatment condition. Bars represent the mean (±SD) of three biological replicates. About 500 mitochondria from 10 cells (five root samples) were counted per condition for *fmt*, and about 100 mitochondria were counted per condition for WT. DNP and ConA led to increased numbers of depolarized mitochondria in the *fmt* mutant root cells (one-way ANOVA; *p < 0.05; **p < 0.01; ***p < 0.001; ****p < 0.0001).

(D) Mitochondrial protein degradation in *fmt* mutant. *Arabidopsis fmt* mutant roots were incubated in DMSO (C), DNP solutions for 1–6 h, or nitrogen starvation (−N) solutions for 1 day. Mitochondrial proteins explained in Figure 4 were analyzed.

(E) Inhibition of mitochondrial protein degradation in *fmt* root cells. Polypeptide intensity values in immunoblots were normalized with that of the SMT1 protein. The graph illustrates the percentage ratios of normalized intensity of the DNP-treated samples to the DMSO control sample. Results from *fmt* samples after 4 h and 6 h treatment and WT after 4 h treatment are shown. Bars represent the mean (±SD; two-way ANOVA; *p < 0.05; **p < 0.01; ***p < 0.001).

See also Figure S3.

blocking the vacuolar transport amplified the DNP effect in *fmt* mutant (Figure 6B), but not in *atg5-1* (n.s. in Figure 1D), suggesting there are other mitophagy pathways in addition to FMT-mediated mitophagy.

FMT is a highly conserved protein with orthologs in evolutionarily distant eukaryotes, including yeast and metazoans.[42] The *Arabidopsis fmt* mutant exhibits comparable phenotypes, including clustered mitochondria next to the nucleus. The *Drosophila* FMT homolog Clueless positively regulates PINK1/Parkin-dependent mitophagy by suppressing mitochondrial fusion.[43] Recent studies have shown that mammalian FMT homolog CLUH could bind RNA to form granules. The CLUH granules are involved in mitophagy and metabolic reprogramming via playing roles in the translation of particular mRNAs.[44,45] Plants lack PINK1/Parkin homologs. It needs to be investigated whether FMT mediates mitophagy by forming stress-activated granules or via a PINK/Parkin-like pathway. Identification of proteins or RNA interacting with FMT during uncoupler treatments could help us understand the role of FMT in mitochondrial quality control.

Mitochondrial recycling and chloroplast biogenesis during de-etiolation

Reprograming the mitochondrial functions in response to nutrient availability is critical for cell survival.[46] In plant cells, photosynthesis in chloroplasts and respiration in mitochondria are coordinated for homeostasis of cellular energy levels and redox status.[47] Our results from greening *Arabidopsis* cotyledons indicated that de-etiolation involves a wave of mitochondrial turnover (Figure 7), probably for rewiring the mitochondrial

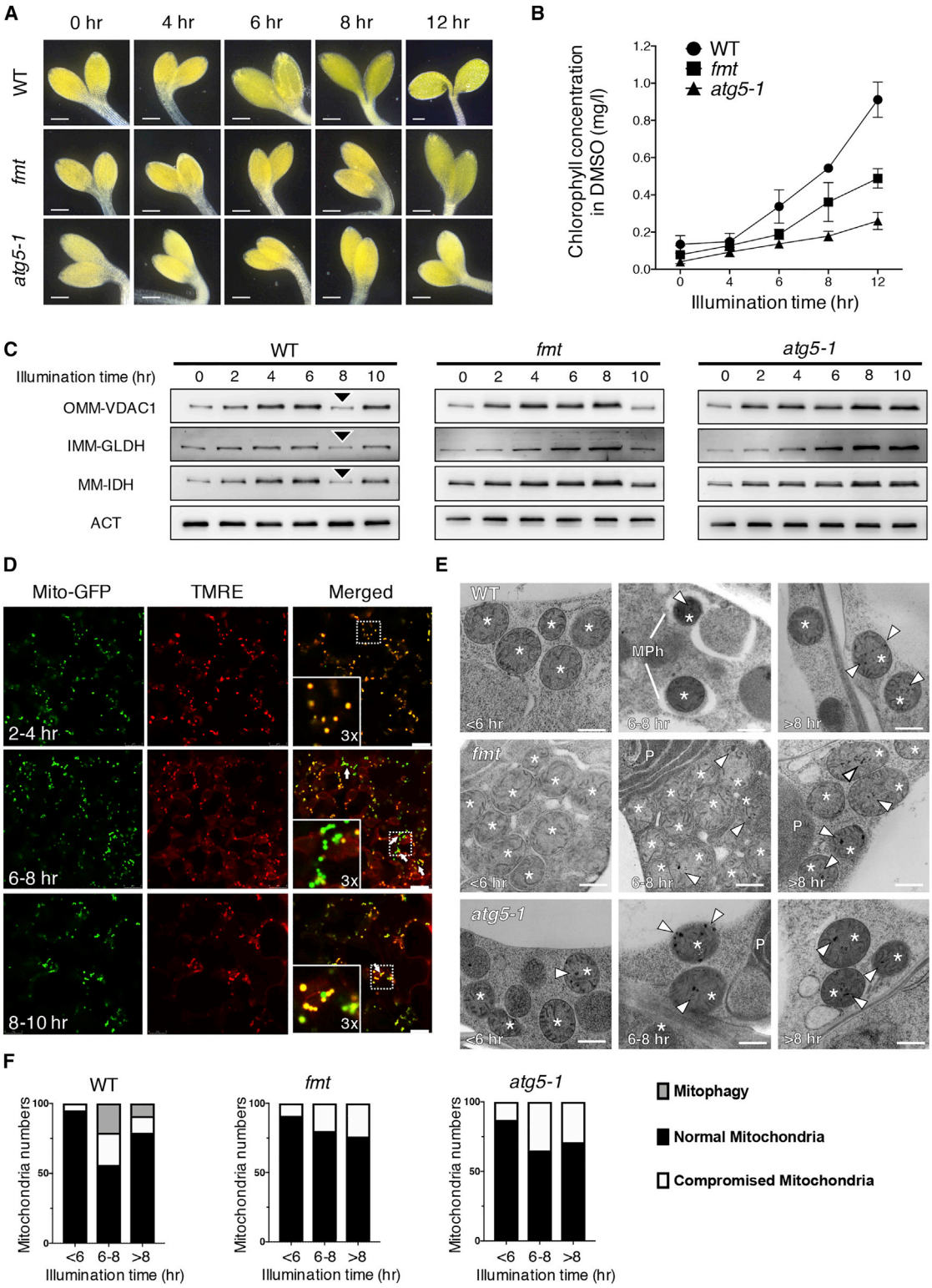

Figure 7. Mitophagy in *Arabidopsis* cotyledon cells during de-etiolation

(A) Cotyledon greening after light exposure in WT, *fmt*, and *atg5-1* seedlings. Darkfield stereo microscopy photos showing WT, *fmt*, and *atg5-1* mutant cotyledons at five time points (0–12 h) after illumination. *Arabidopsis* seedlings were grown for 7 days under darkness before the experiment. Scale bars, 1 mm.

(B) Increase in chlorophyll concentrations after light exposure. The chlorophyll samples from the three genotypes were extracted, and their OD values were measured under 645 nm and 663 nm.

(legend continued on next page)

metabolic network to adapt to photomorphogenesis and salvaging raw materials for chloroplast biogenesis.

In skotomorphogenic seedlings, nutrients reserved in the seed are mobilized to sustain growth and mitochondria are required for the anabolic processes. When light is available, the seedlings become photosynthetically active and capable of autotrophic growth.[48] It was shown that the electron transport chain in mitochondria is decelerated in de-etiolating wheat leaves and chloroplasts and mitochondria are functionally more intertwined.[49] Accumulation of depolarized mitochondria, assembly of mitophagosomes, and rapid changes in mitochondrial protein levels in the greening cotyledon suggest cannibalization of extant mitochondria. We speculate that the developmentally programmed mitophagy could facilitate modulation of the mitochondrial pool and biosynthesis of macromolecules for constructing new organelles. The lack of mitophagosomes and the delay in greening of the *atg5-1* and *fmt* mutant cotyledon agrees with the notion. Altogether, our findings present an example of inter-organelle communication and how mitochondria-chloroplast crosstalk could underlie a major developmental transition in plants.

STAR★METHODS

Detailed methods are provided in the online version of this paper and include the following:

- KEY RESOURCES TABLE
- RESOURCE AVAILABILITY
  - Lead contact
  - Materials availability
  - Data and code availability
- EXPERIMENTAL MODEL AND SUBJECT DETAILS
  - Plant materials
  - Plant growth conditions
- METHOD DETAILS
  - Protein extraction and immunoblot analysis
  - ATG8 de-lipidation assay
  - Immunoprecipitation
  - Confocal microscopy and image processing
  - Immunofluorescence labeling
  - Chlorophyll extraction and measurement
  - TEM analysis, electron tomography, and 3d modeling
- QUANTIFICATION AND STATISTICAL ANALYSIS

SUPPLEMENTAL INFORMATION

Supplemental information can be found online at https://doi.org/10.1016/j.cub.2021.02.034.

ACKNOWLEDGMENTS

We appreciate Dr. Xiaohong Zhuang (Chinese University of Hong Kong) for the *atg5* and *atg7* mutant lines and David Logan and David Macharel for kindly sharing mito-GFP and Friendly-related seeds. We also thank Samantha Krasnodebski for help with the generation of *Arabidopsis* lines. This work was supported by grants from the Research Grants Council of Hong Kong (GRF14126116, GRF14121019, C4012-16E, C4002-17G, andAoE/ M-05/12), Cooperative Research Program for Agriculture Science & Technology Development (project no. 0109532019), and Rural Development Administration, Republic of Korea to B.-H.K. and Austrian Academy of Sciences and Austrian Science Fund (FWF): P32355 to Y.D.

AUTHOR CONTRIBUTIONS

J.M., Y.D., and B.-H.K. conceived and designed the experiments. J.M. performed the confocal microscopy and stereomicroscopy. J.M., Z.L., P.W., and K.K.M. carried out electron microscopy/tomography analysis. J.M. and J.A.F.A. prepared 3D tomographic models. J.M. and W.M. performed immunoblot and pull-down experiments. J.Z., Y.Z., and N.G. did other experiments. J.M., Z.L., J.Z., L.J., Y.D., and B.-H.K. analyzed the data. J.M., Y.D., and B.-H.K. wrote the paper.

DECLARATION OF INTERESTS

The authors declare no competing interests.

Received: August 22, 2020
Revised: November 18, 2020
Accepted: February 15, 2021
Published: March 11, 2021

REFERENCES

1. Youle, R.J. (2019). Mitochondria-striking a balance between host and endosymbiont. Science *365*, eaaw9855.
2. Broda, M., Millar, A.H., and Van Aken, O. (2018). Mitophagy: a mechanism for plant growth and survival. Trends Plant Sci. *23*, 434–450.
3. Pickles, S., Vigié, P., and Youle, R.J. (2018). Mitophagy and quality control mechanisms in mitochondrial maintenance. Curr. Biol. *28*, R170–R185.
4. Palikaras, K., Lionaki, E., and Tavernarakis, N. (2018). Mechanisms of mitophagy in cellular homeostasis, physiology and pathology. Nat. Cell Biol. *20*, 1013–1022.
5. Dikic, I. (2017). Proteasomal and autophagic degradation systems. Annu. Rev. Biochem. *86*, 193–224.
6. Anding, A.L., and Baehrecke, E.H. (2017). Cleaning house: selective autophagy of organelles. Dev. Cell *41*, 10–22.
7. Nguyen, T.N., Padman, B.S., and Lazarou, M. (2016). Deciphering the molecular signals of PINK1/Parkin mitophagy. Trends Cell Biol. *26*, 733–744.
8. Montava-Garriga, L., and Ganley, I.G. (2020). Outstanding questions in mitophagy: what we do and do not know. J. Mol. Biol. *432*, 206–230.
9. Georgakopoulos, N.D., Wells, G., and Campanella, M. (2017). The pharmacological regulation of cellular mitophagy. Nat. Chem. Biol. *13*, 136–146.

(C) Immunoblot analyses of mitochondrial proteins in WT, *fmt*, and *atg5-1* seedlings during de-etiolation. VDAC1, GLDH, IDH, and actin (ACT) were examined for an OMM, an IMM, a matrix (MM), and a loading control protein. Reduced mitochondrial proteins at 8-h samples from WT extracts are marked with asterisks in WT. No such changes were observed in the *atg5-1* and *fmt* mutant lines.
(D) Mitochondria depolarization in WT cotyledon cells. The insets in the merged image panels show enlarged views of the boxed area. Arrows indicate depolarized mitochondria in the cotyledon cells. Scale bars, 8 μm.
(E) TEM micrographs of mitochondria (asterisks) in WT, *fmt*, and *atg5-1* cotyledon cell after light illumination (<6 h, 6–8 h, and >8 h). Dense aggregates in WT, *fmt*, and *atg5-1* mitochondria are marked with arrowheads. P, plastid. Scale bars, 500 nm.
(F) Numbers of normal, compromised, and autophagosome-associated mitochondria in greening cotyledons (<6 h, 6–8 h, and >8 h). Mitochondria were counted from TEM micrographs of WT, *fmt*, and *atg5-1* cotyledon cells.
See also Figure S4.

10. Wauer, T., Simicek, M., Schubert, A., and Komander, D. (2015). Mechanism of phospho-ubiquitin-induced PARKIN activation. Nature *524*, 370–374.
11. Lazarou, M., Sliter, D.A., Kane, L.A., Sarraf, S.A., Wang, C., Burman, J.L., Sideris, D.P., Fogel, A.I., and Youle, R.J. (2015). The ubiquitin kinase PINK1 recruits autophagy receptors to induce mitophagy. Nature *524*, 309–314.
12. Stephani, M., and Dagdas, Y. (2020). Plant selective autophagy-still an uncharted territory with a lot of hidden gems. J. Mol. Biol. *432*, 63–79.
13. Li, F., Chung, T., and Vierstra, R.D. (2014). AUTOPHAGY-RELATED11 plays a critical role in general autophagy- and senescence-induced mitophagy in Arabidopsis. Plant Cell *26*, 788–807.
14. Klionsky, D.J., Abdelmohsen, K., Abe, A., Abedin, M.J., Abeliovich, H., Acevedo Arozena, A., Adachi, H., Adams, C.M., Adams, P.D., Adeli, K., et al. (2016). Guidelines for the use and interpretation of assays for monitoring autophagy (3rd edition). Autophagy *12*, 1–222.
15. Marshall, R.S., and Vierstra, R.D. (2018). Autophagy: the master of bulk and selective recycling. Annu. Rev. Plant Biol. *69*, 173–208.
16. Kellner, R., De la Concepcion, J.C., Maqbool, A., Kamoun, S., and Dagdas, Y.F. (2017). ATG8 expansion: a driver of selective autophagy diversification? Trends Plant Sci. *22*, 204–214.
17. Zess, E.K., Jensen, C., Cruz-Mireles, N., De la Concepcion, J.C., Sklenar, J., Stephani, M., Imre, R., Roitinger, E., Hughes, R., Belhaj, K., et al. (2019). N-terminal β-strand underpins biochemical specialization of an ATG8 isoform. PLoS Biol. *17*, e3000373.
18. Bao, Y., Song, W.M., Wang, P., Yu, X., Li, B., Jiang, C., Shiu, S.H., Zhang, H., and Bassham, D.C. (2020). COST1 regulates autophagy to control plant drought tolerance. Proc. Natl. Acad. Sci. USA *117*, 7482–7493.
19. Liu, F., Hu, W., Li, F., Marshall, R.S., Zarza, X., Munnik, T., and Vierstra, R.D. (2020). AUTOPHAGY-RELATED14 and its associated phosphatidylinositol 3-kinase complex promote autophagy in Arabidopsis. Plant Cell *32*, 3939–3960.
20. Ashrafi, G., and Schwarz, T.L. (2013). The pathways of mitophagy for quality control and clearance of mitochondria. Cell Death Differ. *20*, 31–42.
21. Zhou, Q., Li, H., Li, H., Nakagawa, A., Lin, J.L.J., Lee, E.S., Harry, B.L., Skeen-Gaar, R.R., Suehiro, Y., William, D., et al. (2016). Mitochondrial endonuclease G mediates breakdown of paternal mitochondria upon fertilization. Science *353*, 394–399.
22. Thompson, A.R., Doelling, J.H., Suttangkakul, A., and Vierstra, R.D. (2005). Autophagic nutrient recycling in Arabidopsis directed by the ATG8 and ATG12 conjugation pathways. Plant Physiol. *138*, 2097–2110.
23. Svenning, S., Lamark, T., Krause, K., and Johansen, T. (2011). Plant NBR1 is a selective autophagy substrate and a functional hybrid of the mammalian autophagic adapters NBR1 and p62/SQSTM1. Autophagy *7*, 993–1010.
24. Xiao, B., Deng, X., Zhou, W., and Tan, E.K. (2016). Flow cytometry-based assessment of mitophagy using MitoTracker. Front. Cell. Neurosci. *10*, 76.
25. Yoshii, S.R., Kishi, C., Ishihara, N., and Mizushima, N. (2011). Parkin mediates proteasome-dependent protein degradation and rupture of the outer mitochondrial membrane. J. Biol. Chem. *286*, 19630–19640.
26. Tanaka, A., Cleland, M.M., Xu, S., Narendra, D.P., Suen, D.F., Karbowski, M., and Youle, R.J. (2010). Proteasome and p97 mediate mitophagy and degradation of mitofusins induced by Parkin. J. Cell Biol. *191*, 1367–1380.
27. Lieber, T., Jeedigunta, S.P., Palozzi, J.M., Lehmann, R., and Hurd, T.R. (2019). Mitochondrial fragmentation drives selective removal of deleterious mtDNA in the germline. Nature *570*, 380–384.
28. Twig, G., and Shirihai, O.S. (2011). The interplay between mitochondrial dynamics and mitophagy. Antioxid. Redox Signal. *14*, 1939–1951.
29. El Zawily, A.M., Schwarzländer, M., Finkemeier, I., Johnston, I.G., Benamar, A., Cao, Y., Gissot, C., Meyer, A.J., Wilson, K., Datla, R., et al. (2014). FRIENDLY regulates mitochondrial distribution, fusion, and quality control in Arabidopsis. Plant Physiol. *166*, 808–828.
30. Mai, K.K.K., Gao, P., and Kang, B.H. (2020). Electron microscopy views of dimorphic chloroplasts in C4 plants. Front. Plant Sci. *11*, 1020.
31. Van Dingenen, J., Blomme, J., Gonzalez, N., and Inzé, D. (2016). Plants grow with a little help from their organelle friends. J. Exp. Bot. *67*, 6267–6281.
32. Mizushima, N. (2018). A brief history of autophagy from cell biology to physiology and disease. Nat. Cell Biol. *20*, 521–527.
33. Pohl, C., and Dikic, I. (2019). Cellular quality control by the ubiquitin-proteasome system and autophagy. Science *366*, 818–822.
34. Levine, B., and Kroemer, G. (2019). Biological functions of autophagy genes: a disease perspective. Cell *176*, 11–42.
35. Wang, Y., Zhang, Y., Chen, L., Liang, Q., Yin, X.-M., Miao, L., Kang, B.-H., and Xue, D. (2016). Kinetics and specificity of paternal mitochondrial elimination in Caenorhabditis elegans. Nat. Commun. *7*, 12569.
36. Wei, Y., Chiang, W.-C., Sumpter, R., Jr., Mishra, P., and Levine, B. (2017). Prohibitin 2 is an inner mitochondrial membrane mitophagy receptor. Cell *168*, 224–238.e10.
37. Arimura, S.I. (2018). Fission and fusion of plant mitochondria, and genome maintenance. Plant Physiol. *176*, 152–161.
38. Malka, F., Guillery, O., Cifuentes-Diaz, C., Guillou, E., Belenguer, P., Lombès, A., and Rojo, M. (2005). Separate fusion of outer and inner mitochondrial membranes. EMBO Rep. *6*, 853–859.
39. Burman, J.L., Pickles, S., Wang, C., Sekine, S., Vargas, J.N.S., Zhang, Z., Youle, A.M., Nezich, C.L., Wu, X., Hammer, J.A., and Youle, R.J. (2017). Mitochondrial fission facilitates the selective mitophagy of protein aggregates. J. Cell Biol. *216*, 3231–3247.
40. Sheahan, M.B., McCurdy, D.W., and Rose, R.J. (2005). Mitochondria as a connected population: ensuring continuity of the mitochondrial genome during plant cell dedifferentiation through massive mitochondrial fusion. Plant J. *44*, 744–755.
41. Seguí-Simarro, J.M., and Staehelin, L.A. (2006). Cell cycle-dependent changes in Golgi stacks, vacuoles, clathrin-coated vesicles and multivesicular bodies in meristematic cells of Arabidopsis thaliana: a quantitative and spatial analysis. Planta *223*, 223–236.
42. Cox, R.T., and Spradling, A.C. (2009). Clueless, a conserved Drosophila gene required for mitochondrial subcellular localization, interacts genetically with parkin. Dis. Model. Mech. *2*, 490–499.
43. Wang, Z.H., Clark, C., and Geisbrecht, E.R. (2016). Drosophila clueless is involved in Parkin-dependent mitophagy by promoting VCP-mediated Marf degradation. Hum. Mol. Genet. *25*, 1946–1964.
44. Pla-Martín, D., Schatton, D., Wiederstein, J.L., Marx, M.C., Khiati, S., Krüger, M., and Rugarli, E.I. (2020). CLUH granules coordinate translation of mitochondrial proteins with mTORC1 signaling and mitophagy. EMBO J. *39*, e102731.
45. Sheard, K.M., Thibault-Sennett, S.A., Sen, A., Shewmaker, F., and Cox, R.T. (2020). Clueless forms dynamic, insulin-responsive bliss particles sensitive to stress. Dev. Biol. *459*, 149–160.
46. Spinelli, J.B., and Haigis, M.C. (2018). The multifaceted contributions of mitochondria to cellular metabolism. Nat. Cell Biol. *20*, 745–754.
47. van Lis, R., and Atteia, A. (2004). Control of mitochondrial function via photosynthetic redox signals. Photosynth. Res. *79*, 133–148.
48. Liang, Z., Zhu, N., Mai, K.K., Liu, Z., Tzeng, D., Osteryoung, K.W., Zhong, S., Staehelin, L.A., and Kang, B.-H. (2018). Thylakoid-bound polysomes and a dynamin-related protein, FZL, mediate critical stages of the linear chloroplast biogenesis program in greening Arabidopsis cotyledons. Plant Cell *30*, 1476–1495.
49. Garmash, E.V., Velegzhaninov, I.O., Grabelnych, O.I., Borovik, O.A., Silina, E.V., Voinikov, V.K., and Golovko, T.K. (2017). Expression profiles of genes for mitochondrial respiratory energy-dissipating systems and antioxidant enzymes in wheat leaves during de-etiolation. J. Plant Physiol. *215*, 110–121.
50. Zhuang, X., Wang, H., Lam, S.K., Gao, C., Wang, X., Cai, Y., and Jiang, L. (2013). A BAR-domain protein SH3P2, which binds to phosphatidylinositol 3-phosphate and ATG8, regulates autophagosome formation in Arabidopsis. Plant Cell *25*, 4596–4615.

51. Zhuang, X., Chung, K.P., Cui, Y., Lin, W., Gao, C., Kang, B.-H., and Jiang, L. (2017). ATG9 regulates autophagosome progression from the endoplasmic reticulum in Arabidopsis. Proc. Natl. Acad. Sci. USA *114*, E426–E435.

52. Tamura, K., Shimada, T., Kondo, M., Nishimura, M., and Hara-Nishimura, I. (2005). KATAMARI1/MURUS3 Is a novel golgi membrane protein that is required for endomembrane organization in Arabidopsis. Plant Cell *17*, 1764–1776.

53. Marshall, R.S., Li, F., Gemperline, D.C., Book, A.J., and Vierstra, R.D. (2015). Autophagic degradation of the 26S proteasome is mediated by the dual ATG8/ubiquitin receptor RPN10 in Arabidopsis. Mol. Cell *58*, 1053–1066.

54. Chung, T., Phillips, A.R., and Vierstra, R.D. (2010). ATG8 lipidation and ATG8-mediated autophagy in Arabidopsis require ATG12 expressed from the differentially controlled ATG12A AND ATG12B loci. Plant J. *62*, 483–493.

55. Sauer, M., Paciorek, T., Benková, E., and Friml, J. (2006). Immunocytochemical techniques for whole-mount in situ protein localization in plants. Nat. Protoc. *1*, 98–103.

56. Richardson, A.D., Duigan, S.P., and Berlyn, G.P. (2002). An evaluation of noninvasive methods to estimate foliar chlorophyll content. New Phytol. *153*, 185–194.

57. Kang, B.-H. (2010). Electron microscopy and high-pressure freezing of Arabidopsis. Methods Cell Biol. *96*, 259–283.

58. Wang, P., Chen, X., Goldbeck, C., Chung, E., and Kang, B.-H. (2017). A distinct class of vesicles derived from the trans-Golgi mediates secretion of xylogalacturonan in the root border cell. Plant J. *92*, 596–610.

59. Toyooka, K., and Kang, B.H. (2014). Reconstructing plant cells in 3D by serial section electron tomography. Methods Mol. Biol. *1080*, 159–170.

60. Mai, K.K.K., and Kang, B.-H. (2017). Semiautomatic segmentation of plant Golgi stacks in electron tomograms using 3dmod. Methods Mol. Biol. *1662*, 97–104.

STAR★METHODS

KEY RESOURCES TABLE

REAGENT or RESOURCE	SOURCE	IDENTIFIER
Antibodies		
Rabbit polyclonal anti-GFP	Abcam	Cat# ab290; RRID: AB_303395
Rabbit polyclonal anti-YFP	Agrisera	Cat# AS111776
Rabbit polyclonal anti-mCherry	Abcam	Cat# ab167453; RRID: AB_2571870
Rabbit polyclonal anti-ATG8	Agrisera	Cat# AS142769; RRID: AB_2889398
Rabbit polyclonal anti-ACT	Agrisera	Cat# AS132640; RRID: AB_2722610
Rabbit polyclonal anti-UBQ	Agrisera	Cat# AS08307A; RRID: AB_2256904
Rabbit polyclonal anti-NBR1	Agrisera	Cat# AS142805
Rabbit polyclonal anti-VDAC1	Agrisera	Cat# AS07212; RRID: AB_1031829
Rabbit polyclonal anti-COXII	Agrisera	Cat# AS04053A; RRID: AB_2292247
Rabbit polyclonal anti-GLDH	Agrisera & PhytoAB	Cat# AS06182; RRID: AB_1031731; Cat# PHY0533S
Rabbit polyclonal anti-IDH	Agrisera	Cat# AS06203A; RRID: AB_2123280
Rabbit polyclonal anti-SMT1	Agrisera	Cat# AS07266; RRID: AB_2193665
Rabbit polyclonal anti-ARF1	Agrisera	Cat# AS08325; RRID: AB_1271007
Rabbit polyclonal anti-BiP	Agrisera	Cat# AS09481; RRID: AB_1832007
Rabbit polyclonal anti-PBR	PhytoAB	Cat# PHY0945S
Chemicals, peptides, and recombinant proteins		
Murashige & Skoog Basal Salts	Caisson	Cat# MSP01
Plant-agar	Plantmedia	Cat# 40100072-4
Z-Leu-Leu-Leu-al	Sigma-Aldrich	Cat# C2211-5M
Concanavalin A	Sigma-Aldrich	Cat# L7647-1G
Ethylenediaminetetraacetic acid	Sigma-Aldrich	Cat# ED2SC-250G
Nonidet P-40	Sigma-Aldrich	Cat# I8896-100ML
3,3′-Dithiodipropionic acid di(N-hydroxysuccinimide ester)	Sigma-Aldrich	Cat# D3669-1G
Dimethyl-sulfoxide	Sigma-Aldrich	Cat# D8418-500M
2,4-Dinitrophenol	Sigma-Aldrich	Cat# D198501-1KG
Carbonyl cyanide 4-(trifluoromethoxy) phenylhydrazone	Sigma-Aldrich	Cat# C2920-50MG
phospholipase D	Sigma-Aldrich	Cat# P8398
Tetramethylrhodamine ethyl ester	Thermo Fisher	Cat# T669
MitoTracker Red	Thermo Fisher	Cat# M7512
Complete protease inhibitor cocktail	Roche	Cat# 11873580001
GFP-Trap Magnetic Agarose beads	ChromoTek	Cat# gtma-20
Embed-812 resin	Electron Microscopy Sciences	Cat# 14120
Osmium Tetroxide	Electron Microscopy Sciences	Cat# 19100
Experimental models: organisms/strains		
Arabidopsis: Col-0	[50]	N/A
Arabidopsis: YFP-ATG8e	[50]	N/A
Arabidopsis: mCherry-ATG8e	[50]	N/A
Arabidopsis: atg5-1	[50]	N/A
Arabidopsis: fmt	[29]	N/A
Arabidopsis: Mito-GFP	[29]	N/A
Arabidopsis: Mito-GFP::*atg5-1*	This paper	N/A

(*Continued on next page*)

Continued		
REAGENT or RESOURCE	SOURCE	IDENTIFIER
Arabidopsis: Mito-GFP::*fmt*	[29]	N/A
Arabidopsis: Mito-GFP::mCherry-ATG8e	This paper	N/A
Arabidopsis: Mito-GFP::mCherry-ATG8e::*fmt*	This paper	N/A
Arabidopsis: FMT-YFP	[29]	N/A
Arabidopsis: mCherry-ATG8e::*atg5-1*	This paper	N/A
Software and algorithms		
Excel 2016 v.15.39	Microsoft	https://www.microsoft.com
Prism 8 v.8.0.0	GraphPad Software	https://www.graphpad.com
FIJI v.1.0	NIH	https://imagej.nih.gov/ij/
Photoshop CC v.2017.0.0	Adobe	https://www.adobe.com
IMOD v.4.9	University of Colorado	https://bio3d.colorado.edu/imod/

RESOURCE AVAILABILITY

Lead contact

Further information and requests for resources and reagents should be directed to and will be fulfilled by the Lead Contact, Byung-Ho Kang (bkang@cuhk.edu.hk)

Materials availability

Transgenic plant seeds generated in this study will be made available on request, but we may require a completed Materials Transfer Agreement if there is potential for commercial application.

Data and code availability

This study did not generate datasets or code.

EXPERIMENTAL MODEL AND SUBJECT DETAILS

Plant materials

YFP-ATG8e, mCherry-ATG8e, *atg5-1*, Mito-GFP, Mito-GFP::*fmt* and FMT-YFP seeds were generated for previous studies and acquired from the research groups.[29,50,51] mCherry-ATG8e::*atg5-1*, Mito-GFP x mCherry-ATG8e and Mito-GFP x mCherry-ATG8e::*fmt* were obtained by crossing the previously established lines.[29,50,51] All transgenic lines were genotyped by PCR, and homozygous lines were isolated before experiments.

Plant growth conditions

All *Arabidopsis* seeds were surface-sterilized and germinated on ½ Murashige and Skoog (MS) agar plate in a growth chamber at 21 °C with 16 hour (hr) light – 8 hr dark except for the de-etiolation experiments where seedlings were germinated under darkness.

METHOD DETAILS

Protein extraction and immunoblot analysis

Isolation of mitochondrial membrane proteins and fluorescence protein cleavage assay were carried out as described previously.[50,52,53] Briefly, seven-day-old *Arabidopsis* seedlings were incubated in DMSO (Sigma-Aldrich, D8418-500M), 50 μM DNP (Sigma-Aldrich, D198501-1KG), 50 μm MG132 (Sigma-Aldrich, C2211-5M) or 1 μm ConA (Sigma-Aldrich, L7647-1G) with indicated times in liquid 1/2 MS (Caisson, MSP01) medium when necessary. Seedlings for the nitrogen starvation experiments were germinated on half MS medium agar plate and then transferred to liquid half MS medium without nitrogen for one day. All of the protein samples were subjected to 15% SDS-PAGE. Primary and secondary antibodies were diluted in 1x phosphate-buffered saline (PBS). Antibodies against GFP (Abcam; ab290), YFP (Agrisera; AS111776), mCherry (Abcam; ab167453), ATG8 (Agrisera; AS124769), Actin (ACT; Agrisera; AS132640), Ubiquitin (UBQ; Agrisera; AS08307A), neighbor of BRCA1 (NBR1; Agrisera; AS142805), voltage-dependent anion channel 1 (VDAC1; Agrisera; AS07212), peripheral-type benzodiazepine receptor (PBR; PhytoAB; PHY0945S), cytochrome oxidase subunit II (COXII; Agrisera; AS04053A), L-galactono-1,4-lactone dehydrogenase (GLDH; Agrisera; AS06182 for the immunoblot in Figures 4B and 6C, PhytoAB; PHY0533S for other immunoblots) and isocitrate dehydrogenase (IDH; Agrisera; AS06203A), Cycloartenol-C24-methyltransferase (SMT1; Agrisera; AS07266), ADP-ribosylation factor 1 (ARF1; Agrisera; AS08325), Binding immunoglobulin protein (BiP; Agrisera; AS09481) were obtained from the indicated sources. We

quantified band intensities from three replicate immunoblot analyses using ImageJ (https://imagej.nih.gov/ij/) and Microsoft Excel 2016 (https://www.microsoft.com/). The two-way ANOVA tests and graph preparation were carried out with GraphPad Prism8 (https://www.graphpad.com). Representative results from at least three independent immunoblot analyses were shown in the figures.

ATG8 de-lipidation assay

Protein extraction methods for ATG8-delipidation were explained before.[54] Seven-day-old *Arabidopsis* seedlings were incubated in 50 μM DNP for 2 hours before protein extraction. The total plant lysates were extracted in lysis buffer [50 mM Tris-HCl (pH 8.0), 150 mM NaCl, 0.5 mM Ethylenediaminetetraacetic acid (EDTA) and 1x Complete Protease Inhibitor Cocktail (Roche, 11873580001)] and then centrifuged at 14 000 rpm for 10 min at 4°C. The supernatant was centrifuged at 100 000 g for 1 hr, with the membrane pellet then solubilized in lysis buffer containing 0.5% (v/v) Triton X-100. The solubilized membrane samples were incubated at 37°C for 1 hr with 250 unit/ml of phospholipase D (PLD, Sigma-Aldrich, P8398) or an equal volume of the buffer. Protein samples were subjected to 15% SDS-PAGE in the presence of 6 M urea and analyzed by immunoblot with an anti-ATG8 antibody.

Immunoprecipitation

Protein extraction and immunoprecipitation were performed as described previously.[50] Seven-day-old *Arabidopsis* seedlings were incubated in 50 μM DNP for 2 hr before protein extraction. Total plant lysates were centrifuged at 14000 rpm for 10 min at 4°C. The supernatant was prepared in lysis buffer (10 mM Tris/HCl at pH 7.4, 150 mM NaCl, 0.5 mM EDTA, 5% glycerol, 0.2% Nonidet P-40, and 2 mM dithiobis [succinimidyl propionate] containing 1x Complete Protease Inhibitor Cocktail) and then incubated with GFP-TRAP agarose beads (ChromoTek, gtma-20) for 2 hr at 4°C. The beads were washed five times (4°C) in wash buffer (10 mM Tris/HCl, pH 7.5, 150 mM NaCl, and 0.5 mM EDTA with 1x Complete Protease Inhibitor Cocktail) and then eluted by boiling in 2x SDS sample buffer. Samples were separated by SDS-PAGE and analyzed by immunoblot using indicated antibodies.

Confocal microscopy and image processing

Confocal fluorescence images were acquired using an SP8 laser scanning confocal system with a 63x water-immersion lens (Leica Microsystems). Seven-day-old *Arabidopsis* seedlings were incubated in DMSO, 50 μM DNP, 10 μM FCCP (Sigma-Aldrich, C2920-50MG) or 0.5 μM ConA with indicated times in liquid half MS medium when necessary before imaging. Tetramethylrhodamine ethyl ester (TMRE, Thermo Fisher, T669) and MitoTracker Red (MTR, Thermo Fisher, M7512) were used to stain *Arabidopsis* root cell mitochondria at 500 nm for 10 mins. For visualizing depolarized mitochondria in cotyledon cells, samples from each light exposure group were stained with TMRE for 15 min before confocal microscopy imaging. A sequential acquisition was applied when observing fluorescent proteins. Images were processed with Photoshop CC (https://www.adobe.com) and the microscopy data were evaluated with one-way ANOVA tests using GraphPad Prism8 (https://www.graphpad.com).

Immunofluorescence labeling

The confocal immunofluorescence labeling was performed according to the method in Sauer et al.[55] Seven-day-old *Arabidopsis* seedlings expressing FMT-YFP were fixed with 4% paraformaldehyde in PBS supplement with 0.1% Triton X-100. After procedures of cell wall digestion, plasma membrane permeabilization, and blocking, the roots were incubated with anti-GFP and anti-ATG8 antibody overnight at 4°C for immunolabeling, and then were probed with Alexa 488 goat anti-chicken IgG (Thermo Fisher, Invitrogen, A-11039) and Alexa 568 goat anti-rabbit IgG (Thermo Fisher, Invitrogen, A-11011) secondary antibody for confocal microscopy imaging.

Chlorophyll extraction and measurement

Chlorophyll extraction and concentration measurement were performed as described before.[56] *Arabidopsis* seedlings were germinated under darkness for seven days and then exposed to light. 10 mg of fresh *Arabidopsis* seedlings were collected and ground in 700 μL pre-heated DMSO at 65°C for 30 minutes. The tissues were removed with a centrifuge at 6000 rpm for 10 minutes, and pre-heated DMSO (300 μl) was added to make the final volume 1 ml. The OD value of the extractions were measured at 645 nm for chlorophyll a and 663 nm for chlorophyll b with a NanoDrop spectrophotometer (Thermo Fisher) and chlorophyll concentration was calculated with the Arnon's equations: Chlorophyll a ($g\ l^{-1}$) = $0.0127\ A_{663} - 0.00269\ A_{645}$; Chlorophyll b ($g\ l^{-1}$) = $0.0229\ A_{645} - 0.00468\ A_{663}$; total Chlorophyll ($g\ l^{-1}$) = $0.0202\ A_{645} + 0.00802\ A_{663}$. The experiment was repeated three times for each genotype. Data analysis and graph preparation were carried out with Microsoft Excel 2016 (https://www.microsoft.com/) and Prism8 (GraphPad Software; https://www.graphpad.com), respectively.

TEM analysis, electron tomography, and 3d modeling

For TEM samples preparation, high-pressure freezing, freeze substitution, resin embedding, and ultramicrotomy were performed as described before.[57,58] In brief, Seven-day-old *Arabidopsis* seedlings were incubated in DMSO or 50 μM DNP for indicated times and then rapidly frozen with an HPM100 high-pressure freezer (Leica Microsystems). The samples were freeze-substituted at −80°C for 72 hr, and excess OsO4 was removed by rinsing with precooled acetone. After being slowly warmed up to room temperature over

48 hr, root samples were separated from planchettes and embedded in Embed-812 resin (Electron Microscopy Sciences, Cat. No. 14120). Thin sections (100 nm thick) prepared from sample blocks of each time point were examined with a Hitachi 7400 TEM (Hitachi-High Technologies) operated at 80 kV.

For dual-axis tomography analysis, semi-thick sections (250 nm) were collected on formvar-coated copper slot grids (Electron Microscopy Sciences) and stained with 2% uranyl acetate in 70% methanol followed by Reynold's lead citrate as described previously.[48] Tilt series were collected from 60° to −60° (1.5° intervals) with a 200-kV Tecnai F20 intermediate voltage electron microscopy (https://www.fei.com/). Tomograms were reconstructed according to the method in Toyooka and Kang (2014).[59] To generate models of complicated thylakoid membranes, we used the autocontour command (https://bio3d.colorado.edu/imod/doc/3dmodHelp/autox.html) of the 3dmod software package as explained in Mai et al. (2017).[60]

QUANTIFICATION AND STATISTICAL ANALYSIS

All statistical comparisons were performed on data from three or more independent biological replicates (indicated in figure legends), with similar data variances observed between different groups. All statistical data were calculated and graphed using GraphPad Prism 8 (https://www.graphpad.com) or Microsoft Excel 2016 (https://www.microsoft.com/). We carried out statistical comparisons between different groups from multi-variable and time-course data using two-way ANOVA with Tukey's multiple comparisons test. For data representing a single time-point and condition, we performed statistical comparisons between different groups using one-way ANOVA with Tukey's multiple comparisons test. Two-tailed unpaired Student's t test was performed to compare the difference between two groups. *$p < 0.05$, **$p < 0.01$, ***$p < 0.001$, ****$p < 0.0001$, n.s., no significant difference.

6.5. Root hair lifespan is antagonistically controlled by autophagy and programmed cell death

Root hairs are essential for plant nutrient and water uptake, yet the mechanisms regulating their lifespan remain poorly understood. The study shown in **Chapter 6.6** (Fent et al., 2025) demonstrates that autophagy plays a crucial role in maintaining root hair longevity by suppressing a developmentally programmed cell death (dPCD) pathway. Mutations in autophagy-related genes (*ATG2*, *ATG5*, *ATG7*) lead to premature root hair collapse, accompanied by ectopic activation of dPCD markers and cellular degradation. Genetic complementation and tissue-specific knockout experiments confirm that autophagy acts cell-autonomously to delay dPCD, independent of salicylic acid, jasmonic acid, or ethylene signaling.

The dPCD pathway in autophagy-deficient root hairs depends on the NAC transcription factors ANAC046 and ANAC087, which regulate a conserved gene network associated with cellular senescence. Loss of these transcription factors rescues root hair viability in *atg* mutants, while their overexpression induces premature cell death. These findings reveal an antagonistic relationship between autophagy and dPCD in root hair survival, providing insights into how plants balance cellular maintenance and senescence. The study suggests that modulating autophagy or dPCD could enhance root hair persistence, potentially improving nutrient uptake and stress resilience in crops.

6.6. Appendix Manuscript 3: “Root hair lifespan is antagonistically controlled by autophagy and programmed cell death”

Authors: Qiangnan Feng, Shihao Zhu, Xinchao Wang, Yujie Liu, **Jierui Zhao**, Yasin Dagdas, Moritz K. Nowack

Contribution: For this manuscript, I desgined and performed mitochondria leakage experiment to confirm that Arabidopsis *atg* mutants behave premature root hair death.

Status: This manuscript is currently a preprint on bioRxiv posted on March 19, 2025.

DOI: https://doi.org/10.1101/2025.03.18.643910

Root hair lifespan is antagonistically controlled by autophagy and programmed cell death

Qiangnan Feng[#1,2,3*], Shihao Zhu[#1], Xinchao Wang[#1], Yujie Liu[1], Jierui Zhao[4], Yasin Dagdas[4,5], Moritz K. Nowack[2,3,6,*]

[1]College of Life Sciences, Shandong Agricultural University, Tai'an 271018, China

[2]Department of Plant Biotechnology and Bioinformatics, Ghent University, Technologiepark 71, 9052 Ghent, Belgium

[3]VIB Center for Plant Systems Biology, Technologiepark 71, 9052 Ghent, Belgium

[4]Gregor Mendel Institute (GMI), Austrian Academy of Sciences, Vienna BioCenter (VBC), Vienna, Austria

[5]Heidelberg University, Centre for Organismal Studies (COS), 69120 Heidelberg, Germany

[6]Lead contact

[#]These authors contributed equally to this article.

[*]Correspondence: qiangnan.feng@sdau.edu.cn (Q.F.), moritz.nowack@psb.vib-ugent.be (M.K.N.)

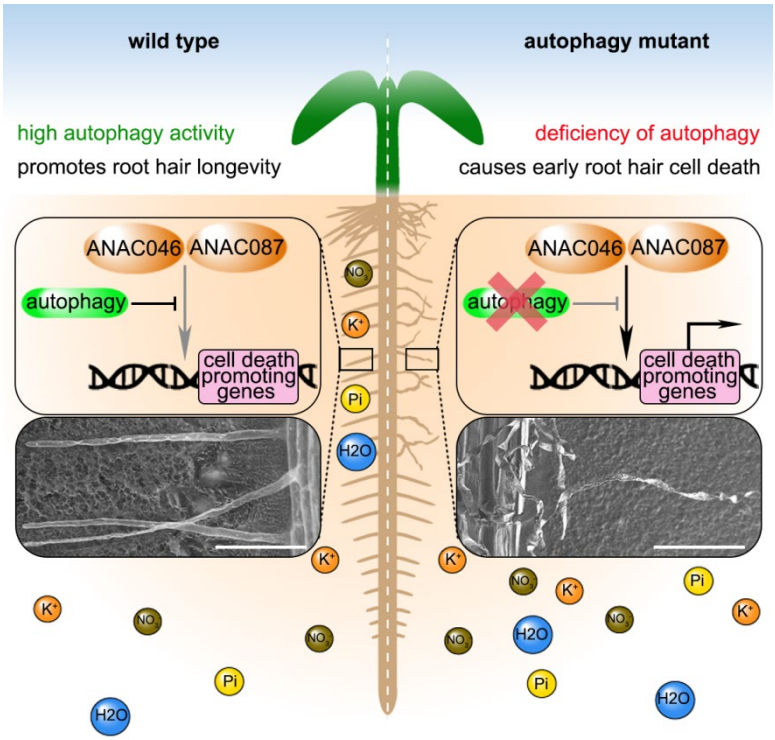

Abstract

Root hairs are tubular tip-growing extensions of root epidermal cells that enhance root surface area for water and nutrient uptake. While mechanisms governing root hair fate, polarity, and tip growth are well understood, the regulation of root hair longevity remains largely unknown. Here, we show that root hair cells employ high levels of autophagy to promote their lifespan. Loss-of-function mutations in the autophagy regulators ATG2, ATG5, or ATG7 induce a premature, cell-autonomous cell death program. This cell death is activated via a gene regulatory network downstream of the NAC transcription factors ANAC046 and ANAC087. Our findings uncover an antagonistic relationship between autophagy and developmentally controlled cell death in root hair lifespan regulation, with potential implications for optimizing plant nutrient and water uptake in crop breeding.

Key words: autophagy, root hair, programmed cell death, PCD, senescence, NAC transcription factor, *Arabidopsis thaliana*

Introduction

Root hairs are important for plant growth and development, since they dramatically increase the root surface area available for water and mineral uptake, improve root anchoring in the soil, and facilitate signaling with the soil microbiome (Grierson et al., 2014). Root hair development occurs in four phases: cell fate specification, initiation of outgrowth in the basal cell region, tip growth maintenance, and growth arrest at maturity (Gilroy and Jones, 2000). The patterning of epidermal cells in root hair and non-root hair cells, and subsequent cellular differentiation is regulated by extensive gene regulatory networks (Vissenberg et al., 2020). Initiation and maintenance of root hair tip growth depends on additional transcription factors, cell wall-modifying enzymes, gradients of calcium and reactive oxygen species, and targeting of active ROPs to specific plasma membrane domains (Honkanen and Dolan, 2016; Zhang et al., 2022; Li et al., 2023). After having reached a certain length, root hairs enter the maturation stage, characterized by vacuolization of the apical root hair region and tip-growth arrest (Grierson et al., 2014). Subsequently, protoplast shrinkage and DNA fragmentation occur, hinting at a controlled degeneration process (Shishkova and Dubrovsky, 2005; Li et al., 2016; Tan et al., 2016). However, the mechanisms and pathways that control root hair life span remain largely unknown.

Both autophagy and programmed cell death have been established as pathways determining cellular life span and organ senescence in animals and plants (Woo et al., 2019; Cassidy and Narita, 2022). Regulated cell death, or programmed cell death (PCD) is a highly organized process occurring in the context of regular development (dPCD), and as part of the reaction to environmental stresses or insults (ePCD) (Daneva et al., 2016). While the regulation of numerous PCD subroutines have been established in animal systems (Galluzzi et al., 2018), the molecular control of PCD in plants appears not to be conserved and is much less understood (Kacprzyk et al., 2024). Plant dPCD is controlled by gene regulatory networks which control the

expression of a suite of specific dPCD signature genes prior to PCD execution (Olvera-Carrillo et al., 2015). NAC transcription factors play key roles in controlling the timely onset of dPCD in several developmental contexts. Some coordinate tissue differentiation and dPCD preparation in a highly cell-type specific manner, e.g. SMB in the root cap (Fendrych et al., 2014) or VNDs in the xylem (Kubo et al., 2005; Ohashi-Ito et al., 2010). Others NAC factors appear to act further downstream in the dPCD regulatory network and are commonly upregulated in several dPCD contexts independent of the tissue type, like ANAC046 and ANAC087 that have been implicated in dPCD processes in the xylem, the root cap, stigmatic papilla cells, the endosperm, and leaves (Kim et al., 2014; Oda-Yamamizo et al., 2016; Gao et al., 2018; Huysmans et al., 2018; Doll et al., 2023).

In contrast to dPCD pathways, autophagy is highly conserved in eukaryotes, and regulated by a suite of established autophagy genes (ATGs). Autophagy acts as a quality control pathway, mediating the degradation of cellular components by targeting them to the lysosomes or vacuoles (Gross et al., 2025). In plants experiencing optimal growth conditions, autophagy operates at basal levels to maintain cellular homeostasis, but starvation and environmental stresses can upregulate autophagic activity to promote plant survival (Agbemafle et al., 2023). In contrast to these pro-survival functions, autophagy can promote the transition to cell death, for instance under nutrient starvation conditions in cell cultures (Teper-Bamnolker et al., 2021). In plant immunity, autophagy has been assigned pro-survival as well as pro-death roles, depending on context (Liu et al., 2005; Hofius et al., 2009). In the Arabidopsis root cap, autophagy has cell-type specific roles: It promotes cell sloughing as well as cell death and corpse clearance in root cap columella cells, but is dispensable for dPCD execution and corpse clearance in lateral root cap cells (Feng et al., 2022; Goh et al., 2022).

Here, we report that defects in the canonical autophagy pathway of Arabidopsis causes the premature onset of dPCD signature gene expression specifically in root hairs. In line with this observation, we find that root hair longevity in different *atg* mutants is reduced by precocious activation of a root-hair specific dPCD process. Cell type-specific ATG knockout and transgene complementation confirmed the cell-autonomous pro-survival role of autophagy in root hairs. Interestingly, root hair cell death depends on ANAC046 and ANAC087, linking the pro-survival role of autophagy in root hairs to the suppression of canonical dPCD pathways.

Results

Root hair cells display intrinsically elevated autophagic activity

Investigating root cell-type specific differences in autophagy processes, we imaged roots of *Arabidopsis thaliana* (Arabidopsis) wild-type and *atg* mutants expressing the autophagy reporter *YFP-ATG8A*. In the wild-type, we detected YFP-ATG8A both freely cytosolic and in a high number of punctate foci representing autophagosomes (APGs) in different root hair developmental stages (Figure 1A). By contrast, in *atg7-2* and *atg5-1* mutants, we detected a predominantly cytosolic YFP signal and significantly less APGs in mature root hair cells (Figure 1B-D), suggesting an upregulation of canonical autophagy in this cell type. Using Concanamycin A (ConA) as a drug to allow quantification of autophagic delivery to the central vacuole, we counted significantly more YFP-ATG8A-positive autophagic bodies in vacuoles of

root hair cells than non-root hair cells, indicating intense autophagy activity also in young root hair cells (Figure 1E-F), suggesting that autophagy is highly activated throughout root hair development.

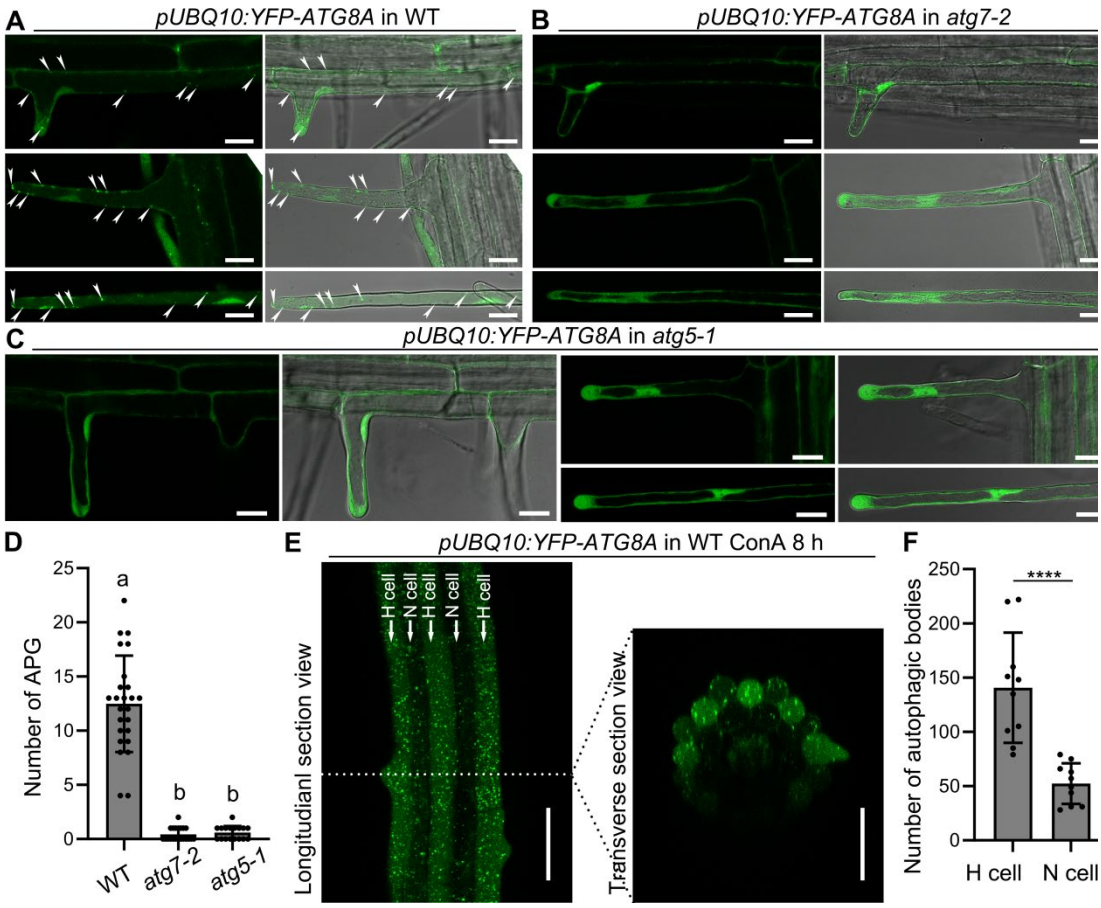

Figure 1. Autophagy activation is increased in root hair cells. A-C, Representative confocal images of root hair cell from 5 days after germination (DAG) expressing *pUBQ10:YFP-ATG8A* in wild-type (WT) (A), *atg7-2* (B) and *atg5-1* (C). White arrows indicate autophagosomes (APGs). D, The quantification of APG in mature root hair cells. Results are means ± SD. 17-25 root hair cells from 5 roots of each genotype were analyzed. Means with different letters are significantly different (one-way ANOVA, Tukey's multiple comparisons test, $P < 0.05$). E, Representative confocal images of roots from seedlings at 5 DAG expressing *pUBQ10:YFP-ATG8A* in WT, *atg7-2* and *atg5-1* mutant treated with 1 µM ConA for 8 h. Non-root hair cell (atrichoblast) and root hair cell (trichoblast) were shown as N cell and H cell, respectively. F, The quantification of autophagic bodies in H cells treated with 1 µM ConA for 8 h as shown in (E). Results are means ± SD. N = 10 cells from 5 roots. **** indicates a significant difference (*t* test, $P < 0.0001$). Bars = 20 µm for A-C, 50 µm for E.

Autophagy deficiency activates a premature dPCD process in root hair cells

To investigate functions of autophagy in root hairs, we investigated root hairs of wild-type and *atg* mutants. While *atg* mutant root hair initiation and tip growth was indistinguishable from the wild type (Supplemental Figure 1A-D), we found collapsed root hairs in all but the most distal parts of 7-day old seedling roots (Figure 2A). Next, we generated transgenic lines expressing a ubiquitously expressed *pUBQ10:ATG5-mCherry* complementation construct in the *atg5-1* mutant background. Three independent lines showed a complete restoration of the

root hair phenotype (Figure 2B), suggesting that autophagy is crucial determinant of root hair cell longevity in Arabidopsis.

To test if root hair collapse displayed dPCD hallmarks, we introgressed promoter-reporters of the dPCD signature genes *PASPA3 and RNS3* (Fendrych et al., 2014; Olvera-Carrillo et al., 2015) into *atg* mutants. While PASPA3 and RNS3 expression in the wild type is restricted to root cap and xylem cells preparing for dPCD (Fendrych et al., 2014; Olvera-Carrillo et al., 2015), *atg* mutants displayed ectopic PASPA3 and RNS3 expression in young root hair cells (Figure 2D-E, Supplemental Figure 1E-F). Notably, the ectopic PASPA3 expression is not present in ATG5-mCherry complementation lines (Figure 2C). In line with reporter expression, we could observe cellular hallmarks of dPCD (Fendrych et al., 2014; Wang et al., 2024), including mitochondrial disintegration, nuclear envelope breakdown, and vacuolar collapse, in *atg* mutant root hairs (Figure 2D-E, Supplemental Figure 1G-H). As root hairs can be easily damaged by microscopy mounting, we followed root hair viability and death in seedlings grown in chambers that allow minimally invasive imaging of plants. In line with our previous results, *atg5-1* mutant root hairs were dead, while wild-type root hairs in the same root region were alive (Supplemental Figure 2A). To address the question whether dPCD in *atg* mutant root hairs occurs ectopically or rather prematurely, we imaged root hairs of 14-day old plants during different stages of secondary growth and periderm development (Wunderling et al., 2018). We found that root hair cells expressed the PASPA3 reporter and subsequently collapsed in the most mature root region just below the hypocotyl (Supplemental Figure 2B, C and F). In *atg2-2* mutants, by contrast, root hairs expressed PASPA3 and subsequently collapsed in a much earlier stage (Supplemental Figure 2D, E and F), suggesting that autophagy deficiency severely reduces root hair life span by early activation of senescence-related dPCD.

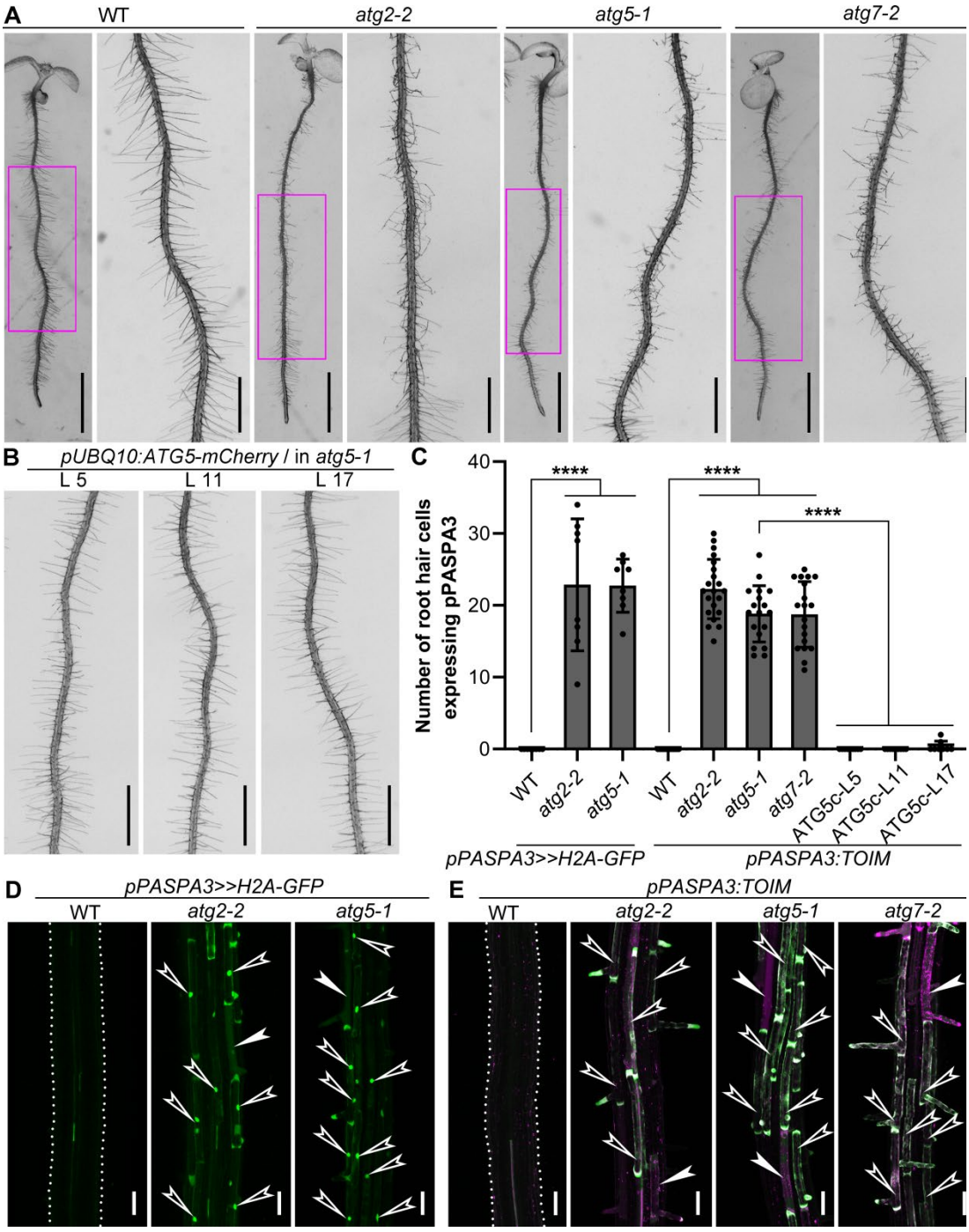

Figure 2. The loss function of autophagy promotes precocious expression of PASPA3 and dPCD onset in root hairs. A, Representative primary roots from 7-day-old seedlings: WT, *atg2-2*, *atg5-1* and *atg7-2*. The right panel of each genotype shows a zoomed image of a part region of the left panel outlined in magenta. B, Representative primary roots from 7-day-old seedlings: three independent lines of *pUBQ10:ATG5-mCherry* in *atg5-1* background. C, The quantification of root hair cells expressing PASPA3 in WT, *atg* mutants and complement lines (ATG5c). The name of lines *pUBQ10:ATG5-mCherry* in *atg5-1* expressing *pPASA3:TOIM* was written as ATG5c. In total, 8-23 roots were analyzed for each genotype. **** indicates a significant difference (*t* test, $P < 0.0001$). D-E, Representative confocal images of roots from 5-day-old WT and *atg* mutants expressing

pPASPA3>>H2A-GFP (D) or *pPASPA3:TOIM* (E). Arrowheads outlined in white indicate that H2A-GFP (D) signals or TOIM (E) were observed in root hair cells of *atg* mutants. White arrowheads indicate that nuclear leakage (D) or vacuole collapse (E) of *atg* mutants. White dotted lines point the profile of root in WT. Bars = 5 mm for A (left panel of each genotype), 1 mm for A (right panel of each genotype) and B, 50 µm for D and E. See also Figure S1 and S2; Movie S1 and S2.

Autophagy promotes root hair longevity in a cell-autonomous fashion

Seeing that autophagy is a systemically active process in plants, we next addressed the question if premature root hair cell dPCD was caused by lack of autophagy specifically in root hairs, or else a more indirect, non-cell autonomous effect of systemic autophagy deficiency. To this end, we generated root-hair specific complementation lines, expressing ATG5-mCherry under the root hair-specific promoter of *ARABIDOPSIS THALIANA EXPANSIN A7* (pE7) (Cho and Cosgrove, 2002; Won et al., 2009). As autophagy has been implicated in xylem maturation (Kwon et al., 2010) and in the restriction of cell death to specific xylem cell types (Escamez et al., 2016; Escamez et al., 2019), we used the xylem- specific promoter IRREGULAR XYLEM1/CELLULOSE SYNTHASE8 (pIRX1) (Turner and Somerville, 1997; Taylor et al., 2000) controlling ATG5-mCherry to test if root hair cell death was dependent on xylem autophagy (Figure 3A). We established three independent lines of *pE7:ATG5-mCherry* that showed a complete rescue of the *atg5-1* phenotype, both the early expression of PASPA3 (Figure 3B) and root hair degeneration (Figure 3C). By contrast, we could not find any line of *pIRX1:ATG5-mCherry* that showed complementation (Figure 3B and D).

Next, we used a tissue-specific knockout approach, CRISPR-TSKO (Decaestecker et al., 2019; Bollier et al., 2021), expressing *Cas9* and a polycistronically attached *P2A-mCherry-NLS* sequence under the pE7 promoter. Combined with previously reported guide RNAs (gRNAs) targeting *ATG2* (Feng et al., 2022), we generated *pE7:Cas9;ATG2* (Supplemental Figure 3A). The construct was transformed into wild-type plants carrying *pPASAP3>>H2A-GFP* (Fendrych et al., 2014), and two independent lines with high expression levels of mCherry-NLS in root hair cells were established (Supplemental Figure 3B). While these lines showed a significant rise of *pPASPA3>>H2A-GFP* activity in root hairs, they did only partially phenocopy the premature root hair collapse of *atg2-2* mutants (Supplemental Figure 3C-D). To test if this is due to the late activation of *pE7* in the course of root hair development, we repeated the experiment with Cas9 driven by the promoter of *ROOT HAIR DEVELOPMENT6* (*pRHD6*) (Figure 3E), which is activated already in the immature root hair cell files in the root meristem (Menand et al., 2007). Three independent lines of *pRHD6:Cas9;ATG2* showed not only early pPASPA3 reporter expression (Figure 3F and 3H), but also a root hair degradation phenotype similar to the *atg2-2* mutant (Figure 3G). Taken together, these results demonstrate a cell-autonomous function of autophagy in promoting root hair longevity by suppressing senescence-induced dPCD.

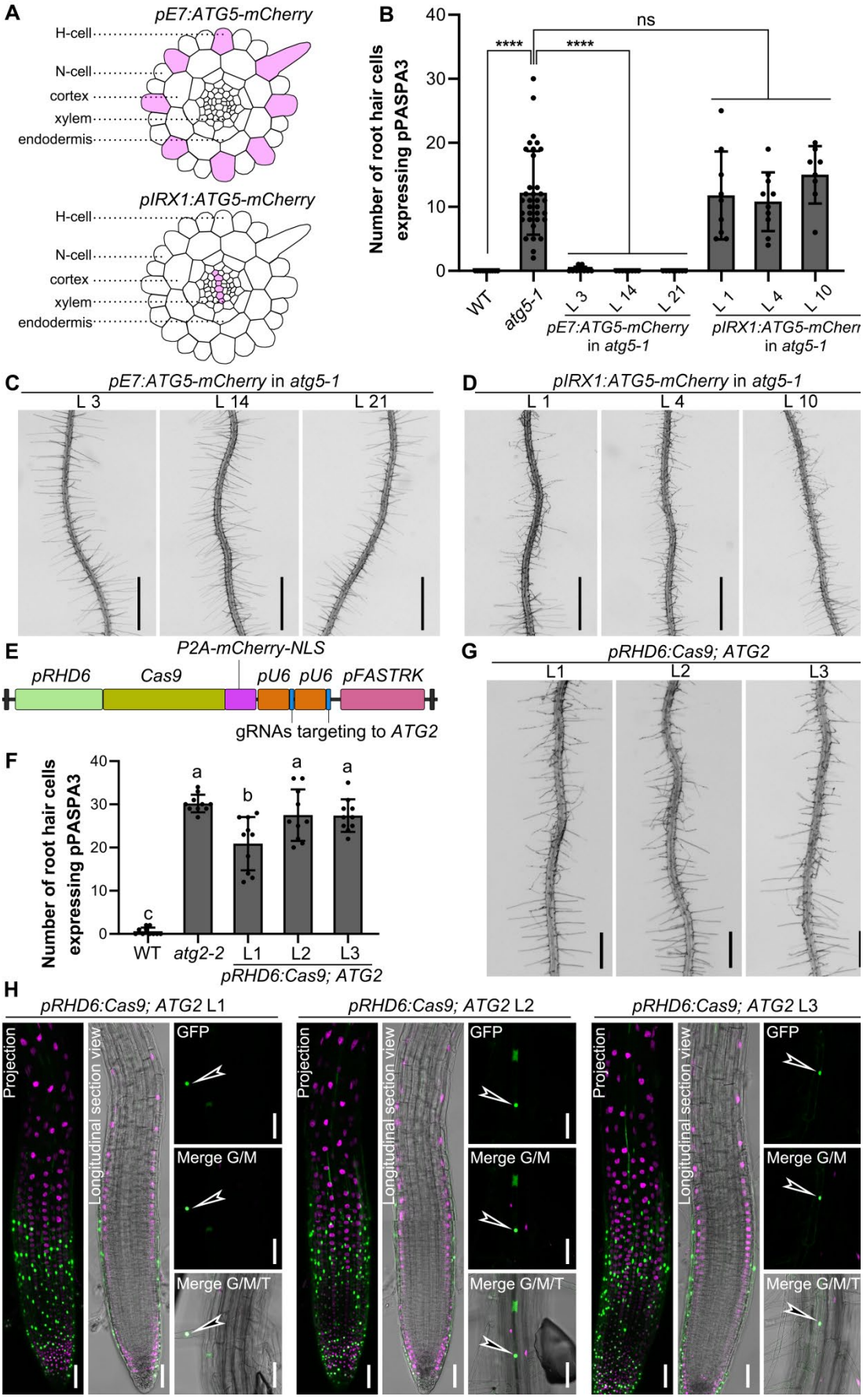

Figure 3. Root-hair-specific complementation and loss of function shows root hair inherent

functions of autophagy. A, Schematic representation of the cross-section of Arabidopsis root. The expression pattern of *pE7:ATG5-mCherry and pIRX1:ATG5-mCherry* is shown as pink in the upper panel and lower panel, respectively. B, The quantification of root hair cell expressing *PASPA3*. Results shown are means ± SD. In total, 8-34 roots were analyzed for each genotype. **** indicates a significant difference (*t* test, P < 0.0001). ns indicates not significant (*t* test, P > 0.05). C-D, Representative primary roots from 7-day-old seedlings: three independent lines of *pE7:ATG5-mCherry* (C) and *pIRX1:ATG5-mCherry* (D) in *atg5-1* background. E, Schematic representation of the vector: *pRHD6:Cas9;ATG2.* The Cas9-P2A-mCherry is driven by root hair specific promoter pRHD6, and two gRNAs targeting to *ATG2* are inserted. F, The quantification of root hair cell expressing *PASPA3*. Results shown are means ± SD. In total, 10 roots were analyzed for each genotype. Means with different letters are significantly different (one-way ANOVA, Tukey's multiple comparisons test, P < 0.05). G, Representative primary roots from 7-day-old seedlings: three independent lines of *pRHD6:Cas9; ATG2*. H, Representative confocal images of three independent lines of *pRHD6:Cas9;ATG2* in *pPASPA3>>H2A-GFP* background. Arrowheads outlined in white indicate the precocious expression of *PASPA3* in root hair cells. Bars = 1 mm for C and D, 500 µm for G, 50 µm for H. See also Figure S3.

Autophagy-deficient root hair degeneration is SA-, JA- and ethylene-independent

The early leaf senescence phenotypes seen in *atg* mutants depends on salicylic acid (SA) signaling (Yoshimoto et al., 2009). To investigate possible analogies between leaf and root hair senescence, we crossed the SA-biosynthesis mutant *sid2* (Nawrath and Métraux, 1999) with the *atg2-2* mutant expressing a *pPASPA3* reporter. Similar to *atg2-2*, the *atg2-2 sid2* double mutant shows early PASPA3 expression and root hair degeneration (Supplemental Figure 3E-G). This was confirmed by the *atg5-1 sid2* double mutant (Supplemental Figure 3H), showing that the *atg* mutant root hair dPCD phenotype does not depend on SA signaling.

Also jasmonic acid (JA) and ethylene have been implicated in senescence modulation (Liao et al., 2022), prompting us to test their involvement in premature root hair degeneration by generating double mutants of *atg2-2* and *atg5-1* with *coi1* (Huang et al., 2014) and *ein2* (Alonso et al., 1999), respectively. All *coi1* and *ein2* double mutant combinations retained the expression of PASPA3 and early cell death phenotype (Supplemental Figure 3), suggesting that neither SA-, nor JA- or ethylene-signaling pathways are responsible for the premature root hair cell death in autophagy mutants.

Autophagy-deficient root hair cell death depends on canonical dPCD regulators

To test the involvement of established dPCD-regulating transcription factors in autophagy-deficient root hair cells, we interrogated their expression patterns using published single-cell RNA-sequencing (scRNA-seq) datasets (Denyer et al., 2019; Wendrich et al., 2020). We found that both *ANAC046* and *ANAC087* are expressed in sc-RNAseq clusters corresponding to root hair cells (Supplemental Figure 4A-C). Investigating the published promoter-reporter lines *pANAC046:NLS-tdTOMATO* and *pANAC046:NLS-tdTOMATO* (Huysmans et al., 2018), we confirmed the root hair cell expression of both transcription factors (Supplemental Figure 4D). Next, we investigated 14-day old roots of wild-type and *anac046 anac087* double mutant plants. Compared with wild type, we found significantly less collapsed root hair cells in the hypocotyl-proximal region of the *anac046 anac087* mutant, suggesting the root hairs of

anac046 anac087 remained viable longer than the wild type ones (Supplemental Figure 4E-F). In addition, we generated *atg2-2 anac046 anac087* triple mutants expressing the PASPA3 reporter (*tri-1*). In parallel, we generated two novel null mutant alleles of *ATG2* (*atg2-8* and *atg2-9*) using published gRNAs (Feng et al., 2022) directly in the *anac046 anac087* double mutant background (*tri-2*, *atg2-8 anac046 anac087*; *tri-3, atg2-9 anac046 anac087*) (Figure 4A, Supplemental Figure 5A). Interestingly, we observed that loss of *ANAC046* and *ANAC087* function was sufficient to suppress the premature root hair cell death phenotype of *atg2* mutants (Figure 4B), but not the early leaf senescence of *atg* mutants (Supplemental Figure 5B-C). By digital-droplet PCR, we demonstrated dPCD signature genes were down-regulated to wild-type levels in these triple mutants when compared with *atg2-2* mutant (Figure 4C), suggesting that NAC transcription factors are indispensable for autophagy-mediated root hair dPCD. By quantifying the number of root hair cells expressing pPASPA3 in *tri-1*, we found that *anac046 anac087* rescues the precocious expression of pPASPA3 of *atg2-2*, confirming the digital-droplet PCR results (Figure 4D).

Finally, we misexpressed ANAC046 under the pE7 promoter, and established two independent lines with root hair cell death in the early stage of root hair formation (Figure 4E). Visually, these lines appear root-hair less (Figure 4F), and show that ANAC046 expression is sufficient to cause root hair cell death.

In sum, these results demonstrate the premature dPCD of root hairs in *atg* mutants dependents on canonical dPCD gene regulatory networks that are shared with established dPCD processes as they occur in the xylem, the root cap, or the endosperm.

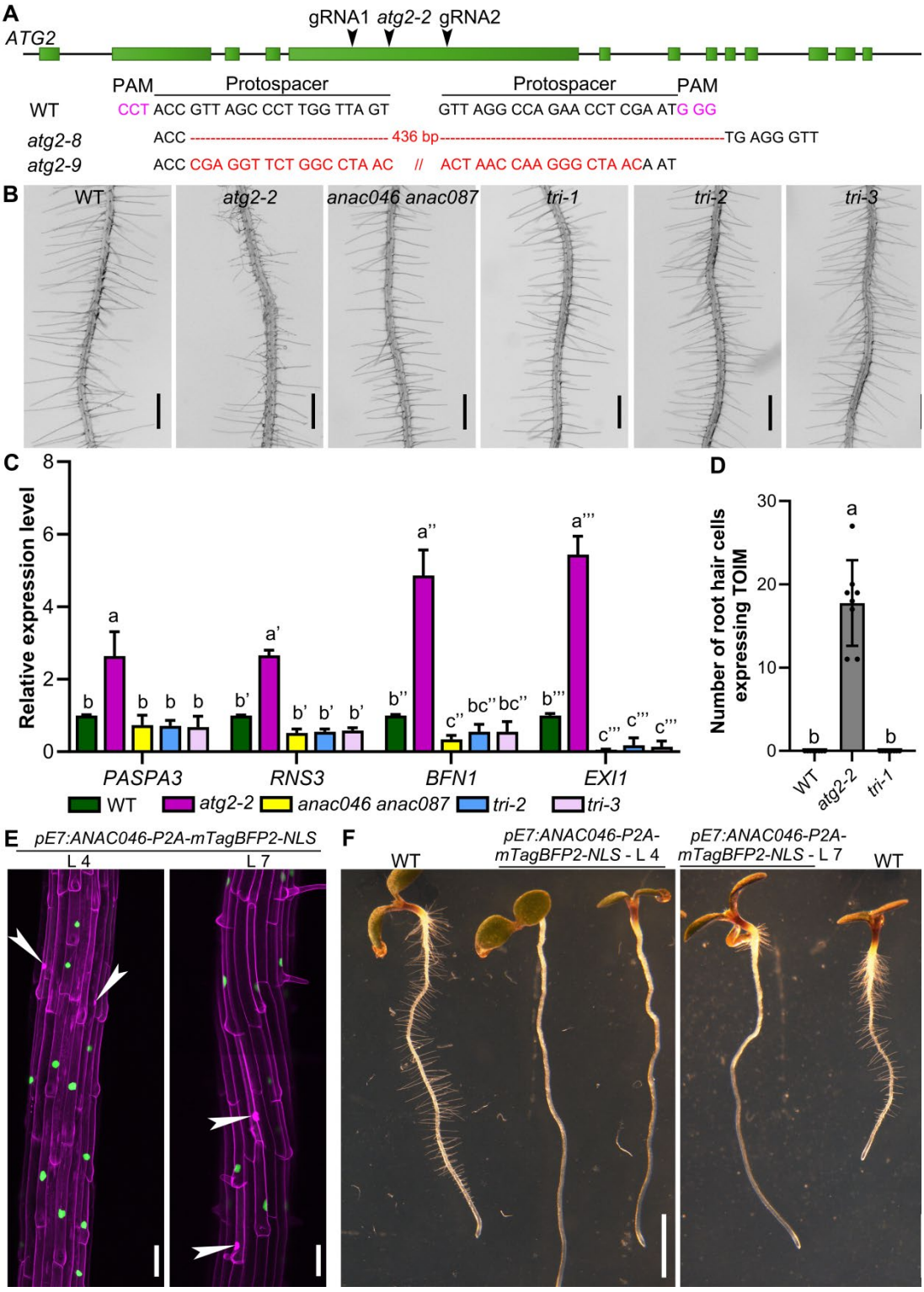

Figure 4. The premature dPCD of root hairs in *atg* mutants dependents on established dPCD gene regulatory networks. A, Schematic illustration of genomic regions of *ATG2*. The *atg2-2* mutation site and Cas9-targeting site are indicated by arrowheads on the genomic loci. Green boxes indicate exon of ATG2. PAM sequences and protospacer sequences are indicated by magenta and black letters, respectively. B, Representative primary roots from 7-day-old seedlings: WT, *atg2-2, anac046 anac087* and three triple mutant lines of *atg2-2 anac046 anac087* (*tri-1*), *atg2-8 anac046 anac087* (*tri-2*) and *atg2-9 anac046 anac087* (*tri-3*). C, Relative expression of PCD-associated genes (*PASPA3*, *RNS3*, *BFN1*,

and *EXI1*) in roots of WT, *atg2-2, anac046 anac087, tri-2* and *tri-3* by digital-droplet PCR (ddPCR) analysis. Results shown are means ± SD. Three independent biological replicates (two-three technical repeats each) were performed. Means with different letters are significantly different for each gene (two-way ANOVA, Tukey's multiple comparisons test, $P < 0.005$). D, The quantification of root hair cell expressing *PASPA3*. Results shown are means ± SD. In total, 8 roots were analyzed for each genotype. Means with different letters are significantly different (one-way ANOVA, Tukey's multiple comparisons test, $P < 0.05$). E, Representative confocal images of roots from 5-day-old seedlings expressing *pE7:ANAC046-P2A-mTagBFP2-NLS* (shown as green) pulse labeled with PI (shown as magenta). White arrowheads point the PI entry. F, Representative images of 5-day-old seedlings: WT and two lines of *pE7:ANAC046-P2A-mTagBFP2-NLS*. Bars = 500 µm for B, 50 µm for E, 2 mm for F. See also Figure S4 and S5.

Discussion

Root hairs as tubular extensions of epidermal cells can represent a substantial portion of the root system surface area (Bates and Lynch, 1996). By increasing the interface area between plant and soil with minimal biomass investment, root hairs crucially contribute to water and mineral acquisition in land plants (Duddek et al., 2023). Both the length and number of root hairs have been implicated in optimizing their function (Cai and Ahmed, 2022). Here, we investigated an additional dimension of root hair performance: their functional longevity. Prompted by the discovery of elevated autophagic activity specifically in root hair cells, we found that autophagy maintains root hair viability by delaying a senescence-induced developmental cell death program.

Root hair development from patterning of fate determination to initiation, elongation by tip growth, and maturation has been intensively studied (Cui et al., 2018). However, little is known on developmentally or environmentally controlled senescence of root hairs, and root age-related processes as a whole has received little attention (Tunc and von Wirén, 2025). In cotton, root hair life span has been determined to last about 3 weeks, depending on the soil moisture content (Xiao et al., 2020). Root hair senescence in Arabidopsis has been described to occur after 2-3 weeks, showing hallmarks of programmed cell death including protoplast retraction from the cell wall and nuclear DNA fragmentation (Li et al., 2016; Tan et al., 2016). It has been shown that root hairs of rice (Oryza sativa) and maize (Zea mays) shrink or collapse in response to reduced soil water contents (Keyes et al., 2017; Duddek et al., 2022). In Arabidopsis, senescing root hairs appear to twist and shrink, reducing less water-holding capacity in comparison with turgid root hairs (Li et al., 2016; Choi and Cho, 2019). Hence, research into the factors determining root hair longevity can reveal new angles towards optimizing plant nutrient use and drought resilience of plants.

Despite having been proposed as a model for PCD research upon stress treatments (Hogg et al., 2011), genes controlling root hair longevity and senescence-induced cell death remained unknown. Our results indicate that autophagy is a key factor to determine root hair lifespan and senescence in Arabidopsis, adding a central aspect to the physiological and developmental roles of autophagy.

Mutants of core autophagy components in Arabidopsis and maize show premature leaf senescence, but otherwise develop normally under optimal growth conditions (Marshall and

Vierstra, 2018). The involvement of autophagy in cellular pro-life and pro-death processes has been discussed controversially (Üstün et al., 2017). In particular, it has become clear that autophagy is not required for major dPCD events such as xylem biogenesis or lateral root cap turnover, despite the upregulation of autophagic activities in these contexts (Courtois-Moreau et al., 2009; Feng et al., 2022). On the contrary, autophagy in leaf senescence has to maintain cellular viability longevity through nutrient recycling, stalling cell death until nutrient mobilization has been completed (Masclaux-Daubresse et al., 2017).

The NAC transcription factors ANAC046 and ANAC087 have been implicated in leaf senescence control (Vargas-Hernández et al., 2022), controlling chlorophyll breakdown by activating known senescence promoters such as NON-YELLOW COLORING1 or STAY-GREEN1 (SGR1) and SGR2 (Oda-Yamamizo et al., 2016). In a differentiation-induced dPCD context such as the root cap, ANAC046 controls expression of dPCD signature genes BIFUNCTIONAL NUCLEASE1, EXITUS1, and RIBONUCLEASE3 (Olvera-Carrillo et al., 2015; Huysmans et al., 2018).

Similar dPCD signatures have been found in root cells during the onset of secondary growth. Interestingly, dPCD signature genes are expressed in root endodermis cells, but have not been found in epidermal root hair or non-root hair cells (Wunderling et al., 2018). As the onset of secondary growth precedes root hair cell death, it is possible that root hair cells have already died before secondary growth sets in, precluding the detection of dPCD signature genes in this context.

While it remains challenging to image root hair cells in a soil context, new techniques as synchrotron-based X-ray computed microtomography might enable us to follow root hair senescence in their natural context (Duddek et al., 2024). It is tempting to speculate that the reduction of root hairs seen in autophagy mutants would seriously compromise water and mineral acquisition in soil. If modulating root hair life span by targeting autophagy and dPCD processes would decrease the need for fertilizers and increase drought resilience, our results can point out exciting new directions in engineering these desirable trait in crop plants.

Acknowledgements

We thank Yu Yang (ZEISS Sigma 360 SEM, ZEISS Microscopy Customer Center Shanghai (ZMCCSH)) provided SEM imaging support. This research was financially supported by the Natural Science Foundation of China (32400293 to Q.F.), by the Natural Science Foundation of Shandong Province (2024HWYQ-060 to Q.F.), Tai-Shan Scholar Program of the Shandong Provincial Government (NO.tsqn202312145 to Q.F.), the European Research Council (ERC) StG PROCELLDEATH 639234 and CoG EXECUT.ER 864952 to M.K.N..

Author contributions

Q.F., M.K.N., and Y.D. analyzed the data, designed the experiments and wrote the article. Q.F. and X.W. prepared the figures. Q.F. and S.Z performed all experiments, except for the following: construction of the vectors *pE7:ATG5-mCherry*, *pIRX1:ATG5-mCherry* and obtaining of the transgenic lines and crosses of *atg* mutants with *sid2*, *coi1*, and *ein2* were done by X.W.; the introducing PCD-reporter line *pRNS3>>HA2-GFP* into *atg* mutants and the quantification of root hair cells expressing of PASPA3 in CRISPR-Cas9 based root hair specific knock out *ATG2* lines were done by Y.L.; mitochondrial leakage experiment was confirmed by J.Z.; M.K.N. performed the imaging of *pANAC046:NLS-tdTOMATO* and *pANAC087:NLS-tdTOMATO* and

imaging of *pUBQ10:TOIM* in imaging chamber.

Declaration of interests

The authors declare no competing interests.

Materials and methods

Plant materials, growth, and transformation

Arabidopsis thaliana seedlings were grown vertically on 1/2 Murashige and Skoog (MS) medium (2.15 g/L MS salts, 1 g/L sucrose, pH 5.8 [KOH], and 1% (w/v) plant agar) in day/night conditions (16 h light, 8 h dark, 21 °C) before analysis, unless stated otherwise.

The Arabidopsis thaliana *atg2-2* mutant allele (EMS, Gln803stop) was reported by (Wang et al., 2011); *atg5-1* (SAIL_129_B07) was reported by (Thompson et al., 2005); *atg7-2* (GABI_655B06) was reported by (Hofius et al., 2009), *anac046 anac087* was reported by (Huysmans et al., 2018). The Arabidopsis lines *pUBQ10::YFP-ATG8A* and *pUBQ10:TOIM* in wild type and *atg5-1* were reported by (Feng et al., 2022), the *pANAC046:NLS-tdTOMATO* and *pANAC087:NLS-tdTOMATO* were reported by (Huysmans et al., 2018). The *pPASPA3>>H2A-GFP* (Olvera-Carrillo et al., 2015), *pPASPA3:TOIM* (Fendrych et al., 2014), *pRNS3>>H2A-GFP* (Olvera-Carrillo et al., 2015), *pUBQ10:YFP-ATG8A* and *pUBQ10:COX4-GFP* (Wang et al., 2024) were introduced into *atg* mutants by cross. Arabidopsis mutant alleles *sid2-1* (Nawrath and Métraux, 1999), *coi1-2* (Huang et al., 2014), and *ein2-1* (Alonso et al., 1999) were used for intermutant crosses with either *pPASPA3:TOIM/atg2-2* or *atg5-1*. *ATG2* CRISPR lines and *ATG5* complement lines were created by stable Arabidopsis transformation using the floral dipping method described before (Clough and Bent, 1998).

Cloning

The 726 bp length fragment of pE7 and the 2946 bp length fragment of pRHD6 were amplified by PCR using p524/p525 and p4540/p4541, respectively. These purified PCR fragments were inserted into pGG-A-ccdb-B module vector via a Golden Gate reaction and obtained Golden Gate entry modules pGG-A-pE7-B and pGG-A-pRHD6-B. pGG-B-Linker-C, pGG-C-Cas9-D, pGG-D-P2A-mCherry-NLS-E, pGG-D-P2A-mTagBFP2-NLS-E, pGG-E-G7T-F, pGG-F-pATU6-26-AarI-G, were reported previously (Decaestecker et al., 2019). pGG-C-ANAC046-D and pGG-F-linker-G were obtained from the VIB-UGent plasmid repository (https://gatewayvectors.vib.be). These entry modules were assembled in pFASTRK-AG with FAST selection marker, resulting in the destination vector pFASTRK-pE7-Cas9-P2A-GFP-NLS-pATU6-26-AarI, pFASTRK-pRHD6-Cas9-P2A-GFP-NLS-pATU6-26-AarI and pFASTRK-pE7:ANAC046- P2A-mTagBFP2-NLS. The destination vector pFASTG-pUBI-Cas9 was reported previously (Decaestecker et al., 2019). Fragment gRNA1-pATU6-26-gRNA2 (ATG2 target) was amplified by PCR as described previously (Feng et al., 2022). These purified PCR fragments were inserted into pFASTR-pE7-Cas9-P2A-GFP-NLS-pATU6-26-AarI or pFASTR-pRHD6-Cas9-P2A-GFP-NLS-pATU6-26-AarI or pFASTG-pUBI-Cas9 destination vector via a Golden Gate reaction. The resulting vectors were named *pE7:Cas9;ATG2*, *pRHD6:Cas9;ATG2* and *pUBI:Cas9;ATG2*.

Gateway entry modules L4-pUBQ10-R1 and L1-ATG5-L2 were described previous (Huysmans et al., 2018; Feng et al., 2022). The fragments of mCherry, pE7 and pIRX1 were amplified by PCR using p73/p74, p508/p509 and p510/p507, respectively. The fragment of mCherry was inserted into pDONRP2R-P3 via BP reaction, resulting in entry vector, R2-mCherry-L3. The fragments of pE7 and pIRX1 were inserted into pDONRP4P1R via BP reaction, resulting in entry vector, L4-pE7-R1 and L4-pIRX1-R1. Entry vectors L1-ATG5-L2, R2-mCherry-L3 were assembled with L4-pUBQ10-R1 or L4-pE7-R1 or L4-pIRX1-R1 into pFASTGB-34GW destination vector via LR reaction and resulting in vectors *pFASTGB-pUBQ10:ATG5-mCherry*, *pFASTGB-pE7:ATG5-mCherry*, *pFASTGB-pIRX1:ATG5-mCherry*, respectively.

All primers for cloning are listed in Supplemental Table 1.

Pharmacological treatments and imaging

For the *pPASPA3>>H2A-GFP* and *pRNS3>>H2A-GFP* confocal imaging, seedlings were mounted on a glass slide in liquid 1/2 MS and imaged on the LSM710 (Zeiss) or LSM880 (Zeiss). For the *pUBQ10:COX4-GFP* confocal imaging, seedling were transferred into imaging chamber 30 min before imaging, and imaged on Nikon AX/AX R . GFP was excited by the 488-nm of the argon laser and detected between 500 and 550 nm.

pUBQ10:YFP-ATG8A seedlings were dipped into 1 µM Concanamycin A (ConA) for 8 h, then mounted on a glass side in 1/2 MS medium and imaged on SP8 (Leica). For the imaging of *pUBQ10:YFP-ATG8A* in root hair, seedlings were mounted on a glass slide in 1/2 MS medium and imaged on LSM880. YFP was excited by the 514-nm line of the argon laser and detected between 525 and 580 nm.

For the *pPASPA3:TOIM* confocal imaging, seedlings were mounted on a glass slide in 1/2 MS. For the *pUBQ10:TOIM* root hair imaging, 3-day-old seedlings were transferred into imaging chamber and kept 11 days growing, then imaged on LSM710 (Zeiss). Imaging of ToIM was performed as described before (Fendrych et al., 2014).

pANAC046:NLS-tdTOMATO and *pANAC087:NLS-tdTOMATO* were imaged as reported previously (Huysmans et al., 2018).

For the *pRHD6:Cas9;ATG2* and *pE7:Cas9;ATG2* in *pPASPA3>>H2A-GFP*, seedlings were mounted on a glass slide in 1/2 MS medium and imaged on LSM880. GFP and mCherry were detected in the different tracks. GFP was excited by the 488-nm of the argon laser and detected between 500 and 550 nm. mCherry was excited by the 561-nm and detected between 600 and 700 nm.

For root hair morphology, roots were imaged directly from petri dish using OLYMPUS SZX16. Quantification of root hair length and identity was performed as described (Huang et al., 2013). All images were processed and analyzed using Fiji (https://fiji.sc/) (Schindelin et al., 2012).

For quantification of root hair survival ratio, 14-day-old primary roots were marked every 1 cm

from the junction of hypocotyl and root to root tip. In the *atg* mutants, the area close to root tip in which root hairs start to undergo collapse was marked as stage 1, the lower area was labeled as minus 1. The corresponding position in WT was labeled the same. For each stage, root hairs were imaged using OLYMPUS SZX16. The number of normal and collapsed root hairs was counted using Fiji. The survival ratio was obtained by the number of normal root hair divided the number of total root hair.

RNA extraction and digital-droplet PCR (ddPCR)

Total RNAs were isolated using a Qiagen RNeasy plant mini kit according to the manufacturer's instructions. About 20-30 roots from 6-day-old seedlings were harvested for RNA extraction per each genotype. ddPCR was performed using the QIAcuity EG PCR Kit according to the manufacturer's instructions. Primers for PCD-associated genes were reported previously (Olvera-Carrillo et al., 2015; Huysmans et al., 2018). GAPDH was used as internal controls (Ryu et al., 2010). RNA extractions and ddPCR were performed for three biological replicates for each genotype, and two or three technical replicates were performed for each sample. The data were normalized against wild-type. All primers for ddPCR are listed in Supplemental Table 1.

Quantification and Statistical Analysis

The statistical details of experiments can be found in the corresponding figure legends. The results of statistical tests can be found in the corresponding Results section. Statistical tests were carried out using GraphPad Prism 9.0.0.

References

Agbemafle W, Wong MM, and Bassham DC. Transcriptional and post-translational regulation of plant autophagy. *J Exp Bot*. 2023:74(19): 6006-6022.

Alonso JM, Hirayama T, Roman G, Nourizadeh S, and Ecker JR. EIN2, a bifunctional transducer of ethylene and stress responses in Arabidopsis. *Science*. 1999:284(5423): 2148-2152.

Bates TR, and Lynch JP. Stimulation of root hair elongation in Arabidopsis thaliana by low phosphorus availability. 1996:19(5): 529-538.

Bollier N, Andrade Buono R, Jacobs TB, and Nowack MK. Efficient simultaneous mutagenesis of multiple genes in specific plant tissues by multiplex CRISPR. *Plant Biotechnol J*. 2021:19(4): 651-653.

Cai G, and Ahmed MA. The role of root hairs in water uptake: recent advances and future perspectives. *J Exp Bot*. 2022:73(11): 3330-3338.

Cassidy LD, and Narita M. Autophagy at the intersection of aging, senescence, and cancer. *Mol Oncol*. 2022:16(18): 3259-3275.

Cho HT, and Cosgrove DJ. Regulation of root hair initiation and expansin gene expression in Arabidopsis. *Plant Cell*. 2002:14(12): 3237-3253.

Choi HS, and Cho HT. Root hairs enhance Arabidopsis seedling survival upon soil disruption. *Sci Rep*. 2019:9(1): 11181.

Clough SJ, and Bent AF. Floral dip: a simplified method for Agrobacterium-mediated transformation of

Arabidopsis thaliana. *Plant J*. 1998:16(6): 735-743.

Courtois-Moreau CL, Pesquet E, Sjödin A, Muñiz L, Bollhöner B, Kaneda M, Samuels L, Jansson S, and Tuominen H. A unique program for cell death in xylem fibers of Populus stem. *Plant J*. 2009:58(2): 260-274.

Cui S, Suzaki T, Tominaga-Wada R, and Yoshida S. Regulation and functional diversification of root hairs. *Semin Cell Dev Biol*. 2018:83: 115-122.

Daneva A, Gao Z, Van Durme M, and Nowack MK. Functions and Regulation of Programmed Cell Death in Plant Development. *Annu Rev Cell Dev Biol*. 2016:32: 441-468.

Decaestecker W, Buono RA, Pfeiffer ML, Vangheluwe N, Jourquin J, Karimi M, Van Isterdael G, Beeckman T, Nowack MK, and Jacobs TB. CRISPR-TSKO: A Technique for Efficient Mutagenesis in Specific Cell Types, Tissues, or Organs in Arabidopsis. *Plant Cell*. 2019:31(12): 2868-2887.

Denyer T, Ma X, Klesen S, Scacchi E, Nieselt K, and Timmermans MCP. Spatiotemporal Developmental Trajectories in the Arabidopsis Root Revealed Using High-Throughput Single-Cell RNA Sequencing. *Dev Cell*. 2019:48(6): 840-852.e845.

Doll NM, Van Hautegem T, Schilling N, De Rycke R, De Winter F, Fendrych M, and Nowack MK. Endosperm cell death promoted by NAC transcription factors facilitates embryo invasion in Arabidopsis. *Curr Biol*. 2023:33(17): 3785-3795 e3786.

Duddek P, Papritz A, Ahmed MA, Lovric G, and Carminati A. Observations of root hair patterning in soils: Insights from synchrotron-based X-ray computed microtomography. *Plant and Soil*. 2024:503(1): 331-348.

Duddek P, Ahmed MA, Javaux M, Vanderborght J, Lovric G, King A, and Carminati A. The effect of root hairs on root water uptake is determined by root-soil contact and root hair shrinkage. *New Phytol*. 2023:240(6): 2484-2497.

Duddek P, Carminati A, Koebernick N, Ohmann L, Lovric G, Delzon S, Rodriguez-Dominguez CM, King A, and Ahmed MA. The impact of drought-induced root and root hair shrinkage on root-soil contact. *Plant Physiol*. 2022:189(3): 1232-1236.

Escamez S, Andre D, Zhang B, Bollhoner B, Pesquet E, and Tuominen H. METACASPASE9 modulates autophagy to confine cell death to the target cells during Arabidopsis vascular xylem differentiation. *Biol Open*. 2016:5(2): 122-129.

Escamez S, Stael S, Vainonen JP, Willems P, Jin H, Kimura S, Van Breusegem F, Gevaert K, Wrzaczek M, and Tuominen H. Extracellular peptide Kratos restricts cell death during vascular development and stress in Arabidopsis. *J Exp Bot*. 2019:70(7): 2199-2210.

Fendrych M, Van Hautegem T, Van Durme M, Olvera-Carrillo Y, Huysmans M, Karimi M, Lippens S, Guerin CJ, Krebs M, Schumacher K, et al. Programmed cell death controlled by ANAC033/SOMBRERO determines root cap organ size in Arabidopsis. *Curr Biol*. 2014:24(9): 931-940.

Feng Q, De Rycke R, Dagdas Y, and Nowack MK. Autophagy promotes programmed cell death and corpse clearance in specific cell types of the Arabidopsis root cap. *Curr Biol*. 2022:32(9): 2110-2119.

Galluzzi L, Vitale I, Aaronson SA, Abrams JM, Adam D, Agostinis P, Alnemri ES, Altucci L, Amelio I, Andrews DW, et al. Molecular mechanisms of cell death: recommendations of the Nomenclature Committee on Cell Death 2018. *Cell Death Differ*. 2018:25(3): 486-541.

Gao Z, Daneva A, Salanenka Y, Van Durme M, Huysmans M, Lin Z, De Winter F, Vanneste S, Karimi M, Van de Velde J, et al. KIRA1 and ORESARA1 terminate flower receptivity by promoting cell death in the stigma of Arabidopsis. *Nat Plants*. 2018:4(6): 365-375.

Gilroy S, and Jones DL. Through form to function: root hair development and nutrient uptake. *Trends*

Plant Sci. 2000:5(2): 56-60.

Goh T, Sakamoto K, Wang P, Kozono S, Ueno K, Miyashima S, Toyokura K, Fukaki H, Kang BH, and Nakajima K. Autophagy promotes organelle clearance and organized cell separation of living root cap cells in Arabidopsis thaliana. *Development*. 2022:149(11).

Grierson C, Nielsen E, Ketelaarc T, and Schiefelbein J. Root hairs. *Arabidopsis Book*. 2014:12: e0172.

Gross AS, Raffeiner M, Zeng Y, Üstün S, and Dagdas Y. Autophagy in Plant Health and Disease. *Annu Rev Plant Biol*. 2025.

Hofius D, Schultz-Larsen T, Joensen J, Tsitsigiannis DI, Petersen NH, Mattsson O, Jorgensen LB, Jones JD, Mundy J, and Petersen M. Autophagic components contribute to hypersensitive cell death in Arabidopsis. *Cell*. 2009:137(4): 773-783.

Hogg BV, Kacprzyk J, Molony EM, O'Reilly C, Gallagher TF, Gallois P, and McCabe PF. An in vivo root hair assay for determining rates of apoptotic-like programmed cell death in plants. *Plant Methods*. 2011:7(1): 45.

Honkanen S, and Dolan L. Growth regulation in tip-growing cells that develop on the epidermis. *Curr Opin Plant Biol*. 2016:34: 77-83.

Huang H, Wang C, Tian H, Sun Y, Xie D, and Song S. Amino acid substitutions of GLY98, LEU245 and GLU543 in COI1 distinctively affect jasmonate-regulated male fertility in Arabidopsis. *Sci China Life Sci*. 2014:57(1): 145-154.

Huysmans M, Buono RA, Skorzinski N, Radio MC, De Winter F, Parizot B, Mertens J, Karimi M, Fendrych M, and Nowack MK. NAC Transcription Factors ANAC087 and ANAC046 Control Distinct Aspects of Programmed Cell Death in the Arabidopsis Columella and Lateral Root Cap. *Plant Cell*. 2018:30(9): 2197-2213.

Kacprzyk J, Burke R, Armengot L, Coppola M, Tattrie SB, Vahldick H, Bassham DC, Bosch M, Brereton NJB, Cacas JL, et al. Roadmap for the next decade of plant programmed cell death research. *New Phytol*. 2024:242(5): 1865-1875.

Keyes SD, Zygalakis KC, and Roose T. An Explicit Structural Model of Root Hair and Soil Interactions Parameterised by Synchrotron X-ray Computed Tomography. *Bull Math Biol*. 2017:79(12): 2785-2813.

Kim HJ, Hong SH, Kim YW, Lee IH, Jun JH, Phee BK, Rupak T, Jeong H, Lee Y, Hong BS, et al. Gene regulatory cascade of senescence-associated NAC transcription factors activated by ETHYLENE-INSENSITIVE2-mediated leaf senescence signalling in Arabidopsis. *J Exp Bot*. 2014:65(14): 4023-4036.

Kubo M, Udagawa M, Nishikubo N, Horiguchi G, Yamaguchi M, Ito J, Mimura T, Fukuda H, and Demura T. Transcription switches for protoxylem and metaxylem vessel formation. *Genes Dev*. 2005:19(16): 1855-1860.

Kwon SI, Cho HJ, Jung JH, Yoshimoto K, Shirasu K, and Park OK. The Rab GTPase RabG3b functions in autophagy and contributes to tracheary element differentiation in Arabidopsis. *Plant J*. 2010:64(1): 151-164.

Li E, Zhang YL, Qin Z, Xu M, Qiao Q, Li S, Li SW, and Zhang Y. Signaling network controlling ROP-mediated tip growth in Arabidopsis and beyond. *Plant Commun*. 2023:4(1): 100451.

Li L, Tan K, Tang XG, Chao XT, Wen CX, D. BZ, Feng HL, Liu WZ, and Su H. Characterization of Programmed Cell Death During the Senescence of Root Hairs in Arabidopsis. 2016:51(2): 194-201.

Liao CY, Wang P, Yin Y, and Bassham DC. Interactions between autophagy and phytohormone signaling pathways in plants. *FEBS Lett*. 2022:596(17): 2198-2214.

Liu Y, Schiff M, Czymmek K, Talloczy Z, Levine B, and Dinesh-Kumar SP. Autophagy regulates programmed cell death during the plant innate immune response. *Cell*. 2005:121(4): 567-577.

Marshall RS, and Vierstra RD. Autophagy: The Master of Bulk and Selective Recycling. *Annu Rev Plant Biol*. 2018:69: 173-208.

Masclaux-Daubresse C, Chen Q, and Havé M. Regulation of nutrient recycling via autophagy. *Curr Opin Plant Biol*. 2017:39: 8-17.

Menand B, Yi K, Jouannic S, Hoffmann L, Ryan E, Linstead P, Schaefer DG, and Dolan L. An ancient mechanism controls the development of cells with a rooting function in land plants. *Science*. 2007:316(5830): 1477-1480.

Nawrath C, and Métraux JP. Salicylic acid induction-deficient mutants of Arabidopsis express PR-2 and PR-5 and accumulate high levels of camalexin after pathogen inoculation. *Plant Cell*. 1999:11(8): 1393-1404.

Oda-Yamamizo C, Mitsuda N, Sakamoto S, Ogawa D, Ohme-Takagi M, and Ohmiya A. The NAC transcription factor ANAC046 is a positive regulator of chlorophyll degradation and senescence in Arabidopsis leaves. *Sci Rep*. 2016:6: 23609.

Ohashi-Ito K, Oda Y, and Fukuda H. Arabidopsis VASCULAR-RELATED NAC-DOMAIN6 directly regulates the genes that govern programmed cell death and secondary wall formation during xylem differentiation. *Plant Cell*. 2010:22(10): 3461-3473.

Olvera-Carrillo Y, Van Bel M, Van Hautegem T, Fendrych M, Huysmans M, Simaskova M, van Durme M, Buscaill P, Rivas S, Coll NS, et al. A Conserved Core of Programmed Cell Death Indicator Genes Discriminates Developmentally and Environmentally Induced Programmed Cell Death in Plants. *Plant Physiol*. 2015:169(4): 2684-2699.

Ryu MY, Cho SK, and Kim WT. The Arabidopsis C3H2C3-type RING E3 ubiquitin ligase AtAIRP1 is a positive regulator of an abscisic acid-dependent response to drought stress. *Plant Physiol*. 2010:154(4): 1983-1997.

Schindelin J, Arganda-Carreras I, Frise E, Kaynig V, Longair M, Pietzsch T, Preibisch S, Rueden C, Saalfeld S, Schmid B, et al. Fiji: an open-source platform for biological-image analysis. *Nat Methods*. 2012:9(7): 676-682.

Shishkova S, and Dubrovsky JG. Developmental programmed cell death in primary roots of Sonoran Desert Cactaceae. *Am J Bot*. 2005:92(9): 1590-1594.

Tan K, Wen C, Feng H, Chao X, and Su H. Nuclear dynamics and programmed cell death in Arabidopsis root hairs. *Plant Sci*. 2016:253: 77-85.

Taylor NG, Laurie S, and Turner SR. Multiple cellulose synthase catalytic subunits are required for cellulose synthesis in Arabidopsis. *Plant Cell*. 2000:12(12): 2529-2540.

Teper-Bamnolker P, Danieli R, Peled-Zehavi H, Belausov E, Abu-Abied M, Avin-Wittenberg T, Sadot E, and Eshel D. Vacuolar processing enzyme translocates to the vacuole through the autophagy pathway to induce programmed cell death. *Autophagy*. 2021:17(10): 3109-3123.

Thompson AR, Doelling JH, Suttangkakul A, and Vierstra RD. Autophagic nutrient recycling in Arabidopsis directed by the ATG8 and ATG12 conjugation pathways. *Plant Physiol*. 2005:138(4): 2097-2110.

Tunc CE, and von Wirén N. Hidden aging: the secret role of root senescence. *Trends in plant science*. 2025.

Turner SR, and Somerville CR. Collapsed xylem phenotype of Arabidopsis identifies mutants deficient in cellulose deposition in the secondary cell wall. *Plant Cell*. 1997:9(5): 689-701.

Üstün S, Hafrén A, and Hofius D. Autophagy as a mediator of life and death in plants. *Curr Opin Plant*

Biol. 2017:40: 122-130.

Vargas-Hernández BY, Núñez-Muñoz L, Calderón-Pérez B, Xoconostle-Cázares B, and Ruiz-Medrano R. The NAC Transcription Factor ANAC087 Induces Aerial Rosette Development and Leaf Senescence in Arabidopsis. *Front Plant Sci*. 2022:13: 818107.

Vissenberg K, Claeijs N, Balcerowicz D, and Schoenaers S. Hormonal regulation of root hair growth and responses to the environment in Arabidopsis. *J Exp Bot*. 2020:71(8): 2412-2427.

Wang J, Bollier N, Buono RA, Vahldick H, Lin Z, Feng Q, Hudecek R, Jiang Q, Mylle E, Van Damme D, et al. A developmentally controlled cellular decompartmentalization process executes programmed cell death in the Arabidopsis root cap. *Plant Cell*. 2024:36(4): 941-962.

Wang Y, Nishimura MT, Zhao T, and Tang D. ATG2, an autophagy-related protein, negatively affects powdery mildew resistance and mildew-induced cell death in Arabidopsis. *Plant J*. 2011:68(1): 74-87.

Wendrich JR, Yang B, Vandamme N, Verstaen K, Smet W, Van de Velde C, Minne M, Wybouw B, Mor E, Arents HE, et al. Vascular transcription factors guide plant epidermal responses to limiting phosphate conditions. *Science*. 2020:370(6518).

Won SK, Lee YJ, Lee HY, Heo YK, Cho M, and Cho HT. Cis-element- and transcriptome-based screening of root hair-specific genes and their functional characterization in Arabidopsis. *Plant Physiol*. 2009:150(3): 1459-1473.

Woo HR, Kim HJ, Lim PO, and Nam HG. Leaf Senescence: Systems and Dynamics Aspects. *Annu Rev Plant Biol*. 2019:70: 347-376.

Wunderling A, Ripper D, Barra-Jimenez A, Mahn S, Sajak K, Targem MB, and Ragni L. A molecular framework to study periderm formation in Arabidopsis. *New Phytol*. 2018:219(1): 216-229.

Xiao S, Liu L, Zhang Y, Sun H, Zhang K, Bai Z, Dong H, and Li C. Fine root and root hair morphology of cotton under drought stress revealed with RhizoPot. 2020:206(6): 679-693.

Yoshimoto K, Jikumaru Y, Kamiya Y, Kusano M, Consonni C, Panstruga R, Ohsumi Y, and Shirasu K. Autophagy negatively regulates cell death by controlling NPR1-dependent salicylic acid signaling during senescence and the innate immune response in Arabidopsis. *Plant Cell*. 2009:21(9): 2914-2927.

Zhang X, Bian A, Li T, Ren L, Li L, Su Y, and Zhang Q. ROS and calcium oscillations are required for polarized root hair growth. *Plant Signal Behav*. 2022:17(1): 2106410.

Supplemental data

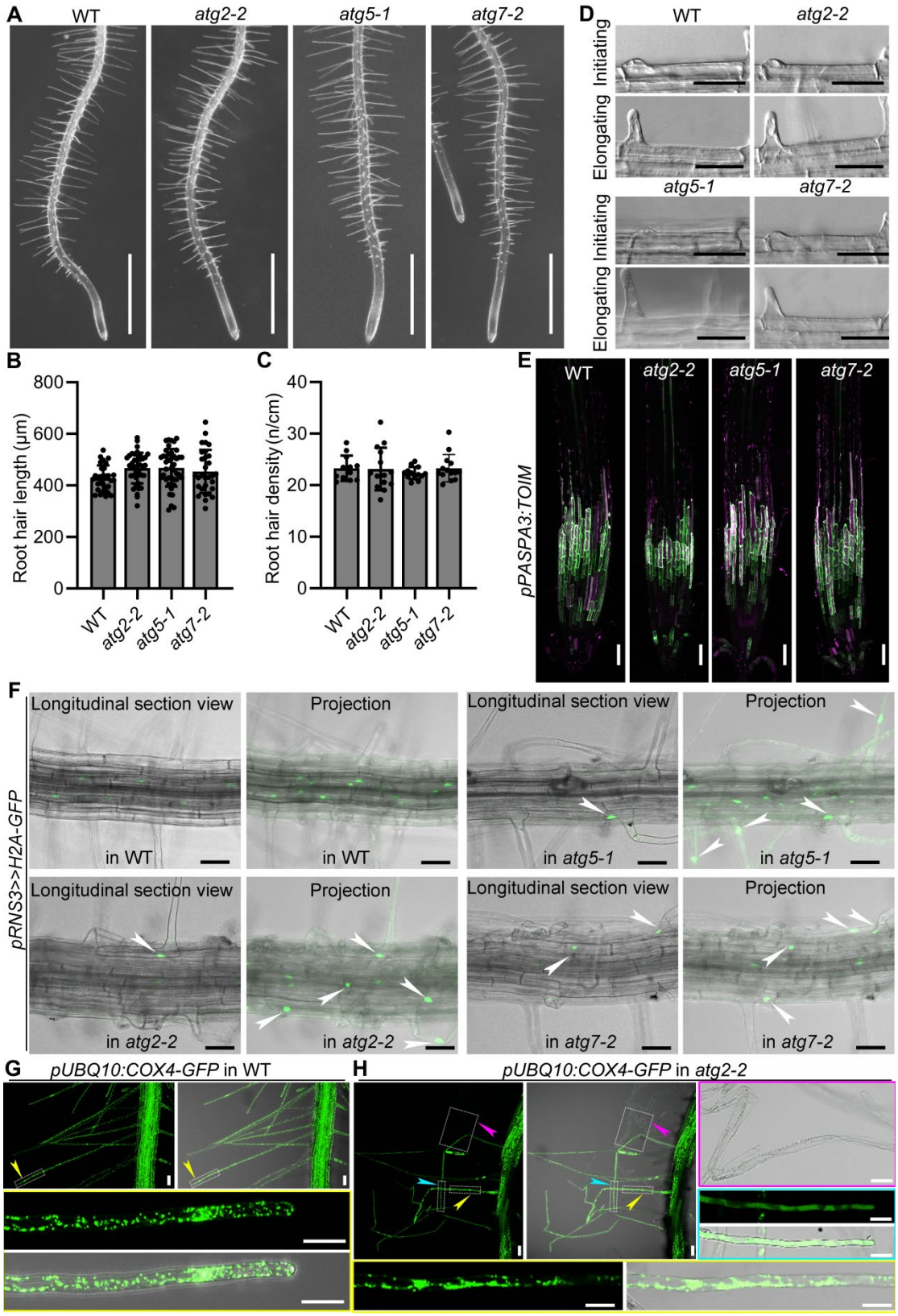

Supplemental Figure 1. Root hair development and marker gene expression in the wild-type (WT) and *atg* mutants. A, Representative primary roots from 5-day-old seedling: WT, *atg2-2*, *atg5-1* and *atg7-2*

seedlings. B-C, The quantification of root hair length (B) or intensity (C) of WT and *atg* mutants. Results shown are means ± standard deviation (SD). Three independent experiments involving 30-42 roots were performed (one-way ANOVA, Tukey's multiple comparisons test, $P > 0.05$). D, Differential interference contrast images of initiating (upper panel) or elongating (lower panel) root hairs from WT and *atg* mutants. E, The *pPASPA3:TOIM* marker showed expression and cell death in the distal and proximal root cap cells and xylem of the *atg* mutants, similar to WT. The eGFP signal is shown in green in the cytoplasm, whereas the mRFP signal is shown in magenta in the vacuole. Merge of both signals indicates vacuolar collapse, a hallmark of cell death. F, Representative confocal images of *pRNS3>>H2A-GFP* signals in 5-day-old WT, *atg2-2*, *atg5-1* and *atg7-2*. White arrowheads indicate that H2A-GFP signals were observed in root hair cells of *atg* mutants. G, Representative confocal images of mitochondria matrix marker *pUBQ10:COX4-GFP* signals in 6-day-old seedlings from WT and *atg2-2*. The zoomed images are shown of a part region of outlined in white dotted lines. Different colored arrowheads indicate different types of root hairs of *atg2-2* mutants. Magenta arrowheads indicate the dead root hairs. Cyan arrowhead indicate the dying root hairs. Yellow arrowheads indicate the living root hairs. Images are shown in z-projection, except the zoomed images in different color lined boxes. Bars = 100 mm for A, 50 µm for D, E, F and G, 20 µm for the zoomed images in G. Related to Figure 2.

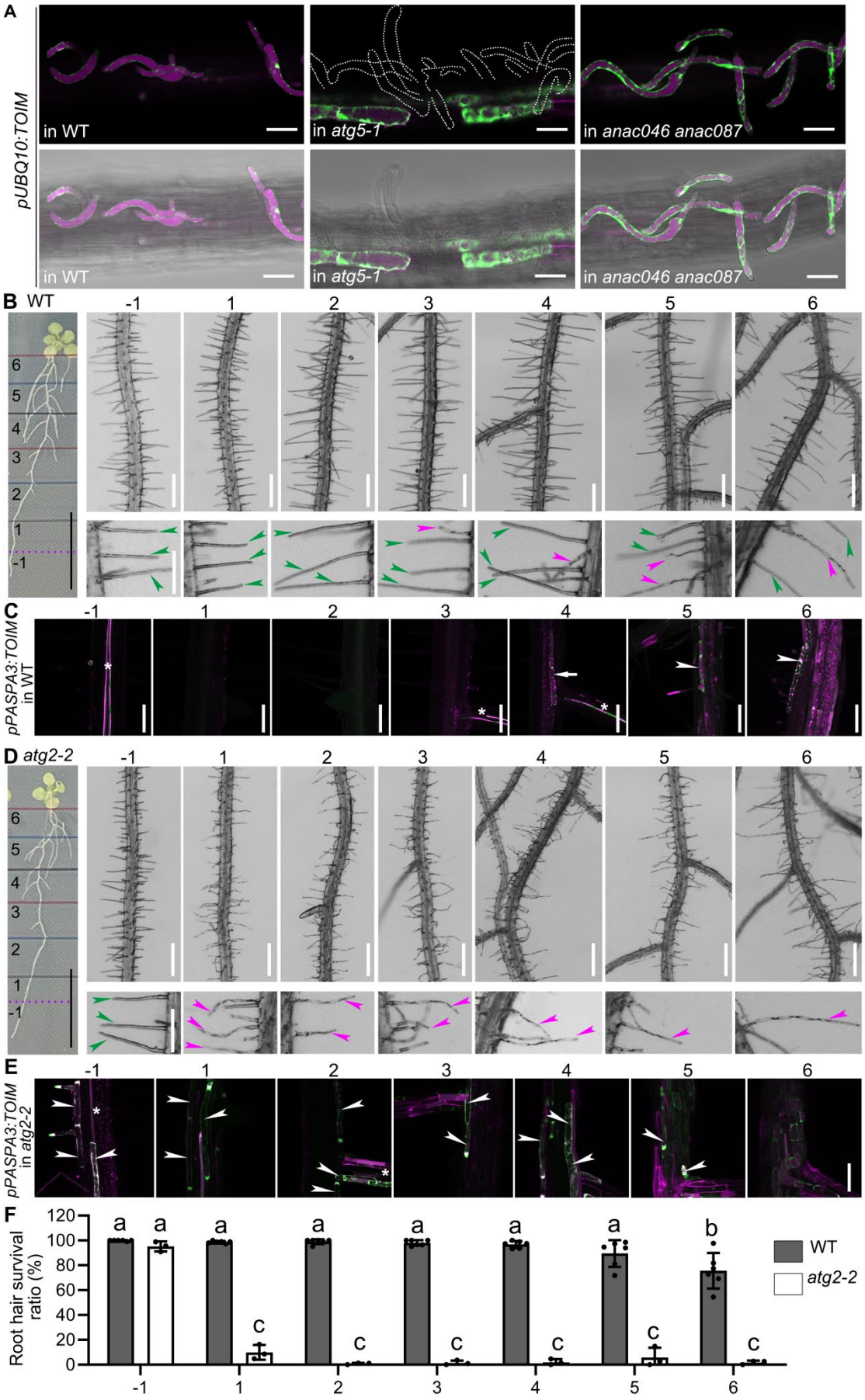

Supplemental Figure 2. *atg* mutants show earlier root hair cell death than the wild type. A, *pUBQ10:TOIM* expression in WT, *atg5-1* and *anac046 anac087* was imaged in the growing chamber. Root hair cells close to first emerged lateral root in 14-day-old seedlings were imaged. *atg5-1* mutant shows premature root hair cell death compared with WT. EGFP signal is shown in green in the cytoplasm, and mRFP signal is shown in magenta in the vacuole. Bars = 50 µm.

B and D, Illustration of a 14-day-old seedling showing the positions corresponding to the different stages (left panel of B and D). Roots at different positions of the root corresponding to from stages -1 to 6 are shown on the right. Lower panel shows a zoomed image of a part region of the upper panel. Green arrowheads indicate living root hair, while magenta arrowheads indicate the dead root hair. Bars = 1.5 cm for left panel, 500 µm for upper panel and 250 µm for lower panel. C and E, Representative confocal images of roots from 14-day-old WT (C) and *atg* mutants (E) expressing *pPASPA3:TOIM*. White arrowheads indicate that TOIM signals were observed in root hair cells. White arrows indicate that TOIM signals were observed in cortex cells suggesting the periderm growth. White asterisks indicate TOIM signals were observed in xylem cells. Bars = 100 µm. F, The quantification of root hair survival ratio. Results shown are means ± SD. At least three independent experiments involving 400-550 root hairs were performed. Means with different letters are significantly different (two-way ANOVA, Tukey's multiple comparisons test, $P < 0.05$). Related to Figure 2.

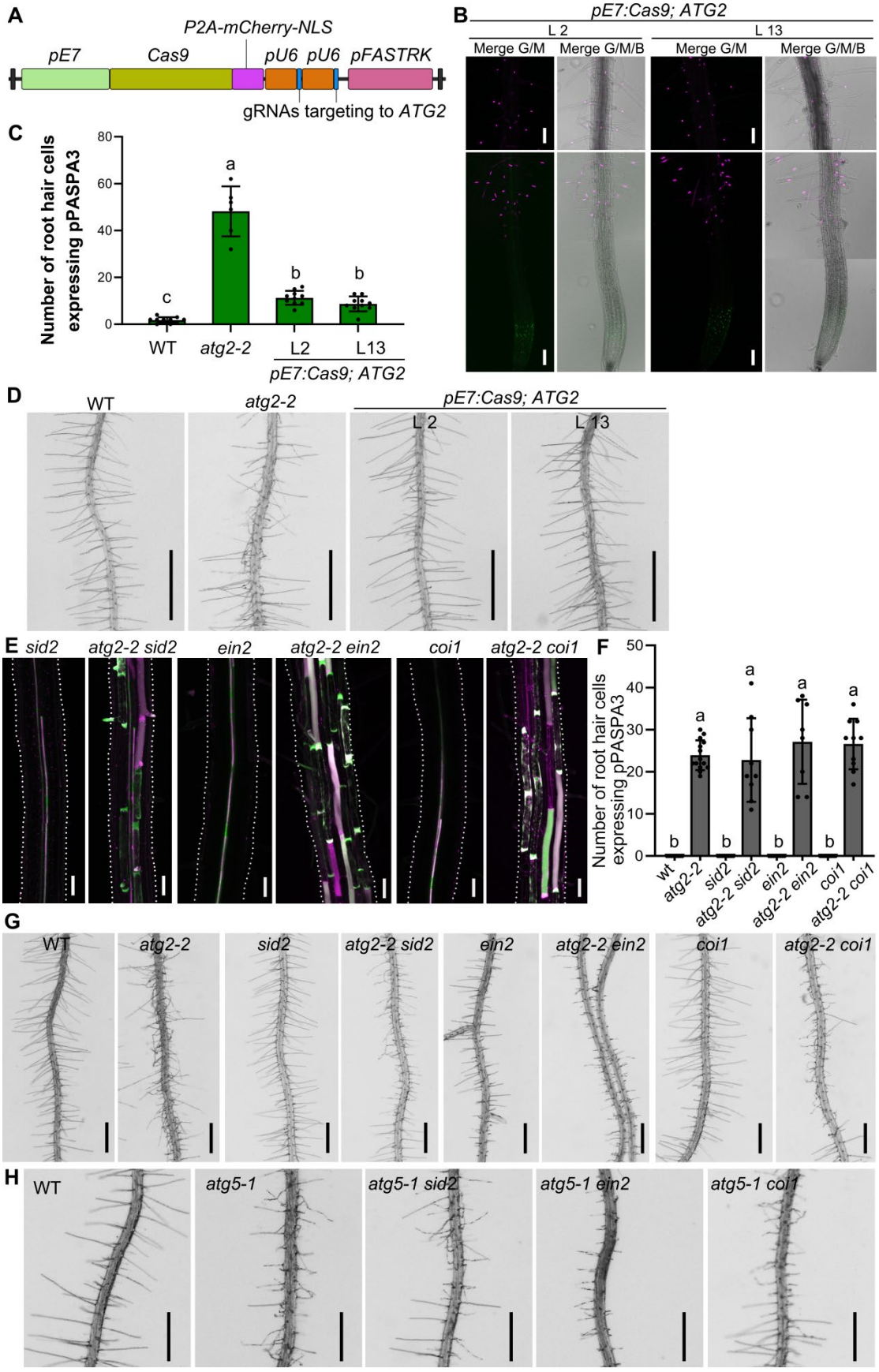

Supplemental Figure 3. Root hair-specific knock out *ATG2*, and independency of the premature root hair phenotype in *atg2* and *atg5* from SA, JA and ethylene signaling. A, Schematic representation of

the vector: *pE7:Cas9;ATG2.* The Cas9-P2A-mCherry is driven by root hair specific promoter pE7, and two gRNAs targeting to *ATG2* are inserted. B, Representative confocal images of two independent lines of *pE7:Cas9;ATG2* in *pPASPA3>>H2A-GFP* background. C, The quantification of root hair cell expressing *PASPA3*. Results shown are means ± SD. In total, 6-10 roots were analyzed for each genotype. Means with different letters are significantly different (one-way ANOVA, Tukey's multiple comparisons test, $P < 0.05$). D, Representative primary roots from 7-day-old seedlings: WT, *atg2-2* and two independent lines of *pE7:Cas9; ATG2*. E, Representative confocal images of roots from 5-day-old seedlings expressing *pPASPA3:TOIM*: *sid2*, *atg2-2 sid2, ein2*, *atg2-2 ein2*, *coi1* and *atg2-2 coi1*. White dotted lines point the profile of root. F, The quantification of root hair cell expressing *PASPA3*. Results shown are means ± SD. In total, 8-14 roots were analyzed for each genotype. Means with different letters are significantly different (one-way ANOVA, Tukey's multiple comparisons test, $P < 0.05$). G, Representative primary roots from 7-day-old seedlings: WT, *atg2-2*, *sid2*, *atg2-2 sid2, ein2*, *atg2-2 ein2*, *coi1* and *atg2-2 coi1*. H, Representative primary roots from 7-day-old seedlings: WT, *atg5-1*, *atg5-1 sid2*, *atg5-1 ein2* and *atg5-1 coi1*. Bars = 100 µm for B, 1 mm for D, 50 µm for E, 500 µm for G and H. Related to Figure 3.

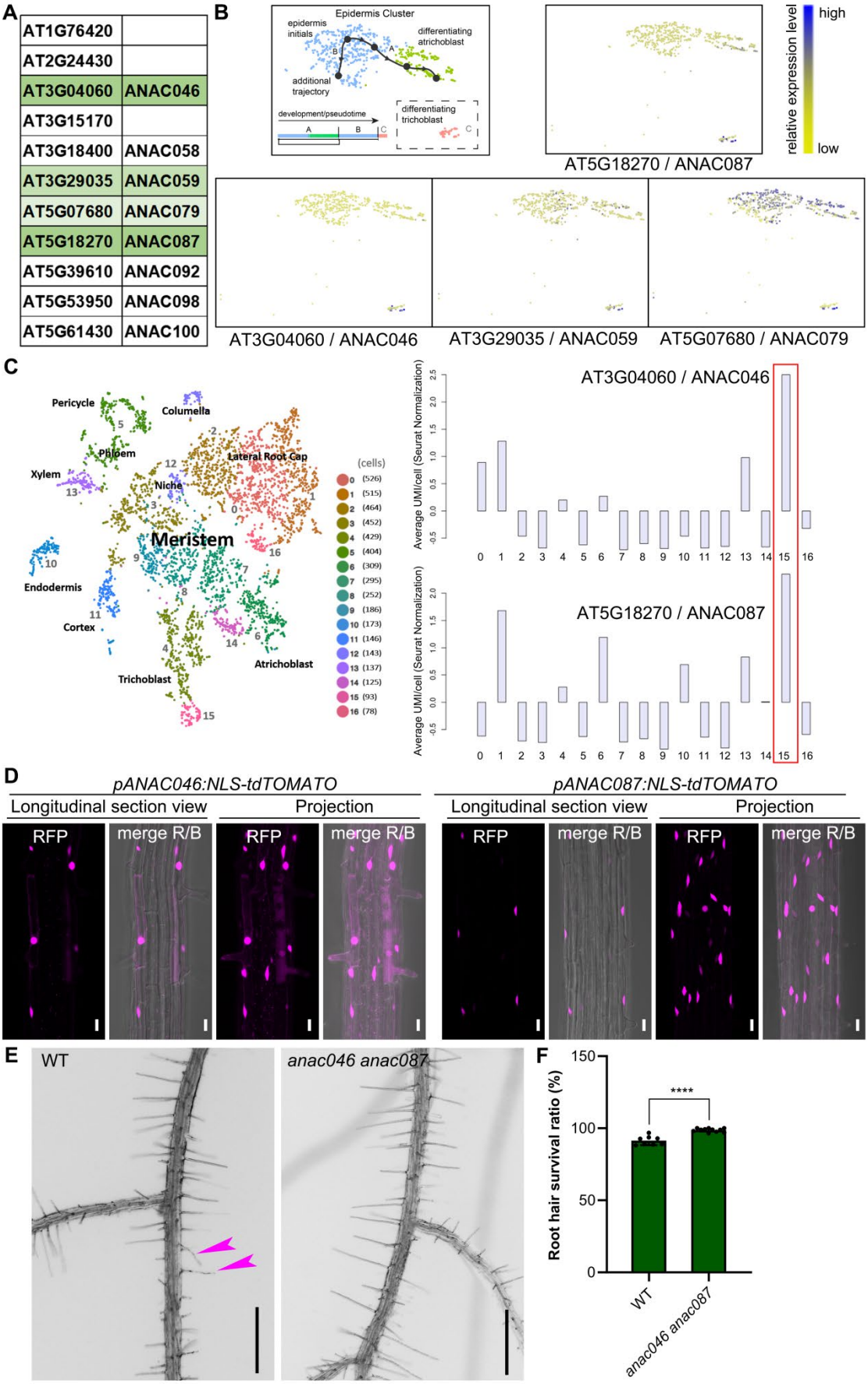

Supplemental Figure 4. Expression analysis of *ANAC046* and *ANAC087* and root hair longevity analysis of *anac046 anac087* mutants. A, ANAC046 family members via PLAZA blast. Green color high light indicate which is detected in sc-RNAseq data, shown as in B. B, Expression pattern of *ANAC046*, *ANAC059*, *ANAC079* and *ANAC087* in epidermis cluster in published sc-RNAseq dataset (Plant sc-Atlas (ugent.be)). C, Expression pattern of *ANAC046* and *ANAC087* in published sc-RNAseq dataset (zmbp-resources.uni-tuebingen.de/timmermans/plant-single-cell-browser/). Red box indicates root hair cluster. D, Representative confocal images of roots from 5-day-old seedlings expressing *pANAC046:NLS-tdTOMATO and pANAC087:NLS-tdTOMATO.* Merges of the RFP/bright field (R/B) are shown at the right. TdTOMATO is shown in magenta. Bars = 20 µm.

E, Representative primary roots from 14-day-old seedlings close to hypocotyl: WT and *anac046 anac087*. Magenta arrowheads indicate the collapsed root hair. Bars = 500 µm. F, The quantification of root hair survival ratio. Results shown are means ± SD. In total, 4000-5300 root hairs from at least 8 roots were analyzed for each genotype. **** indicates a significant difference (t test, $P < 0.0001$). Related to Figure 4.

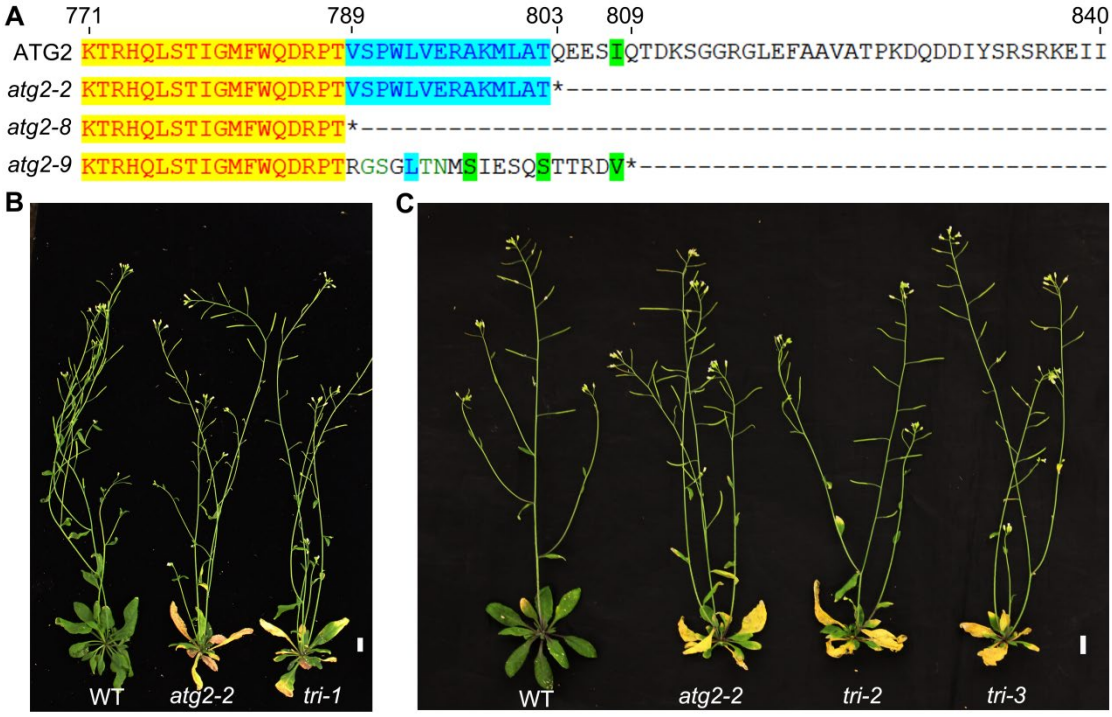

Supplemental Figure 5. Amino acid sequence alignment of *atg2* mutants, and leaf senescence analysis of *atg2-2* versus triple mutants of *atg2 anac046 anac087*. A, Partial amino acid (aa) sequence of ATG2 and the mutants. *atg2-2* has early stop codon at 803 aa. *atg2-8* has early stop codon at 789 aa. While *atg2-9* has different aa from 789 aa on and has early stop codon at 809 aa. B-C, Representative images from 5-week-old plants: WT, *atg2-2*, *tri-1* (*atg2-2 anac046 anac087*), *tri-2* (*atg2-8 anac046 anac087*), *tri-3* (*atg2-9 anac046 anac087*). Bars = 1 cm. Related to Figure 4.

Supplemental table 1. Primers were used in this paper.

Cloning	pEXP7	P524	aagcttGGTCTCAACCTAgagagcgcccggtttg
		P525	GAATTCGGTCTCATGTTtctagcctctttttctttattcttagg
	pRHD6	P4540	aagcttGGTCTCAACCTctcaaagagggacaagaccaaag
		P4541	GAATTCGGTCTCATGTTtagacactaataagtttgataagtgatttttgt
	pEXP7	P508	GGGGACAACTTTGTATAGAAAAGTTGCCAgagagcgcccggtttg
		P509	GGGGACTGCTTTTTTGTACAAACTTGCtctagcctctttttctttattcttagg
	pIRX1	P510	GGGGACAACTTTGTATAGAAAAGTTGCCcagaggaaactcagatgtgatga
		P507	GGGGACTGCTTTTTTGTACAAACTTGCcttcgaattcccctgtttgga
	mCherry	P73	GGGGACAGCTTTCTTGTACAAAGTGGCCATGGTGAGCAAGGGCGAG
		P74	GGGGACAACTTTGTATAATAAAGTTGCTTACTTGTACAGCTCGTCCATGC
ddPCR	RNS3	P5300	GGTTTGCTCCGGGCATTGAA
		P5301	CGACCATGCGGCATAACAGG
	EXI1	P5302	AGGCGGAGTTGGTTGTGGAA
		P5303	CAGCCATTTCGTCAGTCGCC
	BFN1	P5304	TTAGAAGCCGGACCAGCACA
		P5305	TGGTCAGGCCACACACACAA
	PSAPA3	P5306	AGCTCAGGAGGATCCGAAGAA
		P5307	GCTCAGCAGCATAAGCGAGT
	GAPDH	ZP687	TGAAATCAAAAAGCTATCAAGG
		ZP688	CATCATCCTCGGTGTATCCAA

6.7. The autophagy and immune trafficking are negatively regulated by RAB3GAPL in plants

Autophagy and membrane trafficking play pivotal roles in plant stress adaptation and immunity, but their regulatory mechanisms remain incompletely characterized. The study detailed in **Chapter 6.8** (Yuen et al., 2024) identifies Rab3GAPL, a Rab GTPase-activating protein, as a negative regulator of autophagy and immune trafficking in plants. By combining AI-assisted structural predictions with functional assays, this study demonstrates that Rab3GAPL interacts with the autophagy adaptor ATG8 through a conserved AIM motif and suppresses autophagosome formation by deactivating the small GTPase Rab8a.

The research reveals that Rab3GAPL acts as a molecular rheostat, balancing autophagy and immune responses. Overexpression of Rab3GAPL inhibits autophagic flux and disrupts Rab8a-mediated defense secretion, increasing susceptibility to *Phytophthora infestans*. Conversely, silencing Rab3GAPL enhances autophagy and pathogen resistance. These findings uncover a critical regulatory node linking membrane trafficking and autophagy, with implications for engineering stress-resilient crops. The conserved nature of this mechanism across land plants underscores its evolutionary importance in plant-pathogen interactions.

6.8. Appendix Manuscript 4: “A RabGAP negatively regulates plant autophagy and immune trafficking”

Authors: Enoch Lok Him Yuen, Alexandre Y. Leary, Marion Clavel, Yasin Tumtas, Azadeh Mohseni, **Jierui Zhao**, Lorenzo Picchianti, Mostafa Jamshidiha, Pooja Pandey, Cian Duggan, Ernesto Cota, Yasin Dagdas, Tolga O. Bozkurt

Contribution: For this manuscript, I performed confocal experiments and statstical analysis of Figure S3.

Status: This manuscript was published in Current Biology (volume 34, issue 10) on May 20, 2024.

DOI: https://doi.org/10.1016/j.cub.2024.04.002

Article

Current Biology

A RabGAP negatively regulates plant autophagy and immune trafficking

Highlights

- Rab3GAPL binds the core autophagic adaptor ATG8CL through a canonical AIM in plants
- Rab3GAPL functions as a molecular rheostat in adjusting both autophagy and immunity
- Rab3GAPL negatively regulates autophagy and immunity by limiting Rab8a trafficking
- The interplay between Rab3GAPL and Rab8a controls defense secretion upon infection

Authors

Enoch Lok Him Yuen, Alexandre Y. Leary, Marion Clavel, ..., Ernesto Cota, Yasin Dagdas, Tolga O. Bozkurt

Correspondence

yasin.dagdas@gmi.oeaw.ac.at (Y.D.), o.bozkurt@imperial.ac.uk (T.O.B.)

In brief

Yuen et al. reveal the negative regulatory role of Rab3GAPL in plant autophagy and immunity, where it acts as a rheostat, modulating membrane trafficking. Rab3GAPL controls autophagy by binding ATG8 and regulating Rab8a. Independent of its interaction with ATG8, Rab3GAPL also suppresses defense secretion mediated by Rab8a during pathogen infection.

Yuen et al., 2024, Current Biology *34*, 2049–2065
May 20, 2024
https://doi.org/10.1016/j.cub.2024.04.002

CellPress

Current Biology

CellPress
OPEN ACCESS

Article

A RabGAP negatively regulates plant autophagy and immune trafficking

Enoch Lok Him Yuen,[1,4] Alexandre Y. Leary,[1] Marion Clavel,[2,3] Yasin Tumtas,[1] Azadeh Mohseni,[2] Jierui Zhao,[2] Lorenzo Picchianti,[2] Mostafa Jamshidiha,[1] Pooja Pandey,[1] Cian Duggan,[1] Ernesto Cota,[1] Yasin Dagdas,[2,*] and Tolga O. Bozkurt[1,5,6,*]

[1]Department of Life Sciences, Imperial College London, London SW7 2AZ, UK
[2]Gregor Mendel Institute of Molecular Plant Biology, Vienna BioCenter, Dr. Bohr-Gasse, 1030 Vienna, Austria
[3]Max Planck Institute of Molecular Plant Physiology, Am Mühlenberg 1, 14476 Potsdam, Germany
[4]X (formerly Twitter): @EnochYuen
[5]X (formerly Twitter): @Tolga_Bzkrt
[6]Lead contact
*Correspondence: yasin.dagdas@gmi.oeaw.ac.at (Y.D.), o.bozkurt@imperial.ac.uk (T.O.B.)
https://doi.org/10.1016/j.cub.2024.04.002

SUMMARY

Plants rely on autophagy and membrane trafficking to tolerate stress, combat infections, and maintain cellular homeostasis. However, the molecular interplay between autophagy and membrane trafficking is poorly understood. Using an AI-assisted approach, we identified Rab3GAP-like (Rab3GAPL) as a key membrane trafficking node that controls plant autophagy negatively. Rab3GAPL suppresses autophagy by binding to ATG8, the core autophagy adaptor, and deactivating Rab8a, a small GTPase essential for autophagosome formation and defense-related secretion. Rab3GAPL reduces autophagic flux in three model plant species, suggesting that its negative regulatory role in autophagy is conserved in land plants. Beyond autophagy regulation, Rab3GAPL modulates focal immunity against the oomycete pathogen *Phytophthora infestans* by preventing defense-related secretion. Altogether, our results suggest that Rab3GAPL acts as a molecular rheostat to coordinate autophagic flux and defense-related secretion by restraining Rab8a-mediated trafficking. This unprecedented interplay between a RabGAP-Rab pair and ATG8 sheds new light on the intricate membrane transport mechanisms underlying plant autophagy and immunity.

INTRODUCTION

Plants, being sessile organisms, regularly encounter diverse environmental stresses such as temperature fluctuations, drought, and nutrient deficiencies. To adapt and thrive in such dynamic environments, they have evolved to heavily depend on autophagy, a crucial catabolic process that maintains cellular homeostasis.[1,2] Autophagy entails the degradation of unnecessary or harmful cellular components in lysosomes or vacuoles. Moreover, it is instrumental in rapidly reshaping the cellular environment, ensuring the efficient and timely delivery of secretory cargoes to enhance plant resilience against environmental stresses and pathogens. While the specific mechanisms of autophagy in plant immunity are still under exploration,[3] its vital roles are evident, such as sequestering pathogen molecules and viruses for degradation.[4,5] In addition, the evolution of plant pathogens to evade or manipulate autophagy highlights its critical role in plant defense.[6] The reliance of plants on autophagy demonstrates its evolutionary advantage in optimizing plant growth and survival strategies under fluctuating environmental conditions.

Autophagy is a multistep process initiated by the induction of an isolation membrane that expands and closes, forming the mature autophagosomes—atypical vesicles with double membranes.[7] The process of autophagy is orchestrated by a set of highly conserved autophagy-related (ATG) proteins that coordinate the biogenesis and maturation of autophagosomes.[8] Studies in the last decade have revealed that autophagy is not only a bulk degradation process that is triggered during starvation but also encompasses selective pathways that recycle specific cellular components via dedicated cargo receptors, adaptors, or modulators.[9] At the heart of the autophagy machinery lies the ubiquitin-like protein ATG8, which functions as a hub to recruit autophagy cargo receptors and modulatory proteins. The ATG8 gene family exhibits varying degrees of expansion and diversification across plant lineages, with Arabidopsis featuring nine isoforms (ATG8A–I). A phylogenetic analysis conducted within solanaceous plants identified family-specific ATG8 groups, including ATG8A/B/C/D/E/F/H/I-like members, which cluster into four distinct clades.[10] Once ATG8 undergoes lipid modification by the autophagy initiation complex, it becomes embedded within the inner and outer leaflets of the autophagosomal membranes. This localization of lipidated ATG8 is pivotal in coordinating the formation, transport, and fusion events of autophagosomes.[11,12] ATG8-interacting proteins contain short linear motifs termed ATG8-interacting motifs (AIMs, also known as LC3-interacting regions [LIRs][13]). The canonical AIM sequence ([W,Y,F][X][X][L,I,V]) consists of an aromatic amino acid followed by any two amino acids and a hydrophobic residue, which are docked onto the W and L pockets on

Current Biology *34*, 2049–2065, May 20, 2024

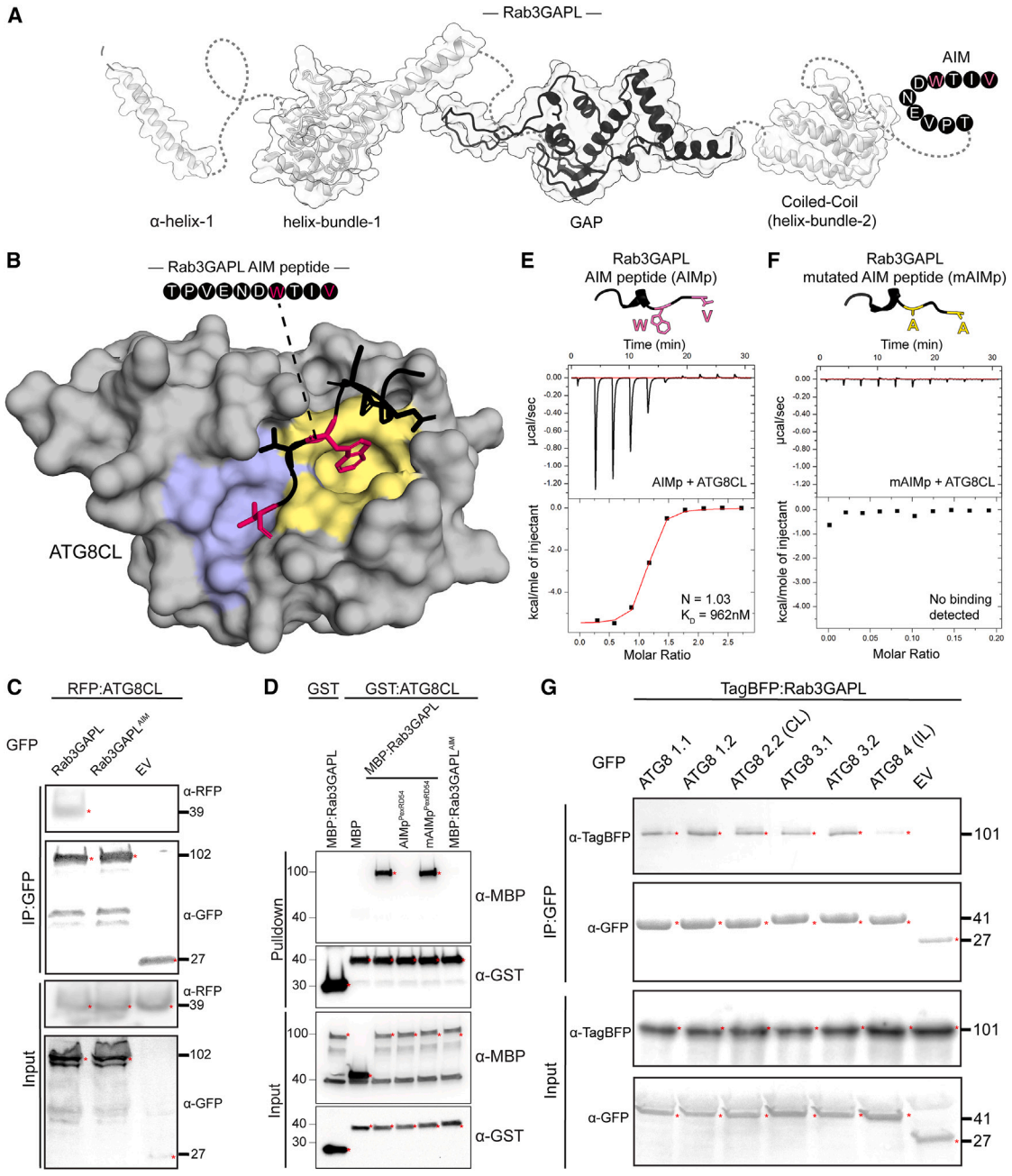

Figure 1. Rab3GAPL binds ATG8CL through a canonical AIM

(A) AF2 model of Rab3GAPL showing different regions (from N-terminal to C-terminal): a long alpha helix (α-helix-1), a helix bundle (helix-bundle-1) upstream of the conserved Rab3GAPL catalytic subunit, a coiled-coil region with a four-helix bundle (helix-bundle-2), and a C-terminal AIM region.

(B) AF2-M predicted structural model of Rab3GAPL and ATG8CL interaction displaying the docking of the Rab3GAPL-AIM peptide to the ATG8CL AIM pocket. Yellow and blue regions highlight W and L pockets on ATG8CL, respectively.

(C) Rab3GAPL binds to ATG8CL via its AIM *in planta*. RFP:ATG8CL was transiently co-expressed with either GFP:Rab3GAPL, GFP:Rab3GAPL^{AIM}, or GFP:EV. IPs were obtained with anti-GFP antiserum. Total protein extracts were immunoblotted. Red asterisks indicate expected band sizes.

(D) *In vitro* GST pull-down assay shows Rab3GAPL-ATG8CL physical interaction is AIM dependent. Bacterial lysates containing recombinant proteins were mixed and pulled down with glutathione magnetic agarose beads. Input and bound proteins were visualized by immunoblotting with anti-GST and anti-MBP antibodies. A peptide derivative of the pathogen effector PexRD54's AIM region (AIMp^{PexRD54}) depleted Rab3GAPL from ATG8CL complexes, whereas the mutated AIM peptide (mAIMp^{PexRD54}) had no effect.

(E) The AIM peptide of Rab3GAPL (Rab3GAPL-AIMp) directly binds to ATG8CL *in vitro*. The binding affinity of Rab3GAPL-AIMp to ATG8CL was determined using isothermal titration calorimetry (ITC). The upper panel shows heat differences upon injection of Rab3GAPL-AIMp into ATG8CL and the bottom panel shows integrated heats of injection and the best-fit line to a single site binding model. K_D = 962 nM, N = 1.03. In the sequence illustration, Rab3GAPL-AIMp is represented in black color, with key AIM residues highlighted in pink for WT Rab3GAPL-AIMp, and in yellow for the mutated version.

(legend continued on next page)

ATG8.[14] The discovery of proteins that carry functional AIMs is crucial for elucidating various aspects of autophagy. We have recently developed an AI-guided pipeline, utilizing Alphafold2-multimer (AF2-M), for prediction of both canonical and non-canonical AIM residues, enabling fast-forward discovery of autophagy receptors and modulators.[15]

Intriguingly, pathogens can exploit ATG8 as a central hub to either undermine antimicrobial autophagy or access nutrient sources within their host cells.[16,17] Previously, we have shown that the Irish potato famine pathogen *Phytophthora infestans* (*P. infestans*) secretes the effector PexRD54. This effector, equipped with a canonical AIM, targets autophagy and preferentially binds to the ATG8CL isoform in potatoes. PexRD54 plays a pivotal role in subverting defense-related autophagy,[18,19] promoting autophagosome formation by mimicking starvation conditions. The autophagic vesicles induced by the pathogen are subsequently redirected to the host-pathogen interface, potentially serving as nutrient resources.[16] Notably, PexRD54 acts as a scaffold between ATG8 compartments and vesicles labeled by the small GTPase Rab8a, likely to channel host lipid sources to stimulate autophagosome biogenesis.[16] It is increasingly evident that vesicle trafficking pathways play a crucial role in both autophagy and immunity.[16,20–22] This aligns with our recent findings, demonstrating that distinct vesicle transport pathways support various selective autophagy processes.[16]

Rab GTPases (Rabs) are key components that regulate vesicle formation, transport, tethering, and fusion events. They have been identified to participate in different stages of autophagy.[23–25] For instance, yeast and plant Rab1 members are crucial for early autophagosome formation,[26,27] while mammalian and plant Rab8a members have also been implicated in autophagy.[16,28] Rabs function as molecular switches that dynamically transit between an active guanosine triphosphate (GTP)-bound state and an inactive guanosine diphosphate (GDP)-bound state. These switches are tightly regulated by guanine nucleotide exchange factors (GEFs) that promote GTP binding and GTPase-activating proteins (GAPs) that catalyze GTP hydrolysis. RabGAPs, in particular, deactivate their Rab substrates, thereby determining their localization and function.[29] Recently, mammalian TBC (Tre2/Bub2/Cdc16)-domain-containing RabGAPs have been discovered to carry functional AIMs and modulate autophagy.[30] Nevertheless, in plants, crucial uncertainties regarding RabGAPs persist, particularly concerning TBC-domain-free RabGAPs. These uncertainties encompass their specific Rab substrates, the trafficking pathways they regulate, and their precise impact on autophagy.

Here, we identified a TBC-domain-free RabGAP protein, Rab3GAPL, as a key regulator of vesicle trafficking that interacts with ATG8 and Rab8a to suppress plant autophagy. Rab3GAPL also modulates immune responses against *P. infestans* by perturbing Rab8a vesicle dynamics and impairing defense-related secretion toward the pathogen interface. We uncovered an intricate interplay between a RabGAP protein, its Rab substrate, and the core autophagy receptor ATG8, underscoring their vital roles in regulating membrane trafficking processes essential for both autophagy and immunity.

RESULTS

A plant RabGAP, Rab3GAPL, directly interacts with ATG8CL through its C-terminal AIM

To uncover the roles of endomembrane trafficking in plant autophagy, we set out to identify vesicle transport regulators that associate with the autophagy machinery. We used our recently established AF2-M-assisted approach[15] to identify candidate trafficking components from our previous proteomics screen of ATG8CL interactors in the solanaceous model plant *Nicotiana benthamiana*.[31] Through AF2-M-assisted re-analysis of the ATG8CL proteome, we identified a Rab GAP that carries specific domains to govern both vesicle trafficking and autophagy. Specifically, this RabGAP comprises the conserved Rab3GAP-like catalytic subunit at its core (Rab3GAPL hereafter), flanked by two helix bundles and an N-terminal alpha helix, alongside a C-terminal AIM (WTIV) that is predicted by AF2-M to bind to the AIM docking site on ATG8CL (Figures 1A, 1B, and S1A). The predicted structure reveals a stable interaction interface between Rab3GAPL AIM and ATG8CL AIM docking sites (Figures 1B and S1A).

To confirm the AIM as the mediator of the interaction between Rab3GAPL and ATG8CL, we substituted the key AIM residues tryptophan and valine with alanine (WTIV > ATIA) and performed co-immunoprecipitation (coIP) assays. We generated N-terminal green fluorescent protein (GFP) fusions of wild-type (WT) Rab3GAPL and its AIM mutant (Rab3GAPL^{AIM}) and investigated their interaction with ATG8CL. In contrast to GFP:Rab3GAPL, neither the GFP:Rab3GAPL^{AIM} mutant nor the GFP control were able to pull down ATG8CL tagged with red fluorescent protein (RFP) from *N. benthamina* protein extracts in the coIP experiments (Figure 1C). This observation demonstrates the specificity of the interaction between Rab3GAPL and ATG8CL, which is dependent on the presence of the C-terminal AIM, as predicted by AF2-M (Figures 1B and 1C). Importantly, the loss of ATG8CL-Rab3GAPL^{AIM} interaction cannot be attributed to altered localization or reduced stability of the AIM mutant, given the comparable protein levels and cytoplasmic localization patterns of both GFP:Rab3GAPL and GFP:Rab3GAPL^{AIM} constructs (Figures 1C and S1B). These findings validate that Rab3GAPL interacts with ATG8CL through its C-terminal AIM, indicating a potential physical interaction between the two proteins.

To further investigate the potential AIM-mediated physical interaction between Rab3GAPL and ATG8CL, we performed *in vitro* glutathione S-transferase (GST) pull-down assays using maltose binding protein (MBP) fusions of Rab3GAPL and Rab3GAPL^{AIM} in combination with GST:ATG8CL or GST (negative control) expressed in *Escherichia coli*. Consistent with AF2-M predictions and *in planta* coIP assays, GST:ATG8CL

(F) No binding was detected between the mutated AIM peptide of Rab3GAPL (Rab3GAPL-mAIMp) and ATG8CL using ITC.
(G) Rab3GAPL binds to different ATG8 isoforms that are transiently expressed in *N. benthamiana*. TagBFP:Rab3GAPL was transiently co-expressed with either GFP:ATG8 1.1, GFP:ATG8 1.2, GFP:ATG8 2.2 (CL), GFP:ATG8 3.1, GFP:ATG8 3.2, GFP:ATG8 4 (IL), or GFP:EV. Ips were obtained with rat monoclonal anti-GFP antiserum. Total protein extracts were immunoblotted. Red asterisks indicate expected band sizes.
See also Figure S1.

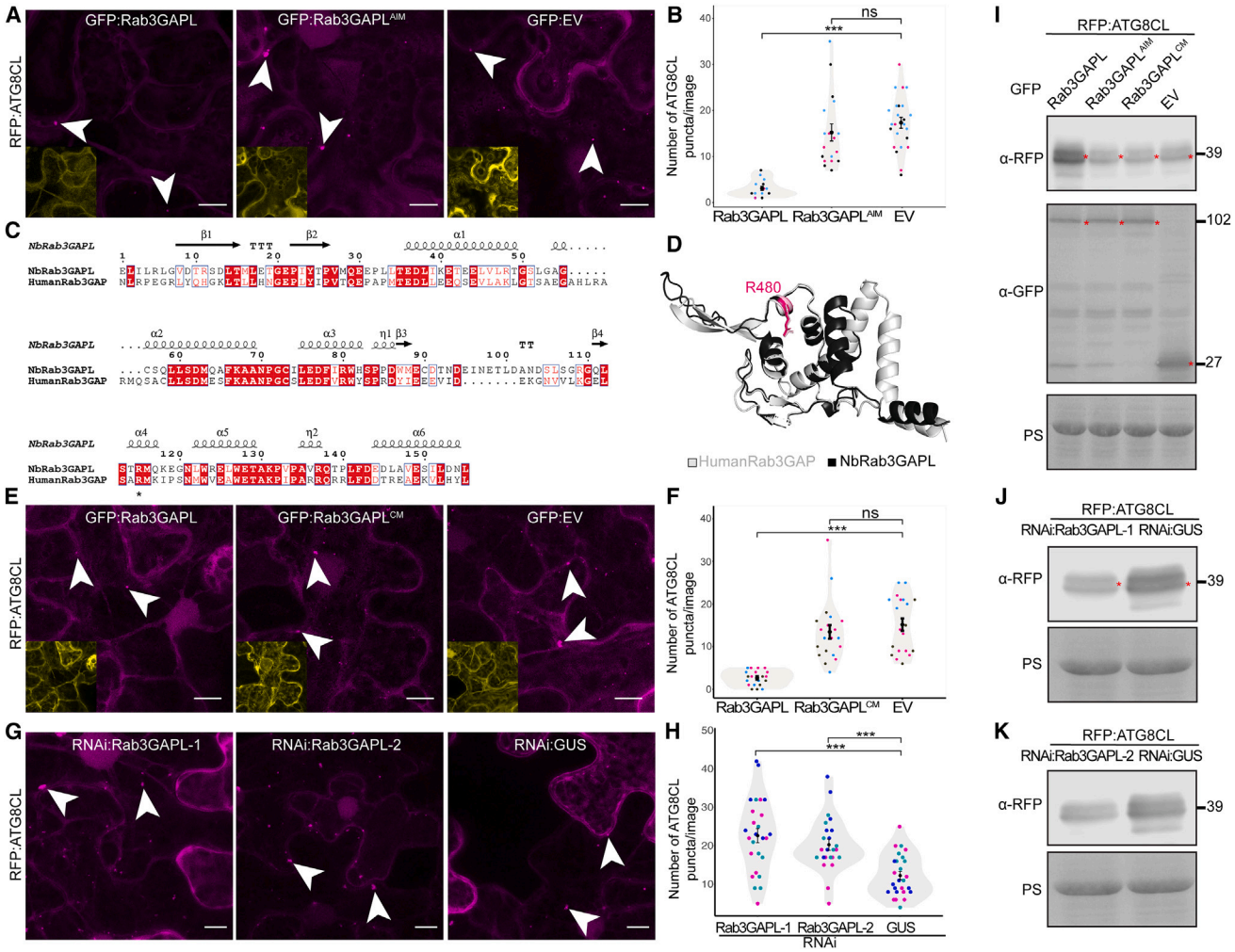

Figure 2. Rab3GAPL suppresses autophagy in an AIM- and catalytic-activity-dependent manner

(A and B) Rab3GAPL reduces the number of ATG8CL autophagosomes in an AIM-dependent manner.

(A) Confocal micrographs of *N. benthamiana* leaf epidermal cells transiently expressing RFP:ATG8CL with GFP:Rab3GAPL, GFP:Rab3GAPL^{AIM}, or GFP:EV. Images shown are maximal projections of 17 frames with 1.3 μm steps. Scale bars represent 10 μm.

(B) Rab3GAPL expression significantly reduces ATG8CL autophagosomes (3.1, n = 18 images) compared with EV control (17.3, n = 18 images), while Rab3GAPL^{AIM} expression has no significant effect on the number of ATG8CL autophagosomes (15.2, n = 18 images) compared with EV control. Statistical differences were analyzed by Mann-Whitney U test in R. Measurements were highly significant when $p < 0.001$ (***).

(C) Amino acid alignment of the GAP domains of human Rab3GAP and *N. benthamiana* Rab3GAPL proteins. * denotes the conserved catalytic arginine finger.

(D) Structural alignment of the GAP domains of human Rab3GAP and *N. benthamiana* Rab3GAPL. Structural predictions were obtained via AF2. The model shows conservation of the positioning of the catalytic arginine finger.

(E and F) Rab3GAPL reduces the number of ATG8CL autophagosomes in a catalytic-activity-dependent manner.

(E) Confocal micrographs of *N. benthamiana* leaf epidermal cells transiently expressing RFP:ATG8CL, with GFP:Rab3GAPL, GFP:Rab3GAPL^{CM}, or GFP:EV. Images shown are maximal projections of 17 frames with 1.5 μm steps. Scale bars represent 10 μm.

(F) Rab3GAPL expression significantly reduces ATG8CL autophagosomes (2.7, n = 20 images) compared with EV control (15.2, n = 20 images), while Rab3GAPL^{CM} expression has no significant effect on the number of ATG8CL autophagosomes (13.5, n = 20 images) compared with EV control. Statistical differences were analyzed by Mann-Whitney U test in R. Measurements were highly significant when $p < 0.001$ (***).

(G and H) RNAi-mediated silencing of Rab3GAPL increases the number of ATG8CL autophagosomes.

(G) Confocal micrographs of *N. benthamiana* leaf epidermal cells transiently expressing RNAi:Rab3GAPL-1, RNAi:Rab3GAPL-2, or RNAi:GUS. Images shown are maximal projections of 17 frames with 1.5 μm steps. Scale bars represent 10 μm.

(H) Silencing Rab3GAPL-1 (22.7, n = 26 images) or Rab3GAPL-2 (20.3, n = 24 images) significantly increases the number of ATG8CL autophagosomes compared with GUS silencing control (12.3, n = 26 images). Statistical differences were analyzed by Welch's t test in R. Measurements were highly significant when $p < 0.001$ (***).

(I–K) Rab3GAPL suppresses autophagic flux in an AIM- and catalytic-activity-dependent manner.

(I) Western blot shows that depletion of RFP:ATG8CL is reduced by GFP:Rab3GAPL compared with GFP:Rab3GAPL^{AIM}, GFP:Rab3GAPL^{CM}, or EV control. Total protein extracts were prepared 4 days post agroinfiltration and immunoblotted. Red asterisks show expected band sizes. Replicate gels are provided (Figure S2E).

(legend continued on next page)

specifically pulled down Rab3GAPL but not its AIM mutant Rab3GAPL^{AIM}. Moreover, Rab3GAPL–ATG8CL interaction was abolished in the presence of the AIM peptide derived from the pathogen effector PexRD54 (AIMp^{PexRD54}) that carries a similar AIM to that of Rab3GAPL (Figure S1C), but not with the mutated AIM peptide (mAIMp^{PexRD54}), providing further support for the AIM-mediated physical binding of Rab3GAPL and ATG8CL (Figure 1D).

To strengthen our findings, we conducted isothermal titration calorimetry (ITC) assays using a synthetic Rab3GAPL AIM peptide (Rab3GAPL-AIMp), which consists of the last 10 amino acid residues of Rab3GAPL that contains the AIM region. The Rab3GAPL-AIMp bound to ATG8CL with high affinity and in a one-to-one ratio (K_D = 962 nM and N = 1.03, based on ITC) (Figure 1E). In contrast, we did not detect any association between the mutated AIM peptide of Rab3GAPL and ATG8CL (Figure 1F). These results conclusively show that Rab3GAP's C-terminal AIM is both necessary and sufficient to directly bind ATG8CL.

In plants, ATG8 has diversified into multiple isoforms (ATG8A–I), forming distinct ATG8 clades that potentially coordinate different selective autophagy pathways.[10,31] Therefore, we next set out to determine the specificity of the binding between Rab3GAPL and other solanaceous ATG8 isoforms. In coIP assays using plant extracts, we observed that Rab3GAPL interacts with various potato ATG8 members exhibiting comparable affinities. Notably, the interaction between Rab3GAPL and the ATG8IL isoform appeared relatively weaker (Figure 1G). This finding suggests that Rab3GAPL may have a broader functional role in autophagy by interacting with multiple ATG8 isoforms. All in all, these results show Rab3GAPL binds to the core autophagy protein ATG8 via a canonical C-terminal AIM.

Rab3GAPL negatively regulates autophagy in an AIM- and GAP-dependent manner

Having established the physical interaction of Rab3GAPL and ATG8CL, we next investigated the role of Rab3GAPL in autophagy. We first investigated the impact of Rab3GAPL on autophagic puncta using confocal laser scanning microscopy (CLSM). To this end, we imaged cells transiently expressing GFP:Rab3GAPL, the AIM mutant GFP:Rab3GAPL^{AIM}, or a GFP control alongside the autophagosome marker RFP:ATG8CL and quantified autophagosome numbers. In cells expressing GFP:Rab3GAPL, we observed a greater than 2-fold reduction in RFP:ATG8CL puncta compared with cells expressing a GFP control. In contrast, GFP:Rab3GAPL^{AIM}-expressing cells did not show any significant difference in the relative amount of RFP:ATG8CL puncta (Figures 2A and 2B). The observed decrease in the quantity of autophagic puncta caused by overexpression of Rab3GAPL, but not its AIM mutant, hints at the possibility that Rab3GAPL negatively regulates autophagy, which relies on its ability to bind ATG8.

To determine the extent to which Rab3GAPL modulates autophagy, we next sought to determine whether the reduction in autophagosome numbers caused by Rab3GAPL overexpression is dependent on the GAP activity of Rab3GAPL. Previously, it was shown that the GAP function of human Rab3GAP was compromised by the mutation of the conserved arginine finger, which typically establishes connections with the γ-phosphate of the GTP nucleotide.[32] The structural alignment of the Rab3GAPL and human Rab3GAP protein sequences revealed that the catalytic arginine finger in the human Rab3GAP is conserved in *N. benthamiana* (R480) with the consensus sequence of LSxRM (Figure 2C). The AF2 predictions of the GAP domains of human and *N. benthamiana* Rab3GAPL showed a high level of structural conservation of the GAP domain architecture with a root-mean-square deviation (RMSD) value of 0.486. Additionally, the catalytic arginine finger was positioned consistently in both predicted structures (Figures 2D and S2A). Based on these observations, we generated the catalytic mutant of the *N. benthamiana* Rab3GAPL (Rab3GAPL^{CM} hereafter) by mutating the conserved arginine at position 480 to alanine (R480A). Unlike GFP:Rab3GAPL, which reduces autophagosome numbers (Figures 2A, 2B, 2E, and 2F), GFP:Rab3GAPL^{CM} did not significantly alter the amount of RFP:ATG8CL-labeled autophagosomes compared with the GFP control (Figures 2E and 2F). Comparing the AF2 models of Rab3GAPL and Rab3GAPL^{CM} did not reveal any global structural alterations resulting from the point mutation (Figure S2B). To further ensure that Rab3GAPL^{CM} is stably expressed and that its overall structure is not disrupted, we tested its stability as well as its ability to associate with ATG8CL *in vivo*. In these assays, we also used a dual mutant of Rab3GAPL (Rab3GAPL$^{CM/AIM}$) carrying both the AIM and GAP mutations as an additional control. Western blots of the plant protein extracts (input) and pull-down assays (output) showed that GFP:Rab3GAPL^{CM} was stably expressed and was able to interact with RFP:ATG8CL, whereas the negative control GFP:Rab3GAPL$^{CM/AIM}$ dual mutant did not associate with ATG8CL (Figure S2C). These results substantiate structural predictions that the overall protein architecture of Rab3GAPL^{CM} is not perturbed. We conclude that the GAP activity of Rab3GAP is required for its ability to suppress ATG8CL-autophagosome numbers.

Next, we determined the effect of *Rab3GAPL* silencing on autophagy by quantifying the number of RFP:ATG8CL-autophagosomes. In contrast with the overexpression results, silencing *Rab3GAPL* with two independent hairpin RNA interference (RNAi) constructs—one targeting the coding region (RNAi:Rab3GAPL-1) and the other targeting the three prime untranslated region (3′ UTR) of *Rab3GAPL* (RNAi:Rab3GAPL-2)—increased the amount of RFP:ATG8CL puncta by greater than 2-fold compared with the β-glucuronidase silencing control (RNAi:GUS) (Figures 2G, 2H, and S2D). A comparison of baseline RFP:ATG8CL puncta between GFP:empty vector (EV) overexpression (Figures 2B and 2F) and RNAi:GUS expression (Figure 2H) revealed a slightly lower puncta count in the latter. This decrease may be due to the activation of RNA silencing machinery by the hairpin constructs, potentially influencing autophagy.

(J and K) Western blots show depletion of RFP:ATG8CL is increased by silencing Rab3GAPL using either of the two silencing constructs, (J) RNAi:Rab3GAPL-1 or (K) RNAi:Rab3GAPL-2, compared with the GUS silencing control. Total protein extracts were prepared 4 days post agroinfiltration and immunoblotted. Red asterisks show expected band sizes. Replicate gels are provided (Figure S2F).
See also Figure S2.

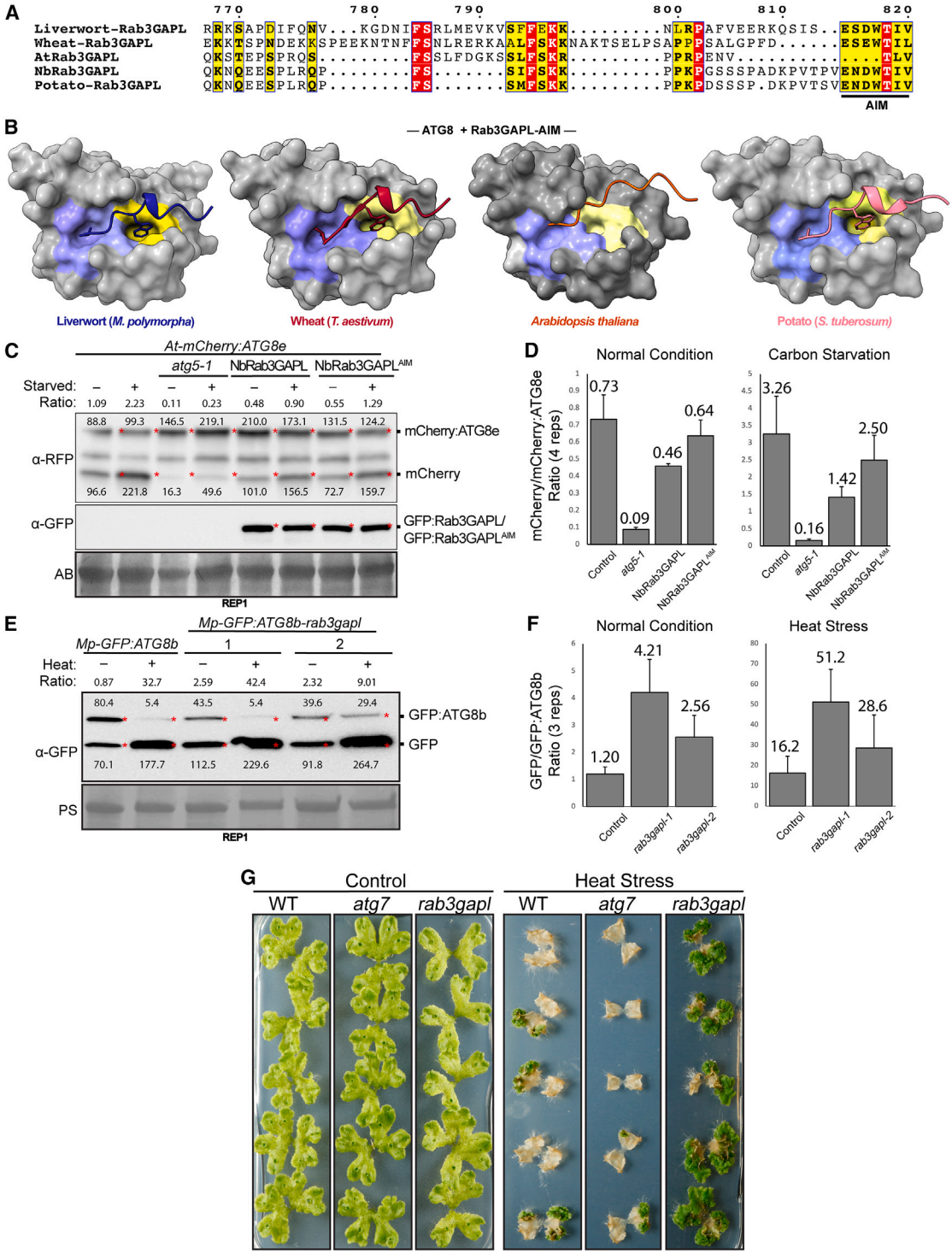

Figure 3. Rab3GAPL suppression of autophagic flux is widely conserved in land plants

(A) Pairwise sequence alignment comparisons of the N-terminals of Rab3GAPL in wheat, Arabidopsis, *N. benthamiana*, potato, and the liverwort *Marchantia polymorpha*. Alignments were obtained using the MUSCLE algorithm and were visualized and color-coded via ESPript 3.0.[33] The AIM is illustrated using a solid line.

(B) AF2-M predictions of ATG8s with Rab3GAPL AIMs sequences from liverwort (*M. polymorpha*), wheat (*Triticum aestivum*), *A. thaliana*, and potato (*S. tuberosum*). Predicted models suggest AIM docking sites (W and L pockets, colored yellow and blue, respectively) on ATG8CL are associated with all tested AIMs except for the Arabidopsis Rab3GAPL AIM sequence.

(C and D) *Arabidopsis thaliana* lines overexpressing Rab3GAPL exhibit reduced ATG8 autophagic flux.

(legend continued on next page)

Nevertheless, in both cases, we see significant differences in the puncta count between Rab3GAPL overexpression (Figures 2B and 2F) or *Rab3GAPL*-silencing (Figure 2H) and their respective controls. Collectively, these results suggest that Rab3GAPL suppresses autophagy via the AIM and GAP domains.

The potential reason for the reduction in autophagy puncta resulting from the overexpression of Rab3GAPL may be attributed to a decrease in autophagosome formation or an increase in autophagosome degradation. To address this, we conducted autophagic flux assays upon overexpression or silencing of Rab3GAPL. We first investigated the impact of Rab3GAPL overexpression on the protein levels of ATG8CL in *N. benthamiana*. To measure autophagic flux, we extracted proteins from *N. benthamiana* leaves co-expressing RFP:ATG8CL in combination with GFP:Rab3GAPL, GFP:Rab3GAPL^{AIM}, and GFP:Rab3GAPL^{CM} or an empty vector control at 4 days post transient expression and performed western blotting. In three independent experiments, overexpression of GFP:Rab3GAPL led to increased relative protein levels of RFP:ATG8CL, whereas overexpression of GFP:Rab3GAPL^{AIM}, GFP:Rab3GAPL^{CM}, or GFP vector control did not show the same effect (Figures 2I and S2E). These results are in line with our findings that only Rab3GAPL, and not its AIM or GAP mutants, modifies the quantity of autophagosomes (Figures 2A, 2B, 2E, and 2F). In accordance with the overexpression assays, the attenuation of Rab3GAPL gene expression through RNAi:Rab3GAPL-1 and RNAi:Rab3GAPL-2 resulted in a decrease in RFP:ATG8CL levels relative to an RNAi construct that targeted GUS (Figures 2J, 2K, and S2F). These results suggest that Rab3GAPL negatively regulates autophagy at the autophagosome biogenesis stage.

The negative regulatory role of Rab3GAPL in autophagy is broadly conserved in land plants

We next investigated whether the regulatory function of Rab3GAPL in autophagy is conserved in other plant species. To test this, we analyzed Rab3GAPL sequences from phylogenetically diverse plants, including wheat, Arabidopsis, *N. benthamiana*, potato, and the liverwort *Marchantia polymorpha*. Our analysis of Rab3GAPL sequences revealed that the GAP domain was conserved across all plant species (Figure S3A). Likewise, the AIM is highly conserved among all tested plant species, with Arabidopsis being the exception. Arabidopsis Rab3GAPL has a deletion in the key AIM residue W, along with upstream negatively charged residues that are known to be essential for interactions with positively charged surface residues of the AIM pocket (Figures 3A and S3A).

The absence of the key AIM residues in Rab3GAPL of Arabidopsis (AtRab3GAPL) raised the question of whether it can bind to ATG8. To investigate this further, we used AF2-M to predict ATG8s in complex with Rab3GAPL sequences used in the MUSCLE analysis. Consistent with the multiple sequence alignment findings, the predicted models revealed that all tested Rab3GAPL proteins possess functional AIMs that occupy the AIM pockets on their respective ATG8 proteins, with the exception of AtRab3GAPL (Figures 3B and S3B). In our expanded analysis across diverse plant lineages, we found that the AIM of Rab3GAPL is broadly conserved among monocots, dicots, lycophytes, bryophytes, and green algae, with a notable exception in the Brassicaceae family, indicating a widespread but not universal conservation pattern (Figure S3C). These results suggest that while the regulatory function of Rab3GAPL in autophagy is largely conserved, it may not be present in certain plant species, including Arabidopsis.

To gain additional insights, we performed a BLAST search of the Rab3GAPL protein sequence against the Brassicales order of flowering plants, which includes Arabidopsis as well as economically important crops such as cabbage, broccoli, mustard, and papaya. Interestingly, while the papaya (Caricaceae) Rab3GAPL carries an intact AIM, Rab3GAPLs from the Brassicaceae and Cleomaceae families, which diverged over 40 million years ago,[34] had deletions in their AIM residues as in the case of Arabidopsis (Figures 3A and S3D). Considering that our results that the AIM residues of Rab3GAPL are critical for autophagy suppression (Figure 2), these findings suggest that the regulation of autophagy by Rab3GAPL may vary among different plant species. Further investigations are required to explore the impact of the loss of AIM in Rab3GAPLs from Brassicaceae and Cleomaceae.

Next, we investigated the potential of heterologous expression of Rab3GAPL from *N. benthamiana* (NbRab3GAPL) to inhibit autophagy in Arabidopsis. To assess this, we stably expressed GFP:NbRab3GAPL or GFP:NbRab3GAPL^{AIM} in Arabidopsis lines that express mCherry:ATG8e and measured the autophagic flux by analyzing the cleavage of mCherry (free mCherry) from mCherry:ATG8e fusion protein through western blotting.[35,36] We analyzed the impact of Rab3GAPL overexpression

(C) Autophagic flux is measured as the ratio of free mCherry to full-size mCherry:ATG8e. The *atg5-1* plants were used as an autophagy-deficient control. Western blots showing the expression of GFP:Rab3GAPL and GFP:Rab3GAPL^{AIM} in At-mCherry:ATG8e transgenic plants. Protein extracts were prepared using 6-day-old seedlings and immunoblotted. The numbers denote the relative band intensity quantified using ImageJ. Replicate gels are provided (Figure S3E).

(D) Bar graphs illustrating that the expression of GFP:Rab3GAPL leads to reduced mCherry/mCherry:ATG8e protein signal ratio in both carbon starvation and control conditions compared with the control plants, while the reduction is less pronounced in the expression of GFP:Rab3GAPL^{AIM}. Each bar represents the average ratio of four individual repeats. Error bars represent standard errors of the mean.

(E and F) *Marchantia polymorpha* Rab3GAPL-KO mutants exhibit increased ATG8 autophagic flux.

(E) Autophagic flux is estimated as the ratio of free GFP to full-size GFP:ATG8b. Western blots illustrating WT and Rab3GAPL-KO mutants in MpEF::GFP:ATG8b background after 6 h of heat stress treatment following 2 h recovery. Protein extracts were prepared using 14-day-old thalli and immunoblotted. The numbers denote the relative band intensity, quantified using ImageJ. Replicate gels are provided (Figure S3I).

(F) Bar graphs illustrating that both Rab3GAPL-KO mutants showed increased GFP/GFP:ATG8b protein signal ratio under heat stress and control conditions compared with the control plants. Each bar represents the average of three individual repeats. Error bars represent standard errors of the mean.

(G) Mp-Rab3GAPL-KO mutants showed enhanced recovery from heat stress compared with WT control plants. ATG7-KO plants were used as an autophagy-deficient control, which showed reduced recovery from heat stress compared with WT control plants. Transgenic plants were incubated either in normal condition (22°C) or heat stress condition (37°C).

See also Figure S3.

on basal autophagy and autophagy induced by carbon starvation by comparing the mCherry signal ratios in the GFP:Rab3GAPL/mCherry:ATG8e and GFP:Rab3GAPL^{AIM}/mCherry:ATG8e lines alongside the *atg5-1* autophagy-deficient mutants that we used as a negative control. As expected, protein extracts from *atg5-1* lines showed lower mCherry/mCherry:ATG8e ratios in both carbon starvation and control conditions, indicating reduced autophagic flux across four independent experiments (Figures 3C, 3D, and S3E). Similarly, plants overexpressing GFP:Rab3GAPL exhibited reduced mCherry/mCherry:ATG8e ratios in both conditions (37.0% decrease and 56.4% decrease in normal and carbon starvation condition, respectively), suggesting decreased autophagic degradation. In contrast, the GFP:Rab3GAPL^{AIM} mutant exhibited a less pronounced reduction in the autophagic degradation of mCherry:ATG8e (12.3% decrease and 23.3% decrease in normal and carbon starvation condition, respectively) (Figures 3C, 3D, and S3E), consistent with the autophagic flux assays in *N. benthamiana* (Figures 2I–2K). Although the slight reduction caused by the AIM mutant may seem unexpected, it aligns with the understanding that neighboring residues of the key AIM residues (W and I) also play crucial roles in interacting with ATG8. Thus, the constitutive overexpression of the AIM mutant could still exert a minor suppressive effect on autophagy. Our observations consistently show a reduction in autophagic flux in different experimental setups or model systems with Rab3GAPL overexpression, albeit to a lesser degree than the disruption caused by *atg5* knockout. It is important to note that Rab3GAPL and ATG5 play fundamentally different roles in autophagy: ATG5 is crucial for initiating autophagy, and its absence halts the process entirely.[37,38] In contrast, Rab3GAPL acts as a nuanced regulator, fine-tuning autophagy by modulating ATG8 interactions, thus affecting autophagic flux subtly rather than stopping it outright. This modulatory effect of Rab3GAPL, akin to adjusting a rheostat, contrasts sharply with the all-or-nothing impact of ATG5 knockout, underlining the importance of recognizing their distinct influences on autophagy. In addition, Arabidopsis cells expressing GFP:Rab3GAPL exhibited reduced autophagic puncta compared with cells expressing the GFP:Rab3GAPL^{AIM} mutant (Figures S3F and S3G). These results indicate that Rab3GAPL from *N. benthamiana* can suppress autophagy in Arabidopsis in an AIM-dependent manner.

It is noteworthy that we employed distinct methodologies in our flux experiments conducted in Arabidopsis and *N. benthamiana*. This choice was necessitated by consistent challenges encountered in detecting free RFP released from RFP:ATG8CL in *N. benthamiana*, as evidenced by prior studies in this model system.[15,16,18] The difficulty is likely attributed to enhanced vacuolar processing or turnover of free RFP in *N. benthamiana*, a phenomenon distinct from that observed in Arabidopsis. Furthermore, variations in the turnover rates of mRFP and mCherry, utilized in Figures 2 and 3, respectively, may also contribute to this observed discrepancy. Consequently, our methodology in *N. benthamiana* flux assays in Figure 2 primarily relied on quantifying total RFP:ATG8CL protein levels as an indicator of autophagic flux.

The conservation of the AIM and GAP domain in liverworts implies their significance in Rab3GAPL function throughout land plants, dating back at least 400 million years. Having observed the interference of Rab3GAPL with autophagic flux in two dicot models, we investigated whether the negative regulation of autophagy by Rab3GAPL is maintained in liverworts. To perform autophagic flux assays, we first generated two independent *M. polymorpha Rab3GAPL* CRISPR knockout mutants, designated as *Mp-rab3gapl-1* and *Mp-rab3gapl-2*, in a GFP:ATG8b background (Figure S3H). We then compared the GFP/GFP:ATG8b protein signal ratios in the WT and mutant genotypes under both control and heat stress conditions across three independent experiments. The GFP/GFP:ATG8b ratios were consistently higher in the *Mp-rab3gapl* mutant lines than in the control plants, indicating increased ATG8 autophagic flux in *M. polymorpha* (3.5-fold and 3.2-fold increase in normal and heat stress condition, respectively, for *Mp-rab3gapl-1*; 2.1-fold and 1.8-fold increase in normal and heat stress condition, respectively, for *Mp-rab3gapl-2*) (Figures 3E, 3F, and S3I). These findings indicate that the knockout of *Rab3GAPL* enhances ATG8 autophagic flux in *M. polymorpha*.

Given the well-established beneficial impact of autophagy on heat stress tolerance and recovery,[39–42] we next investigated whether enhanced autophagic flux observed in *Mp-rab3gapl* mutant lines can boost recovery from heat stress. To assess this, we compared the survival rates of WT plants, *Mp-rab3gapl* mutant lines, and *atg7* mutants deficient in autophagy functionality under heat stress conditions at 37°C, prior to recovery. We observed a notable recuperation from heat stress in the *Mp-rab3gapl* mutant plants compared with WT plants (Figure 3G). In contrast, the autophagy-deficient *atg7* control lines exhibited reduced recovery from heat stress (Figure 3G). These results are consistent with the studies, which showed genetic interference of selective autophagy receptors leading to compromised heat tolerance due to the accumulation of protein aggregates that were highly ubiquitinated under heat stress.[40,41,43,44] However, further evidence is needed to conclude that enhanced recovery from heat stress in *M. polymorpha* is caused by enhanced autophagic activity in the absence of Rab3GAPL. Nevertheless, our results align with the beneficial impact of autophagy in stress tolerance and the role of Rab3GAPL as a negative regulator.

Rab8a, a GTPase implicated in autophagy and immunity, is a substrate of Rab3GAPL

We next sought to identify the Rab GTPase partner of Rab3GAPL in autophagy regulation. We tested the interaction of Rab3GAPL with a panel of candidate Rabs from solanaceous plants—Rab1, Rab2, Rab8a, and Rab8b—identified from our earlier autophagy interactome studies.[16,18,31] As an additional control, we also included a *N. benthamiana* Rab11 member in the interaction assays, as mammalian Rab11 has been implicated in autophagy.[45] The results from our coIP assays indicate that Rab3GAPL strongly interacts with Rab8 members and weakly with Rab2 and Rab11. However, we did not observe any association between Rab3GAPL and Rab1 or the GFP vector control (Figure 4A). AF2-M analysis revealed that Rab3GAPL and Rab8a interact at specific residues, with three being unique to Rab8 (Figures S4A and S4B), potentially explaining the binding affinity of Rab3GAPL for Rab8. These results suggest that Rab8 members are candidate substrates of Rab3GAPL in autophagy regulation. Consistent with this notion, we have previously shown that Rab8a associates with ATG8CL and positively regulates

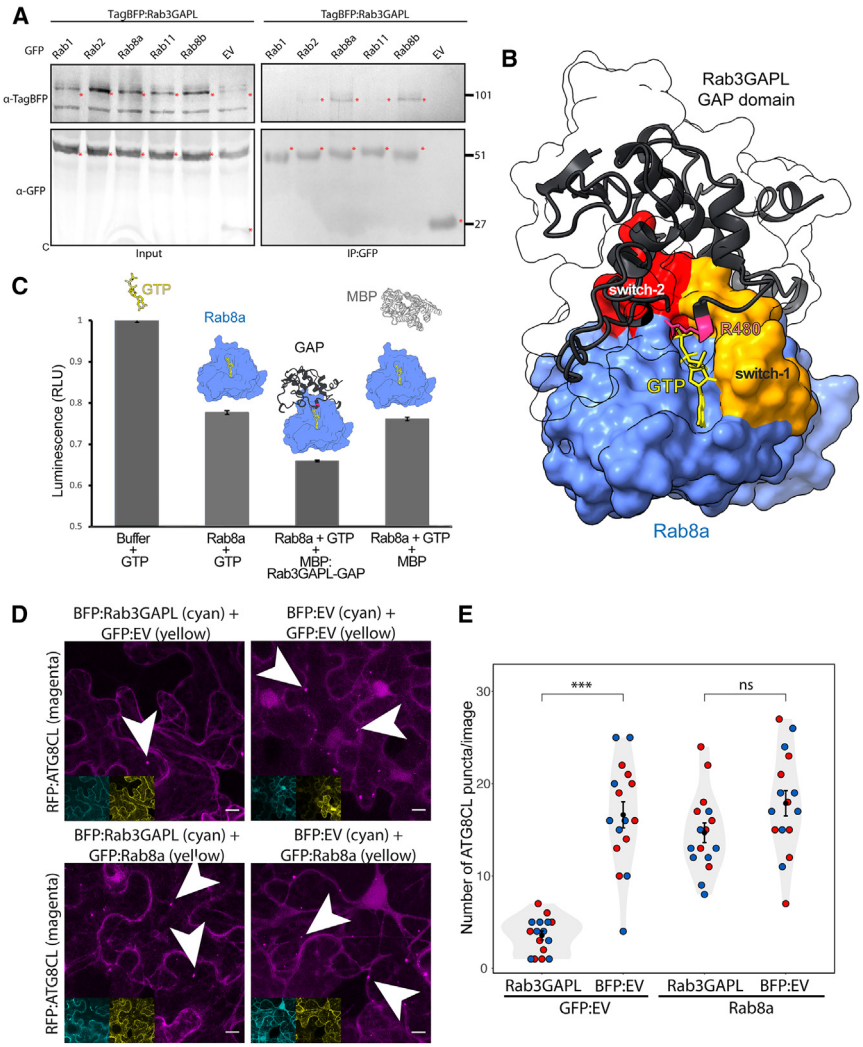

Figure 4. Rab3GAPL interacts with Rab8a and stimulates its GTP hydrolysis activity

(A) Rab3GAPL strongly interacts with Rab8 members and weakly with Rab2 and Rab11 *in planta*. TagBFP:Rab3GAPL was transiently co-expressed with either GFP:Rab1, GFP:Rab2, GFP:Rab8a, GFP:Rab11, GFP:Rab8b, or GFP:EV. IPs were obtained with rat monoclonal anti-GFP antiserum. Total protein extracts were immunoblotted. Red asterisks indicate expected band sizes.

(B) Predicted AF2-M model of Rab8a in complex with the GAP domain of Rab3GAPL. The catalytic arginine residue, R480 (magenta), of Rab3GAPL is positioned across the GTP-binding pocket of Rab8a.

(C) The GAP domain of Rab3GAPL stimulates GTPase activity of Rab8a. A luciferase-based GTPase assay was used to measure the amount of GTP over 120 min at room temperature. Bar graph shows the effect of purified MBP:Rab3GAPL GAP domain or MBP control on the GTPase activity of Rab8a across three repeats.

(D and E) Rab8a overexpression rescues Rab3GAPL-mediated suppression of autophagosome numbers. Images shown are maximal projections of 27 frames with 1 μm step. Scale bars represent 10 μm. Statistical differences were analyzed by Mann-Whitney U test in R. Measurements were highly significant when $p < 0.001$ (***).

(D) Confocal micrographs of *N. benthamiana* leaf epidermal cells transiently expressing GFP:EV or GFP:Rab8a with BFP:Rab3GAPL, or BFP:EV and RFP:ATG8CL.

(E) When GFP:EV is expressed, Rab3GAPL overexpression significantly reduces ATG8CL autophagosome number (3.6, N = 16 images) compared with EV control (16.6, n = 16 images). Contrarily, when GFP:Rab8a is expressed, Rab3GAPL overexpression does not have a significant effect on ATG8CL autophagosome number (14.7, n = 16 images) compared with EV control (17.9, n = 16 images).

See also Figure S4.

autophagy by potentially facilitating the transport of lipids to the phagophore assembly sites (PAS) required for autophagosome biogenesis.[16]

To gain further insights into the Rab3GAPL-Rab8a association, we utilized AF2-M. The predicted AF2 model suggests that the catalytic arginine (R480) of Rab3GAPL is located across the guanine-nucleotide-binding pocket flanking switch-1 and switch-2 regions on potato Rab8a (Figures 4B and S4C), suggesting that Rab8a could be a substrate of Rab3GAPL in plants. Potato Rab8a displayed a high degree of protein sequence conservation, with 68% amino acid identity, and a high degree of structural similarity, with an RMSD value of 0.8, when compared with human Rab8a (Figures S4D–S4F). Leveraging this structural conservation, we performed AF2-guided *ab initio* molecular replacement to obtain potato Rab8a bound to GTP. We replaced the crystal structure of human Rab8a bound to GTP (PDB:6WHE)[46] with the AF2 model of the potato Rab8a (Figures S4E–S4G). The resulting Rab3GAPL-Rab8a-GTP model demonstrated that the catalytic arginine finger of Rab3GAPL is positioned to engage with the GTP-binding pocket of the potato Rab8a and makes contacts with the conserved glutamine from the DTAGQ motif of the switch-2 region of Rab8a (Figures 4B and S4E–S4G). Such interactions between the catalytic arginine and the switch-2 glutamate typically facilitate the nucleophilic attack by a water molecule on the γ-phosphate of GTP, leading to GTP hydrolysis and the subsequent release of inorganic phosphate[47] (Figure S4G).

Based on these findings, we further investigated the interplay between Rab8a and Rab3GAPL by performing biochemical assays. We conducted *in vitro* GAP assays to determine whether Rab3GAPL enhances the GTP hydrolysis activity of Rab8a, using proteins purified from *E. coli*. The titration of 5 μM of purified Rab8a into the GTP reaction buffer led to a significant reduction in free GTP levels compared with the buffer control (Figure 4C), confirming the functionality of purified Rab8a protein. When Rab8a was incubated together with the purified GAP domain of Rab3GAPL, we noted a more pronounced reduction in free GTP levels in the buffer compared with Rab8a alone or using MBP control (Figure 4C). These results indicate that Rab3GAPL

promotes the GTP hydrolysis activity of Rab8a and that Rab3GAPL can function as a conventional GAP for Rab8a.

After establishing the *in vitro* GAP activity of Rab3GAPL on Rab8a, we aimed to elucidate their functional relationship *in vivo*. Using confocal microscopy, we examined whether overexpressing Rab8a could counteract the Rab3GAPL-induced decrease in autophagosome numbers. Echoing our previous findings (Figure 2), Rab3GAPL overexpression with GFP:EV control significantly diminished the RFP:ATG8CL puncta count. Notably, co-overexpressing GFP:Rab8a reversed this Rab3GAPL-induced reduction in ATG8CL puncta (Figures 4D and 4E), suggesting a dynamic interaction between Rab8a and Rab3GAPL in autophagy regulation. To gain further insights, we next silenced Rab8a and assessed its effect on the Rab3GAPL-mediated autophagosome suppression. Consistent with our Rab8a overexpression results (Figures 4D and 4E), silencing Rab8a negated the significant effect of Rab3GAPL-induced reduction in autophagosome numbers (Figures S4H and S4I). It is noteworthy that his result aligns with our previous work showing that silencing Rab8a reduces autophagosome numbers relative to the silencing control.[16] In summary, these outcomes strongly indicate a functional interplay between Rab3GAPL and Rab8a in modulating autophagy, reinforcing the notion that Rab8a is a substrate of Rab3GAPL.

Because Rab3GAPL suppresses autophagy in a manner that relies on its GAP function and ATG8-binding activities (Figures 2A, 2B, 2E, and 2F), we suggest that Rab3GAPL could regulate autophagy by switching off Rab8a at autophagosome biogenesis sites, where ATG8 proteins are actively recruited.[48]

Rab3GAPL increases susceptibility to *Phytophthora infestans* independent of its autophagy suppression activity

Given the recent findings supporting the positive role of Rab8a in autophagy and immunity against *P. infestans*,[16,18] we next investigated whether Rab3GAPL has any impact on pathogen resistance. First, we tested whether Rab3GAPL affects immunity to *P. infestans* in an autophagy-dependent manner by overexpressing the WT Rab3GAPL or its AIM mutant. In four independent experiments, infected leaf patches expressing GFP:Rab3GAPL or GFP:Rab3GAPL^{AIM} showed enhanced disease symptoms, with significant increases in infection lesion sizes compared with the GFP control (Figures 5A and 5B). We validated these results by performing infection assays using a red fluorescent strain of *P. infestans*, 88609td, which allows measurement of pathogen biomass through imaging of hyphal threads via fluorescent microscopy. Consistently, *P. infestans* hyphal growth was significantly higher in leaf patches overexpressing GFP:Rab3GAPL or GFP:Rab3GAPL^{AIM} compared with GFP control samples (Figures S5A and S5B). Intriguingly, the overexpression of the Rab3GAPL^{AIM} mutant, which is impaired in autophagy suppression and ATG8 binding, promoted infection to levels comparable to that of WT Rab3GAPL (Figures 5A, 5B, S5A, and S5B). These results indicate that Rab3GAPL negatively regulates immunity independent of its function in autophagy.

Second, we explored whether enhanced susceptibility phenotype caused by overexpression of Rab3GAPL requires its GAP activity. Notably, overexpression of the GAP mutant (GFP:Rab3GAPL^{CM}) did not cause any difference in *P. infestans* infection lesion sizes compared with the GFP control, unlike the WT GFP:Rab3GAPL construct, which enhanced disease symptoms (Figures 5C and 5D). These findings indicate that the enhanced pathogen growth phenotype caused by Rab3GAPL overexpression is reliant on its GAP activity, suggesting a potential negative regulation of immunity through the restriction of Rab-mediated trafficking.

Third, we conducted infection assays upon downregulation of Rab3GAPL expression. To achieve this, we employed silencing constructs RNAi:Rab3GAPL-1 and RNAi:Rab3GAPL-2, designed to specifically target *Rab3GAPL* in *N. benthamiana* (Figure S2D). In agreement with our overexpression assays, which suggested a negative role of Rab3GAPL in immunity (Figures 5A–5D), the silencing of Rab3GAPL using either RNAi:Rab3GAPL constructs significantly reduced *P. infestans* infection lesion size and hyphal growth compared with the control construct RNAi:GUS (Figures 5E, 5F, S5C, and S5D). These results show that Rab3GAPL acts as a susceptibility factor in a catalytic-activity-dependent, but AIM-independent, manner. Collectively, these findings suggest that the negative regulatory function of Rab3GAPL in defense against *P. infestans* is independent of autophagy, highlighting its involvement in alternative mechanisms of immune regulation.

Rab3GAPL antagonizes Rab8a-mediated defense vesicle dynamics and secretion

Recent studies have revealed the contribution of Rab8a in defense-related secretion and basal immunity against *P. infestans*.[16] Additionally, pathogen effectors specifically target Rab8a to undermine its immune functions, including the secretion of pathogenesis-related protein-1 (PR-1) into the apoplast.[16,49] Given the immunosuppressive role of Rab3GAPL, which is dependent on its GAP activity but not its interaction with ATG8 (Figure 5), we hypothesized that Rab3GAPL negatively regulates defense-related secretion mediated by Rab8a. To test this, we first assessed the impact of Rab3GAPL on defense-related secretory responses by examining its effect on PR-1 secretion. To stimulate endogenous PR-1 induction, we challenged the leaf patches expressing Rab3GAPL and controls with *P. infestans* extract, serving as a pathogen-associated molecular pattern (PAMP) cocktail, at 3 days post infiltration (dpi). Subsequently, we conducted protein extractions from both the apoplast and leaf tissue at 4 dpi. The secretion of PR-1 to the apoplast was drastically reduced in samples expressing Rab3GAPL or Rab3GAPL^{AIM} compared with the GFP vector control. However, the apoplastic levels of PR-1 were unaffected by the catalytic mutant, Rab3GAPL^{CM} (Figure 6A). Although apoplastic PR-1 levels were reduced in samples overexpressing Rab3GAPL and Rab3GAPL^{AIM}, cytoplasmic PR-1 levels reciprocally increased, suggesting that the decrease in apoplastic PR-1 was not due to impaired PR-1 expression (Figure 6A).

Our previous work revealed that Rab8a-labeled vesicle-like structures are deposited around the extrahaustorial membrane (EHM) that envelopes the *P. infestans* haustorium.[16] We reasoned that these Rab8a vesicles could deliver defense compounds to restrict pathogen invasion, whereas Rab3GAPL plays an antagonistic role in regulating Rab8a-mediated transport pathways. Supporting this notion, we observed a notable 74%

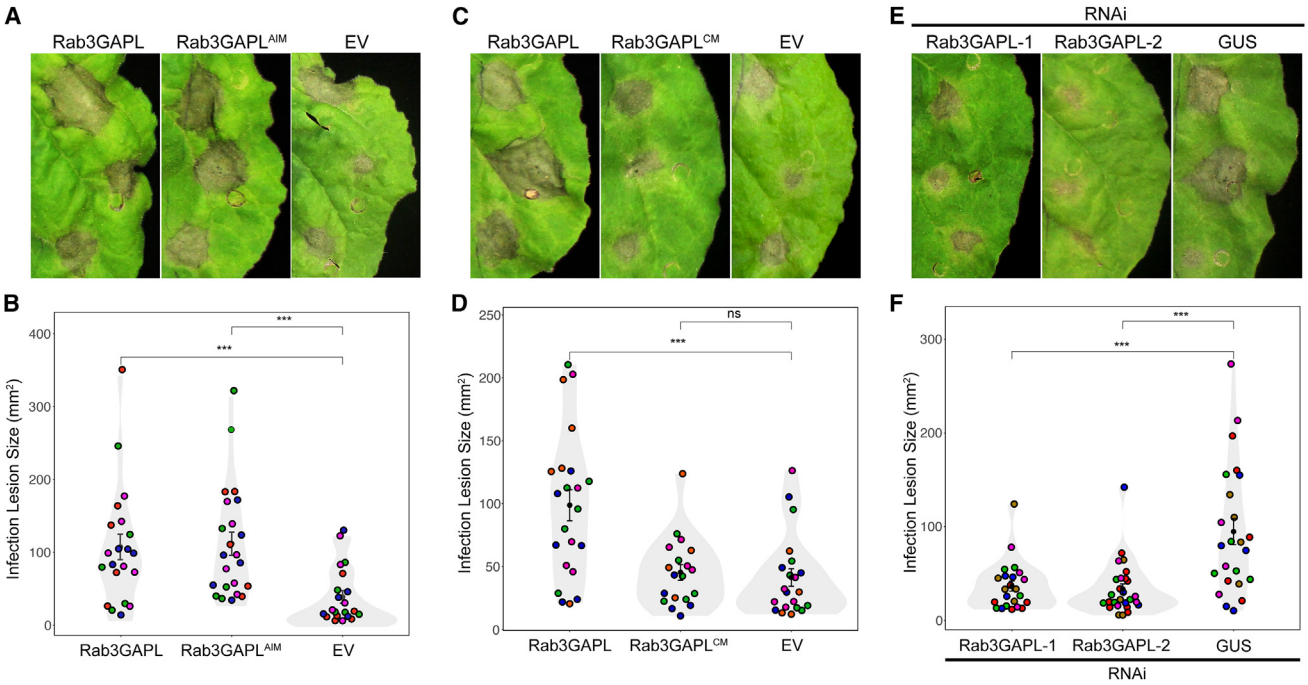

Figure 5. Rab3GAPL increases susceptibility to *Phytophthora infestans* in a catalytic-activity-dependent, AIM-independent, manner

(A and B) Rab3GAPL increases susceptibility to *P. infestans* in an AIM-independent manner.

(A) *N. benthamiana* leaves expressing Rab3GAPL, Rab3GAPL^{AIM}, or EV control were infected with *P. infestans* and pathogen growth was calculated by measuring infection lesion size 7 days post inoculation.

(B) Both Rab3GAPL expression (107.3, $n = 21$ spots) and Rab3GAPL^{AIM} expression (111.8, $n = 23$ spots) significantly increase *P. infestans* lesion sizes compared with EV control (39.0, $n = 21$ spots). Statistical differences were analyzed by Mann-Whitney U test in R. Measurements were highly significant when $p < 0.001$ (***).

(C and D) Rab3GAPL increases susceptibility to *P. infestans* in a catalytic-activity-dependent manner.

(C) *N. benthamiana* leaves expressing Rab3GAPL, Rab3GAPL^{CM}, or EV control were infected with *P. infestans* and pathogen growth was calculated by measuring infection lesion size 7 days post inoculation.

(D) Rab3GAPL expression (98.8, $n = 22$ spots) significantly increases *P. infestans* lesion sizes compared with EV control (45.4, $n = 19$ spots), whereas Rab3GAPL^{CM} expression (41.3, $n = 21$ spots) has no significant effect compared with EV control. Statistical differences were analyzed by Mann-Whitney U test in R. Measurements were highly significant when $p < 0.001$ (***).

(E and F) Silencing *Rab3GAPL* reduces susceptibility to *P. infestans*.

(E) *N. benthamiana* leaves expressing RNAi:Rab3GAPL-1, RNAi:Rab3GAPL-2, or RNAi:GUS control were infected with *P. infestans* and pathogen growth was calculated by measuring infection lesion size 8 days post inoculation.

(F) Both RNAi:Rab3GAPL-1 expression (36.6, $n = 23$ spots) and RNAi:Rab3GAPL-2 expression (33.5, $n = 27$ spots) significantly reduce *P. infestans* lesion sizes compared with RNAi:GUS control (94.8, $n = 24$ spots). Statistical differences were analyzed by Mann-Whitney U test in R. Measurements were highly significant when $p < 0.001$ (***).

See also Figure S5.

reduction in the abundance of Rab8a-labeled vesicles around the haustorium interface upon Rab3GAPL overexpression compared with the vector control (Figures 6B and 6C). We observed a similar decrease in Rab8a vesicle abundance around haustoria when we overexpressed Rab3GAPL^{AIM}. In contrast, expression of Rab3GAPL^{CM} did not affect abundance of Rab8a puncta around haustoria, behaving similarly to the vector control (Figures 6B and 6C). Collectively, our findings provide evidence that Rab3GAPL negatively regulates secretory defenses dependent on Rab8a during the immune response to *P. infestans*. These results also suggest that Rab3GAPL could antagonize focal immune responses targeted to the pathogen interface.

Following up, we examined the potential impact of Rab3GAPL on plant focal immunity. Specifically, we explored whether Rab3GAPL influences callose deposition surrounding *P. infestans* haustoria. Callose deposits play a crucial role in the immune response, especially when pathogens establish specialized host-pathogen interfaces like haustoria for invading host cells.[50–52] We observed around 40% reduction (percentage change of frequency from 50% to 30%) in the occurrence of haustoria with callose deposits upon Rab3GAPL overexpression compared with the vector control, and we noticed a similar decrease in haustoria with callose deposits when Rab3GAPL^{AIM} was overexpressed but not when Rab3GAPL^{CM} was overexpressed (Figures 6D and 6E). These outcomes were not influenced by variations in protein expression, as confirmed by western blots indicating stable and comparable expression of WT Rab3GAPL, Rab3GAPL^{AIM}, and Rab3GAPL^{CM} (Figure S6). These findings, combined with our earlier observations of Rab3GAPL's disruption of Rab8a vesicle dynamics around haustoria, suggest that Rab3GAPL negatively regulates the secretory pathways that are locally deployed at pathogen penetration sites. Moreover, these results provide insights into the

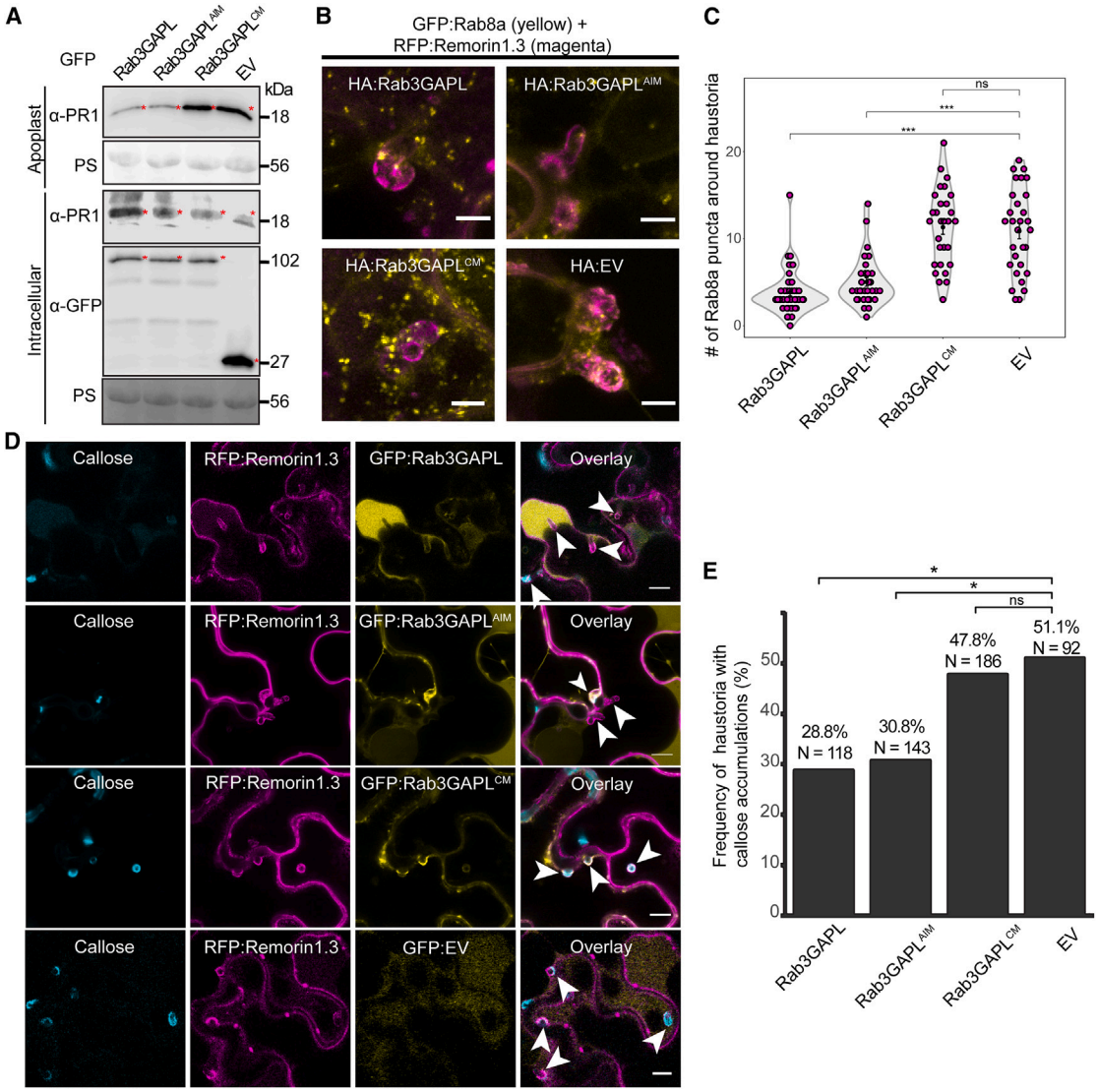

Figure 6. Rab3GAPL suppresses defense-related secretion in a catalytic-activity-dependent manner

(A) Western blot shows that Rab3GAPL and Rab3GAPL^{AIM}, but not Rab3GAPL^{CM}, reduces antimicrobial PR-1 secretion to the apoplast compared with EV control. *N. benthamiana* leaves were infiltrated to express GFP:Rab3GAPL, GFP:Rab3GAPL^{AIM}, GFP:Rab3GAPL^{CM}, or GFP:EV. The leaves were then challenged with *P. infestans* extract at 3 dpi and proteins were extracted from the apoplast and leaf tissue at 4 dpi and immunoblotted. Red asterisks show expected band sizes. PS, Ponceau S staining for RuBisCO as loading controls.

(B and C) Rab3GAPL reduces the number of Rab8a vesicles around haustoria in a catalytic-activity-dependent manner.

(B) Confocal micrographs of *N. benthamiana* leaf epidermal cells transiently expressing GFP:Rab8a and RFP:Remorin1.3 with HA:Rab3GAPL, HA:Rab3GAPL^{AIM}, HA:Rab3GAPL^{CM}, or HA:EV. Images shown are maximal projections of 12 frames with 1.2 μm steps. Scale bars represent 10 μm.

(C) Rab3GAPL expression (3, $n = 42$ haustoria) or Rab3GAPL^{AIM} expression (4, $n = 31$ haustoria) significantly reduces number of Rab8a vesicles around haustoria compared with EV control (11.5, $n = 30$ haustoria), while Rab3GAPL^{CM} expression (12, $n = 29$ haustoria) has no significant effect compared with EV control. Only puncta that are around the haustoria are quantified. Statistical differences were analyzed by Mann-Whitney U test in R. Measurements were highly significant when $p < 0.001$ (***).

(D and E) Rab3GAPL reduces callose deposition at *P. infestans* haustoria in a catalytic-activity-dependent manner.

(D) Confocal micrographs of *N. benthamiana* leaf epidermal cells transiently expressing RFP:Remorin1.3 with GFP:Rab3GAPL, GFP:Rab3GAPL^{AIM}, GFP:Rab3GAPL^{CM}, or GFP:EV. Remorin1.3 acts as a plasma membrane and EHM marker. The leaves were infected with *P. infestans* spores at 1 dpi and stained with aniline blue to visualize callose at 4 dpi. Images shown are single-plane images. White arrows indicate haustoria. Scale bars represent 10 μm.

(E) Bar graphs showing Rab3GAPL expression (28.8%, $n = 118$ haustoria) or Rab3GAPL^{AIM} expression (30.8%, $n = 143$ haustoria) significantly reduce the frequency of callose deposition around haustoria compared with EV control (51.1%, $n = 92$ haustoria), while Rab3GAPL^{CM} expression (47.8%, $n = 186$ haustoria) has no significant effect compared with EV control. Statistical differences were analyzed by chi-squared test in R. Measurements were significant when $p < 0.05$ (*). Protein expression levels of GFP constructs are provided (Figure S6).

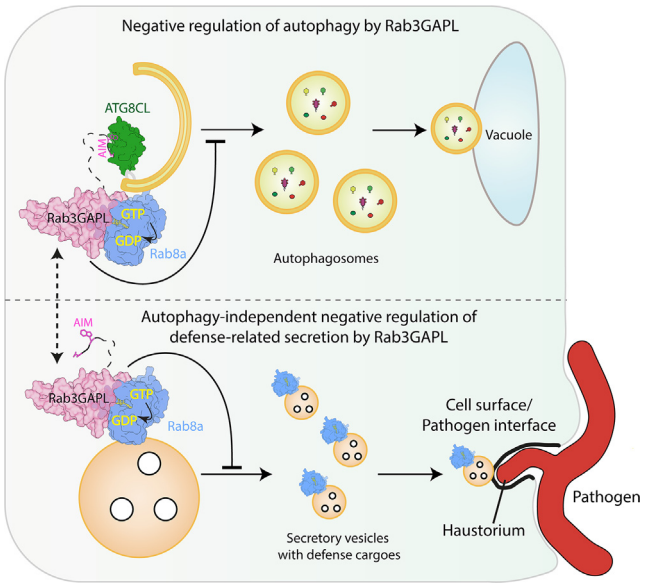

Figure 7. Summary model of the negative regulation of autophagy and immunity by Rab3GAPL

Rab3GAPL toggles between activities to optimize autophagy and defense-related secretion by hindering Rab8a-mediated vesicle trafficking through promoting the GTP hydrolysis of Rab8a. Rab3GAPL suppresses autophagy by binding to ATG8, the core autophagy adaptor, using its ATG8-interacting motif (AIM) and deactivating Rab8a using its GTPase-activating protein (GAP) domain. Beyond autophagy regulation, Rab3GAPL modulates Rab8a-mediated defense-related secretion toward the cell surface/pathogen interface. This immune modulation is independent of its AIM, but dependent on its GAP domain. Consequently, Rab3GAPL functions as a molecular rheostat, dynamically balancing autophagy and immune responses to maintain cellular homeostasis. This model highlights the molecular interplay between a RabGAP-Rab pair and ATG8, providing new insights into the complex membrane transport mechanisms that underpin plant autophagy and immunity.

potential mechanisms underlying the increased susceptibility phenotype observed toward *P. infestans* upon overexpression of Rab3GAPL and its AIM mutant, Rab3GAPL^{AIM} (Figures 5A and 5B).

DISCUSSION

In this study, we investigated the membrane trafficking processes involved in plant autophagy and immunity. Our findings revealed the role of Rab3GAPL as a regulator of vesicle transport that carries a canonical AIM to interact with ATG8 and suppress plant autophagy (Figures 1, 2, S1, and S2). Although the Rab3GAPL AIM is broadly conserved in land plants, some plants in the Brassicales order exhibit mutations in their Rab3GAPL AIM residues, suggesting potential diversification in autophagy regulation (Figures 3A, 3B, S3A–S3D). We also discovered that Rab3GAPL targets Rab8a, an important GTPase involved in autophagy activation and immunity. By stimulating Rab8a's GTPase activity, Rab3GAPL effectively suppresses autophagy (Figure 4).

Interestingly, our findings extend beyond autophagy regulation, as we have uncovered an additional role of Rab3GAPL in negatively modulating immunity toward *P. infestans* that is independent of its ATG8-binding activity (Figures 5 and 6). This modulation relies on the GAP function of Rab3GAPL and involves the inhibition of Rab8a-mediated trafficking diverted toward the pathogen interface (Figures 6B–6E). Our results suggest a model in which Rab3GAPL impedes Rab8a-mediated vesicle trafficking by promoting Rab8a's GTP-to-GDP switch. While Rab8a-mediated trafficking is crucial for autophagy,[16] Rab3GAPL suppresses this process at autophagosome biogenesis sites where ATG8 is enriched. Additionally, Rab3GAPL can subvert defense-related secretion mediated by Rab8a, possibly to mitigate auto-immune responses and to adjust appropriate resource allocation (Figure 7).

In this research, we elucidate the negative impact of Rab3GAPL in plant immunity, particularly highlighting its influence on callose deposition and interaction with Rab8a in defense-related secretion. Our previous research,[16] along with other studies,[49,53] have highlighted the immune functions of Rab8a in defense-related secretion. In light of our new findings, which establish Rab3GAPL as a GAP for Rab8a, we observed that Rab3GAPL influences Rab8a vesicle dynamics around the haustorium and PR-1 secretion (Figures 6A–6C). All these processes are contingent upon the GAP activity of Rab3GAPL. Therefore, we conclude that Rab3GAPL modulates focal immune responses by interfering with the function of Rab8a in defense-related secretion. We propose that Rab3GAPL delicately balances plant immune mechanisms and autophagy, thereby preventing potential harm from overactivation of these vital cellular processes.

Notably, PR-1 is upregulated and secreted in response to various pathogen infections, highlighting its central role in immune responses. This is further emphasized by the diverse range of pathogen effectors targeting PR-1.[54] Our discovery that Rab3GAPL regulates PR-1 secretion suggests a potential widespread role in modulating plant immunity against a variety of pathogens. This hypothesis is reinforced by the well-established role of Rab8 family members in PR-1 secretion and immunity,[16,49] complemented by our findings demonstrating the influence of Rab3GAPL on Rab8a function.

In our investigation, Marchantia Rab3GAPL-KO mutant plants and Arabidopsis lines overexpressing Rab3GAPL exhibited no noticeable differences in growth or development under normal conditions. This observation hints at potential biotechnological applications, such as mutating Rab3GAPL to enhance crop resistance to pathogens and environmental stressors. However, it is important to note that we cannot exclude the possibility of potential trade-offs as we have not conducted comprehensive testing under various stress conditions or evaluated vulnerability to other diseases.

In plants, susceptibility genes such as Rab3GAPL, which are crucial for normal physiology and development, can paradoxically increase vulnerability to pathogens. These genes, often essential and without obvious fitness trade-offs, can be hijacked by pathogens to promote susceptibility.[55–57] Our study highlights the role of Rab3GAPL in this complex interplay, where it modulates immune responses, possibly to prevent resource depletion after pathogen clearance. This underscores the need for balanced immune regulation in plants, as uncontrolled immune activation can disrupt proper growth and other stress responses. Thus, Rab3GAPL exemplifies the intricate context-dependent nature of plant-pathogen interactions,

where susceptibility genes offer a selective advantage in certain environmental conditions or against specific pathogens.

Altogether, our findings uncover an intricate interplay between a RabGAP, its Rab substrate, and the core autophagy machinery, highlighting their essential roles in regulating membrane trafficking processes in both plant autophagy and immunity. The discovery of the role of Rab3GAPL in these processes, along with its potential implications in enhancing biotic and abiotic stress tolerance, presents exciting opportunities for further exploration in basic research and biotechnological applications. In animals, there are several TBC-domain-containing RabGAPs that carry functional AIMs, enabling them to bind ATG8/LC3 and regulate autophagy. However, the question of whether TBC-domain-free plant RabGAPs play regulatory roles in autophagy or immunity remains unknown and warrants further exploration. We envisage that continued research in this field holds promise for the development of novel strategies to fortify crop resilience, improve agricultural sustainability, and ensure global food security in the face of climate change.

STAR★METHODS

Detailed methods are provided in the online version of this paper and include the following:

- KEY RESOURCES TABLE
- RESOURCE AVAILABILITY
  - Lead contact
  - Materials availability
  - Data and code availability
- EXPERIMENTAL MODEL AND SUBJECT DETAILS
  - Plant growth details
  - Pathogen growth details
- METHOD DETAILS
  - Molecular cloning
  - *P. infestans* growth and infection assays
  - Confocal microscopy
  - Structural and sequence analyses
  - Transient gene expression in *N. benthamiana*
  - RNA isolation, cDNA synthesis, and RT-PCR
  - Callose staining
  - Co-immunoprecipitation and blotting analyses
  - *P. infestans* extract preparation
  - Apoplast extraction
  - *A. thaliana* carbon starvation assays
  - Confocal microscopy for Arabidopsis samples
  - *M. polymorpha* heat stress assays
  - ATG8CL purification
  - Rab8a and Rab3GAPL-GAP purification
  - GST pull-down assays
  - Isothermal titration calorimetry (ITC)
  - GTPase activity assay
  - CRISPR/Cas9 construct design in *M. polymorpha*
  - Accession numbers
- QUANTIFICATION AND STATISTICAL ANALYSIS
  - Image processing and data analysis
  - Statistical tests

SUPPLEMENTAL INFORMATION

Supplemental information can be found online at https://doi.org/10.1016/j.cub.2024.04.002.

ACKNOWLEDGMENTS

We acknowledge and thank the Imperial College FILM facility for their technical expertise and the use of their microscopy equipment. We would also like to thank Vienna Biocenter Core Facilities for plant sciences, bio-optics, molecular biology, and protein technology core facilities. We also express our gratitude to the members of the Bozkurt, Dagdas, and Kamoun groups for their suggestions and productive discussion. E.L.H.Y. was funded by BBSRC (ref. BB/X511055/1 and BB/X016382/1). Y.T. and T.O.B. were funded by BBSRC (ref. BB/T006102/1). P.P. was funded by BBSRC (BB/M002462/1). C.D. was funded by BBSRC (ref. BB/M011224/1). M.C. was funded by the VIP2-Marie Curie CoFund program. Research in Y.D.'s lab was funded by Austrian Academy of Sciences, Austrian Science Fund (FWF, P 34944), Austrian Science Fund (FWF, SFB F79), Vienna Science and Technology Fund (WWTF, LS21-009), and European Research Council grant (project number: 101043370).

AUTHOR CONTRIBUTIONS

E.L.H.Y., A.Y.L., T.O.B., and Y.D. conceptualized the study. E.L.H.Y., A.Y.L., M.C., A.M., J.Z., L.P., and T.O.B. contributed to the methodology. E.L.H.Y., A.Y.L., M.C., Y.T., A.M., J.Z., and L.P. carried out validation and formal analysis, in addition to M.J., P.P., C.D., and T.O.B., who conducted the investigation. E.L.H.Y. and T.O.B. curated the data. E.L.H.Y., A.Y.L., M.C., A.M., J.Z., L.P., and T.O.B. performed data visualization. E.L.H.Y., A.Y.L., and T.O.B. wrote the original draft, which was reviewed and edited by E.L.H.Y., Y.D., and T.O.B. E.L.H.Y., A.Y.L., C.D., E.C., Y.D., and T.O.B. were involved in supervising the project, for which the funding was acquired by Y.D. and T.O.B.

DECLARATION OF INTERESTS

T.B. and C.D. receive funding from industry on NLR biology. T.B. and C.D. are founders and shareholders at Resurrect Bio Ltd.

Received: September 1, 2023
Revised: March 11, 2024
Accepted: April 2, 2024
Published: April 26, 2024

REFERENCES

1. Bao, Y., Song, W.M., Wang, P., Yu, X., Li, B., Jiang, C., Shiu, S.H., Zhang, H., and Bassham, D.C. (2020). COST1 regulates autophagy to control plant drought tolerance. Proc. Natl. Acad. Sci. USA *117*, 7482–7493. https://doi.org/10.1073/pnas.1918539117.
2. Yoshimoto, K., and Ohsumi, Y. (2018). Unveiling the molecular mechanisms of plant autophagy—from autophagosomes to vacuoles in plants. Plant Cell Physiol. *59*, 1337–1344. https://doi.org/10.1093/pcp/pcy112.
3. Leary, A.Y., Savage, Z., Tumtas, Y., and Bozkurt, T.O. (2019). Contrasting and emerging roles of autophagy in plant immunity. Curr. Opin. Plant Biol. *52*, 46–53. https://doi.org/10.1016/j.pbi.2019.07.002.
4. Leong, J.X., Raffeiner, M., Spinti, D., Langin, G., Franz-Wachtel, M., Guzman, A.R., Kim, J.G., Pandey, P., Minina, A.E., Macek, B., et al. (2022). A bacterial effector counteracts host autophagy by promoting degradation of an autophagy component. EMBO J. *41*, e110352. https://doi.org/10.15252/embj.2021110352.
5. Hafrén, A., Macia, J.L., Love, A.J., Milner, J.J., Drucker, M., and Hofius, D. (2017). Selective autophagy limits cauliflower mosaic virus infection by NBR1-mediated targeting of viral capsid protein and particles. Proc. Natl. Acad. Sci. USA *114*, E2026–E2035. https://doi.org/10.1073/pnas.1610687114.
6. Leary, A.Y., Sanguankiattichai, N., Duggan, C., Tumtas, Y., Pandey, P., Segretin, M.E., Salguero Linares, J., Savage, Z.D., Yow, R.J., and Bozkurt, T.O. (2018). Modulation of plant autophagy during pathogen attack. J. Exp. Bot. *69*, 1325–1333. https://doi.org/10.1093/jxb/erx425.
7. Liu, Y., and Bassham, D.C. (2012). Autophagy: pathways for self-eating in plant cells. Annu. Rev. Plant Biol. *63*, 215–237. https://doi.org/10.1146/annurev-arplant-042811-105441.

8. Chang, C., Jensen, L.E., and Hurley, J.H. (2021). Autophagosome biogenesis comes out of the black box. Nat. Cell Biol. *23*, 450–456. https://doi.org/10.1038/s41556-021-00669-y.

9. Zaffagnini, G., and Martens, S. (2016). Mechanisms of selective autophagy. J. Mol. Biol. *428*, 1714–1724. https://doi.org/10.1016/j.jmb.2016.02.004.

10. Kellner, R., De la Concepcion, J.C., Maqbool, A., Kamoun, S., and Dagdas, Y.F. (2017). ATG8 expansion: a driver of selective autophagy diversification? Trends Plant Sci. *22*, 204–214. https://doi.org/10.1016/j.tplants.2016.11.015.

11. Nakatogawa, H., Ohbayashi, S., Sakoh-Nakatogawa, M., Kakuta, S., Suzuki, S.W., Kirisako, H., Kondo-Kakuta, C., Noda, N.N., Yamamoto, H., and Ohsumi, Y. (2012). The autophagy-related protein kinase Atg1 interacts with the ubiquitin-like protein Atg8 via the Atg8 family interacting motif to facilitate autophagosome formation. J. Biol. Chem. *287*, 28503–28507. https://doi.org/10.1074/jbc.C112.387514.

12. Taherbhoy, A.M., Tait, S.W., Kaiser, S.E., Williams, A.H., Deng, A., Nourse, A., Hammel, M., Kurinov, I., Rock, C.O., Green, D.R., and Schulman, B.A. (2011). Atg8 transfer from Atg7 to Atg3: a distinctive E1-E2 architecture and mechanism in the autophagy pathway. Mol. Cell *44*, 451–461. https://doi.org/10.1016/j.molcel.2011.08.034.

13. Johansen, T., and Lamark, T. (2020). Selective autophagy: ATG8 family proteins, LIR motifs and cargo receptors. J. Mol. Biol. *432*, 80–103. https://doi.org/10.1016/j.jmb.2019.07.016.

14. Maqbool, A., Hughes, R.K., Dagdas, Y.F., Tregidgo, N., Zess, E., Belhaj, K., Round, A., Bozkurt, T.O., Kamoun, S., and Banfield, M.J. (2016). Structural Basis of Host Autophagy-related Protein 8 (ATG8) Binding by the Irish Potato Famine Pathogen Effector Protein PexRD54*◆. J. Biol. Chem. *291*, 20270–20282. https://doi.org/10.1074/jbc.M116.744995.

15. Ibrahim, T., Khandare, V., Mirkin, F.G., Tumtas, Y., Bubeck, D., and Bozkurt, T.O. (2023). AlphaFold2-multimer guided high-accuracy prediction of typical and atypical ATG8-binding motifs. PLOS Biol. *21*, e3001962. https://doi.org/10.1371/journal.pbio.3001962.

16. Pandey, P., Leary, A.Y., Tumtas, Y., Savage, Z., Dagvadorj, B., Duggan, C., Yuen, E.L.H., Sanguankiattichai, N., Tan, E., Khandare, V., et al. (2021). An oomycete effector subverts host vesicle trafficking to channel starvation-induced autophagy to the pathogen interface. eLife *10*, e65285. https://doi.org/10.7554/eLife.65285.

17. Yuen, E.L.H., Shepherd, S., and Bozkurt, T.O. (2023). Traffic Control: Subversion of Plant Membrane Trafficking by Pathogens. Annu. Rev. Phytopathol. *61*, 325–350. https://doi.org/10.1146/annurev-phyto-021622-123232.

18. Dagdas, Y.F., Belhaj, K., Maqbool, A., Chaparro-Garcia, A., Pandey, P., Petre, B., Tabassum, N., Cruz-Mireles, N., Hughes, R.K., Sklenar, J., et al. (2016). An effector of the Irish potato famine pathogen antagonizes a host autophagy cargo receptor. eLife *5*, e10856. https://doi.org/10.7554/eLife.10856.

19. Dagdas, Y.F., Pandey, P., Tumtas, Y., Sanguankiattichai, N., Belhaj, K., Duggan, C., Leary, A.Y., Segretin, M.E., Contreras, M.P., Savage, Z., et al. (2018). Host autophagy machinery is diverted to the pathogen interface to mediate focal defense responses against the Irish potato famine pathogen. eLife *7*, e37476. https://doi.org/10.7554/eLife.37476.

20. Davis, S., Wang, J., and Ferro-Novick, S. (2017). Crosstalk between the secretory and autophagy pathways regulates autophagosome formation. Dev. Cell *41*, 23–32. https://doi.org/10.1016/j.devcel.2017.03.015.

21. Søreng, K., Neufeld, T.P., and Simonsen, A. (2018). Membrane trafficking in autophagy. Int. Rev. Cell Mol. Biol. *336*, 1–92. https://doi.org/10.1016/bs.ircmb.2017.07.001.

22. Zeng, Y., Li, B., Ji, C., Feng, L., Niu, F., Deng, C., Chen, S., Lin, Y., Cheung, K.C.P., Shen, J., et al. (2021). A unique AtSar1D-AtRabD2a nexus modulates autophagosome biogenesis in Arabidopsis thaliana. Proc. Natl. Acad. Sci. USA *118*, e2021293118. https://doi.org/10.1073/pnas.2021293118.

23. Ao, X., Zou, L., and Wu, Y. (2014). Regulation of autophagy by the Rab GTPase network. Cell Death Differ. *21*, 348–358. https://doi.org/10.1038/cdd.2013.187.

24. Lu, Q., Wang, P.S., and Yang, L. (2021). Golgi-associated Rab GTPases implicated in autophagy. Cell Biosci. *11*, 35. https://doi.org/10.1186/s13578-021-00543-2.

25. Zeng, Y., Li, B., Lin, Y., and Jiang, L. (2019). The interplay between endomembranes and autophagy in plants. Curr. Opin. Plant Biol. *52*, 14–22. https://doi.org/10.1016/j.pbi.2019.05.009.

26. Bansal, M., Moharir, S.C., Sailasree, S.P., Sirohi, K., Sudhakar, C., Sarathi, D.P., Lakshmi, B.J., Buono, M., Kumar, S., and Swarup, G. (2018). Optineurin promotes autophagosome formation by recruiting the autophagy-related Atg12-5-16L1 complex to phagophores containing the Wipi2 protein. J. Biol. Chem. *293*, 132–147. https://doi.org/10.1074/jbc.M117.801944.

27. Zoppino, F.C., Militello, R.D., Slavin, I., Alvarez, C., and Colombo, M.I. (2010). Autophagosome formation depends on the small GTPase Rab1 and functional ER exit sites. Traffic *11*, 1246–1261. https://doi.org/10.1111/j.1600-0854.2010.01086.x.

28. Vaibhava, V., Nagabhushana, A., Chalasani, M.L.S., Sudhakar, C., Kumari, A., and Swarup, G. (2012). Optineurin mediates a negative regulation of Rab8 by the GTPase-activating protein TBC1D17. J. Cell Sci. *125*, 5026–5039. https://doi.org/10.1242/jcs.102327.

29. Itzen, A., and Goody, R.S. (2011). GTPases involved in vesicular trafficking: structures and mechanisms. Semin. Cell Dev. Biol. *22*, 48–56. https://doi.org/10.1016/j.semcdb.2010.10.003.

30. Longatti, A., Lamb, C.A., Razi, M., Yoshimura, S.-i., Barr, F.A., and Tooze, S.A. (2012). TBC1D14 regulates autophagosome formation via Rab11- and ULK1-positive recycling endosomes. J. Cell Biol. *197*, 659–675. https://doi.org/10.1083/jcb.201111079.

31. Zess, E.K., Jensen, C., Cruz-Mireles, N., De la Concepcion, J.C., Sklenar, J., Stephani, M., Imre, R., Roitinger, E., Hughes, R., Belhaj, K., et al. (2019). N-terminal beta-strand underpins biochemical specialization of an ATG8 isoform. PLoS Biol *17*, e3000373. https://doi.org/10.1371/journal.pbio.3000373.

32. Clabecq, A., Henry, J.P., and Darchen, F.o. (2000). Biochemical characterization of Rab3-GTPase-activating protein reveals a mechanism similar to that of Ras-GAP. J. Biol. Chem. *275*, 31786–31791. https://doi.org/10.1074/jbc.M003705200.

33. Robert, X., and Gouet, P. (2014). Deciphering key features in protein structures with the new ENDscript server. Nucleic Acids Res. *42*, W320–W324. https://doi.org/10.1093/nar/gku316.

34. Cardinal-McTeague, W.M., Sytsma, K.J., and Hall, J.C. (2016). Biogeography and diversification of Brassicales: a 103 million year tale. Mol. Phylogenet. Evol. *99*, 204–224. https://doi.org/10.1016/j.ympev.2016.02.021.

35. Bassham, D.C. (2015). Methods for analysis of autophagy in plants. Methods *75*, 181–188. https://doi.org/10.1016/j.ymeth.2014.09.003.

36. Yoshii, S.R., and Mizushima, N. (2017). Monitoring and measuring autophagy. Int. J. Mol. Sci. *18*, 1865. https://doi.org/10.3390/ijms18091865.

37. Phillips, A.R., Suttangkakul, A., and Vierstra, R.D. (2008). The ATG12-conjugating enzyme ATG10 is essential for autophagic vesicle formation in Arabidopsis thaliana. Genetics *178*, 1339–1353. https://doi.org/10.1534/genetics.107.086199.

38. Thompson, A.R., Doelling, J.H., Suttangkakul, A., and Vierstra, R.D. (2005). Autophagic nutrient recycling in Arabidopsis directed by the ATG8 and ATG12 conjugation pathways. Plant Physiol. *138*, 2097–2110. https://doi.org/10.1104/pp.105.060673.

39. Hanaoka, H., Noda, T., Shirano, Y., Kato, T., Hayashi, H., Shibata, D., Tabata, S., and Ohsumi, Y. (2002). Leaf senescence and starvation-induced chlorosis are accelerated by the disruption of an Arabidopsis autophagy gene. Plant Physiol. *129*, 1181–1193. https://doi.org/10.1104/pp.011024.

40. Zhou, J., Wang, J., Cheng, Y., Chi, Y.J., Fan, B., Yu, J.Q., and Chen, Z. (2013). NBR1-mediated selective autophagy targets insoluble ubiquitinated protein aggregates in plant stress responses. PLoS genetics *9*, e1003196. https://doi.org/10.1371/journal.pgen.1003196.

41. Zhou, J., Wang, J., Yu, J.Q., and Chen, Z. (2014). Role and regulation of autophagy in heat stress responses of tomato plants. Front. Plant Sci. *5*, 174. https://doi.org/10.3389/fpls.2014.00174.

42. Thirumalaikumar, V.P., Gorka, M., Schulz, K., Masclaux-Daubresse, C., Sampathkumar, A., Skirycz, A., Vierstra, R.D., and Balazadeh, S. (2021). Selective autophagy regulates heat stress memory in Arabidopsis by NBR1-mediated targeting of HSP90. 1 and ROF1. Autophagy *17*, 2184–2199. https://doi.org/10.1080/15548627.2020.1820778.

43. Zhou, J., Wang, Z., Wang, X., Li, X., Zhang, Z., Fan, B., Zhu, C., and Chen, Z. (2018). Dicot-specific ATG8-interacting ATI3 proteins interact with conserved UBAC2 proteins and play critical roles in plant stress responses. Autophagy *14*, 487–504. https://doi.org/10.1080/15548627.2017.1422856.

44. Zhou, J., Zhang, Y., Qi, J., Chi, Y., Fan, B., Yu, J.Q., and Chen, Z. (2014). E3 ubiquitin ligase CHIP and NBR1-mediated selective autophagy protect additively against proteotoxicity in plant stress responses. PLoS genetics *10*, e1004116. https://doi.org/10.1371/journal.pgen.1004116.

45. Puri, C., Vicinanza, M., Ashkenazi, A., Gratian, M.J., Zhang, Q., Bento, C.F., Renna, M., Menzies, F.M., and Rubinsztein, D.C. (2018). The RAB11A-positive compartment is a primary platform for autophagosome assembly mediated by WIPI2 recognition of PI3P-RAB11A. Dev. Cell *45*, 114–131.e8. https://doi.org/10.1016/j.devcel.2018.03.008.

46. Waschbüsch, D., Purlyte, E., and Khan, A.R. (2021). Dual arginine recognition of LRRK2 phosphorylated Rab GTPases. Biophys. J. *120*, 1846–1855. https://doi.org/10.1016/j.bpj.2021.03.030.

47. Cherfils, J., and Zeghouf, M. (2013). Regulation of small gtpases by gefs, gaps, and gdis. Physiol. Rev. *93*, 269–309. https://doi.org/10.1152/physrev.00003.2012.

48. Shpilka, T., Weidberg, H., Pietrokovski, S., and Elazar, Z. (2011). Atg8: an autophagy-related ubiquitin-like protein family. Genome Biol. *12*, 226. https://doi.org/10.1186/gb-2011-12-7-226.

49. Li, T., Ai, G., Fu, X., Liu, J., Zhu, H., Zhai, Y., Pan, W., Shen, D., Jing, M., Xia, A., and Dou, D. (2022). A Phytophthora capsici RXLR effector manipulates plant immunity by targeting RAB proteins and disturbing the protein trafficking pathway. Mol. Plant Pathol. *23*, 1721–1736. https://doi.org/10.1111/mpp.13251.

50. Bozkurt, T.O., Richardson, A., Dagdas, Y.F., Mongrand, S., Kamoun, S., and Raffaele, S. (2014). The Plant Membrane-Associated REMORIN1.3 Accumulates in Discrete Perihaustorial Domains and Enhances Susceptibility to Phytophthora infestans. Plant Physiol. *165*, 1005–1018. https://doi.org/10.1104/pp.114.235804.

51. Caillaud, M.C., Wirthmueller, L., Sklenar, J., Findlay, K., Piquerez, S.J., Jones, A.M., Robatzek, S., Jones, J.D., and Faulkner, C. (2014). The plasmodesmal protein PDLP1 localises to haustoria-associated membranes during downy mildew infection and regulates callose deposition. PLoS Pathog. *10*, e1004496. https://doi.org/10.1371/journal.ppat.1004496.

52. Micali, C.O., Neumann, U., Grunewald, D., Panstruga, R., and O'Connell, R. (2011). Biogenesis of a specialized plant–fungal interface during host cell internalization of Golovinomyces orontii haustoria. Cell. Microbiol. *13*, 210–226. https://doi.org/10.1111/j.1462-5822.2010.01530.x.

53. Speth, E.B., Imboden, L., Hauck, P., and He, S.Y. (2009). Subcellular localization and functional analysis of the Arabidopsis GTPase RabE. Plant Physiol. *149*, 1824–1837. https://doi.org/10.1104/pp.108.132092.

54. Han, Z., Xiong, D., Schneiter, R., and Tian, C. (2023). The function of plant PR1 and other members of the CAP protein superfamily in plant–pathogen interactions. Mol. Plant Pathol. *24*, 651–668. https://doi.org/10.1111/mpp.13320.

55. Nekrasov, V., Wang, C., Win, J., Lanz, C., Weigel, D., and Kamoun, S. (2017). Rapid generation of a transgene-free powdery mildew resistant tomato by genome deletion. Sci. Rep. *7*, 482. https://doi.org/10.1038/s41598-017-00578-x.

56. van Schie, C.C., and Takken, F.L. (2014). Susceptibility genes 101: how to be a good host. Annu. Rev. Phytopathol. *52*, 551–581. https://doi.org/10.1146/annurev-phyto-102313-045854.

57. Zaidi, S.S.-e.-A., Mukhtar, M.S., and Mansoor, S. (2018). Genome editing: targeting susceptibility genes for plant disease resistance. Trends Biotechnol. *36*, 898–906. https://doi.org/10.1016/j.tibtech.2018.04.005.

58. Hu, S., Ye, H., Cui, Y., and Jiang, L. (2020). AtSec62 is critical for plant development and is involved in ER-phagy in Arabidopsis thaliana. J. Integr. Plant Biol. *62*, 181–200. https://doi.org/10.1111/jipb.12872.

59. Zhao, J., Bui, M.T., Ma, J., Künzl, F., Picchianti, L., De La Concepcion, J.C., Chen, Y., Petsangouraki, S., Mohseni, A., García-Leon, M., et al. (2022). Plant autophagosomes mature into amphisomes prior to their delivery to the central vacuole. J. Cell Biol. *221*, e202203139. https://doi.org/10.1083/jcb.202203139.

60. Norizuki, T., Minamino, N., Sato, M., Tsukaya, H., and Ueda, T. (2022). Dynamic rearrangement and autophagic degradation of mitochondria during spermiogenesis in the liverwort Marchantia polymorpha. Cell Rep. *39*, 110975. https://doi.org/10.1016/j.celrep.2022.110975.

61. Bozkurt, T.O., Schornack, S., Win, J., Shindo, T., Ilyas, M., Oliva, R., Cano, L.M., Jones, A.M., Huitema, E., van der Hoorn, R.A., and Kamoun, S. (2011). Phytophthora infestans effector AVRblb2 prevents secretion of a plant immune protease at the haustorial interface. Proc. Natl. Acad. Sci. USA *108*, 20832–20837. https://doi.org/10.1073/pnas.1112708109.

62. Schindelin, J., Arganda-Carreras, I., Frise, E., Kaynig, V., Longair, M., Pietzsch, T., Preibisch, S., Rueden, C., Saalfeld, S., Schmid, B., et al. (2012). Fiji: an open-source platform for biological-image analysis. Nat. Methods *9*, 676–682. https://doi.org/10.1038/nmeth.2019.

63. R Core Team (2013). R: A Language and Environment for Statistical Computing (R Foundation for Statistical Computing).

64. Wickham, H., and Wickham, H. (2016). Data Analysis (Springer).

65. Mirdita, M., Schütze, K., Moriwaki, Y., Heo, L., Ovchinnikov, S., and Steinegger, M. (2022). ColabFold: making protein folding accessible to all. Nat. Methods *19*, 679–682. https://doi.org/10.1038/s41592-022-01488-1.

66. Meng, E.C., Goddard, T.D., Pettersen, E.F., Couch, G.S., Pearson, Z.J., Morris, J.H., and Ferrin, T.E. (2023). UCSF ChimeraX: Tools for structure building and analysis. Protein Sci. *32*, e4792. https://doi.org/10.1002/pro.4792.

67. Kubota, A., Ishizaki, K., Hosaka, M., and Kohchi, T. (2013). Efficient Agrobacterium-mediated transformation of the liverwort Marchantia polymorpha using regenerating thalli. Biosci. Biotechnol. Biochem. *77*, 167–172. https://doi.org/10.1271/bbb.120700.

68. van West, P., de Jong, A.J., Judelson, H.S., Emons, A.M., and Govers, F. (1998). The ipiO gene of Phytophthora infestans is highly expressed in invading hyphae during infection. Fungal Genet. Biol. *23*, 126–138. https://doi.org/10.1006/fgbi.1998.1036.

69. Duggan, C., Moratto, E., Savage, Z., Hamilton, E., Adachi, H., Wu, C.H., Leary, A.Y., Tumtas, Y., Rothery, S.M., Maqbool, A., et al. (2021). Dynamic localization of a helper NLR at the plant-pathogen interface underpins pathogen recognition. Proc. Natl. Acad. Sci. USA *118*, e2104997118. https://doi.org/10.1073/pnas.2104997118.

70. Yan, P., Shen, W., Gao, X., Li, X., Zhou, P., and Duan, J. (2012). High-throughput construction of intron-containing hairpin RNA vectors for RNAi in plants. PLoS One *7*, e38186. https://doi.org/10.1371/journal.pone.0038186.

71. Chaparro-Garcia, A., Wilkinson, R.C., Gimenez-Ibanez, S., Findlay, K., Coffey, M.D., Zipfel, C., Rathjen, J.P., Kamoun, S., and Schornack, S. (2011). The receptor-like kinase SERK3/BAK1 is required for basal resistance against the late blight pathogen Phytophthora infestans in Nicotiana benthamiana. PloS one *6*, e16608. https://doi.org/10.1371/journal.pone.0016608.

72. Jumper, J., Evans, R., Pritzel, A., Green, T., Figurnov, M., Ronneberger, O., Tunyasuvunakool, K., Bates, R., Žídek, A., Potapenko, A., et al. (2021).

Highly accurate protein structure prediction with AlphaFold. Nature *596*, 583–589. https://doi.org/10.1038/s41586-021-03819-2.

73. Mariani, V., Biasini, M., Barbato, A., and Schwede, T. (2013). lDDT: a local superposition-free score for comparing protein structures and models using distance difference tests. Bioinformatics *29*, 2722–2728. https://doi.org/10.1093/bioinformatics/btt473.

74. Edgar, R.C. (2004). MUSCLE: multiple sequence alignment with high accuracy and high throughput. Nucleic Acids Res. *32*, 1792–1797. https://doi.org/10.1093/nar/gkh340.

75. O'Leary, B.M., Rico, A., McCraw, S., Fones, H.N., and Preston, G.M. (2014). The infiltration-centrifugation technique for extraction of apoplastic fluid from plant leaves using Phaseolus vulgaris as an example. J. Vis. Exp. *94*, 52113. https://doi.org/10.3791/52113.

76. Picchianti, L., Sánchez de Medina Hernández, V., Zhan, N., Irwin, N.A., Groh, R., Stephani, M., Hornegger, H., Beveridge, R., Sawa-Makarska, J., Lendl, T., et al. (2023). Shuffled ATG8 interacting motifs form an ancestral bridge between UFMylation and autophagy. EMBO J. *42*, e112053. https://doi.org/10.15252/embj.2022112053.

77. Sugano, S.S., Nishihama, R., Shirakawa, M., Takagi, J., Matsuda, Y., Ishida, S., Shimada, T., Hara-Nishimura, I., Osakabe, K., and Kohchi, T. (2018). Efficient CRISPR/Cas9-based genome editing and its application to conditional genetic analysis in Marchantia polymorpha. PLoS One *13*, e0205117. https://doi.org/10.1371/journal.pone.0205117.

STAR★METHODS

KEY RESOURCES TABLE

REAGENT or RESOURCE	SOURCE	IDENTIFIER
Antibodies		
GFP mouse monoclonal	ChromoTek	3H9; RRID: AB_10773374
GFP rabbit polyclonal	ChromoTek	PABG1; RRID: AB_2749857
RFP mouse monoclonal	ChromoTek	6G6; RRID: AB_2631395
TagBFP rabbit polyclonal	Evrogen	AB233; RRID: AB_2571743
PR1 rabbit polyclonal	Agrisera	AS10 687; RRID: AB_10751750
Anti-rabbit HRP	Sigma-Aldrich	A9169; RRID: AB_258434
Anti-rabbit AP	Sigma-Aldrich	SAB3700834
Anti-rat HRP	Sigma-Aldrich	A9037; RRID: AB_258429
Anti-mouse HRP	Sigma-Aldrich	SAB3700986
Bacterial and virus strains		
Agrobacterium tumefaciens GV3101 electrocompetent cells	Our laboratory collection	N/A
Escherichia coli DH5α competent cells	Our laboratory collection	N/A
Escherichia coli BL21 (DE3) competent cells	Our laboratory collection	N/A
Escherichia coli Rosetta 2(DE3) competent cells	Our laboratory collection	N/A
Chemicals, peptides, and recombinant proteins		
LB broth (Miller)	VWR	84649
Bacteriological agar	VWR	84609
Plant agar (for Arabidopsis)	Duchefa Biochemie	P1001
Gamborg B5 medium	Duchefa Biochemie	G0209
MS medium	Duchefa Biochemie	M0222
Organic raw whole rye grain seeds	Natural Vita	https://naturalvita.co.uk/shop/nuts-seeds/seeds-for-sprouting/organic-raw-whole-rye-grain-seeds/
Sucrose	Sigma-Aldrich	Product No. S0389
Phusion® High-Fidelity DNA polymerase	New England Biolabs	Catalog # M0530S
TRIzol™ reagent	Invitrogen	Catalog number: 15596026
RQ1 RNase-Free DNase	Promega	Catalog number: M6101
SuperScript™ IV reverse transcriptase	Invitrogen	Catalog number: 18090010
Carolina observation gel	Carolina Biological Supply Company	Item # 132700
Poly(vinylpolypyrrolidone)	Sigma-Aldrich	Product No. 77627
IGEPAL CA-630	Sigma-Aldrich	Product No. I8896
4x Laemmli sample buffer	Bio-Rad	#1610747
cOmplete™ protease inhibitor cocktail	Roche	11697498001
Torin 1	Santa Cruz Biotechnology	CAS 1222998-36-8
Concanamycin A	Santa Cruz Biotechnology	CAS 80890-47-7
LR Clonase™ II Enzyme mix	Invitrogen	Catalog number: 11791020
Hygromycin B	Gibco	Catalog number: 10687010
Sodium phosphate monobasic	Sigma-Aldrich	Product No. S0751
Sodium phosphate dibasic	Sigma-Aldrich	Product No. S7907
Aniline Blue diammonium salt	Sigma-Aldrich	Product No. 415049
Pierce™ Glutathione Magnetic Agarose Beads	Thermo Scientific	Catalog number: 78602
HisTrap FF	Cytiva	17531901
HiLoad 16/600 Superdex 200 pg	Cytiva	28989335
HiLoad 16/600 Superdex 75 pg	Cytiva	28989333

(*Continued on next page*)

Continued

REAGENT or RESOURCE	SOURCE	IDENTIFIER
Critical commercial assays		
PureYield™ Plasmid Miniprep System	Promega	Catalog number: A1223
Wizard® SV Gel and PCR Clean-Up System	Promega	Catalog number: A9281
GTPase-Glo™ Assay	Promega	Catalog number: V7681
Deposited data		
Potato PGSC DM genome v3.4	Sol Genomics Network	solgenomics.net
N. benthamiana genome Nbe_v1.1	NbenBase	nbenthamiana.jp
AF2-multimer predictions of AIMs of Rab3GAPL across diverse plant lineages with ATG8CL	Figshare	Figshare: https://doi.org/10.6084/m9.figshare.24921612
All other AF2-multimer predictions	Figshare	Figshare: https://doi.org/10.6084/m9.figshare.23587575
Experimental models: Organisms/strains		
Nicotiana benthamiana (wildtype)	Our laboratory collection	N/A
Arabidopsis thaliana mCherry:ATG8e (wildtype)	Hu et al.[58]	N/A
Arabidopsis thaliana mCherry:ATG8e-*atg5-1*	Zhao et al.[59]	N/A
Arabidopsis thaliana mCherry:ATG8e-NbRab3GAPL	This study	N/A
Arabidopsis thaliana mCherry:ATG8e-NbRab3GAPL^{AIM}	This study	N/A
Marchantia polymorpha Mp-GFP:ATG8b (wildtype)	Norizuki et al.[60]	N/A
Marchantia polymorpha Mp-GFP:ATG8b-*rab3gapl-1*	This study	N/A
Marchantia polymorpha Mp-GFP:ATG8b-*rab3gapl-2*	This study	N/A
Marchantia polymorpha atg-7	Norizuki et al.[60]	N/A
Phytophthora infestans 88069 isolate (wildtype)	Bozkurt et al.[61]	N/A
Phytophthora infestans 88069 isolate (tdTomato)	Bozkurt et al.[61]	N/A
Oligonucleotides		
All oligonucleotides	This study	Table S1
Recombinant DNA		
All constructs	This study, or otherwise cited	Table S2
Software and algorithms		
Leica Application Suite X	Leica	https://www.leica-microsystems.com/products/microscope-software/p/leica-las-x-ls/
Fiji (ImageJ version 2.14.0)	Schindelin et al.[62]	https://fiji.sc
R (version 4.3.3)	R Core Team[63]	https://www.r-project.org/
ggplot2 (R package)	Wickham[64]	https://ggplot2.tidyverse.org
Origin 7.0	OriginLab	https://www.originlab.com
Image Studio v5.5.4	LI-COR	https://www.licor.com/bio/image-studio/
AlphaFold2.ipynb	Mirdita et al.[65]	https://colab.research.google.com/github/sokrypton/ColabFold/blob/main/AlphaFold2.ipynb
UCSF ChimeraX (version 1.7.1)	Meng et al.[66]	https://www.rbvi.ucsf.edu/chimerax/
ESPript 3.0	Robert and Gouet et al.[33]	https://espript.ibcp.fr/ESPript/ESPript/

RESOURCE AVAILABILITY

Lead contact

Further information and requests for resources and reagents should be directed to and will be fulfilled by the lead contact, Tolga Bozkurt (o.bozkurt@imperial.ac.uk).

Materials availability

Constructs generated in this study are available from the lead contact on request.

Data and code availability

- AF2-multimer predictions data have been deposited at the public repository Figshare and are publicly available as of the date of publication. DOIs are listed in the key resources table. All accession numbers are listed in method details.
- This paper does not report original code.
- Any additional information required to reanalyze the data reported in this paper is available from the lead contact upon request.

EXPERIMENTAL MODEL AND SUBJECT DETAILS

Plant growth details

Wildtype *Nicotiana benthamiana* plants were grown in a controlled growth chamber at 24°C in a mixture of organic soil (3:1 ratio of Levington's F2 with sand and Sinclair's 2-5 mm vermiculite). The plants were exposed to high light intensity and subjected to a long day 16 h light/8 h dark photoperiod. Experiments were conducted using plants that were 4-5 weeks old.

Marchantia polymorpha MpEF1:MpATG8b-GFP plants expressed in Takaragaike-1 (TAK-1, male) were used. The plants were grown on half-strength Gamborg B5 medium containing 1 % agar under 50-60 mmol $m^{-2}s^{-1}$ of white light at 22°C.[67]

For standard *Arabidopsis thaliana* growth, seeds were sown on water-saturated soil containing fertilizer and kept in 16 h light/8 h dark photoperiod with 165 μmol m^{-2} s^{-1} light intensity. For *in vitro* seedling growth, Arabidopsis seeds were surface sterilized in 70% ethanol 0.05% SDS for 15 minutes, rinsed twice in ethanol absolute and dried on sterile paper. Seeds were plated in 1/2 MS + 1% agar + 1% sucrose and stratified for 24-to-48 hours in the dark at 4°C. Plates were then grown in a 16 h light/8 h dark photoperiod. 50 μmol m^{-2} s^{-1} light intensity For selection of Arabidopsis stable lines, transformants were plated on ½ MS media supplemented with kanamycin and resistant seedlings were transferred to soil. Plants were then screened for GFP-Rab3GAP expression using western blot.

Pathogen growth details

WT and tdTomato-expressing *Pytophthora infestans* 88069 isolates were grown on rye sucrose agar (RSA) media in the dark at 18°C for 10 - 15 days before harvesting zoospores.[68] The pathogen strains are detailed in the key resource table. Their sporulating conditions and subsequent experimental steps are described in method details.

METHOD DETAILS

Molecular cloning

Molecular clonings of Rab3GAPL, Rab3GAPL^{AIM}, Rab3GAPL^{CM}, Rab3GAPL$^{CM/AIM}$, Rab1, Rab2, Rab8b and Rab11 were performed using Gibson Assembly as described previously.[18,69] The vector backbone is a pK7WGF2 derivative domesticated for Gibson Assembly. Plasmids were constructed using primers and transformed into DH5α chemically-competent *E. coli* by heat shock. Plasmids were then amplified and extracted by PureYield™ Plasmid Miniprep System (Promega), and electroporated into *Agrobacterium tumefaciens* GV3101 electrocompetent cells. Sequencing was performed by Eurofins. RNA interference silencing constructs (RNAi:Rab3GAPL-1 and RNAi:Rab3GAPL-2) were made using an intron-containing hairpin RNA vector for RNA interference in plants (pRNAi-GG), based on Golden Gate cloning as described previously.[70] RNAi:Rab3GAPL-1 targeted the region between 999 and 1301 bp of *Rab3GAPL*, while RNAi:Rab3GAPL-2 targeted the 3' UTR region of *Rab3GAPL*. After amplifying the target fragments using designed primers, the fragments were inserted into the pRNAi-GG vector both in sense and anti-sense orientation using the overhangs left by BsaI cleavage. The resulting plasmid leads to expression of a construct that folds back onto itself forming the silencing hairpin structure. The subsequent steps of *E. coli* transformation, Miniprep, sequencing and agrotransformation were the same as overexpression constructs. All primers used in this study are detailed in Table S1. Constructs used in this study are detailed in Table S2.

P. infestans growth and infection assays

WT and tdTomato-expressing *Pytophthora infestans* 88069 isolates were grown on rye sucrose agar (RSA) media in the dark at 18°C for 10 - 15 days before harvesting zoospores.[68] Zoospore solution was collected by adding 4°C cold water to the media and incubated at 4°C for 90 minutes. For infection assay, 10 μl droplets of zoospore solution at 50,000 spores/ml were added to the abaxial side (underside) of agroinfiltrated leaves.[71] Leaves were then kept in humid conditions. Microscopy of infected leaves was conducted 3 days post infection. Daylight and fluorescent images were taken at 7 - 8 days post infection, which lesion sizes and hyphal growth were measured in ImageJ.

Confocal microscopy

Confocal microscopy analyses on *N. benthamiana* samples were carried out 3 days post agroinfiltration. Leaf discs for microscopy were taken using size 4 cork borer, live-mounted on glass slides, and submerged in wells of dH2O using Carolina observation gel

(Carolina Biological Supply Company). The slides were imaged using Leica TCS SP8 resonant inverted confocal microscope with 40x water immersion objective lens. The abaxial side of leaf tissue was imaged. The laser excitations for BFP, GFP and RFP tags are Diode 405 nm, Argon 488 nm and DPSS 561 nm respectively. Sequential scanning between lines was performed to prevent spectral mixing from different fluorophores when imaging samples with more than one tag. Confocal images, including Z-stack and single plane images, were analysed in ImageJ.

Confocal microscopy analyses on Arabidopsis samples were carried out via an upright point laser scanning confocal microscope ZEISS LSM800 Axio Imager.Z2 (Carl Zeiss) equipped with high-sensitive GaAsP detectors (Gallium Arsenide), a LD C-Apochromat 40X objective lens (numerical aperture 1.1, water immersion), and ZEN software (blue edition 3.8, Carl Zeiss). GFP signals were excited at 488 nm and detected between 488 and 545 nm. mCherry signals were excited at 561 nm and detected between 570 and 617 nm. For Z-stack imaging, the interval between the layers was set as 1 μm.

Structural and sequence analyses

AF2-multimer was utilized through a subscription to the Google Colab in accordance with their guidelines.[72] The align command in UCSF Chimera (version 1.17) was employed to superimpose the AF2 predictions onto known structures and to show the confidence score of the AF2 predictions using the local distance difference test (pLDDT) scores on the lDDT-Cα metric.[73] The scoring scale ranges from 0 to 100, where 100 corresponds to the highest confidence values. Sequence alignment was performed using the MUSCLE algorithm,[74] and the resulting alignments were visualized and color-coded via ESPript 3.0[33] The proteins and sequences used for AF2 are detailed in Table S3.

Transient gene expression in *N. benthamiana*

Agrobacterium-mediated transient gene expression was conducted using agroinfiltration as previously described.[61] *Agrobacterium tumefaciens* containing the desired plasmid was washed in water and resuspended in agroinfiltration buffer (10 mM MES, 10 mM $MgCl_2$, pH 5.7). BioPhotometer spectrophotometer (Eppendorf) was used to measure the OD_{600} of the bacterial suspension. This suspension was adjusted to a desired OD_{600} depending on the construct and the experiment, and then infiltrated into 3 to 4-week-old *N. benthamiana* leaf tissue using needleless 1ml Plastipak syringe.

RNA isolation, cDNA synthesis, and RT-PCR

For RNA extraction, 56 mg of leaf tissue was frozen in liquid nitrogen. RNA was extracted using TRIzol RNA Isolation Reagent (Invitrogen) according to the user manual. RNA concentration was measured using NanoDrop Lite Spectrophotometer (Thermo Scientific). 2 μg of extracted RNA was treated with RQ1 RNase-Free DNAse (Promega), then used for cDNA synthesis using SuperScript IV Reverse Transcriptase (Invitrogen). cDNA was amplified using Phusion High-Fidelity DNA Polymerase (New England Biolabs). GAPDH level was used as a transcriptional control.

Callose staining

Callose staining was performed as described previously.[61] *N. benthamiana* leaf discs from infected tissue expressing the proteins of interest were collected and rinsed twice in 50% ethanol. They were then rinsed in a sodium phosphate buffer (0.07 M, pH 9.0) for 30 minutes at room temperature. The leaf discs were then incubated with 0.05% w/v aniline blue solution in the phosphate buffer for 60 minutes in the dark at room temperature. Confocal microscopy was followed afterwards.

Co-immunoprecipitation and blotting analyses

Proteins were transiently expressed by agroinfiltration in *N. benthamiana* leaves and harvested 3 days post agroinfiltration. For western blotting experiments, 6 leaf discs were excised using size 4 cork borer (42 mg). For co-immunoprecipitation experiments, 2 g of leaf tissues were used. Protein extraction, purification and immunoblot analysis were performed as described previously.[18,61] Monoclonal anti-GFP produced in rat (Chromotek), polyclonal anti-GFP produced in rabbit (Chromotek), monoclonal anti-RFP produced in mouse (Chromotek), polyclonal anti-tBFP produced in rabbit (Evrogen) were used as primary antibodies. Anti-mouse antibody (Sigma-Aldrich), anti-rabbit antibody (Sigma-Adrich), anti-rat antibody (Sigma-Aldrich) were used as secondary antibodies. Information of antibodies is detailed in Key resources table.

P. infestans extract preparation

Mycelia from a *P. infestans* RSA plate were scraped and suspended in 5 ml of water. The mixture was vortexed for 1 minute and incubated at 95°C for 20 minutes, then filtered using 5-13 μm filter paper. The filtrate was again filtered using a syringe filter with a 0.45 μm pore size. The resulting solution was injected into plants to function as a PAMP cocktail.

Apoplast extraction

Apoplastic proteins were extracted as described previously.[75] Infiltrated *N. benthamiana* leaves were detached and washed in distilled water, then rolled up and inserted in a needleless syringe filled with distilled water. The whole leaves were then infiltrated with the water by creating a negative pressure environment inside the syringe. The leaves were then centrifuged for 10 minutes at 1000g in a Falcon tube. Apoplastic washing fluid was collected at the bottom of the tube and snap-frozen in liquid nitrogen. Leaf tissue was collected from the remaining leaf for immunoblotting analysis.

A. thaliana carbon starvation assays

Arabidopsis seedlings of the indicated genotypes were surface sterilized and added to 3 ml of liquid ½ MS + 1% sucrose, stratified for 24 hours, and grown under constant light with gentle shaking for six days. Seedlings were then washed twice in 3 ml of ½ MS medium with or without 1% sucrose, then left to grow in either ½ MS + 1% sucrose under constant light or in ½ MS without sucrose wrapped in aluminum foil for 24 hours. Proteins were extracted in 2x Laemmli buffer (100mM Tris-HCl pH 6.8, 4% SDS, 20% glycerol, 0.01% bromophenol blue, 1.5% β-mercaptoethanol), treated at 95°C for 5 minutes and quantified using amido black precipitation. 20 μg of total protein were loaded per sample.

Confocal microscopy for Arabidopsis samples

Arabidopsis seeds were sterilized by 70% ethanol + 0.05% Tween 20 (Sigma-Aldrich) for 5 min and were subsequently sterilized by 100% ethanol for 10 min. Sterilized seeds were stored in sterile water at 4°C for 1 d for vernalization. Vernalized seeds were spread on 1/2 MS media plates + 1% agar and vertically grown at 21°C at 60% humidity under LEDs with 50 mM/m2s a and a 16 h light/8 h dark photoperiod for 5 d. 5-d-old seedlings were incubated in 1/2 MS media containing 3 μM Torin 1 (Santa Cruz Biotechnology) and 1 μM concanamycin A (Santa Cruz Biotechnology) for 90 min before imaging. For confocal microscopy, Arabidopsis seedlings were placed on a microscope slide with water and covered with a coverslip. The epidermal cells of root transition and elongation zone were used for image acquisition.

M. polymorpha heat stress assays

Two-week old plants on Gamborg B5 medium containing 1% agar were transformed to 37°C room for 6 hours. After 2 hours recovery, samples were collected in liquid nitrogen. GTEN buffer (10% glycerol, 50 mM Tris/HCl pH7.5, 1 mM EDTA, 300 mM NaCl, 1 mM DTT, 0.1% [v/v] Nonidet P-40/Igepal, Roche cOmplete™ protease inhibitor) was added to grinded-frozen samples. After vortex, samples were centrifuged at max speed for 15 minutes at 4°C for clearing the lysates. Proteins were extracted in 4x Laemmli Buffer (116 mM Tris-HCl pH 6.8, 8% SDS, 4.9% glycerol, 0.01% bromophenol blue, 10 mM DTT) and denatured at 95°C for 5 minutes. Protein concentration was equally adjusted using amido black precipitation. 10 μg of total protein were loaded per sample.

ATG8CL purification

DNA encoding ATG8CL was amplified from GFP:ATG8CL and cloned into the vector pOPINF, generating a cleavable N-terminal 6xHis-tag with ATG8CL. Recombinant proteins were produced using *E. coli* strain BL21 (DE3) grown in lysogeny broth at 37°C to an OD_{600} of 0.6 followed by induction with 1 mM IPTG and overnight incubation at 18°C. Pelleted cells were resuspended in buffer A (50 mM Tris-HCl pH 8, 500 mM NaCl and 20 mM imidazole) and lysed by sonication. The clarified cell lysate was applied to a Ni2+- NTA column connected to an AKTA Xpress system. ATG8CL was step-eluted with elution buffer (buffer A containing 500 mM imidazole) and directly injected onto a Superdex 75 26/600 gel filtration column pre-equilibrated in buffer C (20 mM HEPES pH 7.5, 150 mM NaCl). The fractions containing ATG8CL were pooled and concentrated (concentration determined using a calculated molar extinction coefficient of 7680 $M^{-1}cm^{-1}$ for ATG8CL).

Rab8a and Rab3GAPL-GAP purification

Recombinant proteins were produced using *E. coli* strain Rosetta 2(DE3) pLysS grown in 2xTY media at 37°C to an OD600 of 0.4 – 0.6 followed by induction with 300 μM IPTG and overnight incubation at 18°C. Pelleted cells were resuspended in lysis buffer (100 mM sodium phosphate pH 7.2, 300 mM NaCl, 1 mM DTT) containing Roche cOmplete™ protease inhibitor and sonicated. The clarified lysate was first purified by affinity, by using HisTrap FF (GE HealthCare) columns. The proteins were eluted with a lysis buffer containing 250 mM Imidazole. The proteins were separated by Size Exclusion Chromatography with HiLoad® 16/600 Superdex 200 pg or HiLoad 16/600 Superdex 75 pg, which were previously equilibrated in 50 mM sodium phosphate pH 7.0, 100 mM NaCl. The proteins were concentrated using Vivaspin concentrators (10000 or 30000 MWCO). Protein concentration was calculated from the UV absorption at 280 nm by DS-11 FX+ Spectrophotometer (DeNovix).

GST pull-down assays

Pulldown experiments were performed with *E. coli* lysates as previously described.[76] Briefly, recombinant proteins were produced using *E. coli* strain Rosetta 2(DE3) pLysS grown in 2x TY media at 37°C to an OD_{600} of 0.4 – 0.6 followed by induction with 300 μM IPTG and overnight incubation at room temperature. Pelleted cells were resuspended in lysis buffer (100 mM sodium phosphate pH 7.2, 300 mM NaCl, 1 mM DTT) containing Roche cOmplete™ protease inhibitor and sonicated. 5 μl of glutathione magnetic agarose beads (Pierce Glutathione Magnetic Agarose Beads, Thermo Fisher) were equilibrated with wash buffer (100 mM sodium phosphate pH 7.2, 300 mM NaCl, 1 mM DTT, 0.01% (v/v) IGEPAL). Clarified *E. coli* lysates were mixed with the washed beads and incubated on an end-over-end rotator for 1 hour at 4°C. Beads were washed five times with 1 ml wash buffer. Bound proteins were eluted by adding 50 μl Laemmli buffer. Samples were analyzed by immunoblotting analyses.

Isothermal titration calorimetry (ITC)

Calorimetry experiments were carried out at 15°C in 20 mM HEPES pH 7.5, 500 mM NaCl, using an iTC200 instrument (MicroCal Inc.). For protein:peptide interactions, the calorimetric cell was filled with 90 μM ATG8CL and titrated with 1 mM Rab3GAPL-AIMp (TPVENDWTIV) or Rab3GAPL-mAIMp peptide (TPVENDATIA) from the syringe. A single injection of 0.5 μl of peptide was followed

by 19 injections of 2 μl each. Injections were made at 150 seconds intervals with a stirring speed of 750 rpm. For the heats of dilution control experiments, equivalent volumes of Rab3GAPL-AIMp or Rab3GAPL-mAIMp peptide were injected into the buffer using the parameters above. The titrations were performed at 25°C, but otherwise as above. The raw titration data were integrated and fitted to a one-site binding model using Origin 7.0 software.

GTPase activity assay

To analyze the effect of Rab3GAPL on the GTPase activity of Rab8a, we used a luciferase-based GTPase assay (GTPase-Glo™ Assay Kit by Promega). The assay was carried out as per manufacturer's instructions. 12.5 μl of 2X GTP-GAP solution was prepared containing 5 μM GTP and 1 mM DTT in GTPase/GAP buffer. The solution was mixed with purified MBP:Rab3GAPL GAP domain. 12.5 μl of 5 μM Rab8a was added to each well. The GTPase reaction was initiated by adding 12.5 μl of the 2X GTP-GAP solution to each well. The reaction was incubated for 120 minutes at RT with shaking. 25 μl of reconstituted GTPase-Glo™ Reagent was added to the completed GTPase reaction, which the remaining GTP was converted to ATP. Plate was incubated for 30 minutes at RT with shaking. Then, 50 μl of Detection Reagent was added to all the wells, and incubated for 10 minutes at RT. Finally, luminescence was measured using BioTek Synergy4 plate reader.

CRISPR/Cas9 construct design in *M. polymorpha*

Two sgRNAs were designed based on target sequence (Figure S3E). Both sgRNAs were cloned into pMpGE_En04 entry vector flanked by attL1 and attL2 sequences.[77] Transformants were sequenced and inserted into the pMpGE010 destination vector by LR Clonase II Enzyme Mix (Thermo Fisher). This vector was incorporated into *A. tumefaciens* GV3101+pSoup, which was used to transform GFP-ATG8b-TAK1. Transformants were selected on 10 μM hygromycin,[67] genotyped and sequenced to verify mutations.

Accession numbers

Rab3GAPL (NbenBase: Nbe.v1.1.chr05g03060); StRab1 (RabD2a) (Sol Genomics Network: PGSC0003DMP400023158); StRab2 (RABB1b) (Sol Genomics Network: PGSC0003DMP400022392); NbRab8b (NbenBase: Nbe.v1.1.chr08g05560); NbRab11 (NbenBase: Nbe.v1.1.chr09g37530)

QUANTIFICATION AND STATISTICAL ANALYSIS

Image processing and data analysis

Confocal microscopy images were processed with Leica Application Suite X (LAS X) and Fiji (ImageJ version 2.14.0). Confocal images can be single plane images or Z-stack images depending on the experiment, which is detailed in the figure legends. To quantify autophagosome punctate structures in one channel, the Z stacks were separated into individual images using ImageJ and analyzed. The counting procedure was based on the maxima function in ImageJ to avoid cytoplasmic noises.

Statistical tests

Violin plots were generated using R-4.3.3 (https://www.r-project.org/), bar graphs were generated using Microsoft Excel. Statistical differences were conducted in R using Student's t-test, Welch's t-test, Mann–Whitney U test or chi-squared test depending on the experiment, based on statistical normality and variance. Measurements were significant when $p < 0.05$ (*), $p < 0.01$ (**) and highly significant when $p < 0.001$ (***). All statistical tests and calculations are detailed in Table S4.

6.9. The autophagosome closure is regulated by FREE1 in Arabidopsis

Autophagy is a conserved cellular process critical for maintaining homeostasis under stress conditions, with autophagosome closure being a pivotal yet poorly understood step. While the role of the endosomal sorting complexes required for transport (ESCRT) machinery in autophagosome sealing has been implicated in yeast and mammals, the regulatory mechanisms in plants remain elusive.

As detailed in **Chapter 6.10** (Zeng et al., 2023), using high-resolution microscopy, 3D electron tomography, and proteomic analyses, this study illustrates that FREE1 interacts with the ATG conjugation system and ESCRT-III machinery to mediate autophagosome closure. Mass spectrometry and phosphorylation assays reveal that the energy sensor SnRK1α1 phosphorylates FREE1 at Ser530, enabling its recruitment to phagophores. Genetic and biochemical analyses confirm that phosphorylation-deficient FREE1 mutants fail to support autophagosome sealing, leading to defective autophagy and impaired stress responses. These findings establish FREE1 as a key molecular link between nutrient sensing and autophagosome biogenesis, providing insights into the evolutionary conservation of ESCRT-mediated autophagy regulation.

6.10. Appendix Manuscript 5: “The plant unique ESCRT component FREE1 regulates autophagosome closure”

Authors: Yonglun Zeng, Baiying Li, Shuxian Huang, Hongbo Li, Wenhan Cao, Yixuan Chen, Guoyong Liu, Zhenping Li, Chao Yang, Lei Feng, Jiayang Gao, SzeWan Lo, **Jierui Zhao**, Jinbo Shen, Yan Guo, Caiji Gao, Yasin Dagdas, Liwen Jiang

Contribution: Resources.

Status: This manuscript was published in Nature Communications (volume 14) on March 30, 2023.

DOI: https://doi.org/10.1038/s41467-023-37185-6

nature communications

Article

https://doi.org/10.1038/s41467-023-37185-6

The plant unique ESCRT component FREE1 regulates autophagosome closure

Received: 15 March 2022

Accepted: 3 March 2023

Published online: 30 March 2023

Check for updates

Yonglun Zeng[1,9], Baiying Li[1,9], Shuxian Huang[1,9], Hongbo Li[2], Wenhan Cao[1], Yixuan Chen[1], Guoyong Liu[3], Zhenping Li[1], Chao Yang[2], Lei Feng[1], Jiayang Gao[1], Sze Wan Lo[1], Jierui Zhao[4,5], Jinbo Shen[6], Yan Guo[3], Caiji Gao[2], Yasin Dagdas[5] & Liwen Jiang[1,7,8]

The energy sensor AMP-activated protein kinase (AMPK) can activate autophagy when cellular energy production becomes compromised. However, the degree to which nutrient sensing impinges on the autophagosome closure remains unknown. Here, we provide the mechanism underlying a plant unique protein FREE1, upon autophagy-induced SnRK1α1-mediated phosphorylation, functions as a linkage between ATG conjugation system and ESCRT machinery to regulate the autophagosome closure upon nutrient deprivation. Using high-resolution microscopy, 3D-electron tomography, and protease protection assay, we showed that unclosed autophagosomes accumulated in *free1* mutants. Proteomic, cellular and biochemical analysis revealed the mechanistic connection between FREE1 and the ATG conjugation system/ESCRT-III complex in regulating autophagosome closure. Mass spectrometry analysis showed that the evolutionary conserved plant energy sensor SnRK1α1 phosphorylates FREE1 and recruits it to the autophagosomes to promote closure. Mutagenesis of the phosphorylation site on FREE1 caused the autophagosome closure failure. Our findings unveil how cellular energy sensing pathways regulate autophagosome closure to maintain cellular homeostasis.

Autophagy is an evolutionary conserved process that involves the formation of a double-membrane structure called the autophagosome. Dysregulation of autophagy causes a variety of human diseases, including cancer, neurodegeneration, aging, and pathogen infections. In plants, autophagy plays important roles under adverse environments, likewise nutrient starvation, drought, salt and heat[1]. Genetic studies in yeast have revealed the fundamental roles of autophagy-related (*ATG*) genes in autophagosome biogenesis[2–4]. ATG machinery consists of several functional units: Atg1/ULK1 kinase complex, the ATG14-containing PtdIns 3-kinase complex, the Atg9 vesicle, the Atg2-Atg18 complex, the ATG12 conjugation system, and the ATG8 conjugation system[3,5]. The regulatory roles of the evolutionary conserved energy sensor AMPK on triggering the autophagosome initiation through phosphorylation and activation of ULK1 (unc-51-like autophagy-activating kinase 1)[6–8] and differential regulation of VPS34 (vacuolar protein sorting 34) containing complexes[9] have been unveiled. Albeit how nutrient elicits the autophagosome initiation has been revealed, the degree to which

[1]Centre for Cell & Developmental Biology and State Key Laboratory of Agrobiotechnology, School of Life Sciences, The Chinese University of Hong Kong, Hong Kong, China. [2]Guangdong Provincial Key Laboratory of Biotechnology for Plant Development, School of Life Sciences, South China Normal University, Guangzhou, China. [3]State Key Laboratory of Plant Physiology and Biochemistry, College of Biological Sciences, China Agricultural University, Beijing, China. [4]Vienna BioCenter PhD Program, Doctoral School of the University at Vienna and Medical University of Vienna, Vienna, Austria. [5]Gregor Mendel Institute, Austrian Academy of Sciences, Vienna BioCenter, Vienna, Austria. [6]State Key Laboratory of Subtropical Silviculture, Zhejiang A&F University, Hangzhou, China. [7]CUHK Shenzhen Research Institute, Shenzhen, China. [8]Institute of Plant Molecular Biology and Agricultural Biotechnology, The Chinese University of Hong Kong, Hong Kong, China. [9]These authors contributed equally: Yonglun Zeng, Baiying Li, Shuxian Huang. e-mail: ljiang@cuhk.edu.hk

nutrient sensing impinges on the autophagosome closure remains unknown[10].

The endosomal sorting complexes required for transport (ESCRT) is an evolutionarily conserved, multi-subunit membrane remodeling machinery that can form membrane constrictions in a reverse-topology manner. ESCRT proteins play canonical roles in the biogenesis of multivesicular body (MVB) and the formation of intraluminal vesicle (ILV) that formed inside the MVB by invagination and budding of membrane into the lumen of the endosome[11–13]. The core ESCRT machinery consists of ESCRT-0, ESCRT-I, ESCRT-II and ESCRT-III, VPS4 (vacuolar protein sorting associated 4), LIP5 (lysosomal trafficking regulator interacting protein-5), as well as ALIX (ALG2-interacting protein X)[14]. During ILV formation and MVB biogenesis, the ESCRT machinery assembles in a hierarchical fashion on endosomal membranes. ESCRT-0, the best-characterized complex in MVB biogenesis, acts most upstream and serves as an endosomal clathrin adaptor that recruits ESCRT-I complex. The ESCRT-I complex engages ESCRT-II, which in turn nucleates ESCRT-III polymerization through VPS20 activation. The hexameric AAA+ATPase VPS4 then coincides with LIP5 and ultimately disassembles the ESCRT-III complex to recycle its subunits. In eukaryotes, increasing evidence points to the divergent function of ESCRTs in many cellular processes, including cytokinetic abscission[15], HIV budding[16,17], RNA virus replication[18,19], exosome formation[20], defective nuclear pore complexes clearance[21–24], plasma-membrane (PM) repair[25,26], lysosome repair[27,28], and microautophagy[29,30]. Notably, recent studies indicate that ESCRT complexes also function in autophagosome closure[31–34]. In mammal, the ESCRT-I component VPS37A subunit is required for autophagosome closure, followed by recruitment of the ESCRT-III component CHMP2A[31,32]. In yeast, the ESCRT-III subunit SNF7 interacts with the scaffold protein Atg17 in a VPS21-dependent manner, resulting in the recruitment of ESCRT-III for autophagosome sealing[33,34]. In plants, the bona fide roles of ESCRT in the autophagosome closure remain elusive. Furthermore, how ESCRT complex relocates from MVBs to autophagosomes and regulates autophagosome closure remain largely unknown.

Plants encode most ESCRT isoforms in their genome, including ESCRT-I, ESCRT-II, ESCRT-III, and VPS4/SKD1, with the exception of the canonical ESCRT-0 subunits[35,36]. Accumulating evidence demonstrated the conserved and bona fide functions of plant ESCRTs in endosomal sorting, ILV formation and MVB biogenesis[37–40]. Furthermore, plant ESCRT components are involved in a variety of cellular events including cytokinesis, viral replication, chloroplast turnover, autophagic degradation, hormone signalling, biotic and abiotic stress responses[18,19,41–47]. Intriguingly, plants seem to compensate the missing ESCRT-0 subunit with a plant unique ESCRT protein FREE1 (FYVE DOMAIN PROTEIN REQUIRED FOR ENDOSOMAL SORTING 1). FREE1 works in concert with ESCRT-I to regulate endosomal sorting and ILV/MVB/Vacuole biogenesis[48]. Interestingly, our previous studies have shown that under autophagy inducing conditions, substantial amounts of autophagosomal structures accumulated in the cytoplasm of *Arabidopsis free1* mutants[49]. However, the underlying mechanism remains unknown.

In this study, we demonstrated a mechanistic role of FREE1 in regulating autophagosome closure. Using a combination of biochemical methods, live-cell imaging, high-resolution deconvolution and 3D-electron tomography (ET) analysis, we showed that the autophagosomal structures that accumulated in the *Arabidopsis free1* mutants were largely unclosed autophagosomes in nature. Analysis of the FREE1 interactome during nutrient starvation revealed ESCRT-III machinery and ATG12-ATG5-ATG16 complex as FREE1 interactors. Biochemical analyses further proved that FREE1 forms a complex with ESCRT-III and ATG12-ATG5-ATG16 conjugation system, and directly interacts with the conjugation system substrates the ubiquitin-like proteins ATG8a and ATG8i through a classical AIM (Atg8-interacting motif). Consistently, upon autophagy induction, unsealed autophagosomes were accumulated in the cytoplasm of ATG5 and ESCRT-III mutants. Lastly, immunoprecipitation and mass-spectrum analysis unveiled that FREE1 can be phosphorylated upon nutrient starvation. Interaction and phosphorylation assays demonstrated that KIN10 (SnRK1α1) can directly interact and phosphorylate FREE1. Mutagenesis of the KIN10-targeted phosphorylation site on FREE1 caused the failure of autophagosome closure and defective of plant growth upon starvation. Taken together, during nutrient starvation in plant, the energy sensor SnRK1α1 phosphorylates FREE1 to promote the recruitment of FREE1 to phagophores, and subsequently links the ATG conjugation machinery with ESCRT-III complexes to mediate autophagosome closure. Using the advanced imaging techniques in combination with biochemical methods and genetic approaches, our study comprehensively unveiled the mechanism underlying how nutrient regulates the recruitment of ESCRT machinery to the closing phagophore for achieving autophagosome closure.

Results

FREE1 is required for autophagosome closure

Our previous studies have shown that under autophagy inducing conditions, substantial amounts of autophagosomal structures accumulated in the cytoplasm of the homozygous T-DNA insertional mutants *free1* (*free1*-/-) as well as the dexamethasone (DEX)-inducible FREE1 RNAi mutants (*DEX::RNAi-FREE1*)[49]. To elucidate the possible mechanism underlying autophagosome accumulation in FREE1 mutants, we performed live-cell imaging analysis with deconvolution on transgenic *Arabidopsis* plants expressing YFP-ATG8e in *DEX::RNAi-FREE1*[49]. Upon DEX treatment, the expression level of FREE1 was sufficiently knocked-down in the *DEX::RNAi-FREE1* transgenic plants, while the control DEX treatment exhibited little effect on autophagosome formation in plants (Supplementary Fig. 1a, b and Supplementary Fig. 2a, b). Consistent with our previous study[49], YFP-ATG8e labelled autophagosomes accumulated in *DEX::RNAi-FREE1* mutants upon DEX and autophagic induction by benzothiadiazole (BTH) or BTH and Concanamycin A (ConcA) treatments in comparison to mock (Fig. 1a, b and Supplementary Fig. 2c). Intriguingly, substantial amounts of unclosed autophagosomal structures were observed upon BTH-induced autophagy, while the effects were even more pronounced upon BTH and ConcA treatments (Fig. 1a, b). These results are consistent with the previous findings showing that the specific V-ATPase inhibitor ConcA which blocks autophagic/vacuole degradation may further induce the autophagosome formation in the cytoplasm upon autophagy-induced conditions[50–53], albeit the underlying mechanism remains elusive. Live-cell imaging analysis on the dynamics of ATG8e-positive punctae further showed that the autophagosomes in *DEX::RNAi-FREE1* mutants with DEX treatments were unable to close as compared to *DEX::RNAi-FREE1* mutants without DEX treatments upon autophagic induction (Supplementary Fig. 3, Supplementary Movie. 1, and Supplementary Movie. 2). Biochemical analysis further showed that the lipidated ATG8 and the autophagy receptor NBR1 significantly accumulated in the *DEX::RNAi-FREE1* mutants upon DEX induction with or without BTH treatment, suggesting that the autophagosome initiation and progression remained normal in the FREE1 mutants (Supplementary Fig. 4a, b). Nonetheless, the vacuolar turnover assay showed that the YFP-ATG8 turnover was significantly impeded in *DEX::RNAi-FREE1* mutants upon DEX and autophagy induction, indicating that the unclosed autophagosmes were accumulated in the cytoplasm (Supplementary Fig. 4c). To demonstrate that FREE1 depletion indeed causes the accumulation of unsealed autophagosomes biochemically, we next performed the protease protection assay according to the protocol recently developed in plants (Supplementary Fig. 5a)[54]. Our results showed that the autophagic-receptor NBR1 and ATG8 substantially accumulated in the FREE1 depletion mutants upon DEX treatment (Supplementary Fig. 5b). Notably, the

https://doi.org/10.1038/s41467-023-37185-6

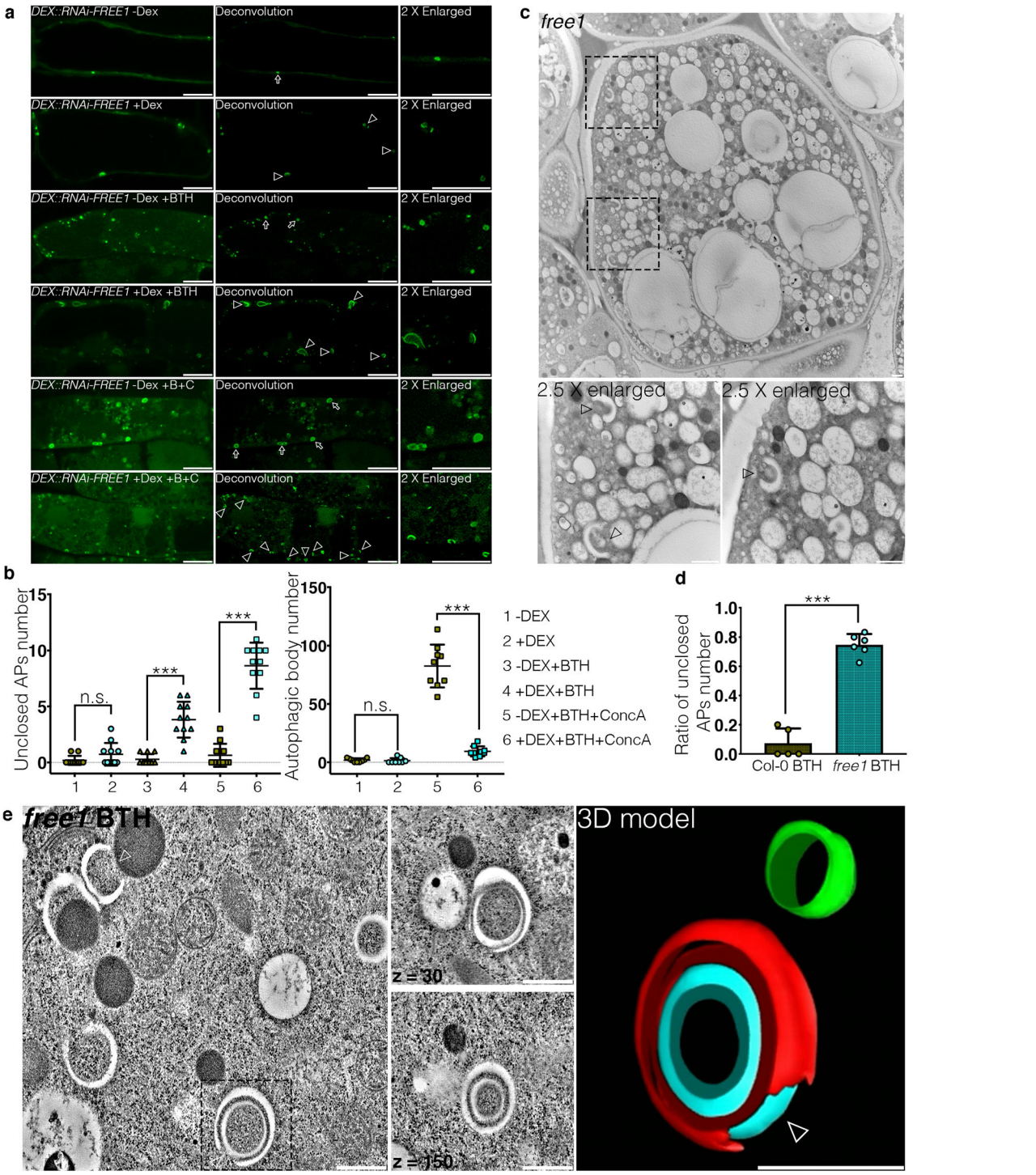

Fig. 1 | FREE1 mutants accumulate unclosed autophagosomes. a Transgenic *Arabidopsis* seedlings expressing YFP-ATG8e in dexamethasone-inducible FREE1 RNAi (*DEX::RNAi-FREE1*) mutants were subjected to mock or autophagy inductions by BTH (Benzothiadiazole, B) or BTH and ConcA (Concanamycin A, C) with or without DEX treatment for 8hrs before confocal laser scanning microscopy (CLSM) observation. Images were further processed by Leica Huygens deconvolution. Arrows and arrowheads indicate the close and unsealed autophagosomal structures, respectively. Scale bars, 10 μm. **b** Quantification analysis of the numbers of unclosed autophagosomal structures in the cytoplasm (left panel) and autophagic bodies inside the vacuoles (right panel) per cross-cell section shown in **a**. Means ±SD; $n = 11$ (left panel) and $n = 9$ (right panel) individual cells per experimental group, one-way analysis of variance (ANOVA), followed by Tukey's multiple test; $^{***}p < 0.001$; n.s., not significant. **c** TEM (transmission electron microscopy) analysis of high-pressure freezing/frozen substituted homozygous *free1* T-DNA insertional mutant root tips upon BTH treatment for 8 h. Black dash boxes indicate the 2.5 X zoom-in areas. Arrowheads indicate examples of the unsealed autophagosomal structures. Scale bars, 500 nm. **d** Quantification analysis of the ratio of the unsealed autophagosomes shown in **c**. Means±SD; $n = 5$ (Col-0 BTH) and $n = 6$ (*free1* BTH) root sections per genotype, two-tailed unpaired *t* test; $^{***}p < 0.001$. **e** 3D electron tomography (3D-ET) analysis of autophagosomal structures in homozygous *free1* T-DNA insertional mutant upon BTH treatment for 8 h. Left panel, individual slice of the 3D-tomography. Right panel, 3D model of the tomography. Black dash box indicates the selected 3D-ET structures for 3D model. Arrowheads indicate examples of the unsealed autophagosomal structures. Scale bars, 500 nm. The red color indicates the autophagosomal structures, while the blue and green color indicate the membrane-bound organelles. All the imaging analysis was repeated at least for three times with similar results.

accumulated NBR1 and ATG8 can be significantly degraded upon proteinase K digestion in the FREE1 depletion mutants (Supplementary Fig. 5b), supporting that the autophagosomes accumulated in the FREE1 depletion mutants are unclosed. Further analysis showed that more accumulation of both the autophagic-receptor NBR1 and ATG8 upon DEX+BTH+ConcA treatments comparing with the DEX+BTH treatments (Supplementary Fig. 5c). To determine the morphology of autophagosomes in FREE1 mutants, we germinated the heterozygous T-DNA insertional mutants of FREE1 (*free1*+/-) and selected the lethal seedlings which were the homozygous (*free1*-/-) mutants[48] for ultrastructural transmission electron microscopy (TEM) and 3D electron tomography (ET) analysis. TEM analysis using the homozygous *free1* T-DNA insertional mutants showed the accumulation of numerous unclosed phagophores in the cytoplasm upon BTH treatment, in sharp contrast to the wild type (WT) cells (Fig. 1c, d and Supplementary Fig. 2d). Immunogold-TEM analysis proved that these unclosed structures in *free1* mutants were positive for the autophagic-markers including ATG1, ATG8, and ATG13 (Supplementary Fig. 6). Further immunogold-TEM analysis on the transgenic plants expressing YFP-ATG8e in *free1* mutants showed that GFP antibodies can substantially label the unclosed autophagosomal structures (Supplementary Fig. 7a), while the GFP antibodies labelling on other intracellular compartments or aggregates could be barely observed (Supplementary Fig. 7b), which are consistent with the live-cell imaging analysis showing the unclosed autophagosmal structures labeled by YFP-ATG8e in FREE1 depletion mutants (Fig. 1a, b, Supplementary Fig. 3, Supplementary Movie. 1, and Supplementary Movie. 2). To further consolidate that the autophagosomes are unclosed in nature, we performed the serial-2D TEM analysis to differentiate the initiated phagophore and unsealed autophagosome, and showed that most of the autophagosomes accumulated in *free1* mutants are unsealed, although they seem to be initiated phagophores or closed autophagosomes in some sections (Supplementary Fig. 8). 3D-tomograms further demonstrated the substantial accumulation of unsealed autophagosomes in *free1* mutant (Fig. 1e, Supplementary Fig. 9, and Supplementary Movie. 3). Taken together, these results indicate that FREE1 is required for autophagosome closure.

ATG conjugation system and its substrates ATG8 coordinate with FREE1 for autophagosome closure

To further elucidate the mechanism underlying FREE1 function in autophagosome closure, we performed multiple rounds of affinity purification-mass spectrometry (AP-MS) analysis using FREE1 as the bait upon carbon starvation (Supplementary Data 1). The autophagosome closure is a relatively transient cellular process, making it challenging to identify its regulators until now. We performed analysis on the MS data through a relative quantification by the IBAQ using MaxQuant software[55]. Although a number of proteins have been identified to be enriched in the GFP-FREE1 groups, we have been focusing on candidates function in MVB sorting/autophagy pathways in the current study because FREE1 performs multiple functions in plants and our study focuses on its function in autophagosome closure. Our analysis showed that the FREE1-interacting candidates that function in MVB sorting/autophagy pathways were enriched in the GFP-FREE1 groups compared to the GFP controls as indicated by the IBAQ (Supplementary Data 1 and Supplementary Fig. 10). Under nutrient starvation, FREE1 associated with ESCRTs, HOPS (homotypic fusion and vacuole protein sorting), Retromer, and TOR kinase complex (Fig. 2a). Interestingly, ATG5 was amongst the interactors, suggesting that the ATG conjugation system may recruit FREE1 to the phagophore for closure (Fig. 2a). Although the yeast two hybrid and FRET analysis showed that FREE1 did not exhibit a direct interaction with components of the ATG conjugation system ATG5, ATG12, ATG16 or other ATG proteins (Supplementary Fig. 11), colocalization and co-immunoprecipitation (co-IP) experiments in *Arabidopsis* protoplasts have shown that the endogenous ATG5, ATG12b and ATG16 associated with FREE1 (Fig. 2b, c). To find out if the ATG conjugation machinery bridged FREE1 to mediate autophagosome closure, we analyzed autophagosome morphology in *atg5-1* mutant. 2D-TEM and 3D-electron tomography analysis of autophagosomes in *atg5-1* mutant have shown the unsealed autophagosomal structures during autophagy induction, comparing to WT Col-0 cells (Fig. 2d–f, Supplementary Fig. 12, and Supplementary Movie. 4). WIPI-1, the close homolog of ATG18 in plants, has been used to analyze the autophagosomal structures in the ATG5 mutants in mammal[56]. We have thus performed confocal analysis with image deconvolution on the ATG18a-GFP in *atg5-1* mutants. In sharp contrast to the Col-0 cells, our results showed that the ATG18a-GFP positive structures are largely unclosed in *atg5-1* mutant cells (Supplementary Fig. 13). Surprisingly, we found that FREE1 directly interacted with the substrates of the ATG conjugation system, i.e. the ubiquitin-like proteins ATG8a, ATG8g, and ATG8i (Fig. 3a and Supplementary Fig. 14a). Notably, phylogenetic trees analysis on the ATG8s in different plant species showed that ATG8a, ATG8g, and ATG8i locate in distinct clades of plant ATG8 paralogs (Fig. 3b). Confocal and super-resolution imaging analysis showed that FREE1 colocalized with ATG8a and ATG8i at the phagophore labeled by ATG5 (Fig. 3c, d). Co-IP (co-immunoprecipitation) and FRET (fluorescence resonance energy transfer) analyses further confirmed the interaction between FREE1 and the specific ATG8 isoforms of ATG8a and ATG8i (Fig. 3e, f). Western blot and quantification analysis further showed the accumulation of full-length eYFP-ATG8i in *atg5-1* mutants as well as full-length mCherry-ATG8i in *atg5-1* mutants compared to WT Col-0 cells upon autophagic induction (Supplementary Fig. 14b, c). Coherently, the ATG conjugation system components accumulated in the FREE1 depletion mutants (Supplementary Fig. 15). In summary, we demonstrated that the ATG conjugation system and its specific substrates may coordinate with FREE1 on the phagophore for autophagosome closure.

FREE1 contains a classical AIM motif essential for the interaction with ATG8

Using Yeast-two hybrid screening, Marshall et al. has shown that ATG8 may interact with FREE1 via typical LDS (LIR docking site)[57], suggesting that FREE1 may contain the classical AIM motif. Our in silico analysis found that W438 I441 on FREE1 could be the potential AIM motif essential for its interaction with ATG8 (Supplementary Fig. 16a). We have thus performed mutagenesis on FREE1 by substituting W438 I441 to A438 A441 to investigate whether FREE1 interacts with ATG8 through the classical AIM motif. Indeed, co-immunoprecipitation (co-IP) and yeast two hybrid analysis showed that mutation of W438 I441 to A438 A441 abolished the interaction between FREE1 and ATG8 (Supplementary Fig. 16b, c). Notably, mutation of the AIM motif on FREE1 significantly inhibited the recruitment of FREE1 to the nascent autophagosomes comparing with wild-type FREE1 in *Arabidopsis* protoplasts (Supplementary Fig. 16d, e), demonstrating that this AIM-dependent interaction was important for the recruitment of FREE1 to the nascent autophagosomes. To further elaborate the function of FREE1 AIM in autophagosome closure, we used the particle bombardment to transfer and express the FREE1 or FREE1^{W438AI441A} in the eYFP-ATG8e/*DEX::RNAi-FREE1* transgenic plants for confocal observation of the autophagosomal structures. Indeed, the mature ring-like autophagosomes can be found in the eYFP-ATG8e/*DEX::RNAi-FREE1* transgenic plants upon FREE1 overexpression, while the FREE1^{W438AI441A} overexpression cannot complement the defective of autophagosome closure in eYFP-ATG8e/*DEX::RNAi-FREE1* (Supplementary Fig. 16f). Taken together, our results demonstrated that FREE1 contains a classical AIM motif, which is essential for its interaction with ATG8, recruitment to autophagosome, and function in autophagosome closure.

https://doi.org/10.1038/s41467-023-37185-6

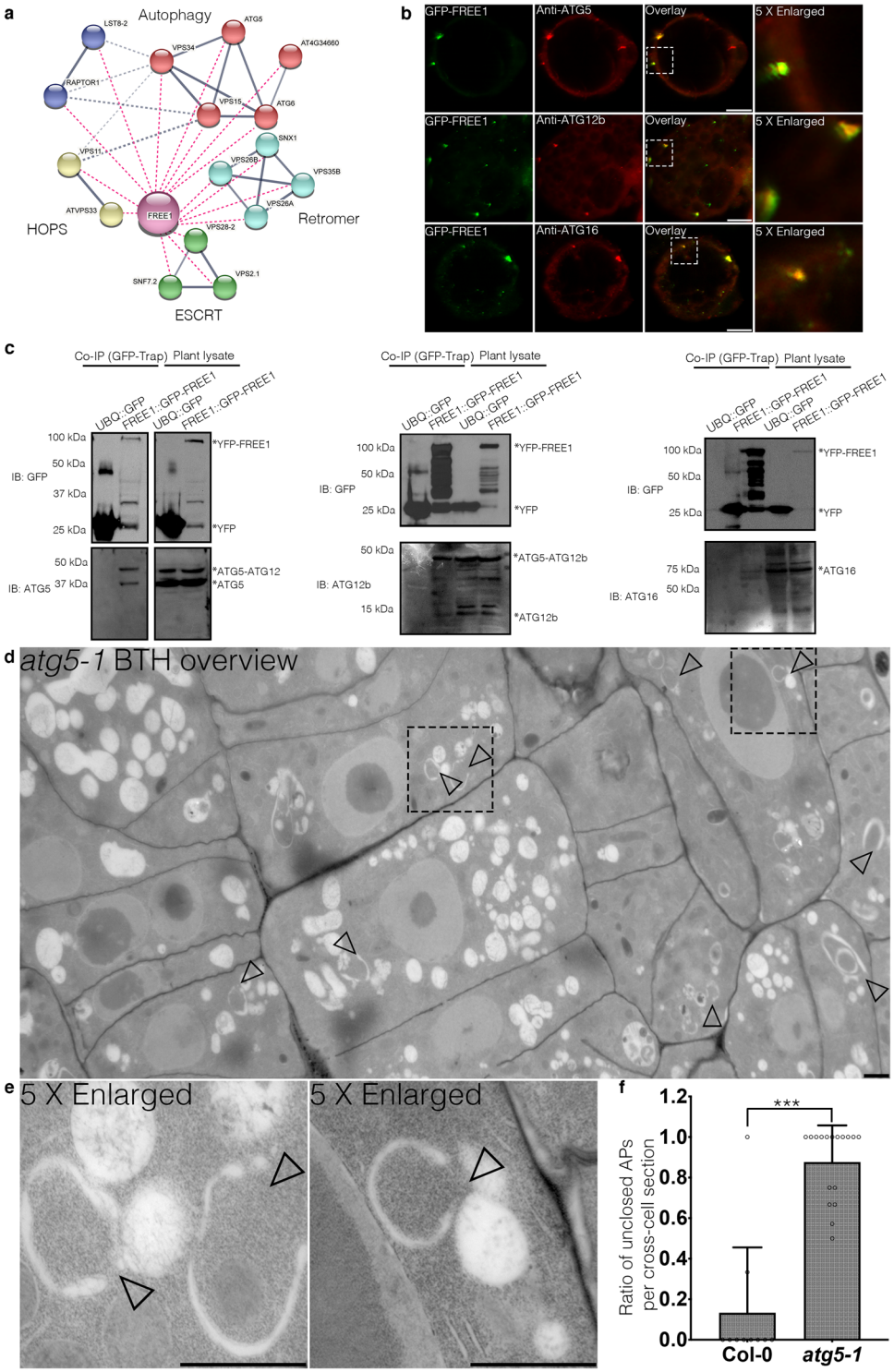

Fig. 2 | FREE1 interacts with ATG conjugation system and ESCRT-III under starvation conditions. a Transgenic *Arabidopsis* seedlings expressing YFP-FREE1 upon autophagy induction by carbon starvation for at least 18 h were subjected to GFP-Trap assay for IP-MS analysis. Identified FREE1-interacting partners were analyzed using STRING. **b** Immunofluorescence labeling of the endogenous ATG conjugation system proteins ATG5, ATG12b or ATG16 in *Arabidopsis* protoplasts transfected with GFP-FREE1 for 24 h before confocal laser scanning microscopy (CLSM) observation. White dash boxes indicate the 5 X enlarged areas. Scale bars, 10 μm. **c** GFP-Trap and co-IP analysis of GFP-FREE1 with endogenous ATG5, ATG12b, or ATG16 using native promoter driven GFP-FREE1 transgenic plants. *Arabidopsis* transgenic plants expressing GFP or GFP-FREE1 driven by the native promoter were subjected to protein extraction and IP with GFP-Trap, followed by western blot analysis with indicated antibodies. **d** Structural TEM analysis of high-pressure freezing/frozen substituted *atg5-1* mutant plant root tips upon BTH treatment for 8 h. Black dash boxes indicated the 5 X zoom-in areas. Arrowheads indicated examples of the unsealed autophagosomal structures. Scale bars, 500 nm. **e** 5 X zoom-in areas from **d**. Arrowheads indicated examples of the unsealed autophagosomal structures. Scale bars, 500 nm. **f** Quantification analysis of the ratio of the unclosed autophagosomal structures (APs) in Col-0 and *atg5-1* mutants per cross-cell section. Means±SD; $n = 10$ (Col-0) and $n = 17$ (*atg5-1*) cells, two-tailed unpaired *t* test; $^{***}p < 0.001$. All the imaging analysis and immunoblots were repeated at least for three times with similar results.

https://doi.org/10.1038/s41467-023-37185-6

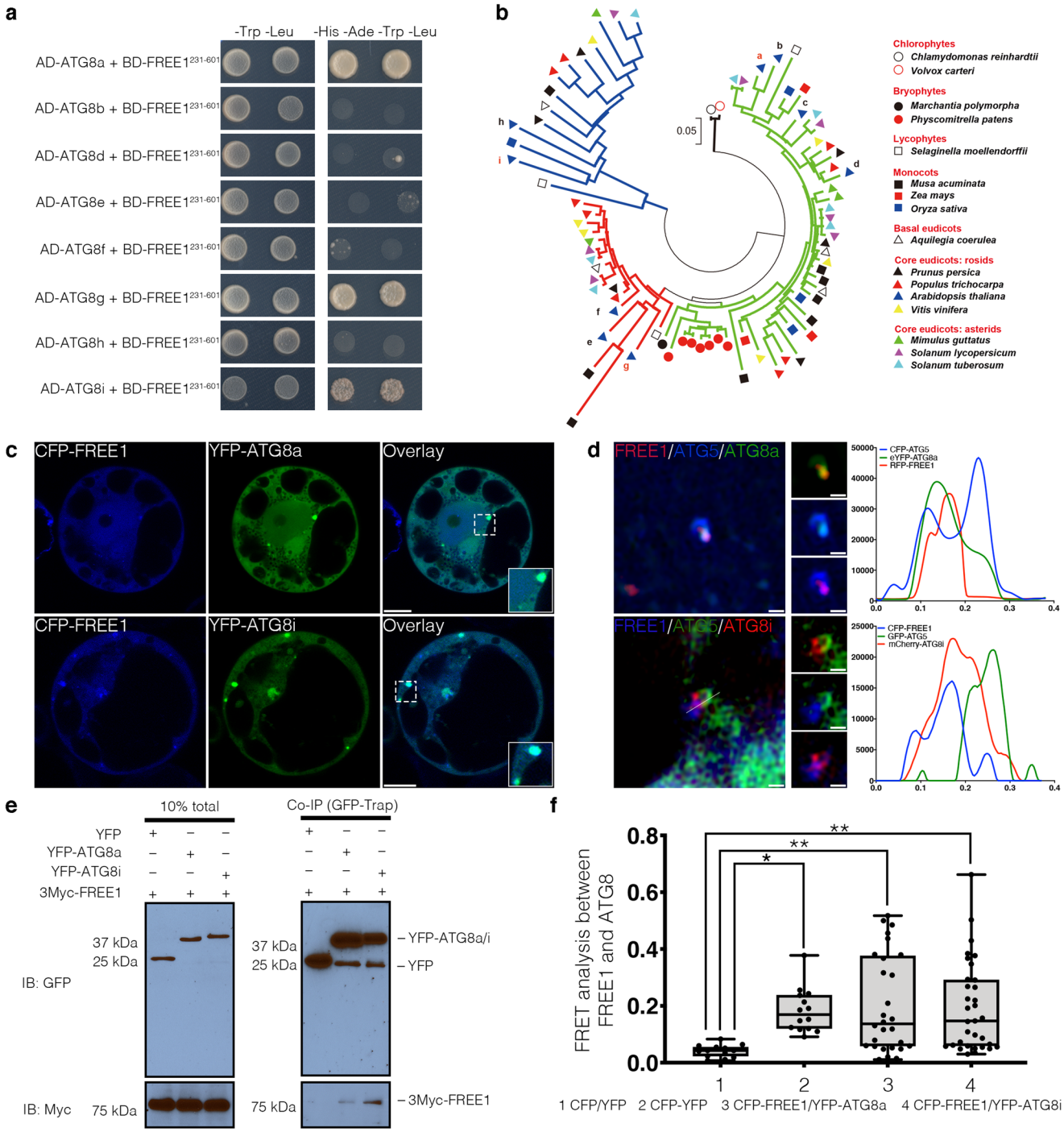

Fig. 3 | FREE1 specifically interacts with the distinct paralogs of ATG8. a Y2H analysis of BD-FREE1$^{231-601}$ (the truncated FREE1 without self-activation on BD vector) with AD-ATG8 isoforms. **b** Evolutionary relationships of ATG8 isoforms. The optimal tree with the sum of branch length=4.32642842 is shown. The tree is drawn to scale, with branch lengths in the same units as those of the evolutionary distances used to infer the phylogenetic tree. **c** Transient expression of CFP-FREE1 with specific ATG8 isoforms YFP-ATG8a and YFP-ATG8i in *Arabidopsis* protoplasts, the transfected protoplasts were cultured for 24 h before CLSM observation. White dash boxes indicate the 2.5 X enlarged insets. Scale bars, 10 μm. **d** *Arabidopsis* protoplasts transfected with FREE1, ATG5 and ATG8a or ATG8i were subjected to structure illuminated microscopy (SIM) analysis. Scale bars, 1 μm. **e** GFP-Trap and co-immunoprecipitation (co-IP) analysis of 3Myc-FREE1 with YFP-ATG8a or YFP-ATG8i using *Arabidopsis* protoplasts. *Arabidopsis* protoplasts co-expressing 3Myc-FREE1 with YFP-ATG8a, YFP-ATG8i, or YFP only were subjected to protein extraction and co-IP with GFP-Trap, followed by immunoblotting with indicated antibodies. **f** FRET analysis between CFP-FREE1 and YFP-ATG8a or YFP-ATG8i in *Arabidopsis* protoplasts. *Arabidopsis* protoplasts were transfected with CFP and YFP (negative control), CFP-YFP (positive control), CFP-FREE1 and YFP-ATG8a, or CFP-FREE1 and YFP-ATG8i, followed by cultured for 24 h before FRET analysis. Means±SD; $n = 14$ (CFP/YFP), $n = 14$ (CFP-YFP), $n = 28$ (CFP-FREE1/YFP-ATG8a), and $n = 33$ (CFP-FREE1/YFP-ATG8i) individual puncta per experimental group, one-way analysis of variance (ANOVA), followed by Dunnett's multiple comparisons test; $^{*}p < 0.05$; $^{**}p < 0.01$. The middle lines of the boxes represent the medians of datasets. The upper and bottom lines of the boxes are the upper quantile and the lower quantile of the data, respectively. The whiskers mark the upper and lower limits of these datasets, respectively. All the imaging analysis and immunoblots were repeated at least for three times with similar results.

ESCRT-III components are recruited by FREE1 onto the autophagosomes to mediate closure

In mammal, ESCRTs components VPS37 and SNF7 are essential for autophagosome closure[31–33]. In yeast, Rab5 GTPase seems to control the recruitment of ESCRT to unsealed autophagosomes through an interaction of the ESCRT subunit SNF7 with Atg17[34]. Several ESCRT components are identified as FREE1 interactors upon starvation (Fig. 2a), we thus set out to investigate the role of ESCRT-III complex in autophagosome closure in plants. To illustrate the ESCRT-III function in plant autophagosome closure, we generated transgenic plants co-expressing eYFP-ATG8e and SNF7.1-RFP, a plant ESCRT-III component[58]. Under nutrient rich conditions, SNF7.1 mainly exhibited cytosolic and punctate patterns, while ATG8e was mainly localized in the cytoplasm (Supplementary Fig. 17a). Upon autophagic induction by BTH treatment, ATG8e-positive punctae appeared and significantly colocalized with SNF7.1 (Supplementary Fig. 17a, b). Further analysis using transient expression in *Arabidopsis* protoplasts demonstrated that SNF7.1 not only exhibited similar localization pattern as previously shown[59], but also localized at the phagophore (Supplementary Fig. 17c). Consistently, another ESCRT-III component VPS20 also localized to the autophagosomes upon autophagic induction (Supplementary Fig. 18a). To analyse the function of ESCRT-III in autophagosome closure, we then generated dominant-negative mutant plants expressing SNF7.1(L22W) (SNF7.1DN), which has been shown to cause the enlargement of the PVC/MVB with a reduced number of intraluminal vesicles (ILVs)[59]. Live cell imaging showed that unsealed ATG8e-positive autophagosomes accumulated substantially while the formation of autophagic bodies were significantly impaired in the SNF7.1DN mutants (Supplementary Fig. 17d, e). Notably, TEM analysis of autophagosomal structures in SNF7.1DN demonstrated that the accumulated autophagosomes in the cytoplasm were unsealed (Supplementary Fig. 17f). 3D electron tomography analysis further confirmed the unsealed nature of autophagosomes in SNF7.1DN mutants (Supplementary Fig. 17g and Supplementary Movie. 5). Consistently, dominant negative mutants of VPS4(E232Q) (VPS4DN), the ATPase-deficient form of VPS4 that causes the enlargement of the PVC/MVB with a reduced number of ILVs[38], also accumulated unsealed ATG8e labelled autophagosomes (Supplementary Fig. 18b, c) and showed significant defects in vacuolar turnover autophagic flux (Supplementary Fig. 18d, e). We next investigated whether FREE1 is required for the recruitment of the ESCRT-III components onto autophagosomal structures to regulate closure. Immunogold-TEM analysis using the antibodies against endogenous plant ESCRT-III component SNF7[58] showed that SNF7 can significantly label the autophagosomal structures in Col-0 wild-type plants, but not the accumulated unclosed autophagosomal structures in *free1* mutants (Supplementary Fig. 19a, b). Our results thus proved that FREE1 is important for the recruitment of other ESCRT components including ESCRT-III onto the autophagosomes. To further consolidate the TEM observations, we next performed the transient expression assay using protoplasts isolated from *Arabidopsis* PSBD suspension culture cells for confocal analysis. Consistently, SNF7.1-GFP failed to be recruited onto the ATG8-positive structures labelled by mCherry-ATG8e in the protoplasts expressing the FREE1 RNAi (Supplementary Fig. 19c, d). Notably, SNF7.1-GFP failed to be recruited onto the ATG8-positive structures in the protoplasts expressing FREE1 RNAi and the AIM motif mutant Myc-FREE1^{W438AI441A} (Supplementary Fig. 19c, d). Nonetheless, the ESCRT-III component SNF7.1-GFP could be sufficiently recruited onto the ATG8-positive structures in the protoplasts expressing FREE1 RNAi and wild-type Myc-FREE1 (Supplementary Fig. 19c, d). Western blot analysis showed the proper overexpression of the FREE1 protein and its mutant variants in the FREE1 RNAi mutants (Supplementary Fig. 19e). Therefore, our results demonstrated that the interaction between FREE1 and ATG8 is required for the recruitment of the ESCRT-III components onto the autophagosome.

Recent studies have demonstrated the importance of ESCRT-I in regulating autophagosome closure in mammal[32], we thus also set out to investigate the potential function of plant ESCRT-I in phagophore sealing. In *Arabidopsis*, all the ESCRT-I components VPS37, VPS23, and VPS28 contain two homologues encoding in the genome. Double mutant of the ESCRT-I components is inapplicable for cellular analysis due to the seedling lethality, while the single mutant does not exhibit obvious growth defective under normal condition[60]. Consistent with recent study[54], phenotypic analysis showed that neither the single mutant *vps23a* nor *vps23b* mutants exhibited comparable autophagy-related phenotype as *atg5-1* and *atg7-2* upon carbon starvation (Supplementary Fig. 20a). TEM results showed that the autophagosomes closed normally in *vps23a-/-vps23b+/-* mutant, which is comparable with the wild-type plants (Supplementary Fig. 20b). Therefore, our current results suggested that VPS23A may either act redundantly with VPS23B in autophagosome closure or do not play role in autophagy. Due to the lethality of the double mutants of VPS23, future study could be carried out to generate micro-RNA mutants of both VPS23A and VPS23B driven by inducible promoter and used for exploring the possible functional roles of ESCRT-I in autophagosome closure. Taken together, our results demonstrated that the interaction between FREE1 and ATG8 is required for the recruitment of the ESCRT-III components onto the autophagosomal structures to regulate autophagosome closure in plants.

Plant energy sensor kinase SnRK1 phosphorylates FREE1

AMPK is a conserved metabolic switch that senses cellular energy status and governs energy homeostasis through its regulation of glucose and lipid metabolism in mammal. The regulatory roles of the AMPK on autophagosome initiation through phosphorylation and activation of ULK1[6–8] and differential regulation of VPS34 containing complexes[9] have been unveiled. In plants, SnRK1 (Sucrose non-fermenting-1 (SNF1)-related kinase 1), the close homolog of the yeast SNF1 (sucrose non-fermenting 1) and the mammalian AMPK families, is a central integrator of energy and stress signalling. Upon sensing energy deficit, nutrient deprivation or darkness, SnRK1 triggers vast metabolic and transcriptional adjustments for homeostasis restoration, survival promotion and environmental adaptation[61]. Surprisingly, our interactome analyses revealed that FREE1 associates with KIN10 (SnRK1α1) during nutrient starvation (Supplementary Data 1 and Supplementary Fig. 10). We thus investigated the localization of FREE1 with KIN10 in *Arabidopsis* protoplasts. Interestingly, FREE1 partially colocalized with KIN10 (Fig. 4a). Both FRET and yeast-two hybrid assay demonstrated the direct interaction between FREE1 and KIN10 (Fig. 4b, c), while co-IP assays in *Arabidopsis* protoplasts further showed that GFP-FREE1 can be co-immunoprecipitated with KIN10-6HA (Fig. 4d). Finally, the in vivo analysis using KIN10-GFP transgenic lines has demonstrated that KIN10 interacts with FREE1 in a nutrient starvation dependent manner (Fig. 4e, f and Supplementary Fig. 21a). In vivo interaction assay using the endogenous promoter driven GFP-FREE1 transgenic plants further confirmed that FREE1 can directly interact with the endogenous KIN10 upon nitrogen starvation (Supplementary Fig. 21b). The interaction between KIN10 and FREE1 prompted us to hypothesize that KIN10 might phosphorylate FREE1 to promote autophagosome closure during nutrient starvation. Indeed, FREE1 can be phosphorylated under nitrogen limiting conditions comparing with mock treatments (Fig. 4g). To identify the potential phosphorylation sites on FREE1, we performed multiple rounds of pull-down and mass-spectrometry analysis during nutrient starvation. Interestingly, Serine at position 530 of FREE1, was phosphorylated upon carbon deprivation (Supplementary Fig. 22a, b). To investigate whether KIN10 can directly phosphorylate FREE1, we performed the semi-in vitro phosphorylation assay. According to previous study[62], KIN10 was first enriched from transgenic seedlings overexpressing KIN10-GFP or KIN10-HA by immunoprecipitation with anti-GFP or anti-HA and then used to

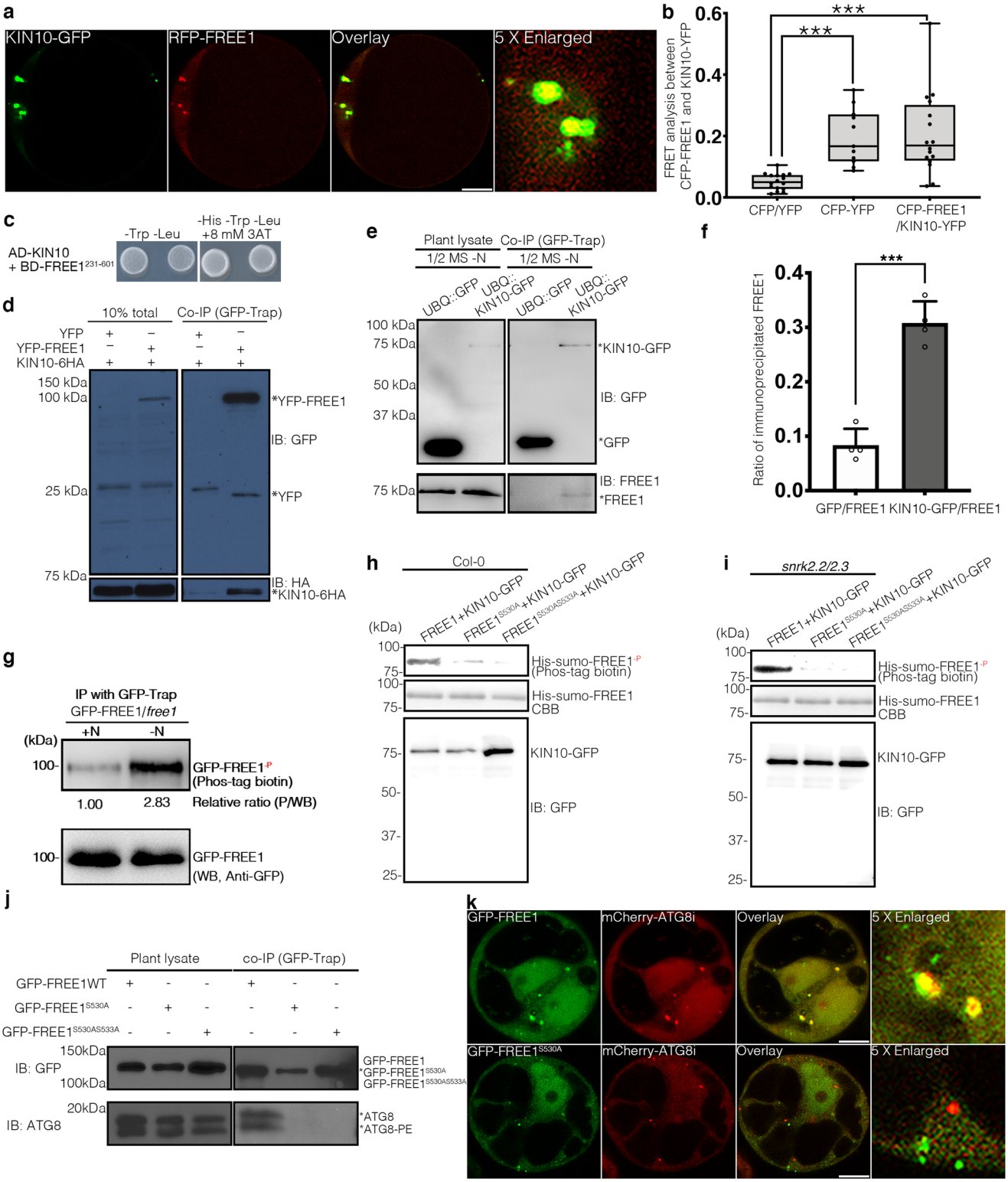

phosphorylate His-sumo-FREE1, His-sumo-FREE1^{S530A}, or His-sumo-FREE1^{S530AS533A} since it also contained the S530A mutation, which was further detected by Phos-tag biotin. Indeed, FREE1 can be phosphorylated in the presence of the activated KIN10-GFP or KIN10-HA, while the negative control GFP only cannot be phosphorylated (Fig. 4h and Supplementary Fig. 23a, b). Importantly, mutation on S530A abolished the phosphorylation of FREE1 by KIN10 (Fig. 4h). FREE1 has been shown to be phosphorylated by SnRK2.2/2.3, promoting its translocation to the nuclei under ABA conditions[63], whereas a recent study has also shown the sequestration of SnRK1 by SnRK2-containing complexes to inhibit SnRK1 signaling[64]. Therefore, to provide the direct evidence of FREE1 phosphorylation by SnRK1 but not by SnRK2.2/2.3 in the semi-in vivo phosphorylation assay, we also used the *Arabidopsis* protoplasts isolated from the *snrk2.2/2.3* mutants for the assay. Consistently, FREE1 can be phosphorylated in the presence of KIN10 purified from the transgenic seedlings expressing KIN10-GFP in *snrk2.2/2.3* mutants background, while the mutation on S530A or S530AS533A abolished the phosphorylation of FREE1 by SnRK1α1

Fig. 4 | KIN10 phosphorylates FREE1 to orchestrate ESCRT machinery function in autophagosome closure. a Transient expression and confocal analysis of the spatial relationship between FREE1 and KIN10 in *Arabidopsis* leaf protoplasts. The transfected leaf protoplasts were cultured for 24 h before CLSM observation. Scale bars, 10 μm. **b** FRET analysis of CFP-FREE1 with KIN10-YFP. *Arabidopsis* protoplasts co-expressing CFP and YFP (negative control), CFP-YFP (positive control), or CFP-FREE1 and KIN10-YFP were cultured for 24hr before FRET analysis. Means±SD; $n = 16$ (CFP/YFP), $n = 11$ (CFP-YFP), and $n = 16$ (CFP-FREE1/KIN10-YFP) individual puncta per experimental group, one-way analysis of variance (ANOVA), followed by Tukey's multiple test; $^{***}p < 0.001$. The middle lines of the boxes represent the medians of datasets. The upper and bottom lines of the boxes are respectively the upper quantile and the lower quantile of the data. The whiskers mark the upper and lower limits of these datasets, respectively. **c** Y2H analysis between AD-KIN10 and BD-FREE1$^{231-601}$ (the truncated FREE1 without self-activation on BD vector). **d** GFP-Trap and co-immunoprecipitation (co-IP) analysis of KIN10-6HA and YFP-FREE1 in *Arabidopsis* protoplasts. *Arabidopsis* protoplasts co-expressing KIN10-6HA with YFP-FREE1, or YFP only were subjected to protein extraction and IP with GFP-Trap, followed by immunoblotting with indicated antibodies. **e** GFP-Trap and co-IP of KIN10 and FREE1 using transgenic plants expressing KIN10-GFP under nitrogen starvation (-N) for at least 18hrs, followed by immunoblotting using GFP and FREE1 antibodies. **f** Quantification analysis of the ratio of co-immunoprecipitated FREE1 by KIN10 shown in **e**. Means±SD; $n = 4$ individual experiments, two-tailed unpaired *t* test, $^{***}p < 0.001$. **g** In vivo phosphorylation of FREE1 upon nitrogen starvation. GFP-FREE1/*free1* transgenic plants were subjected to mock or nitrogen starvation for at least 18 h, followed by protein extraction and IP with GFP-Trap, and subsequent immunoblotting detection by Phos-tag biotin and the indicated antibodies. **h** Semi-in vitro phosphorylation assay of FREE1, FREE1^{S530A} and FREE1^{S530AS533A} proteins by KIN10-GFP purified from the transgenic plants expressing KIN10-GFP. KIN10 was enriched from transgenic seedlings expressing KIN10-GFP by immunoprecipitation with anti-GFP and then used to phosphorylate FREE1, FREE1^{S530A} or FREE1^{S530AS533A} tagged with His-sumo, which was further detected by Phos-tag biotin. **i** Semi-in vitro phosphorylation assay of FREE1, FREE1^{S530A} and FREE1^{S530AS533A} proteins by KIN10-GFP purified from the transgenic plants expressing KIN10-GFP in *snrk2.2/2.3* mutants. KIN10 was enriched from transgenic seedlings expressing KIN10-GFP in *snrk2.2/2.3* mutants background by immunoprecipitation with anti-GFP and then used to phosphorylate FREE1 or FREE1^{S530A} or FREE1^{S530AS533A} tagged with His-sumo, which was further detected by Phos-tag biotin. **j** In vivo interaction between ATG8 and FREE1, FREE1^{S530A}, or FREE1^{S530AS533A} mutant variants. GFP-FREE1, GFP-FREE1^{S530A}, and GFP-FREE1^{S530AS533A} transgenic plants were subjected to nitrogen starvation for at least 18 h, followed by protein extraction and IP with GFP-Trap, and subsequent immunoblotting with indicated antibodies. **k** Transient co-expression of GFP-FREE1 or GFP-FREE1^{S530A} with mCherry-ATG8i in *Arabidopsis* protoplasts. The transfected protoplasts were cultured for 24 h before CLSM observation. Scale bars, 10 μm. All the imaging analysis and immunoblots were repeated at least for three times with similar results.

(Fig. 4i). Furthermore, the in vitro kinase assays were performed using recombinant KIN10 tagged with His-MBP and FREE1 or FREE1^{S530A} tagged with His-sumo, which was further detected by the autoradiography. Indeed, FREE1 can be phosphorylated by the purified KIN10, while the mutation on S530A abolished the phosphorylation of FREE1 by KIN10 in vitro (Supplementary Fig. 23c, d). To further confirm our results *in planta*, GFP-FREE1 or GFP-FREE1^{S530A} were transiently expressed in protoplasts isolated from transgenic plants expressing KIN10-HA upon nitrogen starvation. GFP-FREE1 and GFP-FREE1^{S530A} were enriched by immunoprecipitation with anti-GFP for detection by Phos-tag biotin. Indeed, GFP-FREE1 can be phosphorylated in the protoplasts isolated from the transgenic seedlings expressing KIN10-HA, while the mutation on S530A significantly reduced the phosphorylation of FREE1 by KIN10 (Supplementary Fig. 23e). Taken together, our data demonstrated that KIN10 can directly phosphorylate FREE1 on the S530.

Phosphorylated-FREE1 is essential for the autophagosome sealing and plant growth upon nutrient deprivation

To investigate the functional role of the phosphorylation site on FREE1 in autophagosome closure, we performed biochemical, genetic and cellular analysis to find out whether the Serine at position 530 is essential for the FREE1 function in autophagosome sealing. The homozygous lines of *free1* T-DNA insertional mutants are seedling lethal, which are not suitable for studying the bona fide function of FREE1 in different developmental stages and growth conditions[48]. Thus, we have screened for the CRISPR mutants of FREE1 which are viable under normal growth conditions and identified the *free1*-ct mutant lines (a *free1* weak allele which harbours a deletion of eight nucleotides in the ninth exon region that leads to a change in amino acids or deletion in the C terminus of FREE1)[63]. Albeit the Ser530 is presented in the protein expressed in the *free1*-ct mutant lines, our recent study suggested that these mutants may disrupt the secondary structure and abolish the function of coiled-coil domain of FREE1 which contains the Ser530[63]. Since Ser530 located at the C-terminus of FREE1 protein, we performed the analysis using this recently obtained CRISPR mutant of FREE1, *free1*-ct[63]. Indeed, albeit showing similar growth phenotype as the wild type plants under normal conditions, *free1*-ct exhibited early senescence phenotypes as *DEX::RNAi-FREE1*, SNF7.1DN, VPS4DN and *atg5* mutants upon cellular energy deprivation and nitrogen starvation (Supplementary Fig. 24a-e). We further explored the functional role of Ser530 of FREE1 in the autophagy pathway using the transgenic plants expressing GFP-FREE1 or GFP-FREE1^{S530A} in *free1*-ct mutant background, as well as GFP-FREE1^{S530AS533A}/*free1*-ct that we recently generated since it also contained the S530A mutation[63]. Indeed, *free1*-ct plants exhibited growth defects when cellular energy and nitrogen source were limited, however, overexpressing GFP-FREE1^{S530A} or GFP-FREE1^{S530AS533A} was unable to complement the phenotype, compared to WT Col-0 and GFP-FREE1 complementation lines (Supplementary Fig. 24f, g and Supplementary Fig. 25a, b). We have also generated the phosphomimetic variants of FREE1 transgenic plants expressing the GFP-FREE1^{S530D} or GFP-FREE1^{S530DS533D} in *free1-ct* mutants background for phenotypic analysis. Consistently, overexpressing of GFP-FREE1^{S530D}/*free1*-ct or GFP-FREE1^{S530DS533D}/*free1*-ct was able to complement the defective phenotype as the GFP-FREE1 complementation lines upon carbon starvation (Supplementary Fig. 25c, d). These results suggested that the phosphorylated-FREE1 is indispensable for the plant autophagy.

Notably, GFP-FREE1 can interact with ATG8, while GFP-FREE1^{S530A} and GFP-FREE1^{S530AS533A} cannot be co-immunoprecipitated with ATG8 in planta (Fig. 4j and Supplementary Fig. 26a). Indeed, in vivo interaction assay using the endogenous promoter driven GFP-FREE1 transgenic plants further confirmed that FREE1 can directly interact with the endogenous ATG8 upon nitrogen starvation (Supplementary Fig. 26b). Cellular analysis showed the decreased colocalization of GFP-FREE1^{S530A} with ATG8i in *Arabidopsis* protoplasts (Fig. 4k and Supplementary Fig. 26c), and partial decrement of vacuolar delivery of GFP-FREE1^{S530A} or GFP-FREE1^{S530AS533A} in comparison to GFP-FREE1, GFP-FREE1^{S530D} or GFP-FREE1^{S530DS533D} (Supplementary Fig. 27a, b). Intriguingly, GFP-FREE1^{S530A} failed to co-immunoprecipitate with the ATG conjugation system as well, while GFP-FREE1 can be significantly precipitated by ATG5 and ATG5-ATG12 conjugate (Supplementary Fig. 28 and Fig. 2c), suggesting the importance of S530 for the FREE1-ATG conjugation system interaction. To further elaborate the role of S530 on FREE1 in autophagosome closure, 2D-TEM and 3D-tomography analysis further showed the accumulation of unclosed autophagosomal structures in the *free1-ct*, GFP-FREE1^{S530A}/*free1-ct*, and GFP-FREE1^{S530AS533A}/*free1-ct* lines, while the autophagosomes in the GFP-FREE1^{S530D}/*free1-ct*, GFP-FREE1^{S530DS533D}/*free1-ct*, and GFP-FREE1/*free1-ct* complementation lines were properly sealed upon carbon starvation (Fig. 5a, b and Supplementary Movie. 6). Consistently, we monitored the autophagy flux as previous study[65] and showed that the autophagic bodies were largely absent from the vacuole of the *free1-ct*,

https://doi.org/10.1038/s41467-023-37185-6

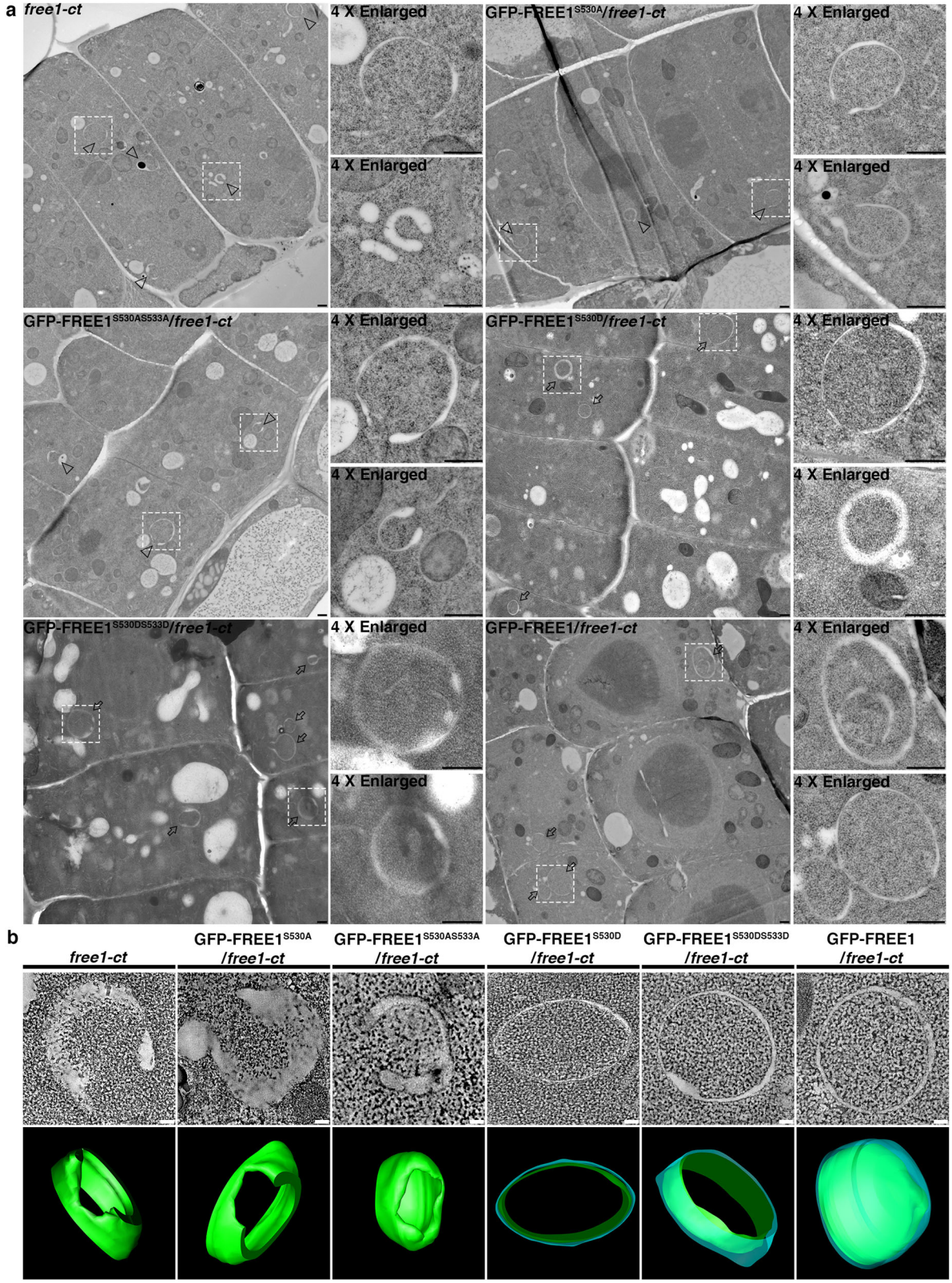

Fig. 5 | The phosphorylation site on FREE1 is essential for the autophagosome closure. a Structural TEM analysis of ultrathin sections prepared from high-pressure freezing/frozen substituted *free1-ct* mutant, GFP-FREE1^{S530A}/*free1-ct*, GFP-FREE1^{S530AS533A}/*free1-ct*, GFP-FREE1^{S530D}/*free1*-ct, GFP-FREE1^{S530DS533D}/*free1*-ct, and GFP-FREE1/*free1-ct* transgenic plant root tips upon carbon starvation for 18 h. White dash boxes indicate the 4 X zoom-in areas. Arrowheads indicate examples of the unsealed autophagosomal structures, while arrows indicate examples of the sealed autophagosomes. Scale bars, 500 nm. **b** 3D electron tomography (ET) analysis of autophagosomal structures in *free1-ct* mutant, GFP-FREE1^{S530A}/*free1-ct*, GFP-FREE1^{S530AS533A}/*free1-ct*, GFP-FREE1^{S530D}/*free1*-ct, GFP-FREE1^{S530DS533D}/*free1*-ct, and GFP-FREE1/*free1-ct* transgenic plant root tips upon carbon starvation for 18 h. Upper panels, individual slices of the 3D-tomography. Lower panels, 3D models of the corresponding tomography. Scale bars, 100 nm. The green color indicates the unclosed autophagosomal structures, while the blue and green color indicate the closed autophagosomes. All the imaging analysis was repeated at least for three times with similar results.

GFP-FREE1^{S530A}/*free1-ct*, and GFP-FREE1^{S530AS533A}/*free1-ct* lines, yet the autophagic bodies were substantially accumulated in the vacuoles of the GFP-FREE1^{S530D}/*free1-ct*, GFP-FREE1^{S530DS533D}/*free1-ct*, and GFP-FREE1/*free1-ct* complementation lines upon carbon starvation and ConcA treatments, suggesting the defective of vacuolar delivery of the unclosed autophagosomal structures in *free1-ct*, GFP-FREE1^{S530A}/*free1-ct*, and GFP-FREE1^{S530AS533A}/*free1-ct* lines (Supplementary Fig. 29a–c).

Biochemically, the lipidated ATG8 significantly accumulated in the *DEX::RNAi-FREE1* mutant protoplasts overexpressing Myc-FREE1^{S530A}, *DEX::RNAi-FREE1* mutant protoplasts overexpressing Myc-FREE1^{W438AI441A}, as well as *DEX::RNAi-FREE1* mutant protoplasts upon DEX induction with or without BTH treatments, while the effects could be restored by overexpressing wild-type Myc-FREE1 in *DEX::RNAi-FREE1* mutant protoplasts (Supplementary Fig. 30a, b). Meanwhile, the autophagy receptor NBR1 substantially accumulated in the *DEX::RNAi-FREE1* mutant protoplasts overexpressing Myc-FREE1^{S530A}, *DEX::RNAi-FREE1* mutant protoplasts overexpressing Myc-FREE1^{W438AI441A}, as well as *DEX::RNAi-FREE1* mutant protoplasts upon DEX induction with or without BTH treatments, while the defects could be recovered by expressing wild type Myc-FREE1 in *DEX::RNAi-FREE1* mutant protoplasts (Supplementary Fig. 30c, d). Lastly, the YFP-ATG8e turnover was significantly impeded in the *DEX::RNAi-FREE1* mutant protoplasts overexpressing Myc-FREE1^{S530A}, *DEX::RNAi-FREE1* mutant protoplasts overexpressing Myc-FREE1^{W438AI441A}, as well as *DEX::RNAi-FREE1* mutant protoplasts upon DEX induction with or without BTH treatments, while the defects could be complemented by overexpressing wild type Myc-FREE1 in *DEX::RNAi-FREE1* mutant protoplasts (Supplementary Fig. 30e, f). Our results thus demonstrated that FREE1^{S530A} failed to complement the defective of FREE1 mutants on ATG8 lipidation, NBR1 turnover, and YFP-ATG8e turnover, indicating that S530 is essential for FREE1 function in autophagosome closure biochemically. Albeit the importance in regulating autophagosome closure, cellular and biochemical analysis showed that S530 on FREE1 is dispensable for the vacuolar transport of Aleurain-mRFP (Supplementary Fig. 31). Our results thus demonstrated that the S530 affects only autophagy but not vacuolar protein transport. To conclude, our data demonstrated that the phosphorylation status of FREE1 is essential for its redistribution to phagophore, function in autophagosome closure, and dedication to plant growth upon nutrient deprivation.

Discussion

Using a combination of 3D electron tomography, proteomic analysis, cellular and genetic approaches, we demonstrated that the ATG conjugation system substrate ATG8 is essential to recruit the ESCRTs machinery for autophagosome completion via a plant unique pleiotropic ESCRT protein FREE1, whose shuttling from endosome to phagophore is tightly regulated by the plant energy sensor SnRK1, by which ATG8 interacts and recruits SnRK1α1-phosphorylated FREE1 onto phagophores for downstream ESCRTs recruitment to regulate autophagosome closure. Our study thus provides hints on the universal underlying mechanism of nutrient sensing and autophagosome closure.

Despite the indispensable role of the ESCRT machinery in autophagosome closure[31–33], exactly how the ESCRT components are translocated from endosome to phagophore upon autophagy induction by nutrient starvation remains unknown in higher eukaryotes. Consistently our study confirmed that the plant ESCRT-III proteins SNF7.1 and VPS20 localize at the autophagosomal structures, while unclosed autophagosomes largely accumulated in SNF7.1 and VPS4 mutants (Supplementary Figs. 17, 18). More intriguingly, we demonstrated that the plant unique ESCRT component FREE1, which has been shown to regulate endosomal sorting and MVB/Vacuole biogenesis in concert with ESCRT-I in *Arabidopsis*[48], is crucial for autophagosome closure. Substantial numbers of "open" phagophores accumulate in *free1* mutants as revealed by high-resolution confocal imaging, ultrastructural transmission electron microscopy, 3D electron tomography, and biochemical analysis (Fig. 1a–e, Supplementary Fig. 2, Supplementary Fig. 3, Supplementary Fig. 4, Supplementary Fig. 5, Supplementary Fig. 6, Supplementary Fig. 7, Supplementary Fig. 8, and Supplementary Fig. 9). These results, together with our previous findings that the autophagic bodies could be barely observed in the vacuole of *free1* mutants comparing with the wild-type Col-0 upon BTH and ConcA treatments[49], suggested that the loss of FREE1 in *free1* mutant strongly blocked the autophagosome closure and the unclosed autophagosomes in *free1* mutants could not be properly fused with the vacuole for degradation under autophagy induction conditions. Surprisingly, our proteomic analysis identified the ATG conjugation system as the potential interactors of FREE1 upon nutrient deprivation (Fig. 2a, Supplementary Fig. 10, and Supplementary Data 1). FREE1 colocalizes and can be co-immunoprecipitated with the components of ATG conjugation system (Fig. 2b, c), whereas FREE1 can directly interact with specific paralogs of ATG8, the substrate of the ATG conjugation system (Fig. 3a–f). It would be of great interest in future study to reveal the mechanism underlying the recognition of FREE1 by specific ATG8s in regulating autophagosome closure and to answer whether the mechanism is evolutionary conserved in other plants. Recent studies have shown that depletion of ATG8 proteins apparently causes the accumulation of "open" autophagosomes in mammalian cells[66,67], whereas deficiency in the ATG conjugation system leads to a significant delay in degradation of the inner autophagosomal membrane and cargo, probably due to the incomplete closure of the autophagosomal structures[68]. However, how the ATG conjugation system contributes to autophagosome closure remains elusive, although it has been speculated that ATG8 proteins may be involved in the recruitment of specific LC3-interacting region (LIR)-containing proteins required for downstream phagophore closure[69]. Intriguingly, FREE1 contains a classical AIM motif, which is required for its interaction with ATG8 as well as its recruitment to autophagosome for closure function (Supplementary Fig. 16a–f). Our study has identified and demonstrated that the plant unique ESCRT protein FREE1 acts as a linker to bridge the ATG conjugation system/ATG8s and ESCRT machinery to regulate the autophagosome closure, thus delineating the underlying mechanism of autophagosome sealing in higher eukaryotes.

Plants respond to abiotic and biotic stresses by fine tuning anabolic and catabolic reactions[70]. SnRK1, a central energy sensor kinase and a chief stress response component in plants, is crucial for catabolic reactions and represses anabolic processes upon energy-depleting stress conditions to support stress tolerance and survival[61,71,72]. SnRK1 is functionally and evolutionarily conserved with the SNF1 in yeast and the AMPK in animals[71]. In plants, SnRK1 has been shown to participate in the autophagy pathway, the important catabolic process for energy and nutrient restoration, via acting upstream of TOR or independently of TOR through direct interaction with ATG1[1,73–75]. Here, we provide multiple evidences on KIN10 in regulating the plant unique ESCRT component FREE1 to function in autophagosome closure. We showed that FREE1 and KIN10 directly interacts with each other (Fig. 4b–f and Supplementary Fig. 21). Indeed, FREE1 can be directly phosphorylated by KIN10 in vivo and in vitro, while the phosphorylation sites on FREE1 are essential for the interaction with ATG8 (Fig. 4g–j, Supplementary Fig. 23, and Supplementary Fig. 26). Genetic, cellular and biochemical analysis further supports the notion that KIN10-mediated phosphorylation of FREE1 is essential for autophagosome closure (Fig. 5a, b, Supplementary Fig. 24, Supplementary Fig. 25, Supplementary Fig. 27, Supplementary Fig. 29, and Supplementary Fig. 30). Notably, recent study has shown that the autophagosome formation is strongly inhibited in *kin10* mutant upon a wide variety of stress conditions[75]. Future study using the micro-RNA mutants of SnRK1α1 and SnRK1α1/SnRK1α2 driven by the DEX-inducible promoter[48] could further increase our understanding of the functional roles of SnRK1 in

autophagosome closure. In mammal, AMPK acts on triggering the autophagosome biogenesis through the activation of ULK1[6–8] and regulation of VPS34 containing complexes[9], which are known regulators in autophagy initiation and progression, respectively. Similarly, KIN10 can phosphorylate ATG1 and ATG6 to regulate plant autophagy pathway[62,73]. Our results provided the first line of evidence to show that the energy sensor also plays pivotal role in regulating the downstream closure step of autophagosome biogenesis. The simultaneously targeting of multi-steps during autophagosome formation by KIN10 may ensure the precise regulation of autophagy upon stresses.

Altogether, our results show that during nutrient starvation, the energy sensor kinase not only suppresses the TOR signalling pathway and induce autophagosome initiation, but also regulates the shuttling of ESCRT machinery from endosomes to autophagosomes to facilitate autophagosome sealing (Fig. 6).

Methods

Plasmid construction

Restriction digestion or Gateway cloning (Invitrogen) were performed to clone the PCR-amplified target genes into the destination plasmids. For the generation of YFP-ATG8i, mCherry-ATG8i, DEX::SNF7.1(L32W), DEX::VPS4(E232Q), VPS20a-GFP, SNF7.1-RFP, KIN10-GFP, and KIN10-HA transgenic plants, PCR-products of ATG8i, SNF7.1(L32W), VPS4(E232Q), VPS20a, and SNF7.1, KIN10 were cloned into corresponding pBI121/1300-UBQ::Gene-GFP/mRFP, pCambia1300-GFP/mRFP, or pTA7002-35S::Gene dexamethasone (DEX)-inducible backbones by restriction digestion and ligation or Gateway. For transient expression constructs used in confocal laser scanning microscopy (CLSM) or co-IP assays, PCR products were cloned into pBI221-UBQ::XFP-gene, 6HA-gene, or 3Myc-gene vectors by restriction digestion and ligation or Gateway. All constructs were confirmed by Sanger sequencing. Constructs and primers used in this study are listed in Supplementary Data 2.

Plant growth and phenotypic analysis

Arabidopsis plant system biology dark-type culture (PSBD) suspension cells were incubated at 25 °C and sub-cultured every 5 days[76]. *Arabidopsis* seeds were surface sterilized and grown on plates with half-strength Murashige and Skoog (MS) growth medium (pH 5.7). Seeds were germinated and grown at 22 °C under a long day (16 h light/8 h dark) photoperiod. For DEX, BTH, or Concanamycin A (ConcA) treatments in CLSM observation, protein extraction analysis, and high-pressure freezing/frozen, 10 μM DEX, 100 μM BTH, and 1 μM ConcA were applied to seedlings for indicated time points before analysis, respectively. For nitrogen or carbon starvation assay, 5-day-old seedlings were transferred to nitrogen source-free or carbon source-free half-strength MS medium for at least 2 weeks before phenotypic analysis and chlorophyll content measurement.

Transgenic lines generation

Transgenic plants were generated by introducing the corresponding genes into the target lines through *Agrobacterium* transformation by floral dip[77]. In general, YFP-ATG8i, mCherry-ATG8i, DEX::SNF7.1(L32W), DEX::VPS4(E232Q), VPS20a-GFP, SNF7.1-RFP, KIN10-GFP, and KIN10-HA cloned into the corresponding pBI121/1300-UBQ::Gene-GFP/mRFP, pCambia1300-GFP/mRFP, or pTA7002-35S::Gene dexamethasone (DEX)-inducible backbones were transformed into *Agrobacterium tumefaciens* GV3101 and then introduced into Col-0 or mutant *Arabidopsis* plants via floral dip. Transgenic plants were selected on MS medium plates containing antibiotics, and homozygous lines were used for further analysis. Double transgenic plants were generated by crossing with previously generated marker lines[78].

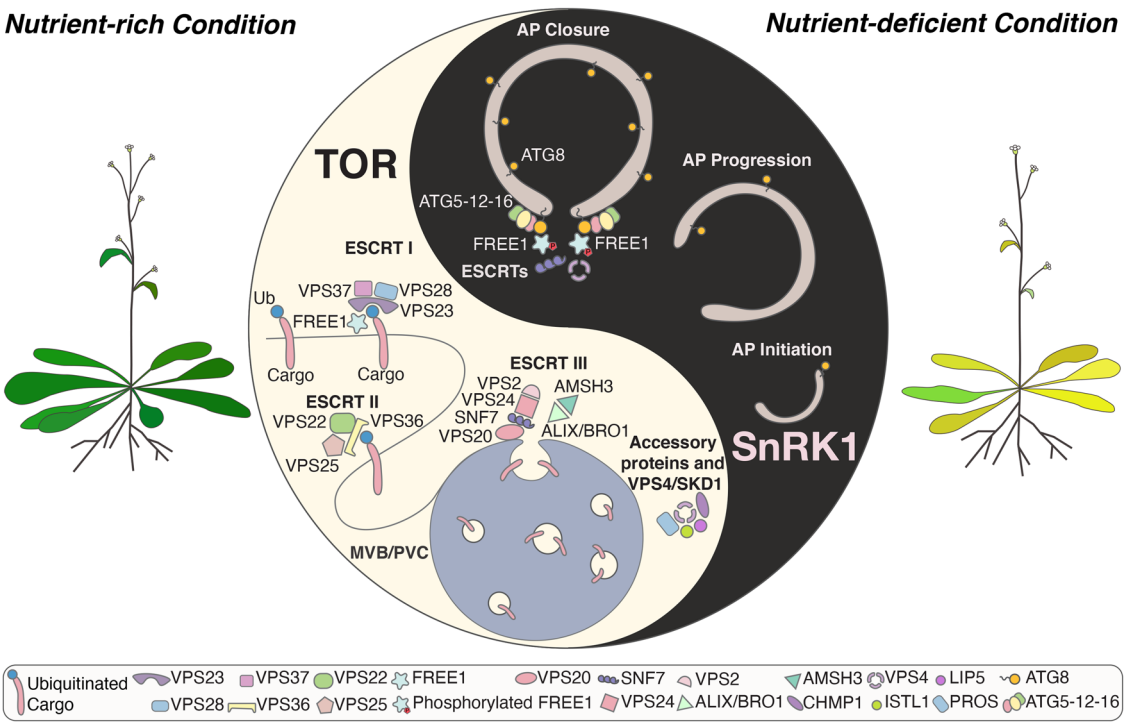

Fig. 6 | Working model of the interplay between the ATG conjugation system and the ESCRT machinery in regulating autophagosome closure in plants. Under nutrient-rich condition, FREE1 functions in endosomal sorting. During nutrient-deficient condition (autophagy induction), SnRK1 phosphorylates FREE1. The phosphorylated FREE1 is then recruited by the ATG conjugation system/ATG8 isoforms and cooperates with the downstream ESCRT machinery to mediate autophagosome closure. TOR, target of rapamycin; SnRK1, SNF1-related protein kinase 1; AP, autophagosome; MVB/PVC, multivesicular body/prevacuolar compartment; ESCRT, endosomal complexes required for transport.

Confocal microscopy and FRET analysis

Confocal fluorescence images were captured by a Leica SP8 laser scanning confocal system with a 63 x water lens and deconvolution. For each analysis, >30 individual cells or >10 individual seedlings were analyzed to represent the majority of samples showing similar expression levels and patterns. Images were further processed by Adobe Photoshop software (http://www.adobe.com). Deconvolution was performed via HyVolution software from Leica. FRET analysis was conducted on the same Leica SP8 confocal system according to the manufacturer's instruction using 405 nm and 514 nm laser. CFP -YFP indicates the fusion of the CFP and YFP protein with a short linker, which is used as a positive control for the FRET analysis. CFP/YFP indicates the co-expression of individual CFP and YFP protein, which is used as a negative control for the FRET analysis. Acceptor photobleaching FRET analysis was conducted on the Leica SP8 confocal system. Briefly, cells expressing various CFP and YFP fusions were used for photobleaching using 514 nm laser in full power intensity. CFP donor fluorescence was imaged before and after bleaching a region of interest of YFP to less than 10% of its initial intensity. FRET efficiency was calculated as Ef =100 × (IPost − Ipre)/Ipost, where Ipre and Ipost stand for the CFP intensities before and after acceptor bleaching, respectively.

Particle bombardment of *Arabidopsis* seedlings

Five-day-old *Arabidopsis* seedlings were carefully transferred to a new MS plate containing 10 μM Dexamethasone in ordered arrangement for 24 h. Gold particles coated with plasmid DNA were prepared and bombarded three times at three different positions into the plants using PSD-1000/He particle delivery system (Gas pressure: 1100 psi; Vacuum: 28 mm Hg; Gap distance between the rupture disk and macrocarrier: 1 cm; Gold particle flight distance between macrocarrier and plant samples: 9 cm) as described previously[79,80]. Plants were kept in dark in the plant growth chamber for 12–24 h before confocal observation.

High pressure freezing and transmission electron microscopy

5 DAG *Arabidopsis* seedling root tips were cut and high-pressure freezing/frozen by the high-pressure freezer (EM PACT2, Leica, Germany) prior to subsequent freeze substitution in acetone containing 0.4% uranyl acetate at −85 °C in an AFS freeze-substitution unit (Leica, Wetzlar, Germany). After gradient infiltration with increasing concentration of HM20, samples were embedded and ultraviolet polymerized for ultra-thin sectioning[48,78]. TEM analysis was performed by observing the ultra-thin section on the grids under the 80 kV Hitachi H-7650 transmission electron microscope (Hitachi High-Technologies Corporation, Japan) with a charge-coupled device (CCD) camera.

3D electron tomography

The electron tomography observation procedures have been described previously[81]. In general, 300-nm-thick sections were observed using a 200 kV Tecnai F20 electron microscope (FEI Company). For each grid, a tilt image stack from at least +51° to −51° with 1.5° increments was collected, while the second axis of tilt image stack was collected by rotating the grid by 90°. Dual-axis tomograms were calculated from pairs of image stacks with the etomo program of the IMOD software package. The 15 nm gold particles at the surface of the sections were used as fiducial markers to align individual images in the tilt series. For model generation, the contours were drawn manually and meshed with the 3dmod program in the IMOD software package.

Proteomics and mass-spectrometry

Proteins were extracted from 5 DAG seedlings in IP buffer (50 mM Tris-HCl, pH 7.4, 150 mM NaCl, 1 mM $MgCl_2$, 20% glycerol, 0.2% NP-40, 1× protease inhibitor cocktail, Roche). The collected supernatant was then co-incubated with GFP-Trap magnetic beads (Chromotek) at 4 °C as instructed by the manufacture handbook. The beads were washed five times with the same ice-cold IP buffer and eluted by boiling in reducing SDS sample buffer before SDS-PAGE gel electrophoresis. The gel was then stained with Imperial™ Protein Stain after SDS–PAGE separation, and proteins were cut out for in-gel trypsin digestion as previously described[82]. In general, the cut gel was dehydrated and rehydrated using acetonitrile and water repeatedly for three times before reducing the disulfide-bond using dithiothreitol (DTT) and iodizing the gel using iodoacetamide (IAA). The gel was further dehydrated using acetonitrile for three times before trypsin digestion at 30 °C overnight. The digested peptide mixture was fractionated by nano-liquid chromatography-MS (nano-LCMS) using an UltiMate 3000 RSLCnano system (Thermo Fisher Scientific). MS data were then acquired with an Orbitrap Fusion Lumus mass spectrometer (Thermo Fisher Scientific). For the phosphorylation sites identification, raw MS/MS data were converted to Mascot generic format (mgf) and were used to search database using an in-house Mascot search engine (Matrix Science) with phosphorylation. For the interactors identification, raw MS/MS data was analyzed with MaxQuant version 2.0.3.1 as described in previous study[55]. The reference sequences of *Arabidopsis thaliana* proteome (Araport11_pep_20220103.fasta) were from TAIR database (arabidopsis.org), which contain 48231 entries. The false discovery rate (FDR) threshold of peptide-to-spectrum match (PSM) and protein were set as 0.05. "Trypsin digestion" and "Orbitrap" were chosen in the parameters setting while other searching parameters were kept as default. The "iBAQ" value was set for label free quantification. Data matrix of protein expression levels in all samples were merged by in-house Perl scripts. The expression value was transformed through $\log_2$(iBAQ+1). Differential expression analyses were performed by using *limma* package. We adopted the default method in *Limma* which uses an Empirical Bayes estimate to "moderate" the standard deviation in the *t*-test denominator using the distribution of all the standard deviations (Moderated paired *t*-test). P-values were adjusted through Benjamini-Hochberg's method for multiple comparisons (https://bioconductor.org/packages/release/bioc/vignettes/limma/inst/doc/usersguide.pdf). The volcano plot was generated by using *ggplot2* package in R.

Yeast two-hybrid

For Y2H analysis, the corresponding PCR products were cloned into the pGBKT7 or pGADT7 vectors (Clontech) (Supplementary Data 2). Plasmids of each pair were co-transformed into the yeast AH109 strain. Transformants were first screened on synthetic drop-out medium lacking Trp and Leu. Positive colonies were further selected on SD medium lacking His, Trp, Leu with 3AT, or His, Trp, Leu and Ade. The experiments were performed independently for at least twice with similar results obtained. Due to the high self-activation activity of full-length FREE1 protein on BD vector, the C-terminal part of FREE1(231–601) was used for the yeast two hybrid assay as previously described[63].

Immunoblotting and co-immunoprecipitation

Seedlings were ground in ice-cold extraction buffer (50 mM Tris-HCl, pH 7.4, 150 mM NaCl, 20% glycerol, 1% Triton, 1× protease inhibitor cocktail, Roche) for protein extraction. Cell debris was removed by centrifugation at 700 *g* then 16,000 *g* at 4 °C. The collected supernatant was then denatured by boiling in reducing SDS sample buffer. Extracted proteins were then applied to gel electrophoresis on 12% SDS-polyacrylamide gel electrophoresis (SDS-PAGE) gels. Immunoblot analysis was performed as previously described[78]. For co-immunoprecipitation (co-IP) analysis, transfected protoplasts or transgenic plants were homogenized in IP buffer (50 mM Tris-HCl, pH 7.4, 150 mM NaCl, 1 mM $MgCl_2$, 20% glycerol, 0.2% NP-40, 1× protease inhibitor cocktail, Roche). Lysates were centrifuged at 16,000 *g* for 4 °C and were incubated with GFP-Trap magnetic beads (ChromoTek) for 2–4 h at 4 °C. After incubation, the beads were washed five times

with ice-cold washing buffer (50 mM Tris-HCl, pH 7.4, 150 mM NaCl, 1 mM $MgCl_2$, 20% glycerol and 0.2% NP-40) and eluted by boiling in reducing SDS sample buffer. Samples were then separated by SDS–PAGE and analysed by immunoblot. Primary antibodies used in this study were anti-FREE1 (homemade), anti-NBR1 (AS142805), anti-ATG8 (Agrisera, AS142769), anti-GFP (Chromotek, 029762), anti-RFP (Abcam, ab125244), anti-HA (Abcam, ab18181), anti-MYC (Santa Cruz, SC789), and anti-SnRK1α1 (Agrisera, AS10919).

In vivo phosphorylation assay

In vivo phosphorylation assay was performed using protoplasts prepared from transgenic plants expressing KIN10-HA upon autophagy induction. GFP-FREE1 or GFP-FREE1^{S530A} were transiently expressed in protoplasts derived from KIN10-HA transgenic plants upon nitrogen starvation for at least 18 h. GFP-FREE1 or GFP-FREE1^{S530A} were further enriched by immunoprecipitation with anti-GFP for further detection by Phos-tag biotin.

Semi-in vitro phosphorylation assay

Semi-in vitro phosphorylation assay was carried out essentially according to the methods described previously[63]. His-Sumo-FREE1, His-Sumo-FREE1^{S530AS533A}, His-Sumo-FREE1^{S530A} fusion proteins were expressed and purified from *E. coil* (Rosseta) with Ni-NTA Resin. HA or GFP-tagged KIN10 proteins were obtained by immunoprecipitation from UBQ::KIN10-HA, UBQ::KIN10-GFP transgenic plants. GFP proteins were obtained by immunoprecipitation from UBQ::GFP transgenic plants. For in vitro kinase assays, immunoprecipitated KIN10-HA, KIN10-GFP, or GFP were incubated with purified His-Sumo-FREE1, His-Sumo-FREE1^{S530A} or His-Sumo-FREE1^{S530AS533A} in 30 µl kinase buffer (10 mM Tris/HCl, pH 7.8, 10 mM $MgCl_2$, 0.5 mM dithiothreitol, 2 mM $MnCl_2$ and 25 mM ATP) for 1 h at room temperature. Samples were separated by SDS-PAGE and transferred to PVDF membrane followed by probing with Phos-tag BTL-111. To observe the total protein amount of His-Sumo fusions and KIN10 proteins used for Phos-tag detection, same amount of protein from each sample was separated by SDS-PAGE followed by either coomassie brilliant blue staining or western blotting analysis with anti-GFP or anti-HA antibody.

In vitro phosphorylation assay

All GST- or His- fusion protein constructs were transformed into *Escherichia coli* BL21 cells and recombinant proteins were induced by 0.5 mM isopropyl-β-D-thiogalactopyranoside (IPTG). After over-night incubation at 16 °C, cells were collected, lysed, sonicated and centrifuged, and recombination proteins (including KIN10, SnAK2, and FREE1) were purified according to the manufacturer's protocol (GE Healthcare Life Science and MERCK). In vitro kinase assays were performed as previously described[83]. Each reaction mixture contained 0.1 mL [γ-^{32}P] ATP (1 µCi) in kinase buffer (20 mM Tris-HCl, pH 8.0, 5 mM $MgCl_2$, 10 mM [^{31}P] ATP, and 1 mM DTT). The kinase assays were performed at 30 °C for 30 min, and then were incubated with 6X SDS loading buffer at 100 °C for 10 min. The samples were separated by 10% SDS-PAGE gels and stained with Coomassie brilliant blue R250 (CBB), and then the gels were exposed to phosphor screens. The autoradiograph (Autorad) signal was detected by a Typhoon 9410 phosphor imager.

Structure-illumination microscopy

Transfected *Arabidopsis* protoplasts samples were imaged on a Nikon NSIM system consisting of a Ti-E stand with Perfect Focus, CFI SR HP Apochromat TIRF 100XC Oil lens, Nikon LU5 laser bed (488 and 561 nm laser lines) and Andor DU-897X-5254 EMCCD camera. For each focal plane, 15 images (5 phases, 3 angles) were captured with the NIS Elements v4.1. SIM images were reconstructed using slice reconstruction in NIS elements. Post-imaging analysis was performed using NIS Elements v4.1.

Molecular evolutionary genetics analysis

The evolutionary history was inferred using the Neighbor-Joining method. The optimal tree with the sum of branch length=4.32642842 is shown. The tree is drawn to scale, with branch lengths in the same units as those of the evolutionary distances used to infer the phylogenetic tree. The evolutionary distances were computed using the *p*-distance method and are in the units of the number of amino acid differences per site. The analysis involved 80 amino acid sequences. All positions with less than 95% site coverage were eliminated. That is, fewer than 5% alignment gaps, missing data, and ambiguous bases were allowed at any position. There were a total of 114 positions in the final dataset. Evolutionary analyses were conducted in MEGA7[84].

Protease protection assay

Protease protection assay was performed as recently described (Supplementary Fig. 5a) with modifications[54]. Roots from seven-day-old *Arabidopsis* seedlings treated with or without DEX/BTH/ConcA were resected and grinded in GTEN-based buffer (GTEN (10% glycerol, 30 mM Tris (pH 7.5), 150 mM NaCl, 1 mM EDTA (pH 8)), 0.4 M sorbitol, 5 mM $MgCl_2$, 1 mM Dithiothreitol (DTT), protease inhibitor cocktail (SIGMA)) in a 3:1 v/w ratio. Lysates were then subjected to low-speed (10 min, 700 x *g*), high-speed (15 min, 12,000 x *g*), and ultra-speed (60 min, 100,000 x *g*) centrifugation to enrich the microsomal fraction containing autophagosomal membranes. The enriched autophagosomal membranes were proceeded for proteinase K digestions (30 ng/µl, 30 min), followed by protein extraction and subsequent western blot detection by NBR1 and Atg8 antibodies.

Quantification and statistical analysis

Confocal quantification: For the autophagosome number quantification in *Arabidopsis* root cells, the ATG8e-positive puncta in the mid-optical section of each root cell were counted, at least 20 individual root cells were used for quantification analysis. For the unclosed autophagosome quantification in *Arabidopsis* root cells, the unclosed ATG8e-positive puncta in the mid-optical section of each root cell were counted, at least 20 individual root cells were used for quantification analysis. For the FRET assay using *Arabidopsis* PSBD protoplasts, over 50 puncta from at least 10 individual protoplasts were used for quantification analysis.

TEM quantification: for the quantification of unclosed autophagosome numbers in *Arabidopsis* root cells, the unclosed APs in the TEM thin section of each root cell were counted and over 20 individual root cells from at least 3 individual high-pressure freezing/frozen substituted *Arabidopsis* roots were used for quantification analysis.

All the data are presented as mean values±SD. Statistical analysis was performed by individual test as indicated using GraphPad Prism version 9.00 for mac (GraphPad Software Inc.). Differences in means were considered statistically significant at $^{*}P < 0.05$. Significance levels are: $^{*}P < 0.05$; $^{**}P < 0.01$; $^{***}P < 0.001$.

Reporting summary

Further information on research design is available in the Nature Portfolio Reporting Summary linked to this article.

Data availability

The authors declare that the data supporting the findings of this study are available in the paper and its supplementary information files. The raw data are available from the corresponding author upon reasonable request. The proteomic data generated in this study have been deposited in ProteomeXchange partner repository under accession code PXD040435. Source data are provided with this paper. The source data for Figs. 1–4, Supplementary Figs. 1, 2, 4–8, 11, 13–19, 21, 23–31 are provided as a Source Data file with this paper. Source data are provided with this paper.

References

1. Signorelli, S., Tarkowski, L. P., Van den Ende, W. & Bassham, D. C. Linking Autophagy to Abiotic and Biotic Stress Responses. *Trends Plant Sci.* **24**, 413–430 (2019).
2. Mizushima, N. A brief history of autophagy from cell biology to physiology and disease. *Nat. Cell Biol.* **20**, 521–527 (2018).
3. Mizushima, N. & Komatsu, M. Autophagy: Renovation of Cells and Tissues. *Cell* **147**, 728–741 (2011).
4. Nakatogawa, H., Suzuki, K., Kamada, Y. & Ohsumi, Y. Dynamics and diversity in autophagy mechanisms: lessons from yeast. *Nat. Rev. Mol. Cell Biol.* **10**, 458–467 (2009).
5. Mizushima, N. The ATG conjugation systems in autophagy. *Curr. Opin. Cell Biol.* **63**, 1–10 (2020).
6. Egan, D. F. et al. Phosphorylation of ULK1 (hATG1) by AMP-Activated Protein Kinase Connects Energy Sensing to Mitophagy. *Science* **331**, 456–461 (2011).
7. Kim, J., Kundu, M., Viollet, B. & Guan, K. L. AMPK and mTOR regulate autophagy through direct phosphorylation of Ulk1. *Nat. Cell Biol.* **13**, 132–U171 (2011).
8. Mack, H. I. D., Zheng, B., Asara, J. M. & Thomas, S. M. AMPK-dependent phosphorylation of ULK1 regulates ATG9 localization. *Autophagy* **8**, 1197–1214 (2012).
9. Kim, J. et al. Differential Regulation of Distinct Vps34 Complexes by AMPK in Nutrient Stress and Autophagy. *Cell* **152**, 290–303 (2013).
10. Sawa-Makarska, J. et al. Reconstitution of autophagosome nucleation defines Atg9 vesicles as seeds for membrane formation. *Science* **369**, 1206–120 (2020).
11. Cui, Y. et al. Biogenesis of Plant Prevacuolar Multivesicular Bodies. *Mol. Plant*. **9**, 774–786 (2016).
12. Henne, W. M., Buchkovich, N. J. & Emr, S. D. The ESCRT Pathway. *Dev. Cell.* **21**, 77–91 (2011).
13. Raiborg, C. & Stenmark, H. The ESCRT machinery in endosomal sorting of ubiquitylated membrane proteins. *Nature* **458**, 445–452 (2009).
14. Schoneberg, J., Lee, I. H., Iwasa, J. H. & Hurley, J. H. Reverse-topology membrane scission by the ESCRT proteins. *Nat. Rev. Mol. Cell Biol.* **18**, 5–17 (2017).
15. Carlton, J. G. & Martin-Serrano, J. Parallels between cytokinesis and retroviral budding: A role for the ESCRT machinery. *Science* **316**, 1908–1912 (2007).
16. Hurley, J. H. & Cada, A. K. Inside job: how the ESCRTs release HIV-1 from infected cells. *Biochem Soc. T.* **46**, 1029–1036 (2018).
17. Sundquist W. I., Krausslich H. G. HIV-1 Assembly, Budding, and Maturation. *Csh Perspect Med* **2**, a006924 (2012).
18. Barajas D., Jiang Y., Nagy P. D. A Unique Role for the Host ESCRT Proteins in Replication of Tomato bushy stunt virus. *Plos Pathog* **5**, e1000705 (2009).
19. Diaz, A., Zhang, J. T., Ollwerther, A., Wang, X. F. & Ahlquist, P. Host ESCRT Proteins Are Required for Bromovirus RNA Replication Compartment Assembly and Function. *Plos Pathog.* **11**, e1004742 (2015).
20. Colombo, M. et al. Analysis of ESCRT functions in exosome biogenesis, composition and secretion highlights the heterogeneity of extracellular vesicles. *J. Cell Sci.* **126**, 5553–5565 (2013).
21. Olmos, Y., Hodgson, L., Mantell, J., Verkade, P. & Carlton, J. G. ESCRT-III controls nuclear envelope reformation. *Nature* **522**, 236–23 (2015).
22. Raab, M. et al. ESCRT III repairs nuclear envelope ruptures during cell migration to limit DNA damage and cell death. *Science* **352**, 359–362 (2016).
23. Vietri, M. et al. Spastin and ESCRT-III coordinate mitotic spindle disassembly and nuclear envelope sealing. *Nature* **522**, 231–23 (2015).
24. Webster, B. M., Colombi, P., Jager, J. & Lusk, P. Surveillance of Nuclear Pore Complex Assembly by ESCRT-III/Vps4. *Cell* **159**, 388–401 (2014).
25. Jimenez, A. J. et al. ESCRT Machinery Is Required for Plasma Membrane Repair. *Science* **343**, 986–98 (2014).
26. Scheffer, L. L. et al. Mechanism of Ca2+-triggered ESCRT assembly and regulation of cell membrane repair. *Nat. Commun.* **5**, 5646 (2014).
27. Radulovic, M. et al. ESCRT-mediated lysosome repair precedes lysophagy and promotes cell survival. *Embo J.* **37**, e99753 (2018).
28. Skowyra, M. L., Schlesinger, P. H., Naismith, T. V. & Hanson, P. I. Triggered recruitment of ESCRT machinery promotes endolysosomal repair. *Science* **360**, 49–4 (2018).
29. Sahu, R. et al. Microautophagy of Cytosolic Proteins by Late Endosomes. *Developmental Cell.* **20**, 131–139 (2011).
30. Liu, X. M. et al. ESCRTs Cooperate with a Selective Autophagy Receptor to Mediate Vacuolar Targeting of Soluble Cargos. *Mol. Cell.* **59**, 1035–1042 (2015).
31. Takahashi, Y. et al. An autophagy assay reveals the ESCRT-III component CHMP2A as a regulator of phagophore closure. *Nat. Commun.* **9**, 2855 (2018).
32. Takahashi, Y. et al. VPS37A directs ESCRT recruitment for phagophore closure. *J. Cell Biol.* **218**, 3336–3354 (2019).
33. Zhen, Y. et al. ESCRT-mediated phagophore sealing during mitophagy. *Autophagy* **16**, 826–841 (2020).
34. Zhou, F. et al. Rab5-dependent autophagosome closure by ESCRT. *J. Cell Biol.* **218**, 1908–1927 (2019).
35. Gao, C. J., Zhuang, X. H., Shen, J. B. & Jiang, L. W. Plant ESCRT Complexes: Moving Beyond Endosomal Sorting. *Trends Plant Sci.* **22**, 986–998 (2017).
36. Winter, V. & Hauser, M. T. Exploring the ESCRTing machinery in eukaryotes. *Trends Plant Sci.* **11**, 115–123 (2006).
37. Buono, R. A. et al. Role of SKD1 Regulators LIP5 and IST1-LIKE1 in Endosomal Sorting and Plant Development. *Plant Physiol.* **171**, 251–264 (2016).
38. Haas, T. J. et al. The Arabidopsis AAA ATPase SKD1 is involved in multivesicular endosome function and interacts with its positive regulator LYST-INTERACTING PROTEIN5. *Plant Cell.* **19**, 1295–1312 (2007).
39. Spitzer, C. et al. The ESCRT-Related CHMP1A and B Proteins Mediate Multivesicular Body Sorting of Auxin Carriers in Arabidopsis and Are Required for Plant Development. *Plant Cell.* **21**, 749–766 (2009).
40. Wang, H. J. et al. VPS36-Dependent Multivesicular Bodies Are Critical for Plasmamembrane Protein Turnover and Vacuolar Biogenesis. *Plant Physiol.* **173**, 566–581 (2017).
41. Katsiarimpa, A. et al. The Deubiquitinating Enzyme AMSH1 and the ESCRT-III Subunit VPS2.1 Are Required for Autophagic Degradation in Arabidopsis. *Plant Cell.* **25**, 2236–2252 (2013).
42. Reyes, F. C. et al. A Novel Endosomal Sorting Complex Required for Transport (ESCRT) Component in Arabidopsis thaliana Controls Cell Expansion and Development*. *J. Biol. Chem.* **289**, 4980–4988 (2014).
43. Spitzer, C. et al. The Endosomal Protein CHARGED MULTIVESICULAR BODY PROTEIN1 Regulates the Autophagic Turnover of Plastids in Arabidopsis. *Plant Cell.* **27**, 391–402 (2015).
44. Valencia, J. P., Goodman, K. & Otegui, M. S. Endocytosis and Endosomal Trafficking in Plants. *Annu Rev. Plant Biol.* **67**, 309–335 (2016).
45. Wang, F., Shang, Y. F., Fan, B. F., Yu, J. Q. & Chen, Z. X. Arabidopsis LIP5, a Positive Regulator of Multivesicular Body Biogenesis, Is a Critical Target of Pathogen-Responsive MAPK Cascade in Plant Basal Defense. *Plos Pathog.* **10**, e1004243 (2014).
46. Wang, F. et al. A Critical Role of Lyst-Interacting Protein5, a Positive Regulator of Multivesicular Body Biogenesis, in Plant Responses to Heat and Salt Stresses. *Plant Physiol.* **169**, 497–49 (2015).

47. Yang, H. L. et al. Overexpression of CHMP7 from rapeseed and Arabidopsis causes dwarfism and premature senescence in Arabidopsis. *J. Plant Physiol.* **204**, 16–26 (2016).
48. Gao, C. J. et al. A Unique Plant ESCRT Component, FREE1, Regulates Multivesicular Body Protein Sorting and Plant Growth. *Curr. Biol.* **24**, 2556–2563 (2014).
49. Gao, C. J. et al. Dual roles of an Arabidopsis ESCRT component FREE1 in regulating vacuolar protein transport and autophagic degradation. *Proc. Natl Acad. Sci.***112**, 1886–1891 (2015).
50. Stephani, M. et al. A cross-kingdom conserved ER-phagy receptor maintains endoplasmic reticulum homeostasis during stress. *eLife* **9**, e58396 (2020).
51. Brillada, C. et al. Exocyst subunit Exo70B2 is linked to immune signaling and autophagy. *Plant Cell.* **33**, 404–419 (2021).
52. Luo, L. et al. Autophagy Is Rapidly Induced by Salt Stress and Is Required for Salt Tolerance in Arabidopsis. *Front. Plant Sci.* **8**, 1459 (2017).
53. Yano, K. et al. Dissection of autophagy in tobacco BY-2 cells under sucrose starvation conditions using the vacuolar H(+)-ATPase inhibitor concanamycin A and the autophagy-related protein Atg8. *Plant Signal. Behav.* **10**, e1082699 (2015).
54. Zhao, J. et al. Plant autophagosomes mature into amphisomes prior to their delivery to the central vacuole. *J. Cell Biol.* **221**, e202203139 (2022).
55. Gemperline, D. C. et al. Proteomic analysis of affinity-purified 26S proteasomes identifies a suite of assembly chaperones in Arabidopsis. *J. Biol. Chem.* **294**, 17570–17592 (2019).
56. Kishi-Itakura, C., Koyama-Honda, I., Itakura, E. & Mizushima, N. Ultrastructural analysis of autophagosome organization using mammalian autophagy-deficient cells. *J. Cell Sci.* **127**, 4089–4102 (2014).
57. Marshall, R. S., Hua, Z. H., Mali, S., McLoughlin, F. & Vierstra, R. D. ATG8-Binding UIM Proteins Define a New Class of Autophagy Adaptors and Receptors. *Cell* **177**, 766–76 (2019).
58. Buono, R. A. et al. ESC RT-mediated vesicle concatenation in plant endosomes. *J. Cell Biol.* **216**, 2167–2177 (2017).
59. Cai, Y., Zhuang, X. H., Gao, C. J., Wang, X. F. & Jiang, L. W. The Arabidopsis Endosomal Sorting Complex Required for Transport III Regulates Internal Vesicle Formation of the Prevacuolar Compartment and Is Required for Plant Development. *Plant Physiol.* **165**, 1328–1343 (2014).
60. Nagel, M. K. et al. Arabidopsis SH3P2 is an ubiquitin-binding protein that functions together with ESCRT-I and the deubiquitylating enzyme AMSH3. *Proc. Natl Acad. Sci.***114**, E7197–E7204 (2017).
61. Baena-Gonzalez, E. & Sheen, J. Convergent energy and stress signaling. *Trends Plant Sci.* **13**, 474–482 (2008).
62. Huang, X. et al. Genetic Analyses of the Arabidopsis ATG1 Kinase Complex Reveal Both Kinase-Dependent and Independent Autophagic Routes during Fixed-Carbon Starvation. *Plant Cell.* **31**, 2973–2995 (2019).
63. Li, H. B. et al. The plant ESCRT component FREE1 shuttles to the nucleus to attenuate abscisic acid signalling. *Nat. Plants.* **5**, 512–524 (2019).
64. Belda-Palazón, B. et al. A dual function of SnRK2 kinases in the regulation of SnRK1 and plant growth. *Nat. Plants.* **6**, 1345–1353 (2020).
65. Liu, Y. et al. Degradation of the endoplasmic reticulum by autophagy during endoplasmic reticulum stress in Arabidopsis. *Plant Cell.* **24**, 4635–4651 (2012).
66. Fujita, N. et al. An Atg4B Mutant Hampers the Lipidation of LC3 Paralogues and Causes Defects in Autophagosome Closure. *Mol. Biol. Cell.* **19**, 4651–4659 (2008).
67. Weidberg, H. et al. LC3 and GATE-16/GABARAP subfamilies are both essential yet act differently in autophagosome biogenesis. *Embo J.* **29**, 1792–1802 (2010).
68. Tsuboyama, K. et al. The ATG conjugation systems are important for degradation of the inner autophagosomal membrane. *Science* **354**, 1036–1041 (2016).
69. Melia, T. J., Lystad, A. H. & Simonsen, A. Autophagosome biogenesis: From membrane growth to closure. *J. Cell Biol.* **219**, e202002085 (2020).
70. Crepin, N. & Rolland, F. SnRK1 activation, signaling, and networking for energy homeostasis. *Curr. Opin. Plant Biol.* **51**, 29–36 (2019).
71. Baena-Gonzalez, E., Rolland, F., Thevelein, J. M. & Sheen, J. A central integrator of transcription networks in plant stress and energy signalling. *Nature* **448**, 938–U910 (2007).
72. Margalha, L., Confraria, A. & Baena-Gonzalez, E. SnRK1 and TOR: modulating growth-defense trade-offs in plant stress responses. *J. Exp. Bot.* **70**, 2261–2274 (2019).
73. Chen, L. et al. The AMP-Activated Protein Kinase KIN10 Is Involved in the Regulation of Autophagy in Arabidopsis. *Front. plant Sci.* **8**, 1201 (2017).
74. Pu, Y. T., Luo, X. J. & Bassham, D. C. TOR-Dependent and -Independent Pathways Regulate Autophagy in Arabidopsis thaliana. *Front. plant Sci.* **8**, 1204 (2017).
75. Soto-Burgos, J. & Bassham, D. C. SnRK1 activates autophagy via the TOR signaling pathway in Arabidopsis thaliana. *Plos One.* **12**, e0182591 (2017).
76. Miao, Y. S. & Jiang, L. W. Transient expression of fluorescent fusion proteins in protoplasts of suspension cultured cells. *Nat. Protoc.* **2**, 2348–2353 (2007).
77. Clough, S. J. & Bent, A. F. Floral dip: a simplified method for Agrobacterium-mediated transformation of Arabidopsis thaliana. *Plant J.* **16**, 735–743 (1998).
78. Shen, J. B. et al. A plant Bro1 domain protein BRAF regulates multivesicular body biogenesis and membrane protein homeostasis. *Nat. Commun.* **9**, 3784 (2018).
79. Wang, X. et al. Trans-Golgi network-located AP1 gamma adaptins mediate dileucine motif-directed vacuolar targeting in Arabidopsis. *Plant Cell.* **26**, 4102–4118 (2014).
80. Wang, H. & Jiang, L. Transient expression and analysis of fluorescent reporter proteins in plant pollen tubes. *Nat. Protoc.* **6**, 419–426 (2011).
81. Cui, Y. et al. A whole-cell electron tomography model of vacuole biogenesis in Arabidopsis root cells. *Nat. Plants.* **5**, 95–105 (2019).
82. Wu, T. et al. Mass spectrometry analysis of the variants of histone H3 and H4 of soybean and their post-translational modifications. *BMC Plant Biol.* **9**, 98 (2009).
83. Zhou, H. et al. Inhibition of the Arabidopsis Salt Overly Sensitive Pathway by 14-3-3 Proteins. *Plant Cell.* **26**, 1166–1182 (2014).
84. Kumar, S., Stecher, G. & Tamura, K. MEGA7: Molecular Evolutionary Genetics Analysis Version 7.0 for Bigger Datasets. *Mol. Biol. Evol.* **33**, 1870–1874 (2016).

Acknowledgements

We thank Prof. Marisa S Otegui from University of Wisconsin-Madison for sharing the SNF7 antibody. This work was supported by grants from the National Natural Science Foundation of China (91854201), the Research Grants Council of Hong Kong (AoE/M-05/12, CUHK 14101219, C4033-19E, C4002-20W, C4002-21EF, C2009-19G, C4041-18E, C2003-22WF, R4005-18, and Senior Research Fellow Scheme SRFS2122-4S01), the Chinese University of Hong Kong (CUHK) Research Committee and CAS-Croucher Funding Scheme for Joint Laboratories to L.J.

Author contributions

Y.Z. and L.J. conceived and designed research. Y.Z., B.L., S.H., H.L., W.C., Y.C., and G.L. performed experiments. Y.Z., W.C., Z.L., and J.G. generated the 3D-electron tomography models. B.L. and S.W.L. performed

proteomic and mass-spectrum analysis. H.L. and G.L. performed the in vitro and in vivo phosphorylation assay. B.L., S.H., Y.C., C.Y., J.Z., J.S., Y.G., C.G., and Y.D. generated resources. Y.Z., B.L., S.H., and L.F. analyzed data. Y.Z. wrote the paper. Y.Z., Y.D., and L.J. edited the paper. L.J. supervised the research.

Competing interests
The authors declare no competing interests.

Additional information
Supplementary information The online version contains supplementary material available at https://doi.org/10.1038/s41467-023-37185-6.

Correspondence and requests for materials should be addressed to Liwen Jiang.

Peer review information *Nature Communications* thanks Santiago Signorelli, Yoshinori Takahashi and the other, anonymous, reviewer(s) for their contribution to the peer review of this work. Peer reviewer reports are available.

7. References

Avin-Wittenberg, T. (2019). Autophagy and its role in plant abiotic stress management. *Plant, Cell & Environment*, *42*(3), 1045–1053.

Bilodeau, P. S., Winistorfer, S. C., Kearney, W. R., Robertson, A. D., & Piper, R. C. (2003). Vps27-Hse1 and ESCRT-I complexes cooperate to increase efficiency of sorting ubiquitinated proteins at the endosome. *Journal of Cell Biology*, *163*(2), 237–243.

Bu, F., Yang, M., Guo, X., Huang, W., & Chen, L. (2020). Multiple functions of ATG8 family proteins in plant autophagy. *Frontiers in Cell and Developmental Biology*, *8*, 466.

Cadena-Ramos, A. I., & De-la-Peña, C. (2024). Picky eaters: Selective autophagy in plant cells. *The Plant Journal*, *117*(2), 364–384.

Chen, H., Dong, J., & Wang, T. (2021). Autophagy in plant abiotic stress management. *International Journal of Molecular Sciences*, *22*(8), 4075.

Datta, S., Kim, C. M., Pernas, M., Pires, N. D., Proust, H., Tam, T., Vijayakumar, P., & Dolan, L. (2011). Root hairs: development, growth and evolution at the plant-soil interface. *Plant and Soil*, *346*, 1–14.

Erlichman, O. A., Weiss, S., Abu Arkia, M., Ankary-Khaner, M., Soroka, Y., Jasinska, W., Rosental, L., Brotman, Y., & Avin-Wittenberg, T. (2023). Autophagy in maternal tissues contributes to Arabidopsis seed development. *Plant Physiology*, *193*(1), 611–626.

Feng, Q., De Rycke, R., Dagdas, Y., & Nowack, M. K. (2022). Autophagy promotes programmed cell death and corpse clearance in specific cell types of the Arabidopsis root cap. *Current Biology*, *32*(9), 2110–2119.

Feng, Q., Zhu, S., Wang, X., Liu, Y., Zhao, J., Dagdas, Y., & Nowack, M. K. (2025). Root hair lifespan is antagonistically controlled by autophagy and programmed cell death. *BioRxiv*, 2003–2025.

Furuta, Y., Yamamoto, H., Hirakawa, T., Uemura, A., Pelayo, M. A., Iimura, H., Katagiri, N., Takeda-Kamiya, N., Kumaishi, K., Shirakawa, M., Ishiguro, S., Ichihashi, Y., Suzuki, T., Goh, T., Toyooka, K., Ito, T., & Yamaguchi, N. (2024). Petal abscission is promoted by jasmonic acid-induced autophagy at Arabidopsis petal bases. *Nature Communications*, *15*(1), 1098. https://doi.org/10.1038/s41467-024-45371-3

Galluzzi, L., Baehrecke, E. H., Ballabio, A., Boya, P., Bravo-San Pedro, J. M., Cecconi, F., Choi, A. M., Chu, C. T., Codogno, P., & Colombo, M. I. (2017). Molecular definitions of autophagy and related processes. *The EMBO Journal*, *36*(13), 1811–1836.

Gao, C., Zhuang, X., Cui, Y., Fu, X., He, Y., Zhao, Q., Zeng, Y., Shen, J., Luo, M., & Jiang, L. (2015). Dual roles of an Arabidopsis ESCRT component FREE1 in

regulating vacuolar protein transport and autophagic degradation. *Proceedings of the National Academy of Sciences*, *112*(6), 1886–1891.

Gao, C., Zhuang, X., Shen, J., & Jiang, L. (2017). Plant ESCRT complexes: moving beyond endosomal sorting. *Trends in Plant Science*, *22*(11), 986–998.

Goh, T., Sakamoto, K., Wang, P., Kozono, S., Ueno, K., Miyashima, S., Toyokura, K., Fukaki, H., Kang, B. H., & Nakajima, K. (2022). Autophagy promotes organelle clearance and organized cell separation of living root cap cells in Arabidopsis thaliana. *Development (Cambridge)*, *149*(11), dev200593. https://doi.org/10.1242/dev.200593

Gross, A. S., Raffeiner, M., Zeng, Y., Üstün, S., & Dagdas, Y. (2025). Autophagy in Plant Health and Disease. *Annual Review of Plant Biology*, *76*.

Guiboileau, A., Yoshimoto, K., Soulay, F., Bataillé, M. P., Avice, J. C., & Masclaux-Daubresse, C. (2012). Autophagy machinery controls nitrogen remobilization at the whole-plant level under both limiting and ample nitrate conditions in Arabidopsis. *New Phytologist*, *194*(3), 732–740. https://doi.org/10.1111/j.1469-8137.2012.04084.x

Guichard, M., Holla, S., Wernerová, D., Grossmann, G., & Minina, E. A. (2024). RoPod, a customizable toolkit for non-invasive root imaging, reveals cell type-specific dynamics of plant autophagy. *Scientific Reports*, *14*(1), 12664. https://doi.org/10.1038/s41598-024-63226-1

Han, S., Yu, B., Wang, Y., & Liu, Y. (2011). Role of plant autophagy in stress response. *Protein & Cell*, *2*, 784–791.

Hofius, D., Li, L., Hafrén, A., & Coll, N. S. (2017). Autophagy as an emerging arena for plant–pathogen interactions. *Current Opinion in Plant Biology*, *38*, 117–123.

Htwe, N. M. P. S., Yuasa, T., Ishibashi, Y., Tanigawa, H., Okuda, M., Zheng, S. H., & Iwaya-Inoue, M. (2011). Leaf Senescence of Soybean at Reproductive Stage is Associated with Induction of Autophagy-Related Genes, GmATG8c, GmATG8i and GmATG4. *Plant Production Science*, *14*(2), 141–147. https://doi.org/10.1626/pps.14.141

Jelínková, A., Malínská, K., & Petrášek, J. (2019). Using FM dyes to study endomembranes and their dynamics in plants and cell suspensions. *Plant Cell Morphogenesis: Methods and Protocols*, 173–187.

Kim, S.-H., Kwon, C., Lee, J.-H., & Chung, T. (2012). Genes for plant autophagy: functions and interactions. *Molecules and Cells*, *34*(5), 413–424.

Kirkin, V. (2020). History of the selective autophagy research: how did it begin and where does it stand today? *Journal of Molecular Biology*, *432*(1), 3–27.

Knævelsrud, H., Søreng, K., Raiborg, C., Håberg, K., Rasmuson, F., Brech, A., Liestøl, K., Rusten, T. E., Stenmark, H., & Neufeld, T. P. (2013). Membrane remodeling by the PX-BAR protein SNX18 promotes autophagosome formation. *Journal of*

Cell Biology, *202*(2), 331–349.

Kurusu, T., Koyano, T., Hanamata, S., Kubo, T., Noguchi, Y., Yagi, C., Nagata, N., Yamamoto, T., Ohnishi, T., & Okazaki, Y. (2014). OsATG7 is required for autophagy-dependent lipid metabolism in rice postmeiotic anther development. *Autophagy*, *10*(5), 878–888.

Kurusu, T., Koyano, T., Kitahata, N., Kojima, M., Hanamata, S., Sakakibara, H., & Kuchitsu, K. (2017). Autophagy-mediated regulation of phytohormone metabolism during rice anther development. *Plant Signaling & Behavior*, *12*(9), e1365211.

Lenz, H. D., Haller, E., Melzer, E., Kober, K., Wurster, K., Stahl, M., Bassham, D. C., Vierstra, R. D., Parker, J. E., & Bautor, J. (2011). Autophagy differentially controls plant basal immunity to biotrophic and necrotrophic pathogens. *The Plant Journal*, *66*(5), 818–830.

Li, F., Chung, T., & Vierstra, R. D. (2014). AUTOPHAGY-RELATED11 plays a critical role in general autophagy-and senescence-induced mitophagy in Arabidopsis. *The Plant Cell*, *26*(2), 788–807.

Li, Y., Xu, X., Qi, G., Cui, D., Huang, C., Sui, X., Li, G., & Fan, Q. (2023). Mechanisms of autophagy function and regulation in plant growth, development, and response to abiotic stress. *The Crop Journal*, *11*(6), 1611–1625.

Liu, F., Hu, W., Li, F., Marshall, R. S., Zarza, X., Munnik, T., & Vierstra, R. D. (2020). AUTOPHAGY-RELATED14 and its associated phosphatidylinositol 3-kinase complex promote autophagy in Arabidopsis. *The Plant Cell*, *32*(12), 3939–3960.

Liu, W., Liu, Z., Mo, Z., Guo, S., Liu, Y., & Xie, Q. (2021). ATG8-interacting motif: evolution and function in selective autophagy of targeting biological processes. *Frontiers in Plant Science*, *12*, 783881.

Liu, Y., & Bassham, D. C. (2012). Autophagy: Pathways for self-eating in plant cells. *Annual Review of Plant Biology*, *63*(1), 215–237. https://doi.org/10.1146/annurev-arplant-042811-105441

Liu, Y., Xiong, Y., & Bassham, D. C. (2009). Autophagy is required for tolerance of drought and salt stress in plants. *Autophagy*, *5*(7), 954–963.

Löfke, C., Dünser, K., & Kleine-Vehn, J. (2013). Epidermal patterning genes impose non-cell autonomous cell size determination and have additional roles in root meristem size control. *Journal of Integrative Plant Biology*, *55*(9), 864–875. https://doi.org/10.1111/jipb.12097

Lornac, A., Havé, M., Chardon, F., Soulay, F., Clément, G., Avice, J.-C., & Masclaux-Daubresse, C. (2020). Autophagy controls sulphur metabolism in the rosette leaves of Arabidopsis and facilitates S remobilization to the seeds. *Cells*, *9*(2), 332.

Luo, L., Zhang, P., Zhu, R., Fu, J., Su, J., Zheng, J., Wang, Z., Wang, D., & Gong, Q. (2017). Autophagy is rapidly induced by salt stress and is required for salt tolerance in arabidopsis. *Frontiers in Plant Science*, *8*, 1459.

https://doi.org/10.3389/fpls.2017.01459

Luo, M., Law, K. C., He, Y., Chung, K. K., Po, M. K., Feng, L., Chung, K. P., Gao, C., Zhuang, X., & Jiang, L. (2023). Arabidopsis AUTOPHAGY-RELATED2 is essential for ATG18a and ATG9 trafficking during autophagosome closure. *Plant Physiology*, *193*(1), 304–321.

Ma, J., Liang, Z., Zhao, J., Wang, P., Ma, W., Mai, K. K., Andrade, J. A. F., Zeng, Y., Grujic, N., & Jiang, L. (2021). Friendly mediates membrane depolarization-induced mitophagy in Arabidopsis. *Current Biology*, *31*(9), 1931–1944.

Marshall, R. S., & Vierstra, R. D. (2018). Autophagy: the master of bulk and selective recycling. *Annual Review of Plant Biology*, *69*(1), 173–208.

Minibayeva, F., Dmitrieva, S., Ponomareva, A., & Ryabovol, V. (2012). Oxidative stress-induced autophagy in plants: the role of mitochondria. *Plant Physiology and Biochemistry*, *59*, 11–19.

Minina, E. A., Moschou, P. N., Vetukuri, R. R., Sanchez-Vera, V., Cardoso, C., Liu, Q., Elander, P. H., Dalman, K., Beganovic, M., Lindberg Yilmaz, J., Marmon, S., Shabala, L., Suarez, M. F., Ljung, K., Novák, O., Shabala, S., Stymne, S., Hofius, D., & Bozhkov, P. V. (2018). Transcriptional stimulation of rate-limiting components of the autophagic pathway improves plant fitness. *Journal of Experimental Botany*, *69*(6), 1415–1432. https://doi.org/10.1093/jxb/ery010

Mizushima, N. (2018). A brief history of autophagy from cell biology to physiology and disease. *Nature Cell Biology*, *20*(5), 521–527. https://doi.org/10.1038/s41556-018-0092-5

Nagel, M. K., Kalinowska, K., Vogel, K., Reynolds, G. D., Wu, Z., Anzenberger, F., Ichikawa, M., Tsutsumi, C., Sato, M. H., Kuster, B., Bednarek, S. Y., & Isono, E. (2017). Arabidopsis SH3P2 is an ubiquitin-binding protein that functions together with ESCRT-I and the deubiquitylating enzyme AMSH3. *Proceedings of the National Academy of Sciences of the United States of America*, *114*(34), E7197–E7204. https://doi.org/10.1073/pnas.1710866114

Olsvik, H. L., Lamark, T., Takagi, K., Larsen, K. B., Evjen, G., Øvervatn, A., Mizushima, T., & Johansen, T. (2015). FYCO1 contains a C-terminally extended, LC3A/B-preferring LC3-interacting region (LIR) motif required for efficient maturation of autophagosomes during basal autophagy. *Journal of Biological Chemistry*, *290*(49), 29361–29374.

Ozkan, P., & Mutharasan, R. (2002). A rapid method for measuring intracellular pH using BCECF-AM. *Biochimica et Biophysica Acta (BBA)-General Subjects*, *1572*(1), 143–148.

Pankiv, S., Alemu, E. A., Brech, A., Bruun, J.-A., Lamark, T., Øvervatn, A., Bjørkøy, G., & Johansen, T. (2010). FYCO1 is a Rab7 effector that binds to LC3 and PI3P to mediate microtubule plus end–directed vesicle transport. *Journal of Cell Biology*, *188*(2), 253–269.

Phillips, A. R., Suttangkakul, A., & Vierstra, R. D. (2008). The ATG12-conjugating enzyme ATG10 is essential for autophagic vesicle formation in Arabidopsis thaliana. *Genetics*, *178*(3), 1339–1353.

Rodriguez, E., Chevalier, J., Olsen, J., Ansbøl, J., Kapousidou, V., Zuo, Z., Svenning, S., Loefke, C., Koemeda, S., & Drozdowskyj, P. S. (2020). Autophagy mediates temporary reprogramming and dedifferentiation in plant somatic cells. *The EMBO Journal*, *39*(4), e103315.

Rose, T. L., Bonneau, L., Der, C., Marty-Mazars, D., & Marty, F. (2006). Starvation-induced expression of autophagy-related genes in Arabidopsis. *Biology of the Cell*, *98*(1), 53–67.

Salazar-Henao, J. E., Vélez-Bermúdez, I. C., & Schmidt, W. (2016). The regulation and plasticity of root hair patterning and morphogenesis. *Development (Cambridge)*, *143*(11), 1848–1858. https://doi.org/10.1242/dev.132845

Sertsuvalkul, N., DeMell, A., & Dinesh-Kumar, S. P. (2022). The complex roles of autophagy in plant immunity. *FEBS Letters*, *596*(17), 2163–2171.

Stephani, M., & Dagdas, Y. (2020). Plant selective autophagy—still an uncharted territory with a lot of hidden gems. *Journal of Molecular Biology*, *432*(1), 63–79.

Stolz, A., Ernst, A., & Dikic, I. (2014). Cargo recognition and trafficking in selective autophagy. *Nature Cell Biology*, *16*(6), 495–501. https://doi.org/10.1038/ncb2979

Sutipatanasomboon, A., Herberth, S., Alwood, E. G., Häweker, H., Müller, B., Shahriari, M., Zienert, A. Y., Marin, B., Robatzek, S., & Praefcke, G. J. K. (2017). Disruption of the plant-specific CFS 1 gene impairs autophagosome turnover and triggers EDS1-dependent cell death. *Scientific Reports*, *7*(1), 8677.

Suttangkakul, A., Li, F., Chung, T., & Vierstra, R. D. (2011). The ATG1/ATG13 protein kinase complex is both a regulator and a target of autophagic recycling in Arabidopsis. *The Plant Cell*, *23*(10), 3761–3779.

Sweeney, P. J., & Walker, J. M. (1993). Proteinase K (EC 3.4. 21.14). *Enzymes of Molecular Biology*, 305–311.

Thanthrige, N., Bhowmik, S. Das, Ferguson, B. J., Kabbage, M., Mundree, S. G., & Williams, B. (2021). Potential biotechnological applications of autophagy for agriculture. *Frontiers in Plant Science*, *12*, 760407.

Vargas, J. N. S., Hamasaki, M., Kawabata, T., Youle, R. J., & Yoshimori, T. (2023). The mechanisms and roles of selective autophagy in mammals. *Nature Reviews Molecular Cell Biology*, *24*(3), 167–185.

Wang, P., Mugume, Y., & Bassham, D. C. (2018). New advances in autophagy in plants: Regulation, selectivity and function. *Seminars in Cell and Developmental Biology*, *80*, 113–122. https://doi.org/10.1016/j.semcdb.2017.07.018

Wang, P., Wang, T., Han, J., Li, M., Zhao, Y., Su, T., & Ma, C. (2021). Plant autophagy:

an intricate process controlled by various signaling pathways. *Frontiers in Plant Science*, *12*, 754982.

Xiong, Y., Contento, A. L., & Bassham, D. C. (2005). AtATG18a is required for the formation of autophagosomes during nutrient stress and senescence in Arabidopsis thaliana. *The Plant Journal*, *42*(4), 535–546.

Yagyu, M., & Yoshimoto, K. (2024). New insights into plant autophagy: molecular mechanisms and roles in development and stress responses. *Journal of Experimental Botany*, *75*(5), 1234–1251.

Yamamoto, H., Zhang, S., & Mizushima, N. (2023). Autophagy genes in biology and disease. *Nature Reviews Genetics*, *24*(6), 382–400.

Ye, H., Gao, J., Liang, Z., Lin, Y., Yu, Q., Huang, S., & Jiang, L. (2022). Arabidopsis ORP2A mediates ER–autophagosomal membrane contact sites and regulates PI3P in plant autophagy. *Proceedings of the National Academy of Sciences*, *119*(43), e2205314119.

Yoshimoto, K., Hanaoka, H., Sato, S., Kato, T., Tabata, S., Noda, T., & Ohsumi, Y. (2004). Processing of ATG8s, ubiquitin-like proteins, and their deconjugation by ATG4s are essential for plant autophagy. *Plant Cell*, *16*(11), 2967–2983. https://doi.org/10.1105/tpc.104.025395

Yoshimoto, K., & Ohsumi, Y. (2018). Unveiling the molecular mechanisms of plant autophagy—from autophagosomes to vacuoles in plants. *Plant and Cell Physiology*, *59*(7), 1337–1344.

Yuen, E. L. H., Leary, A. Y., Clavel, M., Tumtas, Y., Mohseni, A., Zhao, J., Picchianti, L., Jamshidiha, M., Pandey, P., & Duggan, C. (2024). A RabGAP negatively regulates plant autophagy and immune trafficking. *Current Biology*, *34*(10), 2049–2065.

Zeng, Y., Li, B., Huang, S., Li, H., Cao, W., Chen, Y., Liu, G., Li, Z., Yang, C., & Feng, L. (2023). The plant unique ESCRT component FREE1 regulates autophagosome closure. *Nature Communications*, *14*(1), 1768.

Zhao, J., Bui, M. T., Ma, J., Künzl, F., Picchianti, L., de la Concepcion, J. C., Chen, Y., Petsangouraki, S., Mohseni, A., García-Leon, M., Gomez, M. S., Giannini, C., Gwennogan, D., Kobylinska, R., Clavel, M., Schellmann, S., Jaillais, Y., Friml, J., Kang, B. H., & Dagdas, Y. (2022). Plant autophagosomes mature into amphisomes prior to their delivery to the central vacuole. *Journal of Cell Biology*, *221*(12), e202203139. https://doi.org/10.1083/jcb.202203139

Zhao, J., Loefke, C., Yeung, K. C., Chen, Y., & Dagdas, Y. (2025). Cell-type specific autophagy in root hair forming cells is essential for salt stress tolerance in Arabidopsis thaliana. *BioRxiv*, 2003–2025.

Zhuang, X., Chung, K. P., Cui, Y., Lin, W., Gao, C., Kang, B.-H., & Jiang, L. (2017). ATG9 regulates autophagosome progression from the endoplasmic reticulum in Arabidopsis. *Proceedings of the National Academy of Sciences*, *114*(3), E426–

E435.

Zhuang, X., Li, B., & Jiang, L. (2024). Autophagosome biogenesis and organelle homeostasis in plant cells. *The Plant Cell*, *36*(9), 3009–3024.

Zhuang, X., Wang, H., Lam, S. K., Gao, C., Wang, X., Cai, Y., & Jiang, L. (2013). A BAR-domain protein SH3P2, which binds to phosphatidylinositol 3-phosphate and ATG8, regulates autophagosome formation in Arabidopsis. *The Plant Cell*, *25*(11), 4596–4615.